Magnetic-moment measurements by the transient-field and recoil-in-vacuum techniques in fpg-shell nuclei

Author:
Brendan Patrick
McCormick

Supervisory Panel:
Prof. Andrew E. Stuchbery
(Primary supervisor)
Prof. Gregory J. Lane
(Secondary supervisor)
A. Prof. Tibor Kibédi
(Secondary supervisor)

A thesis submitted for the degree of
Doctor of Philosophy of The Australian National University,
in the

Department of Nuclear Physics
Research School of Physics

October 22, 2021

Declaration of Authorship

I, Brendan Patrick McCORMICK, declare that this thesis titled, "Magnetic-moment measurements by the transient-field and recoil-in-vacuum techniques in fpg-shell nuclei" and the work presented in it are my own. I confirm that:

- This work was done wholly or mainly while in candidature for a research degree at this University.
- Where any part of this thesis has previously been submitted for a degree or any other qualification at this University or any other institution, this has been clearly stated.
- Where I have consulted the published work of others, this is always clearly attributed.
- Where I have quoted from the work of others, the source is always given. With the exception of such quotations, this thesis is entirely my own work.
- I have acknowledged all main sources of help.
- Where the thesis is based on work done by myself jointly with others, I have made clear exactly what was done by others and what I have contributed myself.
- The main body of this thesis is not more than 80 000 words in length.

Signed: 

Date: 22/10/2021

"... if I have seen further, it is by standing on the shoulders of giants."

Sir Isaac Newton

"I think I can safely say that nobody understands quantum mechanics."

Professor Richard Feynman

"*Once you eliminate the impossible, whatever remains, no matter how improbable, must be the truth."*

Arthur Conan Doyle

THE AUSTRALIAN NATIONAL UNIVERSITY

Abstract

Department of Nuclear Physics
Research School of Physics

Doctor of Philosophy

Magnetic-moment measurements by the transient-field and recoil-in-vacuum techniques in fpg-shell nuclei

by Brendan Patrick M^{c}CORMICK

Picosecond-lifetime nuclear-state g factors are challenging to measure, with the transient-field (TF) and recoil-in-vacuum (RIV) techniques best able to probe them. The TF is experienced by a swift ion traversing a polarised ferromagnetic material, while RIV relies on hyperfine interactions between the nucleus and its electrons that occur in isolated ions. Both techniques often require independent calibration, a key limitation in their use. The objective of this thesis is to improve the precision of g-factor measurements with these techniques. This was achieved by developing procedures that minimise systematic uncertainty in TF measurements to obtain reliable relative g factors, and then scaling them by developing atomic-structure calculations that enabled absolute g factors to be determined from RIV measurements focused on Na-like ions.

Relative TF measurements were used to determine the 2_1^+-state g-factor ratio between ^{24}Mg and ^{26}Mg, which was then scaled using a literature value of $g(^{24}\mathrm{Mg})$, obtained using RIV, to determine $g(^{26}\mathrm{Mg})$. TF measurements were also performed to obtain 2_1^+-state g-factor ratios between the stable even-A isotopes of Ge and Se, with the first-ever simultaneous measurement performed on isobaric nuclides (^{74}Ge,Se) in a cocktail beam.

An *ab initio* approach to modelling ^{56}Fe 2_1^+ state time-differential RIV data focused on Na-like ions was developed. Time-differential ^{76}Ge and time-integral ^{54,56}Fe 2_1^+ state data were also analysed. The analysis utilised a Monte-Carlo simulation of atomic decays to model the hyperfine interaction through time.

The combined use of relative TF and calibration-independent RIV measurements allowed the determination of precise absolute g-factor values. These were used to interrogate TF-strength calibrations, and shell-model predictions. Together, TF and RIV procedures presented in this work were effective in determining accurate g-factor values with improved precision in picosecond-lifetime nuclear states.

Acknowledgements

First and foremost I wish to thank my primary supervisor, Prof. Andrew Stuchbery, without whom this project would never have been conceived, nor reached fruition. He was a constant source of knowledge, wisdom, assurance, direction, and always ready to make time for a chat. His assistance in drafting this thesis was invaluable. I would also like to thank my secondary supervisors Prof. Gregory Lane and A. Prof. Tibor Kibédi, both for their support during my candidature in various details of graduate student life, their contributions to the drafting of this thesis, and assistance in the running of my experiments. My thanks also go out to Prof. Georgi Georgiev, whose physical insights and keen intellect challenged me to carefully consider my own ideas, and hold myself to a higher standard when developing my methods. I also owe him thanks for his assistance in drafting this thesis.

I owe a great deal of gratitude to the Gamma-Ray Spectroscopy Group at the Nuclear Physics Department, some past and present. Specifically, and in alphabetical order, I would like to thank Aqeel Akber, Ben Coombes, Jackson Dowie, Tomas Eriksen, Matthew Gerathy, Timothy Gray, Nathan Spinks, Bryan Tee Pi-Ern and Yiyi Zhong for their comradery, assistance in my experiments, and limitless source of interesting banter. I also want to thank Petra Rickman for being not just a pleasant and competent administrator, but also a genuinely friendly person. Also, I owe many thanks to the technical staff at the Nuclear Physics department, who were a great source of help whenever I needed assistance with experiments, or any issues relating to the accelerator came up.

I owe thanks to Dr. Rickard du Rietz and Dr. Jörgen Ekman for their aid in understanding the GRASP2018 software package, and for helping me to develop my atomic-structure-calculation scripts.

I would especially like to thank Tomas Eriksen and James Harris for seeing me through the first year of my candidature as my house mates. Better friends will not be found. I would also like to thank my parents, James and Margaret M^{c}Cormick. Without their support of my academic ventures, aspirations and achievements, and during times of financial hardship, I never would have made it this far.

I would like to thank Dr. Mary Gray for time taken out of her busy schedule to proof-read my thesis.

I am grateful to Steve Gunn, Sunil Patel, and Vel from LaTeXTemplates.com, whose works contributed to the LaTeX template used to produce this document, which has been reproduced under the Creative Commons License CC BY-NC-SA 3.0.

Last, and most of all, I want to thank my fianceé, Rosa Gray, who saw me through almost four years of the most academically challenging period in my life. Her support and patience during this challenging time are a true testament to our love.

Contents

List of Figures

List of Tables

Physical Constants

Speed of Light	$c = 2.998 \times 10^{8}\,\mathrm{m\,s^{-1}}$
Bohr velocity	$v_0 = c/137.036$
Nuclear magneton	$\mu_N = 5.050\,784 \times 10^{-27}\,\mathrm{Hz\,T^{-1}}$
Planck's constant	$h = 6.626\,070 \times 10^{-34}\,\mathrm{J\,s}$
Reduced Planck's constant	$\hbar = h/2\pi$

Dedicated to my fianceé, Rosa Gray, without whom my achievements would be hollow…

Chapter 1

Introduction

1.1 Aim

The aim of this thesis is to demonstrate the potential for the use of transient-field and recoil-in-vacuum techniques in a complementary manner to perform g-factor measurements on short-lived ($\lesssim 10^{-11}$ ps) excited states in both stable and radioactive nuclei in the region $Z \sim 30$. These measurements should be demonstrably accurate, and precise, in order to confidently challenge modern nuclear-structure theories and advance the field of nuclear-structure physics.

1.2 Background

The atomic nucleus is a discrete quantum system comprised of two types of interacting baryons: protons and neutrons. The behaviour of the nucleus' constituent protons and neutrons gives rise to a number of macroscopic properties, such as a mass, radius, spin, magnetic dipole moment and electric quadrupole moment. In order to understand the nucleus, the forces through which protons and neutrons interact, primarily being the strong and electromagnetic forces, must be understood. Although electromagnetic interactions are well-understood, nuclear interactions via the strong force are less well known, and challenging to calculate *ab initio*. For most nuclei, models of nuclear structure have been developed so that a more theoretically and mathematically tractable approach can be taken to predict nuclear properties. These nuclear properties must then be measured to validate the models.

The aim of this thesis was to interrogate and validate techniques developed to measure nuclear magnetic dipole moments at the frontier of measurement capability. The availability of radioactive-ion-beam facilities since the 1990s [35], along with their gradual improvement in capability, is elevating our understanding of nuclear structure to new heights. This capability also pushes our experimental techniques to their limits. Nuclear-structure models, such as the multi-configuration nuclear shell model, must be

challenged with new data to test our understanding of nuclear forces, and the assumptions built into these models. Since the 1950s it was suspected that nuclei away from stability (radioactive nuclei) will exhibit deviations from the nuclear models that were developed for stable nuclei [63]. This phenomenon, first observed in the 1960s [224], is well-established today [159]. Radioactive-ion-beam facilities now allow measurements on exotic nuclei far from stability, with which to confront nuclear models. Nuclear magnetic moments (commonly expressed as the dimensionless "g factor") provide a unique probe to test multi-configuration shell-model predictions, due to their sensitivity both to the angular momentum of the constituent nucleons, and the varying contribution of protons versus neutrons, in a given nuclear state. The measurement of magnetic moments requires that the spin-orientation of a nuclear state be measurably perturbed in a magnetic field. However, many states of interest survive for only $\lesssim 10^{-11}$ s; such states will be referred to as short-lived states. In order to induce a measurable spin-rotation or precession over such short timescales, magnetic fields of the order of $\gtrsim 10^2$ T are required [22]. Such strong fields are only produced on microscopic scales by the hyperfine interactions between atomic nuclei and the electrons in their local environment.

Since the 1970s, two techniques have primarily been used to perform g-factor measurements on the aforementioned short-lived states [22]. The first, and most commonly used technique, relies on the hyperfine interaction arising for an ion moving swiftly through a polarised ferromagnetic medium, known as the transient field. The second technique relies on the hyperfine interaction arising between the nucleus and electrons of a free ion as it recoils into vacuum. In both of these techniques, the hyperfine interaction induces a precession in the nuclear spin-alignment within the ion, measurable through a perturbation of the γ rays emitted from the nuclear state as it de-excites.

The transient-field technique has been very successful in measuring g factors in stable nuclei, and is sensitive to not only the magnitude, but also the sign of the g factor [22]. However, the complex ion-solid interactions upon which the transient field depends are poorly understood. To overcome this challenge, the field's strength has been parameterised, but this relies on measurements from alternate methods that are sometimes imprecise or questionable. Its behaviour is also not consistent with the parameterisations across all element and velocity ranges. Furthermore, this technique has proven to be limited in application to radioactive ion beams [204], due to the reduced particle rates, and accumulation of radioactive ions within view of the detectors. This introduces a hard limit on beam intensity, significantly impacting measurement precision within limited beam time.

The recoil-in-vacuum technique has also proven to be a viable technique. The hyperfine interaction for highly stripped light ions, having only one or a few electrons, is calculable from atomic theory. For heavier elements, having many-electron ion ensembles, the hyperfine interaction may be calibrated using the g factors of other isotopes, if known. In this technique only the magnitude, not the sign, of the g factor can be measured. This technique has proven effective for measurements using radioactive ion beams, as it allows for the radioactive ions to pass out of view of the detectors after measurement. However, the hyperfine interaction has proven to be challenging to model in medium-mass elements, and over the few picoseconds after ions have left the solid and enter vacuum.

Used together, the two techniques provide an excellent opportunity to study the properties of both stable and radioactive nuclei along isotopic chains. The transient-field technique allows for measurement campaigns on stable isotopes to be performed, giving relative g-factor values, along with their signs. These relative values can then be scaled by a single absolute measurement using the recoil-in-vacuum technique. Radioactive-ion-beam measurements using the recoil-in-vacuum technique are now feasible, with the hyperfine interaction either calibrated using the known properties of stable isotopes (heavier nuclei), or determined from atomic theory (lighter nuclei). By systematically moving along the nuclear chart, the g factors of short-lived and previously inaccessible states in both stable and radioactive nuclei can be obtained accurately and precisely.

To fully realise the goal of using the transient-field and recoil-in-vacuum techniques together, two challenges must be overcome. First, a standard must be set by which relative g-factor measurements are reliably and robustly performed using the transient-field technique. Second, the complex hyperfine interactions present in the recoil-in-vacuum technique when measuring g factors in medium- and heavy-mass elements must be understood without any calibration measurements, i.e. from the underlying atomic physics. Once these two challenges are surmounted g-factor values may be obtained for nuclei in the fpg-shell space, and beyond, allowing for nuclear structure models to be confronted with the accurate and precise measurements that the theory demands. It is by undertaking such stringent tests of shell-model theory that the field of nuclear-structure physics may advance.

1.3 Thesis Scope

This thesis can be broken into two major components: transient-field measurements and recoil-in-vacuum measurements. For the transient-field component of this project, an experiment was performed in which the nuclear g factors of the first-excited state in stable, even-mass isotopes of germanium and selenium were measured in a relative fashion using the transient-field technique. These measurements were performed with the intention of understanding the relative behaviour of the g factors between these isotopes and elements, and to demonstrate a robust method by which relative g-factor values may be measured. Another experiment was performed with these nuclei using a similar technique, the ion-implantation perturbed-angular-correlation technique, in order to interrogate discrepancies present in a historical measurement of these nuclides, relevant to a widely used parameterisation of the transient-field's strength.

Data from a relative transient-field measurement of the first-excited-state g factors in ^{24}Mg and ^{26}Mg were also analysed. A recent, high-precision g-factor value obtained using the recoil-in-vacuum technique, performed on the ^{24}Mg first-excited state, was used to scale the ^{26}Mg value. This was performed to verify a suspect value in the literature, as well as a proof-of-concept for using a recoil-in-vacuum measurement to scale a transient-field measurement.

For the recoil-in-vacuum measurements, experimental data from both time-dependent and time-integral measurements were analysed with the aim of determining g factors and developing a better understanding of the hyperfine interaction. Two sets of time-differential measurement data were analysed, one on the first-excited state in ^{56}Fe, and the other on the first-excited state in ^{76}Ge. The primary focus of their analysis was to model the time-dependent behaviour of the hyperfine interaction, and use this to determine the g factor. The model developed from the measurement analysis was then used to interpret time-integral measurement data taken on the first-excited states in ^{54,56}Fe. For these nuclear states the g factors had been determined, allowing the hyperfine-interaction model to be tested against the time-integral data.

Finally, the results of these measurements were compared with previous measurements of these nuclear g factors, and compared with contemporary multi-configuration nuclear shell-model calculations. Recent advances in the theory are used to interpret deviations from the models. This thesis then summarises the outcomes of the measurements, and proposes that these two techniques work as complementary approaches with which to probe both stable and radioactive nuclei in the region $Z \sim 30$.

1.4 Thesis Overview

In Chapter 2 the theory underpinning the measurements and analyses performed in this project is presented. Building from basic nuclear-structure principles, models of nuclear structure, along with γ-ray spectroscopy and the use of Coulomb-excitation in nuclear-structure measurements, will be introduced. The particular measurement techniques used in this project, namely the transient-field, ion-implantation perturbed-angular-correlation, and recoil-in-vacuum techniques are described. Details of the atomic-structure-calculation software package used to aid in the analysis of recoil-in-vacuum data are also presented. Finally, the literature motivating this project is reviewed with both a historical and contemporary justification for the work.

In Chapter 3 the instrumentation, data acquisition, and data analysis techniques used in the course of this project are described.

In Chapter 4 the transient-field and ion-implantation perturbed-angular-correlation measurement details, results and analysis are presented. First, the data analysis procedure is described, followed by the methods and results of the relative ^{24,26}Mg transient-field measurements, the Ge and Se isotope transient-field measurements, and finally the Ge and Se ion-implantation perturbed-angular-correlation measurements.

In Chapter 5 a computer program developed during this candidature to model the hyperfine interaction for feasibility testing and analysis of recoil-in-vacuum experiments and data, **RIV Simulate**, is presented. The various features of the program are described, along with comparisons of its outputs to theoretical predictions of effects that are expected to be present in recoil-in-vacuum data.

In Chapter 6 the recoil-in-vacuum measurement details, results and analysis are presented. First, the ^{56}Fe 2_1^+ time-differential measurement methods and results are presented, followed by an in-depth analysis of the time-differential behaviour of the hyperfine interaction using **RIV Simulate**, and finally proposing a new, precise g-factor value. This is followed by a description of the ^{54,56}Fe 2_1^+ time-integral measurement methods and results, and further interrogation of the hyperfine interaction using the understanding developed from the ^{56}Fe 2_1^+ time-differential analysis. Finally, the ^{76}Ge time-differential measurement methods and results are presented, again using the understanding developed in the ^{56}Fe 2_1^+ time-differential measurement to determine the g factor.

In Chapter 7 the hyperfine-interaction model developed while interpreting the recoil-in-vacuum measurements is discussed, highlighting what is understood and where this understanding breaks down. The advances in understanding are then considered in the context of performing accurate and precise g-factor measurements in challenging cases, particularly in radioactive nuclei. The g factors determined in this project are then compared to multi-configuration shell-model predictions, and the discrepancies are interpreted in the context of changing nuclear structure and possible short-falls in the model. The chapter closes with an analysis of the transient-field measurements available in the literature, and using the newly obtained g factors to interrogate the transient-field strength and compare with commonly used parameterisations.

In Chapter 8 the key findings of this project are summarised and conclusions drawn from the results. An argument is made for application of these techniques as complementary experimental probes, which will be necessary in confronting the nuclear shell model with future accurate and precise g-factor measurements, including radioactive nuclei. Such comparisons are necessary to advance the field of nuclear-structure physics.

Chapter 2

Literature Review

As discussed in the introductory chapter, this thesis focuses primarily on using two prominent methods for the measurement of nuclear g factors for excited states of nuclei in the region $Z \sim 30$. These methods are the transient-field technique, and the recoil-in-vacuum technique. Both techniques utilise the large magnetic fields arising from hyperfine interactions between the nucleus and its bound atomic electrons. These large fields are necessary due to the short lifetimes of the states of interest. The ultimate goal in pursuing these measurements is to perform accurate and precise g-factor measurements on these nuclear states, with which nuclear models can be confronted.

In this chapter the physical concepts underlying the experimental work, along with the prerequisite theory required to understand the historical and contemporary motivations of this thesis, will be covered. First, basic nuclear structure theory will be introduced, building to modern concepts that are the primary motivation of much current work in nuclear-structure studies. The conceptual basis underpinning the present nuclear-structure measurements will then be covered, first for general γ-ray spectroscopy, and then more specifically for the implantation perturbed-angular-correlation, transient-field and recoil-in-vacuum techniques, and atomic-structure calculations. The chapter closes with a review of the literature motivating this thesis in particular, providing both a historical and contemporary justification for its undertaking.

2.1 The Structure of the Atomic Nucleus

The scientific revolutions that have resulted from a microscopic understanding of the world around us, in particular those arising from the discovery of atoms and subatomic particles, have outcomes that are ever-present in our modern world. However, even though an enormous amount of progress has been made using the theory of atomic matter, there is still a great deal that we are yet to understand. Measurements on microscopic systems governed by quantum mechanics continue to uncover an increasingly esoteric hierarchy of patterns against which our mathematical capabilities are ever

challenged. An enduring enigma of the natural world is the atomic nucleus and the physics of nuclear matter. The nucleus is a unique quantum physics laboratory, owing to its exhibition of complex many-body interactions mediated by the strong, weak and electromagnetic forces. It exhibits both classical and quantum behaviours, and has a great variety of studiable forms ranging from the "simple" nuclei of hydrogen isotopes, to gargantuan neutron stars.

Much of the information covered in this section has been taken from *Krane's Introductory Nuclear Physics* [127], and any material not explicitly referenced has been sourced from this text. This information can be found in any good introductory textbook on nuclear science, nuclear physics and nuclear models, such as Refs. [42, 47, 185, 223].

2.1.1 Discovery of the Nucleus

The study of nuclear phenomena dates back to the late 19^{th} century, with the discovery of radioactive elements. The early efforts of Becquerel, and the Curies, towards characterising the different radioactive materials began the study of nuclear phenomena. In the early 20^{th} century Rutherford, Geiger and Marsden used these newly discovered radiations to probe the structure of the atom, and consequently uncovered the existence of the nucleus. It was discovered that chemical isotope masses were all approximately integer multiples of the hydrogen atom's mass, and the nuclear charge was the same as the atomic number. With Chadwick's discovery of the neutron in the 1930s the final piece of the nuclear puzzle was in place, and the proton-neutron model, as proposed by Heisenberg, was established [108]. Despite the constituents of the nucleus having been identified almost a century ago, a microscopic description of their interactions still remains a challenge, owing to the sub-nucleonic structure, complexities of the quantum many-body problem, and large energies required to probe them.

2.1.2 Basic Nuclear Structure

The nucleus, composed of a number of nucleons (A), specifically protons (Z) and neutrons (N) ($A = Z + N$), can be described by macroscopic properties such as rest mass, radius, spin, parity, magnetic dipole moment, and electric quadrupole moment. The nucleus is a quantum system, with protons and neutrons being described by their wavefunctions, and, being fermions, obeying the Pauli exclusion principle. As a consequence, discrete, excited nuclear states exist with their own unique radius, spin, and electromagnetic properties. The general structure of the nucleus, and interactions between nucleons, was intensely studied throughout the 20^{th} century. Some significant findings were that the spatial extent of the nucleus is not sharply defined but rather there is a central, approximately constant, nuclear density that gradually drops to zero

at the 'edge' of the nucleus. The distance over which this gradual drop in density occurs is referred to as the "skin thickness". Both the central density and skin thickness are fairly constant across the nuclear chart. Another important observation is the very small number of stable odd-Z, odd-N nuclei and, conversely, the large number of stable even-Z, even-N nuclei. These observations indicate that proton-proton and neutron-neutron pairing is energetically favourable, and has implications for how nucleons may arrange themselves in a structural model.

In the modern era of nuclear physics, the study of nuclear matter focuses on the development of models to predict nuclear structure properties. These models are tested by comparing the measured properties of nuclear states with predictions for nuclei having different Z, N, spin and excitation energy. Through this interplay of theory and experiment, our understanding of the nucleus improves.

In order to understand the complexity of nuclear matter, consider first the atom, having electrons that move in the Coulomb potential of the nucleus. Electron interactions are explained almost solely by the electromagnetic force. The primary sources of electromagnetic interaction are from an approximately radially uniform, central, electrostatic potential, and two-body interactions between electrons. The nucleus and electrons may all be modelled as point-particles, except for in exceptionally high-precision calculations. In contrast, the nucleus consists of two distinct types of baryons experiencing the electromagnetic, strong and weak forces. As the mean field originates from the nucleons themselves, it cannot be precisely modelled by a simple central potential. Protons and neutrons also experience different Coulomb forces due to their differing charge. Nucleons have internal structure, and cannot be treated as point-charges, making the nucleon-nucleon force challenging to model. Three-body forces, which don't need to be accounted for in the atomic picture, also appear to be significant in nuclear interactions [159]. Due to its complexity and quantum nature, an *ab initio* description of atomic nuclei beyond $A \simeq 20$ remains elusive.

The *ab initio* approach has become available only since the early 2000s [154], and has generally been applied to nuclei no heavier than carbon isotopes ($A \lesssim 15$) [16, 50]. The usual approach to the nuclear problem is to make approximations that aim to capture the overall physics, while still remaining mathematically tractable. Due to the success of the atomic shell model in describing the atom, a similar approach has been taken to understanding the structure of the nucleus. As described in the previous paragraph, there are several key differences between atomic and nuclear interactions. However, if structural effects arising from quantum mechanical interactions existed in nuclei, there should be evidence of them. The first key piece of evidence discovered in favour of a

nuclear shell model was the stability of certain numbers of protons and neutrons, termed "magic numbers", which were known as early as 1934 [64]. There tends to be a large number of stable isotopes if Z is magic, or isotones if N is magic, along the nuclear chart. This implies these nucleon configurations are particularly stable, providing evidence for a shell structure.

Another early observation having implications for nuclear structure models was the pairing force between like-nucleons. It is energetically favourable for like-nucleons to pair up. In the case of even-Z, even-N (even-even) nuclei, the ground state always has a net spin of zero, indicating that if nucleons have fixed angular momentum, then they have anti-parallel pairing. Due to this pairing force, two-proton and two-neutron separation energies between even-Z, even-N nuclei were studied across the nuclear chart to reveal trends. When these energies are plotted against the number of nucleons, as shown in Fig. 2.1, a distinct shell structure appears. More evidence suggesting that these magic numbers are analogous to atomic shell closures is that doubly-magic nuclei (both Z and N are magic numbers) have first-excited states with very high energy compared to nearby nuclei, analogous to the noble elements.

To support the hypothesis that the magic numbers correspond to shell closures, a successful shell model of the nucleus must reproduce them. In analogy with the atomic shell model, if a central potential in which nucleons orbit is assumed, then they will require principal (n), angular momentum (l) and intrinsic spin (s) quantum numbers to describe their wavefunction. The magic numbers up to $Z, N = 20$ can be reproduced by solving for the orbital energies using the Schrödinger equation, with an energy Hamiltonian having the form of a potential intermediate between an infinite square-well and a harmonic oscillator. This potential is able to match the approximately uniform nuclear density, and the sharp drop-off in density towards the unbound-particle region (edge of the nucleus). The introduction of a term to the nuclear potential that relates the intrinsic spin and angular momentum, termed the spin-orbit interaction, gives a solution which reproduces the magic numbers observed in all stable nuclei [88, 105]. This spin-orbit term causes a significant splitting in the coupled angular momentum and intrinsic spin, producing two distinct orbital energies for each angular momentum quantum number (with $l = 0$ being the one exception as there is no spin-orbit interaction when the angular momentum has no magnitude). Because of this, nucleon orbitals are described by how l and s are coupled, with total spin $j = l \pm s$ depending on if the coupling is parallel ($+$), or antiparallel ($-$). The ordering of orbital energy levels and shell gaps resulting from the intermediate-form potential is shown in Figure 2.2. This conception of the ordering of nucleons, along with the known pairing force between like nucleons, has been very

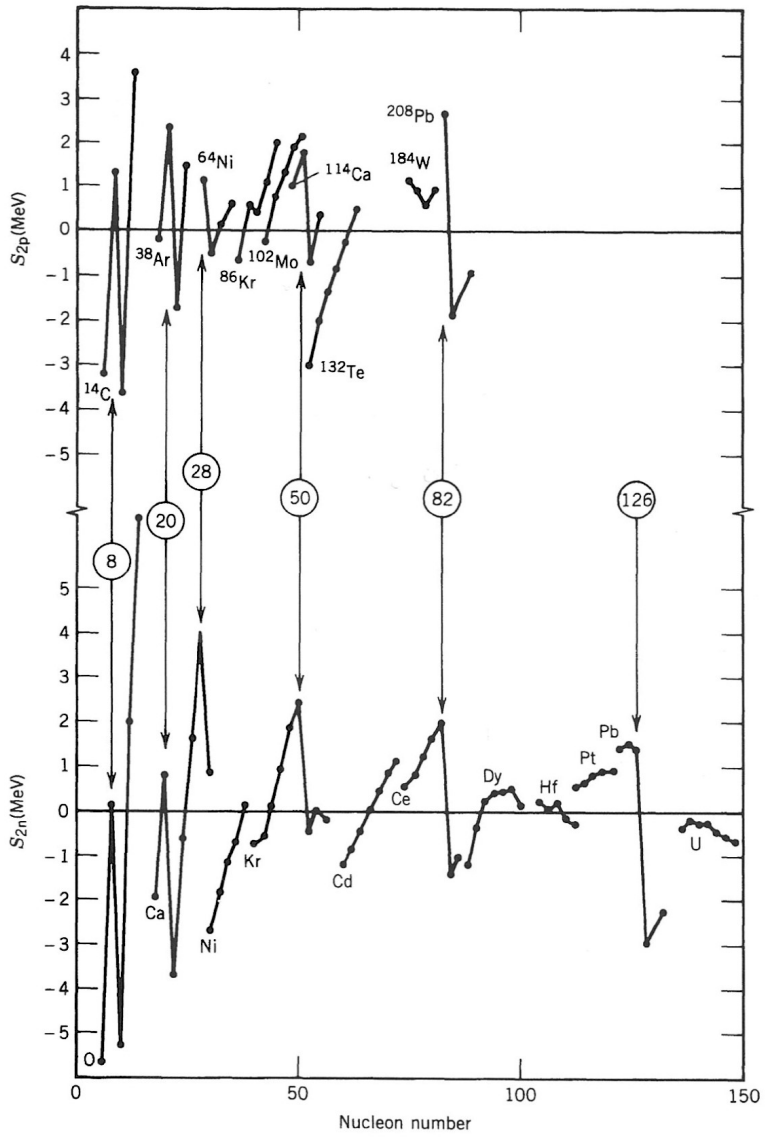

FIGURE 2.1: Plots of the difference between two-proton (S_{2p}) and two-neutron (S_{2n}) separation energies obtained from a smoothly varying, semi-empirical formulation, and from measurements. The S_{2p} energies show sequences of even-Z isotones, with the lowest-Z member indicated, increasing by two protons each step. The S_{2n} energies show sequences of even-N isotopes, increasing by two neutrons each step. The magic numbers (shell closures) are indicated. The shell-closure effect is particularly apparent along the higher-mass sequences where a large, negative discrepancy between measured and predicted values suddenly appears, indicating the pair is more strongly bound. This figure was originally published in Ref. [127].

successful in determining the ground-state properties of spherical nuclei, despite its simplifying assumptions. With this mathematically derived sequence of shell closures, the nuclear shell model was established.

2.1.3 Models of Nuclear Structure

Soon after the establishment of nuclear shells and the order in which orbitals fill, the shell model was used to predict the properties of nuclei having a single, unpaired nucleon (odd-A nuclei). Due to the pairing force, odd-A nuclei should have ground-state properties governed by the odd nucleon. This interpretation is known as the extreme single-particle nuclear shell model. The pairing force results in the spin and parity of the ground state almost always being determined by the spin ($j = l \pm s$) and parity ($\pi = (-1)^l$) of the unpaired nucleon. While this was a good starting point, it was soon found that the accuracy of the shell model's predictions are greatly improved when considering all nucleons outside a closed shell (valence nucleons), particularly for more complex properties like the dipole and quadrupole moments. Excited states in nuclei are also rarely explained by the unpaired nucleon alone. As such, while the extreme single-particle shell model has some predictive power for odd-A nuclei, it says very little about excited states in even-even nuclei, and its usefulness is limited.

Most nuclei, particularly even-even nuclei, have low-energy excited states that are produced by a type of collective behaviour. This is why the extreme single-particle model is unable to accurately predict excited states in many cases. For even-even nuclei one would expect that, to make an excited state, a nucleon pair must be broken, or excited together. Calculated orbital energies predict these states should have energies around 2 MeV. However, a much lower-energy 2^+ or 0^+ state often exists which cannot be explained by any individual nucleon configuration. This behaviour results from correlations between multi-nucleon configurations that lead to collectivity in the form of surface vibrations and/or rotations. Collectivity is also present in odd-A nuclei, in which the paired nucleons of the even core exhibit a collective excitation to which the odd nucleon couples. In other words, the many different ways in which nucleon pairs can be broken and re-coupled to the same spin and parity results in a collective state which is lower in energy than any individual configuration. It is only by understanding the influence of both the single-particle and collective behaviours of nuclei that structural properties can be accurately predicted across the nuclear chart.

Collective excitations have long been interpreted using the "liquid drop" model originally proposed by Gamow [86] and further developed by Bohr and Wheeler

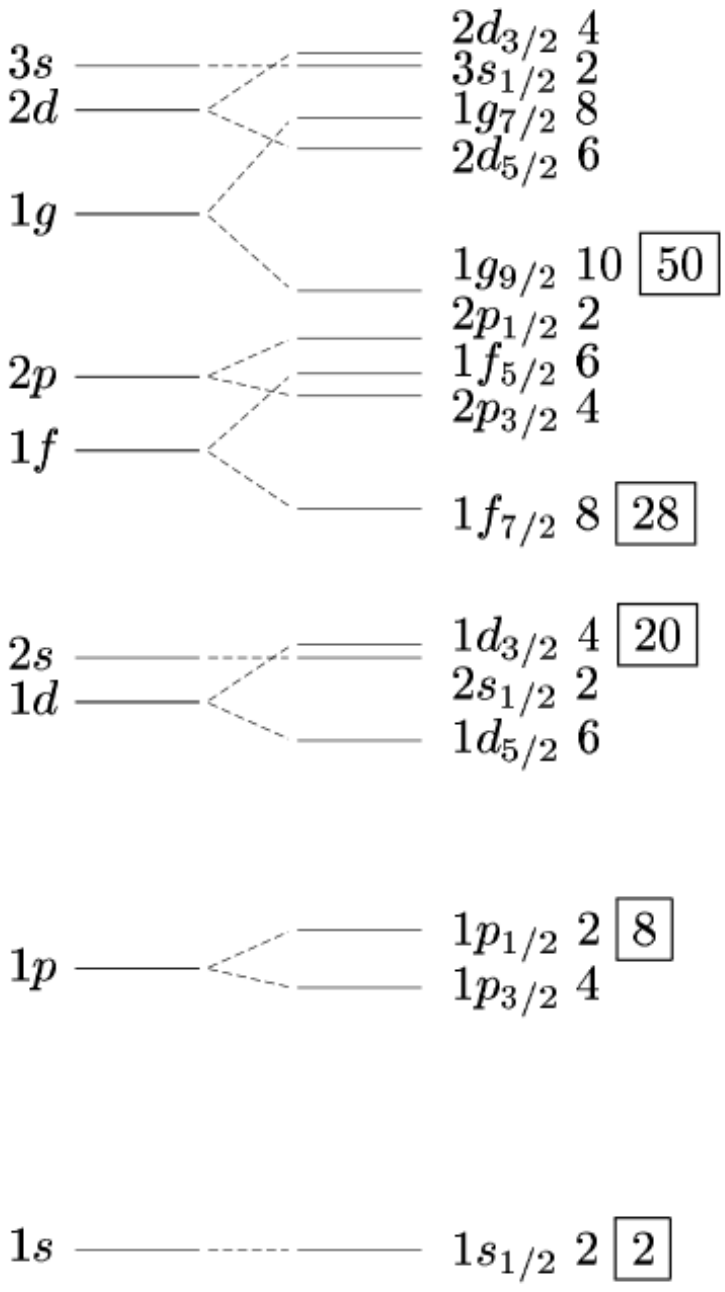

FIGURE 2.2: The energy spacing and ordering of nucleon orbitals, obtained first by the intermediate-form potential well, and then the addition of a spin-orbit term, results in a shell structure with distinct gaps at certain nucleon numbers. These are the so-called "magic numbers". Energy increases from bottom to top. The magic numbers (shell closures) are indicated on the right. Image created by Bakken [15].

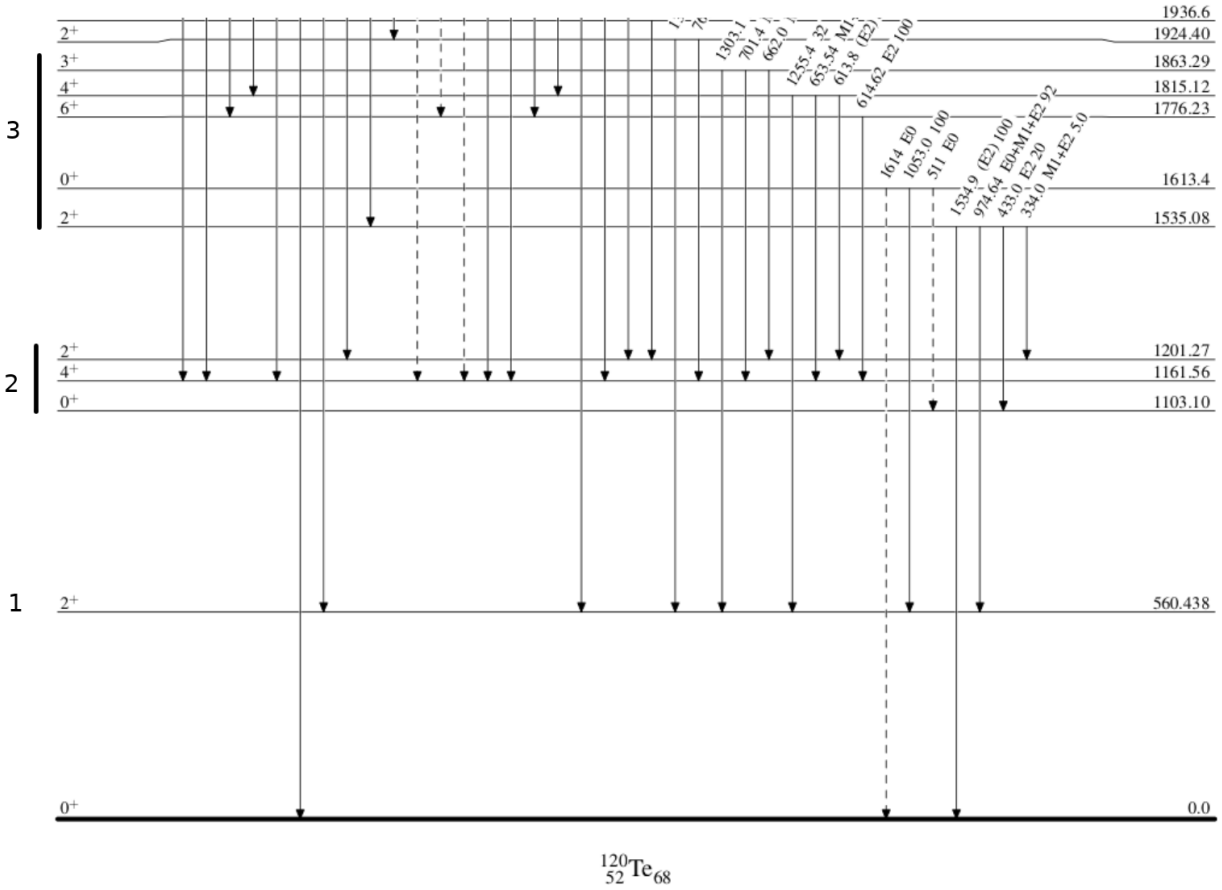

FIGURE 2.3: Level scheme for ^{120}Te, with the collective excited states and the number of quadrupole phonons associated with that state indicated on the left. Note the number of states resulting from the phonon coupling, and the average energy of each cluster of states being evenly spaced. Level scheme obtained from Ref. [124].

to describe nuclear fission [26]. For nearly spherical nuclei, particularly nuclei having $A < 150$ and being near to shell closures, the collectivity can be modelled as a quadrupole vibration that produces a characteristic set of low-energy excited states in even-even nuclei. The vibration occurs around an average, almost spherical shape, although the instantaneous shape of the nucleus is actually non-spherical. Modelling the system as such requires the wavefunction to be symmetric, restricting any excited states to having even parity. Because the nucleus is a quantized system, any vibration connecting two states must also be quantized. This quantum of mechanical energy is termed a "phonon", in analogy to the electromagnetic photon, which also carries energy and angular momentum. A phonon carrying a single unit of angular momentum ($\lambda = 1$) would induce a dipole vibration of the nucleus, requiring the centre-of-mass to move, an unrealistic motion at low energy and spin. A phonon having $\lambda = 2$ (a quadrupole phonon) will produce a vibration with a fixed centre-of-mass. As such, this is the minimum angular momentum such a phonon can carry. A single quadrupole phonon produces a vibration giving rise to a $I^\pi = 2^+$ state, while two phonons give a cluster of three states having $I^\pi = 0^+, 2^+$ and 4^+ states. As each phonon carries similar energy, the average energies of clusters of states arising from them are expected to be spaced evenly apart. The measured energy levels of ^{120}Te, shown in Fig. 2.3, are an example of vibrational excited states. However, in recent years this model has come under suspicion. As large amounts of data from various experimental approaches have become available, and more stringent criteria applied to validate the spherical vibrational model, many nuclei which were once considered to be ideal candidates are proving to not match predicted electromagnetic decays of their states [87]. As such, while it has good predictive capability in many respects, this model may be a caricature of more complex phenomena occurring in the pattern of nuclear excited states.

The single-particle and collective models, as described thus far, are simplifications that describe only exceptional nuclei, and are unable to precisely match measurements for all nuclei. This is because many nuclei exhibit the properties of both models. In some such cases, the single-particle and collective models can be coupled in order to explain observed spins and parities of excited states. For nuclei that are approximately spherical, the approach taken in atomic physics has been adopted: the shell model is used under the assumption that doubly magic nuclei are spherical and inert, providing a stable, central mean-field potential. Valence nucleons are then added, and nucleon-nucleon interactions are allowed (either in a truncated or unrestricted manner), in a valence space generally consisting of orbitals up to the next shell closure. This is the many-particle shell model, and has become an attractive approach since the computational revolution of the 1970s, which made the required computational processing power readily available.

2.1.4 The Many-Particle Nuclear Shell Model

During the 1960s, computer calculations became available for predicting nuclear properties using a multiconfiguration shell model. Solutions could be obtained numerically and parameters varied in order to fit model parameters to experimental data. Cohen and Kurath used such an approach to empirically determine the parameters necessary to describe nuclei in the $1p$-shell space (between ^{4}He and ^{16}O) [51], and were able to successfully validate their model against much of the data avilable at the time [148]. This was an important step in building a complex multiconfiguration shell model against which to test nucleon-nucleon interactions. Much work continued on nuclei in this space and beyond, leading to McGrory and Wildenthal's 1980 review [148], in which they laid out a framework for performing these multiconfiguration shell model calculations. Their review built this framework primarily around its application to *sd*-shell nuclei (from ^{16}O to ^{40}Ca); a tantalising region that presents a virtual laboratory rich in experimental data at the limit of the computational capability of the time. While the results of calculations in this space did not always reproduce exact quantitative features, the reproduction of qualitative spectral features across states exhibiting varying character was a great triumph. Toward the end of the decade, Brown and Wildenthal published a review [40] of progress made in *sd*-shell calculations, and presented an approach in which single-particle energies and two-body matrix elements are obtained from a least-squares fit to the large amount of available spectroscopic and energy data in this region. They refer to the interaction obtained in this manner as the W interaction. Brown and Wildenthal report that interactions derived in this manner show an impressive agreement with experiment, as compared to previous approaches. However, due to their empirical basis they do not give significant insight into the nature of the interactions. The W-interaction approach also requires that large amounts of reliable data be available in any region for which the calculations are to be performed. Finally, it should also be noted that, despite the power of this method, there were still difficulties reproducing states that mix with collective states, as well as with cross-shell excitations [40], owing to limitations in the model and orbital space.

Much of the limitation to advances in realistic shell-model calculations was due to the model spaces becoming increasingly large beyond the *sd* shell. This limitation is continually being overcome with advances in computational power. Another key issue of the time was the determination of the nucleon-nucleon residual interactions in the mean field without resorting to merely fitting experimental data. A solution was eventually provided through advances in the understanding of the *free* nucleon-nucleon (NN) interaction. The free NN interaction has been extensively studied since the 1940s but, due to its complex sub-nucleonic origin, a detailed description was not achieved until the late

1980s. One of the prominent models which utilised this improved understanding of the free NN interaction was the Bonn full model [52]. This model takes the Bonn potential and uses effective-field theory to determine the *effective* NN interaction in the nucleus. This translation of the free NN interaction, as experimentally understood, to the effective interaction present in the nucleus required one-boson-exchange parameterisations. These detailed NN-interaction models reinvigorated the shell model approach to nuclear structure calculation, spurring the investigation of a number of Sn isotopes [10, 65] at the $Z = 50$ shell closure. Efforts continued in exotic nuclei around ^{100}Sn, and neutron-rich ^{132}Sn, as data from RIB facilities has become available, and computational power has become capable [52]. Effective interactions using alternative versions of the Bonn NN interactions have gradually expanded into the pf shell ($28 < Z, N \leq 38$) [110] and full $pfpg$ shell ($28 < Z, N \leq 50$) [111] by the efforts of Honma *et al.* For the latter, nuclei such as Ge and Se isotopes [98, 198] provide a valuable testing ground.

A shell model with orbitals ordered as shown in Fig. 2.2 was very successful at predicting the properties of the stable nuclei experimentally accessible to physicists through the mid-20$^{\text{th}}$ century. However, as early as the 1950s Elliot and Lane [63] pointed out that the one-body spin-orbit term, which was so successful in explaining the magic numbers near stability, could not explain orbital ordering across all nuclei. An additional term in the energy Hamiltonial was required, which not only varied slowly with mass number, but also as particular shells were filled. This was a strong indication that there existed a yet-to-be identified interaction, eventually described as a monopole effect, that arises from a tensor force in the NN interaction [158]. This interaction modifies the magnitude of the spin-orbit interaction, with significant implications for orbital ordering and shell structure. The nucleus ^{11}Be was the first case studied in how orbital filling changes away from stability; this nuclide has its $2s_{1/2}$ orbital lower in energy than the $1p_{1/2}$ [224], contrary to observations in stable nuclei. As more exotic nuclei were probed throughout the 1960s and 1970s, disagreements with expected assignments began to accumulate. The extensive effort of many researchers finally confirmed the disappearance of the $N = 20$ shell gap and coincident onset of collective behaviour in neutron-rich nuclei around $Z = 11$ [193]. This region came to be known as an "island of inversion", and is centred around ^{32}Mg. Nuclei in this particular region exhibit changing neutron (ν) $\nu f_{7/2}$, $\nu p_{3/2}$ and $\nu d_{3/2}$ orbital energies as compared to stable nuclei with the same number of neutrons [193], with the $\nu p_{3/2}$ orbital falling below the $\nu f_{7/2}$. The lowered $\nu p_{3/2}$ orbital is referred to as an "intruder orbital". Consequently, these changing orbital energies remove the $N = 20$ shell closure observed in stable nuclei [227]. Not only have the shell gaps observed in stable nuclei been seen to disappear but new gaps have been seen to form, notably at $N = 16$, 32 and 40 [36, 200, 226]. For example, it was recently shown that ^{54}Ca forms a shell closure at $N = 34$, which is not observed in the higher-Z isotopes

^{56}Ti and ^{58}Cr. In this instance, a tensor force between nucleons in the $\pi f_{7/2}$ and $\nu f_{5/2}$ orbitals reduces the $\nu f_{5/2}$ orbital energy. As protons are removed from the $\pi f_{7/2}$ orbital the gap increases, pushing the $\nu f_{5/2}$ energy above that of $\nu p_{1/2}$ to produce a shell gap at $N = 34$ [201]. This interaction is accounted for in modern shell model approaches by including a monopole interaction between nucleons in different orbitals [159]. The study of these interactions allows for the development and refinement of new interaction models, which in turn improve the nuclear shell-model calculations, enabling them to make predictions further into these exotic regions [160, 163].

As our understanding of the NN interaction has improved, so too have the techniques available to perform the multiconfiguration shell-model calculations. The traditional numerical approach was becoming a computationally daunting challenge as nuclei in the $pfpg$ space and beyond were considered. A solution to this problem is the Monte Carlo Shell Model (MCSM). This approach effectively reduces the number of single-particle interactions in the many-body space by using a stochastic sampling approach designed to favour important components of the wavefunction: application of the quantum Monte-Carlo diagonalisation method to the nuclear many-body problem [161]. In short, it allows the integrals (which are usually solved numerically) to be sampled to the desired precision. By varying the sampling, more valence nucleons can be simultaneously considered, and more single-particle states can be included in any given calculation, allowing for states in larger, more complex nuclei to be calculated. The MCSM's early application allowed for excited nuclear states in ^{32}Mg and surrounding nuclei in the island of inversion to be calculated utilising both the *sd* space, and the pf space beyond, with a unified description of the interaction. Calculations in this $sdpf$ space were beyond reach using previous methods. The predicted 2_1^+ and 4_1^+ energies and $B(E2)$ values are reproduced almost exactly [161]. With the ability to calculate excited states in drip-line and exotic nuclei, a broader test of the theory underlying the shell model could now be undertaken. With calculations for these exotic states now available, experimental techniques must be advanced so that these models may be confronted.

2.2 Nuclear Structure Measurements

When an unstable nuclear state decays, it may emit several radiations before reaching stability. Some radiations alter the nuclear and chemical nature of the nucleus, i.e. change Z and/or N. Common examples are α and β decays, which connect states in different nuclei. The third type of common decay, γ decay, connects different states within the same nucleus. A sequence of possible, characteristic decays which occur in a radioactive nucleus is referred to as a decay scheme. For example, after β decay the newly formed daughter nucleus may be in an excited state. This excited state will undergo one or more γ decays to reach the ground state, which may undergo another β decay and so on until the ground state of a stable nucleus is reached. These excited nuclear states which γ decay can also be produced by nuclear reactions.

Gamma-ray cascades are measured via γ-ray spectroscopy to deduce nuclear level schemes, such as that shown in Fig. 2.3. Because the γ-ray emissions (and any other radiations) conserve energy and angular momentum, information about the states they connect can be inferred. Angular-correlation measurements are one way to obtain such information. By performing experiments in which a nuclear reaction excites states from which γ-ray emissions are measured and angular-correlations are formed, structural information about the nucleus can be obtained.

2.2.1 Gamma-Ray Angular Correlations

A key measurement technique used in nuclear γ-ray spectroscopy is the measurement of the γ-ray intensity at different angles of emission. In its simplest form, two γ-ray detectors, with a known separation angle, measure the intensity of two different, time-correlated γ rays originating from the same nucleus. Each detector measures the intensity of a different γ ray. Changing the angle between the two detectors reveals that the intensity of the second γ ray is a function of the separation angle between the detectors. This is referred to as an angular-correlation measurement. The theory describing angular correlations between nuclear radiations has been established since the 1950s [83]. Angular correlations provide an experimental tool to infer structural information, such as total angular momentum (or spin) I, and parity π, from nuclear excited states.

Consider a state, A, γ decaying to a final state, C, via an intermediate excited state, B. An example decay sequence is illustrated in Fig. 2.4. This scenario can be described as the emission of two successive γ rays from a single radiating system, for which the

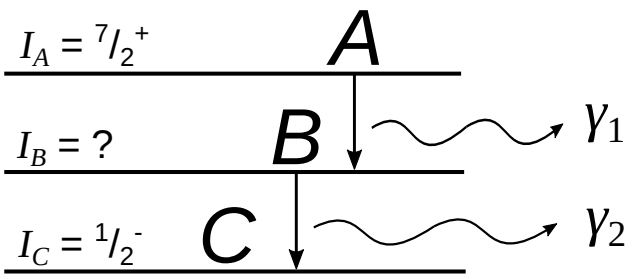

FIGURE 2.4: Illustration of a two-decay sequence connecting three states within the same nucleus. Suppose the initial state A has known spin and parity, and the final state C is the ground state with known spin and parity. There is an intermediate excited state B through which the decay proceeds, with unknown spin and parity. By measuring the angular correlation between γ_1 and γ_2, the spin and parity of state B can be inferred using angular-correlation theory. Note that, in general, the unknown state may be any of the three states A, B or C.

probability amplitude is given by Hamilton's W function [100]:

$$W = \sum_{m_a, m_c, e', e''} |\sum_{m_b} (A_{m_a}|H(\kappa_0', e')|B_{m_b})^* (B_{m_b}|H(\kappa_0'', e'')|C_{m_c})^*|^2, \tag{2.1}$$

where A, B and C represent the required eigenstate quantum numbers of their respective states, m_a, m_b and m_c represent their respective magnetic substates, and H is the Hamiltonian for the transition defined by the direction of propagation κ_0 and polarisation e.

What Eq. (2.1) reveals is that the likelihood of observing a transition between two particular states is related to the angle between the two radiations. The shape of the γ-γ angular correlation, that is the intensity of γ rays across the full angular range, depends on the spin and parity (I^π) of states A, B and C. Therefore, if I^π of two of the states are known, then I^π of the third can, in principle, be inferred. Performing γ-ray spectroscopy measurements on excited nuclei and analysing γ-γ angular correlations allows the identification of many nuclear-state spins and parities in a decay scheme.

A key consideration when performing angular-correlation measurements is a perturbation arising from the interactions between the nucleus and the electrons around it, termed the hyperfine interaction. The hyperfine interaction makes the nuclear magnetic substates non-degenerate, causing their populations to change and thus affecting the probability amplitudes in Eq. (2.1). Goertzel [89], following the form of Eq. (2.1), determined the perturbation arising from the hyperfine splitting of the nuclear substates to

be

$$W = \sum_{m_a,m_b,m_{b'},m_c,e',e''} (A_{m_a}|H(k_0',e')|B_{m_b})^*(B_{m_b}|H(k_0'',e'')|C_{m_c})^* \times (A_{m_a}|H(k_0',e')|B_{m_b'})(B_{m_{b'}}|H(k_0'',e'')|C_{m_c})/(1-i\nu_{m_b,m_{b'}}/2\gamma_B), \quad (2.2)$$

where m_b and $m_{b'}$ signify non-degenerate substates in level B, $\nu_{m_b,m_{b'}}$ is the hyperfine splitting between the substates of B, and γ_B is the oscillator strength of the transition between B and C. The denominator can also be written $1 - i\tau_B(E_{m_b} - E_{m_{b'}})/\hbar$ [1], where τ_B is the lifetime of state B, E_m is the eigenenergy of the non-degenerate magnetic substate, and $\hbar$ is the reduced Planck constant. In cases where $\tau_B(E_{m_b} - E_{m_{b'}}) << 1$, i.e. the nuclear-state lifetime is small and/or the hyperfine splitting is small, Eq. (2.2) reduces to Eq. (2.1). There are two important instances where this is not the case: when the lifetime is sufficiently long, or when the hyperfine splitting is sufficiently large.

Before proceeding, the concept of γ-ray multipolarity needs to be discussed. When a transition occurs between nuclear substates, the emitted γ ray carries away angular momentum and has character relating to the parity of the nuclear states, which is referred to as its *multipolarity*. The multipolarity is specified by whether the transition is *E*lectric or *M*agnetic in nature, and the possible change in spin between the *i*nitial and *f*inal states $|I_i - I_f| \leq L \leq I_i + I_f$. Transitions having an odd value of L and a change in parity are electric, while those having an even value of L and a change in parity are magnetic, and vice-versa for no change in parity [127]. For example, a transition $I^\pi = 2^+ \rightarrow 0^+$ has potential *magnetic-substate* transitions $\Delta I_m = L = 0, 1, 2$, with no change in parity. $L = 1, 2$ will emit γ rays with multipolarity $M1$ and $E2$, respectively, while $L = 0$ has no γ-ray emission. The ratio between the two different multipolarities is termed the mixing coefficient, δ, and relates to the substate populations in the 2^+ state. If there is mixing, the transition is a *mixed* $E2/M1$ *transition*. If only the $E2$ is observed, the transition would be a *pure* $E2$ *transition*.

After Hamilton's theoretical treatment was published, a number of reformulations in the angular-momentum algebra followed, significantly by Racah [175], Lloyd [142], Alder [3], and Fano [70], culminating in a comprehensive review by Biedenharn and Rose [19]. For a γ-γ angular correlation having an unoriented initial state, where both γ-rays are pure multipole, Biedenharn and Rose present the following formula:

$$W(\theta) = \sum_k A_k P_k(\cos\theta), \quad (2.3)$$

where k is an even integer $0 \leq k \leq 2L$, P_k is a k-order Legendre polynomial of $\cos\theta$, and

$$A_k = F_k(L_1 I_A I_B) F_k(L_2 I_C I_B), \tag{2.4}$$

where

$$F_k(L I_n I) = (-)^{I_n - I - 1}\sqrt{2I+1}(2L+1)\langle\ L\ 1\ L\ -1 \mid k\ 0\ \rangle W(\ I\ I\ L\ L\ ;\ k\ I_n\ ), \tag{2.5}$$

in which $\langle\ L\ 1\ L\ -1 \mid k\ 0\ \rangle$ is a vector addition (Clebsch-Gordan) coefficient and $W(\ I\ I\ L\ L\ ;\ k\ I_n\ )$ is a Racah coefficient, evaluated using Racah's techniques [175].

2.2.2 Angular Correlations from Relativistic Particles

The W function for determining the angular correlation of γ radiation from a moving particle is evaluated in the particle's rest frame. When a particle moves faster than a few percent the speed of light, the lab-frame angles defined by the detector positions must undergo relativistic corrections (Lorentz transformation) to match the particle-frame for calculating the angular correlation. A correction to the γ-ray intensity must also be made due to the change in differential solid angle, $d\Omega_\gamma$. Pelte and Schwalm [169] give a formulation for these corrections using two sets of polar coordinates: one defining the particle's direction of motion and the other the γ-ray emission direction. The polar angles are defined in Fig. 2.5. The transformation is performed as follows:

$$\cos\theta_\gamma = \{(\cos\theta'_\gamma - \cos\theta'_p\cos\theta')[1-\beta^2]^{1/2} + \cos\theta'_p(\cos\theta' - \beta)\} \\ /[1-\beta\cos\theta'], \tag{2.6}$$

$$\sin\theta_\gamma\cos\Delta\phi = \{[\sin\theta'_\gamma\cos\Delta\phi' - \sin\theta'_p\cos\theta'][1-\beta^2]^{1/2} + \sin\theta'_p(\cos\theta' - \beta)\} \\ /[1-\beta\cos\theta'], \tag{2.7}$$

$$\sin\theta_\gamma\sin\Delta\phi = \sin\theta'_\gamma\sin\Delta\theta'\frac{[1-\beta^2]^{1/2}}{1-\beta\cos\theta'}, \tag{2.8}$$

where lab-frame quantities are indicated by prime (X') notation, $\Delta\phi = \phi_\gamma - \phi_p$, and $\Delta\phi' = \phi'_\gamma - \phi'_p$. The relative angle between the two directions, θ', is calculated by

$$\cos\theta' = \sin\theta'_p\sin\theta'_\gamma\cos\Delta\phi' + \cos\theta'_p\cos\theta'_\gamma. \tag{2.9}$$

Once the angles are transformed into the particle-frame, the solid-angle correction is applied by multiplying the W function by

$$d\Omega_\gamma / d\Omega'_\gamma = \frac{1-\beta^2}{(1-\beta\cos\theta')^2}. \tag{2.10}$$

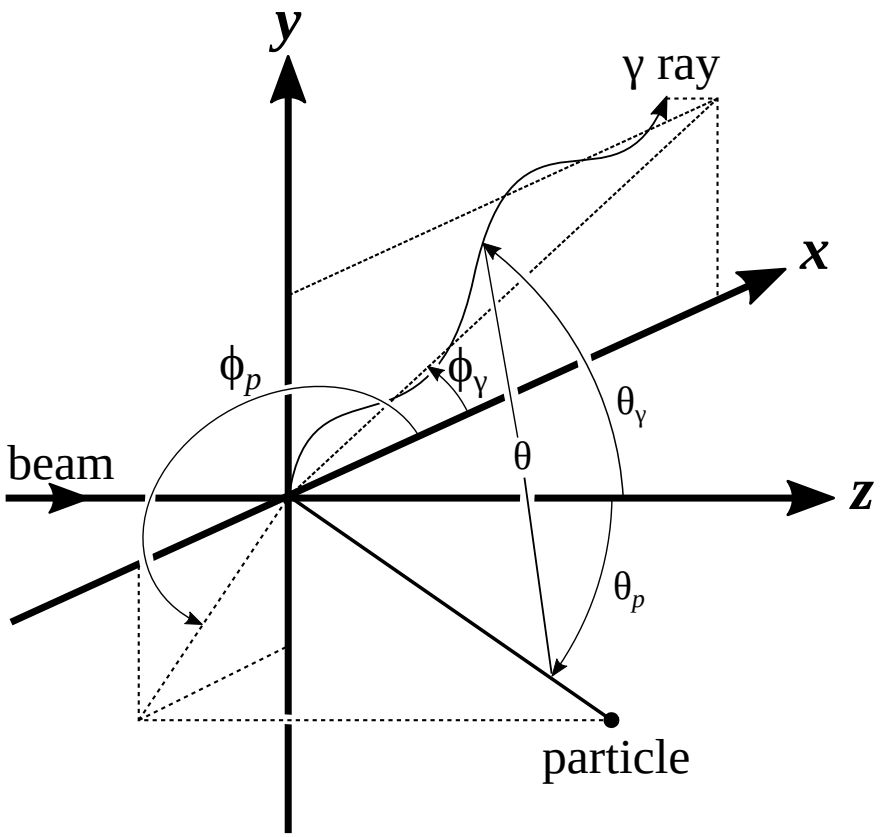

FIGURE 2.5: Definition of the polar angles used in Pelte and Schwalm's formulation of the relativistic correction to transform the lab-frame angles into the particle-frame angles. These definitions are used in all references to relative γ-ray and particle directions, as defined by detector placement. Adapted from Fig. 1.28 in *Heavy Ion Collisions Vol. 3* [24].

2.2.3 Angular Correlations after Coulomb Excitation

Shortly after Biedenharn and Rose's review, Alder *et al.* published a review on progress in nuclear-structure studies using Coulomb excitation [6]. Coulomb excitation is the process by which a nucleus is excited by the Coulomb field of a bombarding nucleus, without the nuclei coming close enough to undergo any strong-force interaction. This is typically achieved using a particle accelerator with its beam impinging on a target of interest. Significantly, Alder *et al.* showed that the differential excitation cross-section (and thereby the transition amplitude) for a particular scattering/deflection angle can be calculated to determine the population of magnetic substates in the excited nuclear state. This information allows the γ-ray distribution from an excited state to be calculated using the

formula:

$$W(\theta) = \sum_k a_k^\lambda A_k P_k(\cos\theta), \tag{2.11}$$

where θ is the angle of the emitted γ ray relative to the beam direction, λ is the change in angular momentum between the two states, $0 \leq k \leq 2\lambda$, and

$$a_k^\lambda = b_k^\lambda / b_0^\lambda, \tag{2.12}$$

where b_k^λ is the transition amplitude parameter, which defines the occupation of a given substate relating to the coupling integer k. This parameter can be integrated across all scattering angles if the exciting particle goes undetected (angular distribution), or calculated for a particular scattering angle (γ-particle angular correlation).

Almost two decades later, Alder and Winther released a comprehensive monograph on the topic of nuclear electromagnetic excitation [5] based largely on previously compiled works [4]. They laid out a formalism [5] in which a spherical statistical tensor, ρ_{kq}, connecting the initial and final state [25] is calculated from the known impact parameters. These parameters are the relative momentum, which can be determined from the beam energy E_b, beam-nucleus mass A_b, and target-nucleus mass A_t; the deflection/recoil angle of the excited nucleus, which is defined by the particle-detector position; and the strength of the Coulomb field, which is determined from the beam and target nuclear charge Z_b and Z_t. In their formalism, a right-handed coordinate system is used in which the beam direction defines the z (quantisation) axis, and the orbital (particle-deflection) plane defines the x axis, in which the x component of the particle velocity during scattering is positive. With this coordinate system defined, spherical polar coordinates are used to express the relative polar angle between the beam (z axis) and emitted γ-ray, θ, and relative azimuthal angle between the scattering plane (z–x axis) and the emitted γ-ray, ϕ, can be used to rotate ρ_{kq} accordingly. When performing a measurement, $\phi = 0$ is often fixed to the x or y axis in the lab frame. In this case, the quantity $\Delta\phi = \phi_\gamma - \phi_p$ is used to rotate ρ_{kq}, where ϕ_γ is the γ-ray detection and ϕ_p the particle detection azimuthal angle relative to the fixed plane. Figure 2.5 gives a visual representation of the angles ϕ_γ and ϕ_p. The "D-function" rotational matrix [5, 25] can then be used to rotate the statistical tensor by the θ and ϕ γ-ray emission angles to obtain the expected γ-ray intensity. At low velocities (less than 1% c) the particle and lab frame-of-reference are approximately equivalent. However, at velocities above a few percent the speed of light, lab angles (defined by the relative angles between the particle and γ-ray detectors) must be transformed into the particle frame-of-reference (see §2.2.2).

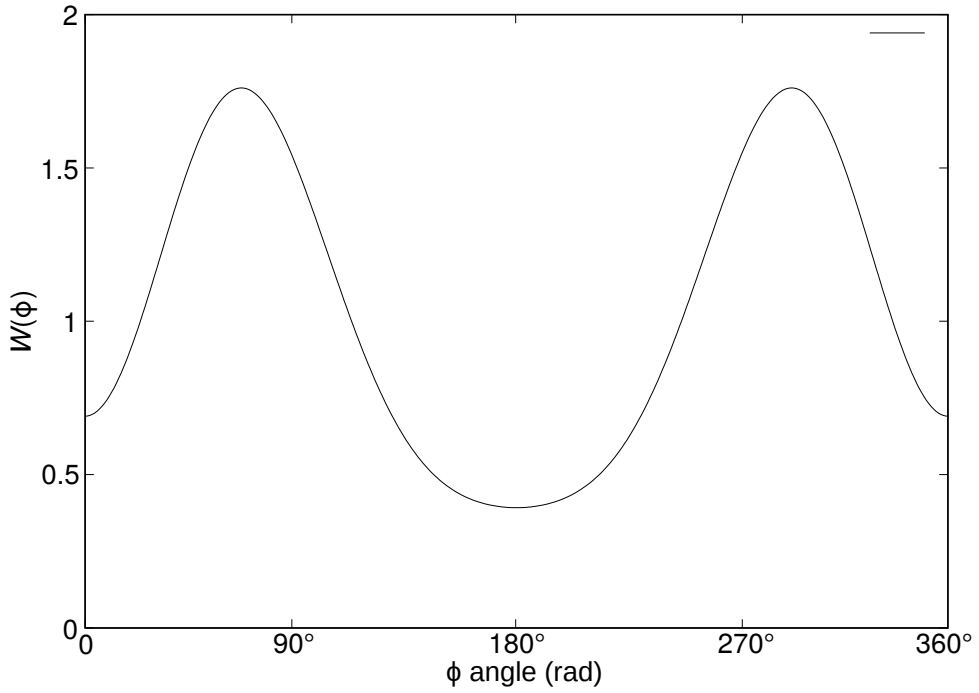

FIGURE 2.6: Example $2^+ \rightarrow 0^+$ angular correlation after Coulomb excitation in inverse kinematics (heavy beam, light target). The decaying nucleus is scattering at a small angle ($\theta_p < 10°$). The angular correlation is around the ϕ angle for a fixed angle $\theta = 45°$. Note the strong anisotropy present in the distribution.

Winther and de Boer developed a computer program that is able to compute the statistical tensor from supplied impact parameter information [4]. Using this program, the alignment of the excited nuclear state after Coulomb excitation, in the form of the statistical tensor, ρ_{kq}, for a given experimental setup can be obtained. In this thesis, the first-excited 2^+ states in even-even nuclei have been studied using Coulomb excitation, resulting in a $0^+ \rightarrow 2^+ \rightarrow 0^+$ transition sequence. The γ-ray angular correlation for such a transition sequence is calculated by

$$W(\theta_p, \theta_\gamma, \Delta\phi) = \sum_{kq} \sqrt{2k+1}\rho_{kq} A_k(L = 2; L' = 2; I_f = 0; I_i = 2) D^{k*}_{q,0}(\Delta\phi, \theta_\gamma, 0), \quad (2.13)$$

where k and q are even integers, $0 \leq k \leq 2L$ and $-k \leq q \leq k$, ρ_{kq} is the statistical tensor, L and L' are the two γ-ray multipolarities $E2$ and $M1$ in a mixed transition, and $D^{k*}_{q,0}$ is the complex conjugate of the rotational matrix that specifies the angular position of the γ-ray detector. $D^{k*}_{q,0}$ is equivalent to a spherical harmonic, and reduces to the Legendre-polynomial terms in cases where there is azimuthal symmetry around the θ and ϕ angles. The A_k coefficient is determined by

$$A_k(LL'I_2I_1) = \frac{1}{1+\delta^2}\{F_k(LLI_2I_1) + 2\delta F_k(LL'I_2I_1) + \delta^2 F_k(L'L'I_2I_1)\}, \quad (2.14)$$

where δ is the mixing ratio between the two multipolarities, and

$$F_k(LL'I_2I_1) = (-)^{I_1+I_2-1}\sqrt{(2L+1)(2L'+1)(2I_1+1)(2k+1)} \times \begin{pmatrix} L & L' & k \\ 1 & -1 & 0 \end{pmatrix} \begin{Bmatrix} L & L' & k \\ I_1 & I_1 & I_2 \end{Bmatrix}, \quad (2.15)$$

where the round brackets represent a Wigner $3J$ symbol and the curly brackets represent a Wigner $6J$ symbol.

This definition of F_k is the generalised form used in Ref. [5], adopted as the γ-ray angular correlation technique matured to maintain phase consistency between different theories [183]. If instead of a mixed-multipole transition, a pure multipole transition is observed (which is the case for a $0^+ \rightarrow 2^+ \rightarrow 0^+$ transition sequence after Coulomb excitation [6]), Eq. (2.13) simplifies to

$$W(\theta) = \sum_{kq} \sqrt{2k+1}\rho_{kq}F_k(L=2; I_f=0; I_i=2)D^{k*}_{q,0}(\phi,\theta,0), \quad (2.16)$$

where

$$F_k(LI_2I_1) = (-)^{I_1+I_2-1}(2L+1)\sqrt{(2I_1+1)(2k+1)} \begin{pmatrix} L & L & k \\ 1 & -1 & 0 \end{pmatrix} \begin{Bmatrix} L & L & k \\ I_1 & I_1 & I_2 \end{Bmatrix}. \quad (2.17)$$

An example angular correlation for this transition sequence is shown in Fig. 2.6.

When performing a measurement, one must also consider the finite size of the γ-ray and particle detectors being used. For a particle detector an additional numerical-integration step can be performed to average the statistical-tensor calculation across the particle-detector's active area, as it varies slowly with small changes in angle. For γ-ray detectors, the solid angle of the detector results in an attenuation of the anisotropy in the measured angular correlation. Taking this into account, the angular correlation formula becomes

$$W(\theta,\phi) = \sum_{kq} \sqrt{2k+1}\rho_{kq}Q_kF_kD^{k*}_{q,0}(\phi,\theta,0), \quad (2.18)$$

where $Q_k = J_k/J_0$ is the solid-angle attenuation factor [184], dependent on the γ-ray energy, detector type and detector geometry. In its simplest form, for a cylindrical detector:

$$J_k = \int_0^{\gamma} P_k(\cos\beta)(1-e^{-\mu x(\beta)})\sin\beta d\beta, \quad (2.19)$$

where γ is the half-opening-angle subtended by the detector, β is the angle of the γ-ray relative to the detector axis, P_k is a k-order Legendre polynomial of $\cos\beta$, μ is the γ-ray absorption coefficient for the detector material, and $x(\beta)$ is the distance traced through the detector by the γ ray at angle β. The Q_k coefficient was originally derived in 1953 by Rose [184], and has become a standard correction in γ-ray spectroscopy techniques [192]. In this thesis, the Q_k coefficients were evaluated using Krane's formulation for coaxial Ge detectors [128].

Finally, the perturbation or attenuation due to the influence of an external electromagnetic field on the angular correlation must be included. This was originally introduced by Goertzel [see Eq. (2.2)], but was reformulated and refined for experimental applications by Abragam and Pound [1]. They introduce the symbol G_k into the angular correlation to represent the external-field perturbation, giving

$$W(\theta,\phi) = \sum_{kq} \sqrt{2k+1}\rho_{kq} G_k Q_k F_k D^{k*}_{q,0}(\phi,\theta,0). \tag{2.20}$$

The external-field perturbation, G_k, may be a time-average or time-integral quantity, or it may be a time-dependent function, $G_k(t)$, depending on the experiment being performed.

In conclusion, through the combined efforts of many researches through the mid-20$^{\text{th}}$ century, from Hamilton's original derivation of the W function through to Alder and Winther's formalism for calculating nuclear alignment after Coulomb excitation, nuclear physicists can reliably and accurately predict γ-ray angular correlations from pure Coulomb-excitation reactions. The capability to calculate angular correlations has allowed a great deal of nuclear-structure research to be performed by measuring γ-ray cascades after radioactive decay and Coulomb excitation reactions, and is the basis for several nuclear spectroscopic techniques in use today. Attention is now turned to such measurement techniques.

2.3 Nuclear Dipole Moments

As discussed in §2.1.2, the nucleus has several properties. Amongst these is the nuclear magnetic dipole moment, μ. It is often reported as the g factor, being the ratio of the magnetic moment to the nuclear spin, $g = {}^{\mu}/_{I} \times {}^{\hbar}/_{\mu_N}$, where μ_N is the nuclear magneton and $\hbar$ is the reduced Planck constant. In order to understand the origin of the magnetic moment, recall that the overall nuclear spin arises from the individual or collective motion, that is the angular momentum and intrinsic spin, of its nucleons. In classical physics, the motion of a charge creates a magnetic field, and circular motion creates a magnetic dipole. The angular momentum of the protons will therefore produce a magnetic dipole moment. In addition to proton angular momentum, the intrinsic quantum spin of both protons and neutrons also generates a magnetic moment that contributes to the overall magnetic moment of the nucleus. Nucleons have their own magnetic dipole moments because they are composed of three quarks. This sub-nucleonic structure gives rise to the intrinsic spin quantum number $s = {}^{1}/_{2}$ and a resulting magnetic dipole moment for both the charged proton, $\mu_p = 2.793\mu_N$, and uncharged neutron, $\mu_n = -1.913\mu_N$ [127]. Together, in a nucleus, the intrinsic magnetic moments of the nucleons and the protons' orbital motion combine to produce a net magnetic dipole moment of the nucleus.

As suggested by the above discussion, the nuclear magnetic dipole moment can be broken down into contributions from the orbital (L) and spin (S) angular momenta of the protons and neutrons. The orbital component depends on the angular momentum of individual protons (l_p) and neutrons (l_n) while the spin component depends on their intrinsic magnetic moments. The nuclear magnetic moment can be separated into a proton and a neutron component: $\mu = \mu_p + \mu_n$ with $\mu_p = g_{l,p}\langle L_p \rangle + g_{s,p}\langle S_p \rangle$, where $g_{l,p}$ and $g_{s,p}$ are the proton orbital and spin g factors, and $\mu_n = g_{l,n}\langle L_n \rangle + g_{s,n}\langle S_n \rangle$, where $g_{l,n}$ and $g_{s,n}$ are the neutron orbital and spin g factors. The magnetic moment of a single free nucleon with angular momentum $j = l \pm s$ is calculated by [127]

$$j = l + \frac{1}{2}, \quad \langle \mu \rangle = [g_l(j - \frac{1}{2}) + \frac{1}{2}g_s]\mu_N, \tag{2.21}$$

$$j = l - \frac{1}{2}, \quad \langle \mu \rangle = [g_l \frac{j(j+\frac{3}{2})}{j+1}\frac{1}{2}\frac{1}{j+1}g_s]\mu_N, \tag{2.22}$$

where g_l and g_s are the orbital and intrinsic-spin g factors, respectively.

Nucleon magnetic moments calculated using Eqs. 2.21 and 2.22 are referred to as Schmidt values. Comparison with odd-A nuclei reveals that the true values for nucleons

bound in nuclei tend to fall between $l \pm s$, indicating that g_s is reduced from the free-nucleon value. Meson-exchange currents and the local influence of nearby nucleons are suspected to cause this reduction from free-nucleon values [127]. Therefore, a reduced value, g_s^{eff}, is used, set depending on the model and orbital space being considered. For even-even nuclei modelled using the collective vibrational model (see §2.1.3), excited nuclear states are expected to have $\langle \mu \rangle / I\mu_N = Z/A$ [127]. This is due to the assumption that nucleons are all paired (cancelling any intrinsic-spin contribution), and all couple to the orbital angular momentum (leaving only the orbital component coupled to spin I). The effective values for g_l are typically $g_{l,p} \simeq 1$ and $g_{l,n} \simeq 0$, meaning

$$\langle \mu \rangle / \mu_N = I \frac{\sum^{Z} g_{l,p} + \sum^{N} g_{l,n}}{Z+N} = I \frac{Z}{A}. \tag{2.23}$$

Measurements tend to be reduced from this theoretical value, as much as 30%, indicating that these assumptions are not completely valid. The shell-model aims to take a middle approach, building the nuclear state from single-particle states all coupling to give expectation values for the components of angular momentum, $\langle L_{p,n} \rangle$, and intrinsic spin, $\langle S_{p,n} \rangle$. Assuming $g_{l,p} = 1$ and $g_{l,n} = 0$, the formula for calculating the nuclear g factor is

$$\langle \mu \rangle / I\mu_N = g = (\langle L_p \rangle + g_{s,p}^{\text{eff}} \langle S_p \rangle + g_{s,n}^{\text{eff}} \langle S_n \rangle) / I. \tag{2.24}$$

In the multiconfiguration shell model, the difference between μ_p and μ_n gives sensitivity to the differing contribution of proton and neutron configurations in nuclear magnetic dipole moments. The pairing force, discussed in §2.1.2, causes nucleons to pair up with antiparallel spin, giving no net contribution to the magnetic moment from the paired nucleons. When they are in their ground state, this results in nuclei with even numbers of protons and neutrons (even-even) having $\mu_Z = 0$ and no net angular momentum ($I = 0$). When a nucleus has an odd number of protons, neutrons, or both, the nucleus has $I > 0$ and $\mu \neq 0$. Another instance where $I > 0$ and $\mu \neq 0$ occurs is when an even-even nucleus is excited from its ground state to states with $I \neq 0$. With $\mu \neq 0$, interactions with magnetic fields can now be measured.

To measure the nuclear g factor, the magnetic moment, $\overrightarrow{\mu}$, of the nucleus must interact with an external, quantifiable field. The interaction with the field is revealed in the resultant energy shift $\overrightarrow{\mu} \cdot \overrightarrow{B}$, or via the torque applied to the nuclear spin $\overrightarrow{\mu} \times \overrightarrow{B}$, which causes the nucleus to precess. The strength of this interaction allows for the determination of the g factor. For long-lived or stable nuclei, the external field can be weak (sub-Tesla strength) and the resulting precession frequency small (to the order of Hertz

or less). The γ-ray angular correlation of an oriented nuclear state will be perturbed by such interactions, as described in §2.2.1. For nuclei with lifetimes down to the nanosecond range, macroscopic magnetic fields produced in the lab (several Tesla) are sufficient to induce a measurable precession of the aligned nuclear spin. For nuclear states with picosecond lifetimes, such as most first-excited 2^+ states, near kilo-Tesla strength magnetic fields are required to induce measurable precessions. Such fields cannot be produced macroscopically, but arise in hyperfine interactions between the nucleus and atomic electrons. Three sources of such strong fields, which have been employed for g-factor measurements, are the hyperfine field experienced by a moving ion within a ferromagnetic solid (transient field), the field between the ions and a ferromagnetic solid once they come to rest (static field), and the hyperfine field present in highly-charged free ions. Techniques utilising these hyperfine fields for g-factor measurements are described in the following subsections.

2.3.1 Perturbed Angular Correlations after Ion Implantation in Polarised Ferromagnetic Materials

The perturbation arising from the interaction of an aligned nuclear state with an external magnetic field provides a valuable method to probe the magnetic dipole moment of excited nuclear states. The strength of the hyperfine interaction experienced by nuclei implanted into a polarised ferromagnetic host is of the order of tens to hundreds of Tesla. The strength of these static hyperfine fields, combined with the strongly anisotropic angular correlations obtained via Coulomb excitation, provides the capability to induce small but measurable precessions ($\Delta\theta \lesssim 2^\circ$) in excited nuclear states having lifetimes of the order of picoseconds [93]. This is referred to as the ion-implantation perturbed angular correlation (IMPAC) techique. In this technique a lighter beam ion, colliding with a heavier target nucleus, is used to recoil-implant the target into a ferromagnetic backing foil. The beam ion Coulomb-excites the target nucleus, and is detected back-scattered in coincidence with de-excitation γ rays from the target nucleus. The target nucleus, with its spin aligned by the Coulomb interaction, rapidly ($\sim$ 1 ps) stops in the ferromagnetic foil and the spin-alignment precesses due to the interaction of its magnetic moment with the static hyperfine field. The precession arising from the interaction is given by [114]

$$\Delta\theta_{\mathrm{SF}} = -g\frac{\mu_N}{\hbar}B_{\mathrm{SF}}\tau e^{-t_s/\tau}, \tag{2.25}$$

where g is the nuclear g factor of the state, μ_N is the nuclear magneton, $\hbar$ is the reduced Planck constant, τ is the lifetime of the state, B_{SF} is the static-hyperfine-field strength, and t_s is the stopping time. Because the measurement is time-integral, the interaction becomes appreciably attenuated in cases where the stopping time is larger than, or

similar in magnitude to, the nuclear state's lifetime.

Grodzins' 1968 review [93] covering this technique examined measurements across several nuclei using this technique, and an alternative technique in which nuclei are able to decay *in situ*, i.e. without being recoil-implanted. A comparison of measurements between the two techniques (implantation versus *in situ*) revealed the presence of an additional component in IMPAC measurements, which in these cases had sign opposite to that of the static hyperfine field. Because the hyperfine-field strength experienced by Ge nuclei at rest in iron is quite small ($\sim$ 7 T) [180], Ge nuclei made for a good candidate to study this additional component. IMPAC measurements on the stable, even-even Ge isotopes indicated that this additional component acts on sub-picosecond timescales, as there was no lifetime dependence across the isotopic chain, covering lifetimes ranging from 2–26 ps [179]. These two pieces of evidence indicated that this additional component originates from a *transient hyperfine field*, which acts as the ions slow in the ferromagnet. The transient field was found to always have a positive sign (aligned with the polarisation of the ferromagnet), whereas the static field may be positive or negative. This means it may enhance or reduce the apparent static-field strength, depending on the sign of the static field. Including this transient field in Eq. (2.25), the measured precession becomes [114]

$$\Delta\theta = g\frac{\mu_N}{\hbar}\left(B_{\mathrm{SF}}\tau e^{-t_s/\tau} - \int_0^{t_s} B_{\mathrm{TF}}[v(t)]dt\right), \tag{2.26}$$

where $B_{\mathrm{TF}}(v)$ is the velocity-dependent transient hyperfine field, and $v(t)$ is the ion velocity at time t. The integral represents the transient-field interaction over the stopping time, which gives rise to a small rotation that acts like an impulse as the ion stops.

In the technique's initial use it was assumed that the static field achieved full strength once the ion stopped. However, there were early hints that the rare-earth elements experienced some lifetime-dependent quenching of the static hyperfine field [93]. It wasn't until the mid-to-late 1990s, three decades after the popularisation of IMPAC, that Stuchbery, Anderssen and Bezakova [9, 220] demonstrated the presence of a quenching effect in the static hyperfine-field interaction in IMPAC measurements across multiple distinct nuclear regions. In IMPAC, the static field does not achieve full strength until the implanted ion comes to rest and the surrounding environment reaches local thermal equilibrium below the Curie temperature. Stuchbery and Bezakova argued that the energy deposited at the implantation site causes a thermal spike, sufficient to induce localised melting of the host. This quenches the static field for several picoseconds. If this is the case, then IMPAC measurements should reveal a reduction of the static-field strength proportional to the lifetime of the probe state. Analysis of IMPAC measurement data revealed that there was a reduction in the static-field strength, indicating a pre-equilibrium

quenching time $t_e \sim 10$ ps. This pre-equilibrium quenching is taken into account by substituting B_{SF}, in Eq. (2.26), with [220]

$$B_{\mathrm{SF}} \rightarrow B_{\mathrm{eff}} e^{-t_e/\tau}, \tag{2.27}$$

where B_{eff} is the effective static-hyperfine-field strength, which may contain radiation-damage effects or other influences and therefore may be a reduced value compared to that found by other methods, and $t_e = 7.3(8)$ ps is the thermal-spike lifetime, as deduced in Ref. [220].

In addition to the observed attenuation owing to the stopping time of the ion, and that arising due to the thermal spike, the effective hyperfine-field strength may also be reduced from its nominal value due to ions coming to rest in non-substitutional sites in the ferromagnetic crystal lattice. While there are loose rules defining the likelihood of a substitutional implantation (the ion comes to rest in the crystal lattice and experiences the full hyperfine field), these generally must be assessed in a case-by-case manner. As such, the static hyperfine-field strength used in Eq. (2.25) may actually be further reduced from its full value, introducing more uncertainty to the analysis of IMPAC measurements. These issues of field-strength reduction owing to the thermal-spike lifetime are significant to states with lifetimes $\tau \lesssim t_e \sim 10^{-11}$ s. When applied to longer-lived states ($\tau \gtrsim 10^{-9}$ s) the effect of the thermal-spike quenching becomes negligible, and instead the non-substitutional fraction becomes the most significant contributor to a reduced hyperfine-interaction strength.

The magnitude of the transient-field effect encountered in IMPAC measurements is a quantity which, during the late 1960s and early 1970s, was challenging to quantify. However, its study led to an entirely new technique by which the magnetic moment of short-lived nuclear states could be probed in a more reliable manner. This technique will now be discussed.

2.3.2 The Transient-Field Effect in Polarised Ferromagnetic Materials

The transient-field (TF) effect arises from an ion-solid interaction occurring for ions moving swiftly through an externally polarised ferromagnetic material. It produces a net magnetic field at the nucleus of these moving ions. It was found that for ions having $Z \lesssim 20$ traversing a ferromagnetic foil with $v_0 < v < Zv_0$, where $v_0 = c/137$ is the Bohr velocity, v is the ion velocity and Z is the atomic number, the strength of the field is of the order of $\sim Z \times 10$ T [191]. This magnitude makes it useful for probing states that interact over picosecond time periods. When aligned nuclei interact with the TF it induces a measurable precession in the spin alignment, causing a perturbation of the

γ-ray angular correlation, which manifests as an angular rotation, $\Delta\theta \simeq 10^{-2}$ rad, over the picosecond interaction time. Since the late 1970s researchers have been studying the TF effect, and utilising it for nuclear dipole-moment measurements, particularly for states with short lifetimes ($\lesssim 10^{-9}$ s) [22].

One of the first hints of the TF effect appeared in a 1966 paper by Grodzins, Borchers and Hagemann [94], then at the Neils Bohr Institute. Using the IMPAC technique (prior to the identification of the transient-field component) they measured the sign of the effective field acting on ^{156}Gd implanted into iron to be opposite to that obtained by non-implantation methods. Later that year, Borchers, Grodzins *et al.*, now of the MIT-Wisconsin group, measured even-A Te ions implanted into iron [29]. They noted inconsistencies between measured hyperfine-field strengths using implantation versus non-implantation methods, and a correlation between nuclear-state lifetimes and measured g factors. Their measurement of anomalously large g factors ($\sim$ 2$\times$ the expected collective Z/A trend) for the Te isotopes led them to propose the presence of a transient field that acted upon the ions as they slowed. Borchers *et al.* subsequently conducted a study of precession angles in nuclei spanning $42 \leq Z \leq 52$ after implantation into Fe, Ni, Co, Gd or Cu foils, and discovered a magnetic field acting upon fast-moving ions in externally polarised ferromagnetic foils [28]. The field was found to be proportional to the ferromagnetic medium's polarised-electron density. They proposed a mechanism by which the field arises due to the capture of polarised electrons by the moving ion from the ferromagnetic host. Soon after, Lindhard and Winther proposed an alternative mechanism to model this phenomenon, in which polarised electrons in the host scatter off the bare charge of the moving nucleus [136]. Their model predicted $B \propto Zv_0/v$. Shortly after, other groups began to observe deviations from Lindhard and Winther's model at higher velocities [59, 81, 82, 90, 101], where the field strength was observed to vary linearly, rather than inversely, with velocity. This led to the revival of the electron-capture mechanism, and consideration of other possibilities.

In the mid-1970s, Eberhart *et al.* observed the TF's linear-velocity dependence for intermediate-velocity Si ions [59], and they revived the mechanism originally suggested by Borchers *et al.* [28], by which the TF effect arises due to the polarised s-orbital electron picked up from the host. In this scenario the TF strength can be expressed, microscopically, as [54, 60]

$$B(v) = \sum_n F_1^{ns}(v)\xi^{ns}(v)B_{ns}, \tag{2.28}$$

where there is a sum over all relevant s-orbital electrons in shells n, $F_1^{ns}(v)$ is the fraction of unpaired n-shell s-orbital electrons at velocity v, ξ^{ns} is the degree of polarisation of these unpaired electrons, and B_{ns} is the Fermi-contact magnetic field experienced by the

nucleus from a single ns electron.

The TF effect is only useful when ions traverse ferromagnetic media with velocity $v_0 < v \lesssim Zv_0$, as above Zv_0 the ion becomes fully stripped and the TF effect decreases significantly. However, across this entire range the degree of ionisation is constantly changing. Consequently, the ion-solid interactions are complex. The task of understanding these interactions is further obscured by a poor understanding of the charge-state distribution of swift ions in solids, and low-velocity stopping of heavy ions. This makes understanding which electrons are contributing to the interaction difficult to model. However, investigations have been undertaken to help understand the varying electron contributions. When recoiling at a few percent of the speed of light, light ions ($Z \lesssim 10$) do not bind their electrons as strongly as heavier ions. As such, light ions will tend to have the $1s$ (K-shell) electron polarised, while heavy ions will have an s-orbital electron at higher n polarised, varying as a function of Z. Eberhart *et al.* [59] estimated that $2s$ electrons were largely responsible for observed precessions in Si recoiling below $3.4v_0$. Later, Dybdal, Eberhart and Rud [54] performed measurements of K-shell ($1s$) vacancies in Si ions recoiling through nickel with $3.9v_0 \leq v \leq 9.0v_0$, and found vacancy fractions of $2-23\%$. Häusser *et al.* [104] determined that for ^{207}Pb ions recoiling between $2.4v_0 \leq v \leq 10.2v_0$ the $4s$ electron was the dominant contributor to the TF. However, there are particular cases in which the moving ion's s-orbital energy is almost equal to that of a particular host electron orbital, as observed for flourine in iron [54], or platinum in iron [211]. In these cases, some fraction of the vacancies being created in the active ns orbit of the moving ion instead go to the host, reducing the net transient-field strength and causing an apparent discontinuity in field strength versus Z. It should be noted that this effect has not been observed for gadolinium hosts, making gadolinium an attractive choice in cases where these discontinuity effects may be present for other host elements.

Due to the ion-solid interactions being poorly understood, the evaluation of Eq. (2.28) from first principles is yet to be achieved. Instead, characterisation of the TF strength for these swift ions has led to the development of four commonly used parameterisations. As these parameterisations were fitted using data sets with distinct velocity ranges and atomic number, it is a natural consequence that they have concluded different relationships as the number of bound electrons changes. Research performed by Eberhardt *et al.* led to the characterisation of a TF strength that was linearly dependent on the ion velocity and atomic number [58, 60]. They proposed

$$B(v, Z) = aZR(Z)v/v_0, \tag{2.29}$$

where Z is the atomic number of the ion, $R(Z) = 1 + (Z/84)^{5/2}$ is a relativistic correction

factor, v is the ion velocity, $v_0 = c/137$ is the Bohr velocity and $a = 11.2(3)$ T is a fitted parameter [58], obtained from available data using fully-magnetised iron hosts. Please note that the uncertainty in a is statistical-only.

Eberhart's linear model argues for a TF mechanism whereby an unpaired, polarised s-shell electron, bound to the moving ion, is responsible for the field [59, 231]. Such polarised electrons are present due to two interactions: atomic spin-exchange interactions (an electron-spin interaction of the ion with polarised electrons of the host transfers polarisation to the ionic electrons); and electron capture-loss processes particular to each ferromagnet [54, 151].

Around this time the newly identified linear dependence of the TF strength on ion velocity motivated the Rutgers group to develop what is known as the thin-foil TF technique, to perform precession measurements free from the static-field effect [33, 34, 102, 191]. Using this method, and systematic measurements mainly on Sm ions in iron, they discovered that the velocity dependence was not linear over the range $2v_0 \lesssim v \lesssim 7v_0$, and proposed a non-linear parameterisation for the field strength

$$B(v, Z) = a' Z^{P_z} (v/v_0)^{P_v} \mu_B N_p, \tag{2.30}$$

where a', P_z and P_v are free-fitted parameters, μ_B is the Bohr magneton and N_p is the polarised-electron density (electrons/cm^3), a value particular to the ferromagnetic element [34, 191]. Together, $\mu_B N_p$ gives the magnetisation of the ferromagnetic foil. The free-fitted parameters were empirically determined to be $a' = 96.7(16)$, $P_z = 1.1(2)$ and $P_v = 0.45(18)$ [191], fitted to precession measurements using elements ranging from O to Sm traversing iron hosts. Measurements of ^{82}Se traversing a gadolinium host were also considered. It was concluded from the ^{82}Se in gadolinium data that these same parameters apply for gadolinium hosts [22], except that the difference in strength is due to gadolinium having a stronger magnetisation (larger N_p) than iron. However, marked deviations from this assumption have since been found [48].

The Chalk River group, exploring the TF effect using the rare-earth elements Tm and Yb, also found an enhanced effect as compared to the Lindhard-Winther model [228]. Further work involving several isotopes of Sm and Gd, along with the analysis of Dy, Tm and Yb isotope data allowed the characterisation of the TF effect in this nuclear region [11, 103]. This led to the proposal of the TF strength for heavy ions recoiling at $1.5v_0 \leq v \leq 6.5v_0$ to be

$$B(v, Z) = a'' Z (v/v_0) e^{-\beta v/v_0}, \tag{2.31}$$

where a'' and β are free-fitted parameters [11]. In their fitting approach, β was first loosely fitted and then set to a fixed value, as a'' and β are correlated. The free-fitted parameters were empirically determined to be $a'' = 19.0(5)$ T for $\beta = 0.12$ in iron hosts [11], and $a'' = 28.1(17)$ T for $\beta = 0.135$ in gadolinium hosts [104].

In recent years Stuchbery [208] developed a TF parameterisation for low-Z ions at high velocities ($v > {}^1/_2 Z v_0$). This parameterisation was obtained by fitting a range of data for ions with $6 \leq Z \leq 16$ in both iron and gadolinium hosts. Stuchbery proposed the parameterisation

$$B(v, Z) = AZ^P (v/Zv_0)^2 e^{-\frac{1}{2}(v/Zv_0)^4}, \tag{2.32}$$

where the magnitude, A, and Z-dependence, P, are fitted parameters, being $A = 1.82(5)$ T and $P = 3$ for iron hosts, and $A = 26.7(11)$ T and $P = 2$ for gadolinium hosts. This parameterisation accounts for the decrease in the TF strength when the ion velocity exceeds Zv_0, at which point few to no electrons remain bound to the ion, making it suitable for high-velocity measurements.

As noted, the discovery that the TF strength increases with velocity led to the development of the thin-foil TF method, pioneered by the Rutgers group [191]. These experiments were performed in conventional kinematics (light beam, heavy target). Beam particles are back-scattered from a target of interest, which has been evaporated onto a ferromagnetic foil, thin enough for the recoiling ions to traverse without stopping, and backed by copper or lead, which provides a field-free environment for recoiling ions to stop in. The back-scattered beam is detected in coincidence with γ rays emitted from the target nuclei, which have recoiled through the ferromagnetic layer and stopped in the field-free backing. This method has been utilised extensively, and with great success, to measure the g factors of picosecond-lifetime nuclear states across the nuclear chart [22]. During the late 1990s a variation on this technique, the inverse-kinematics thin-foil TF method, came into favour due to advances in ion-source and accelerator capability, along with the possibility of using radioactive ion beams [22]. These measurements are performed in inverse kinematics (heavy beam, light target), in which the heavy beam, consisting of the ions of interest, impinges upon a lighter target (e.g. carbon), with recoiling target ions then detected after being forward-scattered. The target layer is backed by the ferromagnetic material, and usually a stopping layer. For nuclei having $A \lesssim 100$ this allows for somewhat higher ion velocities to be achieved during transit of the ferromagnetic host, equating to a stronger TF and larger precession effect. Additionally, due to kinematic focusing, the particle-detection solid angle is much larger in the equivalent centre-of-mass frame. These factors allow for precise measurements with relatively little statistical uncertainty, leaving primarily the uncertainty in the

transient-field calibration as a significant source of error.

Efforts to understand the TF effect have revealed a dependence upon ion velocity and atomic number that, generally, changes smoothly with Z for intermediate-velocity ions, particularly in gadolinium hosts. This means that, even if the absolute scale of the TF strength is unknown, it can be used to scale values relative to an already-known state. Consequently, isotopic chains can be measured efficiently and reliably, relative to a single absolute measurement for one isotope. However, there are some caveats to this approach. The first is that the TF doesn't *always* scale smoothly across a given Z range, or between neighbouring elements, allowing for considerable deviations from the parameterisation [48, 55, 209, 211, 217, 218, 219]. Therefore, if the TF behaviour of an element is unknown, it may not be reliable to calibrate it using a different element. The measurement is also more reliable when the velocity range of the relative measurements is the same or very similar. This reduces uncertainties due to the velocity-dependence of the TF. There are also uncertainties caused by localised reductions in magnetisation that arise from temperature changes and microscopic damage to the host [22, 195]. Considering these issues, the most reliable relative measurement should be made between nuclei of the same, or similar Z that are not near to observed or expected discontinuities in TF strength versus Z, at the same energy, in the same target, with the most ideal scenario being a simultaneous measurement of isobaric nuclides. This means the effect will scale the same for the two cases, and the measured effect ratio should depend only on the g factors and, to a lesser extent, the lifetimes of the nuclear states. As such, selecting an appropriate parameterisation and performing a measurement relative to a known state allows for reliable measurements, while minimising uncertainty due to the TF parameterisation itself.

With recent advances in shell-model calculations of nuclear g factors, precise and accurate experimental g factors are required to probe nucleon-nucleon interactions and test these new predictions [159]. However, due to the aforementioned issues of uncertainty in the TF's absolute magnitude, many TF measurement results are better considered as relative measurements. For nuclei in regions far away from independently determined g-factor measurements, the issue becomes one of finding a suitable method to determine the absolute g-factor values without relying on a parameterisation. As particular elements have already been identified as having unexpected TF behaviour, it is unsafe to assume a parameterisation is correct without being studied relative to an independently established reference. Therefore, absolute independent measurements for nuclei in the aforementioned regions are desirable, so that past measurements via the TF method on these nuclei can be scaled accurately, and future measurements can be made confidently.

2.3.3 Hyperfine Interactions in Recoiling Ions

In Alder's reformulation of the angular-correlation W function [3] the perturbation arising from the hyperfine interaction, introduced by Goertzel [89], was also included. Using Alder's formulation of the angular correlation, Abragam and Pound introduced time dependence to the perturbing component and examined its different forms in particular media: crystalline powder, solid crystals, free atoms/ions, and liquids [1]. They introduced the term G_k to the angular correlation, being the change in anisotropy in the γ-ray angular distribution due to the dipole and quadrupole interactions. In the late 1960s Ben Zvi *et al.* performed experiments to observe the perturbation of the angular correlation from excited 2^+ nuclear states recoiling into low-density gas or vacuum [21]. The hyperfine field, H, acts on the total angular momentum vector F, resulting from the coupling of the isolated nuclear (I) and atomic (J) spin-vectors. The vector coupling is depicted in Fig. 2.7. Two possibilities are proposed for this interaction: the quantity F rapidly fluctuates due to atomic transitions, which also causes the hyperfine-field strength to vary around a mean value, $\overline{H}$, or a large number of static fields up to the limit of large F contribute to a mean hyperfine-field strength $\overline{H}$. If the former case is true, they argued that this fluctuation would result in a perturbation similar to that in liquid. Using Abragam and Pound's formulation for perturbation in a liquid (referred to as the stochastic model), they proposed

$$G_k(t) = e^{-p_k \omega^2 \tau_c t}, \tag{2.33}$$

and

$$G_k = \frac{1}{\tau}\int_0^\infty G_k(t) e^{-t/\tau} dt = \frac{1}{1 + p_k \omega^2 \tau \tau_c}, \tag{2.34}$$

where τ_c is the correlation time (being, in the fluctuating model, the average lifetime of an atomic state) and τ is the nuclear lifetime. For nuclei having $I = 2$, which were studied, $p_0 = 0$, $p_2 = 2$ and $p_4 = 20/3$ for the hyperfine interaction with the nuclear magnetic dipole moment and

$$\omega = \mu_N g \overline{H}/\hbar, \tag{2.35}$$

where μ_N is the nuclear magneton, $\hbar$ is the reduced Planck constant, g is the nuclear g factor and $\overline{H}$ is the mean hyperfine-field strength. Abragam and Pound's model indicates that a hyperfine interaction with the nuclear electric quadrupole moment should also be present, but Ben Zvi *et al.* reported the noteworthy result that, even in the case of strong quadrupole deformation, the quadrupole interaction is absent during the recoil [21]. As such, it has since been largely disregarded, and was not included here.

A comparison of the fluctuating versus static models was unable to distinguish which produced a better fit to the G_k values determined from the measurement [21]. Another

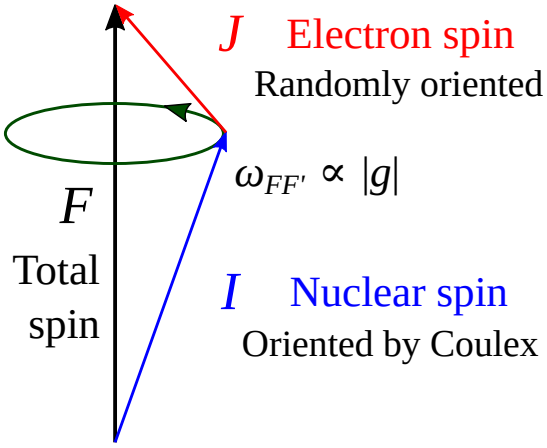

FIGURE 2.7: Vector coupling between the nuclear (I) and electron/atomic (J) spins, combining such that $F = I + J$. The dipole interaction results in a precession about F for any given combination of magnetic substates in I and J with angular frequency $\omega_{FF'}$ [see Eq. (2.39)].

measure available to them was to plot $\omega^2\tau\tau_c$, from the denominator of Eq. (2.34), against τ to verify if the fluctuating model was correct, or $\omega^2\tau^2$ (as $\tau_c = \tau$ in the static model) against τ to verify if the static model was correct. In this comparison the fluctuating model was clearly the better fit to all available data. By measuring the attenuation of angular correlations after Coulomb excitation, and calibrating $\overline{H}$ and τ_c using the known g factor of the 2_1^+-state in ^{152}Sm, they were able to determine the g factors of the excited 2_1^+ states in ^{150,154}Sm and ^{148,150}Nd by fitting G_k values to the measured angular correlations.

A decade later, Goldring *et al.* [92] compared the perturbation observed between varying gas pressures, and vacuum. This paper was motivated by the fitted correlation time ($\tau_c \approx 4$ ps) from Ref. [21] being much smaller than the expected average atomic lifetime ($\overline{\tau_{\text{atomic}}} \sim 10 \times \tau_c$ ps). By reanalysing the data using the static model, they obtained a much longer correlation time, $\tau_c = 150$ ps, more in line with the expected average atomic-state lifetime. This longer correlation time was used to explain the differences observed between the quenching of the hyperfine interaction between ^{152}Sm and ^{150}Sm at increasing gas pressures, a phenomenon that was inexplicable in the fluctuating model alone. The new approach was also able to explain the previous measurements by Ben Zvi *et al.*, provided that the distribution of static fields was broad enough. What they concluded is that the large number of static fields that can originate from the excited atomic states, contributing over the short timescales probed, gives much the same result as a fluctuating field.

Goldring went on to present a formal treatment of the perturbation [91], bringing together the experimental results of many authors. This formalism is as follows.

After recoil into vacuum, the atomic system can be described by a statistical tensor, $\rho_{kq}(J)$. The hyperfine interaction couples the atomic and nuclear ($\rho_{kq}(I)$) systems, producing a system described by the coupled statistical tensor, $\rho_{kq}(FF')$. The tensors are coupled within the range $|I-J| \leq F, F' \leq I+J$, which takes into account all possible couplings of I and J to F, using standard angular-momentum and spherical tensor coupling formulae:

$$\rho_{kq}(FF') = \sum_{k_i k_j q_i q_j} \rho_{k_i q_i}(I)\rho_{k_j q_j}(J)\hat{F}\hat{F}'\hat{k}_i\hat{k}_j\langle k_i k_j q_i q_j|kq\rangle \times \begin{Bmatrix} I & J & F \\ I & J & F' \\ k_i & k_j & k \end{Bmatrix} \quad (2.36)$$

and

$$\rho_{k_i q_i}(I)\rho_{k_j q_j}(J) = \sum_{FF' kq} \rho_{kq}(FF')\hat{F}\hat{F}'\hat{k}_i\hat{k}_j\langle k_i k_j q_i q_j|kq\rangle \times \begin{Bmatrix} I & J & F \\ I & J & F' \\ k_i & k_j & k \end{Bmatrix}, \quad (2.37)$$

where $|I-J| \leq F, F' \leq I+J$, the angled brackets signify a Clebsch-Gordon coefficient, the curly brackets signify a Wigner $9J$ symbol, and $\hat{X} = \sqrt{(2X+1)}$ where X is the relevant symbol.

The time-dependent perturbation arising from the hyperfine interaction is

$$\rho_{kq}(FF';t) = \rho_{kq}(FF';0)e^{-i\omega_{FF'}t}, \quad (2.38)$$

where

$$\omega_{FF'} = \frac{1}{2}\frac{A_J}{\hbar}[F(F+1) - F'(F'+1)], \quad (2.39)$$

in which A_J is the hyperfine coupling constant for the atomic state. Note that $\omega_{FF'}$ varies for each F, F' coupling, resulting in a superposition of different frequencies when $J > 1/2$. The hyperfine coupling constant is related to the hyperfine-field strength, H, and g factor by

$$A_J = \mu_N g \frac{H}{J}. \quad (2.40)$$

At any time t, the nuclear or atomic statistical tensors can be projected from the coupled tensor by

$$\rho_{k_i q_i}(I;t) = \sum_{FF'} \rho_{kq}(FF';t)\hat{F}\hat{F}'\hat{k}_i \begin{Bmatrix} I & J & F \\ I & J & F' \\ k_i & 0 & k \end{Bmatrix} \tag{2.41}$$

and

$$\rho_{k_j q_j}(J;t) = \sum_{FF'} \rho_{kq}(FF';t)\hat{F}\hat{F}'\hat{k}_j \begin{Bmatrix} I & J & F \\ I & J & F' \\ 0 & k_j & k \end{Bmatrix}. \tag{2.42}$$

In a RIV experiment, $\rho_{kq}(I;t=0)$ is determined by the reaction mechanism (in the present work, Coulomb excitation), and $\rho_{kq}(J;t=0) = 0$ for $k,q \neq 0$ by the assumption that the atomic spin is randomly oriented (isotropic).

Through the hyperfine coupling, $\rho_{kq}(J)$ can become oriented. Due to this, when the atomic state undergoes an unobserved optical transition, there is a deorientation,

$$\rho_{kq}(J_f;t+\delta) = \rho_{kq}(J_i;t)U_k(J_iJ_fL), \tag{2.43}$$

where $t+\delta$ represents the post-transition time, and U_k is the deorientation coefficient due to the unobserved radiation connecting an initial state J_i and final state J_f,

$$U_k(J_iJ_fL) = (-1)^{J_i+J_f+L+k}\sqrt{(2J_i+1)(2J_f+1)} \begin{Bmatrix} J_i & J_i & k \\ J_f & J_f & L \end{Bmatrix}. \tag{2.44}$$

When a cascade of optical transitions occurs, a full treatment should include the deorientation of $\rho_{kq}(J)$ for each transition.

If the optical transitions are ignored, the interaction is assumed to be static, and the atomic system is assumed to be isotropic, then the attenuation of anisotropy in the γ-ray angular correlation arising due to the hyperfine interaction can be isolated as

$$G_k(t) = \sum_{F,F'} C_{IJ}^{FF'}(k)e^{-i\omega_{FF'}t}, \tag{2.45}$$

where the angular-momentum-coupling components of Eq. (2.37) reduce to

$$C_{IJ}^{FF'}(k) = \frac{(2F+1)(2F'+1)}{2J+1} \begin{Bmatrix} F & F' & k \\ I & I & J \end{Bmatrix}^2, \tag{2.46}$$

and $w_{FF'}$ is defined in Eq. (2.39).

Because the imaginary components in the spherical statistical tensor $\rho_{kq}(I)$ cancel when oriented by Coulomb excitation, Eq. (2.45) can be re-written as

$$G_k(t) = \sum_{F,F'} C_{IJ}^{FF'}(k) \cos(\omega_{FF'} t), \tag{2.47}$$

emphasising that the attenuation due to the hyperfine interaction manifests as a superposition of cosine functions, with the number of frequencies being determined by the possible couplings of I and J.

Shortly after the experimental work of Ben Zvi *et al.* in the late 1960s [21], Blume presented a time-dependent formulation of the attenuation coefficient in which an arbitrary number of static interactions may occur in sequence [23]. This was a correction to Scherer's work [186], in which time dependence was introduced to the attenuation coefficient in Abragam and Pound's stochastic model. As the formulation proposed is valid for any correlation time, the approach has been employed to determine the attenuation arising from a sequence of different static interactions. A summary of Blume's treatment now follows.

When multiple atomic states contribute to the deorientation in sequence, their effect is multiplicative. Alignment lost through perturbation of a prior state is never regained, fixing a new maximum alignment that is inherited by subsequent interactions. The attenuation coefficient resulting from a sequence of (static) states, G_k^A, is thus

$$G_k^A(t_N) = \prod_i^N G_{k,i}(t_i), \tag{2.48}$$

where A represents a sequence of static states, $G_{k,i}$ is the attenuation coefficient in state i along that sequence [calculated by Eq. (2.45)], t_i is the survival time of state i, and N is the total number of states in the sequence up to time $t_N = \Sigma t_i$.

What Blume's formulation allows for is the calculation of the attenuation coefficient arising from an *atomic-decay cascade*. In an experimental setting there will also be a distribution of charge states, each contributing a large number of atomic-decay sequences with their own G_k^A values. The value expected to be observed experimentally, $\overline{G}_k(t)$, is obtained by averaging, across the charge-state distribution, the respective atomic-decay cascades for each ionic species (charge state):

$$\overline{G}_k(t) = \sum_Q^{N_Q} c_Q \sum_A^{N_A} G_k^A(t)/N_A, \tag{2.49}$$

where Q represents an individual charge state, N_Q is the number of charge-states, c_Q is the fractional population of the charge state, A represents an individual atomic-decay cascade for charge-state Q, and N_A is the number of atomic-decay cascades for each charge state, Q.

Using Blume's formulation, Bosch and Spehl examined the effects of the rapidly fluctuating hyperfine fields, expected to be present in highly stripped free ions, on the time-dependence of the attenuation. They examined two cases: a continuously and rapidly fluctuating field arising due to continuous optical transitions [30], and a singular or rapid cascade of optical transitions to a ground state having a static interaction [32]. In the former case, they demonstrated that the time-dependent attenuation coefficient should resemble an exponential function for short correlation times. In the latter case, they demonstrated that the rapid feeding of a static interaction should result in a phase shift and amplitude reduction in the sum of cosine functions of Eq. (2.47).

Despite the demonstrated applicability of the RIV method, it was largely neglected until 2005, when Stone *et al.* used the RIV technique to measure $g(2_1^+;^{132}\mathrm{Te})$ using a radioactive ion beam (RIB) [204]. The RIV technique allows the unreacted radioactive beam to travel out of view of the γ-ray detectors, avoiding the accumulation of background radiation (a major problem for TF measurements with radioactive ions [204]). Additionally, modern detector arrays allow for the coverage of a large solid angle, a feature that the RIV technique can utilise more effectively than the TF technique. The g factor was determined by calibrating the hyperfine interaction with the known g factors and lifetimes of even-even stable Te isotopes. The success of this approach led to several more RIV measurements using RIB facilities on nearby nuclides [8, 214, 215].

The RIV method, originally developed by Ben Zvi *et al.* and applied by Stone *et al.*, requires that isotopes with known g factors be available to calibrate the hyperfine interaction. However, this need not be the case. In 2010 Stone, Stone and Jonsson used the General Relativistic Atomic Structure Package [119] to calculate the hyperfine-interaction constants for excited states of Te ions present in the 2005 measurement [204] up to 1000 eV, above which energy transitions were considered to be too rapid to have any significant effect [202]. Using Frauenfelder and Steffen's 'static model', in which the atomic lifetime is assumed to be much longer than the nuclear lifetime, they calculated the time-integral G_k for each atomic state in each ion, and took an average of them with a $2J+1$ weighting factor. The result showed good agreement with experiment, demonstrating that, at least for these higher-Z nuclei, an *a priori* and parameter-free approach can be taken, as opposed to the original approach in which the field strength for any given J value was randomly generated by a distribution function. Chen *et al.* [49]

went a step further and applied the Monte-Carlo method to determine the proportions in which different atomic states should be occupied based on their lifetimes. This was achieved by calculating the atomic properties of a large number of excited atomic states, assuming an equal chance of any given state to be initially occupied (with a $2J+1$ weighting), and using the Monte-Carlo method to simulate atomic decays through time using the calculated properties. They were also able to successfully reproduce the measured Te-isotope data. These gradual steps towards a microscopic description of the experiment have slowly moved the analysis technique away from the simple, calibration-dependent approach, towards an *ab initio* approach to understanding the hyperfine interaction in these nuclei.

The aforementioned measurements all employed time-integral (TI) RIV methods. By instead performing a time-dependent (TD) RIV measurement, the nuclear precession frequency resulting from the hyperfine interaction can be observed, with the possibility to identify a single, dominant oscillation due to a strongly populated atomic state. As with TIRIV, the g factor may then be inferred from the oscillation by calibrating the hyperfine-field strength (HFS). When opting for calibration, the advantage of a TD over a TI measurement is that only a single known state is necessary, as the g factor can be scaled by the ratio of the observed oscillations. The effectiveness is this technique was demonstrated by Naqvi *et al.* [153] in the measurement of $g(2_1^+;^{138}\mathrm{Ce})$ relative to $g(2_1^+;^{142}\mathrm{Ce})$. However, while this technique expands the range of nuclei accessible for RIV g-factor measurements, it is limited by the precision of existing g-factor measurements. Therefore, a calibration-independent method is still desirable.

TDRIV allows for calibration-independent measurements when the HFS can be calculated from first principles. This technique was applied in the measurement of $g(2_1^+;^{24}\mathrm{Mg})$ by Kusoglu *et al.* [129]. In Kusoglu's measurement, the ^{24}Mg charge-state distribution was dominated by bare (having no hyperfine interaction) and H-like ions. The H-like HFS was calculated to be $H = 29.09$ kT, with $J = 1/2$. By measuring the hyperfine-interaction frequency of the H-like ground state a precise value of $g = 0.538(13)$ was obtained. This was possible due to the $J = 1/2$ cosine frequency being dominant, allowing ω in Eq. (2.45) to be fitted, and thereby the g factor deduced. This experiment also demonstrated a proof-of-concept modification that allows for RIBs to be used with the TDRIV technique, enabling the capability to make precise excited-state g-factor measurements on radioactive nuclei. For the ^{24}Mg 2_1^+ state the hyperfine-interaction frequency for the H-like ground state was $A_J \sim 8 \times 10^{11}$ Hz, near the limit of the apparatus' capability to resolve. As higher-Z nuclei are considered, the interaction in H-like ions becomes too high in frequency to resolve its time dependence. To

reduce the hyperfine-field strength into the regime where its frequency can again be resolved requires that the recoiling ions have multi-electron charge states. The challenge to calculate the relevant hyperfine interactions then becomes more complex. Time-integral measurements on even-even isotopes of Ge and Se, having multi-electron charge states, produced results that are difficult to interpret [206], but imply that a few low-excitation atomic configurations must be dominant. If this is the case, it may be appropriate to apply a technique like that used by Chen *et al.* Designing experiments that observe the ground-state perturbation owing to Na-like ions may enable accurate g-factor measurements. However, this interaction will be but one component in a much more complex ensemble of atomic states present in both Na-like and other adjacent ionic species. Due to the time dependence, one may also expect the populations to shift over time if the atomic-state lifetimes are of the order of the nuclear lifetime. Modelling this scenario is not a trivial task, but would provide a powerful analysis tool for interpreting TDRIV data for these nuclei in the $Z \sim 30$ region.

2.4 Atomic-Structure Calculations

To model the hyperfine interaction, the atomic-structure information of the relevant charge states must be known. The disciplines of atomic physics and quantum electrodynamics, along with the relative simplicity of the atomic system (compared to nuclei), have produced a number of methodoligies to calculate atomic wavefunctions with high accuracy. The General Relativistic Atomic Structure Package (GRASP) is one particular solution for calculating bound-state atomic wavefunctions and atomic properties. Its origin dates back to 1969, and the publication of an early computer code by Froese Fischer [74]. The approach used the multiconfiguration Hartree-Fock (MCHF) method, in which solutions are obtained using the self-consistent-field method to generate a number of individual configuration states, which are then mixed, to compute atomic wavefunctions. This initial solution laid the foundation for the approaches which have been developed in future versions. Its basis is the assumption that atomic-state wavefunctions can be determined from a linear combination of multi-electron configurations, which in turn are approximated from bound single-electron wavefunctions. This approach was gradually generalised, improved, and relativistic calculation capabilities were introduced [72, 73, 75, 76, 77]. In 1996 the first version of GRASP was released [167], introducing fully relativistic calculation capabilities to Froese Fischer's MCHF atomic structure package. Major updates to GRASP were published in 2007 [120], 2013 [118] and 2019 [79], introducing various improvements and optimisations. GRASP is freely available under the MIT license, and being written in FORTRAN and C++ can be compiled on Linux, OSX and Windows operating systems. It is quite approachable in its use, and is provided with comprehensive documentation and worked examples. Additionally, the software package is still being actively developed. These features make it an attractive software solution for calculating atomic properties.

2.4.1 Obtaining Atomic-State-Function Solutions

In this subsection a general overview is given of how GRASP obtains its solutions, taken from a recent review of the technique by Froese Fischer *et al.* [78], and the document "A practical guide to GRASP2018" provided with the GRASP2018 software package [84]. The properties of a given atomic state, or transition between two states, are calculated from an atomic-state function (ASF). The ASF ideally represents a physical, spectroscopic state of an atom or ion. In the multiconfiguration approach, the ASF is a linear combination of configuration-state functions (CSFs). Each CSF represents a unique combination of one-electron orbitals, with each electron orbital defined by a set of four quantum numbers. In the relativistic case, these are the principal quantum number n, orbital quantum number l, spin quantum number $j = l \pm s$ and magnetic substate m. These single-electron wavefunctions are determined using the Dirac-Coulomb interaction Hamiltonian for the

energy, which takes into account a finite, spherical nuclear size. Slater determinants are used to represent the coupled one-electron orbital products in the CSF so that the wave-function is always anti-symmetric. From this set of CSFs, the ASF is constructed by

$$\Psi(\Gamma J^{\pi}) = \sum_{i=1}^{N} c_i \Phi(\gamma_i J^{\pi}), \tag{2.50}$$

where Ψ is the ASF representing a physical atomic state Γ, having total spin and parity J^{π}, N is the number of chosen CSFs, with each CSF i having an expansion (mixing) coefficient c_i, and a Slater determinant Φ defined by the electron configuration γ_i, having total spin and parity J^{π}.

If the ASF is composed of a single CSF, then the Dirac-Hartree-Fock (DHF) equation can be solved numerically using the self-consistent field method directly. The calculation for ASFs consisting of multiple CSFs (multiconfiguration (MC) DHF) is similar to the single CSF case, however expansion coefficients for each CSF must also be varied to obtain the optimal solution. It should be noted that, when solving the DHF and MCDHF equations, the energy Hamiltonian is fixed, with corrections for variations introduced in stage two. In the second stage, expansion coefficients are further optimised by solving the relativistic configuration interaction (RCI) problem, in which a variable term is added to the energy Hamiltonian to account for electron-electron interactions, and may additionally contain Breit-Pauli (which allows for lifetimes of forbidden transitions to be accurately determined) and QED corrections (which are required for high-precision comparisons with data), if so desired. More information on these topics and methods is available in Refs. [43, 78].

2.4.2 Optimising Convergence of Atomic Properties

Accurate convergence of the ASF solution can be monitored by gradually expanding the number of CSFs in a systematic way. CSFs are typically defined by taking the leading (or lowest-energy) configuration of the ASF as a base, and then allowing either single- or double-electron excitations from this state. CSFs should be considered for single electron excitations that satisfy the following conditions: the quantum numbers ljm remain the same, but n increases (radial correlations); the quantum numbers lm remain the same, but the spin coupling changes (spin-polarisation); the quantum numbers nm remain the same, but the orbital angular momentum changes and possibly spin-coupling changes (orbital polarisation). Double-electron excitations are classified by from where the two electrons originate: two valence electrons (valence-valence); a valence and a core electron (core-valence); or two core electrons (core-core). Recall from Eq. (2.50) that only those CSFs having the same J^{π} as the ASF will be taken into account (spin and parity

must be conserved).

Different atomic properties require different types of electron correlations to converge on accurate solutions. Single-electron correlations should always be considered, but two-electron correlations can rapidly grow the CSF space to an unweidly size, and should be considered carefully. For example, absolute energy levels are sensitive mostly to valence-valence correlations. The dipole oscillator strength (from which the transition rate is determined) is sensitive to core-valence correlations, while the hyperfine-field strength is sensitive to core-core correlations [78]. Generally, CSFs generated from one- and two-electron excitations are sufficient to produce accurate solutions. Convergence can be monitored by expanding the CSF space. This is done by including electrons with higher nl, and/or deeper core-valence and core-core correlations. As nl is increased in the CSF space an atomic property, such as the level energy, should converge on a single value. If sufficient electron correlations have been accounted for, this value should be very close to reality, and in many cases can be compared with the measured values contained in the National Institition of Standards and Technology (NIST) atomic spectral database [178]. The self-consistency of a solution can also be monitored by observing the difference between the two oscillator strength calculation approaches (alternate forms for the dipole operator, or gauges, that are used to determine the transition rate between two atomic states) that GRASP takes, namely the length and velocity forms [43]. Ideally, one would include all CSFs up to the continuum states, however there are practical limitations with computational capacity, time, and obtaining convergence. By this process, atomic properties with accuracy enough to meet the demands of astrophysical observations (better than 1%) can be obtained using GRASP, as has been demonstrated in the literature [78].

2.5 The Present Work

In this thesis, measurements using the transient-field (TF) and recoil-in-vacuum (RIV) techniques have been analysed with the intention of verifying hyperfine-interaction strengths, validating the models underlying the techniques, and obtaining reliable g factors. These objectives are motivated by the desire to obtain accurate and precise g factors with which to confront the nuclear shell model and advance the field of nuclear-structure theory. In addition to these overarching goals, the nuclei studied in this work have their own interest to nuclear-structure studies, which will now be discussed.

2.5.1 The Ge and Se Isotopes

Due to the many-body nature of the nuclear quantum system, nuclei can exhibit particularly intriguing behaviours. One of these is referred to as shape coexistence. Some nuclei in the region $A \sim 70$ exhibit shape coexistence [14, 97, 140, 165, 171], a phenomenon in which two or more nuclear states have distinct shapes with the same spin and parity, close in energy ($\Delta E \lesssim 1$ MeV). Isotope chains which span this region present a unique opportunity to study not only individual nuclei which exhibit shape coexistence, but also the transition of nuclear shapes along the isotopic chains, and their variable exhibition of collective and single-particle behaviour [97, 98, 165, 195]. Two isotopic chains which present interesting and experimentally accessible cases are those of Ge and Se.

The Ge and Se isotopes have a partially filled $\pi f_{5/2}$ orbital, with the stable isotopes ranging from empty neutron $\nu p_{1/2} g_{9/2}$ orbitals (a possible sub-shell closure, $^{70}_{32}\mathrm{Ge}_{38}$), to two-neutrons short of filling the $\nu p_{1/2} g_{9/2}$ orbitals ($^{82}_{34}\mathrm{Se}_{48}$) upto the shell closure at $N = 50$. Speidel *et al.* [195] and Mertzimekis *et al.* [149] suggest that $N = 38$ may be a sub-shell closure for fpg-shell nuclei. If this is true, there should be experimental signatures indicating an increase in collective behaviour in the nuclei at the mid-point of the neutron sub-shell ($^{76}\mathrm{Ge}_{44}$ and $^{78}\mathrm{Se}_{44}$). Therefore, the shell-closure should reveal itself, along the isotopic chain, as a minimum in the 2^+_1-state energy and g factor trend, and maximum in the transition probability amplitude, at the mid-point of the sub-shell. The g-factor minimum should also have a value near the collective limit $g \sim 0.7Z/A$. Measured 2^+_1 energies and $B(E2)$ systematics in the Se isotopes suggest this is the case, evidenced in Fig. 2.8. Concerning the g factors, the $g(2^+_1)$ systematics of the stable, even-even Ge and Se isotopes have been measured using the thin-foil TF technique [98, 130, 166, 195]. For the Se isotopes, there is evidence of an increase in collective behaviour towards ^{78}Se in measured $g(2^+_1)$ trends [195]. This trend appears to exist for the Ge isotopes as well, although the various measurements are not in complete agreement [145], and g-factor measurements beyond the suspected mid-shell at ^{76}Ge are

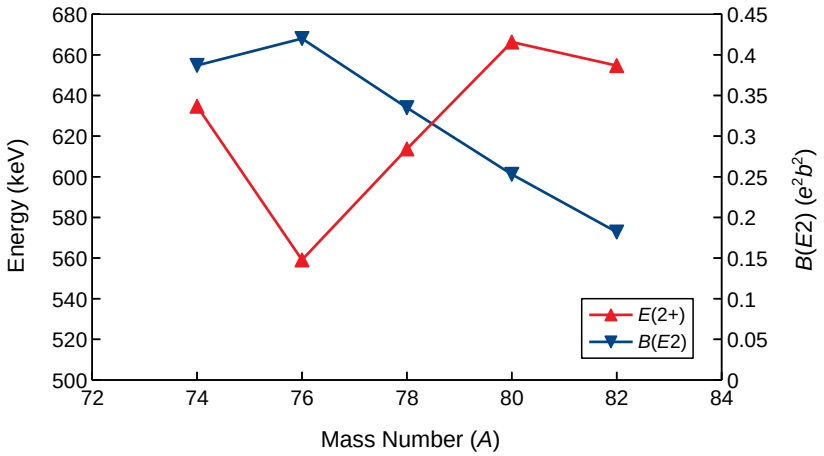

FIGURE 2.8: Systematics of $E(2_1^+)$ and $B(E2)$ values along the Se isotopic chain for the stable, even-even isotopes. There is clearly a minimum in $E(2_1^+)$ and maximum in $B(E2)$ at ^{76}Se, indicating increased collectivity. Values taken from Ref. [179].

yet to be made. As such, firm confirmation of the g-factor values in both the Ge and Se isotope chains is desirable.

In regard to the $N = 38$ shell closure, it is worth noting that fewer excited 2^+ states can be formed by exciting neutrons pairs into the empty $p_{1/2}$ orbital. This comes about because two neutrons in $p_{1/2}$ must couple to $J = 0$. Furthermore, exciting one of the two $p_{1/2}$ neutrons into $g_{9/2}$ cannot form a 2^+ state. Therefore, to form excited 2^+ states at $N = 38$, neutrons must excite from the deeper $p_{3/2}$ and $f_{7/2}$ orbitals. These restrictions can give the appearance of a shell grap at $N = 38$ in the first-excited 2^+-state systematics. Once the $p_{1/2}$ orbital is filled at $N = 40$ the lowest-energy coupling to an excited 2^+ state requires excitation of a pair of neutrons into $g_{9/2}$. Thus, $N = 40$ can also show features of a shell gap.

With accurate and precise g-factor measurements available, the shell model's $pfpg$-shell space capability to predict the change from collective mid-shell behaviour at $N = 44$ to the single-particle behaviour at the $N = 50$ shell gap, for this complex nuclear property, can be rigorously tested. Furthermore, validated methods for performing accurate and precise g-factor measurements on radioactive nuclei approaching the suspected $N = 38$ sub-shell closure, and established $N = 50$ shell closure, will provide more rigorous tests of the shell model.

In addition to the shell-model motivations, there exists an experimental motivation to investigate the Ge and Se isotopes. This arose from the intent to apply the RIV analysis method to Coulomb-excitation data taken on the neutron-rich isotopes $^{78-82}$Ge,

like that obtained at the Holifield Radioactive Ion Beam Facility at Oak Ridge National Laboratory [165]. However, further experiments using the stable Ge and Se isotopes to calibrate the relevant free-ion hyperfine fields found an unexpected difference in the RIV behavior along the two isotope chains [134, 206]. Atomic-structure effects may explain these differences. However, there is also the possibility that the adopted g-factor ratios within and/or between the two isotope chains may be responsible for some, or all, of the observed difference. The desire to verify previous measurements of the relative g factors along and between the Ge and Se isotope chains motivated the present work, along with the nuclear-structure interest. To this end, the relative g factors of the stable, even isotopes of Ge and Se were measured using the thin-foil TF technique in inverse kinematics (beam excitation), and the first case of a relative g-factor measurement using a cocktail beam, in this case of ^{74}Ge and ^{74}Se, was performed [145].

Concerning TF measurements on the Ge and Se isotopes, there are few reliable $g(2_1^+)$ data points in the region $8 \leq Z \leq 62$ against which the TF strength can be calibrated. The original parameterisation by Shu *et al.* (the Rutgers parameterisation) [191] was fitted using precession data from the 2_1^+ states of ^{16}O, ^{20}Ne, ^{24}Mg, ^{28}Si, ^{56}Fe, ^{82}Se, ^{106}Pd, ^{110}Cd, ^{134}Ba, ^{148}Nd, ^{150,152}Sm, and ^{194}Pt ions, with velocities ranging from $2 \lesssim v/v_0 \lesssim 8$. The $g(2_1^+)$ values for many of these nuclei were measured using the implantation perturbed-angular-correlation (IMPAC) technique, which in itself contains a TF component, often accounted for using either the erroneous Lindhard & Winther model, or Eberhart's linear model. Using these values to calibrate a new TF model is therefore partially circular, bringing into question its accuracy. Specific to the present work, examination of the measured ^{82}Se $g(2_1^+)$ value used in the Rutgers calibration [191] reveals that it was originally obtained from an earlier IMPAC measurement [106], performed prior to the characterisation of the TF accepted today. This IMPAC value was reanalysed [34], and cited in the calibration data set. All three papers report a different value for $g(2_1^+;^{82}\,\mathrm{Se})$, with the procedure used to obtain the final value used in the TF calibration rather opaque. It is also now known that the thermal-spike quenching effect, discussed in §2.3.1, may be present, increasing the uncertainty in the IMPAC analysis considerably. Furthermore, the measured precession angle for the ^{82}Se 2_1^+ state is in disagreement with g-factor trends measured by the TF technique. As such, the IMPAC measurement has also been repeated in this thesis to check the previous data and, if possible, to investigate whether the thermal-spike quenching is present. Eliminating this datum from the fit, there are now no calibration points in the region $26 < Z < 46$ for the Rutgers parameterisation. As discussed in §2.3.2, the TF strength can vary unexpectedly in iron hosts, and limited calibration data exists for gadolinium hosts for $Z \sim 30$. Therefore, use of the TF parameterisation to obtain absolute $g(2_1^+)$ values in the Ge and Se isotopes may be considerably more uncertain than reported in the literature, at worst inflating

them to $\pm 20\%$. This uncertainty presents a considerable frustration when comparing the absolute predictions of shell-model calculations against measured values.

Although the accuracy of absolute g factor values determined using the TF parameterisation is questionable, relative values can be reliably determined (see §2.3.2). To obtain reliable, relative g-factor values for the Ge and Se isotopes concerned, a simultaneous measurement between the isobaric nuclei ^{74}Ge and ^{74}Se was performed, in which virtually no systematic uncertainty was present. Other isotopes of the same element were then measured using the same target in a measurement campaign using a sequence of different isotopic beams. This allowed the relative g factors between the two isotopic chains, as well between isotopes of the same chain, to be confidently determined. Then, by obtaining a single, absolute measurement for one of these isotopes, the relative measurements can be scaled without relying on the TF parameterisation. Such a method for performing this calibration measurement is the recoil-in-vacuum technique.

2.5.2 Recoil-In-Vacuum Measurements

The 2_1^+ state in ^{56}Fe presents an important case for TF calibration in the nuclear pf-shell region ($Z \sim 30$). The g factor of the ^{56}Fe 2_1^+ state has been measured relative to the $5/2^-$ state in ^{57}Fe, for which the g factor has been independently obtained [68], using the thin-foil TF technique [56]. As discussed in §2.3.2, this ought to provide a robust measurement, however statistical precision is lacking, and so independent validation remains important. As such, another measurement was performed in 2014 by Stuchbery *et al.* at the ALTO facility at the IPN, Orsay. This measurement was performed using a recently developed plunger device, referred to as OUPS [141], which provides recoil-distance measurement capabilities, making a TDRIV measurement of a high-frequency hyperfine interaction possible. The experiment was optimised to maximise the Na-like charge-state proportion, with an aim to measure the Na-like ground-state frequency ($3s_{1/2}$). However, due to a complex superposition of hyperfine-interaction frequencies, determination of a g-factor value from this dataset had not yet been achieved. This measurement makes for a good case to develop and test a Monte-Carlo analysis approach to the TDRIV data using atomic-structure information calculated using GRASP, and see if an independent g-factor can be extracted and compared with the aforementioned value measured in Ref. [56]. If this can be achieved, it will provide a more precise calibration point for the TF strength, and validate the TDRIV technique for future measurements.

A TDRIV measurement was performed on ^{76}Ge 2_1^+ at ANU's heavy-ion accelerator facility in 2013. However, this experiment was not optimised (as the ^{56}Fe TDRIV experiment was) for a measurement of the Na-like $3s_{1/2}$ frequency. This is because it was

performed to observe the time-dependence of the hyperfine interaction, in order to help interpret time-integral RIV measurements on even-even Ge and Se isotopes performed previously [134]. Although the Na-like state is expected to be small, if not absent, these data provide an alternative data set to test model predictions and to potentially extract a $g(2_1^+)$ value. As such, they were also analysed in the present work. If the approach is successful, an absolute g-factor value will prove valuable in scaling the g factors obtained in the relative Ge and Se isotope TF measurements, or at least inform optimal conditions for a future measurement.

Along with these time-differential data, time-integral RIV data taken on the ^{54,56}Fe 2_1^+ states at ANU in 2014 were also analysed. Comparison of the measured time-integral G_k values to an *ab initio* calculation of the time-integral G_k values, using the Monte-Carlo simulation, will serve to either validate the model, or to investigate any gaps in modelling the hyperfine interaction.

In conclusion, the transient-field technique is an effective way to obtain precise relative g-factor measurements on short-lived ($< 10^{-9}$ ps) nuclear states. However, calibration of the field strength used to obtain absolute g-factor values is a challenge in some regions. The recoil-in-vacuum technique has undergone key developments in the past two decades which make it a promising technique for performing measurements on short-lived states in stable and radioactive nuclei. When combined with atomic-structure calculations, the time-dependent version of RIV has the potential to determine nuclear g factors with improved precision. Together, these two techniques provide the opportunity to perform precise and absolute g-factor measurements on nuclei spanning isotopic chains which cover exotic nuclear regions where the established shells are expected to change, providing valuable data with which to confront shell-model calculations.

2.6 Summary

Despite the field of nuclear physics having existed for over a century, the study of nuclear structure still presents exciting new challenges. A deep understanding of the interactions in nuclear matter evades a complete and fully microscopic explanation. The shell model of the nucleus has proven a valuable tool to improve our understanding. However, it requires continual experimental input and verification. As we push the limits of our theoretical knowledge, we push the limits of our experimental capability, and must develop new techniques with which to obtain the data we need to validate and improve nuclear-structure models. Presently, exotic nuclei in the *sd*- and *fpg*- shell regions are of interest, as they exhibit unusual structural effects relating to their changing collective and single-particle behaviour, and are tractable in shell-model calculations with current computational capabilities. Novel interactions involving sub-nuclear tensor forces, which have been incorporated into shell-model calculations, will test our understanding of this changing behaviour. Radioactive, heavy isotopes of Ge and Se provide interesting testing grounds, however even measurements from the stable isotopes can be used to confront the shell model.

The g factors of first-excited 2_1^+ states may be used to validate finer details of the interactions included in the shell model. The best method for measuring these g factors is presently the transient-field (TF) technique. However, for nuclei in this region its use as an absolute measurement technique is questionable, and no reliable measurements exist against which to scale the field strength. The recoil-in-vacuum (RIV) technique is a viable solution, but a better understanding of the hyperfine interactions which occur for nuclei in this region needs to be obtained before data can be confidently analysed. By combining the established time-differential (TD) RIV technique (with its single-frequency analysis) with the Monte-Carlo approach used to understand the changing superposition of frequencies resulting from multiple charge states and atomic states, calibration nuclei can be established in the region $20 \leq Z \leq 40$, against which the large amount of existing TF data can be reviewed and scaled, if necessary. This technique may also be used to make precise g-factor measurements on excited states in radioactive nuclei, with which to test shell-model interactions.

Chapter 3

Experimental Methodology

This chapter describes the methodology common to experiments undertaken during the research project, in particular the use of detector, electronics and data acquisition systems. It also describes the procedure by which the data were analysed to obtain the information of interest. Two types of experiments have been performed: those utilising the transient and/or hyperfine fields present in polarised ferromagnets, i.e. the TF technique and IMPAC, and those utilising the hyperfine interaction present in an ion after recoiling into vacuum. The theory underpinning these techniques has been described in Chapter 2. Experimental methods regarding transient-field measurements are described in Chapter 4, and recoil-in-vacuum measurements in Chapter 6.

3.1 Radiation Detection

To measure the properties of an excited state of the quantum-mechanical system that is the atomic nucleus, the spatial distribution of its radiations must be predictably perturbed, measured and interpreted. As described in §2.2, angular correlations can be reliably calculated in the absence of extra-nuclear electric and magnetic fields. These angular correlations can be used to determine the spins and parities of nuclear levels. When an electric or magnetic field acts on the nucleus, angular-correlation theory allows for the magnitude of the electromagnetic perturbation to be measured and interpreted, thereby inferring nuclear structure properties of a state, such as the dipole moment, as described in §2.3. Coulomb excitation to a single excited state allows for the direct measurement of γ-particle angular correlations. In order to perform such measurements, particles scattered after Coulomb excitation, and de-excitation γ rays from the nuclear state of interest, are measured in coincidence. The γ-ray angular correlations measured in this way can be calculated, the perturbation determined and, if a suitable magnetic field acts on the nucleus, the nuclear dipole moment inferred. To achieve this, radiation detectors sensitive to energetic particles or γ radiation are used in conjunction with electronic systems that allow for the energy signature and timing information of the scattered particles and decay radiation to be recorded.

3.1.1 Detector Types

In the experimental work presented, two different types of γ-ray detector were used: scintillation detectors and semiconductor detectors. Of the scintillation-detector type, sodium-iodide (NaI) crystals were used in conjunction with a photomultiplier. The detector operation is straight-forward: when a quanta of energy (in the case of interest, a γ ray) interacts with the NaI crystal electrons are excited from the valence band into the conduction band, and then de-excite. This de-excitation results in the emission of light (scintillation). The light is reflected into a photomultiplier tube located at one end of the crystal, inducing an electron cascade and a subsequent electrical pulse. The scintillation light, and therefore the amplitude of the electrical pulse, is proportional to the energy deposited into the crystal. The photomultipliers used have two types of signal output: a DC-coupled anode signal and a linear-response dynode signal. The anode signal is most useful for timing, while the dynode signal gives a more reliable (linear) energy measurement. NaI is a good scintillation crystal for γ-ray measurement due to its transparency to the scintillation light, capability to be produced in large-size single crystals, and the high-Z of iodine, all of which improve detection efficiency. For more information, see Ref. [127]. These features of the NaI detector make it most suitable for γ-ray spectroscopy measurements in which only one γ-ray energy is of interest, or a few well-separated in energy, are present, as they have high detection efficiency but modest energy resolution.

Of the semiconductor-detector type, high-purity germanium (HPGe) detectors were used. These detectors function by producing a charge-depletion zone in the crystal structure of the semiconductor using a kilovolt potential applied across the crystal radius, via a central anode and outer cathode. When ionising radiation penetrates into the crystal and deposits energy into the depletion zone, electrons are excited and accelerated toward the cathode, and holes towards the anode, which produces an electrical pulse having height proportional to the energy deposited. The potential takes several microseconds to be restored, making the pulses quite long compared to other detector types. These pulses are usually fed into a preamplifier which is part of the detector assembly. The preamplifier converts the pulse height from the HPGe crystal into a signal more suitable for transmission and for pulse-processing electronics. The HPGe preamplifiers used have two identical outputs, so the signal can be used for both energy measurement and timing. The timing characteristics of this signal are poor compared to NaI detectors, but this is not of concern in the measurements present in this thesis. For more information, see Ref. [127]. Operation of the HPGe detector makes it most suitable for γ-ray spectroscopy measurements in which different γ rays must be distinguished and correctly identified, as they have high energy resolution.

To detect high-energy particles in coincidence with γ-rays, silicon photodiodes (SiPDs) have been used. When a constant voltage is applied across the SiPD, an equilibrium current flows across the junction. If some kind of ionising radiation interacts with the SiPD, the resistivity of the device changes, causing a change in the current flow. This current change results in a characteristic electrical pulse, proportional to the particle energy [125]. SiPDs make for useful particle detectors as they are effectively 100% efficient in detecting heavy-ion particle impacts. Their small size and low cost are also attractive features, particularly in high-radiation environments, as they can be easily replaced after being damaged by irradiation. Their small size also provides control over the opening angles in Coulomb excitation experiments, allowing the anisotropy in the angular correlation to be maximised. Arrays of these detectors can maintain this anisotropy whilst covering a larger solid angle, are inexpensive to make, and require no complex electronics to setup. However, they offer no pulse-shape discrimination, and are unable to distinguish between different type of particles, making them most suitable for γ-particle coincidence measurements in which a single particle type is expected to be detected in coincidence with the γ rays of interest.

By using NaI and HPGe γ-ray detectors in conjunction with SiPD particle detectors the angular correlation between recoiling or back-scattered particles, and emitted γ rays can be measured.

3.1.2 External Polarising Field

A dual-coil electromagnet, with the windings installed above and below the target holder, allows the generation of a magnetic field that polarises any ferromagnetic materials in the target position. This setup is used for performing IMPAC and transient-field measurements, and the specifics of this setup are discussed in Chapter 4. The electromagnet is powered by a programmable power supply with a custom-built control box capable of ramping up or down the current and reversing the field polarity. The control box also outputs a logic signal indicating the field polarity, and a separate inhibit signal while the current is ramping up or down during the polarity flip. These signals are used in the data acquisition system to determine the field polarity for a given event or veto events during the polarity change.

3.2 Signal Processing and Data Acquisition

3.2.1 Analogue Data Acquisition System

Experimental data acquisition (DAQ) at The Australian National University (ANU) in years prior to 2016 was performed using VME crates consisting of an AlphaVME 5/480 computer and multiple analogue-to-digital converter (ADC) and time-to-digital converter (TDC) cards [172]. This system is controlled using a computer code called Data Collection Program (DCP), which also is used to interpret the recorded data. Because the system requires analogue signal processing before data acquisition, it is referred to as the Analogue DAQ. The basic system has since been migrated to a contemporary platform and remains in use. Data acquisition with the Analogue DAQ operated using an event trigger, which controlled data recording from a number of ADCs and TDCs. Energy signals from γ-ray detectors were obtained by passing a detector output signal through a preamplifier (if required), a linear amplifier, then into an ADC, and finally to the data-acquisition system. After going through the linear amplifier, energy signals from the particle detectors were passed through a linear gate and stretcher (LGS), gated by a single-channel analyser (SCA), which received a signal from the dipolar output of the linear amplifier. This helped to reduce noise, as well as delay the particle-detector pulse to better match that of the γ-ray detector arriving at the ADC.

Timing signals were generated by first passing a detector output through a preamplifier (if required), a timing filter amplifier (TFA) and then a constant fraction discriminator (CFD). These devices generate a timing output pulse whenever a signal above a set threshold is generated by the detector. A flowchart of the electronics setup for the three sets of detectors to produce the master trigger is shown in Fig. 3.1.

In order for the Analogue DAQ to record only meaningful signals, a logic circuit was used to generate a master trigger. This master trigger informed the Analogue DAQ to record incoming digital signals following the trigger. Detector timing signals were used for the logic circuit. The γ-ray detector signals were all put into a single-coincidence logic unit (single output for any input), i.e. an 'OR' gate, and the same was done for the particle detectors. The logic outputs from the 'OR' gates were stretched and delayed as required to have the γ and particle signals overlap. They were then put into a double-coincidence logic unit (single output for at least two inputs). The resulting logic circuit generates a signal whenever any γ-ray and any particle-detector timing signal occur within 400 ns of each other. A third logic signal was generated from the particle single-coincidence logic unit using a down-scaler (1/1000) and was put into the double-coincidence logic unit and also into a TDC. This downscaler signal labels down-scaled

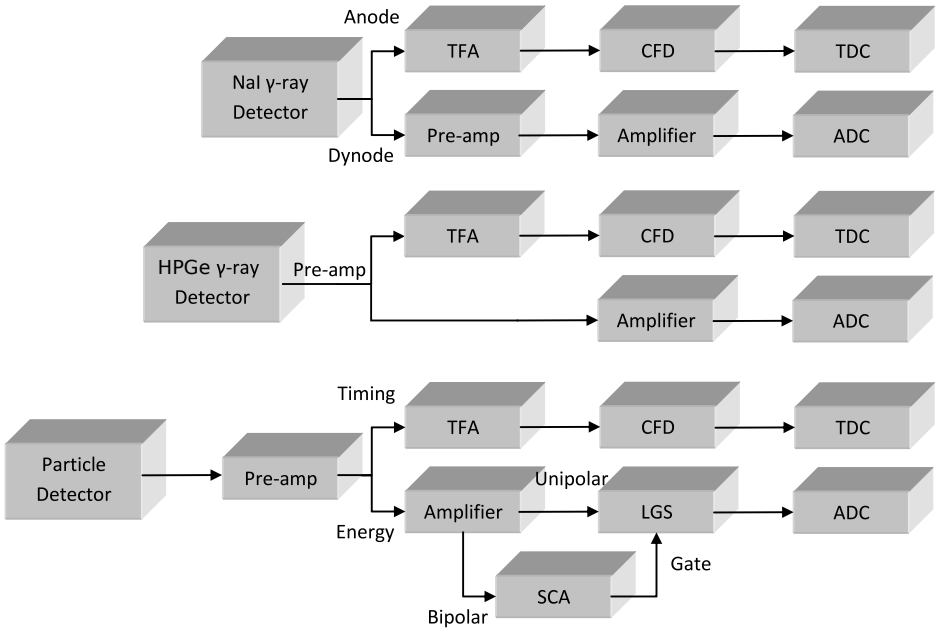

FIGURE 3.1: Electronics setup used to acquire analogue signal from detectors using the Analogue DAQ. Acronyms are described in-text.

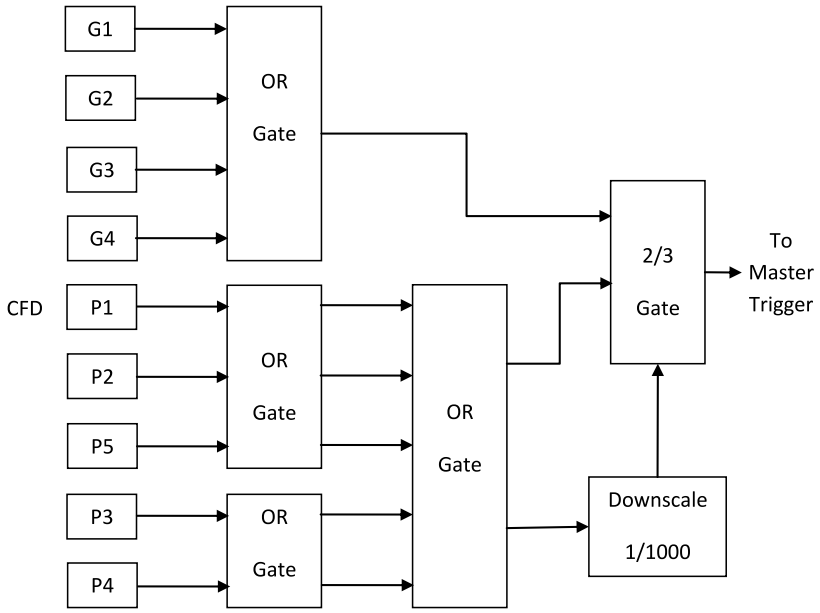

FIGURE 3.2: Logic setup used to produce a master trigger for Analogue DAQ signal acquisition. The 2/3 gate means the logic unit outputs a signal when $\geq$ 2 signals are received. This allows the downscaler signal (intended to be a particle-rate tagger) to occasionally be in coincidence with a γ-particle coincidence event.

particle singles events, which can be used to evaluate differences in particle-detector efficiency. In practice, this information was used to scale the particle-detector count rates in the evaluation of angular correlations. A flowchart of the logic setup is shown in Fig. 3.2. The master trigger, a square logic signal, was then stretched to 10 μs before being passed on to the Analogue DAQ so there was a long acquisition window overlapping the particle and γ-ray signals arriving at the ADCs.

The γ-ray detector time spectra were generated by inputting the γ-ray detector's time signal, and the particle-detector 'OR' logic signal (see Fig. 3.1), into a TDC. This produces a time-difference spectrum between γ-ray and particle events. So that particle detectors could be distinguished in the γ-ray detector time spectrum, as well as the energy spectra, their individual time signals were input into a TDC channel with the master trigger to give time-difference spectra. This was also done for the signal coming from the downscaler (see Fig. 3.1). These spectra give sharp, well-defined peaks that simply serve to identify coincidences with each particular particle detector. TDC outputs were recorded by the Analogue DAQ.

Signals output by the current source regarding the status and polarity of the external polarising field (§3.1.2) were digitised and recorded by the Analogue DAQ. An event counter, connected to the particle singles rate, was used to send the polarity-reversal signal to the current source every $\sim$ 15 min. The signal produced by the current source while the field polarity was changing was used to veto the master trigger, preventing any events from being recorded by the Analogue DAQ during this time.

3.2.2 Digital Data Acquisition System

The Pixie-16 digital pulse processor is produced by the company XIA LLC for nuclear spectroscopy measurements [230]. The fundamental difference between this system and the analogue system is that the Pixie-16 digital pulse processor accepts signals directly from the detector (or detector preamplifier) without any analogue pulse processing. Instead, the pulse is digitised and processed in the system. Digitised pulses are also tagged with a time signal, removing the need for a TDC unit. This makes the setup of this system, once operational, simple and straight-forward. Two Pixie-16 boards, one capable of operating at 100 MHz with 14-bit resolution, and the other operating at 500 MHz with 12-bit resolution, were installed into a PXI crate and interfaced with a Dell PowerEdge R530 running Ubuntu 16.04, which recorded the binary signal stream. This setup is referred to as the Digital DAQ. The system has 16 analogue inputs per board, and is capable of nanosecond timing capabilities using a combination of a 100 MHz clock that gives 10 ns resolution, and a self-generated CFD signal which allows reliable signal

timing down to 1 ns. In the event of a bad CFD signal, the error is recorded and the sub-10-ns timing can be ignored, or the event discarded. Software written by Dr. T. Gray and Dr. M. Gerathy, then PhD students of the Department of Nuclear Physics at ANU, along with the aid of Dr. J. M. Allmond of the Oak Ridge National Laboratory, USA, allows for the setup and control of the Digital DAQ, as well as recording the raw binary datastream. The Digital DAQ acquires data in a triggerless manner, but the acquisition software developed at ANU also allows for coincidence requirements to be specified so only selected, valid coincidence data are recorded.

To have the electromagnet's power supply control box produce signals appropriate for the Digital DAQ, a custom-made electronic signal device was produced by Mr. D. Tempra of the technical team at ANU's Department of Nuclear Physics. This device accepts the signal outputs from the control box and generates a pulse having height particular to the current-source signal. Three different voltage pulses are produced, indicating the polarity status (field up or field down) or if the field is changing. Rather than use the field change signal to veto events, the Digital DAQ instead tags any signals that arrive with the polarity status, which can then be sorted during the analysis procedure.

3.3 Data Analysis

To extract useful information from the data stream, correlations need to be constructed between particular event energies and their relative timing. To process and visualise these data, three different software solutions were used. The first two were used in combination, being TSort and Fitek4, both developed by A. Prof. T. Kibédi at ANU's Department of Nuclear Physics. TSort was used to sort events from the Analogue DAQ output datastream based on specified gating requirements. The sorted events were recorded in the DCP data format. Fitek4 takes the DCP data from TSort and allows visualisation of spectra, fitting of peaks and background, and output of integral peak counts, as well as multiple other functions that were not used in the course of this research project.

The second software package used for data analysis was the ROOT data analysis framework, developed at CERN [41]. In some instances, event data from the Analogue DAQ was converted to the ROOT tree format using software developed at ANU's Department of Nuclear Physics. The Digital DAQ output datastream was always converted into the ROOT tree format using software developed by Dr. T. Gray. Events were created from records which occurred within 1 μs of each other with a multiplicity requirement of two. This ROOT tree could then be analysed to extract γ-particle coincidence events having the appropriate energy and relative timing characteristics, as well as applying any other coincidence requirements (such as the polarising-field direction). Gamma-ray spectra consisting of these events could then be analysed, and photopeak counts obtained for the γ ray of interest.

To extract γ-ray spectra containing valid γ-particle coincidences, three pieces of information must be selected in the data stream (i.e. "gates" defined): the energy of the particles of interest, timing information of the γ-ray detector, and timing information of the particle detector. To obtain these, first the 'raw' (ungated) particle spectrum was projected from the data, which showed the energy region of interest, and was used to set a particle-energy gate. Spectra showing time-differences between individual γ-ray and particle detector pairings, gated by the particle energy, were then projected. This spectrum showed a clear peak that was used as a 'prompt' γ-ray time gate, as well as a flat background of random coincidences. An example spectrum is shown in Fig. 3.3. To obtain γ-particle time spectra from data obtained using the Analogue DAQ, first each particle TDC spectrum was sorted out. These particle TDC spectra show a narrow signal that was used to identify the particle detector that 'fired' in the event. The γ-ray detector TDC spectrum is then projected, applying the particle energy and time gates, producing the γ-particle time spectrum. For data obtained using the Digital DAQ the events each

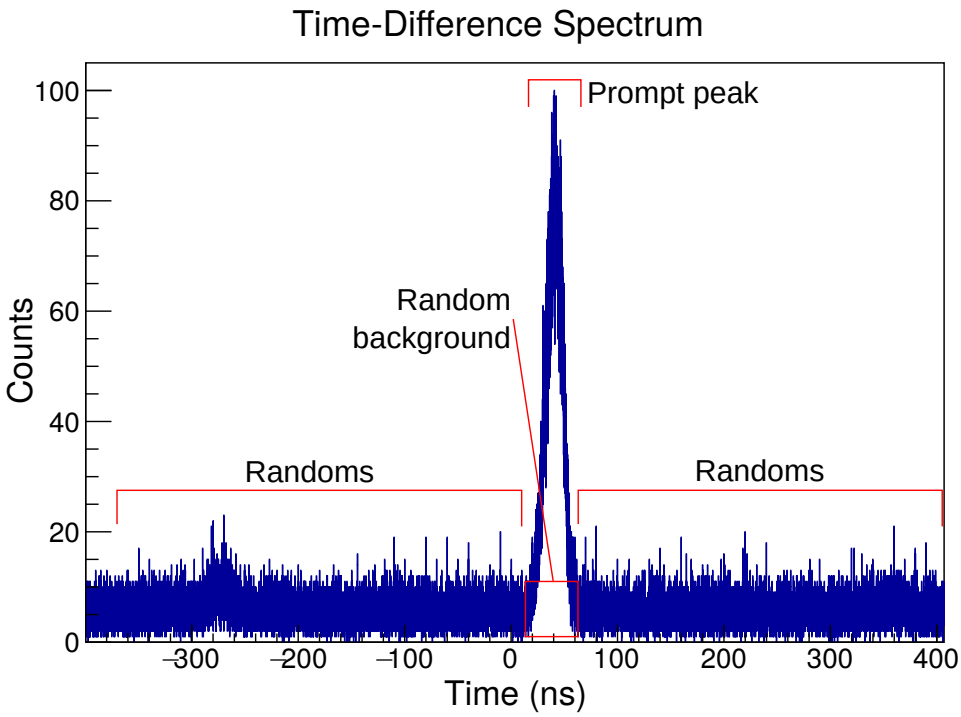

FIGURE 3.3: Spectrum of time-differences between γ-ray events for a single γ-ray detector, and particle events from any particle detector. There is a clear time-correlation peak, or 'prompt' peak, which is used to gate out coincidence events. Regions on either side contain random events, and gates on these regions can be used to deduct the random background from the prompt spectrum. Note that the example data used here were taken from Fig. 4.8.

have a time stamp, and so time-difference spectra are produced by computing the time difference between the signals in the event with the particle-energy gate restriction. Now, the γ-ray energy spectrum containing prompt events can be projected using the prompt time gate and particle energy gates, which produces a γ-ray spectrum containing γ-particle coincidence events and some random-coincidence events. To deduct random coincidences from this spectrum, a γ-ray time gate encompassing the random coincidence regions (flat regions with counts outside of the prompt γ time peak, indicated in Fig. 3.3), along with the usual particle gates, is used to project a random-coincidence spectrum. This spectrum consists of random-chance coincidence events. The spectrum counts are then scaled such that $s = g_{\mathrm{pr}}/g_{\mathrm{rnd}}$, with g_{pr} being the width of the prompt γ time gate, and g_{rnd} the random-coincidence gate. This scaled random-coincidence spectrum is then deducted from the prompt spectrum, which gives the 'true' spectrum. The statistical uncertainty for the true spectrum is obtained from the random-chance spectrum multiplied by s^2, summed with the prompt spectrum. This gives a statistical uncertainty in the true spectrum of $\sigma^2_{\mathrm{true}} = \sigma^2_{\mathrm{pr}} + s^2\sigma^2_{\mathrm{rnd}}$, with σ_{true} equal to the square-root of the counts in the photopeak.

For TF measurements a gate is included to select for the field polarity, which is either 'up', 'down' or vetoed, as described in §3.2.

This careful selection of timing, energy and, in the case of TF experiments, polarity gates, allows for true coincidence events between recoiling particles and γ rays of interest to be sorted out of the data stream. With these events obtained, γ-ray spectra and relevant photopeak counts can be obtained for analysis, in order to determine quantities such as the nuclear g factor.

Chapter 4

Transient-Field Measurements

The transient-field (TF) effect, reviewed in §2.3.2 and outlined below, was utilised to perform nuclear g-factor measurements using Hyperion, ANU's hyperfine spectrometer [213]. Hyperion incorporates two key design features for performing TF measurements: a Sumitomo model RDK 408D cryocooler, used to cool the target to $\sim$5 K via a coldfinger, and shaping of the electromagnet pole pieces, that allows a field strength of 0.09 T to be applied across the target, while keeping stray field to a minimum (negligible) level. These two features eliminate three sources of systematic error: localised heating of the ferromagnetic host near to or above the Curie temperature, magnetic under-saturation of the ferromagnetic host, and stray field causing bending of the beam. Any of these may appreciably affect the measured precession angle, and are difficult factors to quantify. The polarity of the magnetic field is reversed every $\sim$ 15 min as to minimise uncertainties arising from small physical asymmetries, detector placement and efficiency, and other systematic sources. Previous measurements by this method using Hyperion have been described in detail [48, 56, 57, 147].

For perturbation of the nuclear spin-alignment to be meaningfully measured, the coordinate frame must be defined. The coordinate frame defining the particle- and γ-detector angles has its origin at the beam spot on the target. The beam direction defines the z or polar axis ($\theta = 0$) and the magnetic field is applied along the (vertical) y axis, which is along $(\theta, \phi) = (90^\circ, 90^\circ)$ in spherical polar coordinates. This is as depicted in Fig. 2.5. The γ-ray detectors are located in the (horizontal) xz or $\phi = 0$ plane, and the particle detectors were positioned parallel to the xy plane. A typical experimental setup is depicted in Fig. 4.1. When the detected particle is not the nucleus of interest, as in most cases described here, (relativistic) particle scattering solutions [144] were used to obtain the scattering angle of the nucleus of interest. For either case, the scattering solutions were used to obtain the energy of each scattered particle after Coulomb excitation. With the angles and reaction kinematics defined, the spin-precession angle can be determined from the measured perturbation in the angular correlation.

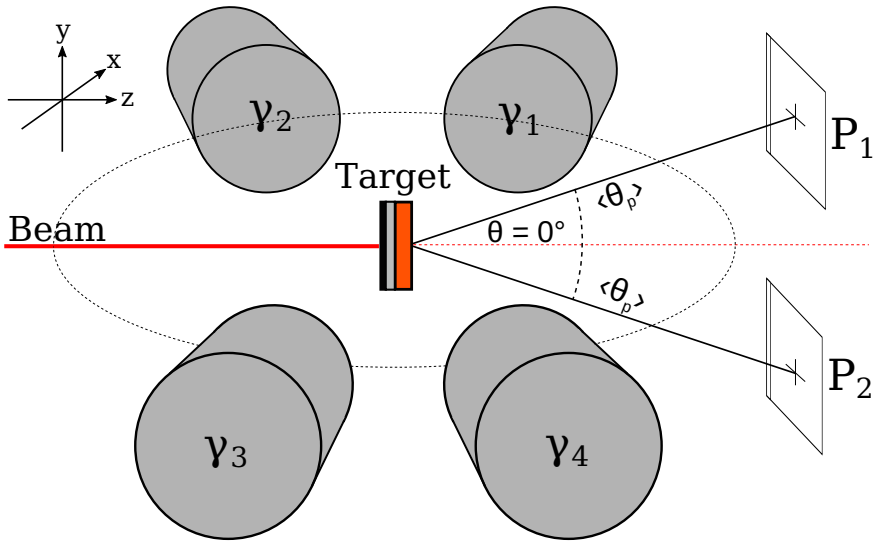

FIGURE 4.1: Setup of a typical thin-foil TF experiment in inverse kinematics. The beam (incoming from the left), consisting of the nuclei of interest, impinges upon a target consisting of three layers, being a target layer, a ferromagnetic host, and a copper backing. After Coulomb excitation of the beam, the target ions are forward-scattered and detected at equivalent scattering angles above or below the beam ($\phi = \pm 90^\circ$) by particle detectors P_1 and P_2 while the nucleus of interest recoils through the ferromagnetic layer and stops in the copper backing. If the experiment is conducted in conventional kinematics, with the target layer now containing the nuclei of interest, then the lighter beam ions will be back-scattered after the collision, and so the particle detectors will be on the left side of the target (see Fig. 4.18). Target nuclei (being the nuclei of interest) will excite and recoil into the ferromagnetic layer and/or copper backing. If the beam remains the nucleus of interest, in conventional kinematics, then the beam nuclei will excite upon the target and be detected forward-scattered. The γ-ray detectors are positioned at equivalent angles in the $x - z$ plane, with forward detectors at $\pm\theta$ and backward detectors at $\pm(180^\circ - \theta)$. Note that, when expressed in spherical coordinates, the detectors are always positioned at positive values of θ, and the phi angle will be $\phi = 0^\circ$ for positive angles and $\phi = 180^\circ$ for negative angles, while $0^\circ \leq |\theta| \leq 180^\circ$.

4.1 Analysis of Transient-Field Data

Several reviews exist describing the determination of nuclear g factors by measuring angular correlations perturbed by the transient field. The most recent comprehensive review was published by Benczer-Koller and Kumbartzki in 2007 [22]. As such, only the essential details of the procedure to determine the g factor will now be presented. The nucleus of interest is Coulomb excited and then recoils into a polarised ferromagnetic layer. In this layer the TF induces a precession of the nuclear spin for ions traversing the ferromagnetic medium. This spin-precession results in a rotation, $\Delta\theta$, in the angular correlation of the de-excitation γ rays, $W(\theta) \rightarrow W(\theta + \Delta\theta)$, in the plane perpendicular to the magnetic field, i.e. the plane in which the γ-ray detectors are located (see Fig. 4.1).

The γ-ray detectors then measure the angular correlation $W(\theta \pm \Delta\theta)$, with the sign of $\Delta\theta$ determined by the direction of the magnetic field, and the sign of the g factor. To obtain the precession angle from a measured coincidence rate, a double ratio of observed counts is formed:

$$\rho_{ij} = \sqrt{\frac{N(\theta_i)\uparrow N(\theta_j)\downarrow}{N(\theta_i)\downarrow N(\theta_j)\uparrow}}, \tag{4.1}$$

where $N(\theta_i)$ and $N(\theta_j)$ represent γ-particle coincidence counts in the photopeak measured in γ-ray detectors i and j at angles $+\theta_\gamma$ and $-\theta_\gamma$, respectively, and $\uparrow$ and $\downarrow$ represent the field direction.

The spin-rotation (precession) angle $\Delta\theta$ is determined from

$$W(\theta \pm \Delta\theta) \simeq W(\theta) \pm \Delta\theta \frac{dW}{d\theta}, \tag{4.2}$$

with $\Delta\theta$ being a small angle ($< 10^\circ$), determined by

$$\Delta\theta = \frac{\epsilon}{S}, \tag{4.3}$$

where

$$\epsilon = \frac{1-\rho}{1+\rho}, \tag{4.4}$$

and S is the logarithmic derivative of the angular correlation at $+\theta_\gamma$

$$S = S(\theta_\gamma) = \frac{1}{W}\frac{dW}{d\theta}\bigg|_{\theta_\gamma}. \tag{4.5}$$

Along with the double ratios used to determine the TF precession effect, it is useful to form 'cross ratios', which should show no net effect, as a check on the validity of the data. Cross ratios are given by Eq. (4.1) with $\theta_i = \theta_\gamma$ and $\theta_j = 180^\circ + \theta_\gamma$. Such symmetrically placed particle and γ-ray detectors should have ρ values distributed around unity or ϵ values distributed around zero; departures from the null effect can indicate systematic errors.

As discussed in §2.2.3, the Winther-de Boer code [4] can be used to compute the statistical tensors required to calculate angular correlations after Coulomb excitation [22, 207, 216]. However, angular correlations were also measured in the present work to verify the experimental setup and analysis procedures. The measured angular correlations can determine if there is any significant offset of the γ-ray detector or particle detector from their nominal positions. Such offsets have little impact on deduced relative precession angles, but can strongly affect absolute values, since S is a strong function of θ_γ at the

detection angles used for the precession measurements.

For short-lived states the precession angle is weakly dependent on the level lifetime, which may be taken into account by expressing

$$\Delta\theta = g\,\Phi(\tau), \tag{4.6}$$

where g is the nuclear g factor and $\Phi(\tau)$ is given by:

$$\Phi(\tau) = -\frac{\mu_N}{\hbar}\int_0^T B_{\mathrm{TF}}[v(t)]e^{-t/\tau}dt, \tag{4.7}$$

in which μ_N is the nuclear magneton, $\hbar$ is the reduced Planck constant, $B_{\mathrm{TF}}[v(t)]$ is the TF strength at the time-dependent ion velocity $v(t)$, τ is the mean life of the state of interest, T is the transit time of the nucleus through the ferromagnetic layer, and t is time.

Stuchbery *et al.* [213] define a figure of merit to guide detector placement for minimising uncertainty in $\Delta\theta$. Expressing this uncertainty as $\sigma_{\Delta\theta}$, it is determined by:

$$\sigma_{\Delta\theta} \approx \frac{1}{2}\frac{1}{S\sqrt{N}}, \tag{4.8}$$

where $N(\theta_i)\uparrow \approx N(\theta_i)\downarrow \approx N(\theta_j)\uparrow \approx N(\theta_j)\downarrow \approx N$ is the count rate in one detector for one field direction. Equation (4.8) shows that $\sigma^2_{\Delta\theta} \propto 1/S^2N$. This makes S^2N a useful figure of merit to maximise in order to reduce the measurement uncertainty. As the counting rate N is proportional to W,

$$S^2N \propto S^2J_0W, \tag{4.9}$$

where $Q_k = J_k/J_0$ is the solid-angle correction factor included in W, which depends strongly on the distance of the γ-ray detector's face to the target, d_γ, and J_0 is proportional to the detector efficiency.

Taking the components of Eq. (4.9) into account, θ and d_γ can be optimised for a given experiment by

$$\sigma^2_{\Delta\theta} \propto [S^2N]^{-1} \propto [S(\theta,\phi,d_\gamma)^2W(\theta,\phi,d_\gamma)J_0(d_\gamma)]^{-1}. \tag{4.10}$$

Stuchbery *et al.* show that the particle-detector geometry can also be optimised, with increased particle-detector size (meaning increased N) generally winning out over anisotropy loss (meaning reduced S) in the angular correlation [213], though this must be evaluated case-by-case, in consideration of the reaction kinematics. Because the

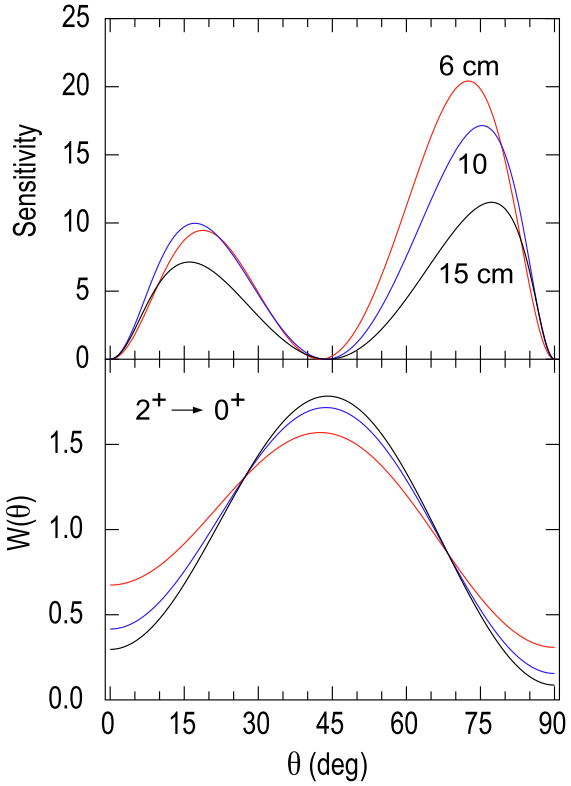

FIGURE 4.2: Plot of the sensitivity ($1/S^2 J_0 W$) versus θ angle for several detector distances d_γ in the top panel, and the angular correlation in the bottom panel. The angular correlation was calculated for a small recoil angle of the nucleus of interest, and $Q_k = J_k/J_0$ was calculated for a cylindrical HPGe detector 7 cm wide by 7 cm long. This figure was adapted from Fig. 4 of Ref. [213].

positioning and sizes of particle detectors were restricted by the available space in the target chamber used for measurements in this project, only γ-ray detector optimisation was considered.

With a fixed particle-detector geometry, plots such as that shown in Fig. 4.2 can be made, which show the interplay between θ_γ and d_γ. Plots like these give a good indication of the angle and distance that will produce the smallest uncertainty for a set amount of beam time. One should also consider how much effect a deviation from the nominal detector angle has on the slope. In order to maximise the sensitivity, whilst also avoiding shadowing of the γ-ray detector due to the target frame, the TF measurements performed during this candidature opted for γ-ray detector angles around $\theta = 65^\circ$.

4.2 Relative $g(2_1^+;\ ^{26}\mathrm{Mg})$:$g(2_1^+;\ ^{24}\mathrm{Mg})$ Measurement

Using the TF technique, a measurement of the ^{26}Mg 2_1^+ g factor relative to the ^{24}Mg 2_1^+ state was performed. This measurement was motivated by a recent successful measurement of $g(2_1^+;\ ^{24}\mathrm{Mg})$ by the time-differential recoil-in-vacuum (TDRIV) technique, and the accepted literature value for $g(2_1^+;\ ^{26}\mathrm{Mg})$ being considerably smaller than predicted by recent, large-basis shell-model calculations. The independent TDRIV measurement provided the opportunity to scale a precise measurement of $g(2_1^+;\ ^{26}\mathrm{Mg})$ relative to $g(2_1^+;\ ^{24}\mathrm{Mg})$, using the TF technique, without relying on a TF-strength parameterisation. It would also help validate the approach of using the TDRIV and TF techniques together to determine the nuclear g factors of challenging, short-lived states in a calibration-independent manner. A single gadolinium target was used to measure 2_1^+-state TF-precession angles in both nuclides. From these, the g-factor ratio was obtained and then scaled using the ^{24}Mg 2_1^+ TDRIV measurement result to give $g(2_1^+;^{26}\mathrm{Mg}) = +0.86(10)$. This value is in strong disagreement with the accepted literature value $g(2_1^+;^{26}\mathrm{Mg}) = +0.50(13)$ [196], but in good agreement with modern shell-model calculations. The success of this measurement shows the potential for TF and TDRIV techniques to be used together for measuring the g factors of short-lived nuclear states.

4.2.1 Methods

A relative measurement of the 2_1^+-state g factors between ^{24}Mg and ^{26}Mg was performed using the thin-foil TF technique by the author, present supervisors, research staff and students in 2014, outside of this candidature. The measurement was performed at ANU's Heavy Ion Accelerator Facility using Hyperion [213]. Beams of ^{24}Mg and ^{26}Mg at an energy of 120 MeV impinged upon, and were Coulomb excited by, a cryocooled, single-layer 9.9 mg/cm^2-thick gadolinium foil. The foil served both as the ferromagnetic layer for the TF precession effect, as well as the reaction target for Coulomb excitation.

Four NaI detectors recorded γ rays, and forward-scattered beam particles were detected by two 6 mm $\times$ 6 mm SiPDs at an average angle of $\pm 37^\circ$, centred at 18.5 mm above and below the horizontal plane. The beam intensity was kept below 2 enA, being limited by the count rate in the particle detectors. The experimental geometry followed that shown in Fig. 4.1, except the target was single-layered and the beam particles were detected forward-scattered. Calculated reaction kinematics and reduced precession angles ($\Phi = |\Delta\theta/g|$) are listed in Table 4.1. Two of the γ-ray detectors (γ_1 and γ_4) were positioned at $\theta_\gamma = \pm 60^\circ$ or $\theta_\gamma = \pm 65^\circ$ while the other two (γ_2 and γ_3) were positioned at $\theta_\gamma = \pm 120^\circ$. The detectors were originally intended to be set

TABLE 4.1: Average reaction kinematics for the 2_1^+ states of ^{24}Mg and ^{26}Mg traversing the gadolinium foil based on calculated Coulomb-excitation cross-sections and Ziegler's stopping powers [115]. $E(2^+)$ is the energy of the first-excited state, $\tau(2^+)$ is the mean life of the first-excited state, E_i is average energy at Coulomb excitation, E_e is the average energy of exit from the foil, $v_i(v_e)$ is the average velocity of the ion at excitation in (exit from) the foil, $\langle v \rangle$ is the average velocity of the ion in the foil, T is the effective transit time, and $\Phi(\tau)$ is evaluated from Eqs. (4.7) and (2.32). $v_0 = c/137$ is the Bohr velocity. The level energies and mean lifetimes are from Refs. [71, 17].

Nuclide	$E(2^+)$ (keV)	$\tau(2^+)$ (ps)	E_i (MeV)	E_e (MeV)	v_i/v_0	v_e/v_0	$\langle v/v_0 \rangle$	T (ps)	$\Phi(\tau)$ (mrad)
^{24}Mg	1369	1.92(9)	97.0	61.7	12.8	10.2	11.5	0.356	38.7
^{26}Mg	1809	0.69(3)	97.8	57.8	12.3	9.47	11.1	0.327	35.0

at $\pm 65°$, but the initial run revealed that the vacuum deorientation of the recoiling ions caused this angle to be less than optimal for the measurement. The angular correlation was measured for ^{24}Mg by varying the detectors denoted γ_1 and γ_4 through angles $\theta_\gamma = 0°, \pm 15°, \pm 30°, \pm 45°, \pm 55°, \pm 60°, \pm 65°$, and $\pm 70°$. For ^{26}Mg the angular correlation was measured at γ-ray detector angles of $\theta_\gamma = \pm 15°, \pm 45°, \pm 60°, \pm 65°$ and $\pm 70°$. Data were recorded using the Analogue DAQ system. Angular correlation data sets were normalised to each other using the downscaled particle count. The data were analysed as per §3.3, using the TSort and Fitek4 software programs to sort out events from the Analogue DAQ data stream, visualise energy and time spectra, and obtain background-subtracted integral photopeak counts.

4.2.2 Results

To obtain the g factor of $^{26}\mathrm{Mg}(2_1^+)$, photopeak counts gated by the field direction were obtained following the analysis procedure described in §3.3. Examples of true-coincidence γ-ray spectra from a NaI γ-ray detector for both ^{24}Mg and ^{26}Mg are shown in Fig. 4.3. The procedure described in §4.1 was followed to obtain ϵ values. Because the Mg ions were allowed to recoil into vacuum, the lab-frame angular-correlation data shown in Fig. 4.4 were fitted to determine the attenuation coefficients G_2 and G_4 (see §2.3.3 for more information), and hence the correct the S values. As the G_2 and G_4 parameters are highly correlated for the available data, they were related through a single $J = 1/2$ electron-spin (H-like) fraction parameter, as described in a previous study of high-velocity ^{24}Mg ions [129] which used a methodology similar to that of the present measurement. Fits returned a $J = 1/2$ fraction of $\sim$50%, in good agreement with the charge-state distribution calculated using the Schiwietz-Grande formula [187] when summing the H-like and Li-like contributions, which both have $J = 1/2$ ground states. The S values obtained

agree well with those obtained allowing G_2 and G_4 to vary freely, but avoided the complications of handling the errors on correlated parameters. While the S values for the forward-placed detectors at $\theta_\gamma = \pm 60^\circ$ and $\pm 65^\circ$ could be determined from the fit to measured angular correlations, those for the backward detectors at $\theta_\gamma = \pm 120^\circ$ were inferred from the fit to the measured angular correlations at forward angles, the difference between $\pm 60^\circ$ and $\pm 120^\circ$ originating only from the effect of the Lorentz boost. The measured effect sizes (ϵ), calculated slopes (S) and deduced precession angles ($\Delta\theta$) are listed in Table 4.2. The relative g factor was determined from a ratio of Eq. (4.6) for ^{24}Mg and ^{26}Mg, then solving for g, as

$$\frac{g(2_1^+;^{26}\,\mathrm{Mg})}{g(2_1^+;^{24}\,\mathrm{Mg})} = \frac{\epsilon(^{26}\mathrm{Mg})}{\epsilon(^{24}\mathrm{Mg})}\frac{S(^{24}\mathrm{Mg})}{S(^{26}\mathrm{Mg})}\frac{\Phi(^{24}\mathrm{Mg})}{\Phi(^{26}\mathrm{Mg})} = \frac{26.9(21)}{18.6(16)} \times \frac{38.7}{35.0} = 1.60(19).$$

Taking $g(2_1^+;^{24}\,\mathrm{Mg}) = +0.538(13)$ gives $g(2_1^+;^{26}\,\mathrm{Mg}) = +0.86(10)$.

The reported uncertainty in $g(2_1^+;^{26}\,\mathrm{Mg})$ is dominated by the statistical precision, but also includes small contributions from the uncertainty in S, and a 2.4% uncertainty assigned to the ratio $\Phi(^{24}\mathrm{Mg})/\Phi(^{26}\mathrm{Mg}) = 38.7/35.0$ to account for uncertainty in the velocity-dependence of the transient field. This uncertainty was estimated by comparing this adopted ratio, evaluated using Eq. (2.32), to an evaluation of $\Phi(^{24}\mathrm{Mg})/\Phi(^{26}\mathrm{Mg})$ under the assumption that $B_{\mathrm{TF}} \propto v$, as per Eq. (2.29). Regardless, the g-factor measurement is effectively independent of the assumed velocity dependence of the transient field because both level lifetimes are longer than the transit time through the gadolinium foil (see Table 4.1). Furthermore, the experimental value of $\Phi_{\mathrm{exp}}(^{24}\mathrm{Mg}) = \Delta\theta/g = 35(3)$ mrad is in agreement with the parameterisation of Eq. (2.32) (see Table 4.1), considering that uncertainties in the gadolinium target thickness ($\sim 5\%$) have been ignored, and that a reduced magnetisation is often found for such relatively thick gadolinium foils [216]. This gives further confidence in the accuracy of the calculated $\Phi(\tau)$ values. Precession

TABLE 4.2: Experimental results for the ^{24,26}Mg TF measurement

Nuclide	$\pm\theta_\gamma$	$\epsilon\times10^3$	S [rad^{-1}]	$\Delta\theta$ (mrad)
^{24}Mg	60	+23.3(35)	−1.299(26)	−18.0(27)
	65	+22.8(69)	−1.294(26)	−17.6(54)
	120	−23.5(25)	+1.229(25)	−19.2(21)
				−18.6(16)[a]
^{26}Mg	60	+35.5(126)	−1.573(31)	−22.6(80)
	65	+46.9(53)	−1.618(32)	−29.0(33)
	120	−37.7(39)	+1.455(30)	−25.9(28)
				−26.9(21)[a]

[a]Weighted average.

angles an order of magnitude larger than the earlier works [61, 196] were observed in the present measurement. Moreover, the same target was used with beam excitation to measure the ratio of 2_1^+-state g factors in ^{24}Mg and ^{26}Mg. As such, the g-factor ratio is determined essentially by the ratio of ϵ values, with relatively small corrections due to differences in S (arising from differences in the particle-frame θ angle and vacuum deorientation), and effective TF strengths which largely cancel when the ratio is taken. These features of the experiment helped to ensure a robust and reliable result.

In conclusion, by virtue of the experimental design, the measurement uncertainty is limited by the counting statistics, with systematic uncertainties having relatively little contribution.

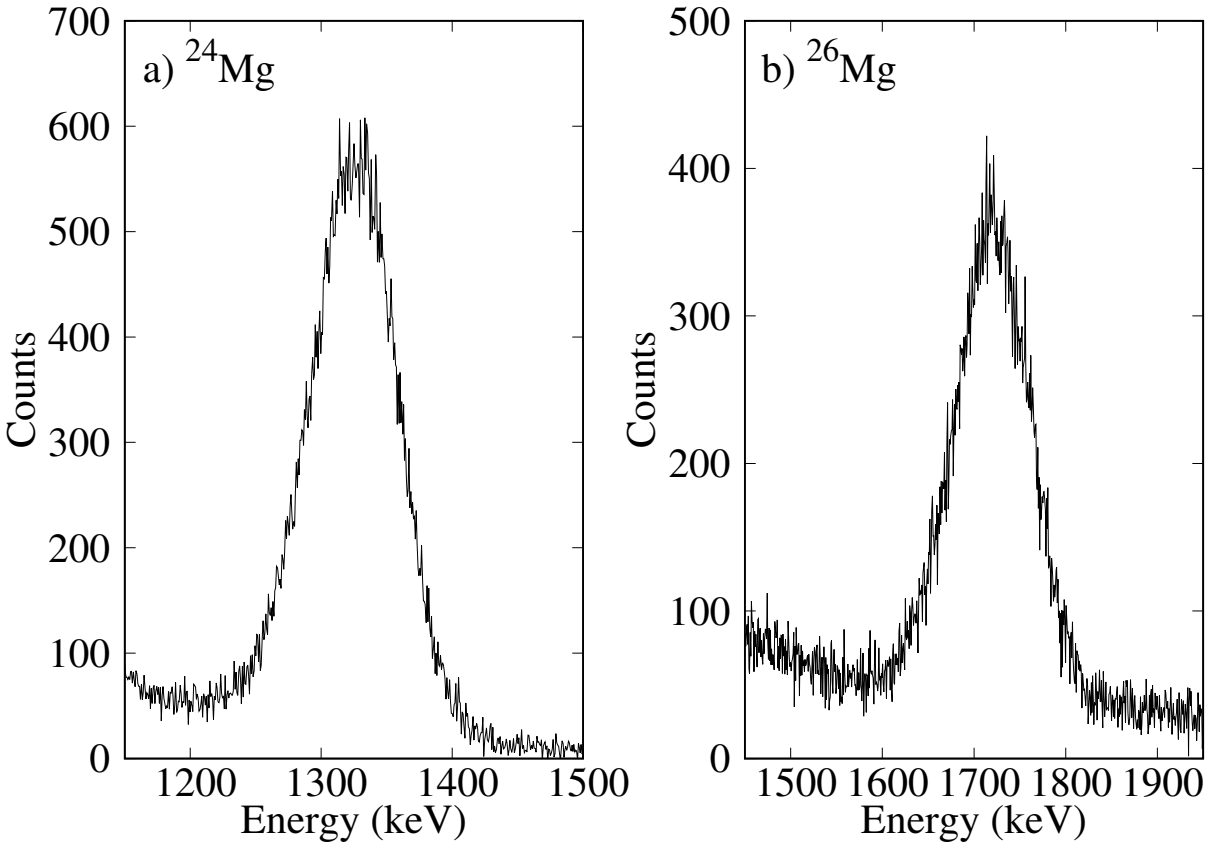

FIGURE 4.3: Photopeak region of the random-subtracted particle-γ coincidence spectra observed in γ_2 (120°) for a) ^{24}Mg and b) ^{26}Mg. The spectra show the field-up, field-down, and both particle detector P_1 and P_2 data summed across all runs.

4.2.3 Discussion

In this project, the g factor of the first-excited 2^+ state in ^{26}Mg was determined relative to the equivalent excited state in ^{24}Mg using the high-velocity thin-foil TF technique. This

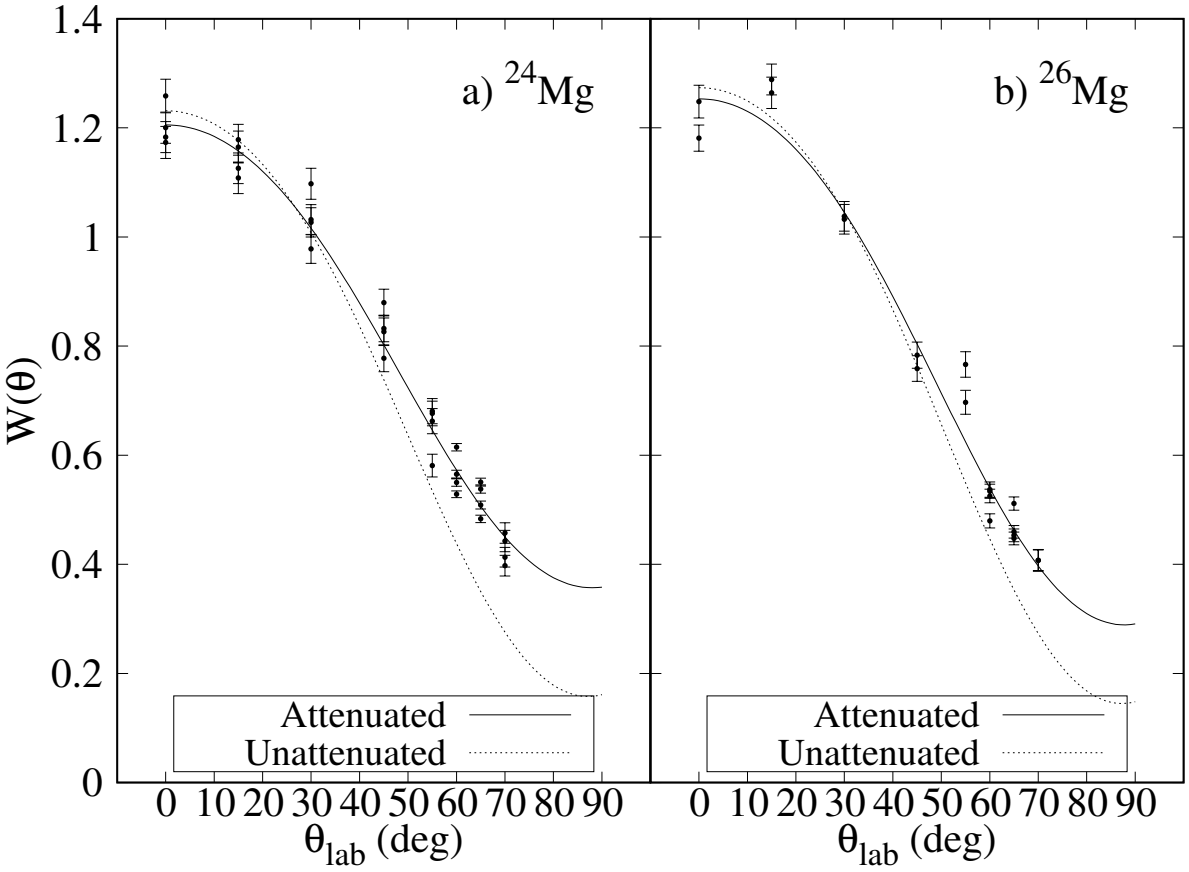

FIGURE 4.4: Angular correlations in the laboratory frame for a) ^{24}Mg and b) ^{26}Mg. The data are shown along with the calculated unattenuated correlation (dotted line) and the fit that is attenuated by vacuum deorientation (solid line).

measurement was motivated by a highly precise measurement of $g(2_1^+;^{24}\,\mathrm{Mg})$ made using the TDRIV technique [129]. A previous measurement of $g(2_1^+)$ had been performed using IMPAC [61] in both ^{24}Mg and ^{26}Mg. The uncertainties in their values were large, but it is curious to note that they obtained $g(2_1^+;^{24}\,\mathrm{Mg}) = 0.42(9)$, smaller than the now accepted $g(2_1^+;^{24}\,\mathrm{Mg}) = 0.538(13)$. This difference will be discussed in Chapter 7. A few years later, the two were remeasured by Speidel *et al.* [196], who suspected the static hyperfine-field strength was underestimated. A dramatically different value was obtained for $g(2_1^+;^{26}\,\mathrm{Mg})$, in strong disagreement with the previous measurement and also with multi-configuration shell-model calculations. The precise $g(2_1^+;^{24}\,\mathrm{Mg})$ value obtained using the TDRIV technique presented the opportunity to reassess these measurements in a manner that virtually eliminated the systematic uncertainty present in the previous measurements by repeating the relative TF measurement using modern methods.

The 2_1^+ state in ^{26}Mg is a challenging state for g-factor measurements. This is due largely to its short lifetime ($\tau = 0.69$ ps), however its small natural abundance of 11% (which affects the beam intensity achievable using a non-enriched sample), combined with the large excitation energy of the state (1.8 MeV), also make the acquisition of the high statistics required for a precise measurement difficult to achieve. To counter this, the high-velocity thin-foil TF technique was chosen, using a gadolinium host as the ferromagnet. This technique and material provide the large magnetic field required ($B_{\mathrm{TF}} \gtrsim 10^3$ T) to measurably precess the ^{26}Mg 2_1^+ state over its short lifetime. By also measuring the ^{24}Mg 2_1^+ state under similar conditions (i.e. during the same experimental run, at the same beam energy), the g-factor ratio between the two states was determined in a manner that has reduced systematic error. This reduction was achieved by implementing several experimental design factors. By using the same target, uncertainties relating to its thickness and magnetisation affected both states equally and are factored-out in the ratio. This is particularly important for gadolinium foils, for which it can be hard to achieve consistent magnetisation. The only potential sources of uncertainty that remained were lattice damage, and potential beam-induced demagnetisation effects due to heavy-ion interactions that might cause differences between the runs with the two different beams. These were minimised by using low-intensity beams ($\sim$ 1 pnA) and by cryocooling the target. The short lifetimes of these two states, being $\tau \lesssim 2$ ps, also have a considerable effect on the measured precession angle. To account for this, a TF-strength parameterisation, developed especially for elements in this region at this high velocity, was used with a lifetime dependence to obtain the reduced precession angle $\Phi(\tau)$, as per Eq. (4.7). When two states, having the same Z and recoiling at similar, narrow velocity ranges are measured relative to each other, uncertain quantities in the TF-strength parameterisation largely cancel,

minimising uncertainty in the parameterisation. By using the same thin ferromagnetic host and having nuclei recoil at similar velocities, the uncertainty in the measurement is reduced almost entirely to the statistical uncertainty of the measurement. Even so, the variation arising from different parameterisations was examined and used as a source of systematic uncertainty in the final reported value, though it was still dominated by the statistical uncertainty. By robustly determining the relative g factor, $g(2_1^+;^{26}\mathrm{Mg})$ was confidently determined using the known $g(2_1^+;^{24}\mathrm{Mg})$ value.

This measurement demonstrated that the g factors of short-lived, excited states can be reliably and precisely determined using the TF technique in a manner free from systematic error and parameterisation issues, supposing a suitable and independent g-factor measurement is available in another isotope of the same element. By using the TDRIV technique as a complementary method, these independent measurements may be obtained, which simultaneously allow the g-factor's sign to be ascertained by the TF technique, and the magnitude of the TF strength to be set using the RIV technique.

4.3 Relative g-factor Measurements in the Ge and Se Isotopes

The first instance of a simultaneous, relative g factor measurement on first-excited 2_1^+ states in the isobaric nuclei ^{74}Ge and ^{74}Se, delivered as a cocktail beam, was performed using the thin-foil TF technique in inverse-kinematics. In addition to this, the stable, even-A isotopes of each element were also measured using the same target and under the same conditions. The aim of this experiment was to obtain relative $g(2_1^+)$ ratios between the isotopes of each element, and between the two isotopic chains, having little to no systematic uncertainty. This experiment was motivated by experimental results obtained from a time-integral RIV experiment on these same isotopic chains, performed previously at ANU [134]. Unexpected differences in behaviour between the two isotopic chains, measured using the RIV technique, proved difficult to interpret using literature g-factor values [98, 195]. This discrepancy may be due to differences in the hyperfine interaction between the two elements. However, it is important to rule out any uncertainty in the relative g factors. Therefore, confirmation of their relative g-factor values, having minimal systematic uncertainty, was sought. It was found that the trend present in the accepted literature g factors for the Ge isotopes differed from the present measurement. However, when comparing instead relative g-factor values in the literature that were obtained using the same target, this discrepancy disappeared. As such, these literature values, and those obtained in the present measurement, were averaged to give precise relative g-factor values across the Ge and Se isotope chains.

4.3.1 Methods

Relative measurements of $g(2_1^+)$ in the stable, even-A isotopes of Ge and Se were performed using the thin-foil TF technique. Data were collected over five separate runs, the details of which are listed in Table 4.3. Of these, runs 1 and 2 were performed during this research candidature, and will now be described. Two cathodes, consisting of a Ge-Se mixture, and Ge alone, were used in ANU's heavy-ion accelerator facility ion source to generate the desired ions. Two separate runs had to be performed as when the ^{76}Ge beam was delivered during run 1, using the Ge cathode, there was isobaric ^{76}Se still present in the beam. This was likely leftover in the ion source from the previous cathode. As the γ-ray energy of the 2_1^+-state decay for these two nuclei could not be resolved, a second run had to be performed after the ion source had been cleaned. In this run, only ^{74}Ge and ^{76}Ge were measured, using a different target of similar constitution to the first. Because the excitation energy of the 2_1^+ state in the ^{74,76}Ge isotopes is amongst the lowest across the two isotope chains, the beam energy for this run was lowered to further reduce excitation of the 4_1^+ state. During run 1, repeated measurements of

TABLE 4.3: Summary of Ge and Se TF measurements. Runs 1 and 2 were performed during this research candidature. Run 3 was performed at ANU in 2015 by the Department of Nuclear Physics spectroscopy group. Runs 4 and 5 were performed at ANU in 2012 by the Nuclear Physics spectroscopy group.

	Run 1	Run 2[a]	Run 3	Run 4[b]	Run 5[b]
Beam Energy (MeV)	190	180	190	190	190
Beam Species	^{70,72,74}Ge, ^{76,78,80,82}Se ^{74}Ge + ^{74}Se[c]	^{74,76}Ge	^{74}Ge + ^{74}Se[c]	^{80,82}Se	^{78,82}Se
Target (C/Fe[Gd]/Cu) (mg/cm^2)	0.48/3.66/5.6	0.37/3.67/10.6	0.28/4.23/3.94	0.28/4.23/3.9	0.5/[5.92]/5.5
ϕ_p	90°	90°	0°, 45°, 90°, 135°, 180°	0°, 45°, 90°, 135°, 180°	0°, 45°, 90°, 135°, 180°
θ_γ, precession	±65°, ±115°	±65°, ±115°	±50°, ±130°	±65°, ±115°	±45°, ±135°
θ_γ, angular correlation	0°, ±30°, ±45°, ±55°, ±60°, ±65°	0°, ±30°, ±40°, ±45°, ±50°, ±55°, ±60°, ±65°, ±75°, ±115°, 235°, ±135°	0°, ±30°, ±45°, ±50°, ±55°, ±65°, ±75°	0°, ±25°, ±55° ±65°, ±88°	

[a] Runs 1 and 2 were separated in time because the ion source was contaminated after running the Se and cocktail beams, and the γ-ray energies associated with ^{76}Ge and ^{76}Se, 562.9 and 559.1 keV, respectively, are too close to separate reliably.

[b] Runs 4 and 5 were consecutive, beginning with the ^{80}Se beam, followed by ^{82}Se and ^{78}Se beams. The target was changed during delivery of the ^{82}Se beam.

[c] Cocktail beam.

TABLE 4.4: Reaction kinematics for the 2_1^+ states of Ge and Se isotopes as the ions traversed the ferromagnetic layer of the target. $E_i(E_e)$ is the average energy at entry into (exit from) the foil, $v_i(v_e)$ is the average velocity at entry into (exit from) the foil, $\langle v \rangle$ is the average velocity through the foil, T is the effective transit time, and $v_0 = c/137$ is the Bohr velocity. τ is the mean life of the 2_1^+ state, taken from Ref. [179]. Figure 4.5 shows the definition of $\langle \theta_p \rangle$ for runs 1 and 2.

Nuclide	E_i (MeV)	E_e (MeV)	v_i/v_0	v_e/v_0	$\langle v/v_0 \rangle$	T(fs)
Run 1 $\langle \theta_p \rangle = 22°$						
^{70}Ge	91.2	10.9	7.25	2.50	4.61	407
^{72}Ge	92.6	11.9	7.20	2.58	4.59	444
^{74}Ge	93.9	12.9	7.15	2.65	4.59	462
^{74}Ge	93.9	12.9	7.15	2.65	4.59	462
^{74}Se	92.8	10.1	7.11	2.35	4.37	480
^{76}Se	94.1	11.1	7.07	2.43	4.41	481
^{78}Se	95.5	12.1	7.03	2.50	4.45	474
^{80}Se	96.9	13.1	6.99	2.57	4.49	467
^{82}Se	98.1	14.1	6.94	2.63	4.51	468
Run 1 $\langle \theta_p \rangle = 0°$						
^{70}Ge	80.2	7.16	6.79	2.03	4.06	452
^{72}Ge	81.8	8.04	6.77	2.12	4.06	495
^{74}Ge	83.4	8.95	6.74	2.21	4.09	513
^{74}Ge	83.4	8.95	6.74	2.21	4.09	513
^{74}Se	82.3	6.78	6.69	1.92	3.86	537
^{76}Se	83.9	7.61	6.67	2.01	3.92	536
^{78}Se	85.4	8.49	6.64	2.09	3.99	523
^{80}Se	87.0	9.39	6.62	2.17	4.04	514
^{82}Se	88.4	10.3	6.59	2.25	4.08	513
Run 2 $\langle \theta_p \rangle = 22°$						
^{74}Ge	91.0	11.5	7.04	2.51	4.44	478
^{76}Ge	92.3	12.5	7.00	2.58	4.48	477
Run 2 $\langle \theta_p \rangle = 0°$						
^{74}Ge	82.0	8.39	6.68	2.14	4.01	525
^{76}Ge	83.6	9.29	6.66	2.22	4.07	520
Run 3						
^{74}Ge	111	13.0	7.76	2.66	4.87	505
^{74}Se	110	10.1	7.74	2.34	4.63	525
Run 4						
^{80}Se	114	13.0	7.57	2.56	4.72	516
^{82}Se	115	13.9	7.51	2.62	4.74	517
Run 5						
^{78}Se	103	18.8	7.30	3.12	4.96	680
^{82}Se	106	21.1	7.20	3.22	4.98	681

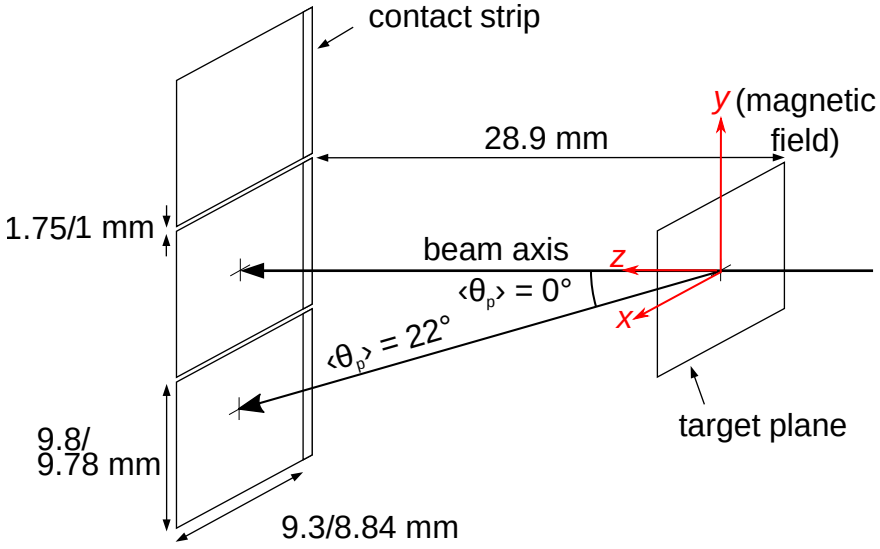

FIGURE 4.5: Experimental geometry for the Ge and Se TF measurement run 1 and run 2 showing the beam axis and the particle detector dimensions (run 1 / run 2). The average scattering angles for the ^{12}C target ions are indicated by $\langle\theta_p\rangle$.

^{74}Ge and ^{74}Se at different time-points allowed for the effect size, and thereby the target condition, to be monitored as the run progressed. Data for runs 1 and 2 were recorded using the Digital DAQ. Run 3 was performed by ANU's Department of Nuclear Physics spectroscopy group in 2015, and runs 4 and 5 in 2012. These data were not previously published, and have been included in this analysis. Data for runs 3–5 were recorded using the Analogue DAQ.

All ion beams were delivered by ANU's 14UD Pelletron accelerator. The beams were incident upon a multi-layer target consisting of a front ^{nat}C layer, an iron or gadolinium foil, and a copper backing. The target details are presented in Table 4.3. For runs 1 and 2, the iron layer was prepared by cutting a $\sim$2 cm$\times$1 cm piece from a large 4.5 mg/cm^2 iron foil and rolling it to the desired thickness of $<$4 mg/cm^2. The foil, now $\gtrsim 2 \times 1$ cm, was then annealed at $\sim$750°C for 30 min under vacuum and its areal density was re-measured. The foil was then cut into two $\sim$1 cm$\times$1 cm pieces. A piece of copper foil of the same size was annealed under the same conditions but only for 10 mins. A very thin layer ($\sim$0.2 mg/cm^2) of indium was then evaporated onto the copper layer, and the iron and copper layers were pressed together under $\sim$1 ton of pressure, with the indium between serving to "glue" the foils together. Finally, the carbon layer was painted onto the iron side of the iron-copper foil. The front ^{nat}C layer served to Coulomb-excite the beam, the central iron or gadolinium foil served as the ferromagnetic host for the TF precession effect, and the copper backing served as a "field-free" environment to stop the recoiling beam particles and provide a good thermal contact. Relevant details of the reaction kinematics are summarised in Table 4.4. Hyperion's cryocooler and

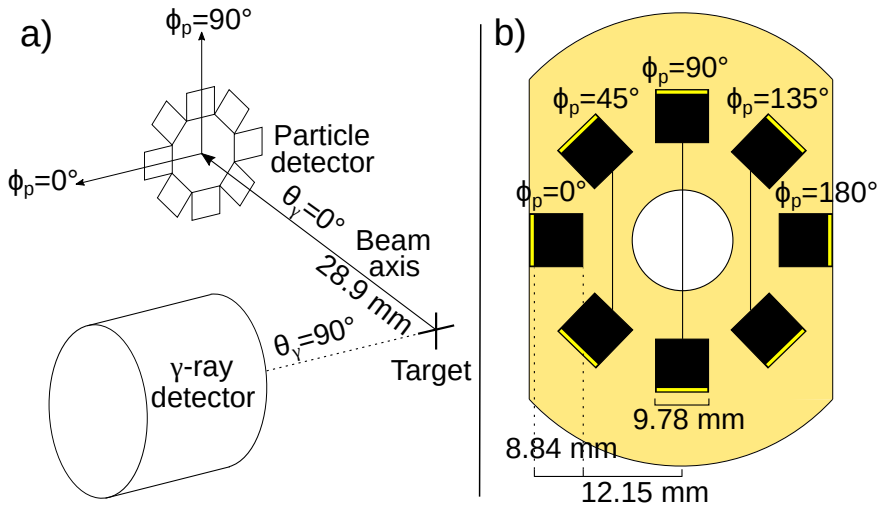

FIGURE 4.6: a) Experimental geometry for the Ge and Se TF measurement runs 3–5 showing the beam axis, a γ-ray detector and the particle detectors. b) A schematic of the particle detector array used in these runs, indicating dimensions and detectors with joined outputs.

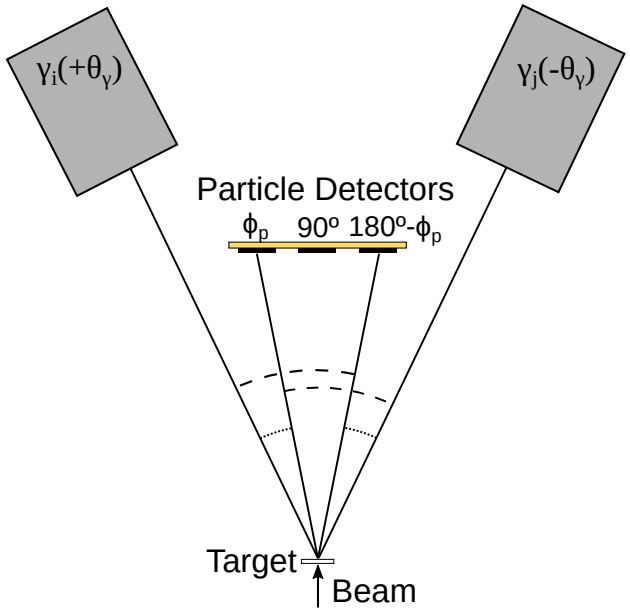

FIGURE 4.7: Illustration of the particle-γ coincidence geometry, drawn from a top-down view. Symmetry is maintained when particle-γ coincidence pairs are formed with γ_i at $+\theta$ paired with the particle detector at ϕ_p and γ_j at $-\theta$ paired with the particle detector at $180^\circ - \phi_p$, shown by the equivalent dotted versus dashed angles. In short, $\gamma_i(\phi_p)$ must be paired with $\gamma_j(180^\circ - \phi_p)$. Figure 4.6 shows the definition of the angle ϕ_p.

electromagnet were operated as described in the chapter introduction (Ch. 4).

Forward-scattered C ions were detected by SiPDs, arranged as shown in Figure 4.5 for runs 1 and 2, and Figure 4.6 for runs 3–5. The central detector for runs 1 and 2 was covered with a 1.7-mg/cm^2-thick mylar sheet to prevent transmitted beam, knock-on target ions, or low-energy electrons (δ rays) from reaching the detector. Four HPGe detectors detected γ rays emitted from the Coulomb-excited beam particles. The setup was as shown in Fig. 4.1. Average particle-detector azimuthal angles (ϕ_p) and γ-ray detector angles (θ_γ) for each run are summarised in Table 4.3. In the following discussion of runs $3-5$, the particle detectors are identified by their absolute ϕ_p angle as indicated in Figure 4.6. The γ-ray detector angles employed for the TF precession measurements were selected to maximise the measured precession effect for the available particle-detector angles [213], see Eq. (4.8). Angular correlations were measured by moving two or three γ-ray detectors through a sequence of different angles with respect to the beam, while the remaining detector(s) remained fixed. The angular-correlation data sets were normalised between runs using particle-γ coincidence counts in the fixed γ-ray detector(s), while particle detectors were normalised to each other using the downscaled count rates within each run.

For runs 1 and 2 the detectors had the usual particle-γ coincidence symmetry with the particle detectors at $\phi_p = \pm 90^\circ$ or $\theta_p = 0^\circ$, so double ratios can be formed in the conventional way [22] for each of the three particle detectors. To calculate ρ_{ij} for runs 3–5 using the detector type shown in Figure 4.6, a modified procedure is required when using counts from the photodiodes with $\phi_p \neq \pm 90^\circ$. This is because the θ-dependent angular correlation, when $\phi \neq \pm 90^\circ$, is not symmetric around $\theta = 0^\circ$. As a result, detectors at $\pm\theta$ are not equivalent, and so detector pairs cannot be formed in the conventional way. Instead, consideration of the equivalent γ-ray-detector θ *and* particle-detector ϕ angles becomes necessary. In spherical polar coordinates, a typical TF experimental setup (as illustrated in Fig. 4.1) has $\phi = 0^\circ$ for γ-ray detectors having $0^\circ \leq \theta \leq 180^\circ$, and $\phi = 180^\circ$ for detectors having $\theta < 0^\circ$ (which, in spherical polar coordinates, will be transformed to their $0^\circ \leq \theta \leq 180^\circ$ equivalent). This means the $\Delta\phi$ values used for calculating the angular correlation become mirrored for γ-ray detectors at negative θ angles. The symmetries required to form the particle-γ coincidences in Eq. (4.1) can be inferred from Figure 4.7, which represents a top-down view of the particle and γ-ray detectors projected onto the horizontal plane. For clarity, Figure 4.7 shows only one pair of particle detectors at angles ϕ_p and $180^\circ - \phi_p$, along with the typical $\phi_p = 90^\circ$ detector. By inspection of Figure 4.7 it can be seen that the relative angle between the γ-ray detector at $+\theta_\gamma$ and the particle detector at ϕ_p is equivalent to that between the γ-ray detector at $-\theta_\gamma$ and the particle detector at $180^\circ - \phi_p$, as indicated by the dotted arcs.

There is another pair of particle-γ combinations with the relative angle indicated by the dashed arcs in Figure 4.7; the angle between detectors at $+\theta_\gamma$ and $180^\circ - \phi_p$ is equivalent to that between the detectors at $-\theta_\gamma$ and ϕ_p. These equivalences visually represent the mirroring of the $\Delta\phi$ angles in pairing the γ-ray and particle detectors. Taking into account the correct spherical polar coordinates, Eq. (4.1) should be constructed such that if $N(\theta_i)$ represents $N(\theta_i, \phi_p)$, then $N(\theta_j)$ must represent $N(\theta_j, 180^\circ - \phi_p)$, and if $N(\theta_i)$ represents $N(\theta_i, 180^\circ - \phi_p)$, then $N(\theta_j)$ must represent $N(\theta_j, \phi_p)$.

The primary objective was to measure g-factor ratios for the Ge and Se isotopes. These were obtained by combining Eq. (4.3) and Eq. (4.6) to give

$$\frac{g_x}{g_y} = \frac{\epsilon_x}{\epsilon_y}\frac{S_y}{S_x}\frac{\Phi_y}{\Phi_x} = \frac{\Delta\theta_x}{\Delta\theta_y}\frac{\Phi_y}{\Phi_x}, \tag{4.11}$$

where x and y signify the two states being measured. The ratio Φ_y/Φ_x must be evaluated based on a parameterisation of the TF strength. For this purpose we have adopted the Rutgers parameterisation [see §2.3.2 and Eq. (2.30)]. Nevertheless, the ratio Φ_y/Φ_x is almost independent of any reasonable choice of parameters. In the evaluation of Φ, the TF strength can be expressed as:

$$B_{\mathrm{TF}}[v(t)] = a_{\mathrm{TF}} Z^{P_Z} (v/v_0)^{P_v}, \tag{4.12}$$

as per Eq. 2.30.

The scale parameter a_{TF} cancels in the Φ ratio, as does the atomic number dependence for ratios within an isotope chain. For nearby atomic numbers, such as for the ratio $\Phi(^{74}\mathrm{Se})/\Phi(^{74}\mathrm{Ge})$, the difference between using the linear Eberhardt ($P_Z = 1$) versus the non-linear Rutgers parameterisation ($P_Z = 1.1$) is 0.6% in this case, a negligible value. $\Phi_y(\tau_y)/\Phi_x(\tau_x)$ is therefore sensitive only to the parameter P_v, and then only if one of the lifetimes is short compared to the transit time of the ion through the ferromagnetic foil. In the cases encountered here, the difference in Φ_y/Φ_x that comes about between the linear versus non-linear parameterisations of the TF strength is altogether negligible. Furthermore, Φ_y/Φ_x is near unity for most of the cases reported here. Therefore, systematic uncertainty owing to the TF parameterisation is negligible in this measurement.

4.3.2 Results

To evaluate the g-factor ratios amongst and between the Ge and Se isotopes, photopeak counts were obtained from background-subtracted integrals of the photopeak region of the $2_1^+ \rightarrow 0_1^+$ transition, after random-coincidence subtraction in particle-γ coincidence

spectra. This procedure was described in §4.1. An example γ-particle time-difference spectrum is shown in Fig. 4.8. An example true γ-ray spectrum for ^{74}Ge from run 1 is shown in Fig. 4.9. Measured angular correlations are shown in Figs. 4.10–4.13. Figures 4.10 and 4.11 compare the angular correlations for the central and outer particle detectors in runs 1 and 2 (see Fig. 4.5). There is a less pronounced dip at $\theta_\gamma = 0^\circ$ for the outer detectors, but the slope at $\theta_\gamma = \pm 65^\circ$ is very similar for both the central and outer detectors. These figures also show that the calculated angular correlations agree very well with experiment and that the angular correlations are almost identical between the isotopes measured. Thus, the ratio S_y/S_x in Eq. (4.11) is very near unity in all cases considered here. Figures 4.12 and 4.13 show angular correlations for the five particle detectors at $\phi_p = 0^\circ$, 45°, 90°, 135°, and 180° in run 3 (see Fig. 4.6). The similarity of the angular correlations for $\phi_p = 90^\circ$ to the almost-equivalent outer detectors in Fig. 4.10 and Fig. 4.11 is evident. Also evident in Fig. 4.12 and Fig. 4.13 is that for $\phi_p = 0^\circ$, 45°, 135°, and 180°, the angular correlation has a pronounced slope at $\theta_\gamma = \pm 45^\circ$ and $\theta_\gamma = \pm 90^\circ$, in some cases of similar magnitude to that at $\theta_\gamma = \pm 65^\circ$ for the conventionally used $\phi_p = 90^\circ$. These differences change the sensitivity function, Eq. (4.8), and consequently the placement of γ-ray detectors indicated for runs 3–5 in Table 4.3.

Precession angles were evaluated as per Eq. (4.3), with $S(\theta_\gamma)$ calculated from angular correlation theory [207, 210, 216], (see §2.2). The measured effect size (ϵ), calculated slopes (S) and resulting precession angles ($\Delta\theta$) are listed in Table 4.5. In order to check that systematic errors were minimal, cross-ratios [22] were calculated for all particle-γ pairs. The cross-ratios, shown in Fig. 4.14, are consistent with a normal distribution around unity, indicating no significant systematic error.

Indirect population of the 2_1^+ state by feeding from the 4_1^+ states was determined from the ^{74,76}Ge and ^{74}Se spectra as these nuclides have the lowest 4_1^+-state excitation energies. Population of the 4_1^+ state was measured to be no greater than $\sim$ 2% of the 2_1^+ state population in the strongest case, and therefore the effect of feeding on the measurement of the 2_1^+-state precession angle was deemed negligible for all isotopes.

The g-factor ratios determined from the measured precession angles and $\Phi(\tau)$ values in Table 4.5 are listed in Table 4.6. The Ge isotopes are referenced to ^{74}Ge, the Se isotopes are referenced to ^{74}Se, and the Ge and Se isotopes are related through the ratio $g(^{74}\mathrm{Se})/g(^{74}\mathrm{Ge})$. The value of this ratio from the cocktail beam data in runs 1 and 3 alone is $g(^{74}\mathrm{Se})/g(^{74}\mathrm{Ge}) = 1.325(77)$. With the additional data collected for ^{74}Ge alone from run 1 the ratio becomes $g(^{74}\mathrm{Se})/g(^{74}\mathrm{Ge}) = 1.338(71)$, which is the value given in Table 4.6. Runs 4 and 5 did not include either of the reference isotopes, ^{74}Ge and ^{74}Se, but they give independent measures of $g(^{80}\mathrm{Se})/g(^{82}\mathrm{Se})$ and $g(^{78}\mathrm{Se})/g(^{82}\mathrm{Se})$,

respectively. These data were included in the evaluation of the g-factor ratios for the Se isotopes relative to ^{74}Se by performing a chi-squared fit to the complete data set using the MINUIT code [117]. Such a procedure gives the correct average values with the correct uncertainties in a straight-forward way. By these means, relative $g(2_1^+)$ values for the even-A Ge and Se isotopes were obtained from the present measurements.

The Rutgers parameterisation was used to set the absolute scale of the relative g-factor measurements. Rather than normalise to a particular reference g factor, a global fit was performed that included the present precession data in Table 4.5 and previous g-factor ratios from Table 4.6. A 10% uncertainty was assigned to the TF strengths for the iron and gadolinium hosts. The reduced chi-squared value from this fit, $\chi^2_\nu = 1.06$, shows the internal consistency of the present measurements and their consistency with the previous g-factor ratios. In the process of fitting these data and testing the sensitivity of the relative g factors to alternative parameterisations of the TF strength, it was observed that assuming a linear velocity dependence [see Eq. (2.29)] for the TF strength gives almost identical g-factor ratios, but has an increased chi-squared value, $\chi^2_\nu = 2.0$. Thus, it is clear that the present g-factor ratios are not sensitive to the velocity dependence of the transient field. The resultant 'absolute' g factors averaged across all measurements are shown in Table 4.7 and in Fig. 4.17.

TABLE 4.5: Calculated TF interaction strength (Φ) and measured effect (ϵ), slope (S) and precession angle ($\Delta\theta$) values for each run. τ is the mean life of the 2_1^+ state. $\Phi(\tau)$ is evaluated from Eq. (4.7) with the velocity-dependent TF strength given by Eq. (2.30). Figure 4.5 shows the definition of $\langle\theta_p\rangle$ for runs 1 and 2.

Nuclide	T (fs)	τ^a (ps)	$-\Phi(\tau)$ (mrad)	$\epsilon(\gamma_{1,4})$ $\times 10^3$	$S(\gamma_{1,4})$	$\epsilon(\gamma_{2,3})$ $\times 10^3$	$S(\gamma_{2,3})$	$-\Delta\theta$ (mrad)
Run 1 $\langle\theta_p\rangle = 22°$								
^{70}Ge	407	1.91	29.3	23.5(48)	−2.67	−23.2(53)	2.90	8.4(13)
^{72}Ge	444	4.75	31.8	17.0(44)	−2.67	−24.4(50)	2.90	7.3(12)
^{74}Ge	462	18.1	33.2	22.7(28)	−2.67	−29.2(31)	2.90	9.2(8)
^{74}Ge	462	18.1	33.2	21.7(45)	−2.67	−31.1(44)	2.90	9.5(12)^b
^{74}Se	480	10.2	35.9	34.8(29)	−2.67	−39.2(29)	2.90	13.3(9)^b
^{76}Se	481	17.8	36.2	30.2(24)	−2.67	−39.6(27)	2.90	12.4(8)
^{78}Se	474	14.0	35.9	30.0(23)	−2.67	−26.2(25)	2.90	10.1(7)
^{80}Se	467	12.3	35.6	31.5(31)	−2.67	−43.6(34)	2.90	13.3(9)
^{82}Se	468	18.6	35.8	40.7(30)	−2.67	−43.6(34)	2.90	15.2(10)
Run 1 $\langle\theta_p\rangle = 0°$								
^{70}Ge	452	1.91	30.7	28.0(57)	−2.90	−31.9(62)	2.81	11.1(16)
^{72}Ge	495	4.75	33.5	22.8(50)	−2.90	−28.0(63)	2.81	9.4(16)
^{74}Ge	513	18.1	35.0	19.4(47)	−2.90	−21.3(52)	2.81	7.6(13)
^{74}Ge	513	18.1	35.0	20.9(63)	−2.90	−24.4(61)	2.81	8.4(17)^b
^{74}Se	537	10.2	38.0	33.7(40)	−2.90	−39.8(40)	2.81	13.7(12)^b
^{76}Se	536	17.8	38.2	35.0(32)	−2.90	−41.7(36)	2.81	14.2(10)
^{78}Se	523	14.0	37.7	30.0(29)	−2.90	−40.1(32)	2.81	12.9(9)
^{80}Se	514	12.3	37.3	29.9(32)	−2.90	−44.1(47)	2.81	13.6(13)
^{82}Se	513	18.6	37.4	39.0(42)	−2.90	−49.3(47)	2.81	16.3(13)
Run 2 $\langle\theta_p\rangle = 22°$								
^{74}Ge	478	18.1	33.8	25.1(19)	−2.89	−29.0(22)	2.83	9.2(5)
^{76}Ge	477	26.9	33.9	23.9(19)	−2.89	−21.5(21)	2.83	7.9(5)
Run 2 $\langle\theta_p\rangle = 0°$								
^{74}Ge	525	18.1	35.4	25.8(26)	−2.90	−36.2(29)	2.84	10.7(7)
^{76}Ge	520	26.9	35.4	27.4(25)	−2.90	−27.6(26)	2.84	9.7(6)
Run 3^c								
^{74}Ge	505	18.1	37.2					9.5(5)^b
^{74}Se	525	10.2	40.3					13.5(6)^b
Run 4^c								
^{80}Se	516	12.3	40.1					13.8(10)
^{82}Se	517	18.6	40.3					17.3(15)
Run 5^c								
^{78}Se	680	14.0	54.3					17.6(8)
^{82}Se	681	18.6	54.5					25.9(13)

^{a}From Ref. [179]. Uncertainties in τ can be neglected in the evaluation of $\Phi(\tau)$.
^{b}Simultaneous measurement of ^{74}Ge and ^{74}Se with cocktail beam.
^{c}Run data analysed outside of this candidature. Only $\Delta\theta$ values were provided.

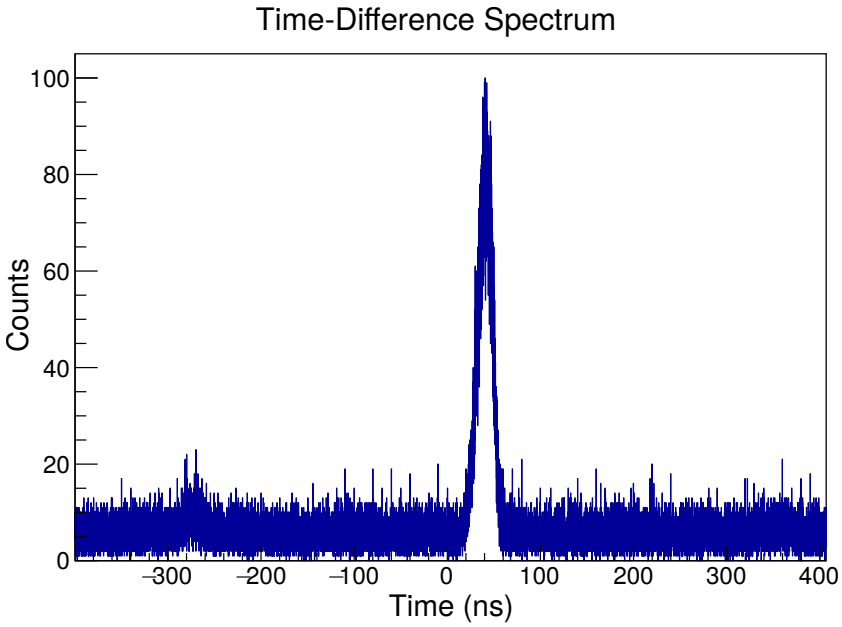

FIGURE 4.8: Example spectrum of time differences from the Ge and Se TF measurement, in this case between γ_1 and P_1 events. Each channel represents the difference between the time stamps on each detector event. There is a clear time correlation between the two detector events indicated by the peak at 40 ns, which was used to sort out the prompt γ-ray spectrum. The level of random coincidences is indicated by the constant background. Although they make only a small contribution, random coincidences under the prompt peak were subtracted in the analysis procedure, as described in §3.3. Note that these data were used as an example time-difference spectrum in Fig. 3.3.

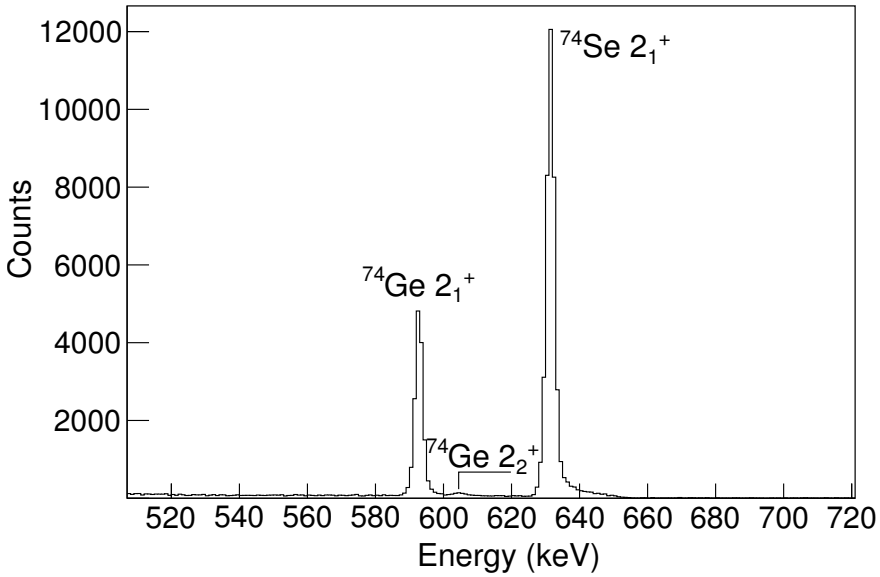

FIGURE 4.9: Spectrum of γ rays at 65° to the beam, in true coincidence with ^{12}C recoils measured during run 1 of the TF experiment ^{74}Ge/^{74}Se cocktail beam. Random coincidences have been subtracted. The resulting spectrum has almost no background. This spectrum represents ∼25% of the data taken for the simultaneous measurement of ^{74}Ge and ^{74}Se during run 1. Excitation of the ^{74}Ge 2_2^+ state is very small ($< 2\%$) and therefore has little-to-no effect on the g-factor measurement.

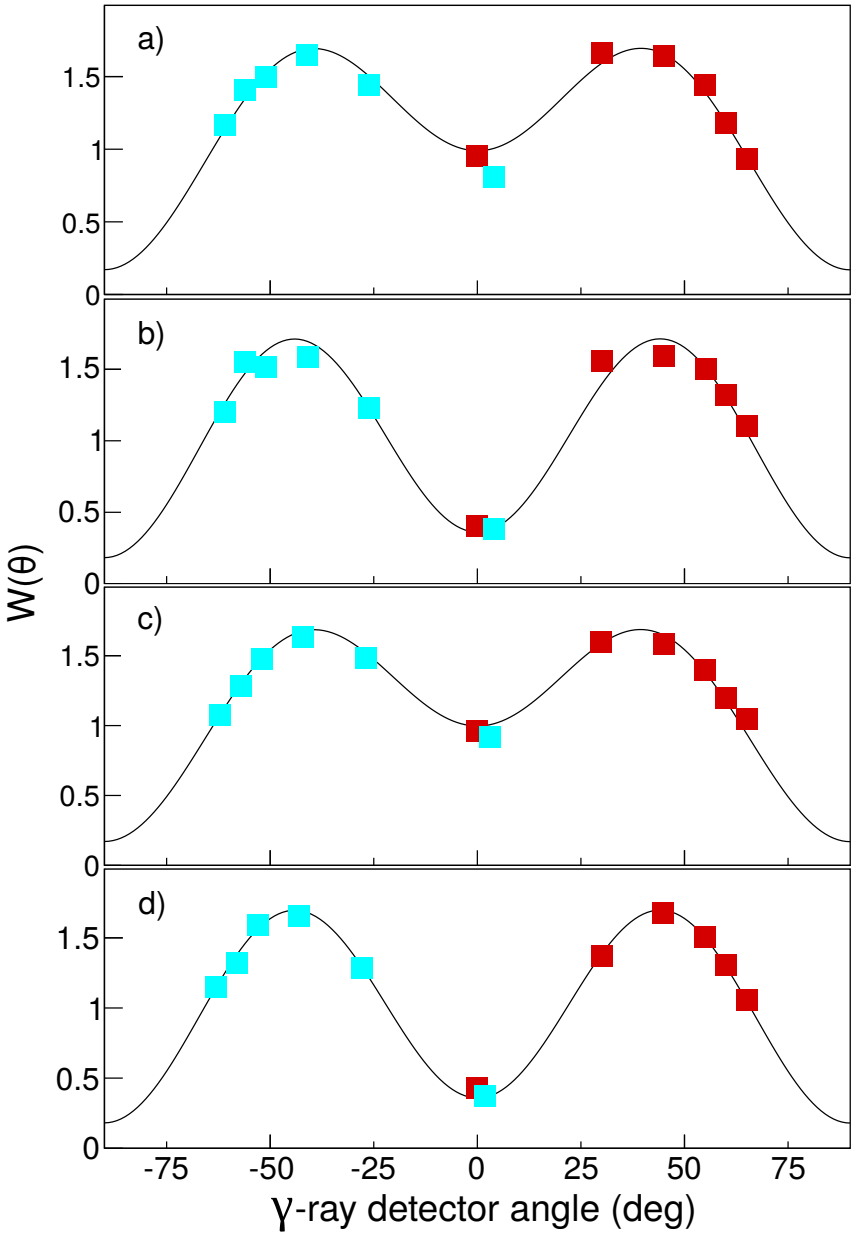

FIGURE 4.10: Angular correlations for the ^{74}Ge and ^{74}Se $2_1^+ \rightarrow 0_1^+$ transitions from the TF experiment run 1 for the two unique particle-detector angles. a) ^{74}Ge, top and bottom particle detectors. b) ^{74}Ge, center particle detector. c) ^{74}Se, top and bottom particle detectors. d) ^{74}Se, center particle detector. Statistical errors are smaller than or similar in size to the data points. Dark red (light blue) points correspond to the γ-ray detector that moves to positive (negative) angles. The measured data are normalised to the theoretical angular correlations shown as continuous lines. Although there is a distinct difference between the correlations for the top/bottom and center particle detectors near 0°, they are similar near $\pm$65°, meaning the two sets of particle detectors have similar sensitivity for the g-factor measurement. An offset of +3° was required on the negative angle data (all taken with the same γ-ray detector) to optimise the fit.

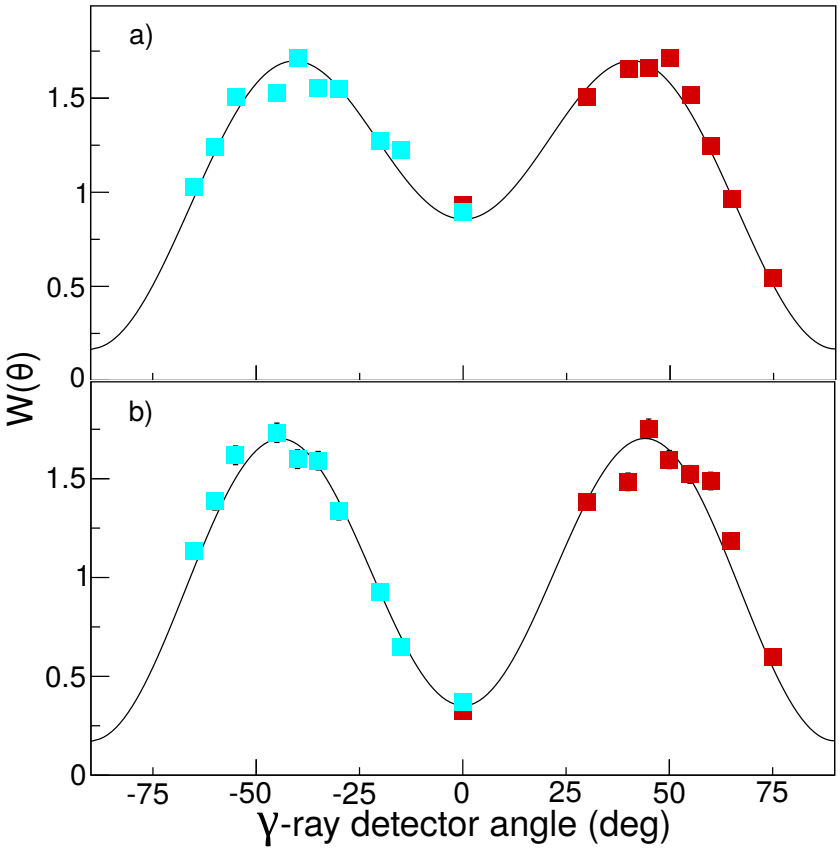

FIGURE 4.11: Angular correlations for the ^{76}Ge $2_1^+ \rightarrow 0_1^+$ transition from the TF experiment run 2 for the two unique particle-detector angles. a) Top and bottom particle detectors. b) Center particle detector. See also the caption of Figure 4.10.

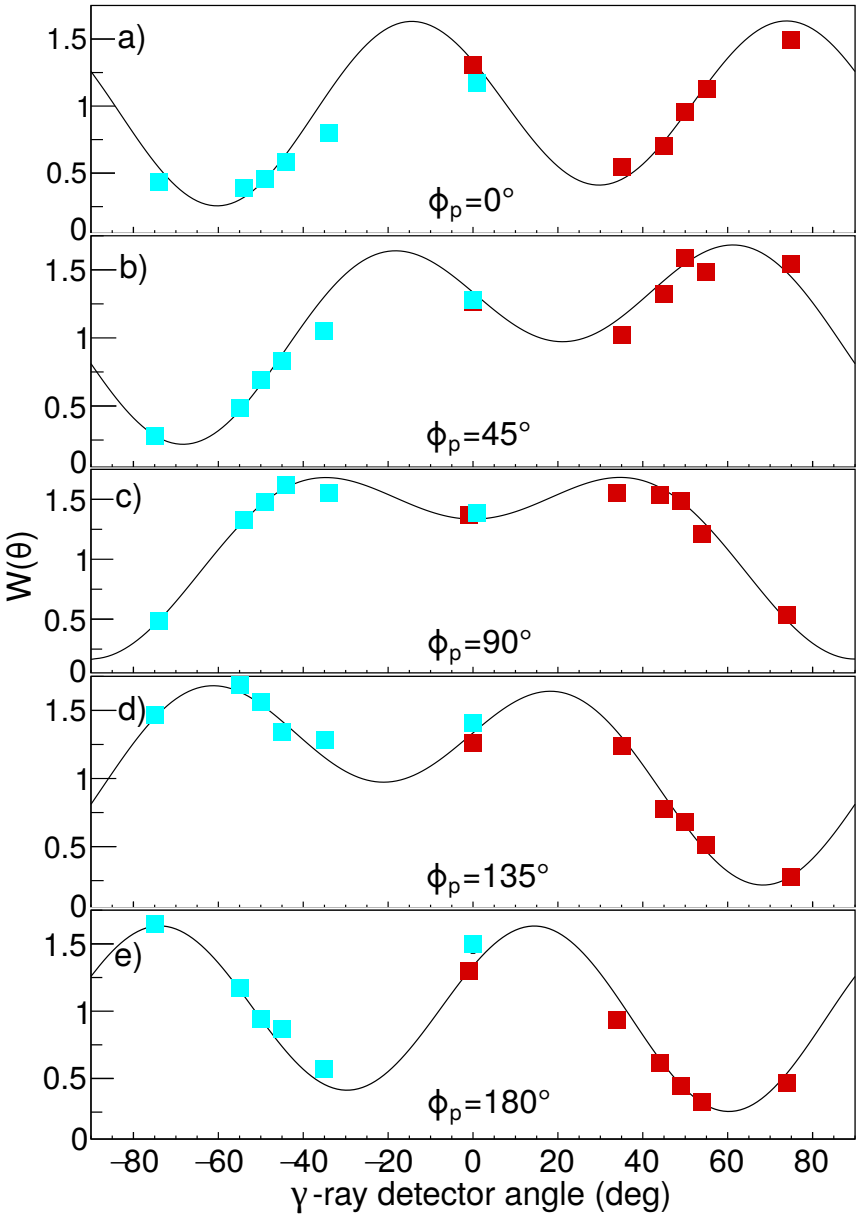

FIGURE 4.12: Angular correlations for the ^{74}Ge $2_1^+ \rightarrow 0_1^+$ transition from the TF experiment run 3, with measurements taken at varying γ-ray detector angles for the five particle detector angles. a) Particle detector at $\phi_p = 0°$. b) Particle detectors at $\phi_p = \pm 45°$. c) Particle detectors at $\phi_p = \pm 90°$. d) Particle detectors at $\phi_p = \pm 135°$. e) Particle detector at $\phi_p = 180°$. The measured data are normalised to the theoretical angular correlations. Dark red (light blue) points correspond to the γ-ray detector that moves to positive (negative) angles. Note the reflection symmetry between the correlations for $\phi_p = 0$ and $\phi_p = 180°$, $\phi_p = 45°$ and $\phi_p = 135°$.

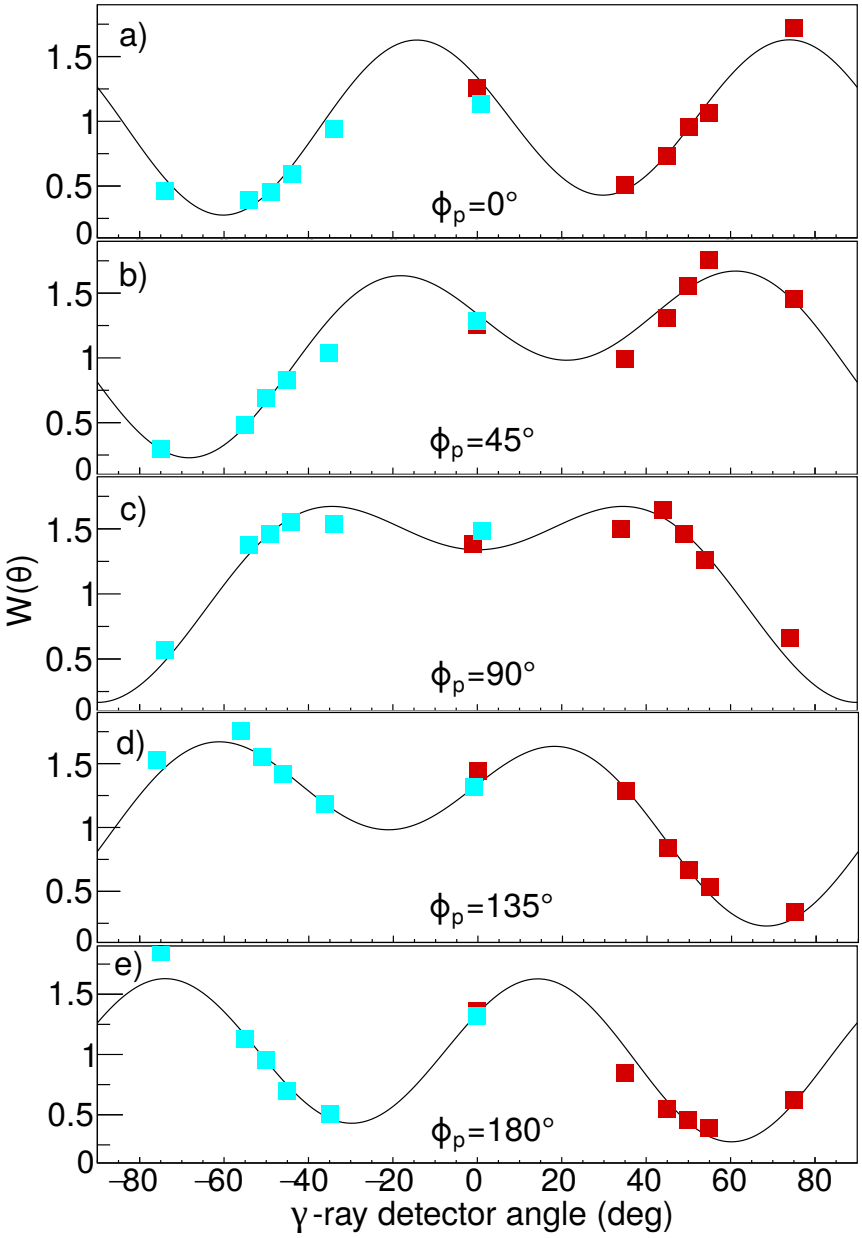

FIGURE 4.13: As for Figure 4.12, for the ^{74}Se $2_1^+ \rightarrow 0_1^+$ transition in run 3.

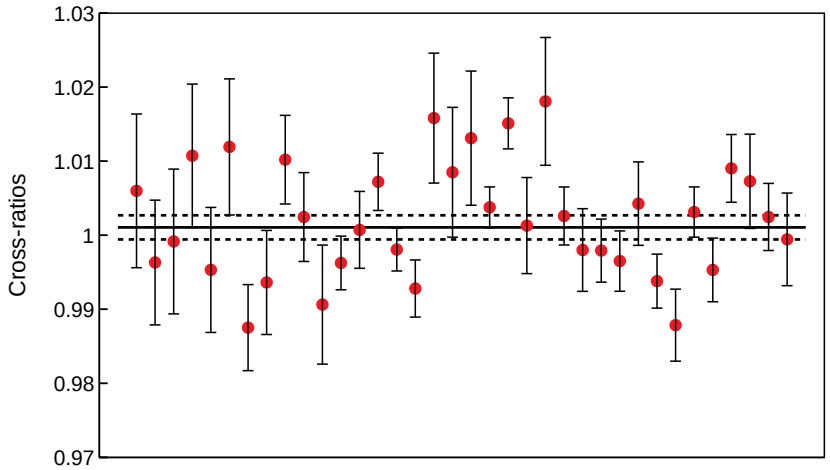

FIGURE 4.14: Cross-ratios for the Ge and Se TF measurement, with the average and 2σ-level indicated. The average deviates very slightly from unity. However, the cross-ratio is still within 2σ of unity, and the small magnitude of the deviation indicates that there is no significant asymmetry.

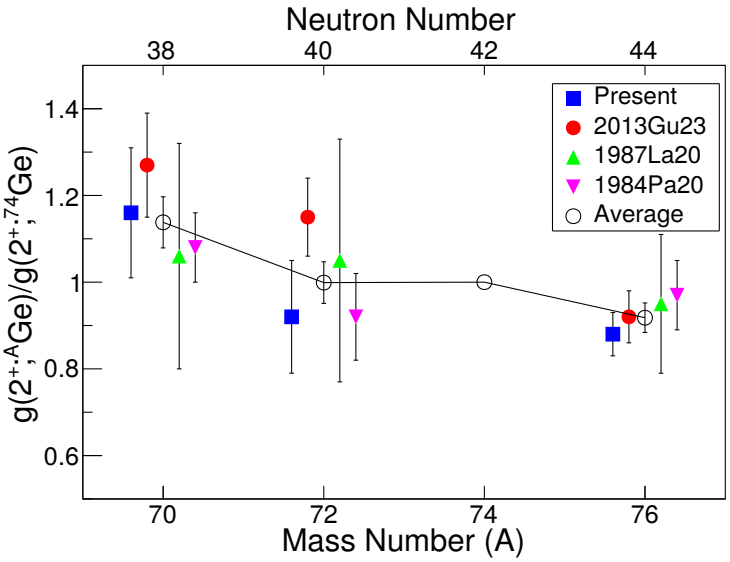

FIGURE 4.15: Ratios of $g(2_1^+)$ in the Ge isotopes relative to ^{74}Ge measured using the TF technique, from present and previous work: 1984Pa20 [166], 1987La20 [130], and 2013Gu23 [98]. Values from Ref. [98] are taken from their target II measurements only. The line connecting the average values serves to guide the eye and emphasise the isotopic trend.

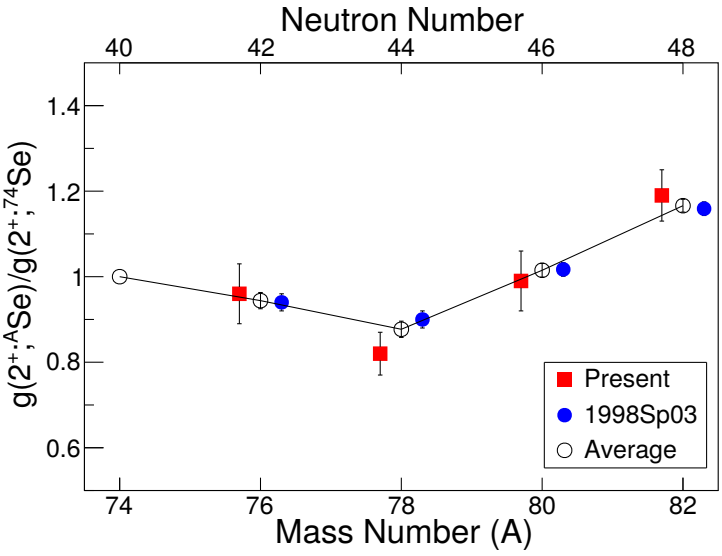

FIGURE 4.16: Ratios of $g(2_1^+)$ in the Se isotopes relative to ^{74}Se measured using the TF technique, from present and previous work: 1998Sp03 [195]. The line connecting the average values serves to guide the eye and emphasise the isotopic trend.

TABLE 4.6: $g(2_1^+)$ ratios measured by the TF technique, from the present and previous work [98, 130, 166, 195].

Ratio	Present	[166]	[130]	[98, 195]	Average
^{70}Ge/^{74}Ge	1.16(15)	1.08(8)	1.06(26)	1.27(12)	1.138(59)
^{72}Ge/^{74}Ge	0.92(13)	0.92(7)	1.05(14)	1.15(9)	0.999(48)
^{76}Ge/^{74}Ge	0.88(5)	0.97(7)	0.95(13)	0.92(6)	0.918(34)
^{74}Se/^{74}Ge	1.34(7)			1.22(8)	1.288(53)
^{76}Se/^{74}Se	0.96(7)			0.942(20)	0.944(19)
^{78}Se/^{74}Se	0.82(5)			0.898(22)	0.877(19)
^{80}Se/^{74}Se	0.99(7)			1.017(16)	1.015(16)
^{82}Se/^{74}Se	1.19(6)			1.159(16)	1.166(15)

4.3.3 Discussion

The isotopic chains of nearby elements allow for the effect of proton-dependent tensor forces on neutron-orbital filling to be examined along isotopic chains. Ge and Se present one such example, and have been the subject of several studies exploring shape changes and orbital ordering in this region [97, 98, 109, 121, 157, 168, 195, 198, 221]. In such studies, the stable isotopes establish a baseline against which isotopes with more extreme proton-to-neutron ratios are compared.

Three separate measurements of the g factors in stable, even-A Ge isotopes have been performed using the TF technique, and are not all in complete agreement (see Table 4.7). The experiments, though all utilising the TF effect, had varying recoil velocities and setups. The g-factor results obtained in the present measurement could not clarify these discrepancies in absolute terms. However, in this project, the primary objective was to determine the relative g factors between and within the isotopic chains of Ge and Se. As such, the challenge of obtaining a reliable, absolute scale of the TF-strength parameterisation was circumvented. The two isotopic chains also present the opportunity to perform a highly robust relative g-factor measurement between isobaric isotopes. The nuclei ^{74}Ge and ^{74}Se were delivered simultaneously by a heavy-ion accelerator, and have sufficiently different excited-state energies that they can be easily distinguished in the γ-ray spectrum. This simultaneous measurement presents the ideal scenario for a relative g-factor measurement, as not only does it have all the advantages described in §4.2.3, but it has the additional advantage that any changes in the target, over time, affect both measurements equally. The isotope chains of each respective element were then measured sequentially, using the same target. In this case, an iron foil was selected as the ferromagnetic host, as it was felt that iron is a more reliable host than gadolinium in this case, due to its higher Curie temperature and thermal properties, and the lower-strength field of the iron host was tolerable. By this method, the g-factor ratios between the Ge

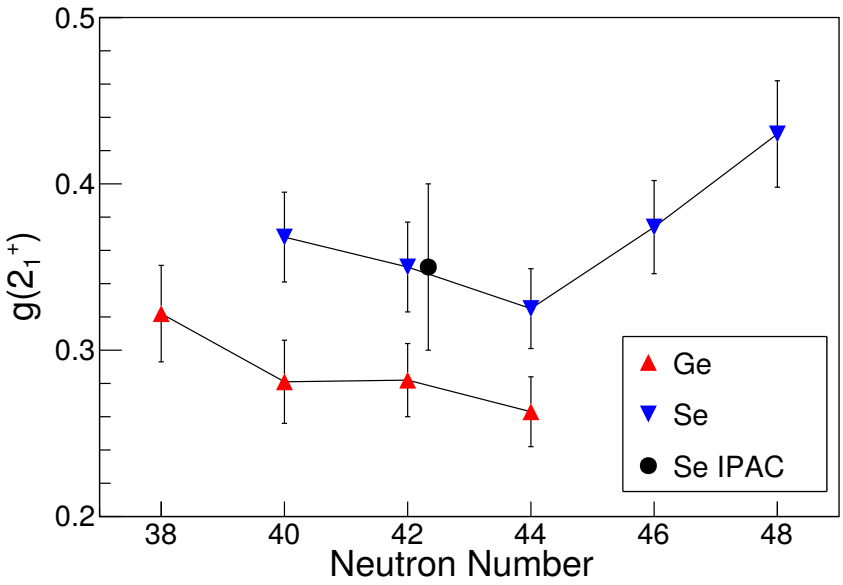

FIGURE 4.17: Comparison of the adopted Ge and Se g-factor values (Table 4.7). There is a shift in magnitude between the two isotope chains but the trend with neutron number appears to be similar. The independently measured integral perturbed angular correlation result for ^{76}Se [152] is shown for reference (slightly displaced from $N = 42$ for clarity).

TABLE 4.7: Measured g factors in Ge and Se using the TF technique. Measurements are ordered chronologically from left to right. Although not explicitly listed, the signs of all g factors in this table are positive.

Nuclide	Present	[166]	[130]	[195, 98]	Average[a]
^{70}Ge	0.330(43)	0.468(26)	0.370(89)	0.44(4)	0.322(29)
^{72}Ge	0.259(36)	0.399(33)	0.367(44)	0.44(2)	0.281(25)
^{74}Ge	0.279(23)	0.433(20)	0.350(22)	0.35(1)	0.282(22)
^{76}Ge	0.261(23)	0.419(23)	0.334(39)	0.32(1)	0.263(21)
^{74}Se	0.360(30)			0.428(27)	0.368(27)
^{76}Se[b]	0.369(33)			0.403(23)	0.350(27)
^{78}Se	0.315(25)			0.384(25)	0.325(24)
^{80}Se	0.374(33)			0.435(27)	0.374(28)
^{82}Se	0.451(35)			0.496(29)	0.430(32)

[a] These results are from a global fit to the present data in Table 4.4 together with previous g-factor *ratios* from Table 4.6. The uncertainties include $\pm 10\%$ uncertainty on the TF parameterisations for the iron and gadolinium hosts.
[b] The only independently determined g factor, by an integral perturbed angular correlation measurement [152], gives $g = +0.35(5)$ for ^{76}Se (see text).

and Se isotopes were obtained in a robust manner with minimal systematic error.

The ratios presently obtained were then compared with the ratios obtained in the other methods, shown in Fig. 4.15 and Fig. 4.16 for Ge and Se, respectively. When comparing the ratios, much of the discrepancy between the different measurements goes away, and the four relative measurements for the Ge isotopes have a reasonable statistical scatter from which an average was taken. The relative Se measurements from the present work and the literature were in good agreement, although the absolute g-factor values vary significantly in magnitude. With these precise ratios now well-established, a single precise and independent g-factor measurement on any of these isotopes can be used to scale the TF strength and confidently obtain absolute $g(2_1^+)$ values for all nine nuclides.

4.4 Ge and Se Implantation Measurements

An ion-implantation perturbed-angular-correlation (IMPAC) measurement was performed on the stable, even-A nuclei of the elements Ge and Se. The purpose of this measurement was to: (i) resolve an inconsistency observed in previously published IMPAC data [106], in which the measured ^{82}Se 2_1^+ precession, relative to the other isotopes, was inconsistent with the g factor values obtained in §4.3.2 and Ref. [195], and (ii) determine if there is a reduction in the hyperfine field strength due to a pre-equilibration effect associated with the violent implantation process (see §2.3.1). Confirmation of the ^{82}Se measurement was motivated due to its use in the Rutgers parameterisation of the TF strength [191]. If this data point is unreliable, it justifies the need to provide new calibration points for the TF in the region $30 \leq Z \leq 40$. As will be shown, it was found that there was good agreement between the literature and present IMPAC measurements, with the exception of ^{82}Se, for which a strong discrepancy was observed. This demonstrated the validity of the measurement at large, and the unreliability of the ^{82}Se data in particular. The Se isotope data also suggested pre-equilibrium quenching of the static-field strength was present, however due to a lack of precision in the measurement a thermal-spike lifetime could not be confirmed with confidence. These two results bring into question the ^{82}Se IMPAC data's use in the Rutgers TF-strength parameterisation.

4.4.1 Methods

The IMPAC technique, described in §2.3.1, was used to perform a measurement of the combined static- and transient-field precession effect in the stable Ge and Se isotopes. The experiment was performed by the author, present supervisors, Mr. Wanli Xing, staff, and students of ANU's Department of Nuclear Physics. At ANU's heavy-ion accelerator facility an aluminium oxide cathode was used in the SSNICS to produce O^- ions. These were injected into the 14 UD Pelletron accelerator to produce a beam of ^{16}O at 35 MeV. The ^{16}O ions impinged upon a triple-layer target having either 0.5 mg/cm^2 $^{\text{nat}}$Ge evaporated onto a 4.6 mg/cm^2 iron foil, or 0.6 mg/cm^2 $^{\text{nat}}$Se evaporated onto a 4.2 mg/cm^2 iron foil, which served as the ferromagnetic host. Both targets were backed by a thick copper foil ($\sim$ 11 mg/cm^2) for thermal contact and to stop the beam, with $\sim$ 1 mg/cm^2 of indium between them, which served to 'glue' the foils together. The ^{70,72,74,76}Ge or ^{74,76,78,80,82}Se nuclei were excited by the ^{16}O beam ions and recoil-implanted into the ferromagnetic host at a depth of $\sim$ 3 μm. Back-scattered ^{16}O ions were detected by two SiPDs at an average scattering angle $\langle\theta_p\rangle = 151^\circ$ and recorded in coincidence with the de-excitation γ rays. The particle detectors were positioned 16.2 mm up-beam of the target with geometry as shown in Fig. 4.18. As per the TF technique description at in the chapter introduction (Ch. 4), the cryocooler and polarising magnet were used to cool the target and polarise the ferromagnetic host, with the magnet polarity reversed every $\sim$15

min. Four HPGe detectors were used to detect γ rays, positioned at $\pm 65^\circ$ (γ_1, γ_4) and $\pm 115^\circ$ (γ_2, γ_3), arranged as per Fig. 4.1. For the run using the Ge target, angular correlations were measured at $\pm(0^\circ, 25^\circ, 35^\circ, 45^\circ, 55^\circ, 65^\circ$ and $70^\circ)$ by moving γ_1 (positive angles) and γ_4 (negative angles), while leaving γ_2 and γ_3 fixed.

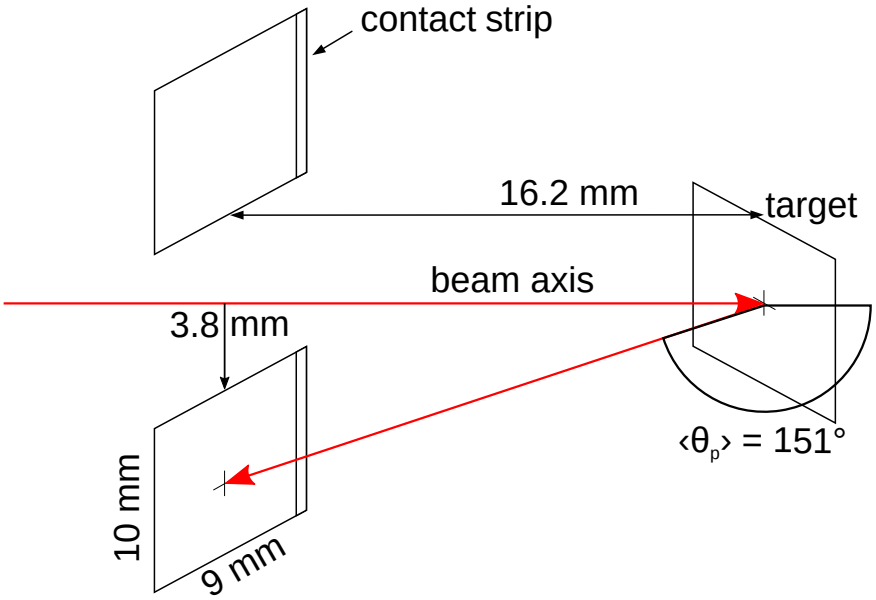

FIGURE 4.18: Back-scattered particle detector layout for the Ge and Se IMPAC measurement.

4.4.2 Results

The data were analysed in the same manner as the TF data, described in §4.1. The triggerless Digital DAQ data were converted into 1 μs-correlated events in the ROOT tree format, and γ-ray spectra containing either field-up or field-down γ-particle coincidence events were sorted out. An example γ-particle time-difference spectrum is shown in Fig. 4.19. A gate was placed around the peak at -150 ns to project the prompt spectra, and around the surrounding regions for random coincidence spectra. Figure 4.20 shows a 'true' γ-ray spectrum from γ_1 for the Se target, and Fig. 4.21 shows the same for the Ge target. Background counts under the photopeak were obtained by fitting a Gaussian with a Doppler tail plus a linear background function to the photopeak, and then subtracting the linear (background) component from the raw photopeak counts. Figure 4.21 shows that the ^{73}Ge excited-state γ-ray is very close to the ^{72}Ge 2_1^+ γ ray. These peaks had to be fitted together, with the smaller ^{73}Ge peak subtracted from the integral photopeak counts along with the background.

To determine the presence of pre-equilibrium quenching of the static field, the TF component must be subtracted from the measured precession angles. The hyperfine field experienced by Ge implanted in iron is $B_{\mathrm{SF}}(\mathrm{Ge}Fe) = 6.0(2)$ T [176], an order of magnitude smaller than that for Se in iron, being $B_{\mathrm{SF}}(\mathrm{Se}Fe) = 67.9(10)$ T [205]. Due to the

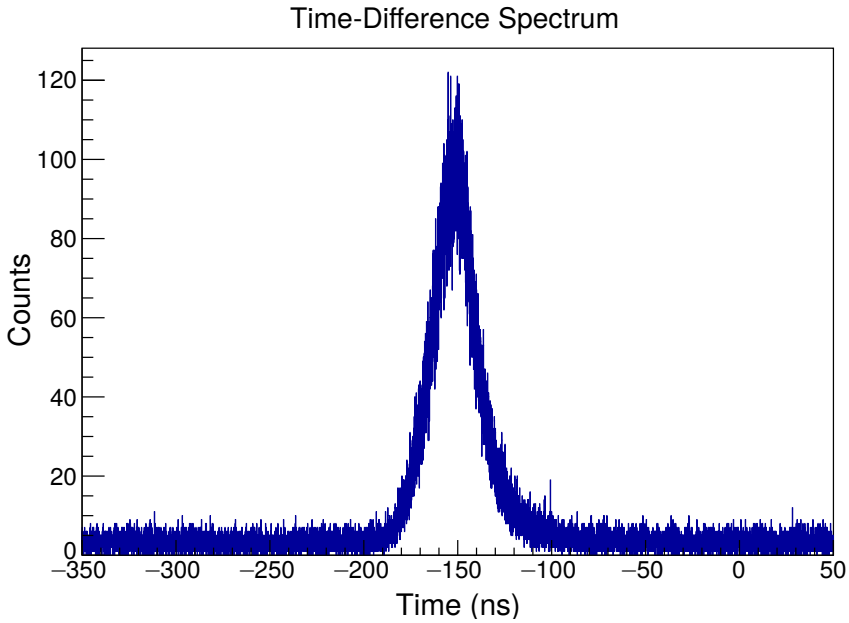

FIGURE 4.19: Spectrum of time differences from the Ge IMPAC measurement, between γ_1 P_1. There is a clear time correlation between the two detector events indicated by the large peak at -150 ns, which was used to sort out the prompt γ-ray spectrum.

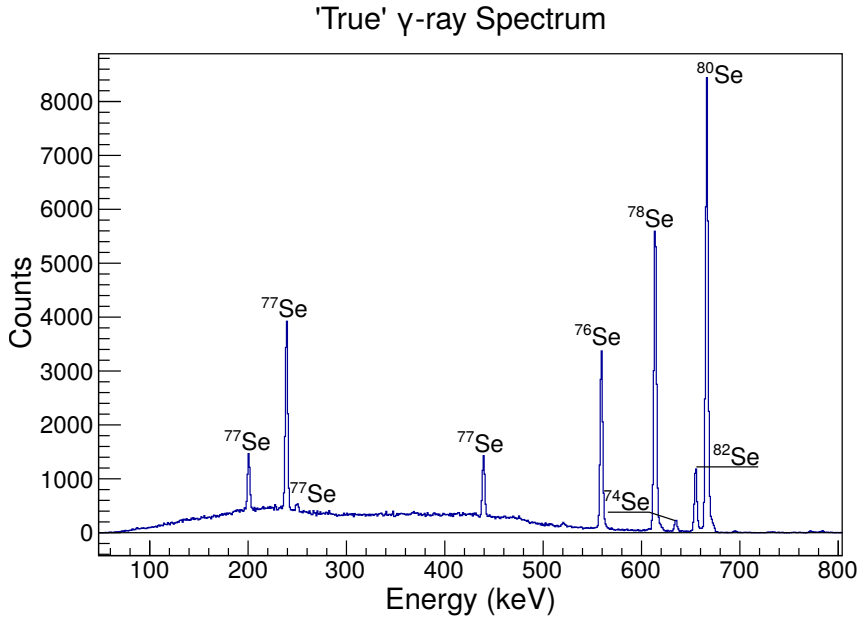

FIGURE 4.20: 'True' γ-ray spectrum from the Se IMPAC measurement target from γ_1, summed across both particle detectors without field-up or field-down gating. Note only γ-rays from the excited states of Se isotopes and Compton scattering are present.

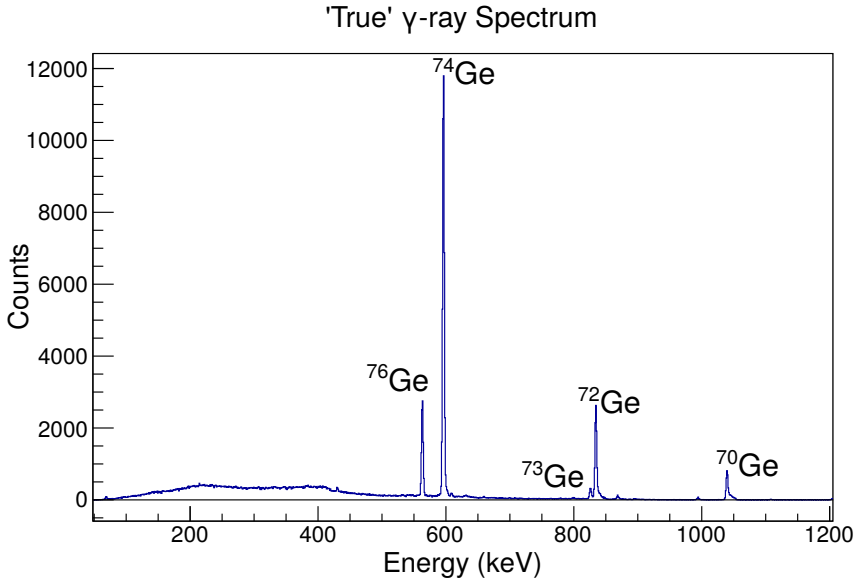

FIGURE 4.21: 'True' γ-ray spectrum from the Ge IMPAC measurement target from γ_1, summed across both particle detectors without field-up or field-down gating. Note only γ-rays from the excited states of Ge isotopes and Compton scattering are present.

TABLE 4.8: Measured effect values, calculated S, and resulting precession angles obtained from the IMPAC measurement of the stable, even-A Ge and Se isotopes. Uncertainty in S has been omitted due to its small value relative to the measurement uncertainties. The present mesaured precessions are listed alongside those reported in Ref. [106] in the last two columns.

Nuclide	$\epsilon(\gamma_{1,4})$ $\times 1000$	$S(\gamma_{1,4})$	$\epsilon(\gamma_{2,3})$ $\times 1000$	$S(\gamma_{2,3})$	$-\Delta\theta_{\text{exp}}$ (mrad)	$-\Delta\theta_{\text{lit}}$ (mrad)
^{70}Ge	47.0(126)	−2.98	−37.2(148)	2.98	14.2(31)	11.2(15)
^{72}Ge	55.7(80)	−2.98	−42.9(95)	2.98	14.1(22)	9.9(17)
^{74}Ge	31.7(37)	−2.98	−28.7(43)	2.98	11.1(12)	11.3(13)
^{76}Ge	25.4(78)	−2.98	−45.3(91)	2.98	12.9(22)	9.9(15)
^{74}Se	11.9(27)	−2.98	−103(31)	2.98	17.2(70)	
^{76}Se	69.2(71)	−2.98	−90.8(83)	2.98	26.9(26)	27.1(15)
^{78}Se	58.9(53)	−2.98	−81.6(62)	2.98	23.2(21)	24.0(16)
^{80}Se	65.2(45)	−2.98	−72.1(53)	2.98	23.1(20)	23.9(11)
^{82}Se	130(12)	−2.98	−129(14)	2.98	44.0(43)	29.5(8)

TABLE 4.9: Transient-field precession angles obtained from Ge isotope IMPAC measurement. The experimentally measured precession angle (exp) is composed of a TF and a static field (SF) component: $\Delta\theta_{exp} = \Delta\theta_{TF} + \Delta\theta_{SF}$. For the Ge isotopes $\Delta\theta_{TF} >> \Delta\theta_{SF}$, and therefore $\Delta\theta_{exp} \simeq \Delta\theta_{TF}$. Because there is a lifetime dependence in $\Phi(\tau)$ these values were calculated using the Rutgers TF parameterisation, Eq. (4.7) and Eq. (2.30), with $\tau(2_1^+)$ values taken from Ref. [179], and used to scale $\Delta\theta_{TF}$. The average $g(2_1^+)$ values from Table 4.7 were adopted.

Nuclide	τ^a (ps)	$-\Delta\theta_{exp}$ (mrad)	$\Phi(\tau)$ (mrad)	$-\Delta\theta/g\Phi(\tau)$
^{70}Ge	1.91	11.8(13)	33.5	1.09(16)
^{72}Ge	4.75	11.4(14)	38.9	1.05(16)
^{74}Ge	18.1	11.2(9)	42.3	0.94(10)
^{76}Ge	26.9	10.9(12)	43.2	0.96(13)
Average				$\langle 0.99(7) \rangle$

TABLE 4.10: Effective-field-strength values, B_{eff}, in the IMPAC measurement. The experimentally measured precession angle is composed of a TF and a static-field (SF) component: $\Delta\theta_{exp} = \Delta\theta_{TF} + \Delta\theta_{SF}$. Here, $\Delta\theta_{SF}$ was obtained by multiplying the weighted-average value from Table 4.9 by $\Phi(\tau)$ to scale the TF component in a manner less dependent on the absolute scale of the parameterisation, then subtracting it from $\Delta\theta/g$ and dividing by the attenuation factor $e^{-t_s/\tau}$ due to the stopping time. The stopping time, $t_s = 1.3$ ps, was determined from reaction kinematics and Ziegler's stopping powers [232]. Because there is a lifetime dependence in $\Phi(\tau)$, these values were calculated using Eq. (4.7) and Eq. (2.30). The average $g(2_1^+)$ values from Table 4.7 were adopted, and $\tau(2_1^+)$ values were taken from Ref. [179].

Nuclide	τ (ps)	$-\Delta\theta$ (mrad)	$\Phi(\tau)$ (mrad)	$-\Delta\theta_{SF}/g$ (mrad)	B_{eff} (T)
^{74}Se	10.22(22)	17.2(70)	38.8	9(20)	17(40)
^{76}Se	17.76(42)	26.0(25)	39.8	35(10)	41(11)
^{78}Se	13.98(38)	23.7(13)	40.1	33(7)	50(11)
^{80}Se	12.29(30)	23.7(9)	40.1	24(6)	40(10)
^{82}Se	18.6(5)	44.0(43)	41.2	62(13)	69(15)

large difference in the strength of B_{SF} between these two elements in iron (which makes the static-field contribution for the Ge isotopes effectively negligible) and the known g-factor ratios determined in §4.3, the TF component of the Se IMPAC measurement can be approximated by scaling the precession angle of the Ge isotopes. This approximation was then used to subtract the TF contribution from the Se isotope precession angles to obtain their static-field component. Table 4.9 shows the determination of B_{TF} from the Ge isotope data, and Table 4.10 shows the deduced B_{SF} values for the Se isotopes. It should be noted that the average value from Table 4.9 $\langle \Delta\theta/g\Phi \rangle \simeq 1$ indicates the consistency of the TF parameterisation at the two distinct velocity ranges sampled in the IMPAC versus TF measurements. The resulting effective field values (B_{eff}) are shown plotted against τ^{-1} in Fig. 4.22, along with an exponential fit matching the form $B_{eff} = B_{SF}e^{-t_e/\tau(2_1^+)}$. The fit gives $t_e = 11(10)$ ps and $B_{SF} = 98(68)$ T. The uncertainties on these values are large, but the values are consistent with the literature value for the hyperfine-field strength $B_{SF} = 67.9(10)$ T [205] and the thermal-spike lifetime $t_e = 7.3(8)$ ps as determined in Ref. [220]. When $B_{SF} = 67.9$ T is fixed in the fit, $t_e = 5.5(18)$ ps is obtained, still consistent with the thermal-spike lifetime in Ref. [220]. While this is not a definitive result, it does suggest that there is a pre-equilibrium quenching of the field strength, and this effect will have an influence on the result of any IMPAC measurements.

An alternative way to probe the value of t_e, as well as other factors which may reduce B_{SF}, is to compare the g factors as obtained from IMPAC theory to those obtained from the TF measurement in §4.3. As discussed in §2.3.1, the precession angle measured using IMPAC consists of a TF component acting on the moving ion, and a static-field component acting on the ion once it comes to rest. The theoretical reduced precession angle, Φ (i.e. the precession angle evaluated for $g = 1$), may be computed using a parameterisation of B_{TF}, a known B_{SF}, and ion stopping powers. As discussed in §2.3.1, the average B_{SF} experienced by the ion may be attenuated if it does not alloy well with the host material. This can cause the ion to come to rest in interstitial (or 'bad') sites, where the hyperfine interaction is reduced or absent. A measurement of the hyperfine-field strength experienced by ^{75}Se ions implanted into iron [44] used the ion-channeling technique to observe what proportion of Se ions were coming to rest at substitutional versus interstitial sites. It appeared that all ions were located in substitutional sites. Therefore, if there is any reduction of B_{SF} for the Se ions associated with the final site of the Se ion in the iron host, it should be small.

In §4.3.2, $g(2_1^+)$ values for the stable Ge and Se isotopes were determined by using the TF technique with the field strength scaled using the Rutgers parameterisation. The TF precession component in the IMPAC measurement was determined using the Rutgers parameterisation, under the assumption that it is valid at both the high velocity in

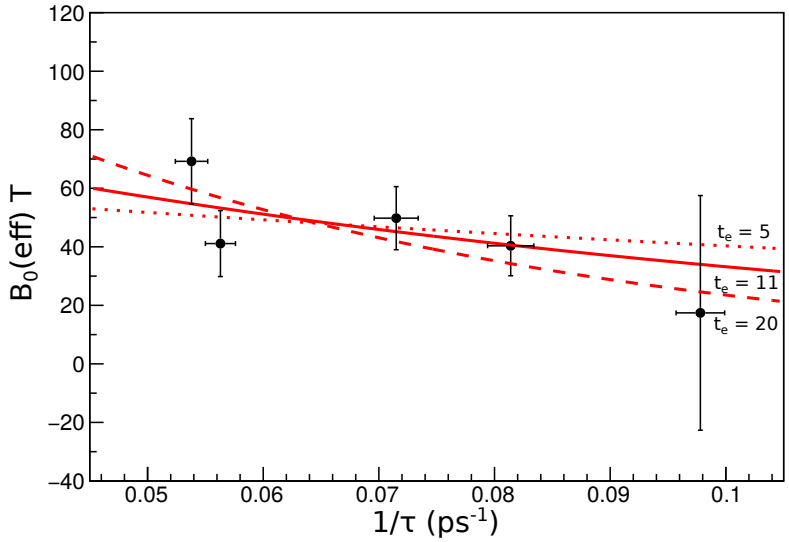

FIGURE 4.22: Effective field strength, $B_{\text{eff}} = \Delta\theta_{\text{SF}}/g\tau\mu_N/\hbar$, versus $1/\tau$ for the Se IMPAC measurement. The solid red line is a fit to $B_{\text{eff}} = B_{\text{SF}}e^{-t_e/\tau(2_1^+)}$, giving $t_e = 11(10)$ ps and $B_{\text{SF}} = 98(68)$ T. Fit lines with $t_e = 5$ ps and $t_e = 20$ ps are shown as the dotted and dashed lines for comparison.

the TF measurement, and the low velocity in the IMPAC measurement. The static-field component was computed using Eqs. (2.26) and (2.27), with a stopping time $t_s = 1.3$ ps determined using Ziegler's stopping powers [232]. The g factors were then determined by $g = {}^{\Delta\theta}/_{\Phi}$. To determine the thermal-spike lifetime t_e, it was varied until the difference between the IMPAC- and TF-measurement g factors was minimised, giving $\chi^2_\nu = 0.83$. The resulting plot is shown in Fig. 4.23, along with a straight line to guide the eye, which has minimised to a thermal-spike lifetime $t_e = 4.5(17)$ ps. The uncertainty on this value does not take into account uncertainties inherent to the ion-stopping process and TF parameterisation, and hence is underestimated. As such, it seems consistent with the value determined by Stuchbery and Bezakova [220], being $t_e = 7.3(8)$ ps, and the value obtained in Fig. 4.22. When determining this value, the static field was set to its full strength. The reductions in the static-field strength owing to the thermal-spike lifetime and non-substitutional implantation sites are correlated. However, the value obtained by this fitting procedure is smaller than either the value obtained from the exponential fit, or that suggested in Ref. [220]. Therefore, it seems the ion-channeling measurement in Ref. [44] correctly deduced the strongly substitutional implantation of Se ions into an iron lattice.

4.4.3 Discussion

The IMPAC technique was widely used for g-factor measurements through the late 1960s and early 1970s, as was discussed in §2.3.1. Many of these measurements used the now

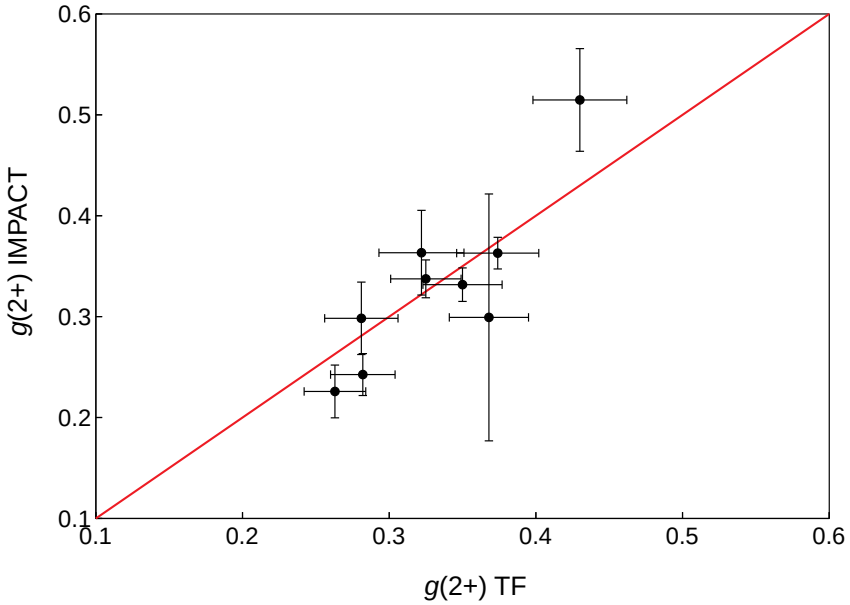

FIGURE 4.23: Plots of $g(2_1^+)$ values for the Ge and Se isotopes obtained from the IMPAC precession angles against the average values obtained from the TF measurement (see Table 4.7). The thermal-spike lifetime, $t_e = 4.5(17)$, was obtained by varying its value until the fitted line gave $y = x$.

outdated Lindhard-Winther model of the TF strength to determine the spin-precession component belonging to the TF [93]. The now dated Lindhard-Scharff-Schiott (LSS) stopping powers were often used to evaluate the energy loss and stopping of ions in the ferromagnetic host. The invalidity of the Lindhard-Winther parameterisation and imprecision of the LSS stopping powers at low energy mean that these older measurements may be quite inaccurate. Furthermore, in the late 1990s Stuchbery and Bezakova [220] demonstrated that the static hyperfine field experienced by the implanted ions after they have come to rest is also quenched for a duration, owing to a localised thermal spike arising from the implantation process. That this effect is not accounted for in these older measurements only adds further uncertainty to the effective static field, particularly for states having short lifetimes ($\tau \lesssim 10^{-11}$ s). This potential inaccuracy is important, as several of the calibration points used in the Rutgers parameterisation [191] were obtained from IMPAC measurements, of particular relevance being the ^{82}Se 2_1^+ measurement by Heestand *et al.* [106]. The Rutgers parameterisation obtains the $g(2_1^+;^{82}\mathrm{Se})$ valued used in its calibration from Ref. [106], the only calibration point between $26 < Z < 46$. With this value brought into question, the precise behaviour of the transient field through this region is uncertain.

The present IMPAC measurement aimed to repeat the measurement reported in Ref. [106], intending to check the measured precession angle of the ^{82}Se 2_1^+ state, and also to determine if the pre-equilibrium quenching effect may be present, and to what

extent. To achieve this, the precession angles of both Ge and Se isotopes were measured. The two measurements obtained similar precession angles across the two isotopic ranges, with the exception of ^{82}Se. In this case, the present measurement found the precession angles to be $\sim 1.5\times$ larger than in Ref. [106], well outside of measurement uncertainty. As the ^{82}Se 2_1^+ state has the longest lifetime among the even-A stable Se isotopes, the static-field reduction should also be the smallest. Still, despite having the longest lifetime, the static field will be reduced by 34%, assuming a thermal-spike lifetime $t_e = 7.3$ ps as determined by Stuchbery and Bezakova [220]. According to the reduced precession angles reported in Table 4.10, and the calculated static-field precession effect, the TF and static-field should contribute almost equally to the measured precession. Taking into account the thermal-spike quenching, the g factor could be up to $\sim 20\%$ larger. This quenching effect, as well as the large discrepancy between the present measurement and Ref. [106], limit the usefulness of the ^{82}Se 2_1^+ g factor in the calibration of the TF strength. Exclusion of this value from the calibration leaves no data points in the range $26 < Z < 46$. Therefore, the magnitude of the TF-strength parameterisation, as applied to TF measurements of the Ge and Se isotopes in the literature, may be considerably more uncertain than reported.

4.5 Calibration of the Transient-Field Strength

In this section, previous measurements using the TF effect in iron and gadolinium foils will be scrutinised. First, measurements will be compared with calculations using the newly obtained ^{56}Fe $g(2_1^+)$ value, to be presented in Chapter 6, with the aim of checking existing TF calibrations and differences between iron and gadolinium hosts. It will be shown that iron-host data closely matches the parameterisation, and that gadolinium-host measurements are strongly dependent upon foil magnetisation. Then, the TF measurements in the Ge and Se isotopes from §4.3.2 will be compared with literature values to examine consistency and attempt to identify the source of discrepancies in the published $g(2_1^+)$ values. It will be shown that a reanalysis of the iron-host data brings the present and literature measurements into agreement, while the gadolinium-host measurements appear to inflate the g factors due to the Rutgers parameterisation possibly underestimating the TF strength in this host.

4.5.1 ^{56}Fe Measurements

With a value for $g(2_1^+)$ in ^{56}Fe firmly assigned (see Chapter 6), the various TF measurements of the ^{56}Fe 2_1^+ state may be compared to parameterisations. Table 4.11 shows measured TF precession angles of ^{56}Fe in an iron host from the literature [101], along with calculated $\Delta\theta$ values using the Rutgers parameterisation. Measured precession angles in gadolinium are also shown [56, 66] along with the Rutgers parameterisation, and the linear parameterisation. There is good agreement between the calculated and measured values in the iron host. However, the uncertainty in these measurements is also quite large. Gadolinium is a different case to iron, because the magnetisation of the foil usually doesn't reach maximum saturation, and therefore must be measured to be accurately known. In neither experiment was the magnetisation of the gadolinium foil measured. Between the two measurements, there is also a key difference in the foil preparation: one used an evaporated gadolinium foil, and used a rolled and annealed gadolinium foil. The variation between these two measurements will now be explored.

A key parameter when using gadolinium hosts is the foil magnetisation. Using the Rutgers parameterisation, the magnetisation of the gadolinium foil would have to be $M = 0.225$ T to match the precession angles observed by Ernst *et al.* [66]. This M value represents a fully saturated gadolinium foil, however the authors predict a demagnetisation effect. The measurements of East *et al.* [56] are both larger than the Rutgers parameterisation, having $M = 0.225$ T. *Although these deviations are not statistically significant ($\lesssim 2\sigma$), potential explanations will be explored.*

TABLE 4.11: Measured 2_1^+ precession angles in ^{56}Fe traversing an iron or gadolinium foil. For iron hosts, this is compared with the Rutgers TF parameterisation [191] with $M = 0.175$ T. For gadolinium hosts, this is compared with the Rutgers TF parameterisation, having $M = 0.225$ T, as well as a linear parameterisation [194]. These calculations use the newly determined $g = 0.546$ (see §6.2.7) in the hyperfine interaction, and Ziegler's SRIM 2013 stopping powers [232] to determine energy loss through the target. Foil details and calculated kinematic details (entry energy E_{in}, exit energy E_{out}, and resulting transit time T) are listed. The precession angle $\Delta\theta$ was calculated as per Eq. (4.6).

	Foil (mg/cm^2)	E_{in} MeV	E_{out} MeV	T ps	$\Delta\theta_{\text{measured}}$ mrad	$\Delta\theta_{\text{Rutgers}}$ mrad	$\Delta\theta_{\text{linear}}$ mrad
Ref. [191]	Fe 2.3	65.0	19.0	0.258	8.9(17)	8.7	
Ref. [191]	Fe 1.3	56.0	29.2	0.139	4.9(11)	4.8	
Ref. [191]	Fe 2.3	56.0	13.3	0.292	8.2(16)	9.3	
Ref. [101]	Fe 1.75	56.0	21.3	0.201	6.4(18)	6.7	
Ref. [66]	Gd 3.6	42.0	8.9	0.548	19.7(6)	20.3	19.6[a]
Ref. [66]	Gd 3.6	48.4	11.9	0.491	19.5(5)	19.1	19.6[a]
Ref. [56]	Gd 3.4	36.9	7.8	0.554	22.0(12)	19.8	21.8[b]
Ref. [56]	Gd 3.4	30.7	5.6	0.635	21.1(13)	20.9	21.5[b]

[a] Linear TF parameterisation with $a = 17 \times 0.83$.
[b] Linear TF parameterisation with $a = 17 \times 0.97$.

One explanation for the observed precession-angle deviations is that the Rutgers parameterisation is overestimating the TF strength, and the foil magnetisation in Ernst's measurement is smaller than East's. Alternatively, the TF strength may not follow the non-linear trend of the Rutgers parameterisation. To explore the latter possibility, a linear parameterisation, taking $a = 17.0$ T [194], was used. The linear parameterisation best matches the measurements of Ernst *et al.* if the magnetisation is 83% of its maximum strength, and 97% to match the measurements of East *et al.*. Curiously, Ernst *et al.* suggest a demagnetisation coefficient $G_{\text{beam}} = 0.83$, owing to a hypothesised demagnetisation of the foil due to a heavy-beam-ion energy-deposition effect [116]. To explore this effect, the beam enegy-loss in the two measurements was investigated. The average energy-loss in gadolinium for the ^{56}Fe beam ions in the measurements of Ernst *et al.* versus East *et al.* was $\langle dE/dx \rangle = 7.9$ (130 MeV) and 8.7 (145 MeV) MeV/mg cm^{-1}, and $\langle dE/dx \rangle = 7.5$ (inner) and 8.7 (outer) MeV/mg cm^{-1}, respectively. According to the precession effects presented in Ref. [116], Fig. 3, the heavy-ion-induced demagnetisation effect should be almost the same in the two measurements. Therefore, this effect is either negligible, absent, or small compared to the differing magnetisation of the two foils.

The method of foil preparation was notably different between the two gadolinium-host measurements, with Ernst *et al.* using an evaporated gadolinium foil, while East *et al.* used a rolled and annealed gadolinium foil. It is possible that the evaporated foil may

have an appreciably weaker magnetisation than the rolled and annealed foil. It seems that the difference between the two measurements is better explained by differing inherent magnetisation between the two foils due to their methods of preparation, rather than heavy-ion-beam attenuation. However, the possibility remains that the Rutgers parameterisation with $M = 0.225$ T is correct and the deviation observed for East's measurement is statistical, or owing to some other unknown factor.

4.5.2 Ge and Se Measurements

TF measurements on Ge isotopes present a good case to examine the consistency of the TF-strength between different experiments and ferromagnetic hosts. This is because measurements in the literature, as shown in Table 4.7, fall into two categories: the measurements by Lampard *et al.* [130] and Pakou *et al.* [166], which used an iron ferromagnetic host in regular kinematics; and the measurements by Gürdal *et al.* [98], which used a gadolinium host in inverse kinematics. The reported average magnitude of $g(2_1^+)$ for the Ge isotopes is fairly similar in the measurements of Lampard *et al.* and Gürdal *et al.*, and are also in good agreement with the re-evaluated IMPAC data measured by Fahlander *et al.* [69]. The values reported by Pakou *et al.*, however, have a larger average magnitude, significantly different from the values reported by Lampard *et al.* To investigate the source of this discrepancy, the precession angle measured for ^{74}Ge 2_1^+ using an 85 MeV ^{32}S beam in Ref. [166] was compared to that in Ref. [130], which used a 75 MeV ^{34}S beam. The calculation of $\Phi(\tau)$ as per Eq. (4.7) was performed using Ziegler's SRIM 2013 stopping powers [232]. The Rutgers TF-strength parameterisation was used, as by Pakou *et al.*, and gave $g(2_1^+;{}^{74}\mathrm{Ge}) = +0.367(9)$ and $g(2_1^+;{}^{74}\mathrm{Ge}) = +0.359(22)$ for the precession measurements of Pakou *et al.* and Lampard *et al.*, respectively. Note that, though these uncertainties are statistical only, the resultant g factors are in good agreement. The former measurement also sampled the TF over a considerably wider range owing to its thicker target, though the ranges do completely overlap. This agreement spurred the reanalysis of the precession angles measured by Pakou *et al.* and Lampard *et al.* using the Rutgers parameterisation. The results from this reanalysis, along with those reported by Fahlander *et al.* and Gürdal *et al.*, are shown in Fig. 4.24. The reanalysis reveals that there is no major discrepancy between any of the measurements. This highlights the trouble when using a TF-strength parameterisation: the calculation of $\Phi(\tau)$ depends on the stopping powers, numerical integration methods and TF parameterisation used, and so results may vary if these dependencies are not controlled.

The agreement between the g factors from the reanalysed precession measurements of Pakou *et al.* [166] and Lampard *et al.* [130] is an interesting case, as it allows for possible

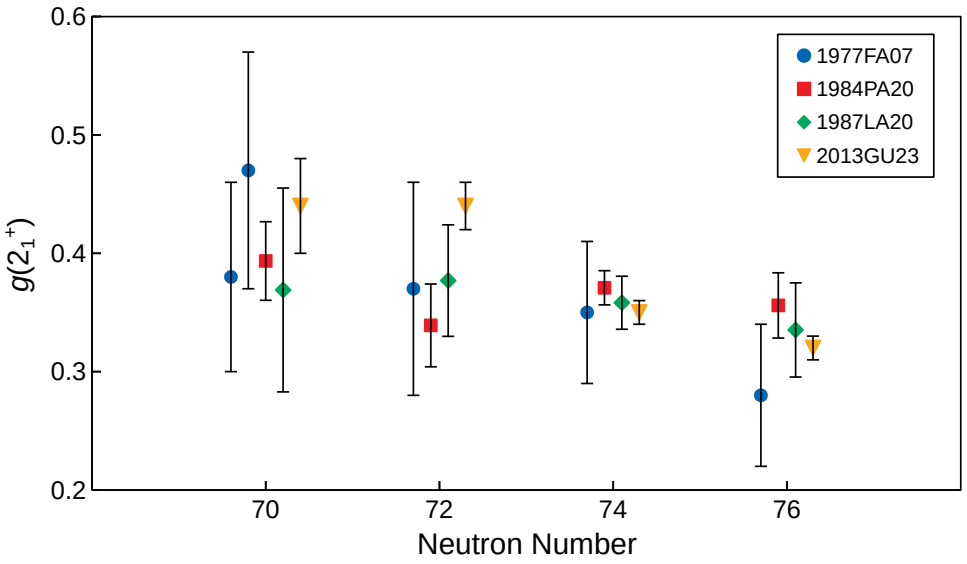

FIGURE 4.24: Reported (1977FA07 [69], 2013GU23 [98]) or reanalysed (1984PA20 [166], 1987LA20 [130]) $g(2_1^+)$ values in the stable, even-A isotopes of Ge. The values from 1984PA20, which were in strong disagreement, have decreased significantly in magnitude in the re-evaluation of $\Phi(\tau)$, as described in-text. This brings the four measurements into good agreement.

identification of the beam demagnetisation effect proposed by Jakob *et al.* [116]. Figure 2 in Ref. [116] indicates that, for a TF effect caused by the 3*s* electron in iron, the demagnetisation effect should begin once beam energy loss reaches $dE/dx \gtrsim 13$ MeV/mg cm^{-2}. In the measurement of Pakou *et al.*, most beam ions have energy loss through the target well under the demagnetisation threshold value, whereas the measurements of Lampard *et al.* are almost at this threshold. The agreement between the two indicates that this threshold has not been reached in the latter measurements. This is not surprising, as the effect should only just be becoming apparent, and is anticipated to be small. However, it is curious to note that, with the exception of ^{72}Ge, the measurements of Pakou *et al.* give systematically larger g factors. These larger g factors may indicate that the demagnetisation effect is beginning to reduce the precession angles measured by Lampard *et al.*, and thereby the reported g factors. However, at the level of precision in these two measurements, the demagnetisation effect cannot be confirmed. Furthermore, as discussed in the previous paragraph, a small variation in inherent magnetisation is the more likely cause of any observed differences between measurements.

In the measurements by Gürdal *et al.* [98], ^{74,76}Ge were measured in both iron and gadolinium hosts under similar conditions to the present ^{74,76}Ge TF measurements, providing the opportunity for a critical comparison. The first thing to note is that the iron-host $g(2_1^+)$ values reported by Gürdal *et al.* and in §4.3.2 are smaller than the gadolinium-host values. Because the Rutgers parameterisation (used by Gürdal *et al.*) was developed using iron-host data, it is plausible that the parameterisation for

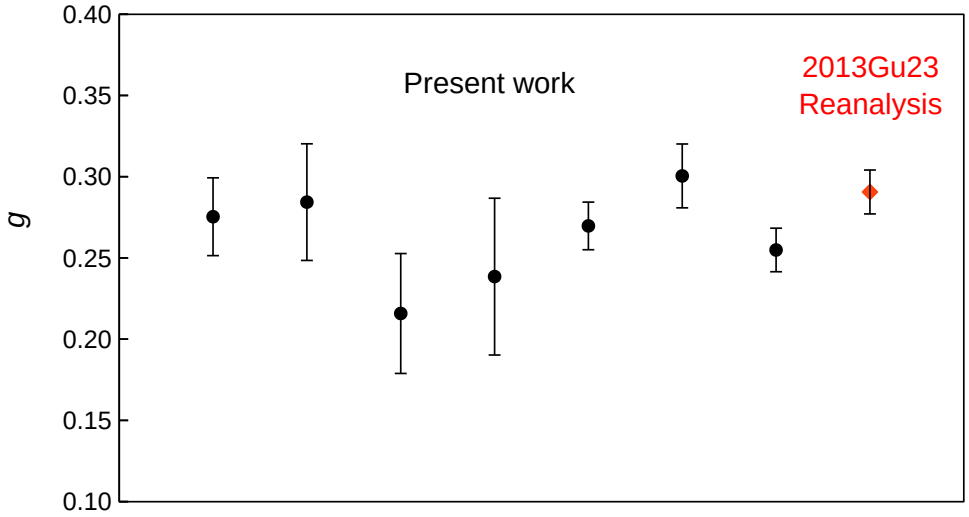

FIGURE 4.25: Measurements of $g(2_1^+;^{74}\mathrm{Ge})$ from the present work and the iron-foil (target III) results from Ref. [98]. The g factors have been evaluated from the measured precession angles as per Eq. (4.6), using the Rutgers parameterisation (see §2.3.2) and Ziegler's SRIM 2013 stopping powers [232]. The measurements are all in good agreement.

gadolinium hosts is underestimating the TF strength, resulting in inflated g factors. However, $g(2_1^+)$ reported by Gürdal *et al.* from iron hosts is still larger than obtained in this project. Focusing now on ^{74}Ge, reanalysis of $\Phi(\tau)$ for the iron host reduces the g factor to $g(2_1^+;^{74}\mathrm{Ge}) = +0.290(13)$. Figure 4.25 shows this value plotted alongside the values obtained from the varying measurements reported in §4.3.2, and are all in good agreement. This discrepancy between $\Phi(\tau)$ calculated by Gürdal *et al.* and that obtained in this work appears to arise from the stopping powers used. In the calculation of Gürdal *et al.*, the ions make a faster transit through the host, reducing $\Phi(\tau)$ and thereby giving a larger g factor. Using Ziegler's SRIM 2013 stopping powers, the ion loses more energy through the target, making a slower transit and thereby giving a smaller g factor. This shows that the TF strength in iron is consistent between the two measurements, and that the Rutgers parameterisation appears to overestimate the gadolinium-host field strength, if the Rutgers parameterisation is assumed to be valid for iron hosts.

In §4.3.2 the relative g-factor values were scaled using the Rutgers TF parameterisation to give averaged absolute g factors, listed in Table 4.7. Comparison of these with the literature values indicates that, in the measurements presented in this thesis, both the Ge and Se values are smaller than the average literature values by $\sim$ 12% in Se and $\sim$ 20% in Ge. In the case of the Se isotopes, the magnitude of the TF has been scaled using $g(2_1^+;^{82}\mathrm{Se}) = +0.496(29)$ [195] (as discussed in §4.3.3), a value obtained from both iron- and gadolinium-host precession data [34, 195]. Meanwhile, the Ge isotope values have been determined solely from TF parameterisations, and are dominated

by the statistical precision of the gadolinium-host measurements of Gürdal *et al.* [98]. The measurements performed in this project differ from any in the literature due to the sole use of an iron host in inverse-kinematics. The g-factor results obtained in §4.3.2 being smaller in magnitude than the literature, for both Ge and Se, indicates that the Rutgers parameterisation for gadolinium hosts underestimates the field strength as compared to iron, resulting in relatively larger g factors. This is further confirmed by the agreement of the ^{74}Ge iron-host precession data measured by Gürdal *et al.* with measurements performed in this project (see Fig. 4.25). The larger discrepancy between Ge measurements performed in this project and the literature, as compared to the Se measurements, also confirms this, as the Ge data in the literature were largely made using gadolinium hosts, whereas the Se data in the literature uses both gadolinium and iron hosts equally. Furthermore, the unambiguous agreement observed for ^{56}Fe in iron, presented in the previous subsection, suggests that the $g(2_1^+)$ values obtained from the present measurement are more accurate than the values reported from or calibrated using gadolinium-host measurements, though this cannot be firmly concluded.

In conclusion, while arguments can be made about the relative over or underestimation of the TF strength between iron and gadolinium hosts observed in the Ge and Se isotopes, a determination of the TF strength's accuracy for these measurements cannot be confidently made until a precise, independent g-factor measurement is obtained.

4.6 Summary

The TF method, and the calibrations used to obtain absolute g factor values from it, have positive and negative aspects. They provide a means to perform precise g-factor measurements on what may be otherwise inaccessible states, but also provide a false assurance of the measured g factor's magnitude, particularly in isolated measurements without any reference state for calibration. Much of the g-factor data in the literature has been obtained using the TF effect, with alternative measurements being dated and imprecise, and based on different TF parameterisations. Re-evaluation of some data with a consistent set of stopping powers has resolved some discrepancies in reported g factors, however absolute g-factor values obtained by the TF method remain a challenge in many cases: certain elements or regions appear to exhibit deviations from the proposed calibrations. This makes an accurate calibration of the TF strength across the entire nuclear chart a challenge that has not yet been achieved. A complementary technique against which to calibrate the TF strength in any given measurement is urgently required.

Relative measurements along isotopic chains, using the thin-foil TF technique, eliminate much of the uncertainty in the TF calibration by sampling it over short and largely overlapping velocity ranges, whilst also utilising the same target to eliminate uncertainties in thickness and magnetisation. The results presented and discussed in §4.2 demonstrate the effectiveness of such an approach. The Ge and Se isotopes, with their accurately and precisely obtained ratios, could have their magnitudes firmly set by a single absolute measurement. The RIV technique is a good candidate to complement the TF technique, but has been restricted in its use due to challenges in developing an *ab initio* understanding of the hyperfine interactions involved. With the advances in modelling the hyperfine interaction in TDRIV measurements presented in the previous chapter, these two techniques provide the opportunity to measure both the sign and magnitude of $g(2_1^+)$ values in previously inaccessible nuclear states.

Chapter 5

RIV Simulate: A Recoil-In-Vacuum Data-Analysis Toolkit

This chapter describes **RIV Simulate**, a collection of computer programs written during this doctoral candidature for POSIX-compliant operating systems. **RIV Simulate** is a toolkit to aid in both the setup and feasibility testing of nuclear g-factor measurements using the recoil-in-vacuum (RIV) technique, as well as the analysis of RIV angular-correlation data and determination of the g factor from measurements on ions having multi-electron charge-state distributions. A reading of this chapter is necessary as a precursor to Chapter 6, however the experimental descriptions in Chapter 6 also serve to help understand the application of this program. As such, certain details presented here may be more easily understood in a subsequent reading after Chapter 6, and may be best understood when read in parallel.

The hyperfine interactions arising within the multi-electron ionic species of a charge-state distribution present a unique challenge when interpreting the g factor from measured angular correlations. The physics underlying these hyperfine interactions was reviewed in §2.3.3, along with cases in which successful g-factor measurements have been performed using the RIV technique. These successful published cases differ from the cases considered here as, in the former, isotopes with known g factors existed against which a calibration of the hyperfine interaction could be made and, in the latter, the analysis only needed to consider the hyperfine interaction of a single, simple atomic state. In the present work, an *ab initio* approach has been taken to interrogate the complex problem of interpreting an ensemble of charge states (ionic species), amongst which multiple atomic states contribute, potentially with changing populations through time. The challenge of modelling this system was handled by taking a Monte-Carlo approach, as suggested by Stone, Stone and Jonsson [202] and as implemented by Chen *et al.* [49] for interpreting time-integral RIV measurements. The atomic-structure package GRASP2018 was used to calculate the required atomic properties, as described in §2.4. A toolset was developed consisting of a Monte-Carlo simulation, G_k and angular-correlation plotting routines, an energy loss, kinematics and

charge-state-distribution calculator, and χ^2 minimisation (fitting) routines.

It shall be clarified now that in this chapter, and the next, the convention has been adopted to refer to ionic species (charge states) by their atomic analogue, i.e. the equivalent element having the same number of bound electrons, n_e. For example, if an iron atom, having nuclear charge $Z = 26$, is ionised to a charge-state having $Q = +15$, then it will be referred to as a Na-like ionic state, as $Z - Q = n_e = 11$.

5.1 Monte-Carlo Approach

To calculate the time-dependent attenuation of the angular correlation by an *ab initio* approach, the hyperfine interaction of each contributing ionic species, and their associated ground- and excited-atomic-state configurations, should be considered. The initial population of excited atomic states, which determines the atomic decay chains, also needs to be defined. Finding an exact mathematical solution to the time-dependent attenuation arising from all these variables is not practical. Instead, the numerical Monte-Carlo method has been used to obtain a solution by conducting a "virtual experiment", using properties obtained from atomic-structure calculations.

5.1.1 Atomic-Decay Cascades

The first piece of information required is the charge-state distribution of the ions of interest as they emerge from the target into vacuum. This can be obtained from a measurement for the particular beam/target combination chosen, or calculated using an empirical parameterisation such as those published by Nikolaev and Dmitriev [155] or Schiwietz and Grande [187]. After defining the charge-state distribution, and thereby the ionic species present, the initial atomic-state populations must be set. The initial atomic-state populations, however, are ill-defined for ions emerging into vacuum. In the approach taken by Chen *et al.* [49] it was assumed that there is an equal probability of any atomic state to be populated, a uniform distribution across all states produced by the allowed electron excitations in the GRASP calculation. In addition to this basic distribution, Boltzmann, Maxwell-Boltzmann and Gaussian energy-distribution functions have been included as options in the present approach, as well as the capability to populate only a specific level. The functions are parameterised using a 'temperature' parameter T, and for the Gaussian distribution also a width parameter σ. The temperature parameter represents the average energy in a given ionic system relating to the atomic-excited-state energies. The function's form defines how this energy is distributed across each simulated ionic species. The effect of different distributions and average energies can then be examined and compared to experimental results. With the charge-state distribution and

atomic-state populations defined, the atomic-structure calculations can then be used to generate single-ion events consisting of atomic-transition cascades, numbering in the tens of thousands (a typical experimental measurement). The procedure to generate an event is as follows:

For a given ionic species an initial atomic state is randomly selected following the chosen population distribution. This is achieved by summing the energy function of the chosen distribution for all atomic states (and optionally including a $2J+1$ weighting as per the procedures of Stone *et al.* [202] and Chen *et al.* [49]) and using a uniformly distributed random number to choose a state. Specifically,

$$P_{\text{sum}} = \sum_{a=1}^{N} d(E_a) \times (2J_a + 1), \tag{5.1}$$

$$P_a = R \times P_{\text{sum}}, \tag{5.2}$$

where P_{sum} is the sum of probabilities for all atomic states calculated for the chosen ionic species, N is the number of atomic states, d is a function representing the chosen energy distribution and includes the parameter T (and σ for the Gaussian distribution), E_a is the atomic-state energy, the $2J_a + 1$ term is the optional weighting, J_a is the spin of the atomic state, and R is a random number evenly distributed between $(0, 1]$. P_a is used to select an atomic state at random, which is done by selecting state a having the value P_a in its sum range, such that

$$\sum_{i=1}^{a-1} d(E_i) \times (2J_i + 1) < P_a \leq \sum_{i=1}^{a} d(E_i) \times (2J_i + 1), \tag{5.3}$$

or, if $a = 1$,

$$0 < P_a \leq d(E_1) \times (2J_1 + 1). \tag{5.4}$$

Once an initial atomic state has been selected a nuclear survival time for the event is then generated by

$$t_N(\tau_N) = -\log_e(R) \times \tau_N, \tag{5.5}$$

where τ_N is the nuclear-state lifetime, and R is a random number evenly distributed between $(0, 1]$.

The following procedure is then iterated (after initialising the cumulative atomic survival time t_c to zero):

1. An atomic survival time t_a is randomly generated for each available transition using Eq. (5.5), with $\tau = 1/A_a$ instead of τ_N, A_a being the partial transition rate. The transition with the shortest survival time is selected.

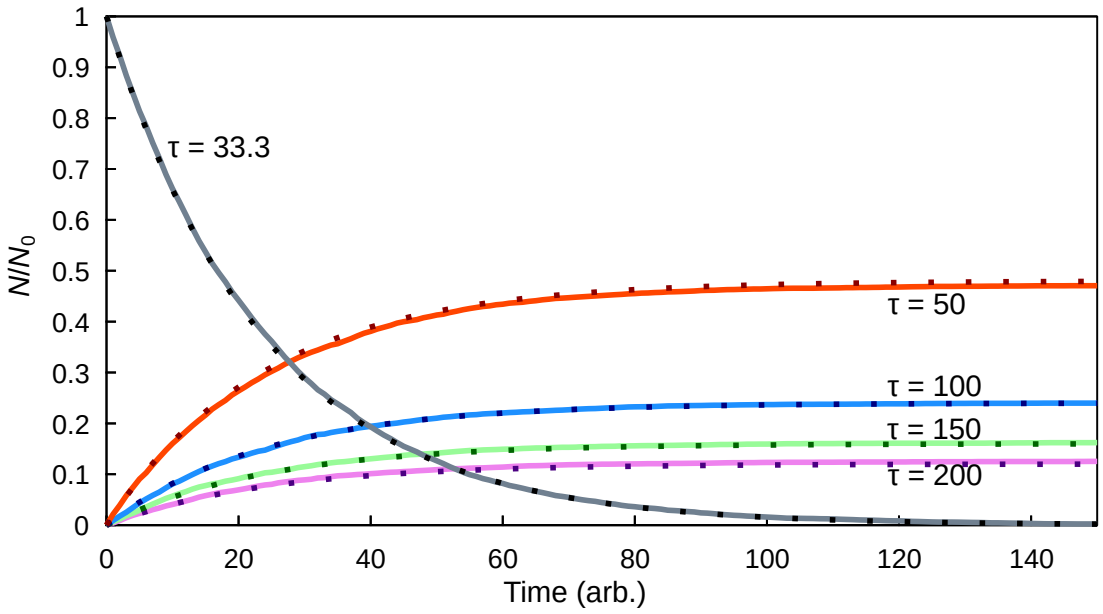

FIGURE 5.1: Comparison of the two decay approaches described in-text, being the single atomic-lifetime and branching-ratio method versus the Monte-Carlo simulation partial-transition-rate method. The dots represent the values calculated using Eq. (5.6) with a single atomic lifetime and a branching ratio $I = \lambda_a/\lambda$, and the lines represent the values obtained using the Monte-Carlo approach described in §5.1.1 with partial transition rates. The mother state is allowed to decay into one of four daughter states, with their respective lifetimes indicated. The agreement between the dotted and solid lines shows that the mathematical and Monte-Carlo approaches are equivalent.

2. If the nuclear survival time t_N is less than $t_a + t_c$, or there are no available transitions, set $t_a = t_N - t_c$ and end the event. Otherwise, add t_a to t_c.

3. Set the atomic state to that chosen as a result of the first step, for the next iteration.

Atomic levels and t_a values are recorded for each iteration. This procedure produces an event consisting of a number of atomic-level references and survival times, with a cumulative atomic survival time equal to the nuclear survival time.

It should be clarified that the selection of a new atomic state occurs based on the calculated individual oscillator strengths (i.e. partial transition rates), rather than a single atomic lifetime and branching ratios. This approach is valid because

$$N\lambda = N_0\lambda e^{-t\lambda}, \tag{5.6}$$

$$\log_e(N/N_0) = -t\lambda, \tag{5.7}$$

$$-\log_e(N/N_0)\frac{1}{\lambda} = t, \tag{5.8}$$

can also be represented as a sum over separate decays in which

$$\lambda = \sum_{l=1}^{n} \lambda_l, \tag{5.9}$$

$$-\frac{\log_e(N/N_0)}{\sum_{l=1}^{n} \lambda_l} = t, \tag{5.10}$$

$$-\sum_{l=1}^{n} \frac{\lambda_l}{\log_e(N/N_0)} = \frac{1}{t}, \tag{5.11}$$

where N is the population of states at time t, N_0 is the initial number of states ($t = 0$), n is the total number of available transitions, λ is the transition rate of the atomic state, and λ_l is the partial transition rate of transition l.

For any given population fraction N/N_0 of a mother state, the proportions between each daughter state are the ratio λ_l/λ. From Eq. (5.11) it follows that $1/t_{\text{part}} = -\lambda_a/\log_e(N/N_0)$, and therefore the partial decay rate is proportional to λ_l. As such, a value of t generated by substituting N/N_0 with a uniformly distributed random number, as per Eq. (5.5), will give the correct branching ratios when the same value of N/N_0 (the random number) is used. Hence, when sampled across the range $[0, 1]$, a faster partial transition will give, on average, a smaller value of t, and vice-versa.

Through the Monte-Carlo approach, the survival time generated using Eq. (5.5) from each partial transition rate represents the sum over $\lambda_a/\log_e(N/N_0)$ in Eq. (5.11) across a uniformly sampled range of N/N_0. This is how the branching ratios are maintained in the random sampling procedure. The outcome of using this approach versus the purely mathematical approach of Eq. (5.6) is shown in Fig. 5.1, and reveals almost no difference between the two, particularly in the mother state's decay rate. Note that it is assumed any non-$E1$ (i.e. forbidden) transition strength is weak enough to disregard.

With a number of atomic-decay-cascade events now generated across the charge-state distribution, Eq. (2.49) can be used to calculate the $G_k(t)$ values. These data can also be used to examine the population of atomic states through time, as well as the effect of different distributions and temperature parameters on observable frequencies in the $G_k(t)$ plots.

5.1.2 Rapid versus Slow Transitions

Atomic-structure calculations reveal that the high-energy atomic states of relevance to the present work are all very short-lived, decaying away on sub-picosecond to few-picosecond timescales. When transition cascades occur on such short timescales

and have several steps in the decay chain, the resulting attenuation appears as a quasi-exponential function [31, 30]. When a large number of atomic states are populated and their population remains relatively static over the measurement time, this also results in the perturbation appearing as a quasi-exponential function [92]. Both of these characteristics appear for ionic species with multiple valence electrons, and both mechanisms contribute to the resulting quasi-exponential behaviour: there are many populated excited atomic states that are close in energy, resulting in rapid, multi-step transition cascades leading to a large number of longer-lived, low energy states becoming populated.

For ionic species with a single electron outside a closed shell, such as Na-like ions, low-lying excited states can have lifetimes much greater than the nuclear 2_1^+-state lifetimes, to the order of hundreds of picoseconds. Short-lived ($\tau \leq 1$ ps), high-energy states will rapidly feed these long-lived states, which then slowly feed the ground state, and/or other low-energy excited states with long lifetimes. Bosch and Spehl mathematically derived the effect on the time-dependent attenuation resulting from an atomic state being fed by a large number of short-lived, higher-energy states [32]. They determined that there is a phase shift and amplitude reduction of the $G_k(t)$ cosine function proportional to the average lifetime of the feeding states. By performing a Monte-Carlo simulation using a test set of atomic transitions this effect was qualitatively reproduced for single transitions, as shown in Fig. 5.2. The phase shift and amplitude reduction do not match the formulas presented in Ref. [32] exactly, but this is not surprising considering that they describe a somewhat different decay scenario. The simulation result does converge on the solution in Ref. [32] for feeding states with very long lifetimes ($\gtrsim 100$ ps), counter to their formulation in which the feeding states are expected to be very short lived ($\lesssim 0.1$ ps). An exact mathematical description of the interactions arising from these decay cascades would be difficult to achieve, however the Monte-Carlo simulation allows these effects to be explored.

5.1.3 $G_k(t)$ Calculations for Single Atomic States

It can be useful to calculate the $G_k(t)$ plots arising from a small number of individual atomic states, rather from a Monte-Carlo simulation. This is particularly true in cases where the charge-state distribution or atomic-state distribution is not well-known or understood, as these often distinct individual states can provide insight into the population of particular ionic species. The user can choose the number of atomic states to input and provide their spin, J, hyperfine-field strength, B, and occupation. A superposition of particular frequencies can then be assembled and their occupations varied to develop

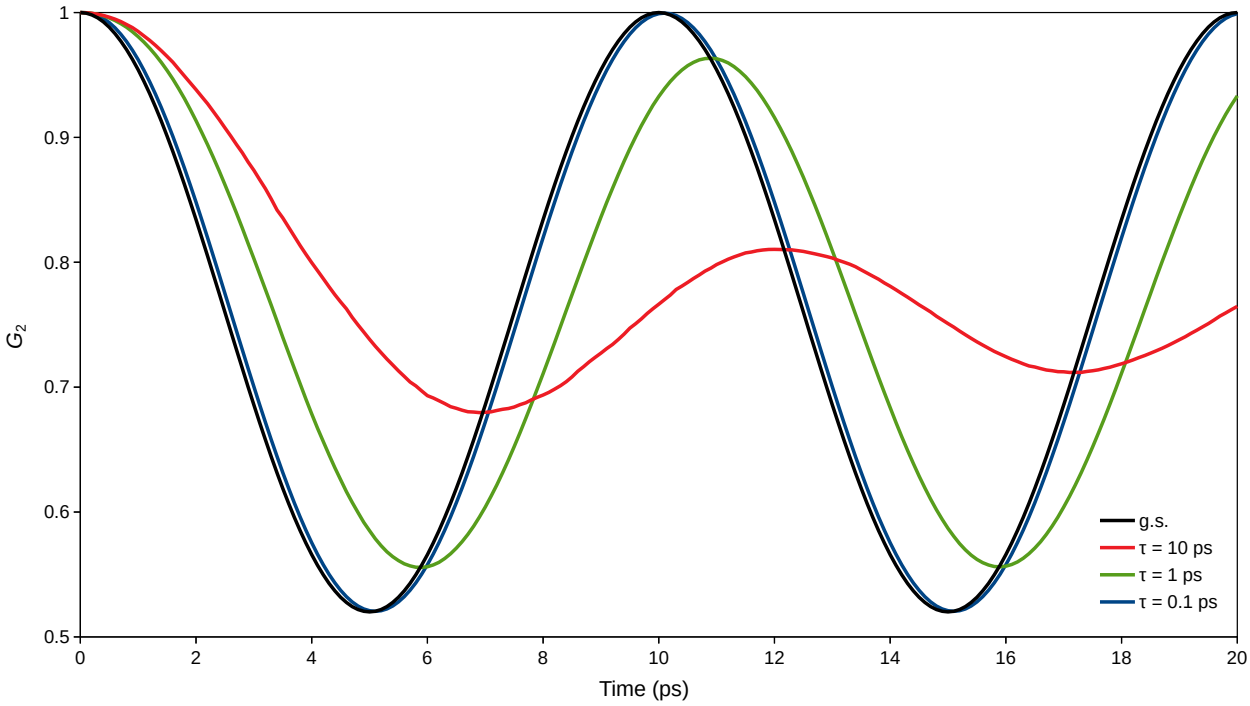

FIGURE 5.2: G_2 versus time plot of a $J = 1/2$ ground-state frequency with a 10 ps period, either fully populated from $t = 0$, or initially unpopulated and being fed by one of three excited states, each having a lifetime of either $\tau = 10$, 1 or 0.1 ps. There is a clear amplitude reduction and phase shift, which is proportional to the lifetime of the feeding state [32].

an intuitive understanding, for example, of the measurement data and identify particular features in the time-dependent $G_k(t)$ values, without interference from states having weak hyperfine interactions that will reduce the amplitude of frequencies important over the ion flight-time covered by the measurement. Additionally, by tweaking each atomic state's occupation, this method may be used to interrogate the influence of low-lying atomic states from different ionic species on the measured time-dependent attenuations. These occupations ought to allow insight into the population of particular ionic species, and whether the chosen atomic states are strongly occupied over the time-span interrogated by the measurement.

5.1.4 Frequency Superposition

Considering the overall character of the ionic species discussed in §5.1.2, there are three categories into which they can be classified: those with a dominant ground state and/or long-lived low-energy states with distinguishable cosine-like frequencies in $G_k(t)$ (e.g. Na-like), those exhibiting quasi-exponential character in $G_k(t)$ (e.g. Al-like), and those with dominant $J = 0$ states that have little or no attenuation effect (e.g. Ne-like). Their combined interaction ought to present itself in the $G_k(t)$ trend as a superposition of the

measurable frequencies from the first category, with their amplitude reduced by contributions from the second and third categories. Such a trend is illustrated in Fig. 5.3. *Therefore, by identifying the major contributing frequencies in time-dependent attenuation coefficients, $G_k(t)$, it should be possible to determine a g factor without the need to accurately model all the contributing ionic species and excited atomic states.*

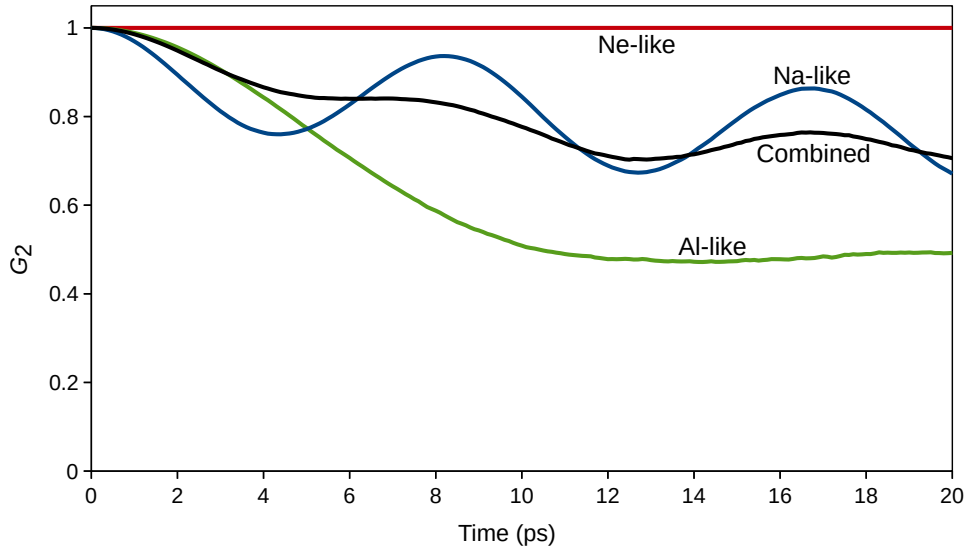

FIGURE 5.3: G_2 versus time plot of a Monte-Carlo simulation having an initial atomic-state distribution following a Boltzmann function with average energy $T = 30$ eV for Na-like, Ne-like, and Al-like ionic species, and a superposition of all three in equal parts. The Na-like case shows a clear (cosine) oscillation from the dominant $J = 1/2$ ground state, with its amplitude reduced by the slower frequencies of the long-lived, low-energy excited states. The Ne-like case is assumed to be dominated by the $J = 0$ ground-state, causing no attenuation. The Al-like case has a large number of low-energy excited states (many of which are short-lived), that rapidly decay into a large number of relatively static states. This behaviour gives the quasi-exponential shape of G_2. In the combined case the amplitude of the Na-like ground-state G_2 oscillation is reduced owing to the smooth Ne-like and Al-like contributions. This attenuation of the Na-like component highlights the importance of an optimised charge-state distribution.

5.2 Atomic-Structure Calculations

To calculate the required atomic-structure properties for the $Z \sim 30$ nuclei concerned in this project, GRASP2018 [79] was used. While the theoretical basis underpinning the calculations is common to any atomic configuration to be calculated, the information about obtaining convergence relates specifically to calculations performed for atomic configurations having 9–13 electrons. The GRASP2018 software package was described in §2.4. To reiterate the key points: atomic properties are obtained for atomic-state functions (ASFs) and transitions between them, and atomic-state functions are calculated from a linear combination of configuration-state functions (CSFs), which are Slater determinants built from user-specified single-electron configurations. Equation (2.50) shows that any CSF having the same parity π and angular momentum J can contribute to a given ASF. To obtain the most accurate solution, one would include CSFs up to the continuum states. However, this is impractical as convergence becomes more difficult and computation time becomes longer as the number of CSFs increases. As such, one should choose CSFs that have the most significant mixing coefficients. While these mixing coefficients aren't known before obtaining the solution, most with significant magnitudes can be included by following the procedure in §2.4.

In the present context, the goal was to simulate spectral cascades for atomic configurations having 9–13 electrons. Spectral cascades, that is sequences of atomic transitions, which involve reconfiguration of only valence-shell electrons, are solely being considered due to the time-scales over which the hyperfine interaction is expected to be observed, that is the picosecond timescale. The high-energy atomic configurations that may result in Auger and X-ray emissions occur of the order of sub-picosecond timescales, too small to significantly affect the hyperfine frequencies observed in time-differential RIV experiments. The approach taken to calculate the properties of atomic states involved in spectral cascades has been to calculate ASFs having leading terms that are valence configurations, up to atomic level energies nearing the ionisation energy. Because high-energy excited states produced by valence configurations are typically short-lived and have $B_{\mathrm{HF}} \sim 0$, their effect on the time-dependent frequencies to be observed in $G_k(t)$ is almost null. As such, for the atomic configurations concerned (9–13 electrons) it was deemed unnecessary to calculate all the way out to the ionisation energy, and so spectral configurations were restricted to those with principal quantum number $n \leq 6$. By applying these restrictions, atomic-state configurations relevant to the picosecond measurement timescale and ionic species expected were selected for, while keeping the configuration space computationally tractable.

The most important property to calculate accurately is the hyperfine-field

strength (HFS), followed by the transition rates. As such, CSFs were generated having a single-electron excitation from the deep core ($n = 1$) electrons to improve the calculated HFS. Transition rates were improved by allowing single and double excitations from the outer-core electrons, having principal quantum number $n = 2$ ($Z - Q > 10$) or $n = 1$ ($Z - Q \leq 10$). The CSF space was increased by intervals of n up to a value where the number of CSFs exceeded $\sim 10^8$, at which point computation time was already quite long on the available computing resources ($\gtrsim$4 weeks). For ionic species with $Z - Q > 10$ the ASFs were resticted to level energies below 1000 eV where necessary, as per the suggestion in Ref. [202, 203]. This restriction had to be relaxed for ions at or just below the neon shell closure due to the large energy gap, and instead were taken to only two shells beyond the shell closure, as these states were expected to rapidly and directly decay to the ground state. Once solutions were obtained, the calculated energy levels were compared to those in the US National Institute of Standards and Technology database for atomic spectra [178], and found to agree to the level of 1% in all cases, and 0.1% in most. These comparisons were helpful in determining whether the radial wavefunctions had converged on an accurate solution. Another way convergence was assessed was to compare the results of the two oscillator-strength (partial transition rate) calculation approaches (alternate forms for the dipole operator, or gauges) GRASP takes, namely the length and velocity forms [43]. Disagreement indicates the solution is not self-consistent. Most partial transition rates were found to agree better than 1%, with poor agreement only observed for slow transitions from high-energy states, which were deemed unimportant in the present context due to the unlikeliness of their population or observation. Tables showing these comparisons for the important ionic species (F-like, Ne-like, Na-like) can be found in Appendix D. With the atomic-structure properties calculated, and having confidence the wavefunctions have converged on good solutions, the Monte-Carlo simulation can be performed.

The scripts used to perform GRASP calculations and obtain the atomic-structure properties used in this project can be made available upon request to the thesis author.

5.3 Calculation of G_k Values

The calculation of the attenuation in the angular correlation owing to the hyperfine interaction in free ions, G_k, is described in detail in section §2.3.3. The Monte-Carlo simulation events allow for a G_k value or the perturbation of the nuclear tensor at any given time to be calculated. The user may also specify if they wish to calculate the γ-ray angular correlation for the unshifted (stopped), Doppler-shifted (in-flight), or stopped plus in-flight (summed) components. These events can be separated in the Monte-Carlo simulation by comparing how long the nuclear state survives for, t_N, to the specified flight time, t_f. Experimentally, t_f is the time the ion takes from leaving the target foil and impacting into the stopping foil. Ion events with nuclear states that decay prior to t_f, i.e. $t_N < t_f$, are classified as in-flight decays. Those having $t_N \geq t_f$ are classified as stopped. Depending on the user's selection, the event is vetoed from or allowed in the calculation. $G_k(t)$ values for allowed events are then calculated by either perturbing the tensor as per Eqs. (2.36–2.43) or calculating G_k for the event as per Eq. (2.48). Stopped events are evaluated at t_f, and in-flight events are evaluated at the nuclear decay time t_N. The $G_k(t)$ value is then averaged across all events and all atomic states as per Eq. (2.49) to give the G_k value expected to be measured. When the calculation is performed for the stop component using individually specified atomic states, instead of using the Monte-Carlo simulation, then the perturbation or $G_k(t)$ values are calculated directly using Eq. (2.38) or Eq. (2.45), respectively, and are evaluated at t_f. The values are then linearly combined, weighted by their fractional population. If the user has specified that the in-flight or summed components are to be calculated, then nuclear decays must now be accounted for. This is handled by performing the Monte-Carlo simulation for each individual atomic state, allowing nuclear decays but no atomic decays. The resulting simulation is then used to calculate $G_k(t)$ as described for the Monte-Carlo procedure.

Two approaches to calculating the attenuation in the angular correlation have been described: the full treatment involving the perturbation of a coupled atomic and nuclear statistical tensor; and the isotropic approximation in which G_k is computed as a coefficient of the nuclear tensor. These will now be discussed, and the difference between the two approaches examined.

5.3.1 Coupled-Tensor Approach

The coupled-tensor approach, while more computationally involved, is the full treatment of the coupled nuclear and atomic tensor's evolution in time due to an atomic hyperfine interaction. As described in §2.3.3, the coupled tensor, $\rho(FF')$, is obtained using Eq. (2.36). The nuclear tensor is obtained using the Winther-de Boer code, and the initial atomic tensor is assumed to be that of an isotropic electronic configuration. The

coupled tensor is formed from these two, and perturbed as per Eq. (2.38), introducing alignment into the atomic tensor. Each time an atomic transition occurs the nuclear and atomic tensors are projected out, and then the deorientation arising from the unobserved atomic transition is applied to the atomic component, as per Eq. (2.43). The two tensors are then recoupled and further perturbed until another transition occurs, repeating the procedure just described, or either the flight time t_f or the nuclear survival time t_N is reached. In this sequence, alignment is gained by the atomic tensor through its interaction with the nuclear tensor, and then some alignment is lost from the system with each atomic transition.

5.3.2 Isotropic Approach

Goldring's formulation for calculating $G_k(t)$, shown in Eq. (2.45), was obtained by assuming that the statistical atomic-state orientation is not only initially isotropic, but that it does not evolve in time with the nuclear tensor. This formulation was derived for the recoil-in-gas technique, where the atomic state is changed by collisions with gas molecules, that frequently 'reset' the atomic alignment. This assumption considerably reduces the number of calculations as the assumption of a static isotropic atomic tensor greatly reduces the angular-momentum coupling algebra present in the coupled-tensor approach down to that presented in Goldring's formulation, which is now simplified into the $C_{IJ}^{FF'}(k)$ component and a cosine function [see Eq. (2.46)].

5.3.3 Comparison of Approaches

In order to determine if there is any significant difference between the full treatment and the isotropic assumption in the Monte-Carlo simulation, the two methods were used to calculate $G_k(t)$ plots for two different ionic species. The results of these two calculations are shown in Fig. 5.4. They were performed using a uniform excited-state distribution so that a large number of transitions would be observed. Calculations were performed for a Na-like ionic species, having some thirty excited states, and an Al-like ionic species, having hundreds of excited states. In both cases, there is no observable difference between using the isotropic and coupled-tensor approaches. This may be due to either an insignificant amount of perturbation transferring from the atomic tensor to the nuclear tensor, or may be due to the large amount of sampling in the propagation of the atomic population preventing any overall orientation from forming in the atomic tensors. As such, while the option to perform the calculation using the coupled-tensor approach has been retained, the isotropic approach is the preferred method due to its simplicity. Hence it has been used in all further calculations discussed here and in Chapter 6, unless otherwise noted.

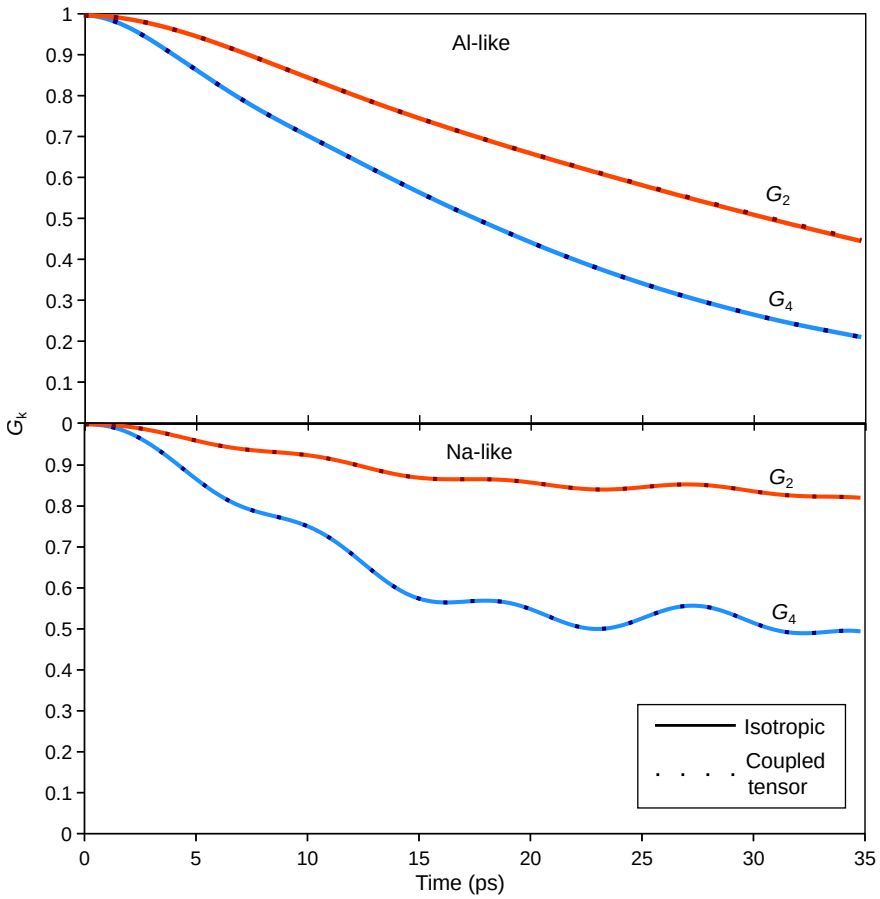

FIGURE 5.4: Comparison of the isotropic calculation approach (solid lines) and the coupled tensor approach (dotted lines) described in §5.3.1. The calculations are based on ^{56}Fe Al-like and Na-like ionic species with a large number of atomic states initially populated. This was done to maximise the number of transitions in order for the effect of deorientation due to unobserved atomic transitions to be most evident. As shown in the plot, there is no observable difference between the two calculations.

5.4 Experimental Setup

So that theoretical angular correlations can be calculated, the user must input the details of the experiment. The user must specify the beam nuclide, beam energy, target details (number of layers, elements/isotopes and thicknesses), ground-state spin, excited-state spin, excited-state energy, transition probability amplitude ($B(E2)$ in units e^2b^2), particle-detector details (either square detectors at a certain radius from the beam axis with user-specified ϕ angles, or a segmented ring detector with inner and outer radius and angular coverage of each segment) and γ-ray detector details (length and radius of the cylindrical crystal, distance from target, radius of 'dead core' if present, θ and ϕ angles). This information allows the calculation of kinematics details, energy loss in the target, statistical tensors after Coulomb excitation (Coulex), average recoil velocity, and solid-angle attenuation factors for the γ-ray detectors.

Kinematics calculations [144] are used to determine the energy of detected particles after Coulex (being either beam or target particles), whilst also taking into account energy loss [232] through the target layer before excitation, at scattering angles across a detector segment (rectangular or annular), and compute an average statistical tensor and recoil velocity. The average tensor is calculated by making ten horizontal and vertical divisions across the detector face, and ten divisions through the target depth, calculating the tensor in each division using the Winther-de Boer code [4], and then computing the composite Simpson's rule integral (weighted by the scattering angle and excitation cross-sections, and the particle-detector-segment solid angle) divided by the step width. The γ-ray-detector information is used to calculate the solid-angle attenuation factor Q_k in the angular correlation using Krane's [128] method. Gamma-ray and particle detector θ and ϕ angles, along with the recoil velocity, are used to determine relativistic abberation and Lorentz boost corrections using Pelte and Schwalm's solution [169] for Doppler-shifted photopeak counts and angular shifts from the particle-frame to the lab-frame (See §2.2.2). Only with this experimental information can accurate theoretical angular correlations be computed for comparison with data.

5.5 Input of Measurement Data

To fit parameters to measured angular-correlation data, the user must be able to input the photopeak count data. RIV Simulate can read an ASCII file containing a γ-particle detector coincidence ID (γ-p ID), ion flight time, photopeak count, photopeak count uncertainty and time uncertainty, separated by either spaces or a tab character. The γ-p ID is an array-style identifier obtained by $i_{\gamma p} = i_\gamma n_p + i_p$, where $i_{\gamma p}$ is the γ-p ID, i_γ is the zero-indexed (i.e. counting from zero, not one) γ-ray-detector number, n_p is the number of particle detectors, and i_p is the zero-indexed particle-detector number, as input into the experimental setup (see §5.4). Once i_γ and i_p are obtained from the γ-p ID the θ and ϕ angles are obtained from the experimental setup inputs. By using a γ-p ID the fitting routine will automatically compute the correct theoretical angular correlation and select the γ-ray detector Q_k coefficient. Following the γ-p ID should be a flight time t of the ion, the photopeak counts N, uncertainty in N, and optionally uncertainty in t. The photopeak counts do not need to be normalised to the theoretical angular correlation in the data file; they can be provided as direct photopeak counts. These will be normalised around the ϕ-dependent angular correlation for each γ-ray detector. If definitive γ-ray and particle detector identification is not possible, the user may also setup the experimental details with a single particle detector specified, and a dummy γ-ray detector for which a Q_k value is computed. This will indicate to the program that the ASCII data file will instead specify a θ and relative ϕ angle ($\phi_\gamma - \phi_p$) instead of a γ-p ID, and at the user's specification use the Q_k of the dummy detector. In this style of data file, the angular-correlation data points must be normalised to the theoretical angular correlation before being input, as automatic normalisation between unknown γ-particle pairings would be unreliable. For Doppler-shifted photopeak counts the θ and ϕ values for each data point are adjusted to the nucleus frame-of-motion using either a user-specified recoil velocity or a value calculated by the kinematics and energy-loss routines to apply the relativistic abberation and Lorentz boost corrections described in §5.4. An example of each type of data input file can be found in Appendix C.

5.6 Data-Analysis Tools

A number of tools have been developed to aid both in feasibility testing of experimental setups (i.e. planning experiments), as well as the interpretation and analysis of data. Many tools generate gnuplot [222] scripts so that output data can be quickly visualised. Others report χ^2 minimisation information from fits to the charge-state distribution, atomic-state population, and g factor. The details of each program are described in this section.

5.6.1 Energy Loss in Targets

In order to interrogate an experimental setup, the user is able to calculate energy loss through a single or layered target, and the average recoil velocity of beam and recoil particles detected by a square or annular particle detector. The charge-state distribution of the ion of interest may also be calculated using the parameterisations developed by Nikolaev and Dmitriev [155] or Schiwietz and Grande [187], with customisable fit parameters for the former. A user-supplied routine for calculating the charge-state distribution may also be used in the program by providing a pre-compiled object file and using the correct switch at compilation. Instructions to do this are included with the software documentation. The user specifies a beam nuclide, beam energy, a number of layers in a target foil, their elemental/isotopic composition and thickness, (optionally) the details of a plunger foil following the target, the layer in which the nuclei of interest excite, whether the beam or target is excited in the reaction, nuclear-excited-state transition information, and particle-detector shape and geometry. Average entry and exit energies are calculated for each specified layer, taking into account reaction kinematics and weighting by Coulomb-excitation cross-sections and solid-angles across the detector face. If any reaction kinematics are unsafe in the head-on collision, the user will be notified. This information can be used to determine if recoil or beam particles will stop or pass through a specified foil, in particular the stopping/plunger foil. Charge-state distribution calculations allow the user to optimise beam energy, target thicknesses and/or recoil angles to produce the optimal charge-state populations. Using this tool, a user can optimise their experimental design to perform a robust measurement of ideal frequencies for a g-factor measurement.

5.6.2 Atomic-State-Population Heatmaps

The Monte-Carlo simulation approach, described in §5.1.1, allows for the tracking of atomic-state populations through time. At 1 ps intervals the population data are obtained from the Monte-Carlo event array and written to a comma-separated value (csv) file format for easy viewing in spreadsheet software. A gnuplot script is also generated

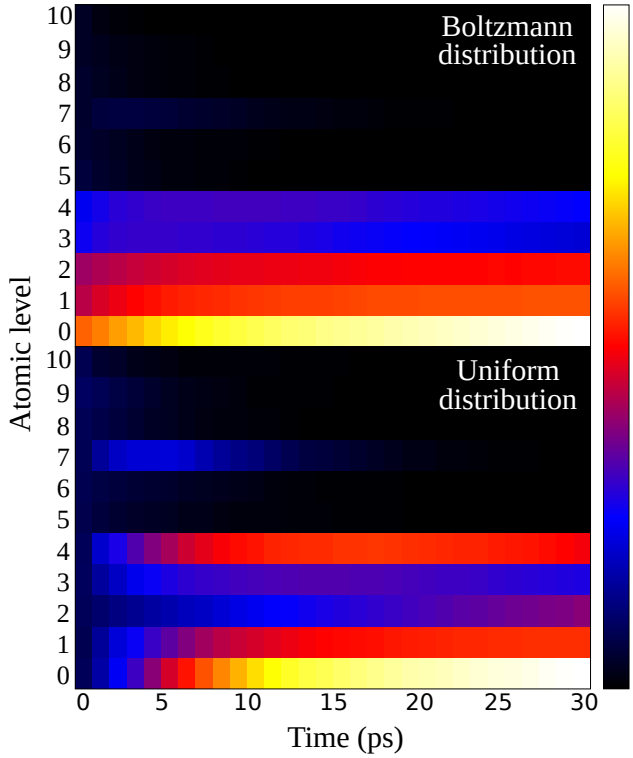

FIGURE 5.5: Example heatmaps produced by RIV Simulate from a ^{56}Fe Na-like ionic species, one having a Boltzmann distribution of excited atomic states with $T = 100$ eV and the other a uniform distribution. The y axis shows the energy-ordered level index. The temperature scale is set relative to the most intense population on the plot. Higher-excited states, which feed the lower states, are included in these calculations but not shown.

that instructs gnuplot to produce a heatmap of the populations through time, with the colour scale set relative to the most populated state. Example heatmaps comparing initial state populations having either a Boltzmann or uniform distribution are shown in Fig. 5.5. These heatmaps allow for a fast, intuitive assessment of the timescales over which certain atomic states are important, and how long-lived states change over time via feeding and decay. Should the user want to perform further analysis of the atomic-state populations they can access the time-dependent population data directly in the csv file.

5.6.3 $G_k(t)$ and Angular-Correlation Plotting

After a Monte-Carlo simulation has been performed or single states have been input, a plot of G_k vs t can be produced, as well as θ- or ϕ-dependent theoretical angular correlations at chosen time points. Using the $G_k(t)$ plots, the dominant frequencies for a given charge-state or atomic-state distribution can be visualised, and the effect of changing either distribution explored. In many cases a realistic possibility for a g-factor measurement requires several periods of a dominant, simple (i.e. $J = 1/2$) frequency. By

using a g-factor estimate, the length of time and number of steps required to perform a robust measurement can be interrogated. After deciding on an ideal charge-state distribution and measurement time, θ- or ϕ-dependent angular correlations can be printed. By examining the angular correlations expected at certain detector positions, those having maximal anisotropy and count rates, which provide the best statistics and measure of $G_k(t)$, can be selected.

5.6.4 Free-Fitting G_k Values to Measured Angular Correlations

The G_k coefficients can be free-fitted to experimental ϕ-dependent angular correlation data using a χ^2 minimisation procedure. This is performed in a straight-forward manner by varying G_2 and G_4 values across the range $-1 \leq G_k \leq 1$ and calculating the resulting angular correlation. A χ^2 value is then obtained from comparison with the experimental data. Initially the G_k values are stepped through their ranges by $s_{\text{step}} = 0.1$ and a χ^2 curve is obtained. The step size is then reduced by $1/10^{\text{th}}$ and the procedure repeated in a narrower range around the G_k χ^2 minimum: $G_k^{\text{min}} \pm (s_{\text{step}} \times 10)$. This range narrowing is repeated until a user-defined precision is reached, where the precision level p results in a minimum step size $s_{\text{step}} = 10^{-p}$. As discussed in §2.2.1 the angular-momentum coupling for the $E2$ transitions results in sums over $k = 0, 2$, and 4. For the angular correlations observed here, G_2 and G_4 are correlated variables. This means, when fitting an angular correlation, that a decrease in one variable can be countered by an increase in the other. As a result, it is possible for the χ^2 value to minimise to unrealistic ratios between the two values. For simple atomic states, such as a pure $J = 1/2$ state, the ratio between G_2 and G_4 can be fixed, simplifying their fitting. The ratio between G_2 and G_4 can also be fixed based on the Monte-Carlo simulations, or calculations using a linear combination of individual atomic states. In the present procedure the uncertainty is handled by treating G_2 and G_4 as co-variate. When the uncertainty in G_2 is being determined, G_4 is simultaneously minimised, and vice-versa. This approach gives realistic, although possibly over-estimated uncertainties. Also, because a strict relationship between the two cannot be defined, the relative magnitude between G_2 and G_4 at their χ^2 minima may not be correct. However, the unrestrained relationship makes this approach able to distinguish, to some extent, the spin of the contributing states as G_2 and G_4 will exhibit differing frequencies for $J > 1/2$. This fitting process is also sensitive to the detector placement and reaction kinematics, as unperturbed angular correlations must be calculated quite precisely. Deviations from the expected kinematics and geometry can cause the theoretical angular correlation to poorly fit the measurement data, which should be considered. Overall, a free fit to G_2 and G_4 is useful in revealing frequency trends present in the measured data, and as will be shown in Chapter 6, it is a powerful tool for initially

interpreting experimental data, but should not be uncritically taken as giving true, absolute values.

5.6.5 Calculating and Fitting $R(t)$ Values

The anisotropy in the angular correlation depends on G_2 and G_4. Due to the complications which may arise when fitting these as free parameters, as described in §5.6.4, another measure of the change in anisotropy of the angular correlation through time is desirable. One such method is by directly determining the degree of anisotropy present at any given time point. In the ϕ-dependent angular correlation, the count rate at any given $\Delta\phi$ angle will either increase, $W^{\uparrow}$, or decrease, $W^{\downarrow}$, as anisotropy is lost from the unperturbed angular correlation at $t = 0$. For each γ-ray detector the coincident particle detectors can be categorised as $W^{\uparrow}$ or $W^{\downarrow}$. This categorisation depends on their $\Delta\phi$ value in the ϕ-dependent angular correlation.

Figure 5.6 shows the difference between several angular correlations with $G_2, G_4 < 1$ and the unperturbed angular correlation when $G_2 = G_4 = 1$. The error bars show the standard deviation across the varying values of G_2 and G_4. Figure 5.6 shows that while there are clearly defined cross-over points at which the deviation minimises, it does not fall to zero. This means that the $\Delta\phi$ range defining $W^{\uparrow}$ and $W^{\downarrow}$ is not the same for every value of G_2 and G_4. However, the small deviation at these cross-over points means that an average across the entire dataset will give the correct assignment in most cases. When designing an experiment, these cross-over points may be determined, and detector placement at these positions avoided to eliminate this issue. The plot in Fig. 5.6 gives the $\Delta\phi$ ranges defining $W^{\uparrow}$ and $W^{\downarrow}$ assignment, with regions having $\Delta W > 0$ being $W^{\uparrow}$ and $\Delta W < 0$ being $W^{\downarrow}$. **RIV Simulate** automatically generates this plot by free-fitting the G_k values and then taking the average difference between the fitted angular correlation at each time point and the unperturbed angular correlation to assign each γ-particle detector pair to the group $W^{\uparrow}$ or $W^{\downarrow}$.

With each γ-particle detector pair categorised, a geometric average of the ratio between each available pairing can be formed [129] by

$$R(t) = \left(\prod_{i=1}^{n} \frac{W_i^{\uparrow}(t)}{W_i^{\downarrow}(t)} \right)^{1/n} \tag{5.12}$$

where $R(t)$ is the geometric average ratio, n is the number of ratios, and $W(t)$ is the count rate for a given γ-particle combination at time t.

To maximise the sensitivity to the change in anisotropy, specific $W^{\uparrow}/W^{\downarrow}$ pairs should be formed. When $|dW/dt|$ is at its largest for a $W^{\uparrow}$ and $W^{\downarrow}$ ratio the sensitivity to the changing anisotropy will also be at its largest. $|dW/dt|$ is proportional to the anisotropy

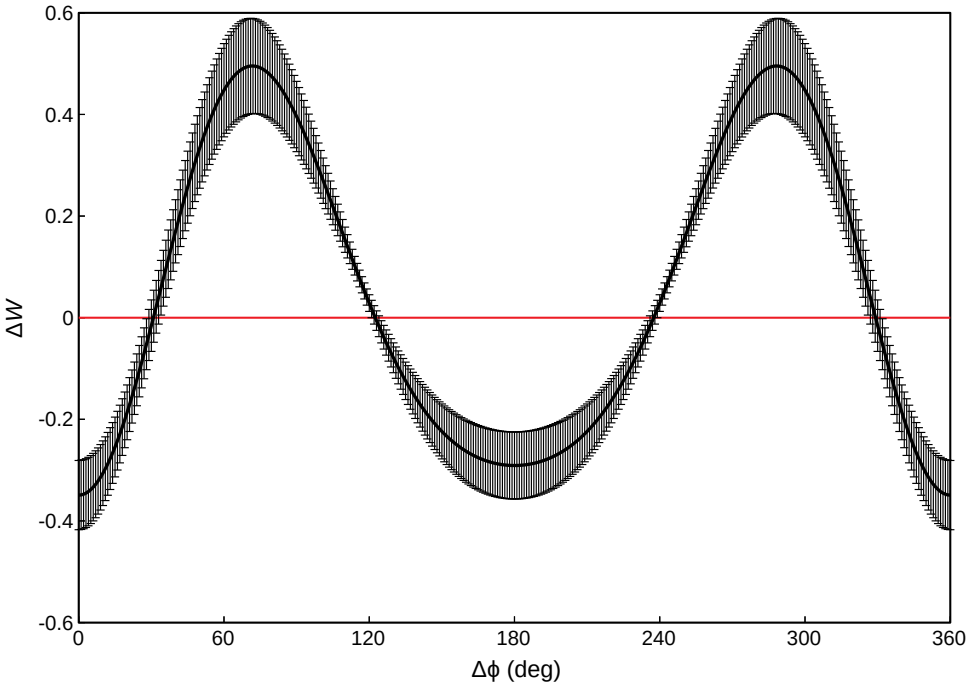

FIGURE 5.6: This plot shows the average difference, ΔW, between the theoretical unattenuated angular correlation $G_2 = G_4 = 1$ and fitted angular correlations having $G_2, G_4 < 1$ at several different time points, using the data from §6.1. The γ-particle detector pairs having $\Delta\phi$ values where $\Delta W < 0$ will be categorised as $W^{\uparrow}$, and $\Delta W > 0$ will be categorised as $W^{\downarrow}$. The magnitude of ΔW is proportional to the change in anisotropy. The error bars show the standard deviation across the average. It is worth noting that the deviation minimises at the 'cross-over' points $\Delta W = 0$, meaning that these cross-over points are consistent across the data-set.

in the unperturbed angular correlation. Therefore, γ-particle detector pairs can be ordered by increasing $|\Delta W|$ (see Fig. 5.6). The pairings are then made from the $W^{\uparrow}$ and $W^{\downarrow}$ lists. If the angular correlation is isotropic (i.e. $G_2 = G_4 = 0$), then $R(t) = 1$ for any possible pairing of data points in the angular correlation. Conversely, when the anisotropy is maximal (i.e. $G_2 = G_4 = 1$ at $t = 0$), then $R(t)$ can form the smallest possible value, being the ratio between the $W^{\uparrow}$ and $W^{\downarrow}$ data points having the largest $|\Delta W|$ values. Therefore, the first-listed pairings will have the most sensitivity to changes in anisotropy, and sensitivity will decrease down the list. To control the sensitivity, an allowed ratio range can be set. The range is normalised so that the sensitivity range, as set by the user, is between 0 and 1. The maximum sensitivity is defined by the first detector pair in the list, having the smallest *ratio* value. By increasing the lower limit on the sensitivity range the detector pairings with no sensitivity to the change in anisotropy will be removed from the $R(t)$ average, while reducing the upper limit on the sensitivity range will remove those detectors most sensitive. Higher sensitivity ranges should be examined to accentuate the desired oscillations in a given measurement, while lower sensitivity ranges may be used to verify that there is a 'null' effect.

One key advantage of this approach over fitting the ϕ-dependent angular correlation at each time point is that it is not as sensitive to the experimental geometry, reaction kinematics, or to normalisation between γ-ray detectors. However, it is also less able to distinguish contributions from atomic states with $J > 1/2$ spin, which present as complex frequency patterns in the $R(t)$ function that obfuscate the simple frequencies sought. The issue of attenuation owing to unknown factors, which can significantly confound direct angular-correlation and G_k fits, is also easily handled by introducing an offset into the $R(t)$ function when fitting to measurements. The offset allows attenuation owing to unknown, omitted, or uncontrolled sources to be compensated for, meaning that fewer atomic states can be included in a given fit. The important oscillations that will be used to determine the g factor can then be fitted more directly, with fewer parameters and less interference. By this method, frequencies can be elucidated and their time-dependence observed in a straight-forward manner which, in the right experimental conditions, can provide a robust fitting approach to determine the g factor.

5.6.6 Parameter Fitting Using the Monte-Carlo Simulation

After a Monte-Carlo simulation has been performed G_k values, angular correlations and $R(t)$ values can be calculated. In the Monte-Carlo-simulation fitting procedure there are four components that may be varied: the charge-state distribution (having a population parameter for each charge state), the atomic-state distribution (having the temperature parameter T and/or σ depending on which distribution function is chosen),

the plunger zero-time offset, and the nuclear g factor. The charge-state distribution is, ideally, an independently parameterised or measured quantity. The atomic-state distribution is presently a poorly known quantity, both in its distribution and its average energy. In Ref. [134] the experimental data were able to be fitted using a Boltzmann distribution having an average energy $T = 200$ eV, although this fit may not be unique in its ability to describe the data. The fit indicates that this shape has good potential to match the distribution of excited atomic states. Using a robust measurement on a state with a known g factor, this quantity could be more firmly understood; however for the purposes of this work it is considered a free parameter to be explored.

When fitting to angular-correlation data, any and all of the parameters discussed may be allowed to vary in the minimisation. In this multivariate space many local minima may exist. To find the deepest/true minimum a segmented 'landscape' fit is performed followed by a local minimisation. As in §5.6.4, the user specifies a precision level, p, such that there is a minimum step size $s_{\text{step}} = 10^{-p}$. Before this minimum step size is used, a landscape fit is performed which calculates χ^2 across the range $0 \leq T, \sigma \leq 1000$ eV, and a user-specified g-factor range, if these parameters are chosen to be varied. The step size across the range is $s_{T,\sigma} = 10$ eV, and is allowed to fall to $s_{T,\sigma} = 1$ eV for $p > 2$. Across the g factor range the step size is $s_{\text{g}} = 10 \times s_{\text{step}}$. If the user specifies that the charge-state distribution should be varied, this is performed in a separate routine which dynamically fits the occupation of each charge state at each landscape step. In this approach, all charge states begin as having equal population, and are co-varied, step by step, until a χ^2 minimum is found. The minimisation is iterated over, reducing the step size until $s \leq 0.001$ (0.1%). In testing, dynamically fitting the charge-state distribution in this manner fits the charge-state occupation parameters to the same values for a wide range of different starting values, showing it is a robust approach. This is fortunate, as handling a landscape fit with n^{th} dimensional parameters (n being the number of charge states), in addition to the existing landscape procedure, is incredibly computationally intensive. If the user specifies that the zero-time offset should be varied, this is also dynamically minimised as there is little risk of falling into a false minimum, and to reduce computational load. Across the landscape, χ^2 is calculated for each combination of stepped parameters chosen to be varied. After this procedure the set of values at the χ^2 minimum is selected. From these values a dynamic minimisation is performed at the smallest step size, s_{step}. If the g factor is varied, its uncertainty is obtained using the resulting χ^2 minimisation curve, allowing re-minimisation of any other variable parameters. This landscape to dynamic fit approach is intended as a compromise between falling into a false minimum and reducing computational load.

Ideally, the charge-state and atomic-state distributions can be firmly set, leaving the

g factor alone to be freely varied. However, due to the poorly understood physics governing the atomic-state distribution, it is recommended that the user, when fitting the g factor, also allows it to vary. This means the uncertainty obtained through the χ^2 minimisation curve will account for re-minimisation of the atomic-state distribution's temperature parameter. Alternatively, this parameter can be fixed at different values in order to observe its effect on the g factor. When allowing too many parameters to vary simultaneously there can be issues with over-fitting and unrealistic results. This is particularly true when allowing the charge-state distribution in a Monte-Carlo simulation to vary along with the atomic-state distribution. Recalling the discussion in §5.1.4 regarding the characteristic $G_k(t)$ behaviour of different ionic species, as the average energy of a distribution is increased the attenuation takes on a quasi-exponential character regardless of the ionic species, which can lead to false minima with unusual charge-state populations and average energies. The user is advised to carefully consider the results of fits and explore the parameters thoroughly using the χ^2 sweep calculations (to be described) before accepting a fit value.

5.6.7 Parameter Fitting Using Individual Atomic States

The procedure followed here is very similar to that described in §5.6.6, the differences being that there is no longer a temperature parameter, and the charge-state distribution is conceptually replaced with a list of atomic-state occupations. These individual-state occupations may vary in an unrestricted manner, or be grouped by their ionic species and share a specified population value. If individual states are grouped, the occupation of individual states belonging to each specified ionic species always sums to the population of the ionic species. This makes individual atomic-state occupations, the plunger zero-time offset, and the g factor, the available parameters in the fit. Because the occupation of single atomic states can be difficult to ascertain, it is recommended that this parameter be allowed to vary, and the Monte-Carlo simulation heatmap used to interrogate if these occupations are realistic. To simplify the fit, the relative populations are fixed through time. The variation of atomic-states through time is only handled in the Monte-Carlo simulation.

In comparison with the Monte-Carlo simulation, the individual-state approach has the disadvantage of not handling changing populations and frequency-amplitude attenuation through time, or phase shifts, arising from atomic decays (see §5.1.2). The advantages are that it provides much more control over, and sensitivity to which atomic-state frequencies are important in the fit, particularly over a constrained time interval. However, the effect of changing populations and phase shifts can be explored using the

routine described in the next section. Again, the user is advised to thoroughly interrogate fit results and ensure they are well-understood before accepting them.

5.6.8 χ^2 Sweep Calculations

In order to aid the user in understanding the results and consistency of certain fits, as well as the correlation between g and varied parameters, a routine exists that allows the user to sweep the g factor across a range of values at a specified precision level, while allowing the charge-state population or individual-atomic-state occupation, temperature parameter (if applicable), and the plunger zero-time offset to vary with g. If the user has specified individual atomic states, there is also the option to allow phase shifts for each individual atomic state.

This function compliments the automated parameter fits as it allows the user to interrogate how fit parameters are varying with g, how different parameters affect the χ^2 curve, and also check that no deeper minima exist in the fit region. It can also reveal whether strong correlations or unusual fluctuations exist between the g factor and other parameters. Finally, the χ^2 curves it generates are useful in verifying that correct uncertainties in fitted values and true minima have been obtained, particularly for fits using Monte-Carlo simulations, in which the random-sampling process introduces fluctuations in the fit results.

5.7 Summary

In this chapter the details of the software package **RIV Simulate** have been described. **RIV Simulate** provides a means to design RIV experiments using a number of tools, such as atomic-state heatmaps resulting from chosen atomic-state distributions, $G_k(t)$ plots for specified charge-state distributions, ϕ-dependent angular correlations for specified γ-ray-detector and particle-detector geometries, and plotting of individual-state frequencies alone or in superposition to inform the choice of appropriate plunger distances in a measurement. **RIV Simulate** is also capable of fitting parameters to data sets, specifically the charge-state distribution in a measurement, the atomic excited-state distribution of the ionic species, and most importantly, the nuclear g factor. For the nuclear g factor, statistical uncertainties can also be obtained using the χ^2 minimisation curve. Parameters can be freely varied, and sweeps across g-factor ranges can be performed to investigate correlations between parameters. With the specifics of how **RIV Simulate** works now described, its application to experimental data analysis will be presented in the next chapter.

Chapter 6

Recoil-In-Vacuum Measurements

In this section, the experimental details of time-differential (TD) and time-integral (TI) recoil-in-vacuum (RIV) measurements are reported, along with the analysis of data obtained from these experiments using the **RIV Simulate** computer code described in Chapter 5. A description of the RIV technique can be found in §2.3.3. The coordinate frame defining the particle- and γ-ray-detector angles in these measurements has its origin at the beam spot on the target. The beam direction defines the z or polar axis ($\theta = 0$). These experiments aim to measure ϕ-dependent angular correlations, where $\phi = 0$ is defined as the γ-ray and particle detector having the same azimuthal angle. Each γ-ray detector measures a ϕ angular correlation in coincidence with a radially symmetric particle-detector array positioned parallel to the xy plane and down-beam of the target, which provides the ϕ-dependence. Please refer to Fig. 2.5 for a visual representation of these polar angles. In the time-dependent variation, a plunger device is used to adjust the position of a stopping foil, which serves to quench the hyperfine interaction at the moment of impact. The analysis of the TDRIV data allowed for several dominant hyperfine interactions to be identified in an *ab initio* fashion, while the TIRIV data reveals that there are components of the hyperfine interaction that require further research to understand.

All of these experiments were performed prior to the commencement of this project. The ^{56}Fe 2_1^+-state TDRIV data were collected at IPN, Orsay, with the provided angular correlation data and nuclear lifetime already extracted from the spectroscopic data. For the other measurements, the collected spectroscopic data was analysed and interpreted by the author.

6.1 ^{56}Fe Time-Dependent Recoil-In-Vacuum Measurement

The aim of this experiment was to measure the time-dependent vacuum deorientation of the ^{56}Fe 2_1^+ state using the recoil-in-vacuum technique and determine the g factor from the $G_k(t)$ trend (see §2.3.3). By optimising the charge-state distribution (CSD) to predominantly produce Na-like ions, the data were intended to allow the determination of the nuclear g factor of the ^{56}Fe 2_1^+ state using the hyperfine interaction with the Na-like atomic $J = 1/2$ ground state. The experiment was therefore designed to maximise the fraction of Na-like ions in the CSD, whilst also Coulomb-exciting the ^{56}Fe nucleus to the 2_1^+ state. CSD measurements were also performed, and an empirical parameterisation of the CSD of iron ions recoiling out of nickel was determined. The ^{56}Fe 2_1^+-state lifetime was also extracted from the TDRIV data and provided. In the present work, this value was averaged with measurements available in the literature to provide a high-precision value. The TDRIV data provide the opportunity to test an *ab initio* model that seeks to calculate the hyperfine-interaction strength in free ions, based on atomic-structure theory. Analysis of the TDRIV data using this model will be presented in the next section, §6.1. Validation of the model will serve to improve precision for future g-factor measurements using this technique.

6.1.1 Methods

The experiment was conducted at the Accelerateur Linéaire et Tandem á Orsay facility at the Institut de Physique Nucléaire, Orsay, in 2014 by Prof. Andrew Stuchbery (The Australian National University, Australia), Dr. Alain Goasduff and Prof. Georgi Georgiev (Centre de Sciences Nucléaire et de Sciences de la Matiére (CSNSM), Orsay, France), and Dr. Asli Kusoglu (CSNSM, Orsay, France and Instanbul University, Turkey), assisted by staff and students J. Ljungvall, I. Matea, T. Konstatinopoulos, K. Gladnishki, A. Gottardo and D. Yordanov. A 130 MeV ^{56}Fe beam was incident upon a target having 0.30 mg/cm^2 of carbon painted onto a 0.67 mg/cm^2 nickel foil. Beam particles were excited on the carbon layer and recoiled out of the nickel. Down-beam of the target was an eight-fold segmented plastic annular particle detector. This detected recoiling carbon ions at forward angles. The inner-radius of the detector segments was 39 mm, outer-radius was 47 mm, and each segment subtended a ϕ angle of 30°. The particle detector was located 70 mm down-beam of the target. Recoiling beam particles were stopped in a 5.8 mg/cm^2 nickel foil (the stopping foil). The Orsay Universal Plunger System (OUPS) plunger device [141] was used to measure the time dependence of the hyperfine interactions. OUPS uses an electronically controlled stage capable of maintaining a consistent distance between the target and stopping foils. OUPS is capable of adjusting the stopping-foil position along the beam axis in order to perform a time-dependent

measurement. Consistent inter-foil distances were maintained using a feedback mechanism that continuously read the capacitance beween foils to determine the inter-foil distance and adjusted the stage position accordingly. Coincident γ rays were detected at forward angles by the ORGAM [85] γ-ray-detector array, and at backward angles by the MINIBALL [229] γ-ray-detector array.

The CSDs of ^{56}Fe ions traversing nickel foils at various energies were measured at ANU's heavy-ion accelerator facility by Prof. Andrew Stuchbery and Dr. Matthew Reed. Beams of ^{56}Fe at energies of 40, 50, 55, 60, 70, 80 and 100 MeV were delivered by the 14 UD Pelletron accelerator onto a $\sim$0.1 mg/cm^2 nickel target. Energy loss through the target was calculated to be $\sim$ 2 MeV for all beam energies using Zeigler's stopping powers [232]. The accelerator switching magnet (normally used to select a beam line), was used to bend individual charge states into a suppressed Faraday cup and measure the beam current for each charge state, hence determining the CSD. Similar measurements were also performed using a self-supporting 0.5 mg/cm^2 carbon target.

6.1.2 Results

The raw data obtained in this experiment were analysed, and angular correlation data provided, by Dr. Asli Kusoglu (CSNSM, CNRS/IN2P3, Université Paris-Sud, and Department of Physics, Faculty of Science, Istanbul University) and Dr. Alain Goasduff (CSNSM, CNRS/IN2P3, Université Paris-Sud). Due to the fragmented statistics from, and poorly defined geometry of, the MINIBALL array, those data were excluded from the analysis. Angular correlations measured by the ORGAM array can be found in Appendix B.1. Figure 6.1 shows a sum γ-ray spectrum of γ-particle coincidences, showing that the measurement is clean of interfering γ rays and that the Doppler shift is sufficiently large for separation of the in-flight and stop peaks.

The charge-state distribution (CSD) data were provided by Prof. Andrew Stuchbery. The CSDs at each beam energy were fitted using a skew-normal distribution [46], which was found to be an ideal shape in Ref. [134]. It is also the expected form, as the well-known CSD parameterisations of Nikolaev and Dmitriev [155], and Schiweitz and Grande [187] both use normal distributions to fit the data, and skew is expected to be introduced for CSDs near to atomic shell closures (Ne-like ions in the present case). The skew-normal distribution is calculated by [46]:

$$P(x) \propto \phi(x)\Phi(\alpha x), \tag{6.1}$$

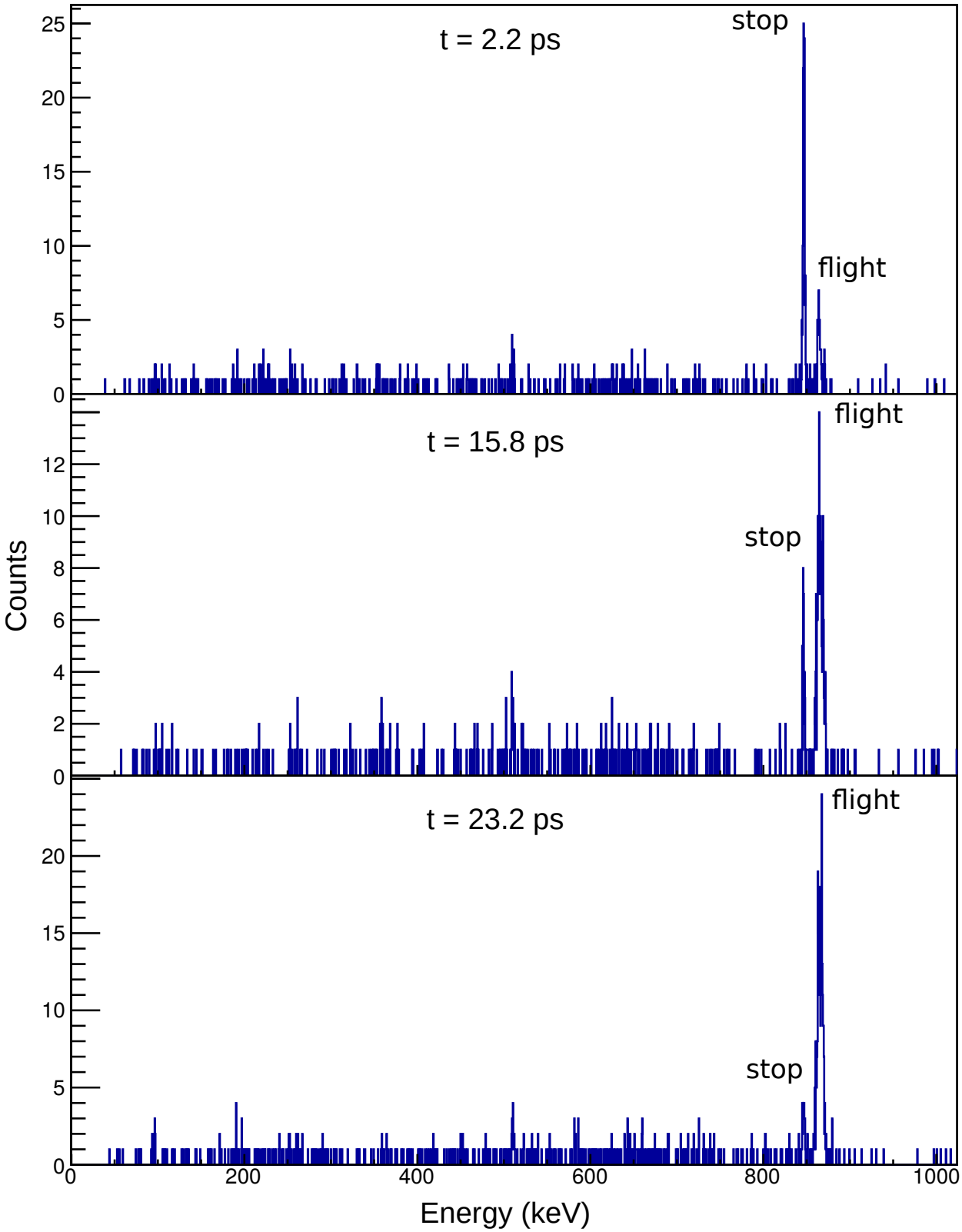

FIGURE 6.1: TDRIV ^{56}Fe γ-ray spectrum from a single ORGAM detector in coincidence with events from a single particle detector at three distinct flight times. These spectra show the peaks are well-separated, and that there is neither background nor Doppler tail under the ^{56}Fe 2_1^+ stop peak.

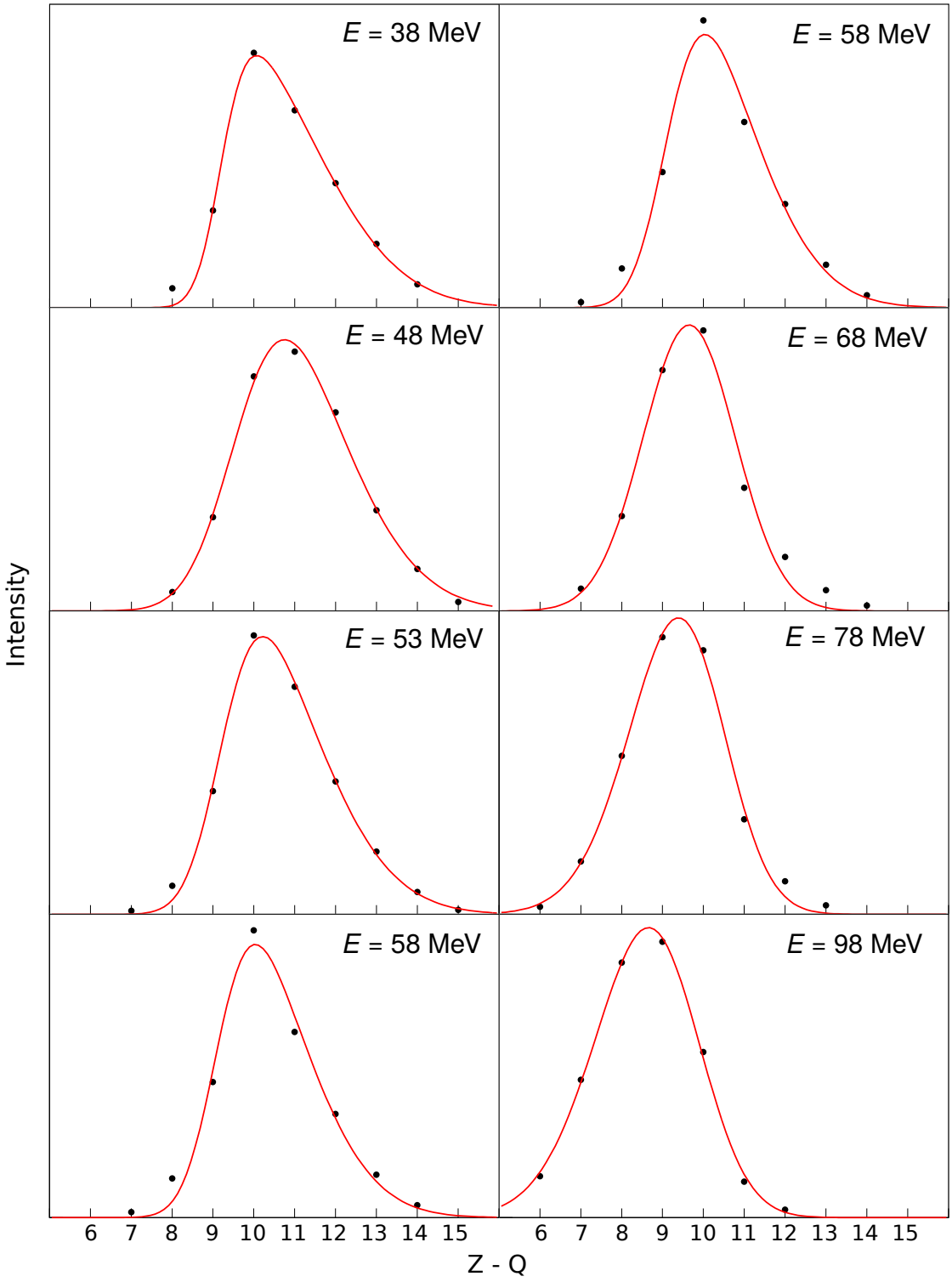

FIGURE 6.2: Measured CSDs of ^{56}Fe ions emerging from a nickel foil at various energies, fitted using skew-normal distributions. Note that $E = 58$ MeV has been duplicated for comparison.

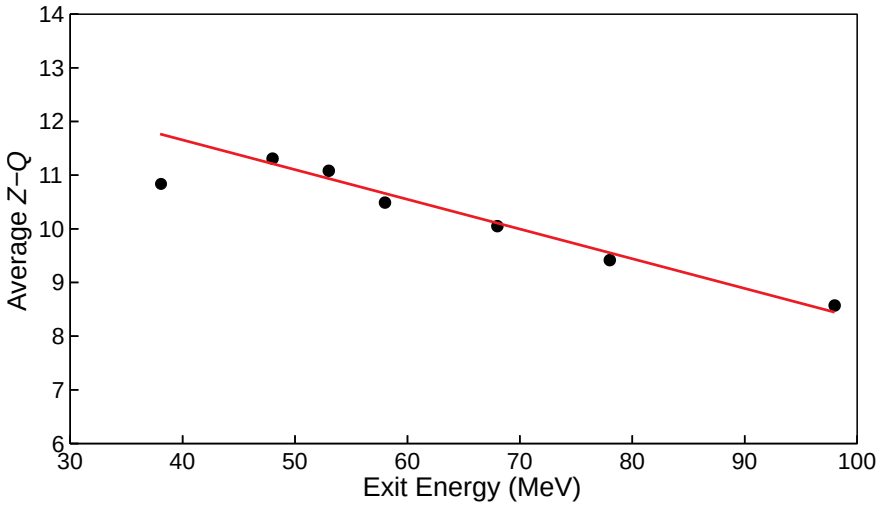

FIGURE 6.3: The empirical average $Z - Q$ values, $\overline{m}$, of the measured CSDs versus the energy of the ions as they exit the foil. There is a strong linear relationship between $\overline{m}$ and the exit energy. The $E = 38$ MeV point was excluded from the fit because it is an outlier and outside of the range of interest (see text).

where

$$\phi(x) = \frac{1}{\sqrt{2\pi}} e^{-x^2/2}, \tag{6.2}$$

and

$$\Phi(x) = \int_{-\infty}^{x} \phi(t)dt = \frac{1}{2}[1 + \text{erf}(x/\sqrt{2\pi})], \tag{6.3}$$

where $\text{erf}(x)$ is the Gaussian error function of Eq. (6.2). Note that, because $\text{erf}(x)$ cannot be evaluated analytically, numerical approaches supplied by the GNU Scientific Library [143] and CERN's ROOT [41] have been used.

Because CSD data are not normally distributed around zero, the variable x is substituted by $x \to (x - \xi)/\omega$, changing Eq. (6.1) to

$$P(x) = \frac{2}{\omega}\phi(\frac{x-\xi}{\omega})\Phi(\alpha\frac{x-\xi}{\omega}). \tag{6.4}$$

Note that the variables ξ and ω are analogous, but not directly equivalent, to μ (the mean) and σ (the variance) in the normal-distribution function.

The skew-normal distribution was fitted to the CSDs using ROOT's fitting function [41], varying ξ, ω, α, and a scaling parameter, a. The resulting fits are shown in Fig. 6.2, and the parameters obtained from these fits (excluding a) are listed in Table 6.1. The empirical mean $Z - Q$ values, $\overline{m}$, were calculated for each foil exit energy from the measured CSDs, and are also listed in Table 6.1. These were plotted against the foil exit energy, shown in Fig. 6.3, and were consistent with a linear trend across this energy

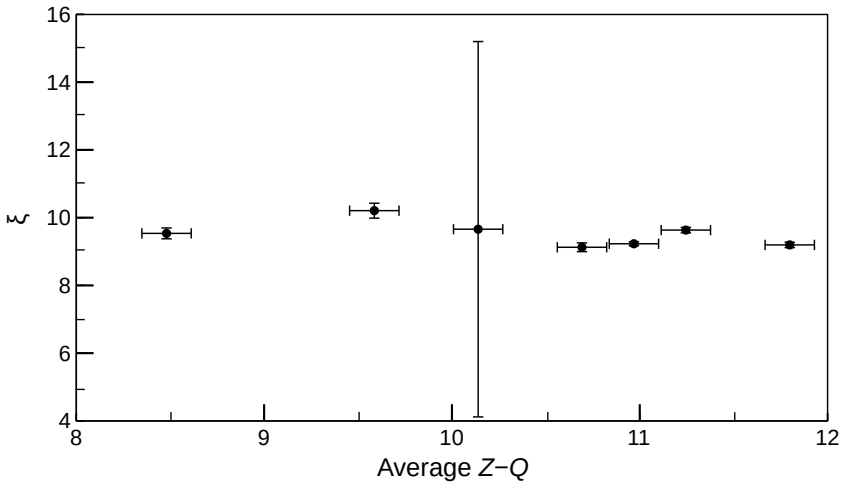

FIGURE 6.4: The fit parameter ξ versus $\overline{m}(E)$. There is no apparent relationship between ξ and $\overline{m}(E)$ across this energy range, with ξ having an average value $\xi = 9.347$. The large uncertainty in the $Z - Q \simeq 10$ data point may be due to the distribution becoming very close to a normal distribution at this energy.

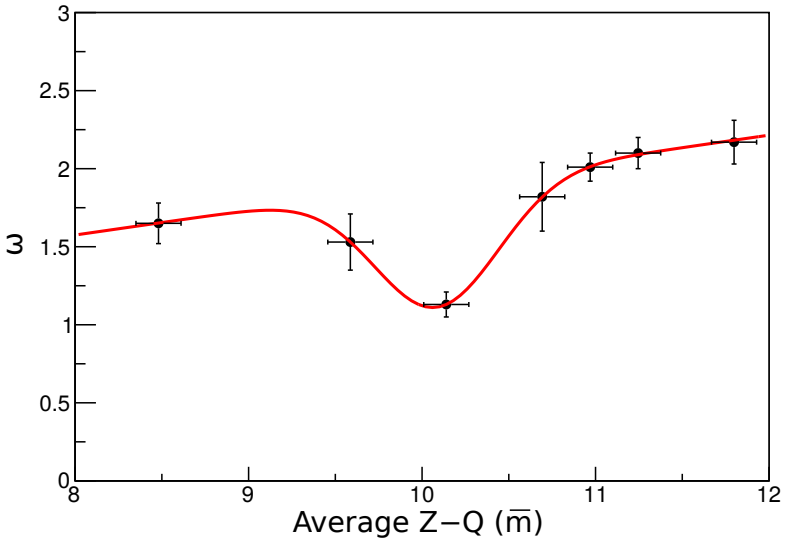

FIGURE 6.5: The fit parameter ω versus $\overline{m}(E)$. The relationship appears to be linear across the range, with an inverted Gaussian allowing for the narrowing of the distribution, and the consequent dip in the ω vs $\overline{m}$ trend, when centred over Ne-like ions ($\overline{m} = 10$).

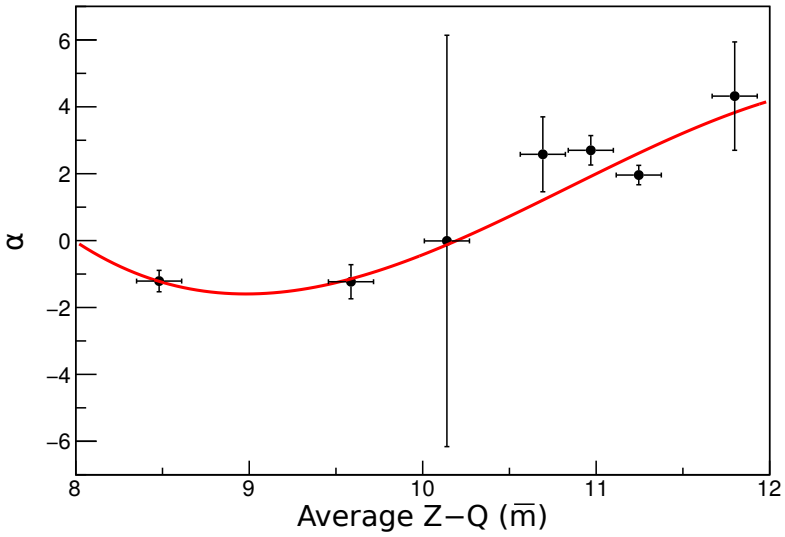

FIGURE 6.6: The fit parameter α versus $\overline{m}(E)$. The fit shows an asymmetric relationship around $\overline{m} = 10$. Hence, a 3$^{\text{rd}}$-degree polynomial function was used to fit the trend. The large uncertainty in the $Z - Q \simeq 10$ data point may be due to the distribution becoming very close to a normal distribution at this energy.

TABLE 6.1: Values obtained from fitting the skew-normal-distribution parameters (ξ, ω and α) to the charge-state measurements shown in Fig. 6.2, as well as the empirical mean at each energy ($\overline{m}$). The large uncertainties in the fitted values of ξ and α for $E = 68$ MeV is likely due to the distribution at this energy nearing $Z - Q = 10$ and becoming closer to a normal distribution, allowing the two correlated parameters to fit a wider range, and consequently inflating their uncertainty.

Exit Energy (MeV)	ξ	ω	α	$\overline{m}$
38	9.19(8)	2.17(14)	4.32(162)	10.76(13)
48	9.63(8)	2.10(10)	1.96(29)	11.31(13)
53	9.23(6)	2.01(9)	2.70(44)	11.08(13)
58	9.12(13)	1.82(22)	2.58(112)	10.49(13)
68	9.66(554)	1.13(8)	-0.01(615)	10.05(13)
78	10.21(22)	1.53(18)	-1.23(51)	9.42(13)
98	9.53(16)	1.65(13)	-1.21(32)	8.57(13)

range, with the exception of the $E = 38$ MeV point. Recoiling ^{56}Fe ions are expected to have energy in the range $49 \lesssim E \lesssim 55$ MeV. Due to the $E = 38$ MeV point being an outlier, and outside of this range, it was excluded. The fit gives the formula:

$$\overline{m}(E) = 13.869 - 0.0553E. \tag{6.5}$$

Using Eq. (6.5), the mean $Z - Q$ as a function of energy, $\overline{m}(E)$, was then calculated for each foil exit energy, and used to identify trends with the skew-normal-distribution parameters. An uncertainty determined from the average deviation of the empirical $Z - Q$ values from the calculated values, being ± 0.13, was assigned. Fitted values of ξ, ω and α were then plotted against $\overline{m}(E)$, shown in Fig. 6.4, Fig. 6.5, and Fig. 6.6, respectively. The plot of ξ versus $\overline{m}(E)$ shows no apparent correlation, and that these values are consistent across the energy range. As such, a weighted-average value $\xi = 9.347$ was adopted. The plot of ω versus $\overline{m}(E)$ in Fig. 6.5 was best fit using an inverted Gaussian added to a linear function. Across the range, ω appears to increase with $\overline{m}(E)$, but drops around $\overline{m}(E) = 10$. This seems sensible, because ω represents the width of the skew-normal distribution. This result indicates that the width narrows as more electrons are stripped, and electrons become more tightly bound, but also that there is additional binding at $Z - Q = 10$, the neon shell-closure. This fit gives the formula:

$$\omega(\overline{m}) = 0.160\overline{m} + 0.296 - 0.796e^{-(\overline{m} - 10.086/0.504)^2}. \tag{6.6}$$

The plot of α versus $\overline{m}(E)$ in Fig. 6.6 was fit to a 3$^{\text{rd}}$-degree polynomial. This function was chosen to capture the changing skew across the present range as $\overline{m}(E)$ passes from the regions away from the shell-closure (where the CSD is expected to follow a normal distribution, i.e. $\alpha = 0$), through the shell-closure, where $\alpha \sim 0$ is also expected. This fit gives the formula:

$$\alpha(\overline{m}) = -0.248\overline{m}^3 + 8.062\overline{m}^2 - 84.810\overline{m} + 289.447. \tag{6.7}$$

Kinematics calculations [144] indicate that the energy of excited ^{56}Fe ions resulting from recoiling carbon ions impacting across the angle subtended by the particle detector is 49.6–55.6 MeV. By using Eq. (6.5), Eq. (6.6), Eq. (6.7), and the average value $\xi = 9.347$ to calculate the skew-normal CSD across the detector face, weighting appropriately for excitation-probability, solid-angle and scattering intensity, the CSD listed in Table 6.2 and shown in Fig. 6.7 is obtained. The single-energy CSDs listed in Table 6.2 show that there is little variation in the CSD expected across the detector face due to the narrow energy range. With the CSD empirically determined, the analysis of the angular-correlation

TABLE 6.2: Expected CSD for ^{56}Fe ions in the Orsay TDRIV experiment, integrated over the annular-style detector's angular opening, recoiling with average velocity $\beta = 0.04463$ and covering the range $49.6 \leq E \leq 54.6$ MeV, using Eqs. (6.4–6.7) and $\xi = 9.347$. The expected CSD was calculated using RIV Simulate's target energy-loss routine. For reference, the CSD at the lower energy limit $E \sim 49$ MeV and the upper energy limit $E \sim 55$ MeV are also shown.

$Z - Q$	Ionic Species	$P(49.6 \leq E \leq 54.6$ MeV)	$P(E = 49$ MeV)	$P(E = 55$ MeV)
8	O-like	2.8%	2.0%	4.7%
9	F-like	14.1%	13.2%	15.9%
10	Ne-like	27.7%	28.2%	27.0%
11	Na-like	26.8%	27.2%	25.8%
12	Mg-like	16.7%	16.9%	15.8%
13	Al-like	7.8%	8.1%	6.9%
14	Si-like	2.9%	3.1%	2.3%

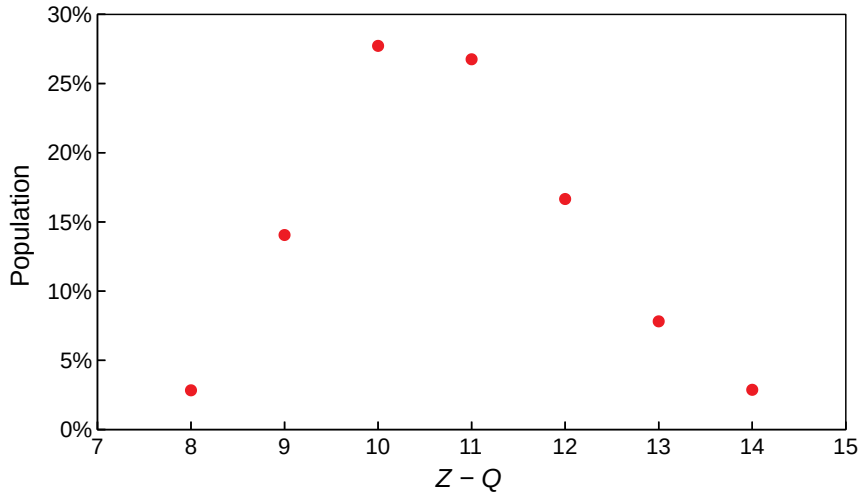

FIGURE 6.7: Expected CSD for ^{56}Fe ions in the Orsay TDRIV experiment, integrated over the annular-style detector's angular opening and recoiling with average velocity $\beta = 0.04463$, using Eqs. (6.4–6.7) and $\xi = 9.347$.

data may proceed with more confidence.

The ^{56}Fe 2_1^+ state's lifetime was measured from the observed Doppler shift between the stop and flight peaks across the γ-ray detector array. This analysis was performed by the original experimenters, and not in this project. They reported $\tau(2_1^+;^{56}\text{Fe}) = 8.43(50)$ ps. Using this value, and all the available values in the literature, a re-evaluation was performed to determine a new, precise value. The average was obtained using AveTools [123], a code developed to determine averages with uncertainties using the "Limitation of Relative Statistical Weight", "Normalised Residual Method" and "Rajeval Technique" statistical approaches [177]. Lifetimes from Refs. [2, 7, 12, 18, 20, 27, 45, 53, 62, 67, 99, 107, 122, 126, 132, 135, 138, 150, 156, 170, 173, 197, 225]

were used with AveTools. The data points from Refs. [12, 20, 138] (1960An07, 1962Be18, 1972Li28) were identified in the averaging procedure as severe outliers, and as such were excluded. With these removed, the remaining data points showed good consistency, obtaining $\tau(2_1^+;^{56}\mathrm{Fe}) = 9.27(13)$ ps with $\chi^2_\nu = 1.07$ in all three averaging methods. Figure 6.8 shows a visual representation of the fit result. This value was used for the ^{56}Fe 2_1^+ lifetime in calculations performed in the following section.

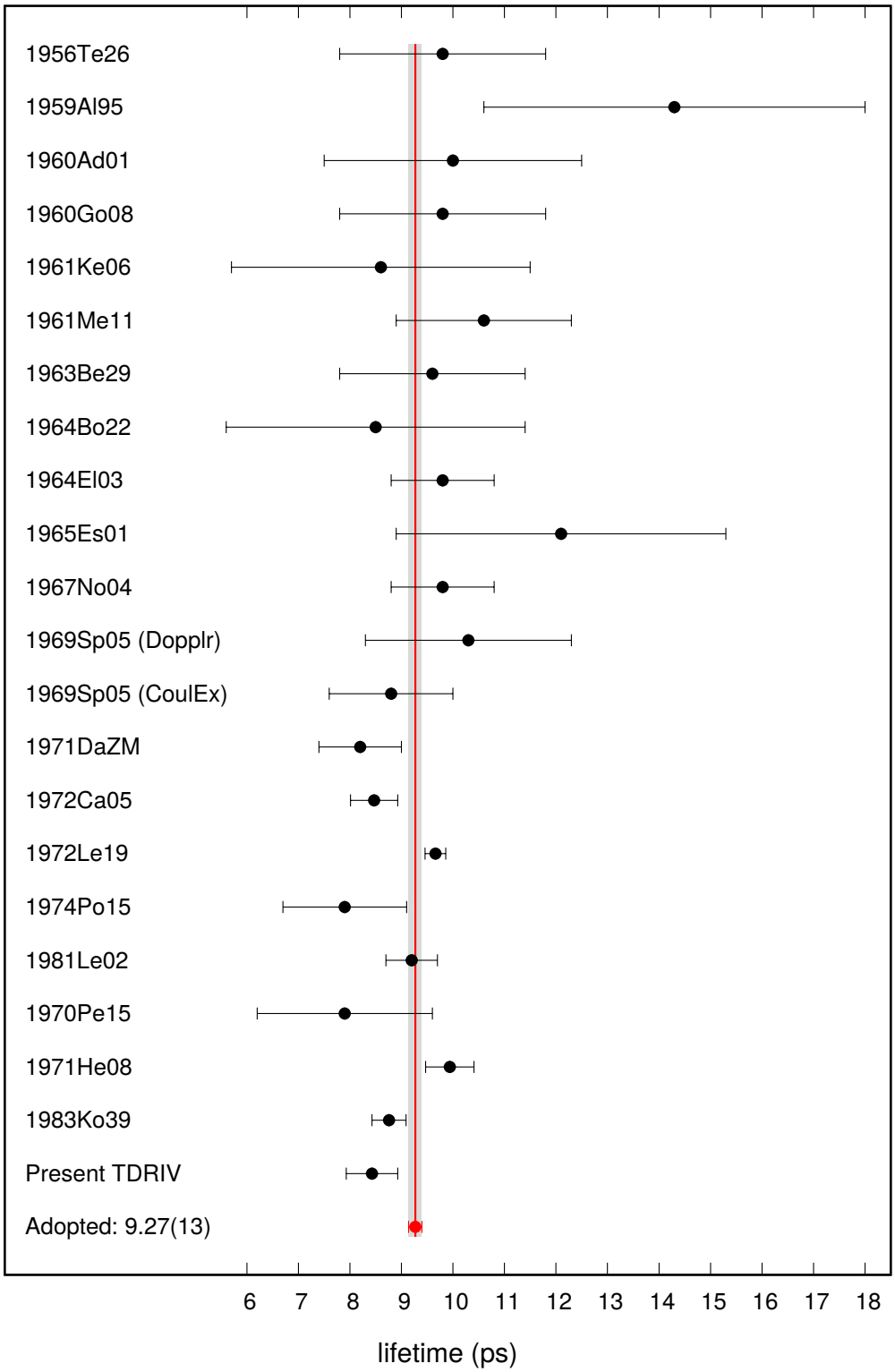

FIGURE 6.8: Lifetime measurements of the ^{56}Fe 2_1^+ state available in the literature, along with that obtained in the ^{56}Fe TDRIV measurement. AveTools [123] was used to obtain the average with uncertainty. Nuclear Science References codes have been used here, and bibliographic references can be found in-text.

6.2 ^{56}Fe Time-Differential Recoil-In-Vacuum Analysis

The ^{56}Fe 2_1^+-state TDRIV data provided from the experiment at the ALTO facility at the IPN, Orsay, were analysed using **RIV Simulate**, both with the intention of determining a $g(2_1^+)$ value, as well as a demonstration of the capabilities of the **RIV Simulate** computer program. A conference proceeding describing a preliminary analysis has been published by the author and collaborators [146]. A more thorough analysis is presented here, specifically of the data collected using the ORGAM γ-ray-detector array. These data were chosen due to the array having all detectors at equivalent angles $\theta = 46.5^\circ$ with well-defined geometry, which allows for ϕ-dependent angular correlations to be easily visualised and robustly fitted. Additionally, these detector crystals were large enough to record sufficient statistics at each time-point. In contrast, the MINIBALL detector-array crystals had poorly defined geometry and variable θ angles, with low count rates in each crystal segment. As such, they were excluded. Through the analysis of the ORGAM data, using the RIV Simulate toolkit, the hyperfine interaction was interrogated, and a $g(2_1^+)$ value for ^{56}Fe was determined. It should be noted that in the following section the data from the stopped component of the measured γ-ray peaks was the primary focus of the analysis, as it is most sensitive to the oscillations used to determine the g factor. Hence, where G_k values are referred to in the following section, they should be assumed to be the G_k^{stop} component, unless otherwise specified.

It will be shown that the ground and first-excited atomic states in the F-like and Na-like species were able to almost completely explain the observed oscillations in the $G_k(t)$ trend (§6.2.4 below). By fitting the $R(t)$ function of the angular-correlation data, consistent g-factor values were obtained using both individual-state and Monte-Carlo-simulation fits (§6.2.7 below). Modelling of the in-flight component of the data revealed the presence of a strong hyperfine-interaction component resembling the F-like ground state (§6.2.9 below). Modelling of the hyperfine interaction present in the stop-component of the TDRIV data, using individual atomic states and the Monte-Carlo simulation, was able to determine $g = +0.546(19)$.

6.2.1 Target Energy Loss and Kinematics

In the experiment, ^{56}Fe nuclei were accelerated to 130 MeV and impinged upon a reaction foil comprised of a 0.30 mg/cm^2 carbon layer as the target, backed by 0.67 mg/cm^2 of nickel. For this target composition, the target energy-loss routine (described in §5.6.1) indicates that the average recoil velocity of ions detected by the plastic ring-style detector agrees with the value of $\beta = 0.04463(12)$ obtained from the Doppler shift of the flight

energy peak. The target energy-loss routine was used to calculate the charge-state distribution (CSD) shown in Table 6.2 using the empirical parameterisation proposed in §6.1.2. The target and particle-detector details were used in the experimental setup routine to calculate the statistical tensors defining the spin-alignment of recoiling ^{56}Fe 2_1^+-state ions coincident with the detected forward-scattered carbon ions. With these target and geometry details confirmed, angular correlations can be reliably calculated so as to identify perturbations owing to the hyperfine interaction.

6.2.2 Free-Fitted $G_k(t)$ Values

The first step taken in the data analysis was to free-fit G_k values to the data set using RIV Simulate's G_k free-fitting routine (see §5.6.4 for more details). The resulting free-fitted $G_k(t)$ values are shown in Fig. 6.9. It should be noted that with free minimisation of the G_k values, $\chi^2_\nu = 1.296$ was obtained across the entire dataset, which is notably larger than unity. Figure 6.10 shows a comparison of angular-correlation fits at two time points from the free-fitted G_k values, one having $\chi^2_\nu = 0.918$ (lower end of the χ^2 range) and the other having $\chi^2_\nu = 1.902$ (upper end of the χ^2 range). There is a significant amount of scatter present in the poorer fit. The source of this issue is unknown, but may be due to some systematic error (e.g. the beam being off-centre or bad normalisation between detectors), that there were issues with the γ-ray or particle detectors during the particular run (e.g. unstable voltage supply), or that there were issues extracting clean photopeak counts in the analysis (e.g. bad peak-to-background ratios in the γ-particle coincidence pair), which can cause irregular behaviour in some of

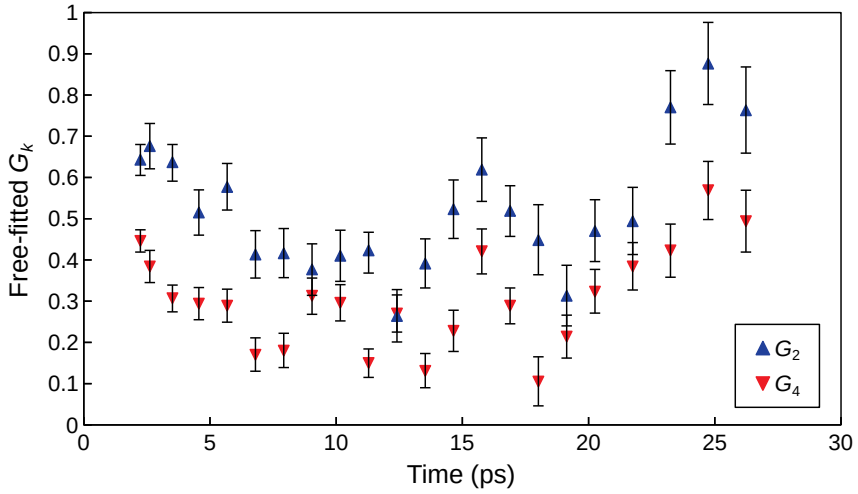

FIGURE 6.9: Time-differential ^{56}Fe G_k values obtained by free-fitting G_2 and G_4 to the measured angular correlations (see Appendix B.1) as described in §5.6.4. For this fit $\chi^2_\nu = 1.296$. The interaction appears rather complex, however there is clear structure with which the dominant hyperfine interactions can be identified, as described in §6.2.2.

the angular-correlation data points. Regardless, these issues, while worsening the $G_k(t)$ fits, should have little effect on the overall analysis due to the larger number of γ-ray and particle detector pairings contributing to each angular-correlation measurement.

Inspection of the free-fitted $G_k(t)$ data points in Fig. 6.9 shows that the early time-points (< 10 ps) appear to have some structure, but are dominated by a rapid decline. This most likely indicates one of two things: that many rapid atomic transitions are occurring, giving the quasi-exponential shape as described in §5.1.2, or that a single, dominant hyperfine field is responsible. In the former case, a reduced maximum anisotropy will be fixed here, but, in the latter case, anisotropy may be restored at a future time. Beyond $t \sim 5$ ps the G_2 and G_4 values follow differing frequencies, converging with $G_2 \simeq G_4 << 1$ near 10 and 12 ps, behaviour necessitating a $J > 1/2$ atomic state. From 12–19 ps there appears to be a single period of a strong oscillation in both G_2 and G_4, more indicative of a $J = 1/2$ state. A significant degree of anisotropy is then restored at around 23 ps, suggesting that the rapid decline near $t = 0$ is largely due to a dominantly populated atomic state. These are clear structural markers that can be used to identify which hyperfine interactions are contributing most strongly. They therefore determine which atomic states should be used to describe the $G_k(t)$ trend, and hence determine the g factor.

6.2.3 Monte-Carlo Simulations

To fit the g factor, it is important to understand which atomic states contribute most strongly to the overall hyperfine interaction, and give rise to features that can be identified. To interrogate which states will most likely contribute, Monte-Carlo simulations were performed with the ionic species corresponding to the charge states indicated in Table 6.2 to explore how the population of atomic states for each ionic species varies through time. These were performed without the $2J + 1$ weighting suggested by Stone *et al.* [202], as preliminary fitting attempts revealed that it dramatically worsened the fit. The $2J + 1$ weighting worsened the fit by causing the high-spin states to effectively increase in occupation, causing a relative reduction in the occupation of the low-spin, low-energy states that contribute most strongly to the hyperfine interaction. The Monte-Carlo simulations helped to understand which atomic states will be dominantly occupied, and therefore which frequencies should be observed in the measurement. The simulations were performed having the initial excited atomic states for each ionic species follow a Boltzmann distribution with average energy $T = 200$ eV. This value was chosen as it should give a wide occupation of low-energy atomic states expected in the system after recoil. However, its value does not critically affect the following discussion.

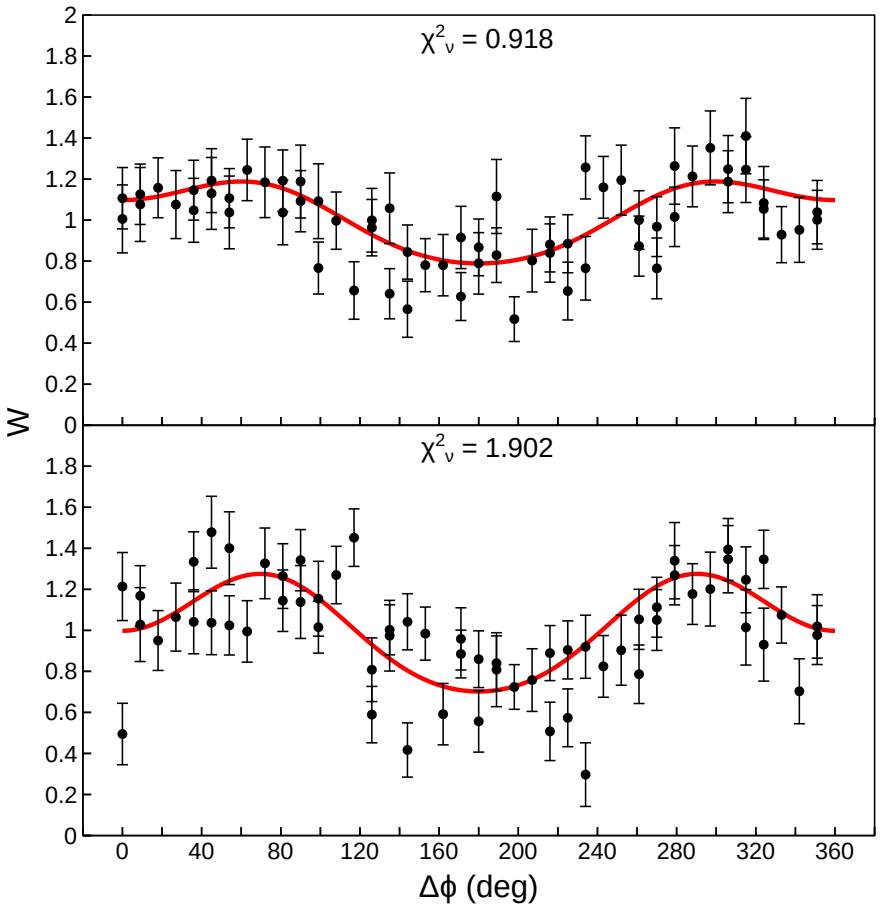

FIGURE 6.10: Two example angular correlations from the obtained free-fitted G_k values at $t = 14.6$ ps and $t = 15.8$ ps. The upper panel shows a good fit, with $\chi^2_\nu \simeq 1$, while the lower panel shows a poor fit, with $\chi^2_\nu \simeq 2$. The poorer fit has appreciably more scatter in the data points, as well several low-count outliers.

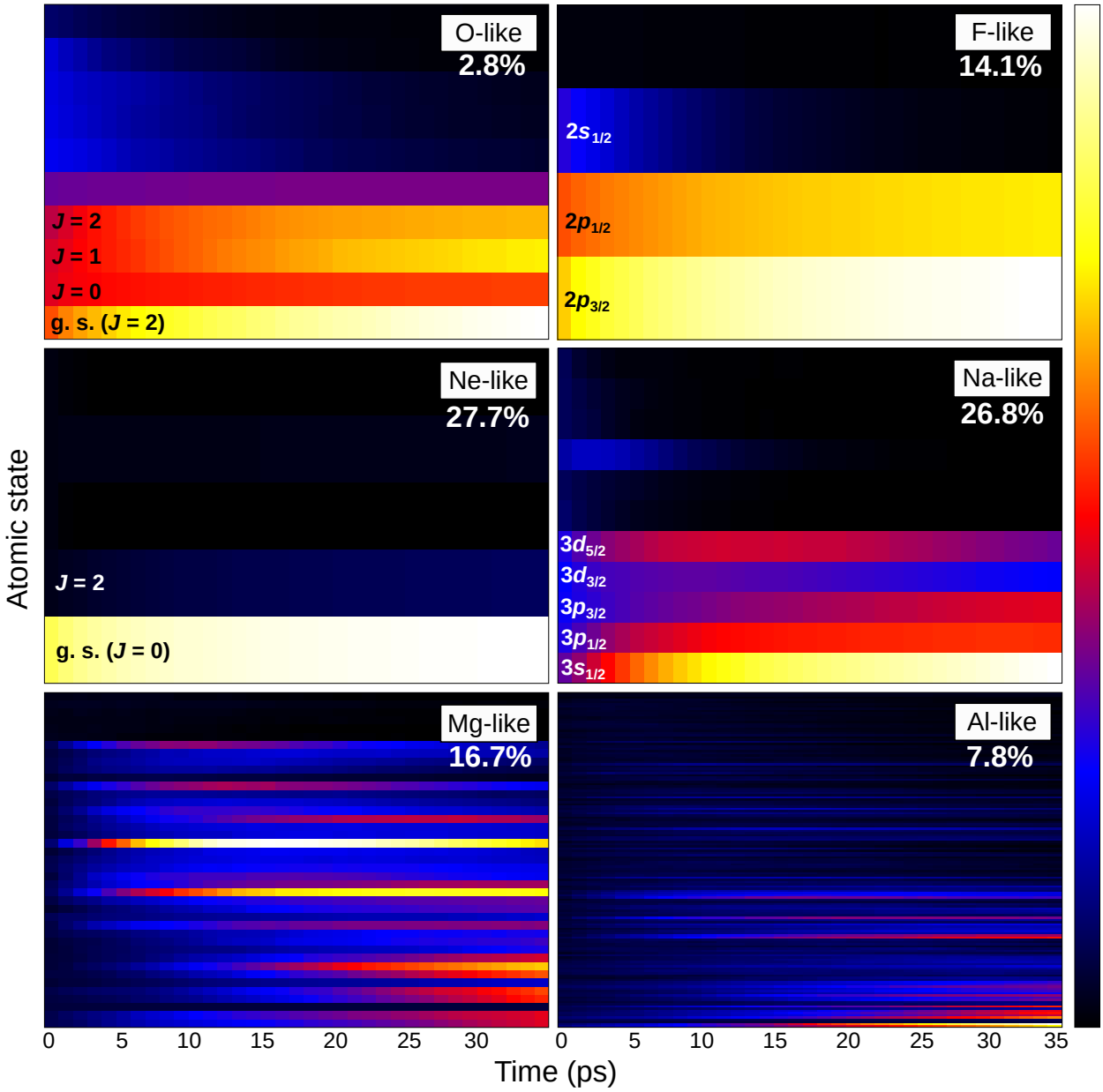

FIGURE 6.11: ^{56}Fe atomic-state heatmaps obtained from Monte-Carlo simulations of the CSDs listed in Table 6.2. Each row is a different atomic state, starting with the ground state and ascending in order of energy. Important states have been labelled for reference in-text. The initial population of excited atomic states follows a Boltzmann distribution having average energy $T = 200$ eV, **without** a $2J + 1$ weight. Additional higher-energy excited states were populated than are shown in these heatmaps, but rapidly decay into the shown states. (When viewing a copy of this thesis, note that rows should be clearly separated. Some PDF viewers will smear the colour gradient together. Try using a different PDF viewer if this is the case.)

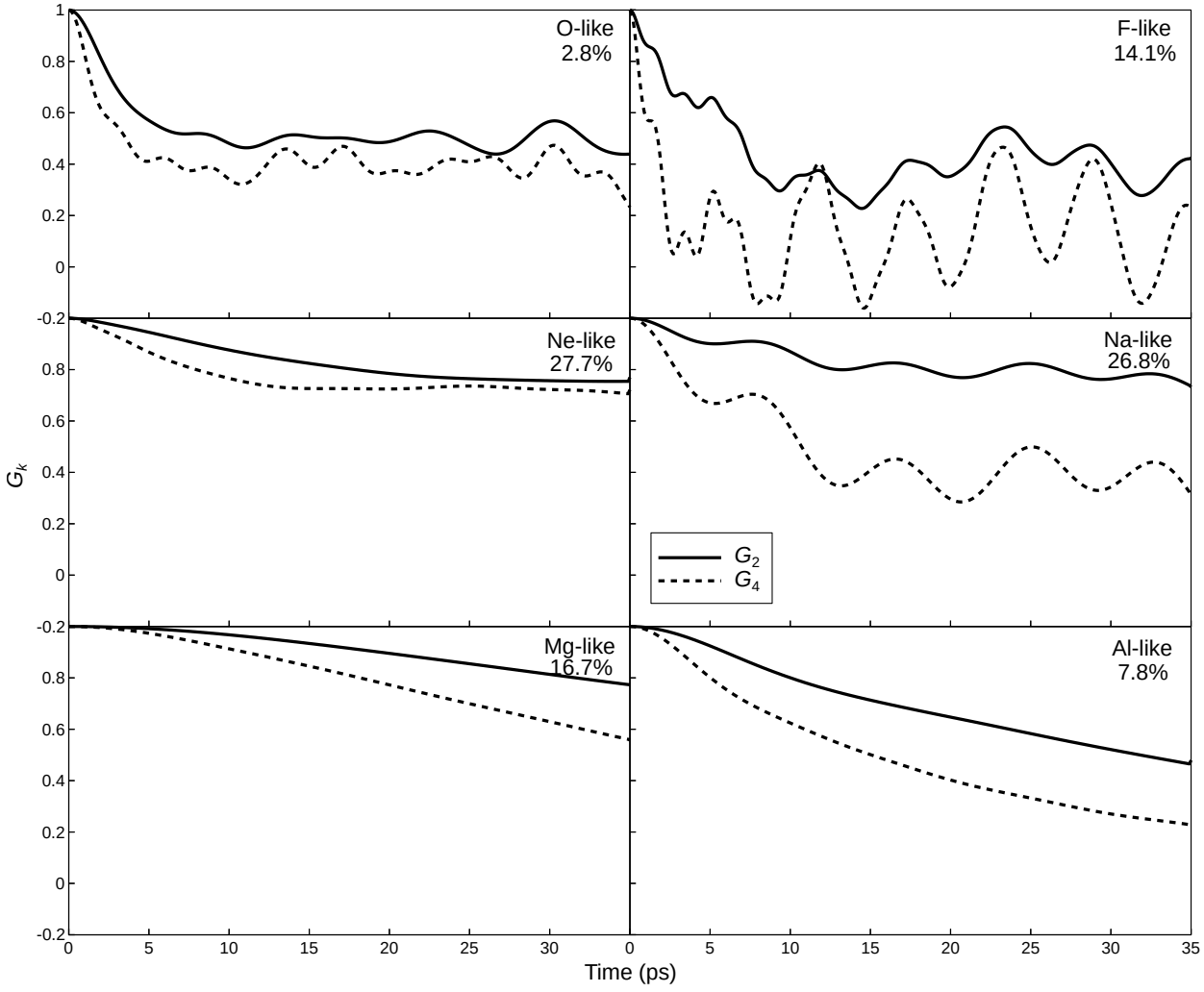

FIGURE 6.12: ^{56}Fe $G_k(t)$ plots resulting from Monte-Carlo simulations of the six CSDs shown in Fig. 6.11. These have been calculated with initial excited atomic states following a Boltzmann distribution with average energy $T = 200$ eV. $G_k(t)$ were evaluated having $g(2_1^+; \mathrm{Fe}^{56}) = +0.51$, as previously reported [56].

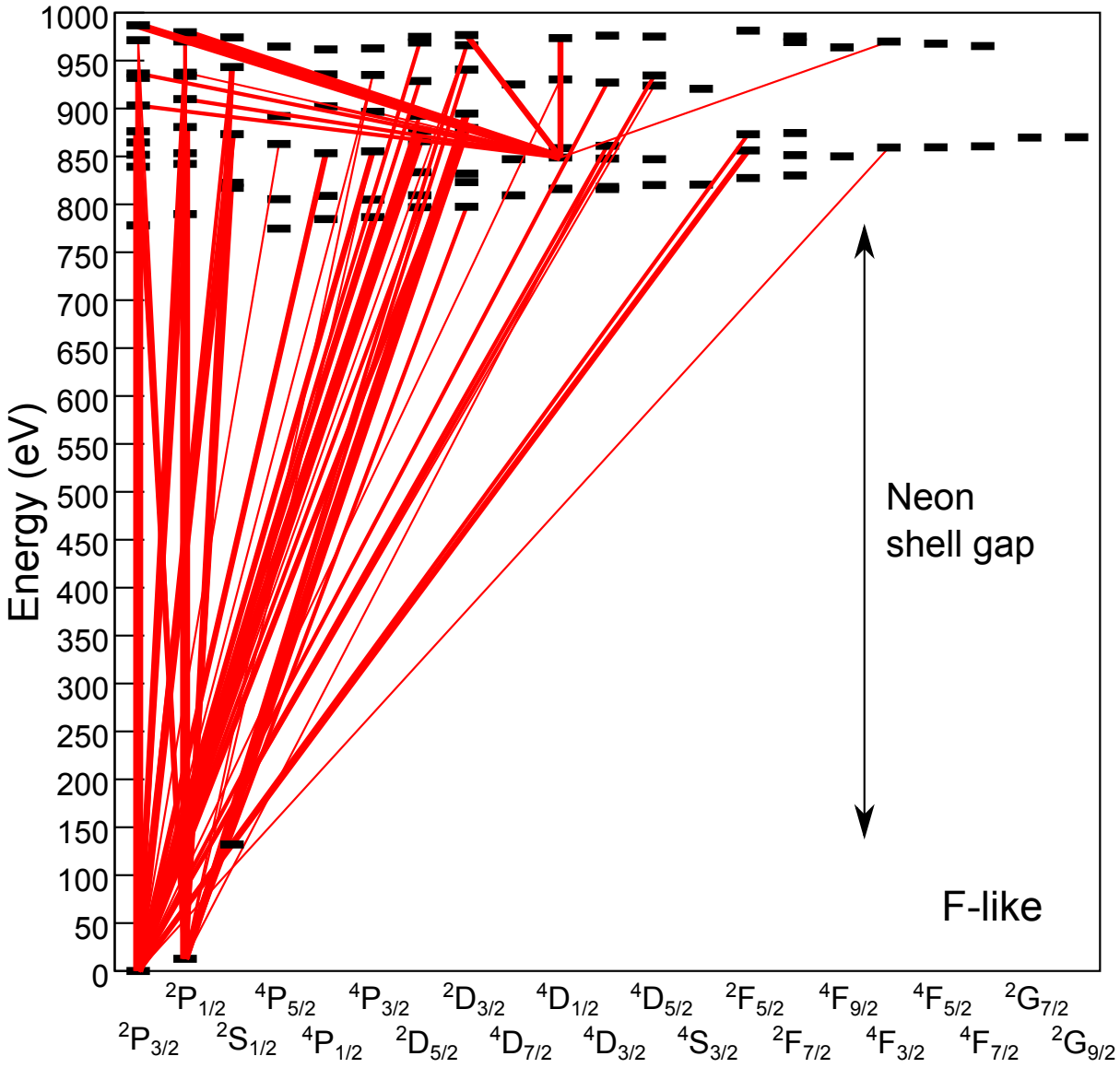

FIGURE 6.13: Grotrian-style diagram of $E1$ atomic transitions in F-like Fe ions. Atomic states have been labelled using *spectroscopic notation*, in columns. This was necessary to simplify the labelling. The $2p_{3/2}$, $2p_{1/2}$ and $2s_{1/2}$ electron-hole states (labelled in Fig. 6.11) correspond to the lowest-energy $^2P_{3/2}$, $^2P_{1/2}$ and $^2S_{1/2}$ states. The line thickness is logarithmically proportional to the transition rate, and transitions slower than $\tau = 10$ ps are not shown. Most transitions strongly feed the lowest two states, though some have slower transition rates and instead become effectively trapped in these higher-energy atomic states over the ^{56}Fe 2_1^+ nuclear-state lifetime. It is also interesting to note the $\sim$ 840 eV state to which the higher states feed without any strong decays out. However, the Ne-like shell gap prevents any significant occupation of these states.

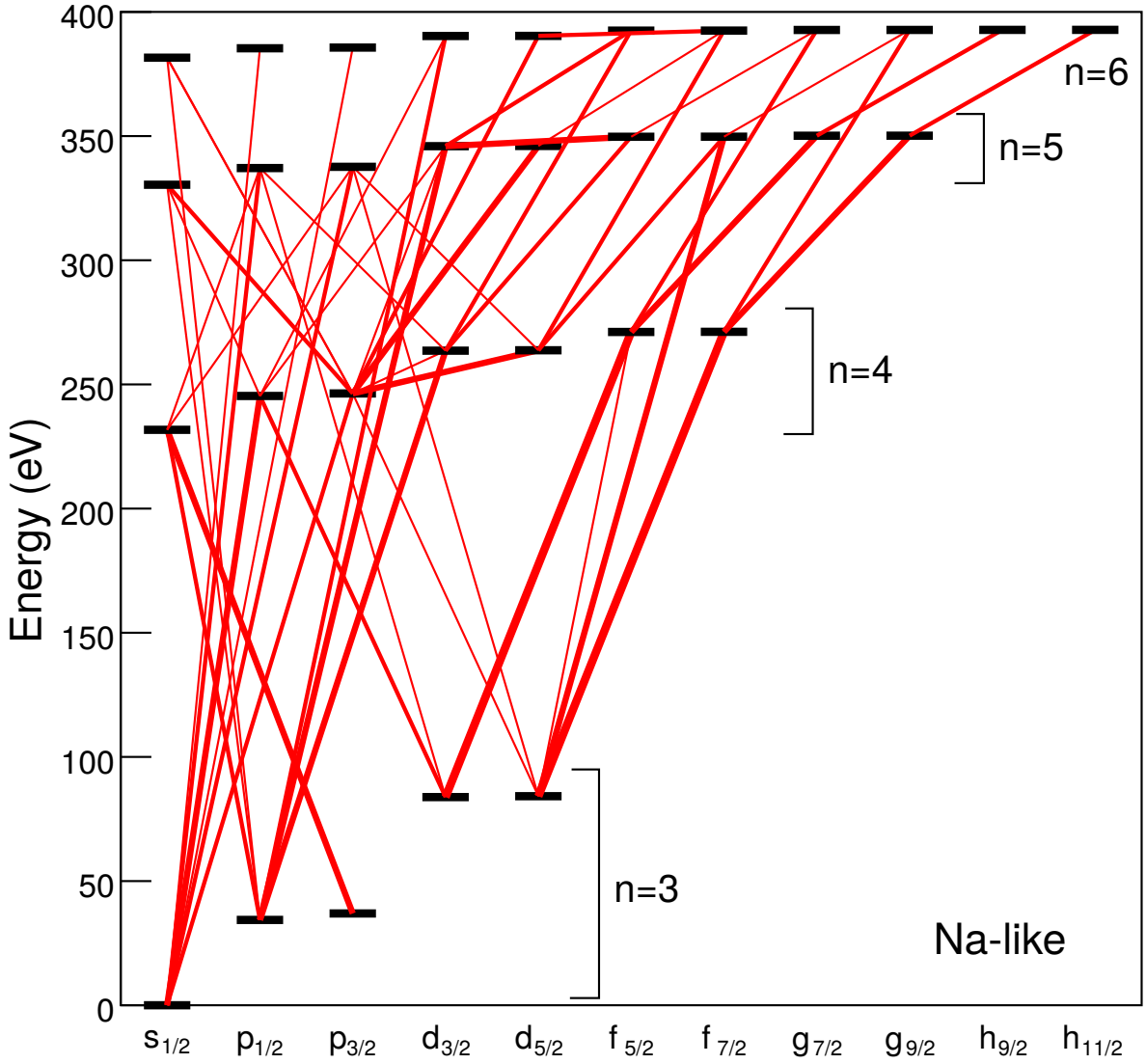

FIGURE 6.14: Grotrian-style diagram of $E1$ atomic transitions in Na-like Fe ions. Atomic states have been labelled by standard electron-configuration notation of the outermost electron (the neon core remains static), in columns. The principal quantum number of the outermost electron is indicated on the figure. The line thickness is logarithmically proportional to the transition rate, and transitions slower than $\tau = 100$ ps are not shown. Most transitions strongly feed the lowest five states.

Figure 6.11 shows the resulting time-dependent occupation of atomic states in each ionic species through time, in the form of a heatmap. Atomic-state occupation is represented by colour, rising linearly from black (none), through blue, red, yellow, and then white. White is set to the most intensely occupied state at any point in the time range, with all other occupations referenced to this. The heatmap is intended to give an intuitive feel for the intensity of atomic-state occupation through time. Significant atomic states (those belonging to strongly populated ionic species, and having significant occupation through time) have been labelled. Figure 6.12 shows the $G_k(t)$ plots resulting from the simulated atomic-state occupation for each ionic species. An interpretation of the information in these two figures will now be presented.

O-like ions have similar initial occupation of the ground and first three excited states, which are then fed and/or decay at different rates. The resulting $G_k(t)$ trend appears as a superposition of single frequencies contributed by the $J > 0$ excited states, with their amplitude reduced by the $J = 0$ ground state. The combination of the oscillations cancelling due to interference, and the $J = 0$ ground state reducing the oscillation amplitudes, causes the overall $G_k(t)$ trend to appear rather flat, with only a little structure.

F-like ions only have notable occupation of the first three states. This is because fluorine, being one electron removed from neon, must excite electrons across the neon atomic shell gap to occupy the higher-excited states. These three occupied states are the $2p_{3/2}$ (ground state), $2p_{1/2}$ (first-excited or spin-flip) and $2s_{1/2}$ (second-excited) electron-hole states. The $2s_{1/2}$ mostly feeds the $2p_{3/2}$ via an $E1$ transition, while the $M1$ transition between $2p_{1/2}$ and $2p_{3/2}$ is hindered, and therefore is not expected to be observed over the experimental timescale. Transitions between the atomic energy levels are illustrated in Fig. 6.13, and show that many of the higher-energy states have strong transitions to the lowest two energy states. The $G_k(t)$ plot shows strong, single-frequency behaviour with high-amplitude oscillations, owing to the dominant occupation of the two $2p$ atomic states, with a small contribution from the $2s$ state at early times.

Ne-like ions have dominant occupation of the ground state from $t = 0$ due to the atomic shell gap. The small number of excited states have large spin, and so their transition back to the ground state is hindered, but should only weakly contribute to the hyperfine interaction. The $G_k(t)$ plot shows no frequency character, with G_2 and G_4 initially weakly declining, owing to the small occupation of excited states, before becoming fixed. Overall, the dominant ground-state occupation means the Ne-like ions will contribute little to the attenuation in the angular correlation. Instead, the Ne-like ions will cause a reduction in the overall amplitude of the hyperfine interaction

frequencies from other ionic species, once averaged.

Na-like ions initially have many excited states, which quickly decay into the ground ($3s_{1/2}$), and first four excited states ($3p_{1/2}$, $3p_{3/2}$, $3d_{3/2}$ and $3d_{5/2}$). These low-energy excited states are long-lived (having $\tau \gtrsim 100$ ps), meaning that they will slowly feed into the ground state, causing an amplitude reduction in the ground state's oscillations over time. The $G_k(t)$ plot shows some single-frequency character, which will become dominant as $T \to 0$. The rapid transitions of the higher-energy states to the lower-energy states are illustrated in Fig. 6.14, which reinforce this single-state character. At this energy ($T = 200$ eV) the single-frequency amplitudes are reduced by occupation of the long-lived, low-energy states that have weak hyperfine interactions ($B_{\mathrm{HF}} \simeq 0$), as well as due to feeding. This results in a somewhat quasi-exponential shape.

Mg-like and Al-like ions have a multitude of populated states that are continually changing occupation, which will give their $G_k(t)$ trend a quasi-exponential character. The $G_k(t)$ plots show that this is indeed the case, particularly for the Al-like ions.

In conclusion, these simulations reveal that the low-energy atomic states in the strongly populated F-like and Na-like ionic species are the best candidates to associate with the high-frequency structural features discussed in §6.2.2.

6.2.4 Individual Atomic-State Contributions

A better understanding of the hyperfine interaction present in this measurement can be obtained by considering a handful of individual atomic states, instead of the full Monte-Carlo simulation. If this approach is valid, the contribution of strongly occupied atomic states should be evident in the $G_k(t)$ trend. In consideration of the free-fit $G_k(t)$ plot in Fig. 6.9 and the simulation $G_k(t)$ plots in Fig. 6.12, it appears that the quasi-exponential attenuation resulting from the Mg- and Al-like ions makes only a small contribution. The free-fit $G_k(t)$ trend must therefore be dominated by frequencies from only a few low-energy states.

As discussed in §6.2.3, the F-like and Na-like ionic species are the only ones that will contribute observable frequencies, and so their low-energy and ground states were examined. For Na-like, five low-lying atomic states, being $3s_{1/2}$, $3p_{1/2}$, $3p_{3/2}$, $3d_{3/2}$ and $3d_{5/2}$, were rapidly populated. Of these five, only the $3s_{1/2}$ and $3p_{1/2}$ states have hyperfine interactions with observable periods over the measurement time-span. The $3p_{3/2}$, $3d_{3/2}$ and $3d_{5/2}$ states serve only to reduce the amplitude of the $3s_{1/2}$ and $3p_{1/2}$ frequencies and lower the overall G_k values through time. For the F-like charge state

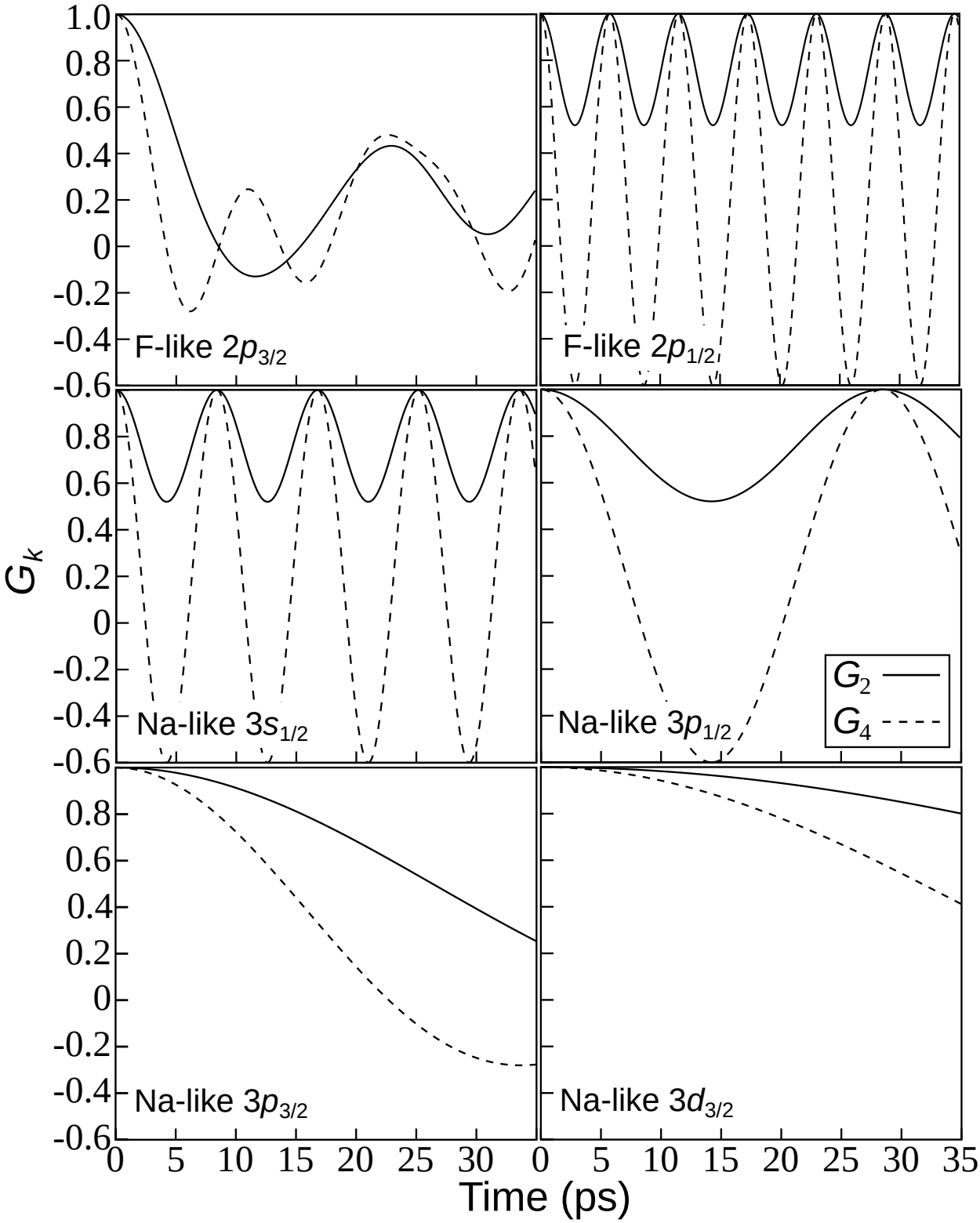

FIGURE 6.15: Individual ^{56}Fe-ion $G_k(t)$ plots for F-like $2p_{3/2}$, F-like $2p_{1/2}$, Na-like $3s_{1/2}$, Na-like $3p_{1/2}$, Na-like $3p_{3/2}$, and Na-like $3d_{3/2}$ states. The Na-like $3d_{5/2}$ state was not shown as its hyperfine interaction is so weak that it causes no appreciable attenuation over this time-span. These were evaluated with $g(2_1^+; \mathrm{Fe}^{56}) = +0.51$ [56].

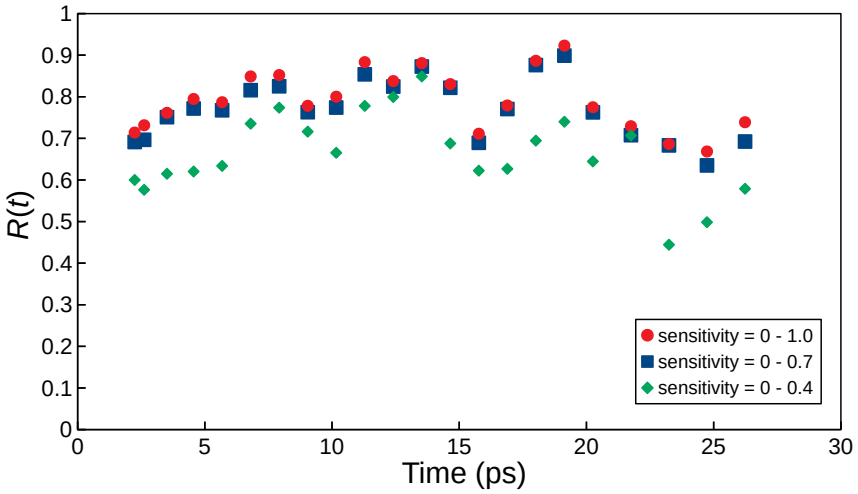

FIGURE 6.16: Comparison of calculated ^{56}Fe-data $R(t)$ values expanding the sensitivity range from the lower limit, $0-0.4$, to the upper limit, $0-1.0$. While there is a small loss in frequency amplitude as the range is expanded, there is more consistency between the data points (a smoother trend). Due to its improved consistency, the sensitivity range $0-1.0$ was chosen for fitting.

the ground and first-excited states ($2p_{3/2}$ and $2p_{1/2}$ holes) are dominantly populated from $t = 0$, and both have observable frequencies over the measurement time-span. The $G_k(t)$ plots arising from the hyperfine interaction with each individual state, adopting $g = +0.51$ [56], are shown in Figure 6.15. Individual examination of these trends, and comparison with the $G_k(t)$ trends in Fig. 6.9, should reveal which states are strongly contributing.

Already, the restoration of anisotropy after 20 ps, owing to the combined effect of $3p_{1/2}$ and $2p_{3/2}$, is evident. The interference between $3s_{1/2}$ and $2p_{1/2}$ creates a constructive peak at $t \simeq 16$ ps, but they interfere less constructively at other times. The $2p_{3/2}$ also exhibits a strong, rapid decline from $t = 0$ followed by G_2 falling below G_4, owing to the $J = 3/2$ spin, around 10 ps. If there is any contribution from the $3p_{3/2}$ and $3d_{3/2}$ states, it is quite weak. This is expected if the average-energy of the atomic-state distribution is actually much smaller than 200 eV. It appears to be a robust conclusion that these frequencies explain several structural details observed in the free-fitted $G_k(t)$ plot, making them good candidates with which to fit the g factor.

6.2.5 $R(t)$ Plots

While the information gained from inspecting the free-fitted G_k plots has allowed insight into the atomic states contributing to the hyperfine interaction, it is also useful to calculate and plot $R(t)$ values from the data (see §5.6.5 for information on calculating $R(t)$ values) and compare them to the free-fitted $G_k(t)$ plot to confirm consistency

between the observed frequencies. This is helpful because the $R(t)$ function avoids the complications introduced through fitting the correlated G_2 and G_4 variables. As discussed in §5.6.5, when computing the $R(t)$ function, the number of γ-particle pairs used can be varied, which affects the resulting plot. To recap: each pairing used to calculate $R(t)$ has a sensitivity determined by the ratio of the $W(\theta, \phi, t = 0)$ values, with values closer to zero having more sensitivity, and values closer to unity having less sensitivity, to changes in G_k. By increasing the acceptance, or sensitivity range, more detector pairings are included (reducing uncertainty), but sensitivity to changes in G_k, and therefore the hyperfine interaction frequencies, is lost. Figure 6.16 shows how the $R(t)$ plot changes as the sensitivity range is increased. As more data points are included, the amplitude of the oscillations decreases. However, the consistency across the overall trend improves and the oscillations in the $R(t)$ trend become more defined. The improved consistency in the $R(t)$ trend, and only small loss in oscillation amplitude, led to the sensitivity range $0 - 1$ being chosen for all future calculations.

Comparison of the free-fitted $G_k(t)$ values in Fig. 6.9 to the $R(t)$ values in Fig. 6.16 (noting that the $R(t)$ trend appears as opposite phase to the $G_k(t)$ trend) confirms the more general features identified in the free-fitted $G_k(t)$ plot, but avoids the complications introduced through fitting the correlated G_2 and G_4 parameters. The $R(t)$ function also gives only a single value for each time point against which to fit the angular correlation, which allows for a scalar offset to be applied without introducing the complicated correlations that would arise from applying such an offset to the G_k values. Such an offset is able to compensate for unknown but consistent deorientation effects that may be caused, for example, by an off-centre beam spot on the target, or the reaction geometry differing from expectation. However, the free-fitted G_k trend remains useful for its ability to tease out the relationship between G_2 and G_4, which is sensitive to the spin of the contributing atomic states. With these factors considered, the $R(t)$ plots were chosen to proceed with the g factor fitting attempts, with atomic-state contributions informed by the free-fitted G_k trend.

6.2.6 Parameter Fitting

Two approaches may be taken in fitting the $R(t)$ trend. The hyperfine interaction and resulting G_k values used to calculate the $R(t)$ trend can be obtained using a Monte-Carlo simulation, or from individual atomic states. As discussed in §6.2.4, there is reason to believe that fitting individual states will be effective for these data. Fitting individual atomic states also allows more control over the fitting procedure, and its interrogation. However, before proceeding with a set of differing atomic states, a simpler option was

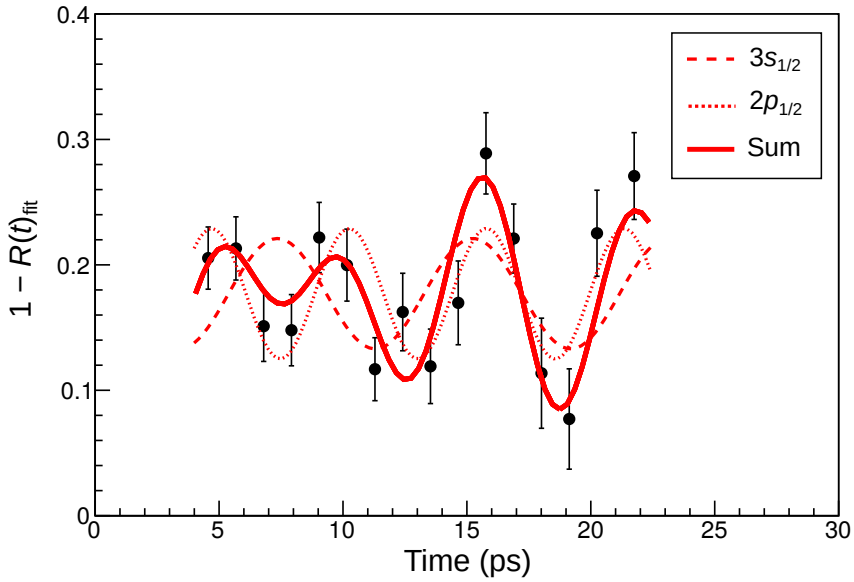

FIGURE 6.17: Result of the ^{56}Fe $3s_{1/2}$ and $2p_{1/2}$ double-cosine fit as per Eq. (6.8), showing also the separate $3s_{1/2}$ and $2p_{1/2}$ cosines. Note the strong constructive interference at $t \simeq 16$ ps.

explored to establish an initial g factor estimate. The $R(t)$ plots in Fig. 6.16 reveal discernible oscillations over the time-span 4–22 ps. Figure 6.15 shows that only the Na-like $3s_{1/2}$ and F-like $2p_{1/2}$ hyperfine-interaction frequencies are fast enough to have full periods across this time span. As they are both $J = 1/2$ states, the interaction will be in the form of a cosine function. Therefore, the data were fitted using a two-cosine function:

$$1 - R(t)_{\text{fit}} = a_s \cos(\omega[t - \delta_s]) + a_p \cos(1.423\omega[t - \delta_p]) + c, \tag{6.8}$$

giving $a_s = 0.035(12)$, the amplitude of the $3s_{1/2}$ frequency, and $a_p = 0.059(11)$, the $2p_{1/2}$ amplitude; $\omega = 0.792(29)$ rad/ps, the angular frequency of the $3s_{1/2}$ hyperfine interaction; $\delta_s = -0.64(75)$ ps, the phase shift in the $3s_{1/2}$ frequency; $\delta_p = -0.95(58)$ ps, the $2p_{1/2}$ phase shift; and $c = 0.176(8)$, the amplitude offset for both cosine terms. The 'inverse' function $1 - R(t)$ was fitted so as to have the cosines in the correct phase. The value 1.423 is the ratio between the $2p_{1/2}$ and $3s_{1/2}$ angular frequencies, fixed using the calculated hyperfine interaction constants obtained from GRASP. For this fit, $\chi^2_\nu = 0.923$. The ratio of 0.6:1 between the $3s_{1/2}$ and $2p_{1/2}$ cosine magnitudes seemed somewhat unrealistic. As the values had quite large uncertainties, the ratio was slowly adjusted until the fit gave $\chi^2_\nu = 1.00$. This resulted in $a_s = 0.044$ and $a_p = 0.052$, which were fixed. The remaining parameters then minimised to $\omega = 0.796(27)$ rad/ps, $\delta_s = -0.54(70)$ ps, $\delta_p = -0.84(53)$ ps and $c = 0.177(8)$, all with approximately the same uncertainty as obtained at the true χ^2 minimum. The result of this fit is shown in Fig. 6.17.

From this fit the g factor is determined as the ratio of the fitted angular frequency to

the calculated angular frequency for $g = 1$, such that $\omega = g\omega_{g=1}$. The angular frequency of the hyperfine interaction for $3s_{1/2}$ having $g = 1$ is $\omega_{g=1} = 1.502(15)$ rad/ps. The fitted angular frequency therefore gives $g = \omega/\omega_{g=1} = 0.527(19)$ when a_s and a_p were allowed to vary, and $g = \omega/\omega_{g=1} = 0.530(18)$ when a_s and a_p were fixed to give $\chi^2_\nu = 1.00$. Because the two results are statistically indistinguishable, the fit with fixed a_s/a_p will be discussed further. In this fit, time offsets of $\delta_s = -0.54(70)$ ps for $3s_{1/2}$ and $\delta_p = -0.84(53)$ ps for $2p_{1/2}$ were obtained. Because there is expected to be little to no feeding of the $2p_{1/2}$ state, the offset of -0.84 ps may be considered as a zero-time offset in the plunger, $t_0 = -0.84$ ps. This would make the smaller offset of $3s_{1/2}$ actually a positive phase shift $\delta = +0.30$ ps. This small degree of phase shift is expected due to feeding from excited atomic states in the Na-like ion. However, the discussion of these phase shifts should be considered with caution, as the uncertainty in these values is large, and overlapping. For $\chi^2_\nu = 1.00$ the $2p_{1/2}$ amplitude is 1.2 times the strength of $3s_{1/2}$, though the initial fit shows that there are large uncertainties in these values. There is expected to be some loss in amplitude of the $3s_{1/2}$ state due to feeding, as well as lost intensity to other excited states. Therefore, this ratio of $2p_{1/2}$ to $3s_{1/2}$ is not unreasonable, especially considering the large uncertainty. Ideally, these values would be constrained by theory or measurement, which is possible using the **RIV Simulate** fitting routines. Regardless, this analysis gives a promising g-factor value, being more precise than any previously reported value, and within uncertainty of the previously reported $g = +0.51(5)$ [56]. With this reference-point set, more comprehensive fitting procedures may proceed with greater confidence.

Six atomic states were identified in §6.2.4 for fitting. A seventh state, having $B_{\mathrm{HF}} \simeq 0$, was also included. This state primarily represented the strong Ne-like $J = 0$ ground state, but may also represent contributions from any states having weak hyperfine interactions, e.g. the Na-like $3d_{5/2}$. In the first instance, the g factor was fitted to the $R(t)$ function across the experimental data covering the time-span 4–22 ps (as in the double-cosine fit) using these seven states, and to the longer 0–27 ps range. For these fits, individual-state occupations were allowed to vary in two ways: *unrestricted* minimisation, in which each individual-state occupation can take any value; or *restricted* minimisation, in which individual atomic states were grouped by ionic species, and the sum of individual-state occupation's for each ionic species was fixed as per the CSD in Table 6.2. The attenuation as modelled by the Monte-Carlo simulation was also fitted to the 0–27 ps range. The resulting fits to the $R(t)$ function are shown in Fig. 6.18. The best-fit values are listed in Table 6.3.

The g factors obtained in the individual-state and Monte-Carlo fits are consistently larger than that obtained in the double-cosine fit. They also have smaller t_0 offsets,

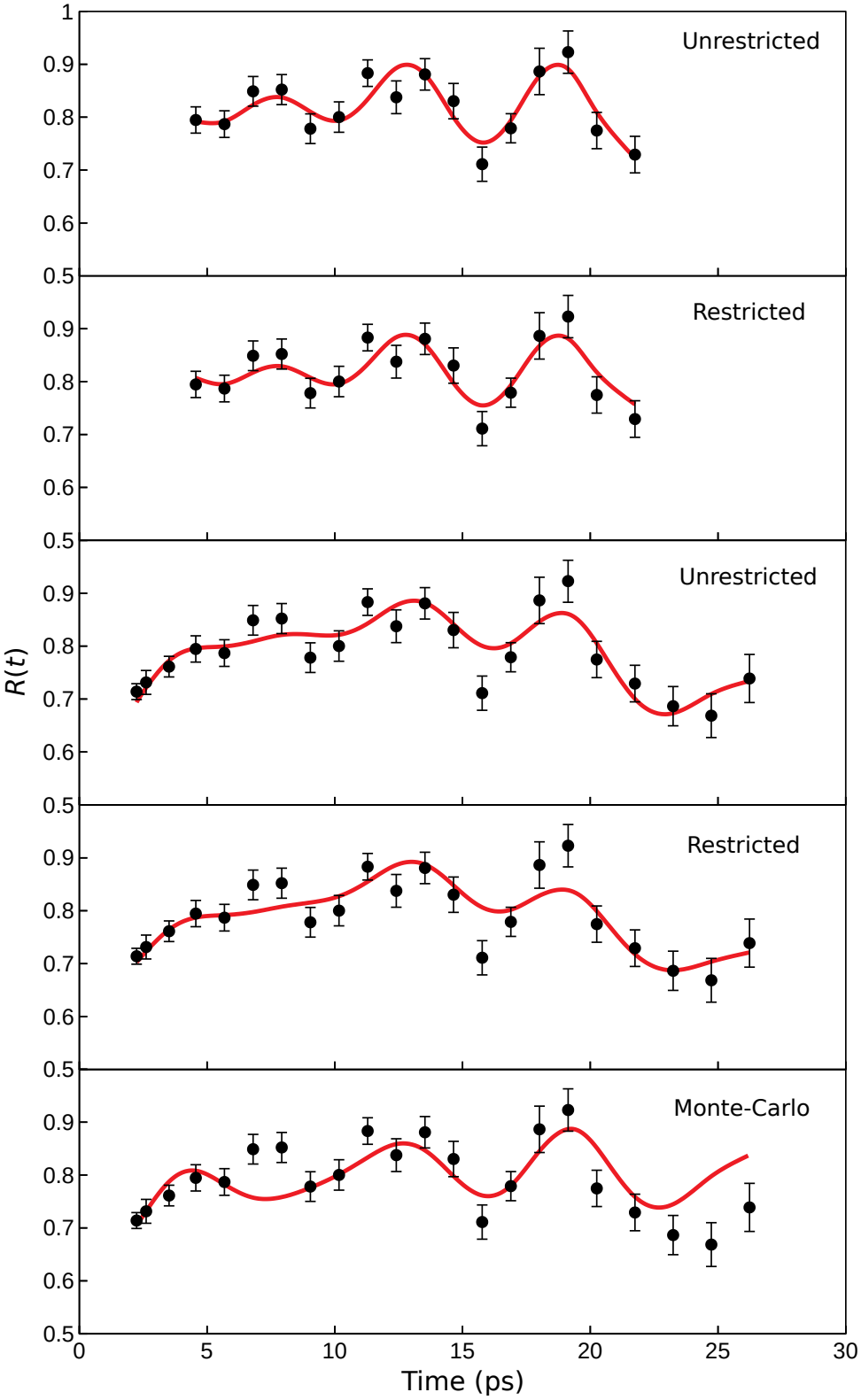

FIGURE 6.18: Results of the ^{56}Fe-data $R(t)$-function fit using the seven individual atomic states (described in-text) across the 4–22 ps and the 0–27 ps time-spans, and the Monte-Carlo simulation. The zero-time offset, t_0, was allowed to vary, and individual-state occupation phase shifts, δ, were allowed using the χ^2 sweep routine (see §5.6.8), with occupations either unrestricted, or having maximum occupation shared amongst states of the same ionic species, fixed by the CSD as described in-text. Fitted values are listed in Table 6.3.

TABLE 6.3: Best-fit values from fits to the $R(t)$ function across the time-span 4–22 ps to the seven individual atomic states described in-text, and 0–27 ps to the individual atomic states, as well as the Monte-Carlo simulation. The time-zero offset (t_0) was allowed to vary in the Monte-Carlo fits and the individual-state fits, as well as the occupation and phase shift (δ) in the individual-state fits. Minimisation of individual-state occupations falls into two categories: *unrestricted* minimisation, in which each individual-state occupation could take any value; or *restricted* minimisation, in which individual atomic states are grouped by ionic species, and the sum of individual-state occupation's for each ionic species was fixed as per the CSD in Table 6.2. Uncertainties have not been evaluated for quantities other than the g factor as these were not primarily of concern when the codes were written.

					Occupation (%), δ (ps)						
	χ^2_ν	g	t_0 (ps)	$R(t)$ offset	$3s_{1/2}$	$3p_{1/2}$	$3p_{3/2}$	$3d_{3/2}$	$2p_{3/2}$	$2p_{1/2}$	$B_{\mathrm{HF}} \simeq 0$
Cosine fit											
4–22 ps	0.998	0.530(18)	-0.84	0.177	46, 0.30					54, 0	
Individual states, unrestricted											
4–22 ps	0.801	0.546(10)	-0.29	0.164	14, 0.58	6, 0	0	0	18, 1.37	14, 0	48, 0
0–27 ps	1.183	0.537(9)	-0.04	0.104	13, 0.13	13, 0	0	6, 16	30, 0.57	7, 0	32, 0
Individual states, restricted											
4–22 ps	0.870	0.550(11)	-0.22	0.217	13, 0.63	8, 0	0	19, 22	7, 1.54	14, 0	40, 0
0–27 ps	1.369	0.544(15)	+0.15	0.147	11, 0.35	19, 0	0	9, 24	16, 0.57	5, 0	40, 0
Monte-Carlo simulation											
0–27 ps	2.618	0.554(12)	+0.55	0.154	Boltzmann distribution, $T = 30$ eV						

and reduced uncertainty in the g factor. This shows the importance of including all relevant atomic states in the fit: observing only a subset of the interacting states (e.g. only those having $J = 1/2$) can give a less accurate and less precise result. The $R(t)$ offset values are a scalar offset added to the $R(t)$ function across the entire time-span. These offsets either emulate a decrease in average anisotropy (positive value) or an increase (negative value). They indicate how close the hyperfine interaction arising from the included states are to the absolute reduction in anisotropy (i.e. the magnitude of the G_k values) observed in the measurement, with larger-magnitude offsets indicating a larger discrepancy. Offsets obtained across the 4–22 ps time-span are $\sim 50\%$ larger than the 0–27 ps time-span, which is reasonable as fitting the entire time-span should cause the fit to better match the overall interaction. In all of the individual-state fits, positive phase shifts are seen for $3s_{1/2}$ and $2p_{3/2}$. The fitted phase shifts are larger in the 4-22 ps datasets, and smaller in the 0–27 ps datasets, but consistent between the unrestricted and restricted fits. Since the $3s_{1/2}$ and $2p_{3/2}$ states should be strongly fed (as they are ground states), this result is expected. The somewhat long-lived $2s_{1/2}$ state ($\tau \lesssim 8$ ps), which strongly feeds the $2p_{3/2}$ state, may be the reason for the $2p_{3/2}$ phase-shift being larger than that of the $3s_{1/2}$. That the phase shift is smaller in the 0–27 ps dataset may be due to the precise early time points, in which the feeding is still underway, consequently reducing the apparent magnitude.

According to the CSD in Table 6.2, the ionic species should have *relative* populations 21% F-like, 40% Ne like and 39% Na-like. These relative populations, and the heatmaps in Fig. 6.11, indicate that states contributing to the $B_{\mathrm{HF}} \simeq 0$ fraction should be dominant. Across the 4-22 ps range, the $B \simeq 0$ (Ne-like) contribution is indeed observed to be dominant when occupation is unrestricted, however the relative populations of the F-like and Na-like ionic species are fitted to be 32% and 20%, respectively. This may indicate that the CSD present in the experiment is actually weighted more towards the F-like ions than the Na-like. A less realistic distribution is observed in the unrestricted fit to the 0–27 ps range, which gives 37% F-like, 32% Na-like and 32% Ne-like. In this fit, the occupation of the $3d_{3/2}$ state, with $\delta = 16$ ps, is actually behaving as a $B \simeq 0$ state. This is because the already weak hyperfine interaction is prevented from perturbing the spin-alignment until $t = 16$ ps, and causes almost no attenuation over the remaining 9 ps. As such, it may be 'stealing' intensity from the Ne-like $B \simeq 0$. If this is the case, the distribution should instead be 26% Na-like, 38% Ne-like and 37% F-like, which is more realistic. These two unrestricted fits suggest that the CSD has larger F-like, and smaller Na-like, proportions than the empirical nickel-target parameterisation obtained in §6.1.2.

In the restricted fits, the populations of ionic species shown in Table 6.2 are enforced.

With this restriction in place, the population of the Na-like $3s_{1/2}$ and $3p_{1/2}$ states remains the same for the 4–22 ps time span, with the required increased intensity going into the $3p_{3/2}$ and $3d_{5/2}$ states. These two states both have large phase shifts that, as previously mentioned, serve only to make them behave as $B \simeq 0$ states, and may instead be representing contributions not only from these two states, but also from the Mg-like and Al-like ions. Nonetheless, the $3s_{1/2}$ and $3p_{1/2}$ occupations are consistent across this time range. Continuing to examine the 4–22 ps fit, the forced reduction in the overall F-like intensity reduced the $2p_{3/2}$ occupation, leaving $2p_{1/2}$ occupation much the same as in the unrestricted fit. This shows the importance of $2p_{1/2}$ in fitting this region.

Comparing now the unrestricted to restricted fits across the 0–27 ps range, there is a notable increase in the Na-like $3p_{1/2}$. This increase likely compensates for the restoration in anisotropy, near 25 ps, no longer provided by the F-like $2p_{3/2}$ state, which concurrently halves in occupation. The higher-frequency $3s_{1/2}$ and $2p_{1/2}$ states retain almost the same occupation (decreasing only slightly), indicating consistency in these values, as was seen in the 4–22 ps fits. The Na-like $3d_{3/2}$, with $\delta = 24$ ps, is again indistinguishable from a $B \simeq 0$ contribution, and increases in occupation over the longer time-span, likely due to the importance of the Mg-like and Al-like species across the longer time scale. Overall, the occupation of Na-like $3s_{1/2}$ is insensitive to the range or restrictions in the fit, averaging around 13% of the total hyperfine interaction. The contribution of the $2p_{1/2}$ state is clearly sensitive to the fitting region. Figure 6.18 shows that, when fitting the 4–22 ps range, the fit passes through the time points at $t \simeq 6,7$ ps, whereas in the 0–27 ps range it does not. This is due to the presence or absence of a strong oscillation owing to $2p_{1/2}$ in this region. Inclusion of the $t < 4$ ps time points forces a reduction in the $2p_{1/2}$ occupation, and concurrent increase in $2p_{3/2}$ to reproduce these early time points. When the occupation of $2p_{1/2}$ is considered relative to $2p_{3/2}$, the values obtained from fits across 0–27 ps match better with the occupation expected from the heat map, suggesting that these are more realistic fits. That fitting to the larger dataset gives a more realistic result is good confirmation of its validity.

The Monte-Carlo fit takes into account the hypothetical contribution of all excited states as initially occupied following a Boltzmann distribution of the ground and excited states. The CSD was fixed to the values indicated in Table 6.2. Apart from the g factor, the fit had only two other free parameters, being the average energy of the Boltzmann distribution, T, and the zero-time offset, t_0. These minimised to $T = 30$ eV and $t_0 = +0.55$ ps. The small value of T (relative to the atomic excited-state energies) indicates that, for this modelling, dominant occupation of the ground and first few excited states from $t = 0$ gives the best fit. This result matches the findings of Stuchbery in the analysis of Ge and Se RIV data [206]. That t_0 is a small but non-zero value is also reassuring, as some

small degree of time-zero offset is expected, due to the uncertainty in experimentally determining the true value of $t = 0$ for the time-dependent hyperfine interaction. The simulation of these excited states through time models the effect of feeding on phase-shifts and amplitude attenuation, and maintains realistic proportions between the ionic species and excited states, granted that the initial excited-atomic-state distribution resembles reality. Figure 6.18 shows that through the time points up to $t \leq 22$ ps the fit captures the $R(t)$ trend well, particularly in the range $9 \leq t \leq 22$ ps. However, the points at $t \simeq 6,7$ ps, and $t > 22$ ps were poorly fitted. Excluding these poorly fitted points reduces the χ^2 to $\chi^2_\nu = 1.152$. There may be issues with the angular-correlation measurements for these particular time points, but this seems unlikely to have occurred at both early and late times. Instead, these deviations may indicate that there is additional behaviour that the Monte-Carlo simulation is unable to capture. Another possibility is that the CSD is changing through time, perhaps due to the deposition of carbonised oil or from damage to the target over time. Regardless, there is clearly agreement with the overall trend, providing good validation to this approach.

6.2.7 Interpreting the Fit Results

There appears to be a (small) correlation between the fitted g factor and the F-like population versus Na-like population. The relative populations also appear sensitive to whether the early and late time points are included in the fit. On average, in the restricted versus unrestricted fits, the g factors were larger when restricted, and smaller when unrestricted. The same trend was seen between the 4–22 ps and 0–27 ps ranges, with the average g factors being larger in the former, and smaller in the latter. Looking more carefully at the occupations of individual states obtained in each fit, the increased g factors across the 4–22 ps range correlate with a reduced $2p_{3/2}$ occupation. Across the 0–27 ps range the g factor is also seen to increase with reduced $2p_{3/2}$ occupation (and the concurrent increase in $3p_{1/2}$ occupation). However, despite the appreciable change in $2p_{3/2}$ occupation, the fitted g factors do not vary dramatically. The largest fitted g factor was obtained in the Monte-Carlo fit, which had the population of ionic species fixed to the values in Table 6.2. Figure 6.19 shows all the fitted g-factor values plotted together. There is no significant variation between them, and they are consistent with the previously [33] and currently [56] accepted literature values, also shown. Taking a weighted average of the presently fitted values (excluding the double-cosine fit), $g = +0.546$ is obtained, with the sign determined by the transient-field technique [56]. Adopting $g = +0.546$, the uncertainty in the double-cosine fit was chosen as a conservative estimate (being the largest). A further 1% uncertainty in the hyperfine-interaction frequency of those states to which the g-factor determination is sensitive (i.e. those having observable oscillations: $3s_{1/2}$, $3p_{1/2}$, $2p_{3/2}$ and $2p_{1/2}$) was also added in quadrature.

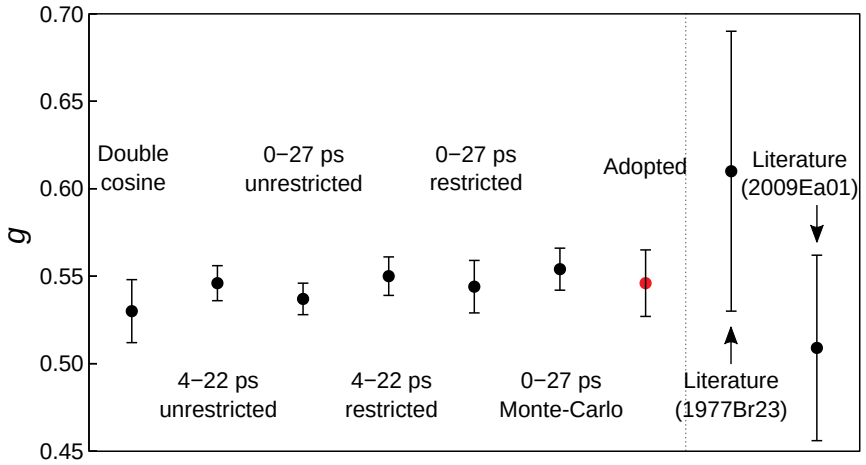

FIGURE 6.19: ^{56}Fe TDRIV data 2_1^+-state g factors obtained from the various fitting approaches, shown alongside the adopted value from Brennan *et al.* [33] (1977Br23), and the value measured by East *et al.* [56] (2009Ea01). They are all in excellent agreement. A weighted-average of the $R(t)$ fit values (excluding the double-cosine) was adopted, taking the uncertainty to be that from the double-cosine fit (being the largest) and adding, in quadrature, 1% uncertainty for each important atomic-state hyperfine-interaction strength. This gives $g = +0.546(19)$, which is consistent with the previously and presently adopted literature values, but has greatly improved precision.

This gives $g(2_1^+;^{56}\mathrm{Fe}) = +0.546(19)$, a value that encompasses all the $R(t)$ fit values (excluding the double-cosine fit) and almost their entire uncertainty range. It also has good consistency with previous measurements, while also having greatly improved precision.

6.2.8 Investigating the Large F-like Fraction

In the unrestricted individual-state fits to the $R(t)$ function, a stronger F-like than Na-like fraction was obtained for both the 4–22 ps and 0–27 ps timespans. This result contradicts the empirically determined CSD expected for the ^{56}Fe ions recoiling out of nickel. However, it was noted after the experiment was completed that carbon residue had built up on the back-side of the target, i.e. the surface out of which the ions recoil. In addition to the nickel-target charge-state-distribution measurements, carbon-target measurements had also been performed. Figure 6.20 shows that at almost equal recoil velocities (being approximately the average recoil velocity in this measurement), the CSD of ^{56}Fe ions recoiling out of carbon, instead of nickel, has an inversion of the F-like and Na-like fractions as compared to the Ne-like. If the observed carbon build-up were thick enough to affect the CSD, then this can easily explain the larger F-like fraction suggested by the unrestricted fits. The time points in the measurement were taken in chronological sequence, and so the precise, early time points ought to have

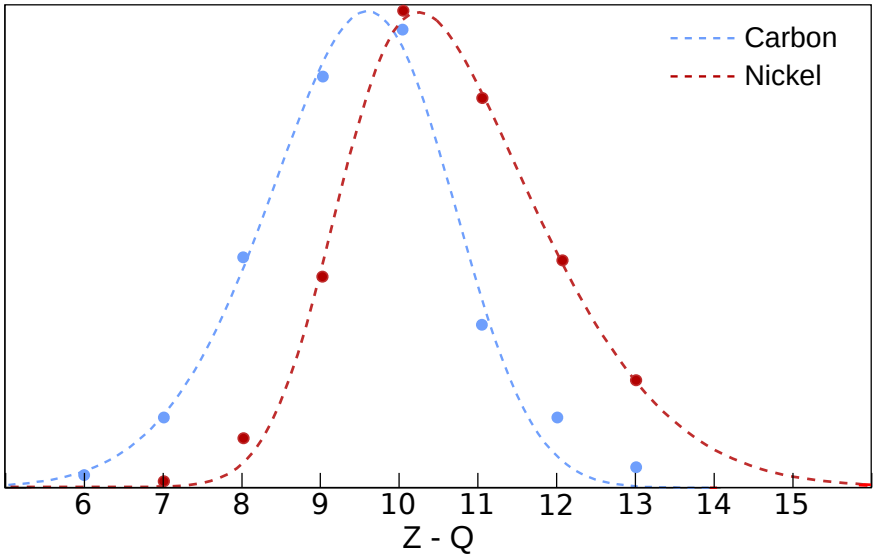

FIGURE 6.20: Measured CSDs of ^{56}Fe ions recoiling out of a carbon (blue) or nickel (red) target with $E_{\text{recoil}} \simeq 53$ MeV, approximately the average recoil energy in the ^{56}Fe TDRIV measurement. Note the near inversion of the F-like ($Z - Q = 9$) and Na-like ($Z - Q = 11$) fractions between the two targets.

very little carbon build up (the target had already been in the chamber for a half-day when the first time-point measurement began). That the 0–27 ps range, containing the precise, early time points, fitted a smaller F-like fraction than the 4–22 ps time-span fits further suggests that carbon build-up was altering the CSD. If the carbon build-up was significant by the latter time-points in the run, the Mg- and Al-like fractions may have fallen to nearly zero, as suggested in Fig. 6.20. This would help to explain the strong restoration of anisotropy at later times, which is difficult to reproduce with the Mg- and Al-like contributions required by the nickel-target CSD. This is a potential pitfall in this measurement technique, as not only could the CSD differ from expectation (resulting in the measurement not being optimal), but it may be changing through time. However, the sensitivity of this technique to the atomic-state contributions appears to have correctly identified a strong F-like fraction owing to carbon build-up on the target.

Another effect that carbon build-up on the stopping foil may have is the generation of events with no vacuum attenuation ("time-zero" events). This is due to primary ^{56}Fe beam particles passing through the target foil and exciting on the built-up carbon on the stopping foil. The recoiling carbon ions will then be detected forward-scattered in effectively the same geometry as the target foil. The energies would be almost the same, making these events indistinguishable. This would further help to explain the degree of restoration of anisotropy observed at later times that the model cannot reproduce.

If the CSD of ^{56}Fe ions is closer to that measured out of carbon than nickel (see Fig. 6.20), then it would be valuable to observe how a CSD with a larger F-like fraction

TABLE 6.4: CSD of ^{56}Fe ions approximating the relative F-like, Ne-like and Na-like proportions suggested by the unrestricted $R(t)$ fits shown in Table 6.3.

$Z-Q$	Ionic Species	Population
8	O-like	11.5%
9	F-like	24.2%
10	Ne-like	28.9%
11	Na-like	20.3%
12	Mg-like	8.7%

and smaller Na-like affects the Monte-Carlo fit. A new CSD was approximated by varying the average foil exit energy until a distribution having relative populations 33% F-like, 40% Ne-like and 27% Na-like was obtained, which matches the proportions suggested by the unrestricted fits. This new CSD is shown in Table 6.4, and was used to fix the population of ionic species in a Monte-Carlo simulation $R(t)$ fit. The objective of performing this fit was to understand how much an increased F-like proportion (and consequent introduction of O-like ions) would affect the g factor obtained from the Monte-Carlo fit. From this fit, $g = 0.569(11)$ was obtained, and the resulting plot is shown in Fig. 6.21 as the solid red line, alongside the fit using the nickel-target CSD, shown as the dashed blue line. Curiously, the carbon-target CSD g factor being larger than the nickel-target is contrary to the single-state fit results, which found a decrease in the g factor with the increased F-like fraction. This behaviour may indicate that the O-like ions are significantly influencing the fitted g factor. The nickel-target fit better-captures the early time-point data and dominant oscillations. In contrast, the carbon-target fit oscillates too rapidly, falling on the early side of the trend, and missing the early time-point data. As such, it appears as though the carbon-target CSD is over-estimating the measured g factor, and that the true value is unlikely to be significantly larger than the adopted value $g = +0.546(19)$.

6.2.9 Analysis of In-Flight Angular Correlations

The previous sections have been concerned with modelling the hyperfine interaction observed in the angular correlations originating from the stop peak of the measured de-excitation γ rays. In addition to the stop-peak angular correlations, which are most sensitive to atomic-state oscillations in the $G_k(t)$ trend (and therefore are most suitable for determining the g factor), the angular correlations originating from the in-flight (i.e. Doppler-shifted) component are revealing of the average strength of the hyperfine interaction. These angular correlations originate from the states that have decayed before reaching the plunger foil, which introduces an exponential attenuation component $e^{-t/\tau}$,

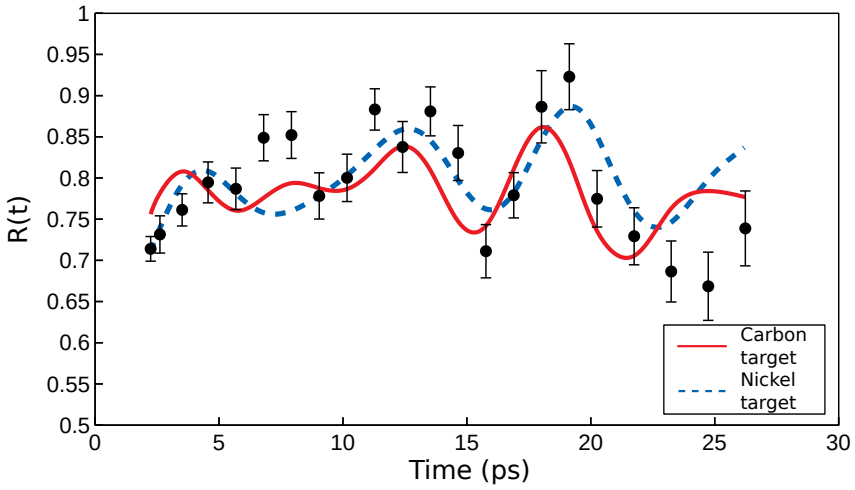

FIGURE 6.21: Comparison of two Monte-Carlo simulation fits to the ^{56}Fe TDRIV $R(t)$ values having different CSDs. The red solid line is the Monte-Carlo simulation fit with the larger F-like proportion, having the CSD shown in Table 6.4. The blue dashed line is the fit with the larger Na-like proportion, having the empirically determined CSD shown in Table 6.2.

dependent upon the nuclear-state's lifetime. Therefore, the in-flight $G_k(t)$ trend should resemble an exponential-decay curve.

Figures 6.22 and 6.23 show the $G_k(t)$ values obtained from the in-flight angular correlations using the G_k free-fitting routine, along with various fits. The exponential-decay component in the data is clear, and as the time becomes large compared to the nuclear lifetime the $G_k^{\text{flight}}(t)$ values approach the $G_k(t = \infty)$ values that are obtained in a time-integral measurement. The $G_k(t)$ trend indicates that there is a strongly deorienting hyperfine interaction acting from the earliest times. The relative magnitude between G_2 and G_4 also indicates that this interaction is dominated by atomic states having $J > 1/2$, and/or rapidly fluctuating atomic states. Fits to the in-flight $G_k(t)$ trend are more sensitive to the absolute magnitude of the $G_k(t)$ values as compared to the stopped component, in which the oscillations are more important. However, the major contributing atomic states should be the same for both the in-flight and stop data.

It was shown in §6.2.8 that, due to carbon build-up on the target, the centroid of the CSD is closer to F-like ions than Na-like. If this is true, it should be reflected in the in-flight data. To investigate this, two Monte-Carlo-simulation fits were performed to the angular-correlation data using the nickel- and carbon-target CSDs. Angular-correlation data were fitted (rather than the $R(t)$ function) because sensitivity to the magnitude of the attenuation is most important for the in-flight data. Individual-state fits were also performed, with the occupation of individual atomic states either restricted to the nickel- or carbon-target CSD, or allowed to minimise in an unrestricted manner. In the

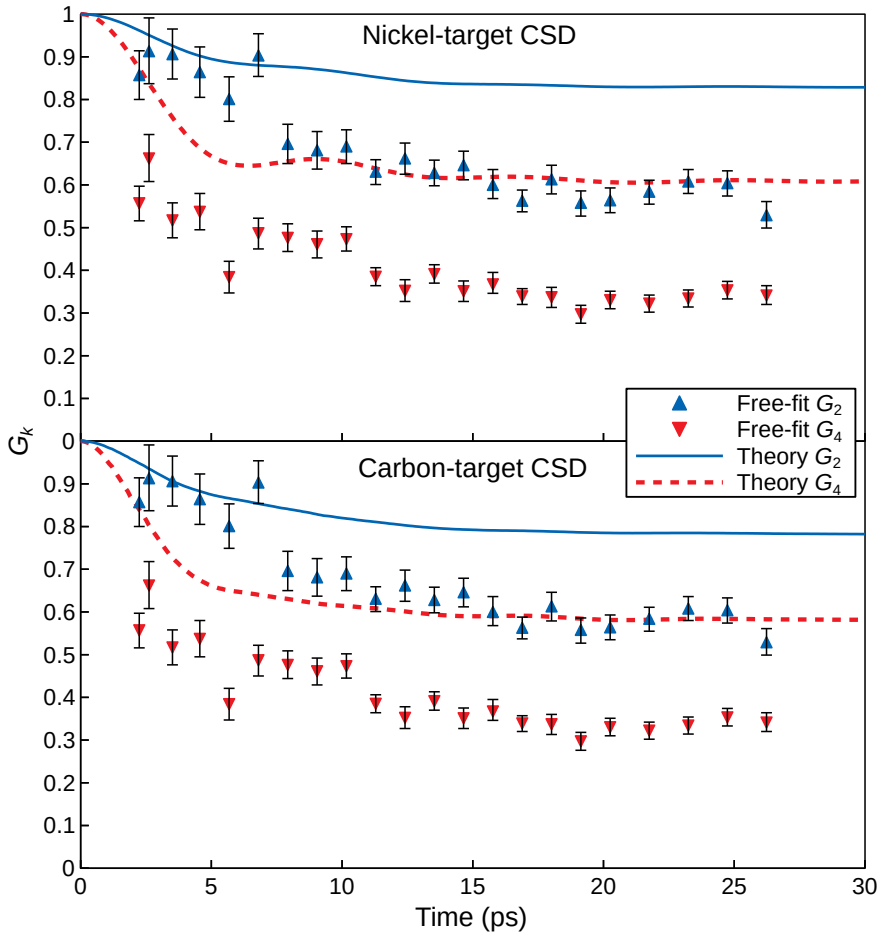

FIGURE 6.22: Fits to the in-flight component of the ^{56}Fe 2_1^+-state TDRIV measurement using the Monte-Carlo simulation, constrained either to the CSD expected from the nickel target, or the carbon target. The fit details are listed in Table 6.5. It is clear that neither CSD is able to reproduce the magnitude of the free-fitted G_k values.

individual-state fits the atomic states in O-like ions arising from the ground configuration ($1s^2 2s^2 2p^4$), and the first-excited state in the Ne-like ions were included. This is because these states will have a significant impact on the $G_k(t)$ magnitude, which was less important to capture in the individual-state fits. These fits were all performed using the adopted value of $g = +0.546$. Due to the sensitivity of these fits to the zero-time offset (owing to the exponential-decay component) the zero-time offset was fixed to $t_0 = 0$ ps to simplify the fits. This decision was justified because the fitted offsets in Table 6.3 were all quite small ($|t_0| < 1$ ps) and averaged around $t_0 \simeq 0$ ps. The fit results for the Monte-Carlo simulations are shown in Fig. 6.22, and for the individual-state fits in Fig. 6.23. Fitted parameters are listed in Table 6.5.

The Monte-Carlo fit results (Fig. 6.22) show that neither CSD was able to reproduce the strong deorientation observed. The individual-state fits (Fig. 6.23) were able to capture the strong deorientation due to occupation of the Ne-like $J = 2$ excited state,

TABLE 6.5: Best-fit values obtained from fits to the in-flight component of the TDRIV angular-correlation data. Occupation uncertainties have not been determined as this was not the primary goal when the codes were written.

				Occupation (%)									
				Na-like		F-like		Ne-like		O-like			
	χ^2_ν	$G_2(\infty)$	$G_4(\infty)$	$3s_{1/2}$	$3p_{1/2}$	$2p_{3/2}$	$2p_{1/2}$	$J=0$	$J=2$	g.s.	$J=1$	$J=2$	$J=0$
Nickel-target CSD													
Monte-Carlo	2.989	0.830	0.612	Boltzmann distribution, $T = 1$ eV									
Individual-state	1.436	0.644	0.312	39	0	21	0	5	36				
Carbon-target CSD													
Monte-Carlo	2.241	0.784	0.582	Boltzmann distribution, $T = 27$ eV									
Individual-state	1.318	0.593	0.341	24	0	27	1	10	24	0	0	14	0
Unrestricted occupation													
Individual-state	1.304	0.582	0.340	9	0	12	15	11	26	13	0	14	

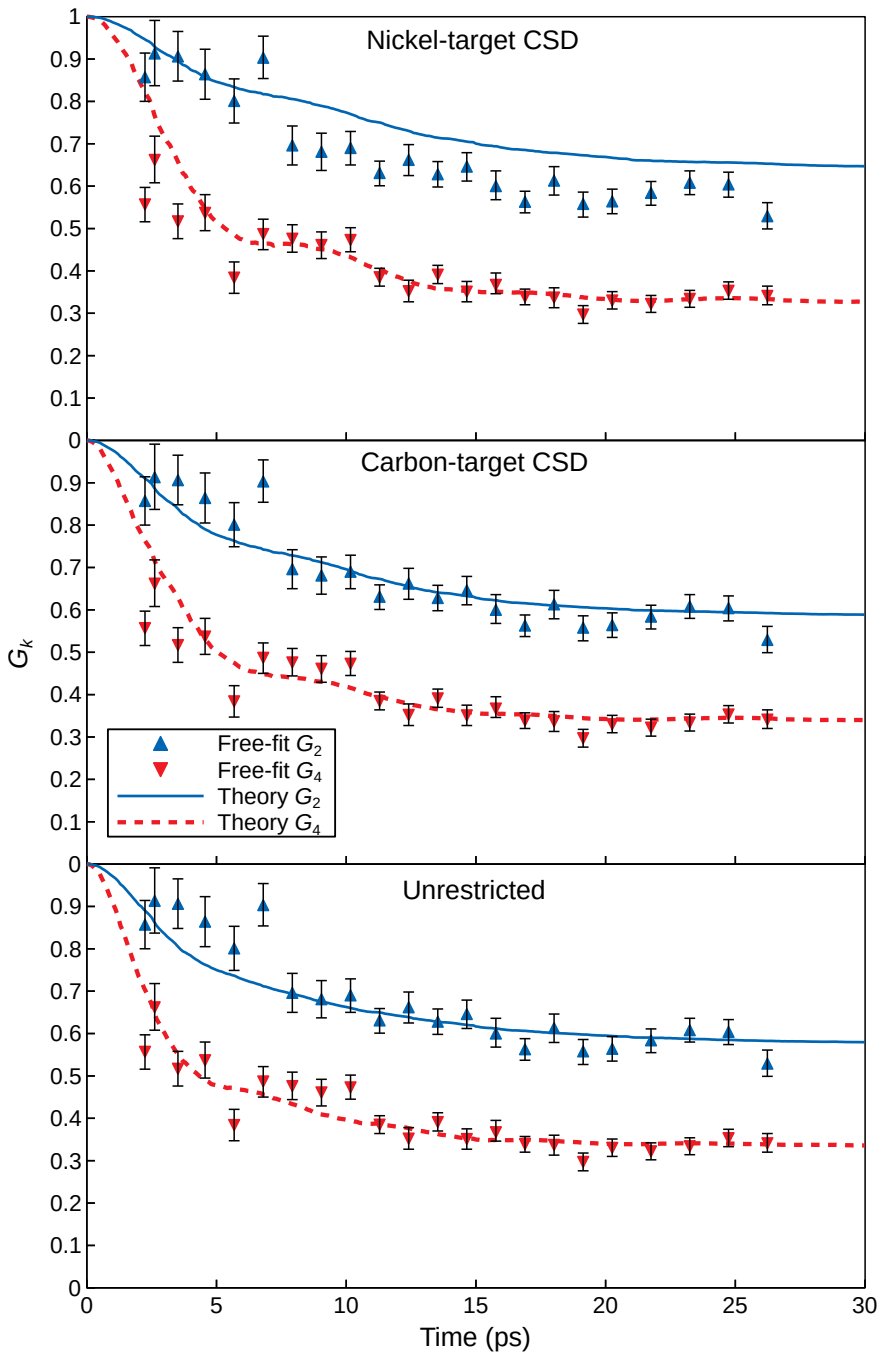

FIGURE 6.23: Fits to the in-flight component of the ^{56}Fe 2_1^+-state TDRIV measurement using individual atomic states expected to contribute strongly to the interaction (see in-text). Individual-state occupations were either restricted to the nickel-target CSD, carbon-target CSD, or unrestricted. The fit details are listed in Table 6.5. It is curious to note that while the carbon-target and unrestricted fits better match the observed magnitude of G_2 and G_4, the nickel-target fit possibly better captures the early oscillation most visible in G_4 ($t \lesssim 15$ ps).

with the unrestricted fit giving only a small improvement over the restricted fit using the carbon-target CSD. It is immediately clear from these fits that the centroid of the CSD is closer to F-like ions than to Na-like. What is also clear is that the Monte-Carlo-simulation fits were unable to capture the observed deorientation, regardless of the CSD used. The unrestricted individual-state fit indicates that the Ne-like fraction is largest, with equal parts F-like and O-like. Comparing the unrestricted individual-state fit to the fit restricted to the carbon-target CSD, the ratio of the Ne-like ground state to the excited state remains the same. With the forced reduction in the O-like occupation, the ground-state falls to 0% while the $J = 2$ state remains at 14%. Most dramatically, the similar proportion of F-like $2p_{3/2}$ and $2p_{1/2}$ in the unrestricted fit goes almost completely to the $2p_{3/2}$ state in the restricted fit, though the overall F-like fraction is almost the same. The similar χ^2_ν and steady occupation of F-like and Ne-like ions between the unrestricted and restricted fits, indicates that contributions from these states can be modelled. The large proportion of Ne-like $J = 2$ and selective occupation of O-like $J = 2$, which contradict the occupations suggested by the heatmap, may be compensating for unaccounted deorientation arising from core-hole excited states and rapid transitions in the first few picoseconds, and warrants further investigation.

A key component when modelling the absolute $G_k(t)$ values observed in the in-flight component is their sensitivity to the contributions from core-hole excited atomic states (e.g. $[\mathrm{He}]2s^1 2p^6 3s^2$ in Na-like ions), which have lifetimes $\tau \lesssim 5$ ps. The atomic-structure calculations performed for the Monte-Carlo simulation only include valence configurations. This is almost certainly the reason why the Monte-Carlo-simulation fits are unable to model the in-flight component. The individual-state fits are unable to account for the decay of these states, and additional effects due to rapidly fluctuating states. The individual-state fits do, however, give some insight into the long-term atomic-state contributions. Unfortunately, the relative occupations will likely be skewed by deorientation arising from the strong, fluctuating core-hole atomic states. It is possible that the unexpectedly large occupations of the Ne-like and O-like $J = 2$ states approximate the average interaction of these unaccounted-for states. However, such investigations are outside the scope of this project. Measuring the $G_k(t)$ trend over the early timescales which these states are expected to significant contribute ($t < 2$ ps) will allow for more detailed modelling, and hence a better understanding of the hyperfine interaction to be developed. Already, the Monte-Carlo simulation is capable of modelling decays from these core-hole states, but their atomic-structure properties must be calculated. With the calculated properties available, early time-point data ought to allow for the initial occupation of these states to be modelled and the full behaviour of the in-flight component to be predicted. Such understanding will be important when the model is applied to the interpretation of the ^{54,56}Fe time-integral RIV data in §6.3.

6.2.10 Conclusion

In order to determine the 2_1^+-state g factor from the ^{56}Fe TDRIV dataset, several different approaches were taken to fitting the $R(t)$ trend. To guide the fitting attempts, the Monte-Carlo simulation was first used to understand which atomic states within the ionic species present should contribute significantly to the hyperfine interaction. Once these states were identified, their individual hyperfine interaction frequencies were used in fitting attempts. First, a preliminary fit was performed, whereby a double-cosine function, representing two states having $J = 1/2$ spin and large hyperfine interaction frequencies, was fit. Following this, the identified atomic states were fitted to the $R(t)$ function, with $G_k(t)$ values appropriately calculated from theory (see §2.3.3). These individual states were allowed to vary in occupation, either in an unrestricted manner, or limited by the population of the ionic species to which they belonged. Finally, a Monte-Carlo simulation was used to compare these results with the comprehensive atomic-decay simulation. Similar g factor values were obtained from all fits, agreeing within uncertainties.

While there was strong agreement between the fitting approaches described in §6.2.6, there are still uncertainties relating to the precise occupation of individual atomic states through time. Considerable uncertainty also remains surrounding the overall behaviour of the hyperfine interaction, evidenced by the in-flight angular-correlation fits. The presence of core-hole (deep vacancy) states followed by a cascade of Auger and photon emissions may explain this additional deorientation. Measurements extending to earlier, possibly sub-picosecond time points would improve this understanding. A plunger device and particle-detector setup has been developed at ANU's Research School of Physics, with the capability not only to probe these early time points, but to simultaneously probe differing CSDs, for future measurements.

In conclusion, the task of fitting the complex hyperfine interaction arising from this charge-state ensemble has many variables, but a methodical and stepwise approach has allowed the extraction of a precise g factor from the unique oscillations present in the stop-component of the $G_k(t)$ measurement. Further measurements are warranted, to a) develop a better understanding of the hyperfine interaction arising within these ions, particularly over sub-picosecond timescales, and b) allow for a more confidently (and precisely) determined g factor.

6.3 ^{54,56}Fe Time-Integral Recoil-In-Vacuum Measurement

A time-integral RIV measurement was performed on the 2_1^+ states in ^{54,56}Fe to complement the TDRIV measurement described in §6.1. The difference between the lifetime of the 2_1^+ states in ^{54,56}Fe presents an opportunity to compare the behaviour of the hyperfine interaction over brief ($\tau \sim 1$ ps) and intermediate ($\tau \sim 10$ ps) timescales, and further test the *ab initio* model implemented in **RIV Simulate**. Analysis of the ^{54,56}Fe 2_1^+-state TIRIV data, using **RIV Simulate**, found that Monte-Carlo simulations using only valence-state atomic configurations were unable to model the observed magnitude of the deorientation. As was proposed in the analysis of the in-flight TDRIV data in §6.2.9, these results suggested that additional components of the hyperfine interaction are present that valence atomic states alone are unable to account for, specifically the presence of core-hole excited atomic states that live for $\tau \lesssim 5$ ps. Using atomic-structure calculations that take these core-hole excited states into account, it may be possible to describe time-integral vacuum deorientation if the initial distribution of states is accurately modelled. The hyperfine interactions over these early timescales ($t \lesssim 1$ ps) warrant additional measurements to probe them, as to validate and improve the *ab initio* description of the hyperfine interactions for $Z \sim 30$ nuclei with CSDs near to the neon atomic shell closure. Developing such an understanding is important for accurately interpreting the results of radioactive-ion-beam measurements using the TIRIV technique for $Z \sim 30$ nuclei.

6.3.1 Methods

A measurement of the time-integral vacuum attenuation in the 2_1^+-state angular correlation of ^{54}Fe and ^{56}Fe was performed in inverse kinematics using the RIV technique by Prof. Andrew Stuchbery, A. Prof. Tibor Kibédi, and Mr. Asif Ahmed in April 2013. The measurement was performed using ANU's Hyperfine Spectrometer [213]. The ANU's 14 UD Pelletron accelerator was used to produce beams of ^{54}Fe and ^{56}Fe at 110 MeV. The 110 MeV beam nuclei were Coulomb excited on a single-layer 0.5 mg/cm^2 carbon target. The ^{54}Fe or ^{56}Fe ions recoiled into vacuum at small scattering angles, while carbon ions were detected forward-scattered using an annular-style detector (see Fig. 4.6 for reference) located 27 mm down-beam of the target. Eight particle detectors were radially spaced 12.5 mm from the beam to the detector edge, with detectors at equivalent ϕ angle having their outputs coupled to give five particle-detector channels (P_1–P_5), with average angles $\phi = 0°, 45°, 90°, 135°, 180°$, respectively. The active area of the SiPD chips used was 8.8 × 9.8 mm, with an average scattering angle $\langle\theta\rangle = 30°$. Coincident γ rays were detected using two NaI detectors (γ_1 and γ_4) positioned alternately at $\pm 90°$ or $\pm 45°$ for each isotope and energy, and two HPGe detectors fixed at $\pm 135°$ (γ_2 and γ_3). Data were acquired using the Analogue DAQ. Coincident γ-ray spectra were obtained by gating

using appropriate time signals from the γ-ray and particle detectors, as well as energy signals from the particle detectors. Variation in efficiency between particle detectors was accounted for by normalising yields using the downscaled particle singles rate.

6.3.2 Results

The data were collected over three runs for each Fe isotope. The details of each run can be found in Table 6.6. For both isotopes, runs 2 and 3 were analysed together as they had the same detector angles.

TABLE 6.6: Run details for the ^{54,56}Fe TIRIV experiment.

	Isotope	γ_1 angle (deg)	γ_4 angle (deg)
Run 1	^{54}Fe	90°	−90°
Runs 2 & 3	^{54}Fe	45°	−45°
Run 1	^{56}Fe	45°	−45°
Runs 2 & 3	^{56}Fe	90°	−90°

The data were analysed, by the author, as described in §3.3. Data were converted into the ROOT tree format and γ-ray spectra containing γ-particle coincidence events were obtained by gating on the γ-ray- and particle-detector time spectra. Example HPGe and NaI γ-ray-detector time spectra are shown in Fig. 6.24 and Fig. 6.25, respectively. Note there is a long tail on the higher side of the prompt time peak in the HPGe spectrum in Fig. 6.24 due to low-energy γ-ray events, that are mostly Compton background. Data were analysed with no random-coincidence gate in the high region, and with a random coincidence gate set from channels 4200–4350. There was no difference in the photopeak counts, and so gates on both the low and high region were included. Example 'true' γ-ray spectra for ^{54}Fe and ^{56}Fe for both the HPGe and NaI γ-ray detectors are shown in Figures 6.26–6.29. Tables of photopeak counts (scaled using the singles rate in particle detector pair 3) and plots of angular correlations for each run can be found in Appendix B.2.

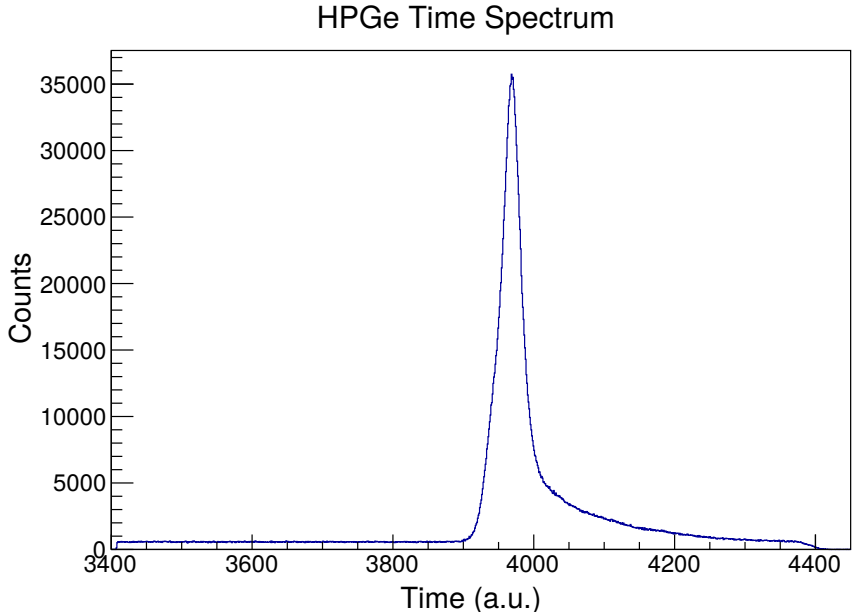

FIGURE 6.24: Spectrum of time differences between a HPGe γ-ray detector, in this case γ_2, and any particle-detector signal. There is a clear time correlation indicated by the large peak, which was used to obtain the prompt γ-ray spectrum. Gates to determine random coincidences were set on the low and high sides of the prompt peak. The long tail of the prompt peak is mainly due to Compton events that are of no consequence to the measurement.

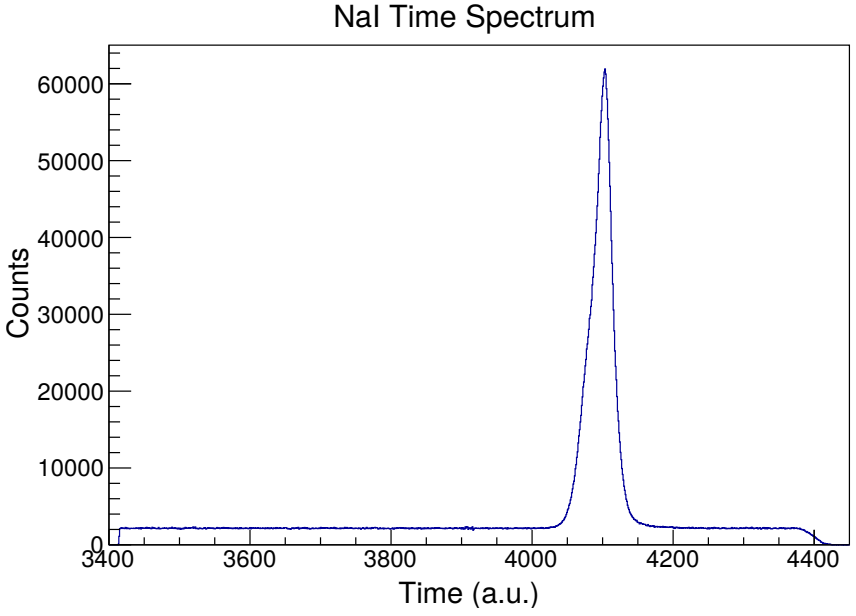

FIGURE 6.25: Spectrum of time differences between a NaI γ-ray detector, in this case γ_1, and any particle-detector signal. There is a clear time correlation indicated by the large, which was used to obtain the prompt γ-ray spectrum. Note that the tail is absent in comparison to the HPGe time spectrum in Fig. 6.24. Gates on both sides of the peak were used to obtain random-coincidence spectra.

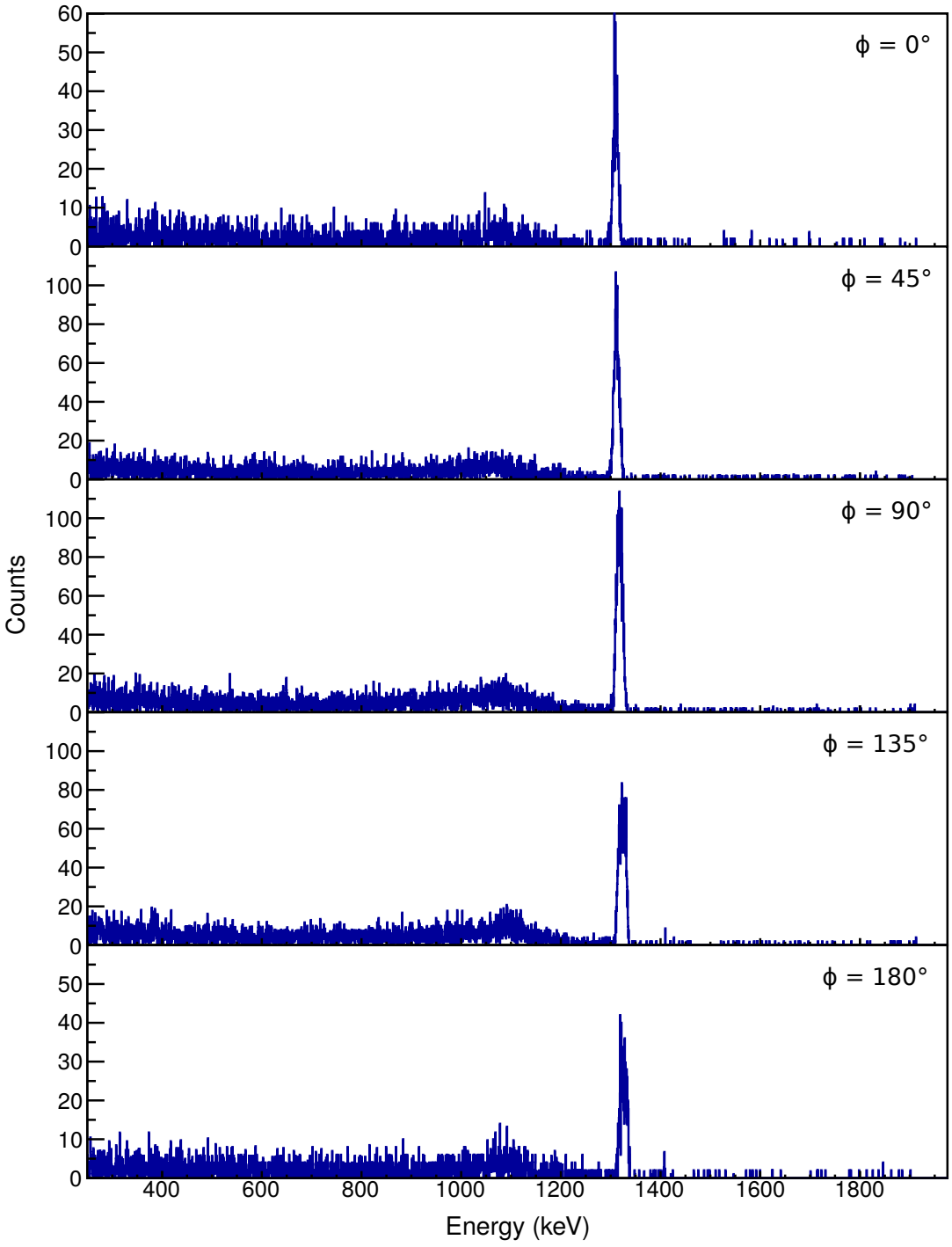

FIGURE 6.26: 'True' ^{54}Fe γ-ray spectrum in coincidence with each particle-detector, from γ_2 (HPGe), run 1. Observed γ-rays come only from the excited, Doppler-shifted ^{54}Fe 2_1^+ state and Compton scattering. A minuscule unshifted ^{56}Fe 2_1^+ peak is visible in the $\phi = 135°, 180°$ panels due to uneven subtraction (negative counts in the subtracted peak are not shown).

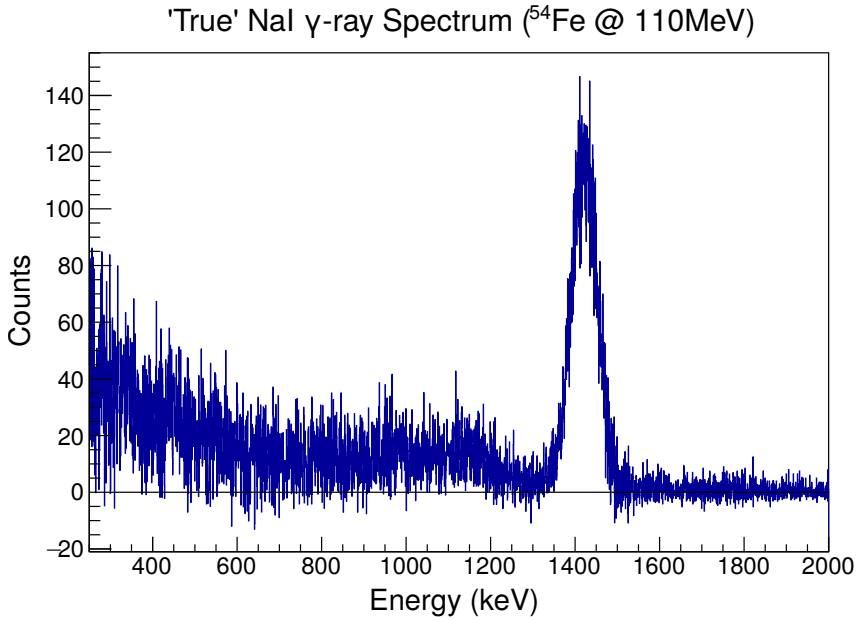

FIGURE 6.27: 'True' ^{54}Fe γ-ray spectrum with all particle-detector coincidences summed, from γ_1 (NaI). Observed γ-rays come only from the excited ^{54}Fe 2_1^+ state and Compton scattering. The zero-count line has been extended across the horizontal length for clarity.

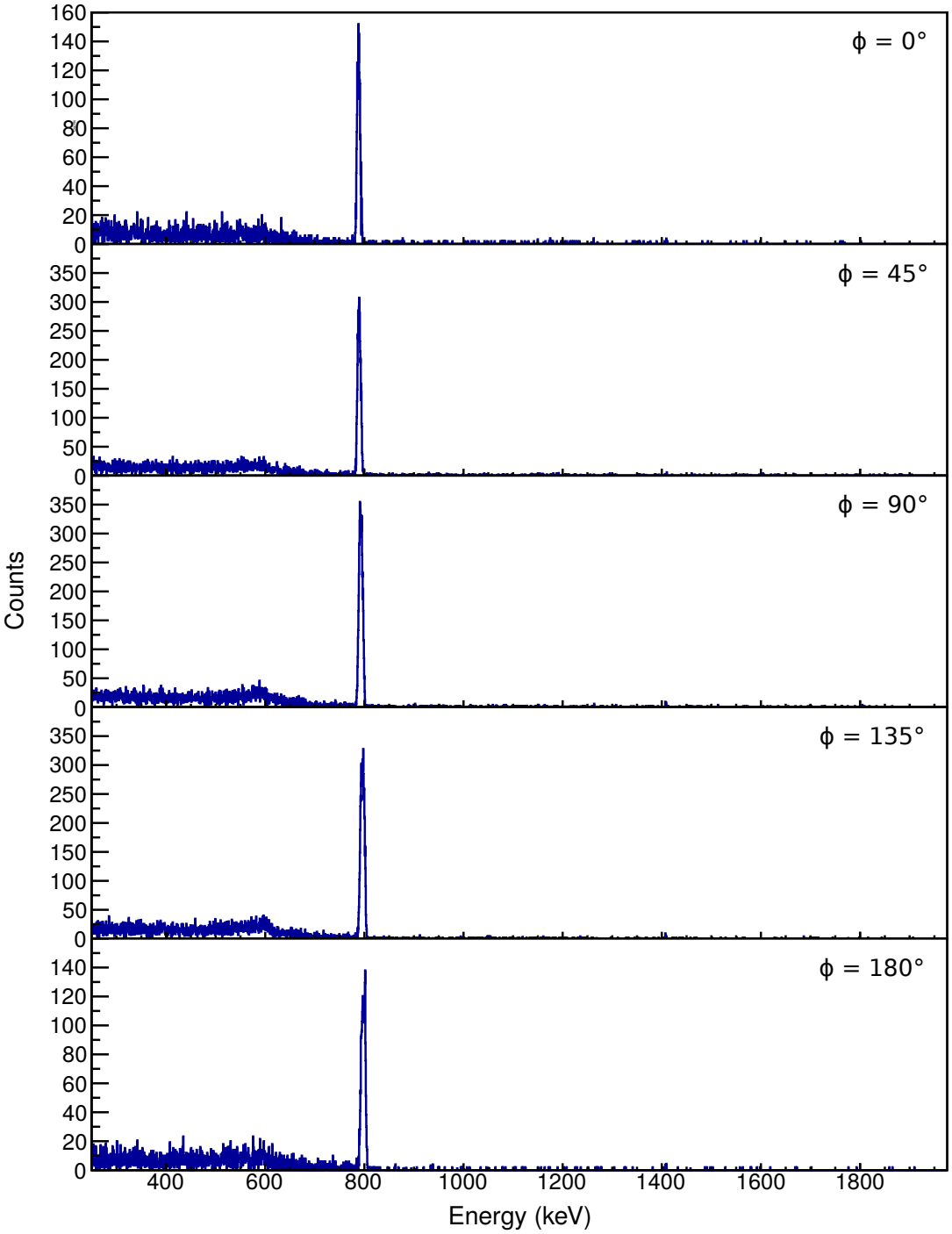

FIGURE 6.28: 'True' ^{56}Fe γ-ray spectrum in coincidence with each particle-detector, from γ_2 (HPGe), run 1. Observed γ-rays come only from the excited, Doppler-shifted ^{56}Fe 2_1^+ state and Compton scattering.

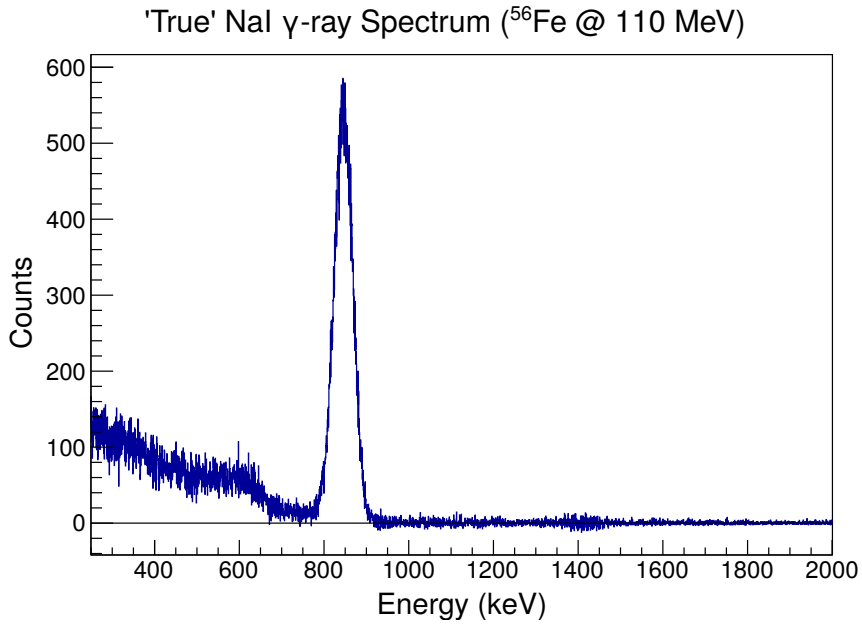

FIGURE 6.29: 'True' ^{56}Fe γ-ray spectrum with all particle-detector coincidences summed, from γ_1 (NaI). Observed γ-rays come only from the excited ^{56}Fe 2_1^+ state and Compton scattering. The zero-count line has been extended across the horizontal length for clarity.

TABLE 6.7: Approximate CSD for Fe ions recoiling at $E_{\text{rec}} \simeq 50$ MeV out of a carbon target.

$Z - Q$	Ionic species	Population
7	N-like	3%
8	O-like	13%
9	F-like	27%
10	Ne-like	34%
11	Na-like	15%
12	Mg-like	6%

The first step taken in the analysis was to obtain free-fitted $G_k(\infty)$ values using RIV Simulate, as per §5.6.4. The fitted $G_k(\infty)$ values are listed in Table 6.8. The fitted angular correlations are shown in Fig. 6.30. The uncertainties on the data points were inflated until the fits gave $\chi^2_\nu = 1.000$ so that the uncertainties in the fitted $G_k(\infty)$ values were appropriate. Immediately, it is obvious that the ^{54}Fe ions experience less deorientation than the ^{56}Fe ions; this is expected due to the lifetime of the ^{56}Fe 2^+_1 state being almost 10 times longer than that of the ^{54}Fe 2^+_1 state, and $G_k(\infty) \propto g\tau$ as per Ref. [206].

The next step in the analysis was to determine the expected CSD for the Fe ions recoiling out of the carbon target. Charge-state-distribution measurements of ^{56}Fe recoiling out of a carbon target (see Fig. 6.20) were used to approximate the CSD expected (see Table 6.7) in this measurement.

The CSD shown in Table 6.7 is very similar to that expected in the TDRIV ^{56}Fe measurement from a carbon target. Comparison of the ^{56}Fe 2^+_1 $G_k(\infty)$ values presently measured to those obtained from fitting the in-flight component of the TDRIV measurement on ^{56}Fe (see §6.2.9) reveals good agreement between the two, indicating that the hyperfine interactions present in both measurements were similar. The lifetime of the ^{54}Fe 2^+_1 state is almost an order of magnitude smaller than that of the ^{56}Fe 2^+_1 state. Because the two isotopes will experience almost identical hyperfine interactions (due to recoiling at almost the same velocity and therefore having almost the same CSD), the difference between the two isotopes' $G_k(\infty)$ values should depend only on the state lifetime and g factor. This provides an opportunity to probe potential differences in the hyperfine interaction between short timescales ($\tau \sim 1$ ps) with $g \sim 1$, and longer timescales ($\tau \sim 10$ ps) with $g \sim 0.5$, and whether the Monte-Carlo simulation can describe both cases using the same initial atomic-excited-state distribution.

In fitting, the values $g(2^+_1;^{56}\text{Fe}) = +0.546$ (obtained in §6.1) and $g(2^+_1;^{54}\text{Fe}) = +1.02$ were used, the latter obtained by scaling the relative measurement performed by East *et*

TABLE 6.8: ^{54,56}Fe 2_1^+-state $G_k(\infty)$ values obtained by free-fitting G_2 and G_4 to the measured angular correlations, and using the Monte-Carlo simulation with the CSD listed in Table 6.7.

	Free-fitted			Monte-Carlo simulation			
Isotope	$G_2(\infty)$	$G_4(\infty)$	χ^2_ν	$G_2(\infty)$	$G_4(\infty)$	T	χ^2_ν
^{54}Fe	0.847(24)	0.725(18)	1.000[a]	0.936	0.832	180 eV	2.15
^{56}Fe	0.569(14)	0.410(10)	1.000[a]	0.721	0.550	940 eV	10.20

[a] Uncertainties in angular-correlation data-points were inflated until $\chi^2_\nu = 1.000$.

al. [57] using $g(2_1^+;^{56}\,\mathrm{Fe}) = +0.546$. Uncertainties were omitted as they do not affect the following discussion. The data were fitted using **RIV Simulate**'s Monte-Carlo simulation, with the initial excited-atomic-state distribution described by a Boltzmann function, as used in §6.1. The fit results are shown in Table 6.8. Comparison of the $G_k(\infty)$ values obtained from the Monte-Carlo simulations to the free-fit values shows that the loss of anisotropy modelled by the decays is not strong enough to match the data, with the deviation worsening over the longer ^{56}Fe 2_1^+ lifetime. This result further confirms the findings in §6.2.9, this being that the Monte-Carlo simulation, using only valence configurations, is unable to model the observed vacuum attenuation. The deviation worsening over the longer lifetime indicates that the missing hyperfine-interaction strength arises from states acting over the ^{56}Fe 2_1^+ lifetime. However, the possibility remains that the assumption about the form of the initial distribution of excited atomic states may not allow for the correct proportion of states necessary to explain the observed deorientation.

To interrogate the potential contribution of individual atomic states from the ionic species expected to be present, individual-state fits were performed. The individual states comprised the low-lying atomic states in O-like, F-like and Na-like ions, as well as the ground and first-excited state in Ne-like ions; these are expected to be the dominant contributors over the ^{56}Fe 2_1^+ lifetime. Fits were performed using $g(2_1^+;^{54}\,\mathrm{Fe}) = +1.02$ and $g(2_1^+;^{56}\,\mathrm{Fe}) = +0.546$, with the atomic states belonging to each ionic species having their occupation restricted by the CSD in Table 6.7. The resulting (fitted) occupations are shown in Table 6.9. When fitting individual atomic states, the $G_k(\infty)$ values obtained are in good agreement with the free-fitted $G_k(\infty)$ values ($\chi^2_\nu \simeq 1$) for both the ^{54}Fe and ^{56}Fe 2_1^+ states. For the O-like and Ne-like ions the occupation goes almost entirely into the $J = 2$ state. For the short-lived ^{54}Fe 2_1^+ state ($\tau \sim 1$ ps), atomic states having weak hyperfine interactions (e.g. the Ne-like ground state) are completely absent. For the longer-lived ^{56}Fe 2_1^+ state ($\tau \sim 10$ ps), the same O-like $J = 2$ occupation is observed, and the Ne-like is still dominated by the $J = 2$ excited state. Comparing the F-like occupations, it is worth noting that the excited $2s_{1/2}$ occupation, having $\tau \lesssim 8$ ps, disappears for the ^{56}Fe fit, and instead occupation goes entirely to the $2p_{3/2}$ ground state. This suggests that the short-lived F-like $2s_{1/2}$ is influential over the 1 ps range, but does not have a

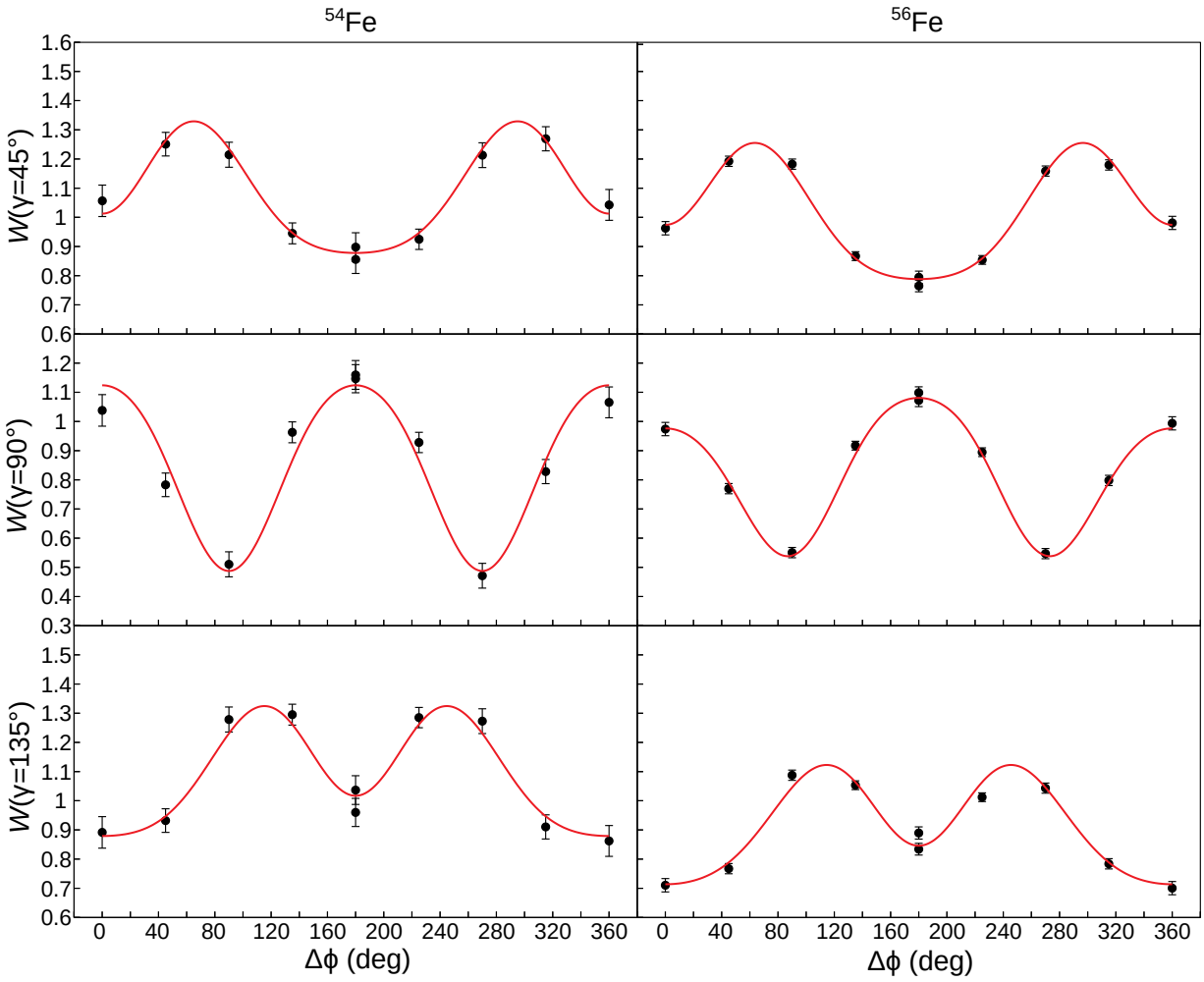

FIGURE 6.30: Measured angular-correlation data points overlaid with theoretical angular correlations having the free-fitted G_k values shown in Table 6.8.

significant impact over the 10 ps range, as should be expected. The Na-like occupations present a strange case, with the $3s_{1/2}$ ground state fully occupied for the ^{54}Fe fit, and unoccupied for ^{56}Fe. Instead, the ^{56}Fe fit puts the intensity into the weakly interacting $3p_{3/2}$ and $3d_{3/2}$ states. This is an unrealistic outcome, as ground-state occupation should dominate over the longer time-span, and the two isotopes should have the *same* initial distribution of atomic states. The Na-like $3p_{3/2}$ and $3d_{3/2}$ may instead be mimicking the Mg-like contribution, or other higher-excited atomic states, which have been left out in the individual-state fits. The overall conclusion to be drawn is that $J > 1/2$ atomic-state interactions, and/or atomic-decay sequences, must contribute strongly to the measured hyperfine interaction.

6.3.3 Discussion

Modelling the time-integral hyperfine interaction for $Z \sim 30$ nuclei, with short-lived nuclear states ($\tau \lesssim 10$ ps), is a complex task. Many atomic states across the ion ensemble are anticipated to contribute significantly to the interaction, with some having $B \sim 15$ kT hyperfine fields but living for only femtoseconds, others having $B \sim 5$ kT hyperfine fields and acting over picoseconds, and others having $B \lesssim 1$ kT fields but living much longer than the nuclear-state lifetime. That the occupation of states is in flux over these timescales further complicates the model. The Monte-Carlo simulation (using only valence atomic states) was used to model the observed vacuum deorientation. The results (see §6.3.2) showed that the valence states alone are not sufficient to explain the measured vacuum deorientation, and/or that assumptions regarding the initial distribution of excited atomic states were incorrect. To help probe the latter possibility, individual-state fits were performed to determine the static-state occupations best able to explain the observed deorientation.

Over the brief ^{54}Fe 2_1^+ lifetime ($\tau = 1.2$ ps), contributions from core-hole excited states are expected to be significant. This is because atomic-structure calculations predict these states to survive for several picoseconds. Over the short ^{54}Fe 2_1^+ lifetime there will also be many atomic transitions occurring. Such a scenario is not well-approximated by a static superposition of atomic states. Regardless, the atomic-state occupations obtained in Table 6.9 should reveal the character of the contributing states. Indeed, the absence of any occupation of weakly interacting atomic states strongly suggests that core-hole states with strong hyperfine fields are significantly contributing. The absence of any Ne-like ground-state ($J = 0$) occupation also suggests that these ions may be highly excited.

TABLE 6.9: Individual atomic-state occupations resulting from fits to the ^{54,56}Fe time-integral angular-correlation measurements, using the states identified as most likely to contribute in §6.2.4. Occupation uncertainties have not been determined as this was not the primary goal when the codes were written.

	$G_2(\infty)$	$G_4(\infty)$	O-like				F-like			Ne-like		Na-like				χ^2_ν
			g.s.	$J=1$	$J=2$	$J=0$	$2p_{3/2}$	$2p_{1/2}$	$2s$	g.s.	$J=2$	$3s$	$3p_{1/2}$	$3p_{3/2}$	$3d_{3/2}$	
^{54}Fe	0.888	0.726	0%	0%	15%	0%	22%	0%	8%	0%	38%	17%	0%	0%	0%	1.108
^{56}Fe	0.554	0.393	0%	0%	15%	0%	30%	0%	0%	6%	32%	0%	0%	12%	5%	1.132

Over the ^{56}Fe 2_1^+ state lifetime ($\tau \sim 10$ ps), the core-hole excited states are expected to have less influence, and ground-state configurations should become more important. The fit results in Table 6.9 for ^{56}Fe are almost the same as for ^{54}Fe, with two notable differences: the F-like ions completely occupy the ground state, and the Na-like ions have no ground-state occupation. The former makes sense, as the F-like atomic states should preferentially and rapidly decay to the ground state. The latter, however, seems unrealistic, as we expect Na-like ground-state occupation to increase significantly with time. Therefore, this change may reflect the contribution from Mg-like ions and other weakly interacting, long-lived states, as was concluded in §6.3.2.

Comparing to the in-flight TDRIV fits in §6.2.9, it can be seen that the strong O-like $J = 2$ contribution is matched in all fits. This state has the largest hyperfine-field strength at $B \simeq 17$ kT. Barring preferential occupation of this state, the O-like $J = 2$ occupation may be compensating for core-hole excited states and rapid decays not included in the fit. That it fits the same proportion in all cases, for both time-integral and time-differential data, and unrestricted or restricted atomic-state occupation, warrants further investigation. Such investigations should consist of a Monte-Carlo simulation that includes core-hole excited states, as these states and their fast transitions are important factors to consider when modelling absolute G_k values.

It should be noted, fits that have $\chi^2_\nu \simeq 1$ can be obtained for both the ^{54}Fe and ^{56}Fe data by simply using the F-like $2p_{3/2}$ and Ne-like $J = 0$ ground-state at approximately $\sim 70\%$ and $\sim 30\%$ occupation, respectively. This shows the challenge in interpreting time-integral data: fitting such a range of atomic states (i.e. a large parameter space) without strong constraints makes finding true and realistic minima difficult. The task is further complicated by the effect that fluctuating atomic states (rapid sequences of transitions) have on the magnitude of G_2 and G_4. This is why *ab initio* modelling of the atomic behaviour is important for time-integral measurements. If the effect that atomic-decay cascades have on magnitude of G_2 and G_4 is ignored, then the simple F-like $2p_{3/2}$ and Ne-like $J = 0$ may be interpreted as approximating the dominant spin and average strength of the hyperfine interaction taking place. This is because the ratio between G_2 and G_4 is sensitive to the atomic spin. For example, Fig. 6.31 shows the in-flight component of $G_k(t)$ for several $J = 1/2$ atomic states, and Fig. 6.32 shows the same for two $J = 3/2$ states. In the $J = 1/2$ case, the value of G_2 is similar, no matter how large the field strength is. In the $J = 3/2$ case, G_2 and G_4 can be much closer in magnitude. Therefore, if $J = 1/2$ or $J = 0$ interactions are dominant, or the hyperfine interactions are weak, then G_2 will be close to unity, and the ratio of G_2 to G_4 will not be near unity. If $G_2 \lesssim 0.75$ is measured, and the ratio of G_2 to G_4 isn't significantly greater than unity, then strongly interacting atomic states with $J > 1/2$ must be contributing. However, to reiterate, this

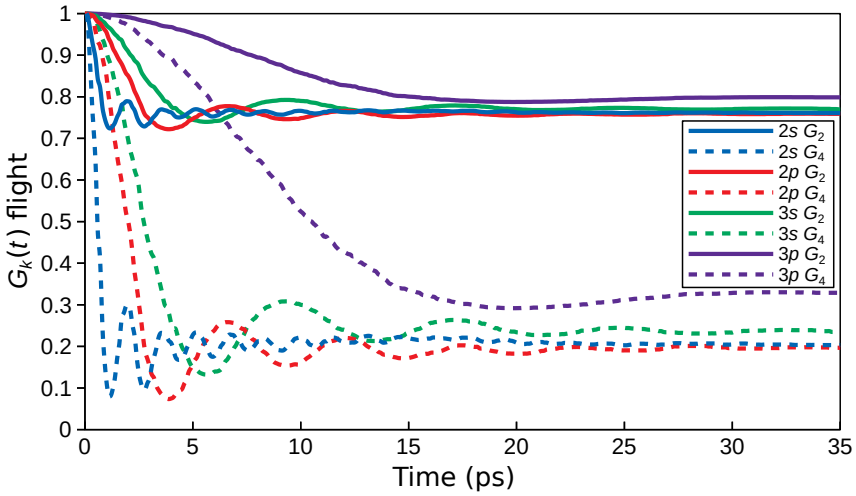

FIGURE 6.31: Plots of the in-flight component of $G_k(t)$ for the $J = 1/2$ F-like $2s$, $2p$ and Na-like $3s$, $3p$ states using the ^{56}Fe 2_1^+ lifetime $\tau = 9.3$ ps. Despite the large range of hyperfine-field strengths covered by these states ($2 \leq B \leq 30$ kT), the resulting $G_k(\infty)$ values are all quite similar, and $G_2 > 0.75$ in all cases.

is assuming that atomic-decay cascades, i.e. from core-hole excited states, may be ignored, which is not likely to be the case. However, that a F-like $2p_{3/2}$ and Ne-like $J = 0$ state together can fit the data so well, suggests that the F-like ground-state is a dominant component of the hyperfine interaction across the nuclear state's lifetime. However, beyond this rudimentary analysis, time-differential measurements must be performed to thoroughly tease out the individual states that are contributing within an ionic ensemble.

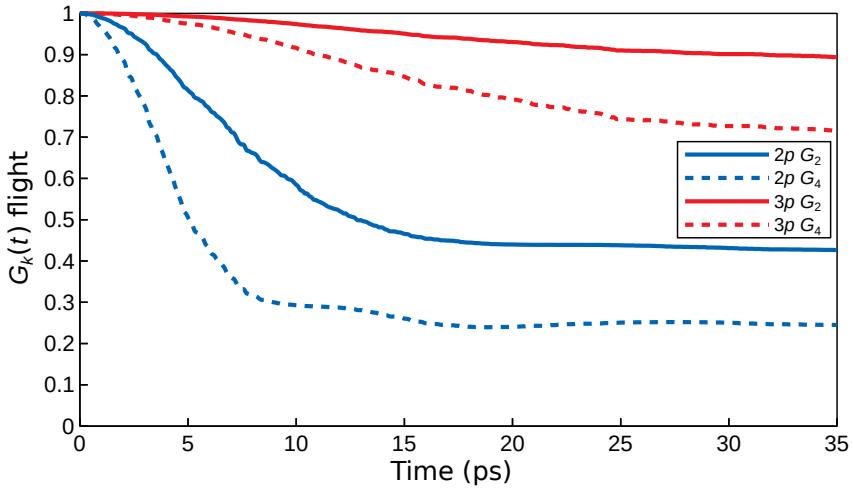

FIGURE 6.32: Plots of the in-flight component of $G_k(t)$ for the $J = 3/2$ F-like $2p$ and Na-like $3p$ states using the ^{56}Fe 2_1^+ lifetime $\tau = 9.3$ ps. The two states have somewhat similar hyperfine-field strengths as compared to the range of $J = 1/2$ states, however the resulting $G_k(\infty)$ values differ greatly. The relative magnitude of G_2 and G_4 is also dramatically different from the $J = 1/2$ case in Fig. 6.31, while the result for $2p_{3/2}$ better matches the relative magnitude of the free-fitted values. It should be noted that atomic-decay cascades having the appropriate lifetime and hyperfine-field strength can also reduce the magnitude of G_2 and G_4 in a similar fashion.

6.4 ^{76}Ge Time-Dependent Recoil-In-Vacuum Measurement

The aim of this experiment was to observe the time-dependent attenuation in the angular correlation of the ^{76}Ge 2_1^+ state. This experiment was motivated by the discrepancy observed in measured time-integral vacuum-attenuation coefficients, $G_k(\infty)$, between 2_1^+ states in Ge and Se isotopes [134, 206]. The experiment aimed to reproduce the charge-state distribution (CSD) present in the time-integral measurement using ^{76}Ge, with a recoil velocity $\beta \sim 0.045$, therefore having a charge-state distribution centred on Si-like ions, as per the parameterisation presented in Ref. [134]. It is expected that some Na-like fraction was present in the measurement, so the data were analysed to see if a g factor could be extracted from the hyperfine interaction with the Na-like atomic ground state. It was found that the quasi-exponential contribution of the majority of the ionic states to the $G_k(t)$ trend allowed for the weak Na-like $J = 1/2$ ground-state oscillation to be isolated. A simple cosine function was fit to this oscillation, after deducting the quasi-exponential component, and allowed $g(2_1^+)$ to be determined. However, due to large uncertainties in the data points, and in allowing a time offset in the fit, $g(2_1^+)$ could not be precisely deduced. Instead, a range $0.27 \leq g \leq 0.32$ was proposed.

6.4.1 Methods

A measurement of the time-dependent vacuum attenuation in the 2_1^+-state angular correlation of ^{76}Ge was performed in inverse kinematics using the RIV technique by Prof. Andrew Stuchbery, A. Prof. Tibor Kibédi, and Mr. Asif Ahmed in April 2013. The ANU's 14 UD Pelletron accelerator was used to produce a beam of $^{76}Ge^{13+}$ at an energy of 180 MeV. The beams were Coulomb excited on a dual-layer target having ~ 0.3 mg/cm^2 of carbon on 0.83 mg/cm^2 of nickel, backed by 0.50 mg/cm^2 of iridium. The iridium served to reduce the average charge of the recoiling Ge ions, in turn giving the measured $G_k(t)$ trend a more quasi-exponential character. The ^{76}Ge ions recoiled out of the iridium into vacuum at small scattering angles, while carbon ions were detected forward-scattered using a ring of 8 SiPD detectors with layout and dimensions as shown in Fig. 6.33. Particle detector outputs were paired by equivalent ϕ angle (vertically), as indicated by the dashed lines. The particle-detector array was located 26.7 mm down-stream of the target. Coincident γ rays were detected using four HPGe detectors positioned in the z-x (horizontal) plane at $\theta = 45°$, $\phi = 0°$, $180°$ (γ_1, γ_4) and $\theta = 135°$, $\phi = 0°$, $180°$ (γ_2 and γ_3). The overall detector setup was the same as in Fig. 4.1. HPGe detectors were chosen for use due to their superior energy resolution, capable of resolving Doppler-shifted γ rays emitted from nuclei in flight from unshifted γ rays emitted at rest. Data were acquired using the Analogue DAQ. Variation in efficiency between particle detectors was

accounted for by using the downscaled particle singles rate. Time-dependent measurements were enabled using ANU's recoil-distance plunger. The plunger device operated mechanically, using a worm drive adjusted with a dial having 1/1000-inch graduations to move a stopping foil along the beam axis. The simple, robust design is reliable, but unable to compensate for small changes in distance due foil deformation resulting from beam heating and pressure (as OUPS [141] can). The small recoil angle of the ^{76}Ge ions, owing to the reaction kinematics and particle-detector positions, means that the distance between the target foil and the stopping foil can be used to determine the ion's flight time, and thereby the hyperfine interaction time. The position of the stopping foil was adjusted using a micrometer dial. This dial turned a wormscrew rated to make positional adjustments to the foil of the order of 10^{-5} m. At ion velocities of $\sim 5\%\ c$, this equates to 10^{-12} s time steps. A thick nickel foil was used to stop the recoiling ^{76}Ge ions, but it was thin enough to allow forward-scattered carbon ions to reach the particle detector.

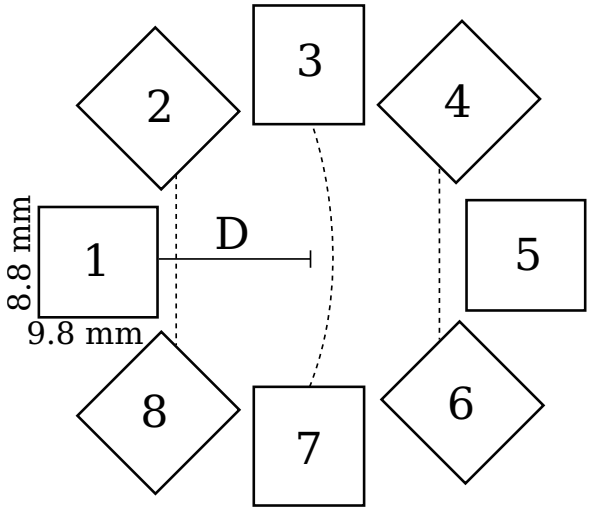

	D (mm)	ϕ
1:	9.5	0°
2:	9.3	45°
3:	7.9	90°
4:	9.6	135°
5:	10.0	180°
6:	9.3	225°
7:	7.7	270°
8:	9.6	315°

FIGURE 6.33: Layout of SiPD particle detectors in the annular-style detector for the ^{76}Ge TDRIV experiment, shown on the left. The dashed lines indicate detector output pairing. The SiPD chips were not perfectly placed, so there is some variation in their radial distances and alignment (details at right), making the ϕ angles slightly smaller than intended in some cases.

6.4.2 Results

The data were acquired over seventeen runs for a sequence of plunger separations. Particle detector 3 failed, so that particle detector pair 3 (P_3) was actually particle detector 7 only. The details of the analysed runs, specifically the plunger distance and time, can be found in Table 6.10. The data were converted into the ROOT tree format, and analysed by the author using the established procedure in §3.3. An example γ-particle time-difference spectrum is shown in Fig. 6.34, while 'true' γ-ray spectra at forward and backwards angles are shown in Fig. 6.35 and Fig. 6.36, respectively. Tables of photopeak

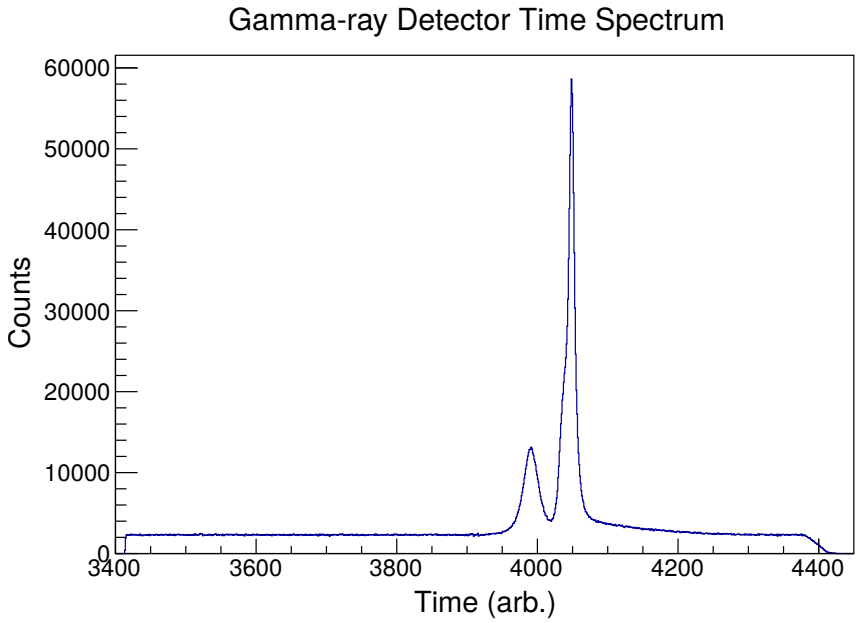

FIGURE 6.34: Example time-difference spectrum between γ-ray detector γ_1 and any particle in the ^{76}Ge TDRIV measurement. There is a clear time correlation indicated by the large peaks at channels 3990 and 4100, which were used to sort out the prompt γ-ray spectrum. Two peaks are visible due to P_4 (lower peak) having different timing characteristics from the other particle detectors (higher peak). Gates were set on the lower and higher side of the two peaks to obtain random-coincidence spectra.

counts and angular-correlations plots for each run can be found in Appendix B.3.

To determine the velocity of the recoiling ions the Doppler shift in the γ-ray energy was used. The energy of a measured γ ray emitted from a relativistic ion is given by [169]:

$$E = E_0 \frac{1-\beta^2}{1-\beta\cos\theta_\gamma}, \tag{6.9}$$

where E is the measured γ-ray energy, E_0 is the γ-ray energy in the rest frame, β is the ion velocity, and θ_γ is the relative angle between the ion's direction of motion and the γ ray, i.e. the lab-frame detector angle.

The mean ion velocity was determined by varying β until the minimum deviation across all measured E/E_0 ratios was obtained. It was found to be $\beta = 0.0451(5)$. This is in good agreement with kinematics [144] and energy-loss [232] calculations, which give $\beta = 0.0456$. This value was then used to convert each run's micrometer reading, relative to the run having the smallest foil gap (run 17), to an expected relative flight time, taking into account the ion's recoil angle. To determine the zero time and verify the flight times, a logarithmic decay curve was plotted. The unshifted peak counts represent the undecayed fraction N, and the sum of the shifted and unshifted counts represents

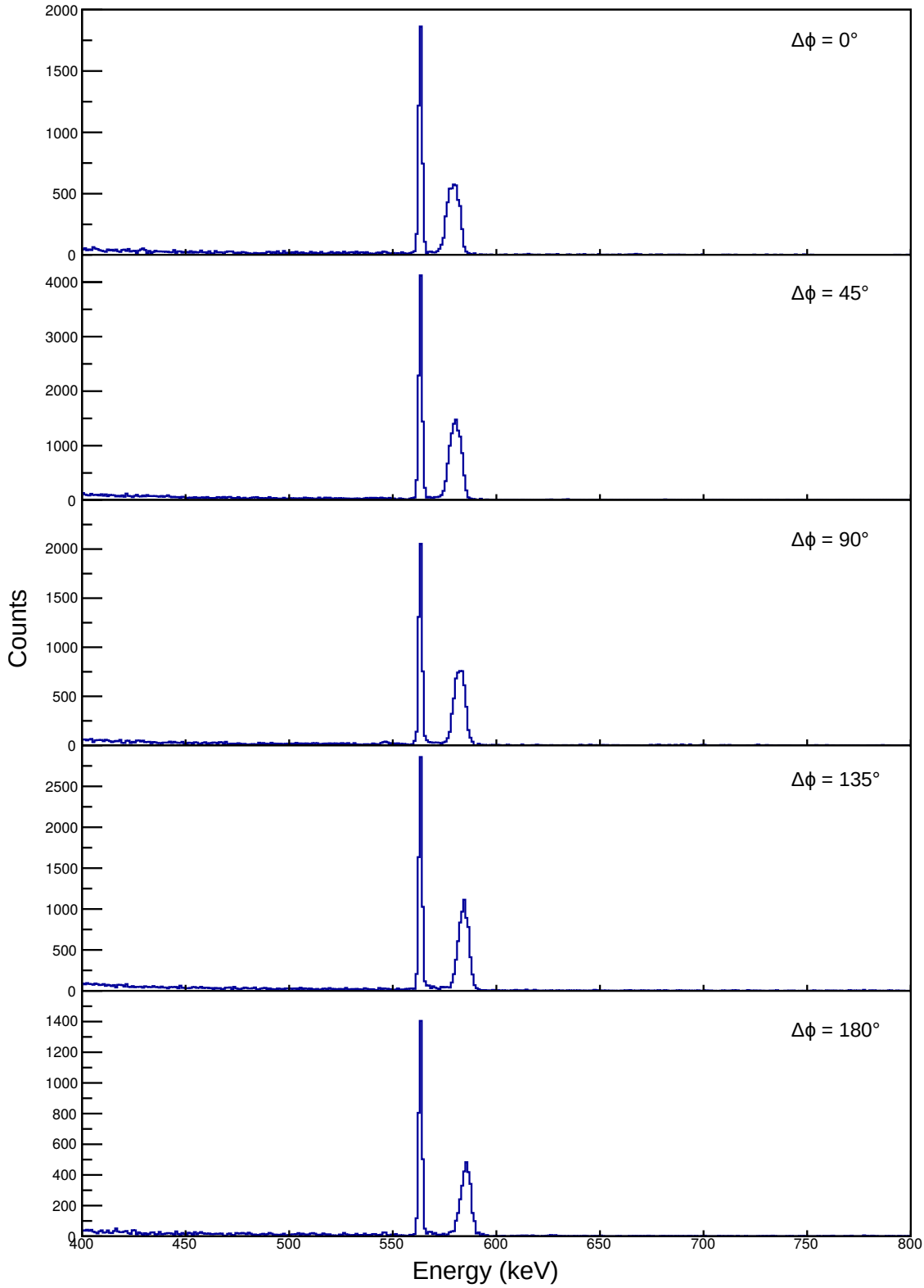

FIGURE 6.35: 'True' γ-ray spectra from the ^{76}Ge TDRIV measurement, run 7, showing separate particle coincidences with $\gamma_1 = 45°$ (forward angle). Note that there is almost no background. Decays originating from stopped nuclei form the narrow, lower-energy peak, while those in flight form the broader, higher-energy peak; they are clearly separated in the spectra.

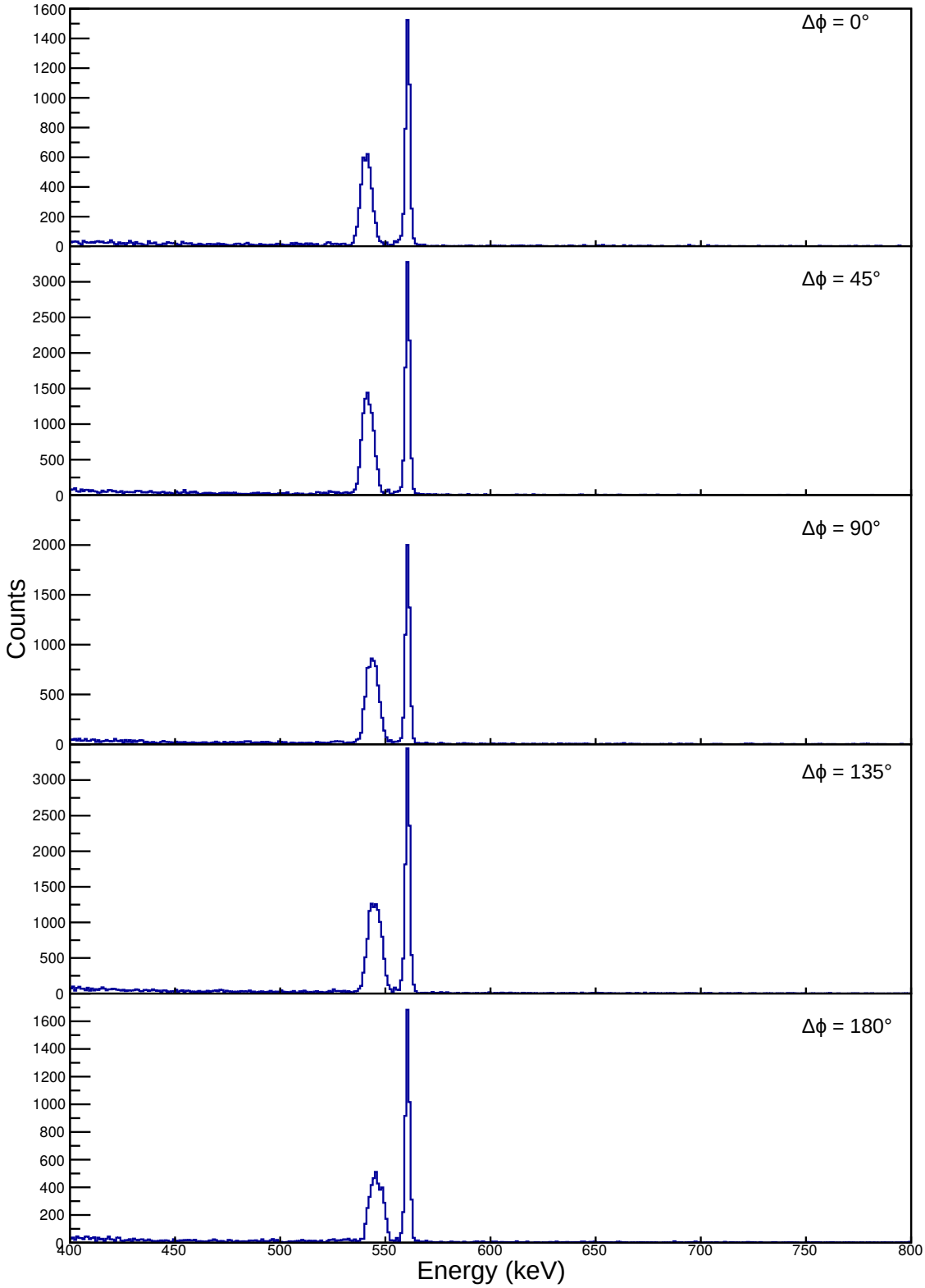

FIGURE 6.36: 'True' γ-ray spectra from the ^{76}Ge TDRIV measurement, run 7, showing separate particle coincidences with $\gamma_2 = 135°$ (backward angle). Note there is almost no background. Decays originating from stopped nuclei form the narrow, higher-energy peak, while those in flight form the broader, lower-energy peak; they are clearly separated in the spectra.

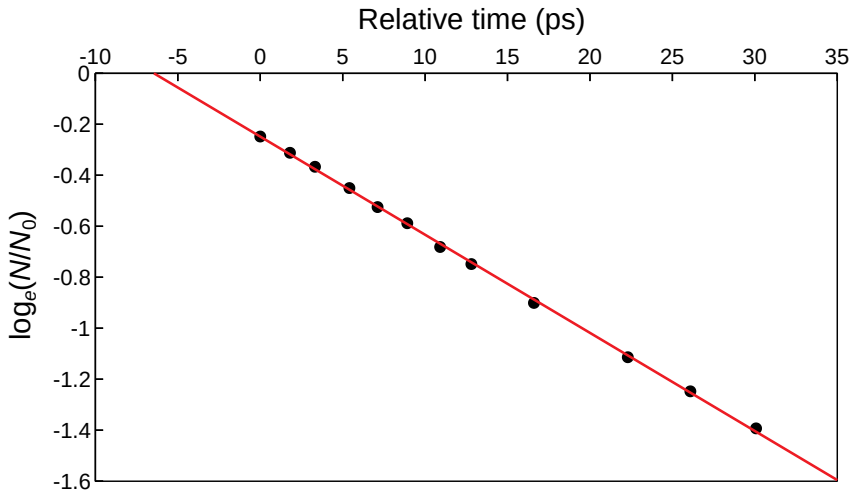

FIGURE 6.37: ^{76}Ge TDRIV measurement logarithmic decay curve, showing the natural logarithm of the undecayed fraction versus the ion flight time. The fit was minimsed using ROOT's fitting routine [41], obtaining $\chi^2_\nu = 0.9582$. Uncertainties in both relative time and $\log_e(N/N_0)$ are approximately the size of the data points. The fitted lifetime of the ^{76}Ge 2^+_1 state is $\tau = 26.04(17)$ ps, in good agreement with the literature value of 26.3(3) ps [133], and the ion flight time to the run 17 plunger position (leftmost point at relative time zero) is 6.48(15) ps.

the total fraction N_0. By taking the peak counts and then correcting for changes in the angular correlation due to the vacuum deorientation (G_k values, obtained from free-fitting the data), and the relative detector efficiency between the shifted and unshifted peak energies, values of N and N_0 were obtained for each run. The logarithmic decay curve in Fig. 6.37 plots $\log_e(N/N_0)$ against the relative times. The data show a linear dependence, and strong agreement was found between the fitted lifetime of the ^{76}Ge 2^+_1 state, being $\tau = 26.04(17)$ ps, and the accepted literature value of 26.3(3) ps [133]. These two features validate the use of the calibration to set the time-zero offset and obtain time points for each run, which are listed in Table 6.10.

The CSD of ^{76}Ge ions was estimated using the parameterisation determined by Leslie [134]. Leslie used an aluminium, rather than an iridium target, but found that the Nikolaev-Dmitriev charge-state parametrisation [155] more closely matched the measurements than the Schiwietz-Grande parametrisation [187]. As the Nikolaev-Dmitriev parametrisation does not account for the Z of the target, the Schiwietz-Grande parameterisation was used to scale the distribution from the distribution centroid expected out of an aluminium target to an iridium target. The resulting CSD is shown in Table 6.11.

TABLE 6.10: Plunger micrometer setting and flight time for each run in the ^{76}Ge TDRIV experiment. The average recoil velocity and angle of the ^{76}Ge ions were $\beta = 0.0451(5)$ and $\theta_p = 8.6°$. Times were obtained by $t = -\log_e(N/N_0) \times 26.04$ as determined from Fig. 6.37. Micrometer readings are considered accurate to 2.5 μm.

	Relative Distance (μm)	Time (fit) (ps)
Run 17	0.0(25)	6.46(16)
Run 1	24.0(25)	8.12(16)
Run 2	45.0(25)	9.55(16)
Run 3	73.0(25)	11.72(17)
Run 4	96.0(25)	13.67(18)
Run 5	121.0(25)	15.32(18)
Run 6	147.0(25)	17.74(19)
Run 7	173.0(25)	19.49(20)
Run 16	224.0(25)	23.46(22)
Run 13	301.0(25)	29.01(25)
Run 14	353.0(25)	32.49(27)
Run 15	406.0(25)	36.27(29)

6.4.3 Analysis

The TDRIV data were analysed to determine a value of $g(2_1^+; ^{76}\mathrm{Ge})$. Unlike the ^{56}Fe TDRIV experiment, this CSD was not optimised on Na-like ions, but was instead centred on Si-like ions. As such, it may be challenging to extract a g factor from these data. As for the ^{56}Fe case (§6.1), the first step taken in the analysis was to free-fit the G_k values. The result of this fit is shown in Fig. 6.38. There is a quasi-exponential trend, with a weak oscillation visible from 10–20 ps. The oscillation appears to be present at the later time points, but the points are spaced too sparsely to be sure. This overall trend in $G_k(t)$ is expected from the CSD in Table 6.11, as it is dominated by ionic species with multiple valence electrons, which are expected to strongly exhibit this quasi-exponential character. The only atomic state expected to contribute toward the observed weak oscillation over this time period, at this frequency, is the Na-like $3s_{1/2}$ ground state. In this case, the best approach to fitting would be to isolate and fit the Na-like $3s_{1/2}$ frequency in the data directly, as per the preliminary approach taken in §6.2.6.

To isolate this oscillation, the $R(t)$ function was calculated, shown in Fig. 6.39. Across the entire time-span there is little structure. However, the range $10 \leq t \leq 25$ ps appears to have two periods of some oscillation. Expecting this to be caused by the Na-like $3s_{1/2}$ interaction, a cosine fit was performed as in §6.2.6, this time with only a single cosine frequency. But, before this was performed, an exponential function was fitted to the data from $10 - 25$ ps, and deducted from the data points to remove the quasi-exponential

TABLE 6.11: Expected CSD of ^{76}Ge ions recoiling out of iridium, corresponding to the detection of C target nuclei measured across a particle-detector face. This distribution is based on the parametrisation proposed in Ref. [134], which was developed for the same velocity regime as this experiment. The Schiwietz-Grande parameterisation was used to scale the distribution centroid expected from an Al target to an Ir target.

$Z - Q$	Ionic Species	Population
11	Na-like	3.3%
12	Mg-like	9.2%
13	Al-like	18.1%
14	Si-like	25.0%
15	P-like	24.4%
16	S-like	15.8%
17	Cl-like	8.2%
18	Ar-like	2.6%

component and isolate the oscillation. The residual data were then fitted to:

$$1 - R(t)_{\text{fit}} = a\cos(\omega[t-\delta]) + c, \tag{6.10}$$

where the fitted values of the parameters are the cosine amplitude $a = 0.0186(42)$, the angular frequency $\omega = 1.065(80)$ rad/ps, the phase shift $\delta = 2.3(9)$ ps, and the cosine offset $c = -0.0021(3)$. The $\chi^2_\nu = 0.161$. The fit result is shown in Fig. 6.40, and gives $g = +0.318(24)$ accounting for 1% uncertainty in the GRASP $3s_{1/2}$ calculation, added in quadrature. The sign is known from the transient-field measurement in §4.3.2. This value is in excellent agreement with that obtained by Gürdal *et al.* using the TF technique [98]. The large phase shift has a considerable uncertainty, and may indicate over-fitting of the data. When the phase shift is fixed to $\delta = 0$, the fitted value falls to $\omega = 0.899(15)$ rad/ps, giving $g = +0.269(5)$. This value is in excellent agreement with the value measured in §4.3, also using the TF method, but disagrees with the value fitted when δ is allowed to vary. The uncertainty, however, is dramatically underestimated due to fixing the δ parameter. Adopting the same percent uncertainty as obtained for $g = +0.318(24)$ gives $g = +0.269(20)$, and the uncertainties now almost overlap at 1σ. With conditions so poorly optimised for making this measurement, it is difficult to determine where between these two values the g factor truly lies. The small χ^2 also means that a large range of g-factor values can give $\chi^2_\nu \leq 1$, and so the possibility remains that the true value may be outside of this range. Nevertheless, the strongly attenuated Na-like ground-state oscillation has, remarkably, suggested a value of $+0.27 \lesssim g \lesssim +0.32$. The result suggests that a future experiment, with optimised conditions, will be able to determine $g(2_1^+;^{76}\text{Ge})$ with high precision.

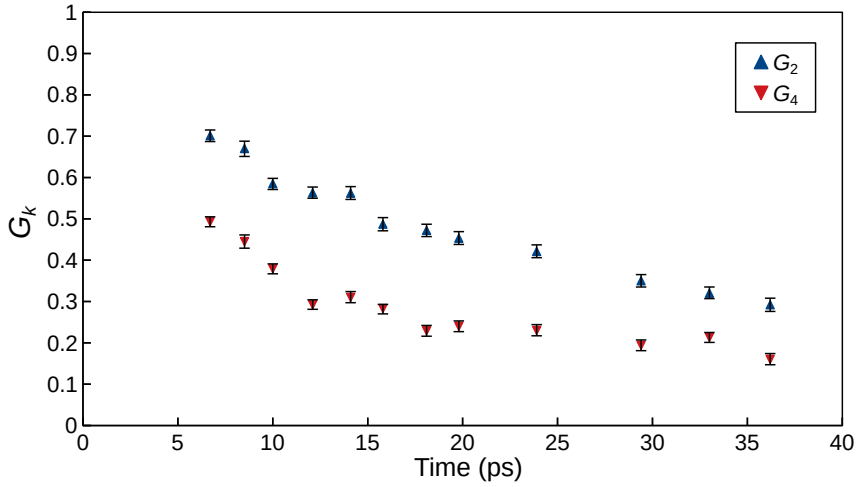

FIGURE 6.38: Time-differential ^{76}Ge-data G_k values obtained by free-fitting G_2 and G_4 to the measured angular correlations (see Appendix B.3) as described in §5.6.4. Quasi-exponential states clearly dominate the interaction with a strongly attenuated oscillation visible from 10–20 ps.

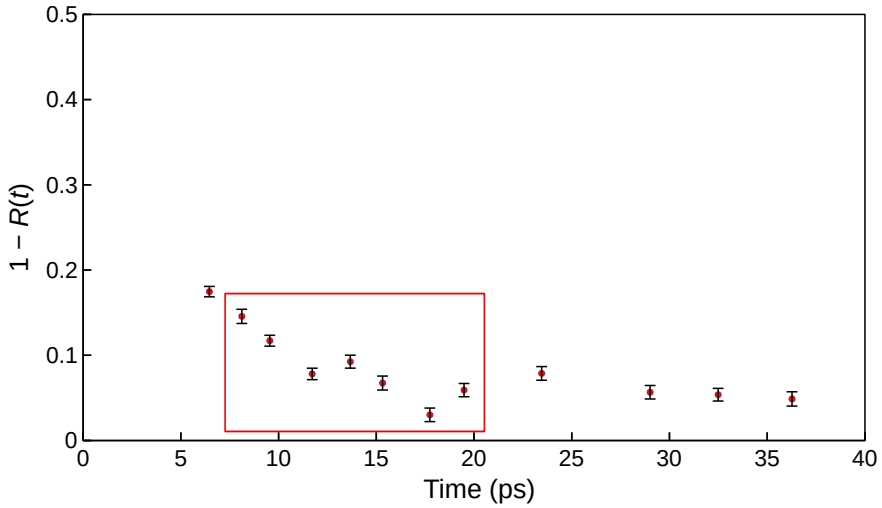

FIGURE 6.39: ^{76}Ge-data $R(t)$ plot. The region in which the suspected Na-like $3s_{1/2}$ frequency is visible is indicated.

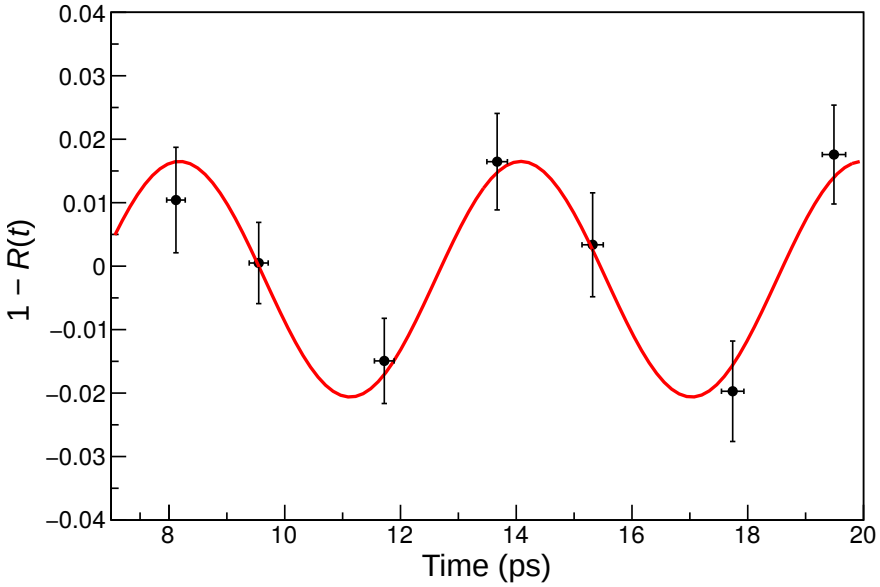

FIGURE 6.40: Result of the fit to the ^{76}Ge data using Eq. (6.10).

6.5 Free-Ion Hyperfine Interactions in $Z \sim 30$ Nuclei

In this section the results of the RIV measurements presented in this chapter will be scrutinised. In particular, the challenge of understanding both the time-integral (TI) and time-differential (TD) RIV data that is available for ^{54,56}Fe will be examined, along with ways to improve or optimise measurements for $Z \sim 30$ nuclei. The strengths and weaknesses of the two TDRIV measurements on ^{56}Fe and ^{76}Ge will be examined, and proposals made for performing measurements to further interrogate the hyperfine interaction, as well as optimisations to improve the reliability of g-factor values obtained via this technique. It will be argued that a charge-state distribution (CSD) centred between Na-like and Mg-like ions will provide the best measurement for determining the g factor for $Z \sim 30$ nuclei. Finally, these optimisations will be examined with a view to apply them to radioactive-ion-beam (RIB) measurements. It will be shown that these optimisations are important for maximising precision when performing $g(2_1^+)$ measurements using RIBs.

6.5.1 Previous Measurements and the Challenge of $Z \sim 30$ Nuclei

The RIV technique has been utilised for nuclear g-factor measurements in short-lived excited states since the 1960s, and is still undergoing advances in its application and methodology today. However, it was also around this time that the transient-field (TF) effect was identified, and methods utilising the TF would instead come to dominate the literature. As early as 1975, the TDRIV technique was used to measure $g(2_1^+)$ for ^{24}Mg and ^{20}Ne [113]. The simple hyperfine interactions present in highly stripped, low-Z ions, provide the opportunity to measure $g(2_1^+)$ in an absolute manner. For these low-Z ions, H-like 1s and Li-like 2s electrons almost solely contribute to oscillations in the measured anisotropy at moderate recoil velocities ($\sim$ 5% c), making for a simple, direct measurement of their frequency and thereby the g factor. While this approach is effective for nuclei having $Z \lesssim 14$, the H-like 1s hyperfine-interaction frequency, which scales with Z^3, becomes unresolvable as higher-Z nuclei are considered. To reduce the hyperfine-interaction frequency back into a measurable range, higher-n (shell) electrons must be utilised. In the case of $Z \sim 30$ nuclei, the Na-like ground state (3s) is a more experimentally accessible atomic state for using to measure $g(2_1^+)$. For even heavier nuclei, with longer-lived 2_1^+ nuclear states ($\tau \sim 10^{-9}$ s), time-integral measurements may instead be performed without the need for optimising on ionic species with a $J = 1/2$ ground state. However, in such measurements, the hyperfine interaction must be calibrated to determine the g factor of unknown states. Such are the varied applications of this technique across the nuclear chart, and also the challenges as Z is increased.

The success of the TIRIV measurement of $g(2_1^+)$ in radioactive ^{132}Te [204], generated interest in utilising these techniques to analyse TIRIV data available for radioactive ^{78,80,82}Ge. Measurements of $g(2_1^+)$ in the stable, even-A Ge isotopes had been published repeatedly in the literature, along with those for the stable, even-A Se isotopes. It was supposed that these could be used to calibrate the hyperfine interaction and thereby determine $g(2_1^+)$ in the ^{78,80,82}Ge radionuclides. Unfortunately, calibration of the hyperfine interaction, as performed by Leslie [134], proved to be problematic [206]. The TDRIV $g(2_1^+)$ measurement on ^{56}Fe, described in §6.1, also proved challenging to interpret, initially. The hyperfine interaction presented unexpected features that resulted from a number of strongly populated atomic states from F-like and Na-like ions contributing together, a more complicated scenario than originally modelled, and much more complex than the simple H-like contribution observed for ^{24}Mg. It was this stumbling block that had slowed progress in applying this technique to $Z \sim 30$ nuclei, until now.

$Z \sim 30$ nuclei present a middle ground between $Z \lesssim 14$ nuclei, for which simple H-like ions may be used, and $Z \gtrsim 50$ nuclei, for which measurements utilising an empirical calibration suitable for ions having considerably more bound electrons ($\gtrsim 14$ electrons) and longer-lived nuclear states ($\tau \sim 10^{-9}$ s) may be used. For the $Z \sim 30$ nuclei, which have 2_1^+ lifetimes of the order of picoseconds, the strong hyperfine interactions present in highly stripped ions are necessary to obtain accurate $g(2_1^+)$ values from TIRIV measurements. Unfortunately, these ion ensembles can contain significant contributions from Na-like and F-like states, which have been demonstrated to have strong, single-frequency contributions. Such ion ensembles are not well-approximated by the empirical static model used in the analysis of the ^{132}Te TIRIV $g(2_1^+)$ measurement, as presented by Stuchbery and Stone [212]. Hyperfine interactions with H-like ions for $Z \sim 30$ nuclei are too high in frequency to resolve with current apparatus. Going to less-stripped Li-like ions is still challenging, although more feasible. However, the co-generation of Be-like ions will contribute atomic states that will create complex hyperfine interactions to disentangle; hence, the CSD will need to be tightly controlled and centred over Li-like, with smaller contributions from He-like and Be-like. As such, Na-like ions seem to be the most viable option, particularly for Coulomb excitation, so long as the F-like contribution is kept minimal. These factors in TIRIV and TDRIV measurements will be discussed in the remainder of this section.

6.5.2 Atomic-State Contributions to the Hyperfine Interaction

Strong contributions from single atomic states may present unexpected hyperfine interactions when not properly accounted for. When the ^{56}Fe 2_1^+ TDRIV measurement

(§6.3) was originally proposed, preliminary modelling suggested that the Na-like ground-state ($3s$) and first-excited-state ($3p_{1/2}$) oscillations would be visible against a smooth, declining quasi-exponential slope. Such a quasi-exponential slope was apparent in the ^{76}Ge TDRIV measurement (§6.4.2), however the Na-like ground-state oscillation was too weak. The ^{56}Fe TDRIV measurement instead revealed an unexpected, strong deorientation at early times, with multiple interfering frequencies and restoration of anisotropy at later time points (§6.2.2). Analysis of these frequencies found a strong F-like ground-state ($2p_{3/2}$) oscillation was required to explain the measured trend (§6.2.6). An empirical determination of the CSD found that a F-like contribution, while considerably stronger than expected, was still not strong enough to fully explain this trend. Regardless, the measured oscillations were well-explained using the F-like and Na-like ground and first-excited states, along with a Ne-like $B \simeq 0$ contribution, when allowing for an offset in the $R(t)$ function to which the data were fitted. This analysis demonstrated that consideration of each observable ground and low-energy atomic state from the ion ensemble allows for the identification of the components contributing to the hyperfine interaction.

Fits to both the ^{56}Fe time-dependent stop (§6.2.7) and in-flight data (§6.2.9), as well as the time-integral data (§6.3.2), always found a dominant F-like $2p_{3/2}$ component when state occupations were allowed to vary in an unrestricted manner. This result could not be explained using the CSD expected for a nickel target. The time-dependent in-flight ^{56}Fe and time-integral ^{54,56}Fe measurements also showed that this deorientation is not rapid ($\tau \lesssim 1$ ps), but occurs over the lifetime of the ^{56}Fe 2_1^+ state (§6.3.3). The restoration of anisotropy at later time points, observed in the time-dependent measurement (see Fig. 6.9), is evidence that the initial deorientation must be owing, in part, to the persistent occupation of a single state from early timepoints. It was observed after the ^{56}Fe TDRIV measurement that carbon residue had built up on the target, and was suspected of altering the CSD. It was found that the measured CSD of ^{56}Fe out of carbon matched much more closely to the unrestricted fits to the TDRIV data. That the observed deorientation of the in-flight component in the TDRIV measurement (§6.2.9) matched well with the TIRIV measurement (§6.3.2) supports the hypothesis that carbon build-up was increasing the F-like relative to the Na-like fraction. Thus, the conclusion that the F-like fraction was greater than expected is firm, although it cannot explain all the observed features of the observed G_k trend.

The contribution of short-lived (sub-picosecond) core-hole excited states may significantly affect the magnitude of G_k values in both time-integral and time-differential measurements, although formation of $R(t)$ ratios in TDRIV measurements can reduce any sensitivity to such effects when determining the g factor (§6.2.7). A more thorough

measurement is suggested to probe this interaction, in which different CSDs may be compared to observe the effect on the absolute magnitude of the $G_k(t)$ trend, and time points that will allow the $t < 2$ ps region to be probed. An apparatus has been developed at ANU that will allow such a measurement, consisting of a plunger device that is anticipated to be capable of measuring time points beginning at $t < 1$ ps, and a two-ring particle-detector array that, due to the angular separation between the rings (and consequent differing recoil velocities), will allow for two different CSDs to be measured simultaneously. This means the hyperfine interaction can be probed in two ways: by measuring angular correlations at very early timepoints, that will allow for the behaviour of the hyperfine interaction over the short timescales to be identified; and observation of how the hyperfine interaction differs between two separate CSDs, that will allow critical comparisons to be made with the hyperfine-interaction model and observed vacuum deorientation. The objective of such a measurement is a consistent description of the features in the $G_k(t)$ data that are similar and dissimilar for two overlapping CSDs.

Analysis of the ^{56}Fe (§6.1) and ^{76}Ge (§6.4) TDRIV data has demonstrated that the hyperfine frequencies present at later times ($t \gtrsim 5$ ps) can be modelled using hyperfine interactions associated with the ground and lowest-excited atomic states of the ionic species present to determine the nuclear g factor. This capability is a triumph for this technique, and will allow for future measurements to be carried out with the confidence that *ab initio* modelling of the hyperfine interaction can allow the g factor to be extracted from TDRIV data for nuclei around $Z \sim 30$. The lessons learned about optimising the experimental parameters for such measurements will now be discussed.

6.5.3 Optimal g-factor Measurements By Time-Differential Recoil-In-Vacuum

The ideal TDRIV measurement would present a simple, $J = 1/2$ cosine oscillation from a maximally occupied atomic state for the determination of the g factor. The TDRIV measurements analysed in the present work, while containing this oscillation, represent two examples of non-optimal CSDs: the ^{56}Fe measurement presented a complex superposition of oscillations owing to the CSD including a significant F-like fraction that was not expected, while the ^{76}Ge measurement had almost no oscillations owing to the small Na-like fraction and the dominance of ionic species exhibiting quasi-exponential $G_k(t)$ trends. By examining the optimal features in each of these two measurements, an ideal CSD can be determined.

States having $J > 1/2$ contribute a complex set of frequencies to the observed $G_k(t)$

trend. These states, therefore, obfuscate what would ideally be a straight-forward analysis of a simple cosine frequency from a $J = 1/2$ state. Such a complex superposition was seen in the ^{56}Fe measurement, owing to the $2p$-electron hole in the F-like ions. The F-like ions' ground state has $J = 3/2$, causing G_2 and G_4 to oscillate at different frequencies. In its first-excited (spin-flip) $J = 1/2$ state, the frequency is very similar to the Na-like $3s$ state, creating a complex interference pattern that further obfuscates the observation of a simple cosine oscillation (see Fig. 6.17). The measurement has revealed that any significant contribution from the F-like ions is undesirable for the direct observation of the Na-like $3s$ state's oscillation. When originally designed, the ^{56}Fe measurement was expected to have a CSD centred on Na-like ions, with a small F-like fraction. The build-up of carbon on the back side of the target seems a likely explanation for the F-like fraction being stronger than expected.

The sensitivity of the measurement to the F-like fraction highlights the importance of using an empirically determined CSD, rather than the approximate solutions provided by Nikolaev and Dmitriev, or Schiweitz and Grande. This is particularly relevant to the CSDs desired for $Z \sim 30$ nuclei, which are near to the neon atomic shell closure and therefore exhibit non-Gaussian distributions. It is also strongly suggested that the ion recoil velocity is measured from the Doppler shift before the beam-energy is finally set, owing to uncertainties that may be present in the target thickness. Both of these steps were taken for the ^{56}Fe TDRIV measurement: the CSD out of the target material was empirically determined, and the beam energy was adjusted to give the optimal velocity. What was not expected was that carbon build-up over the run lifetime could also present an issue, as a thin layer of carbon deposited on the back of the target can appreciably shift the CSD to higher charge states. Therefore, steps should also be taken to prevent the build-up of carbon on the target foil (e.g. clean vacuum, cold shield). As a further precaution, the C/Ni layers of the target could be reversed to guarantee the ions recoil out of carbon, as to select an appropriate recoil energy to obtain the desired CSD.

In contrast to the ^{56}Fe measurement, the ^{76}Ge measurement had almost all of the ionic species that were present contribute a quasi-exponential character to the measured $G_k(t)$ trend. This was evident in Fig. 6.38, although there appeared to also be a small-amplitude oscillation. The lack of any expected competing frequencies made the isolation of the weak Na-like atomic-ground-state contribution straight-forward. Comparison of the G_k trends from the ^{76}Ge measurement and the ^{56}Fe measurement indicate that an optimised CSD should be focused on Na-like and Mg-like states, having lesser populations of Ne-like and Al-like, with little-to-no F-like. That the charge states follow a skew-normal distribution near the neon shell closure (see §6.1.2) should allow for fine-tuning of the Na-like fraction, while keeping the F-like fraction minimal. The simulated $R(t)$ plot from

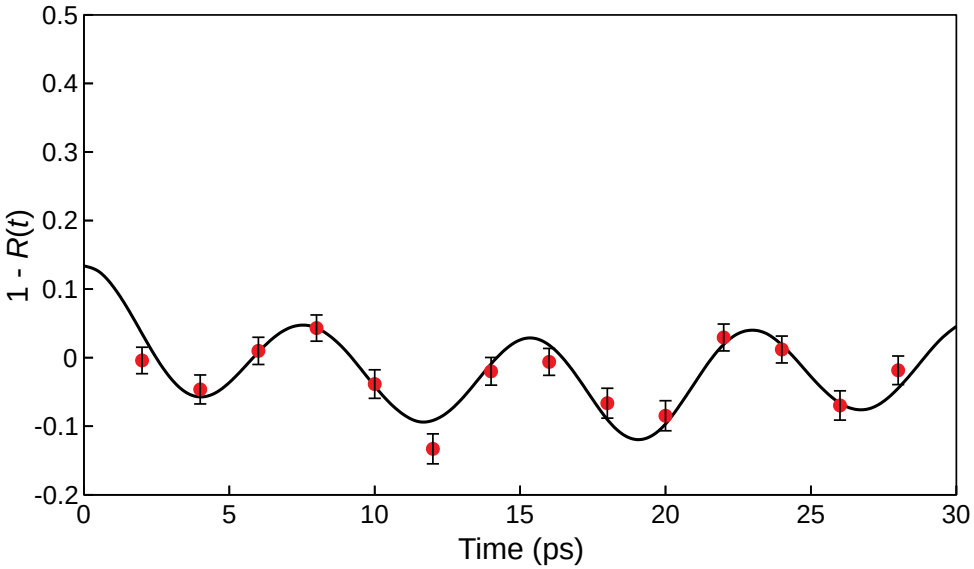

FIGURE 6.41: Simulated $R(t)$ plot for a TDRIV ^{56}Fe 2_1^+ measurement, with data at 2 ps intervals and having 2% uncertainty. The CSD used in this simulation was 4% F-like, 23% Ne-like, 29% Na-like, 25% Mg-like and 15% Al-like. The Na-like 3*s* ground-state oscillation is readily identifiable with no interfering frequencies. Such a CSD would be ideal for a TDRIV measurement on any $Z \sim 30$ nuclide.

such an optimal CSD is shown in Fig. 6.41. By identifying and subtracting the quasi-exponential component, the Na-like ground-state oscillation can be isolated and precisely fitted to determine $g(2_1^+)$ in $Z \sim 30$ nuclei. With an optimal CSD identified, attention will now be directed to the application of the TDRIV technique to RIBs.

6.5.4 Recoil-In-Vacuum Measurements Using Radioactive-Ion Beams

As previously discussed, and indicated in the literature [129, 204, 206, 212], the RIV technique provides a viable means to probe excited-state g factors in radioactive nuclei produced as beams by RIB facilities. Such experiments may be designed so that not only can the g factor of a given state be determined, but by performing Coulomb excitation as well, the energy level, $B(E2)$ and lifetime of an excited state can be determined in a single experimental run, providing valuable data with which to test shell-model predictions for excited states in exotic nuclei.

Time-integral (TI) RIV measurements are ideal for RIB measurements due to the radionuclides being able to pass out of view of the detectors. This prevents the accumulation of radionuclides, and consequent saturation of the detectors with unwanted decay radiation, that would occur in a typical TDRIV measurement. For TIRIV, careful calibration and detailed *ab initio* modelling of the hyperfine interaction will be important.

A TDRIV measurement, in conjunction with relative measurements using the transient-field technique, will allow for the g factors of several nuclear states amongst isotopes of the same element to be determined in an absolute manner. TIRIV measurements on these states will then allow for the precise calibration of the hyperfine interaction. With the proper calibration, TIRIV data measured using RIBs can be confidently interpreted to determine $g(2_1^+)$. By optimising the CSD, the acquisition time necessary to achieve the desired precision may be reduced, allowing the possibility to perform alternative measurements, such as multi-step Coulomb-excitation, during the same beam time. From a single beam time, level energies, excitation amplitudes, and g factors may be obtained for several states, providing valuable data with which to confront the nuclear shell model.

6.6 Summary

In this chapter, the experimental procedures and results for several time-differential and time-integral recoil-in-vacuum measurements were presented, with a particular focus on understanding the hyperfine interaction present in ^{56}Fe ions with a charge-state distribution centred around Ne- and Na-like ionic species. For the ^{56}Fe 2_1^+-state measurement, a g factor was obtained, albeit with minor reservations about its accuracy in light of the complications surrounding the charge-state distribution (CSD). A simplified analysis procedure also allowed $g(2_1^+; ^{76}\mathrm{Ge})$ to be loosely determined, despite the measurement being poorly optimised for this purpose.

The hyperfine interaction causing time-integral vacuum attenuation in Fe ions, and its behaviour between lifetimes of $\tau \lesssim 1$ ps and $\tau \simeq 10$ ps was modelled. Components of the hyperfine interaction relating to valence atomic configurations, which become dominant over tens of picoseconds, have been modelled and seem able to explain the oscillatory features observed time-differential data. This understanding will inform the optimisation of future experiments, allowing for g-factor measurements with improved precision. However, the influence of core-hole excited states on the overall magnitude of the hyperfine interaction is poorly understood, and will require carefully designed experiments to probe, as well as additional modelling. A future measurement, capable of exploring early time points ($t \lesssim 2$ ps), will improve our understanding and ability to model the hyperfine interaction. Such a measurement will be possible using a newly developed plunger device at ANU, that was designed to be coupled to a two-ring particle-detector array capable of measuring two distinct CSDs simultaneously.

In conclusion, **RIV Simulate** and the TDRIV technique have proven able to model the hyperfine interaction with the goal of determining nuclear g factors for nuclei in this region, particularly with well-informed experimental design, whilst also presenting the opportunity to understand the sub-picosecond hyperfine interaction for better analysis of time-integral measurement data.

Chapter 7

Nuclear Shell-Model Interpretations of $g(2_1^+)$ Values

As discussed in Chapter 2, the goal of many experimental endeavours is to measure nuclear properties with which to confront the nuclear shell model. In this work several $g(2_1^+)$ values were obtained, either directly from data or by reanalysis. In this chapter the g-factor results obtained in Chapter 4 and Chapter 6 will be compared to and interpreted in the context of modern shell-model theory and multi-configuration shell-model calculations, along with previous interpretations. It will be shown that nuclear g-factor systematics provide a valuable probe for interrogating the changing orbital occupation of protons and neutrons in the wavefunction for isotope chains near to islands of inversion, and in nuclear regions which exhibit changing collective and single-particle behaviour.

7.1 ^{24,26}Mg

Excited states in ^{24}Mg present an interesting case of a self-conjugate nucleus that develops collective features. Being self-conjugate, it has equal valence protons and neutrons in the *sd*-shell space, and has been calculable within the multi-configuration shell model since the 1970s [61, 148]. The naïve interpretation from its nucleon configuration, with equal numbers of valence protons and neutrons in the same shell, is that the g factor of the first-excited state will be $g(2_1^+) = +0.5$. Deviations from this limit indicate differences in coupling of proton and neutron configurations. Calculations indicate that the g factor should be slightly larger than $g = +0.5$. Today, $g(2_1^+;^{24}\mathrm{Mg}) = +0.538(13)$ has been firmly assigned, in excellent agreement with the value $g = +0.543$ obtained by multi-configuration *sd*-shell calculations using the USDB interaction Hamiltonian. For the nucleus ^{26}Mg, the accepted literature value, measured by Speidel *et al.*, of $g(2_1^+;^{26}\mathrm{Mg}) = +0.50(15)$ [196] deviates greatly from the USD shell-model-calculation value of $g = +0.959$, but was in good agreement with a multishell Hartree-Fock calculation at the time of publication [96]. This value was in stark contrast to the previously measurement by Eberhardt *et al.*, being $g(2_1^+;^{26}\mathrm{Mg}) = +0.97(18)$ [61, 231].

These measurement discrepancies will now be examined.

The earlier measurement by Eberhardt *et al.* was obtained using IMPAC [61], whereas the value of Speidel *et al.* was used the thin-foil TF technique [196]. Speidel's measurement was motivated by a perceived issue with the doubling of $g(2_1^+)$ between ^{24}Mg and ^{26}Mg, and a now dated hypothesis regarding the electromagnetic properties of $A = 4n + 2$ nuclei being consistent across this region. Between the publication of Eberhardt *et al.* and Speidel *et al.*, the static hyperfine field strength for Mg in iron was measured, and found to be an order of magnitude stronger than the extrapolated value used by Eberhardt *et al*. Speidel *et al.* suggested that this underestimation caused the measured precession in ^{24}Mg to be much smaller (as the static field has sign opposite to the transient), and hence the ^{26}Mg g factor appeared larger. However, at the time it was not known that the pre-equilibrium quenching of the static field, owing to the thermal-spike lifetime, would cause the static-field component to be almost null for these short-lived isotopes. Therefore, while the assertion that the static-field component was underestimated is correct, the magnitude of the reduction was much smaller than expected. In the measurement by Speidel *et al.*, $g(2_1^+;^{24}\text{Mg})$ was measured relative to $g(2_1^+;^{26}\text{Mg})$ by exciting nuclei in a Mg target in regular kinematics using an α-particle beam. A weakly polarising field of 0.02 T was applied to the foils, containing an iron ferromagnetic host. Discrepancies in foil preparation, the weak polarising field, uncertainties in the TF calibration, and the small lifetime of the ^{26}Mg 2_1^+ state, may have all contributed to the erroneous result.

The value obtained in the present work, $g(2_1^+;^{26}\text{Mg}) = +0.86(10)$, followed the ideal of the measurement by Speidel *et al.* [196], whereby $g(2_1^+;^{26}\text{Mg})$ was measured relative to $g(2_1^+;^{24}\text{Mg})$. However, as discussed in §4.2.3, systematic uncertainties in the measurement were almost completely eliminated, and a much stronger polarising field was used without inducing appreciable beam-bending by virtue of the apparatus design (see introduction in Chapter 4). The value obtained was in good agreement with Zalm's reanalysis of Eberhardt's measured $g(2_1^+;^{26}\text{Mg})$ value [231], while being slightly smaller as alluded to in Ref. [196]. It is also in agreement with modern shell-model calculations.

With $g(2_1^+;^{26}\text{Mg})$ confidently evaluated, shell-model calculations, and the influence of different active spaces and interactions in their predictions of nuclear behaviour around the ^{32}Mg island of inversion can be interrogated. Figure 7.1 shows measured $E(2^+)$, $B(E2)$ and $g(2^+)$ values for even-A isotopes of Mg compared with shell-model calculations performed using NuShellX [39] with the USDB interaction Hamiltonian [182] in the *sd*-shell space. Calculations have also been performed for $g(2_1^+)$ in ^{30,32}Mg using the Monte-Carlo shell model in the *sdpf* space [162]. The large difference between $g(2_1^+)$

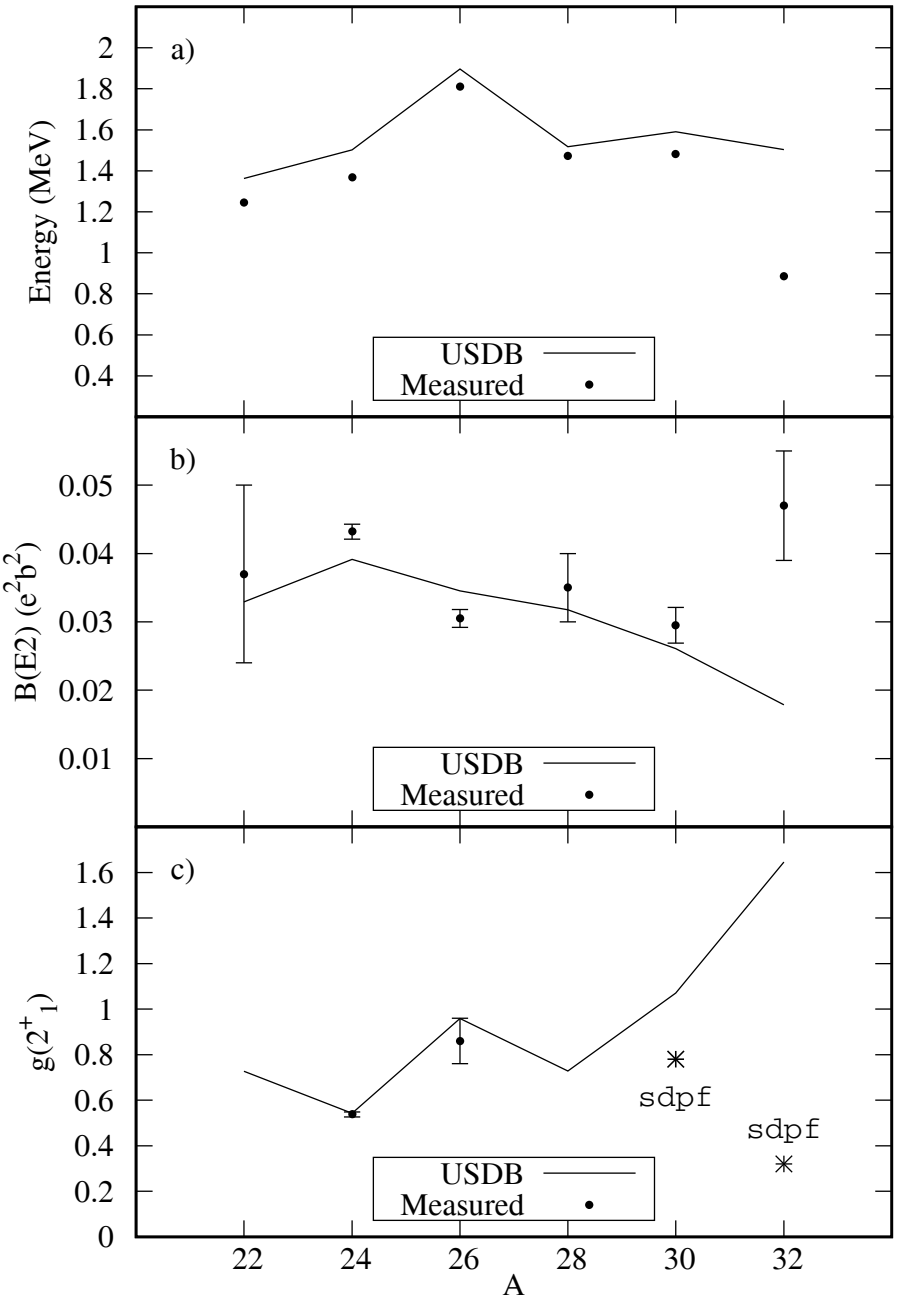

FIGURE 7.1: Comparison between shell model calculations using the USDB interaction Hamiltonian, and experiment, for the magnesium isotopes from $22 \leq A \leq 32$ a) $E(2_1^+)$ energies, b) $B(E2)$ rates, and c) g-factor values [179, 188, 71, 17, 189, 190, 164]. The theoretical g factors for ^{30}Mg and ^{32}Mg in a more realistic (for the island of inversion) $sdpf$ model space are also shown by the stars [162].

TABLE 7.1: Spin composition of 2_1^+ states in ^{24,26}Mg as determined by shell-model calculations using the USDB interaction Hamiltonian.

J_n	J_p	Weight (%)	
		^{24}Mg	^{26}Mg
2	0	25.64	17.05
0	2	25.64	52.04
2	2	19.66	9.59
2	4	8.60	7.17
4	2	8.60	3.85

in ^{24}Mg and ^{26}Mg is indicative a shell effect owing to the two additional neutrons. The spike in $E(2^+)$ and dip in $B(E2)$ at ^{26}Mg suggest the presence of a subshell closure. Indeed, ^{26}Mg (having $N = 14$) fills the $\nu d_{5/2}$ orbital, which appears to be behaving as a sub-shell closure. Table 7.1 shows a breakdown of the proton and neutron spin contributions to the ^{24,26}Mg 2_1^+ states, and indicates that when the $\nu d_{5/2}$ orbital is filled, $J = 2$ two-proton excited states ($\nu(0^+) \otimes \pi(2^+)$) become dominant over two-neutron states ($\nu(2^+) \otimes \pi(0^+)$), whereas they are equal in ^{24}Mg. This causes a near doubling of $g(2_1^+)$ in ^{26}Mg, an increased $E(2^+)$ and a reduced $B(E2)$.

The USDB interaction is able to reproduce the trends and magnitudes in the measured observables up to $N = 30$. At $N = 32$, however, changing nuclear forces have deformed the nucleus to the extent that the $N = 20$ shell closure is no longer firm, and significant occupation of the pf orbitals beyond $N = 20$ must be considered. The sd-shell space is unable to account for this behaviour, instead predicting an increased $E(2_1^+)$ and $g(2_1^+)$, and a reduced $B(E2)$ as the shell-closure is approached. By extending to the the $sdpf$ space, calculations are able to account for this behaviour. The agreement between $E(2^+)$ and $B(E2)$ values up to $N = 30$ indicates that these observables are not as sensitive to the weakening shell-gap as $g(2^+)$ may be, which already gives a noticeable disagreement between the two calculations at ^{30}Mg. This indicates that $g(2_1^+)$ values may actually have sensitivity to the changing single-particle energy levels along isotopic chains approaching an island of version, and deviations in $g(2_1^+)$ may be visible at ^{28}Mg if precise measurements are made. Such precise $g(2_1^+)$ measurements on radioactive nuclei, however, are challenging. The TDRIV technique, utilising the electron-reset foil as applied by Kusoglu *et al.* [129], is the ideal technique for such measurements, and already data on $g(2_1^+;^{28}\text{Mg})$ has been collected by this method (pending analysis with another institution). Further measurements on ^{30,32}Mg could provide important validation for shell-model calculations and modern configuration-interaction models in this interesting region.

7.2 ^{54,56,58}Fe

Precise g factors for nuclei in the pf shell space provide an interesting opportunity to study the softening and even disappearance of the $Z, N = 28$ shell closure in neutron-rich nuclei [112], as well as changing single-particle energies for the $\nu 1f_{5/2}$, $\nu 2p_{1/2}$ and $\nu 1g_{9/2}$ orbitals. An island of inversion similar to that around ^{32}Mg has been suggested to appear in neutron-rich Fe nuclei [139]. This was interpreted from the modelling required to explain the large increase in $B(E2)$ between ^{62}Fe and ^{64}Fe, with the latter having neutron excitations into an intruder orbital. Another study compared the predictive power of pf-space shell-model calculations versus a truncated fpg-space calculation, and found that while the ordering of ^{61}Fe excited states was handled by the pf space, it was unable to reproduce the ^{63}Fe ordering [199]. The authors suggest that a monopole correction is responsible for this discrepancy, further supporting the idea of this island of inversion. If there is some change to the ordering of the neutron orbitals for Fe nuclei, it might have a measurable effect in the ^{56}Fe 2_1^+-state g factor, which may be used to confront the shell model.

Up until 2009 only two g-factor measurements had been performed on the ^{56}Fe 2_1^+ state that did not utilise a TF-strength calibration. These were radioactivity measurements; a resonance scattering measurement and observed perturbation of the angular correlation in a $0^+ \rightarrow 2^+ \rightarrow 0^+$ sequence by Metzger [150], and a measurement of the perturbation in the γ-γ angular correlation in a $4^+ \rightarrow 2^+ \rightarrow 0^+$ cascade by Appel and Mayer [13]. These two measurements used $\tau(2_1^+) = 10.6$ ps in the evaluation of the g factor. A new value, $\tau(2_1^+) = 9.27(13)$ ps, was evaluated in this project (See §6.1.2). The older radioactivity measurements [13, 150] were reanalysed using this new lifetime, choosing $B_{\mathrm{HF}} = 33(1)$ T from Ref. [180]. A weighted avereage of the two gives $g = +0.61(11)$. In 2009 a new g-factor value was measured for this state by East *et al.* [56], using the TF technique. In this instance, however, the state was measured relative to the first-excited $5/2^-$ state in ^{57}Fe, having a well-established g factor. This measurement determined $g = +0.49(6)$. In §6.1 a new value for the g factor has been determined, $g = +0.546(19)$, in good agreement with these three previous measurements. It is also worth noting that the ^{56}Fe 2_1^+-state precession data measured by Ernst *et al.* [66], evaluated using the Rutgers parameterisation, gives $g = +0.55(3)$, also in agreement with the present value. East *et al.* also published a measurement of $g(2_1^+)$ values for ^{54,58}Fe relative to $g(2_1^+;^{56}\mathrm{Fe})$ [57], again using the TF technique. Rescaled $g(2_1^+)$ values, obtained using $g(2_1^+;^{56}\mathrm{Fe}) = +0.546(19)$ with these relative measurements, are listed in Table 7.2, along with the pf-space shell-model calculations reported in Ref. [112]. With the improved precision of these values, critical comparisons with these shell-model predictions can be made with confidence.

TABLE 7.2: Newly evaluated $g(2_1^+)$ values for ^{54,56,58}Fe along with pf-space shell-model calculations. The signs of the g factors are all positive.

	$g(2_1^+)$	
Isotope	Measured	Shell model [112]
^{54}Fe	1.020(50)	1.094
^{56}Fe	0.546(19)	0.592
^{58}Fe	0.499(33)	0.605

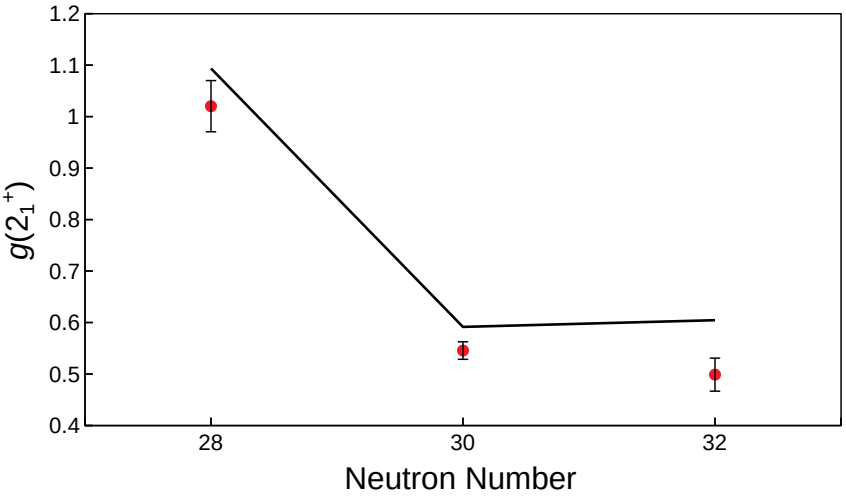

FIGURE 7.2: Values from Table 7.2 plotted for visual comparison. The pf-space shell-model calculations [112] have a slightly larger magnitude than the measured values, with the discrepancy growing larger as N increases.

Figure 7.2 shows the newly determined ^{54,56,58}Fe $g(2_1^+)$ values alongside the pf-space shell-model calculations reported by Honma *et al.* [112]. East *et al.* [57] suggested that the smaller values of the Fe isotope g factors were indicative of some occupation of the $\nu g_{9/2}$ orbital, which calculations using only the pf space cannot account for. The comparison in Fig. 7.2 indicates that while the effect is not as large as East *et al.* suggest, the improved precision shows that there is an increasing deviation between the measurements and the shell-model calculations as N increases. This reduction of the measured g factors relative to the pf-model calculations could possibly be attributed to some occupation of the $\nu g_{9/2}$ orbital. Therefore, fpg-space shell-model calculations may be necessary to achieve agreement at this level of precision. Furthermore, isotopes beyond ^{56}Fe, approaching the potential island of inversion at ^{64}Fe, may require a full fpg-basis space to be accurately predicted, as has already been observed for nearby isotopes of Co [181]. However, without $g(2_1^+)$ systematics that extend into the neutron-rich isotopes, this cannot be confirmed. Instead, this deviation may relate more to effective nucleon g factors used in the calculation, rather than the proton orbital occupation.

In conclusion, by scaling a relative measurement of the less abundant ^{54,58}Fe nuclei against ^{56}Fe with a TDRIV measurement, precise $g(2_1^+)$ values have been obtained for the three nuclei and allowed for a critical comparison with the theory, again demonstrating the complementary use of these techniques.

7.3 Stable Even-A Ge and Se Isotopes

The stable, even-A isotopes of Ge and Se cover the range $38 \leq N \leq 48$, notionally from an empty $\nu 2p_{1/2}$ orbital through to the $\nu 1g_{9/2}$ orbital being two neutrons away from the $N = 50$ shell closure. For these two elements, with $Z = 32, 34$, nominally the $\pi 2p_{3/2}$ orbital is filled and the $\pi 1f_{5/2}$ is either empty or has two protons. The difference in neutron behaviour between these two isotopic chains is not expected to be significantly affected by the $\pi 1f_{5/2}$ orbital's occupation or lack thereof, although it will influence the magnitude of the g factors. In stable nuclei the filled $\nu 2p_{1/2}$ orbital ($N = 40$) should be a sub-shell closure in spherical nuclei, with implications for trends in the Ge- and Se-isotope systematics. This sub-shell closure has been probed using notionally doubly-magic $^{80}_{40}Zr_{40}$ [137] and $^{68}_{28}Ni_{40}$ [37]. The former showed strong deformation and therefore no shell closure, whereas the latter showed indicators of a subshell closure. It is tempting to explain this as the gap between the $1f_{5/2}2p_{1/2}$ orbitals and the $1g_{9/2}$ orbital changing as Z increases, however neither Fe nor Zn show evidence of a $N = 40$ sub-shell closure in their $E(2^+)$ and $B(E2)$ systematics, and mass studies on nuclei in this region further confirm this [95]. One study suggests the behaviour of ^{68}Ni can instead be explained as a neutron excitation [131]. Together, this evidence indicates that $N = 40$ is not a sub-shell closure in $pfpg$-shell nuclei.

The results from the even-A Ge and Se isotopes presented in §4.3.2 are shown in Fig. 7.3, along with the adopted literature values, and shell-model calculations spanning $38 \leq N \leq 50$ using a ^{56}Ni core and the JUN45 [111] and jj44b [38] interactions, performed using NuShellX [39]. Table 7.3 shows the results of these shell-model calculations. Listed are the $g(2_1^+)$ values along with a breakdown of the orbital and spin contributions from the proton and neutron configurations, as used in Eq. (2.24). Recalling the TDRIV $g(2_1^+; ^{76}\text{Ge})$ result from §6.4, the TF-measurement results from this project can be considered as a lower bound, and the literature values as an upper bound. Viewed as such, it appears that the shell-model calculations are able to predict the magnitude of the g factors within the experimental uncertainty. Considering now the experimental data points, the $g(2_1^+)$ trend could indicate that as $N \to 44$ there is a gradual increase in collectivity, after which $g(2_1^+)$ returns to single-particle behaviour as $N \to 50$. This suggests that the $2p_{1/2}1g_{9/2}$ orbitals may together form a sub-shell spanning $38 \leq N \leq 50$, however a neutron closure at $N = 38$ has also been excluded based on systematics along the Ge isotope chain [98]. What has been confirmed, is that the relative behaviour of nuclei through this region has proven difficult to model. Gürdal *et al.* [98] report, for the Ge isotopes, that as the $\nu g_{9/2}$ orbital is filled (i.e. as N increases), neutron excitations from the fp orbitals decrease and, consequently, proton excitations become increasingly dominant, resulting in increased $g(2_1^+)$. The $g(2_1^+)$ values are calculated using Eq. (2.24)

and the effective nucleon g factors, giving

$$g(2^+) = (\langle L_p \rangle + 3.91\langle S_p \rangle - 2.68\langle S_n \rangle)/2. \tag{7.1}$$

Considering now the values of $\langle S_p \rangle$ and $\langle S_n \rangle$ from Table 7.3, $3.91\langle S_p \rangle \approx 0$ and $2.68\langle S_n \rangle \approx 0.2$. From these two approximations, the $g(2_1^+)$ values along the isotopic chains may be described by,

$$g(2^+) \approx (\langle L_p \rangle - 0.2)/2. \tag{7.2}$$

Similar behaviour can be anticipated for the jj44b interaction. Thus, the shell-model-calculation trends shown in Fig. 7.3 reflect, primarily, the proton orbital contribution to the angular momentum, and hence small variations in $\langle L_p \rangle$ directly impact on the calculated g factor. If this interpretation is reflective of the reality, then the measured g-factor trends represent the changing proton orbital contribution with changing N. The shell-model calculations presented by Gürdal *et al.* [98] indicate that the changing proton contribution is driven by the reduced number of neutron holes in the fp orbitals as N increases. The experimental data from the Se isotopes shows that this changing behaviour is smooth, with a turning point at $N = 44$ after which proton contributions begin to increase. For the Ge isotopes, the trend is not so smooth, with $g(2_1^+;^{72}\mathrm{Ge}) \simeq g(2_1^+;^{74}\mathrm{Ge})$. The lack of protons in the $\pi 1f_{5/2}$ orbital may be responsible for this deviation from the smooth behaviour seen in the Se isotopes. The spin-isospin tensor force predicts that introducing two $1g_{9/2}$ neutrons (at ^{74}Ge) should cause a change in the $\pi 1f$ spin-orbit splitting, moving the $\pi 1f_{7/2}$ orbital closer to the fermi surface. If this occurs, then the $Z = 28$ shell closure will be weakened, and therefore the ^{56}Ni core used in the present calculations becomes less valid. Instead, a $^{48}_{20}\mathrm{Ca}_{28}$ core becomes more suitable. The importance of proton excitations across the $Z = 28$ shell gap for nuclei in this region was demonstrated by Srivastava and Ermamatov [198], who showed that shell-model calculations using a $^{48}_{20}\mathrm{Ca}_{28}$ core with an effective fpg interaction produced $B(E2)$ and quadrupole-moment values in better agreement with measurements than those using a $^{56}_{28}\mathrm{Ni}_{28}$ core. Using this same method, Srivastava performed calculations for $g(2_1^+)$ in the even-A Ge isotopes [174]. Figure 7.4 shows these values alongside the measured values, and the $pfpg$-space calculations using the JUN45 and jj44b interactions. For the most part, there is good agreement between the ^{48}Ca-core fpg-interaction and ^{56}Ni-core jj44b-interaction calculations, with the exception of $g(2_1^+;^{74}\mathrm{Ge})$. Their agreement indicates that inclusion of the $\pi 1f_{7/2}$ orbital into the proton active space does not improve $g(2_1^+)$ predictions in these nuclei, and that pfg orbitals are more important for predicting $g(2_1^+)$ in these states.

For the exotic Ni and Cu nuclei having $N > 40$, monopole migration of the $\pi 1f_{5/2}$

orbital is predicted by shell-model calculations employing the V_{MU} interaction [159] as neutrons fill the $\nu 1g_{9/2}$ orbital along the isotopic chains. This is depicted in Fig. 7.5. The monopole migration leads to an inversion of the $\pi 1f_{5/2}$ orbital with the $\pi 2p_{3/2}$ between $N = 44, 46$. Intrusion of the $1f_{5/2}$ orbital below the $\pi 2p_{3/2}$ has been experimentally observed along the ^{71,73,75}Cu isotope sequence [80]. If the $1f_{5/2}$ orbital intrusion is occurring along the Ge and Se isotope chains, increased collectivity should also be observed as the $\pi 1f_{5/2}$ and $\pi 2p_{3/2}$ orbital energies converge, becoming almost equal in energy at $N = 44$. From $N = 44$ to $N = 50$, the lowest-energy excited proton configurations would arise from unpaired protons in the $\pi 1f_{5/2}$ orbital, rather than the $\pi 2p_{3/2}$. According to the Schmidt values for these two orbitals, the $\pi 2p_{3/2}$ g factor is more than three times stronger than the $\pi 1f_{5/2}$ using $g^{\text{eff}} = 0.7g^{\text{free}}$, and even greater using free values. The reordering of these two orbitals may be why the g factor continues to decrease past $N = 42$, despite the diminishing number of neutron pf holes. If the tensor force in the present shell-model calculations is not correctly accounting for these monopole migrations, then they will be unable to predict the experimentally observed behaviour of the $N = 42, 44$ isotopes, despite obtaining what appears to be correct magnitudes. Correct magnitudes are likely obtained because the central term of the interaction Hamiltonian, to which the magnitude is sensitive, is the dominant and most robustly fitted component, whereas the subtler two-body interactions are not fitted so well for these mid-shell nuclei. Only through an improved understanding of these two- and three-body interactions can the shell model's capability to predict the behaviour across the breadth of the nuclear chart be strengthened.

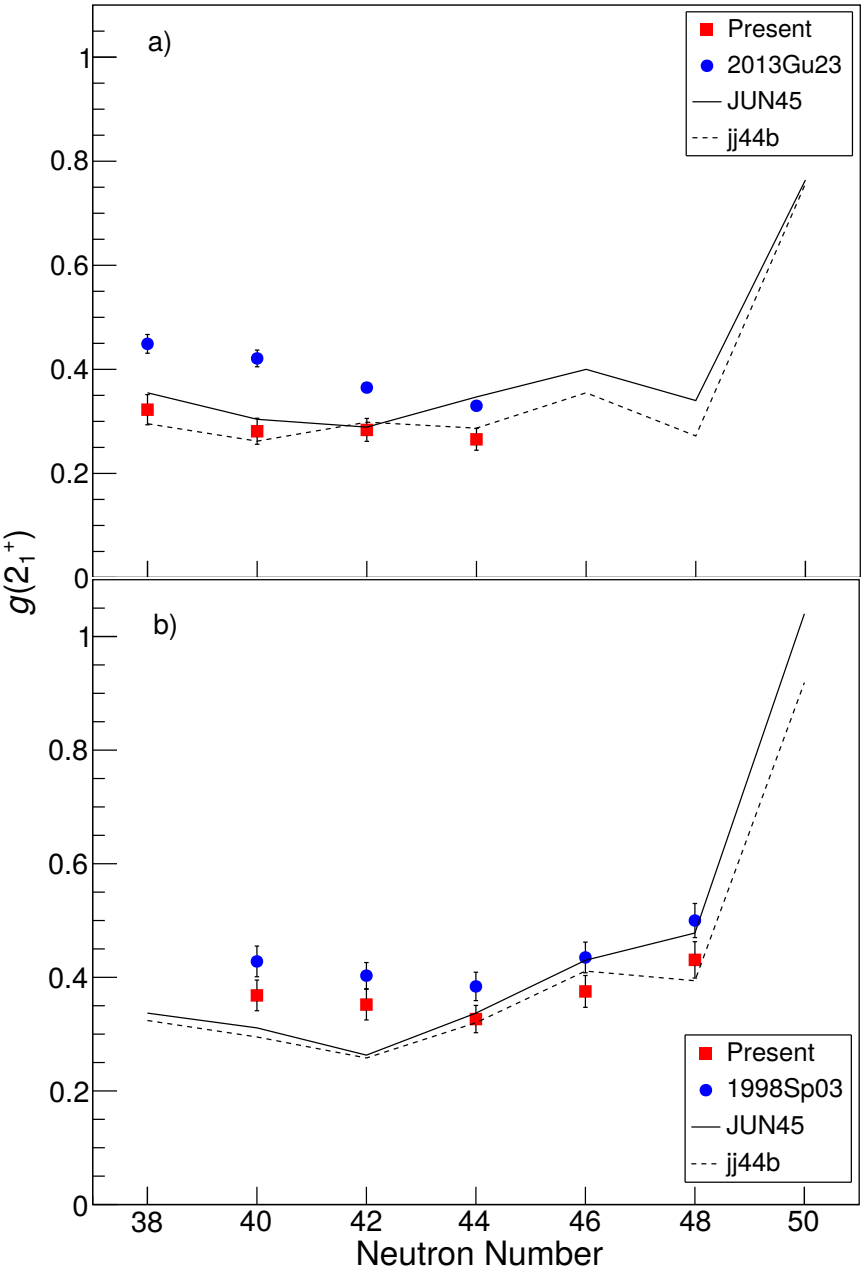

FIGURE 7.3: Measured 2_1^+-level g factors for a) Ge and b) Se isotopes from the present work (red squares) and the literature (blue circles). Previous work is designated by the Nuclear Science Reference code, namely 2013Gu23 [98] and 1998Sp03 [195]. Shell-model calculations using the JUN45 and jj44b interactions are shown as solid lines and dashed lines, respectively. Experimental g factors from Ref. [98] shown in panel a) are their reported weighted-averages that include the previous measurements [166, 130] along with their own data. (See also Table 4.7.)

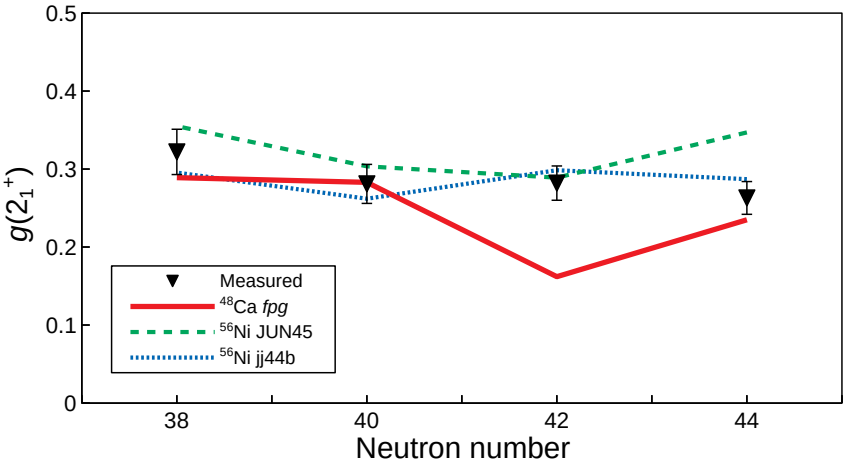

FIGURE 7.4: Comparison between shell-model calculations for $g(2_1^+)$ in the stable, even-A isotopes of Ge, alongside the values presented in §4.3.2. The JUN45 and jj44b interactions use a $^{56}_{28}\mathrm{Ni}_{28}$ core, while the fpg interaction uses a $^{48}_{20}\mathrm{Ca}_{28}$ core. Inclusion of the $\pi 1f_{7/2}$ orbital in the active space appears to lower the average g factor, and causes the value for ^{74}Ge to be greatly reduced. Apart from ^{74}Ge, the ^{48}Ca-core fpg calculation agrees well with the jj44b interaction using the ^{56}Ni core, indicating that proton excitations from the $\pi 1f_{7/2}$ orbital are not important for $g(2_1^+)$ in these nuclei.

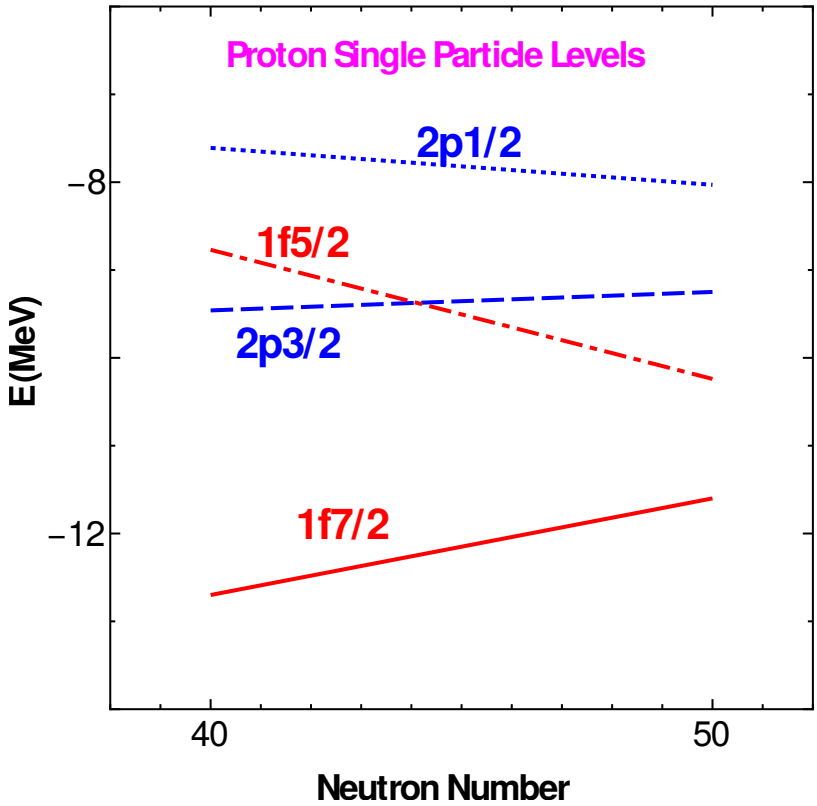

FIGURE 7.5: Calculated proton single-particle energies versus neutron number in exotic Ni isotopes, showing the effect of the $\pi + \rho$ tensor force as the $\nu 1g_{9/2}$ orbital fills. This figure was originally published in Ref. [158], Fig. 4.

TABLE 7.3: Component breakdown of the Ge and Se 2_1^+-state magnetic-moments (μ) for the JUN45 interaction [111].

Z	A	N	$\langle L_p \rangle$	$\langle S_p \rangle$	$\langle L_n \rangle$	$\langle S_n \rangle$	μ_p	μ_n	μ	$g(2^+)$
32	70	38	0.772	0.0044	1.192	0.0297	0.790	-0.079	0.710	0.355
32	72	40	0.760	0.0023	1.176	0.0605	0.769	-0.162	0.607	0.304
32	74	42	0.770	0.0032	1.150	0.0764	0.782	-0.205	0.578	0.289
32	76	44	0.897	0.0039	1.018	0.0813	0.912	-0.218	0.694	0.347
32	78	46	1.017	0.0027	0.895	0.0852	1.028	-0.228	0.800	0.400
32	80	48	1.002	-0.0120	0.907	0.1033	0.955	-0.277	0.679	0.339
32	82	50	2.162	-0.1622	0.000	0.0000	1.528	0.000	1.528	0.764
34	72	38	0.847	-0.0123	1.110	0.0469	0.799	-0.126	0.673	0.337
34	74	40	0.814	-0.0104	1.132	0.0568	0.773	-0.152	0.621	0.310
34	76	42	0.745	-0.0025	1.174	0.0787	0.735	-0.211	0.525	0.262
34	78	44	0.866	0.0064	1.044	0.0814	0.891	-0.218	0.674	0.337
34	80	46	1.044	0.0090	0.865	0.0822	1.079	-0.220	0.859	0.429
34	82	48	1.163	0.0064	0.744	0.0869	1.188	-0.233	0.955	0.478
34	84	50	1.972	0.0279	0.000	0.0000	2.081	0.000	2.081	1.041

7.4 Summary

In this chapter g factors measured in this project, and attained through rescaling based on the present work, have been compared with shell-model predictions. Small discrepancies between measurement, and the empirically derived jj44b-, JUN45- and pfg-interaction Hamiltonians were found. These discrepancies were interpreted through the lens of monopole migration. These investigations suggest behaviour in the mid-shell configuration mixing that present shell-model calculations are unable to fully capture.

The complementary use of transient-field and recoil-in-vacuum techniques has allowed for $g(2_1^+)$ in ^{26}Mg and ^{54,56,58}Fe to be determined with improved precision, enough to reveal discrepancies with shell-model calculations. This opens up the possibility for future measurements in the $Z \sim 30$ and the ^{32}Mg island-of-inversion regions on both stable and radioactive nuclei to be made with confidence. With such measurements available, even more stringent tests of shell-model calculations may be undertaken.

Chapter 8

Conclusion

In this thesis, the feasibility of performing precise and accurate g-factor measurements on short-lived collective states in $Z \sim 30$ nuclei was investigated. Two techniques were explored for such measurements: the thin-foil transient-field technique in inverse-kinematics, and the time-differential recoil-in-vacuum technique. The TF technique is effective for measurements using stable-isotope beams, however calibration of the field strength remains a challenge. Despite the calibration issue, the transient-field technique is an effective means for performing *relative* measurements, particularly when ion velocity, and foil magnetisation and thickness are controlled, as the absolute scale of the field strength factors out. Isobaric nuclei may also be measured simultaneously, allowing for measurements almost completely free from systematic uncertainty. However, this must be performed with caution, as the TF strength may vary sharply between certain elements in iron hosts.

The RIV technique has shown promise for obtaining precise and accurate g-factor measurements. It has special advantages for measurements using radioactive beams (see §2.3.3). However, application of this technique to $Z \sim 30$ nuclei is challenging due to the complex hyperfine interactions present. A Monte-Carlo simulation of the atomic states contributing to the interaction, developed during this project, allowed for a step-wise approach to the analysis. Confounding effects resulting from atomic transitions were modelled, the varying effects owing to different ionic states categorised, and the dominant atomic states contributing strong oscillations to the hyperfine interaction were identified, and then fitted to obtain the g factor. Further details of the hyperfine interaction remain to be investigated, such as the influence of core-hole excited states, however these processes were shown to be less important for modelling the TDRIV data beyond ~ 5 ps. Through this procedure parameters for experimental optimisation were realised, and tools were developed to help probe them for future experiments.

Together, these techniques provide the opportunity to obtain the aforementioned g factors in an accurate and precise manner for nuclei spanning isotopic chains and neighbouring elements.

8.1 Relative g-factor Measurements Using the Transient-Field Technique

Two distinct sets of thin-foil transient-field measurements were performed in this thesis: a relative measurement between the ^{24}Mg and ^{26}Mg 2_1^+ states at high velocity, and a relative measurement between the 2_1^+ states of the stable, even-A isotopes of Ge and Se in inverse kinematics. The first case of a simultaneous measurement of isobaric nuclides in a cocktail beam, in this instance being ^{74}Ge and ^{74}Se, was also performed.

In the ^{24,26}Mg measurement a gadolinium foil was chosen as the ferromagnetic host, due to the stronger transient field experienced by ions. The stronger field was necessary to maximise the precession effect, which is small due to the low-Z and short lifetimes of the ^{24,26}Mg 2_1^+ states. In addition to cryocooling to 5 K, beam currents were kept low to prevent any localised heating that may affect the foil's magnetisation. The relative $g(2_1^+)$ value in ^{26}Mg was scaled using the published ^{24}Mg value, obtained independently using the TDRIV technique. This new value was in strong disagreement with the accepted literature value, but in good agreement with current shell-model calculations (performed by B. A. Brown, see §7.1) and also with the only other value available in the literature.

For the Ge- and Se-isotope measurements an iron foil was chosen to be the ferromagnetic host due to the higher Curie temperature of iron and because extensive experience collected at the ANU HIAF has shown that iron foils consistently achieve near to the saturation magnetisation when polarised by an external field of the order of 0.1 T. Velocity ranges almost completely overlapped across all isotopes, removing virtually all uncertainty in the velocity dependence of the transient-field strength. The simultaneous measurement of ^{74}Ge and ^{74}Se delivered as a cocktail beam ensured that the only uncertainty in determining the $g(2_1^+)$ ratio between the two isobars was in the Z-dependence of the transient field, which is expected to vary smoothly across this region. The resulting ratios were compared with previously published measurements, from which the g-factor ratios were obtained using precession measurements from a single target, and used for comparison. While absolute comparisons of g-factor values showed disagreement, the single-target g-factor ratios from the literature were in agreement. These were combined in weighted averages to obtain precise g-factor ratios, which now require only a single, independent measurement of $g(2_1^+)$ in one of the isotopes to scale the rest, as was done in the Mg measurement.

8.2 Precise g-factor Measurements Using the Recoil-In-Vacuum Technique

The time-differential recoil-in-vacuum technique offers a unique opportunity to determine nuclear-excited-state g factors to high precision with comparatively small systematic uncertainty. This is made possible by the work of Goldring *et al.* [91], and atomic-structure calculations performed by GRASP [84], that allow the calculation of the hyperfine interaction in free ions to very high accuracy. This approach has been successfully applied to light nuclei in which only a single bound electron is responsible for the hyperfine interaction.

A measurement of the 2_1^+-state in ^{56}Fe using the TDRIV technique was performed on multi-electron ion ensembles that exhibited a complex hyperfine interaction due to the multiple ionic states and excited-atomic-state configurations present. A Monte-Carlo simulation was used to model how the occupation of excited atomic states may change through time, and how the resulting hyperfine interaction would affect the measured angular correlations. From these simulations, several atomic states from F-like and Na-like ions were identified as strongly contributing to the hyperfine interaction. Potential effects arising from atomic transitions were also examined, and accounted for by allowing variable average occupation and phase offsets in the hyperfine-interaction frequencies. Together, these were then used to fit the data and determine the g factor.

Another TDRIV measurement, performed on ^{76}Ge, was analysed with the intention of both observing the behaviour of the hyperfine interaction through time, and identifying the possible presence of a frequency with which to determine $g(2_1^+)$. Because the measurement was not optimised for a g-factor measurement, a firm value for $g(2_1^+)$ could not be determined from the weak Na-like frequency present. However, a range for the g-factor value was still obtained, despite the weak contribution.

Aspects of both the ^{56}Fe and ^{76}Ge measurements informed the design of future experiments, indicating the importance of having a strong $J = 1/2$ atomic-state contribution with which to determine $g(2_1^+)$, while also minimising the presence of other atomic states which will contribute high-frequency oscillations to the hyperfine interaction. Ions having multiple valence electrons give a superposition of many atomic states that produce a smooth, quasi-exponential time dependence that is relatively innocuous in the measurements described here.

For nuclei in the region $Z \sim 30$, measurements should be performed with charge-state distributions centred between Na-like and Mg-like ions. This is desirable because

a strong Na-like contribution is required with little interference. The ^{76}Ge measurement showed that the lower-charged ions ($>$ 11 bound electrons) contribute the quasi-exponential attenuation-coefficient behaviour, noted above, to the hyperfine interaction, which is easy to model and does not interfere with the Na-like $3s_{1/2}$ frequency. This is in stark contrast to the ^{56}Fe measurement, in which the F-like fraction was very strong and confounded a straight-forward interpretation of the results. By centring the charge-state distribution closer to Mg-like, a strong Na-like contribution may still be obtained, while the Ne-like and Al-like charge states will not contribute any interfering oscillations in the overall time-dependent attenuation coefficients. The conclusion of the present work is that $g(2_1^+)$ measurements may be performed on nuclei in this region for stable ion beams with confidence, and precision.

8.3 Obtaining g-factors Spanning Isotope Chains and Neighbouring Elements

During this project $g(2_1^+)$ of ^{26}Mg and ^{56}Fe have been determined, free from uncertainties in transient-field-strength calibration, and with good precision. The relative $g(2_1^+)$ values between the stable, even-A isotopes of Ge and Se have also been determined with good precision. A range for the absolute g factor is suggested from the ^{76}Ge TDRIV data.

The ^{26}Mg value is in good agreement with the *sd*-space shell-model calculations, but deviations are expected as N increases towards the island of inversion. The newly determined value for ^{56}Fe, presented in this thesis (see §6.2) has been used to scale existing relative measurements of $g(2_1^+)$ for ^{54,58}Fe [57], and deviations from predictions of large-basis shell-model calculations begin to emerge. It is possible that these deviations are related to increasing proximity to the potential island of inversion at ^{64}Fe. The $g(2_1^+)$ values may have increased sensitivity to the occupation of the $\nu 1g_{9/2}$ orbital compared to the $E(2^+)$ and $B(E2)$ systematics. There are also notable discrepancies between the relative values of $g(2_1^+)$ along the Ge and Se isotopes (i.e. N dependence). A future measurement of ^{74}Ge or ^{76}Ge using the TDRIV technique would allow the g factors to be accurately scaled.

With firmly assigned g factors for the Fe, Ge and Se isotopes, the next step in this experimental regime should be to expanded into the even-Z isotope chains between iron and germanium by performing simultaneous transient-field measurements of isobaric ^{58}Fe and ^{58}Ni, and ^{70}Ge and ^{70}Zn. Relative isotopic measurements within each element have largely been made using the transient-field technique, which can then be reliably scaled using the relative isobaric measurements. The present work suggests that sequences of such measurements made using the *same* target give reliable relative g factors. Such measurements, though potentially challenging due to the short 2_1^+-state lifetimes of the isobaric nuclei and relative isotopic abundances, can be achieved using stable-beam facilities. With reliable 2_1^+-state g-factors and lifetimes available, time-integral recoil-in-vacuum measurements can be made on the stable isotopes, interpreted using the Monte-Carlo simulation model developed in this project, and then used to calibrate the hyperfine-interaction strength. With the hyperfine-interaction strength accurately calibrated, $g(2_1^+)$ can then be determined in radioactive nuclei from time-integral recoil-in-vacuum measurements using radioactive ion-beam facilities. With measurements on radioactive nuclei available, $g(2_1^+)$ values across the region spanning $26 \leq Z \leq 34$, and the neutron shell-closures from $28 \leq N \leq 50$, will enable a thorough test of shell-model calculations in the fpg space to be undertaken.

Appendix A

Publications

The following are publications either authored by or co-authored by the thesis author, or regarding experiments in which the thesis author was involved during the research candidature.

J. T. H. Dowie, T. Kibédi, D. G. Jenkins, A. E. Stuchbery, A. Akber, H. A. Alshammari, N. Aoi, A. Avaa, L. J. Bignell, M. V. Chisapi, B. J. Coombes, T. K. Eriksen, M. S. M. Gerathy, T. J. Gray, T. H. Hoang, E. Ideguchi, P. Jones, M. Kumar Raju, G. J. Lane, B. P. McCormick, L. J. McKie, A. J. Mitchell, N. J. Spinks and B. Tee Pi-Ern, "Evidence for shape coexistence and superdeformation in ^{24}Mg", *Physics Letters B, volume 811, 135855 (2020).* DOI: 10.1016/j.physletb.2020.135855

M. S. M. Gerathy, G. J. Lane, A. E. Stuchbery, G. D. Dracoulis, T. Kibédi, A. Akber, L. J. Bignell, B. J. Coombes, J. T. H. Dowie, T. J. Gray, B. Q. Lee, B. P. McCormick, A. J. Mitchell and N. Palalani, "γ-ray and conversion-electron spectroscopy of the high-spin isomer in ^{145}Sm", *Physical Review C, volume 102, 044319 (2020).* DOI: 10.1103/PhysRevC.102.044319

T. K. Eriksen, T. Kibédi, M. W. Reed, A. E. Stuchbery, K. J. Cook, A. Akber, B. Alshahrani, A. A. Avaa, K. Banerjee, A. C. Berriman, L. J. Bezzina, L. J. Bignell, J. Buete, I. P. Carter, B. J. Coombes, J. T. H. Dowie, M. Dasgupta, L. J. Evitts, A. B. Garnsworthy, M. S. M. Gerathy, T. J. Gray, D. J. Hinde, T. H. Hoang, S. S. Hota, E. Ideguchi, P. Jones, G. J. Lane, B. P. McCormick, A. J. Mitchell, N. Palalani, T. Palazzo, M. Ripper, E. C. Simpson, J. Smallcombe, B. M. A. Swinton-Bland, T. Tanaka, T. G. Tornyi and M. O. de Vries, "Improved precision on the experimental $E0$ decay branching ratio of the Hoyle state", *Physical Review C, volume 102, 024320 (2020).* DOI: 10.1103/PhysRevC.102.024320

T. J. Gray, A. E. Stuchbery, B. J. Coombes, J. T. H. Dowie, M. S. M. Gerathy, T. Kibédi, G. J. Lane, B. P. McCormick, A. J. Mitchell and M. W. Reed, "Hyperfine fields at ^{66}Ga, ^{67,69}Ge implanted into iron and gadolinium hosts at 6 K, and applications to g-factor measurements", *Physical Review C, volume 101, 054302 (2020).* DOI: 10.1103/PhysRevC.101.054302

B. J. Coombes, A. E. Stuchbery, J. M. Allmond, A. Gargano, J. T. H. Dowie, G. Georgiev, M. S. M. Gerathy, T. J. Gray, T. Kibédi, G. J. Lane, B. P. McCormick, A. J. Mitchell, N. J. Spinks and B. Tee Pi-Ern, "Emerging nuclear collectivity in $^{124-130}$Te", *European Physics Journal Web of Conferences, volume 232, 04003*. DOI: 10.1051/epjconf/202023204003

J. T. H. Dowie, T. Kibéedi, A. E. Stuchbery, A. Akber, A. Avaa, L. J. Bignell, M. V. Chisapi, B. J. Coombes, T. K. Eriksen, M. S. M. Gerathy, T. J. Gray, T. H. Hoang, E. Ideguchi, P. Jones, M. Kumar Raju, G. J. Lane, B. P. McCormick, A. J. Mitchell and B. Tee Pi-Ern, "Evidence for shape coexistence in ^{52}Cr through conversion-electron and pair-conversion spectroscopy", *European Physics Journal Web of Conferences, volume 232, 04004*. DOI: 10.1051/epjconf/202023204004

B. P. McCormick, A. E. Stuchbery, A. Goasduff, A. Kusoglu and G. Georgiev, "Modelling hyperfine interactions for nuclear g-factor measurements", *European Physics Journal Web of Conferences, volume 232, 04009 (2020)*. DOI: 10.1051/epjconf/202023204009

B. P. McCormick, A. E. Stuchbery, B. A. Brown, G. Georgiev, B. J. Coombes, T. J. Gray, M. S. M. Gerathy, G. J. Lane, T. Kibédi, A. J. Mitchell, M. W. Reed, A. Akber, L. J. Bignell, J. T. H. Dowie, T. K. Eriksen, S. Hota, N. Palalani and T. Tornyi, "First-excited state g factors in the stable, even Ge and Se isotopes", *Physical Review C, volume 100, 044317 (2019)*. DOI: 10.1103/PhysRevC.100.044317

A. E. Stuchbery, B. P. McCormick, T. J. Gray and B. J. Coombes, "Pushing the limits of excited-state g-factor measurements", *European Physics Journal Web of Conferences, volume 178, 02005 (2018)*. DOI: 10.1051/epjconf/201817802005

B. P. McCormick, A. E. Stuchbery, T. Kibédi, G. J. Lane, M. W. Reed, T. K. Eriksen, S. S. Hota, B. Q. Lee and N. Palalani, "Probing the $N = 14$ subshell closure: g factor of the ^{26}Mg(2_1^+) state", *Physics Letters B, volume 779, pages 445-451 (2018)*. DOI: 10.1016/j.physletb.2018.02.032

Appendix B

Angular-Correlation Plots

B.1 ^{56}Fe TDRIV ACs

This appendix section contains angular-correlation (AC) plots obtained from the γ-ray detectors in ORGAM in the time-differential recoil-in-vacuum (TDRIV) measurement on the 2_1^+ state in ^{56}Fe, described in §6.1. The data are separated by plunger distance.

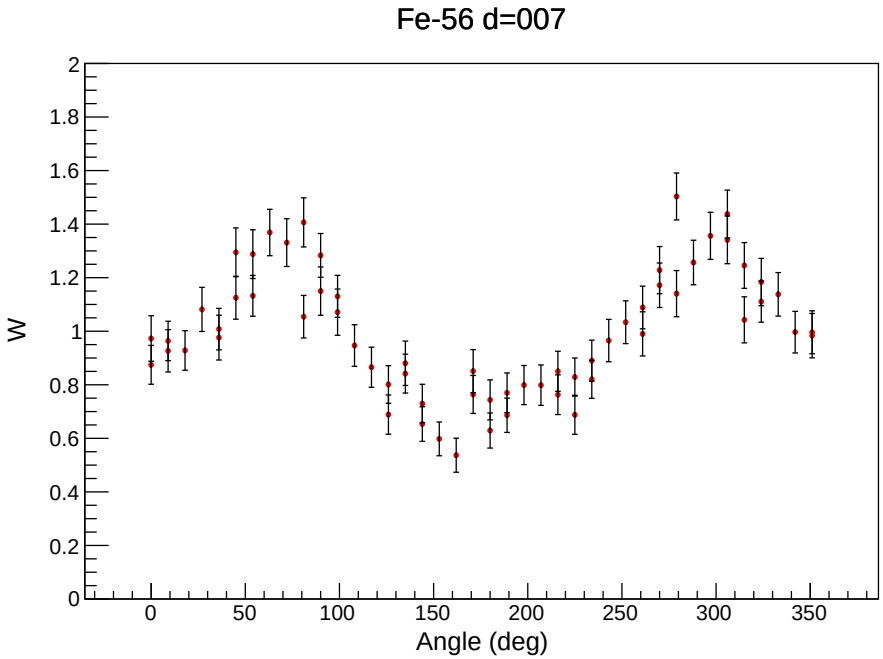

FIGURE B.1: ^{56}Fe TDRIV ϕ-dependent AC. γ-ray detectors $\theta = 46.5°$, time = 2.24 ps. See §6.1 for experimental details.

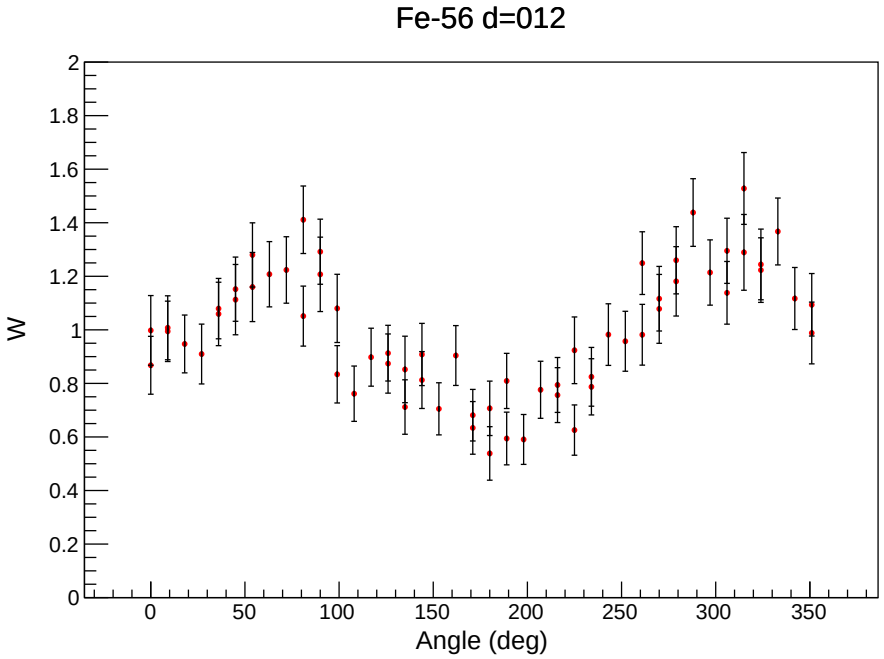

FIGURE B.2: ^{56}Fe TDRIV ϕ-dependent AC. γ-ray detectors $\theta = 46.5°$, time = 2.62 ps. See §6.1 for experimental details.

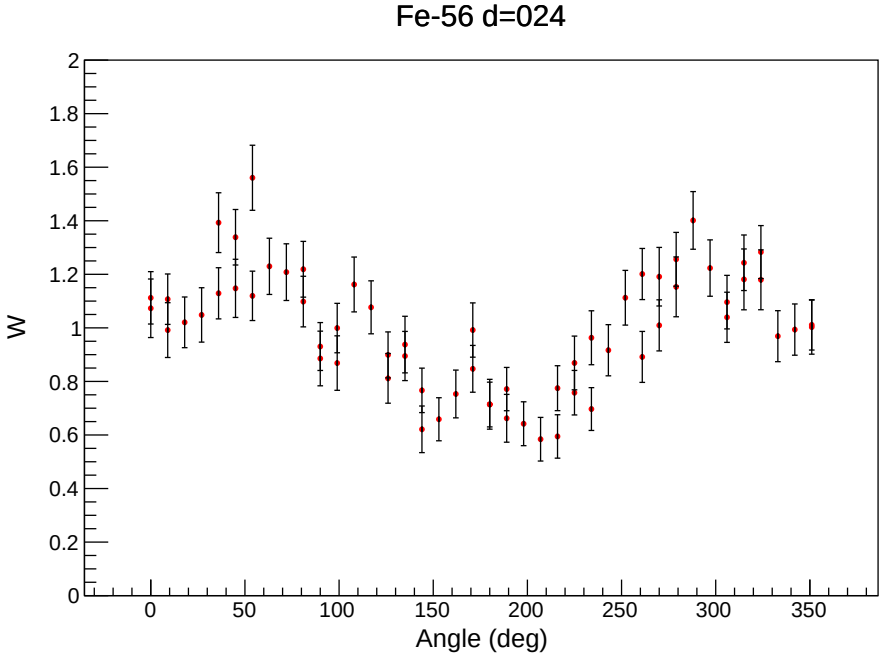

FIGURE B.3: ^{56}Fe TDRIV ϕ-dependent AC. γ-ray detectors $\theta = 46.5°$, time = 3.51 ps. See §6.1 for experimental details.

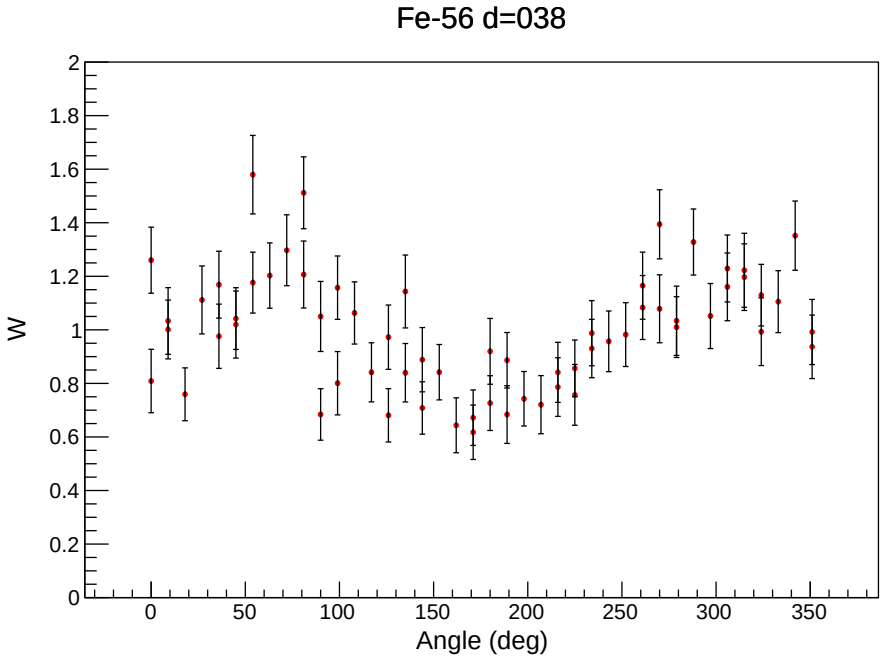

FIGURE B.4: ^{56}Fe TDRIV ϕ-dependent AC. γ-ray detectors $\theta = 46.5°$, time = 4.56 ps. See §6.1 for experimental details.

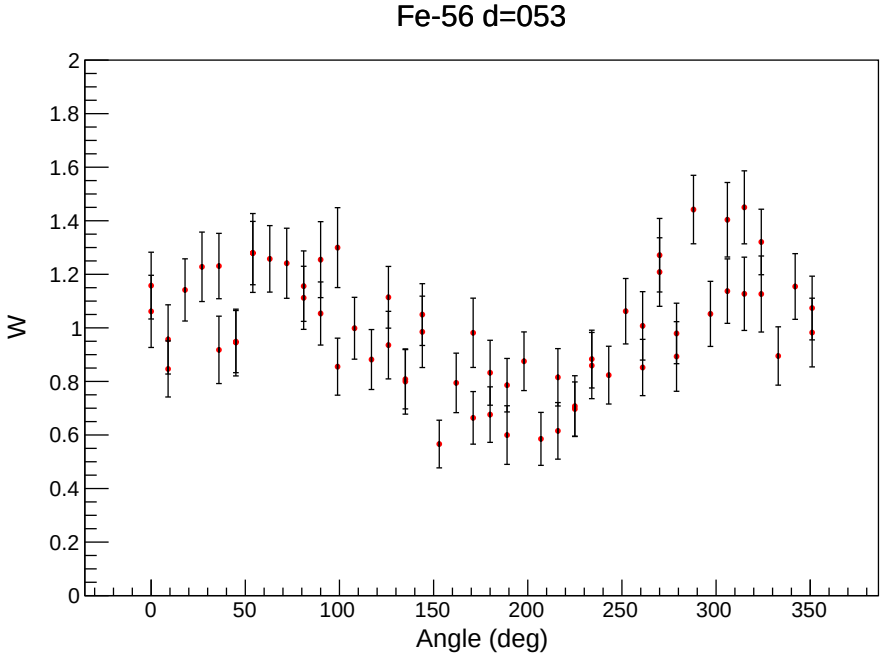

FIGURE B.5: ^{56}Fe TDRIV ϕ-dependent AC. γ-ray detectors $\theta = 46.5°$, time = 5.68 ps. See §6.1 for experimental details.

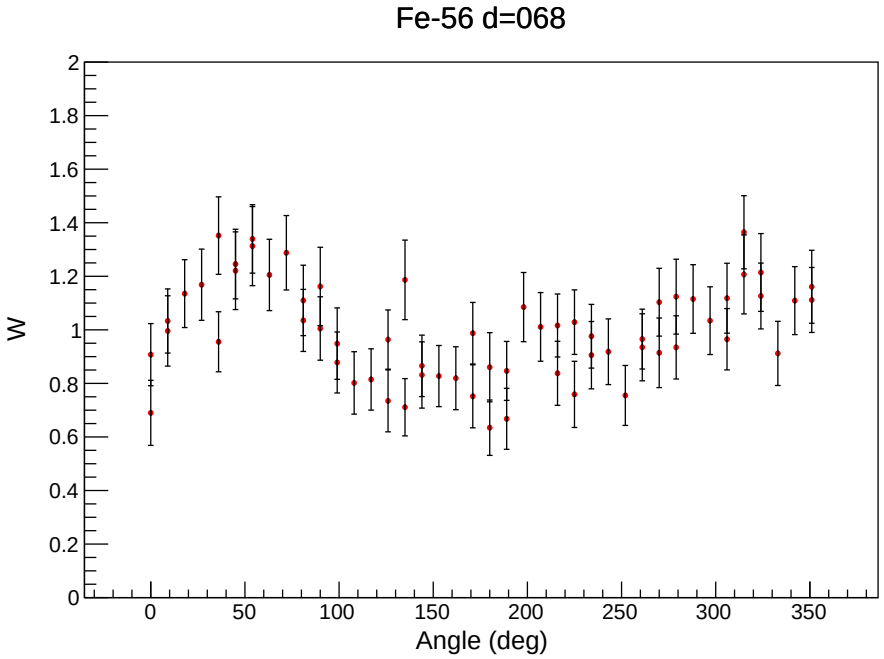

FIGURE B.6: ^{56}Fe TDRIV ϕ-dependent AC. γ-ray detectors $\theta = 46.5°$, time = 6.80 ps. See §6.1 for experimental details.

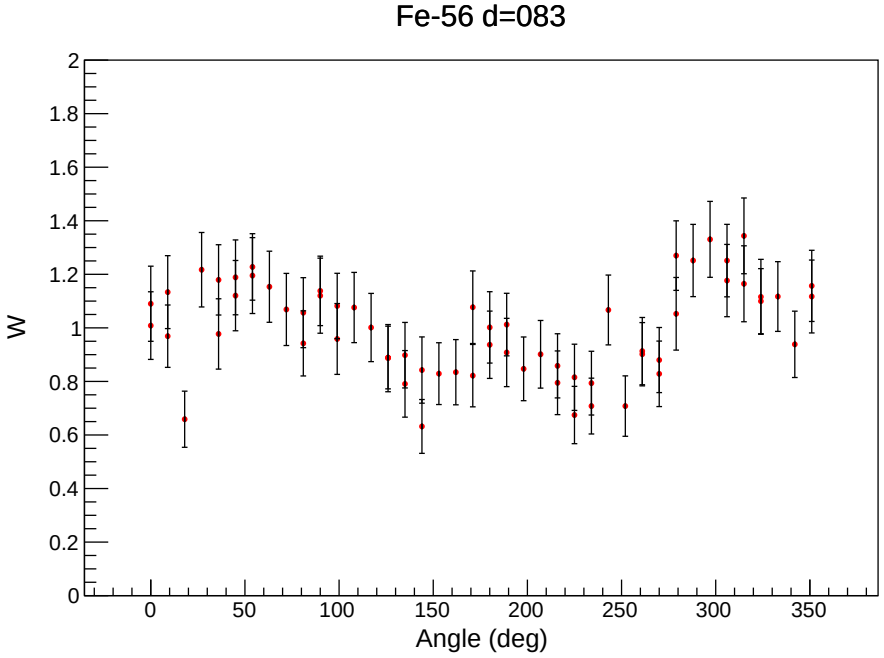

FIGURE B.7: ^{56}Fe TDRIV ϕ-dependent AC. γ-ray detectors $\theta = 46.5°$, time = 7.92 ps. See §6.1 for experimental details.

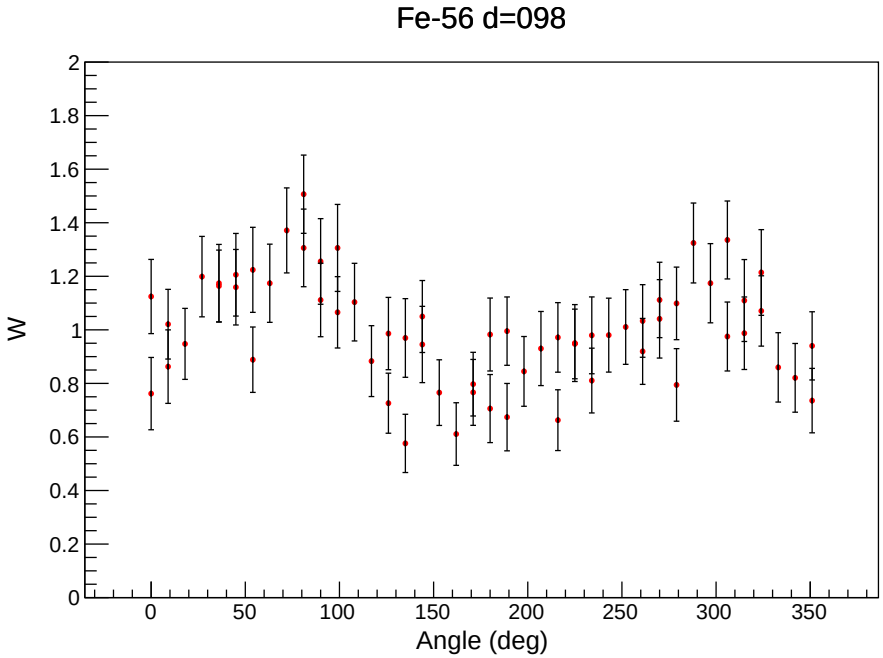

FIGURE B.8: ^{56}Fe TDRIV ϕ-dependent AC. γ-ray detectors $\theta = 46.5°$, time = 9.04 ps. See §6.1 for experimental details.

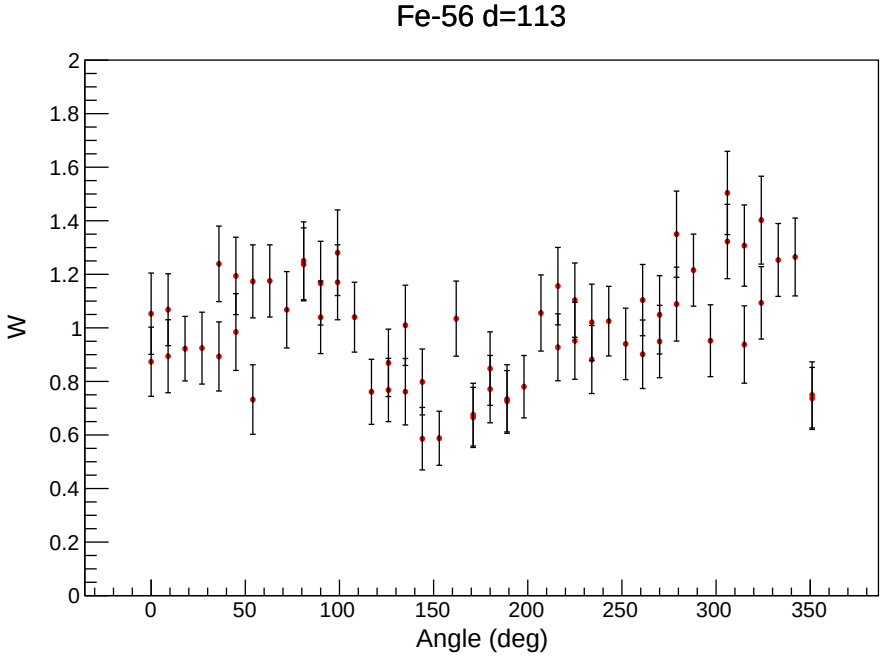

FIGURE B.9: ^{56}Fe TDRIV ϕ-dependent AC. γ-ray detectors $\theta = 46.5°$, time = 10.2 ps. See §6.1 for experimental details.

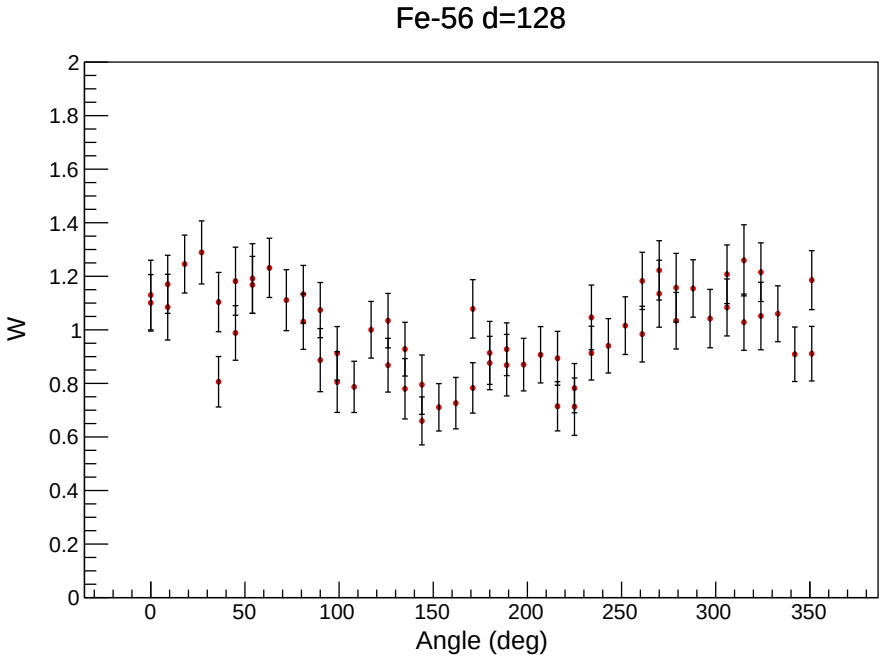

FIGURE B.10: ^{56}Fe TDRIV ϕ-dependent AC. γ-ray detectors $\theta = 46.5°$, time = 11.3 ps. See §6.1 for experimental details.

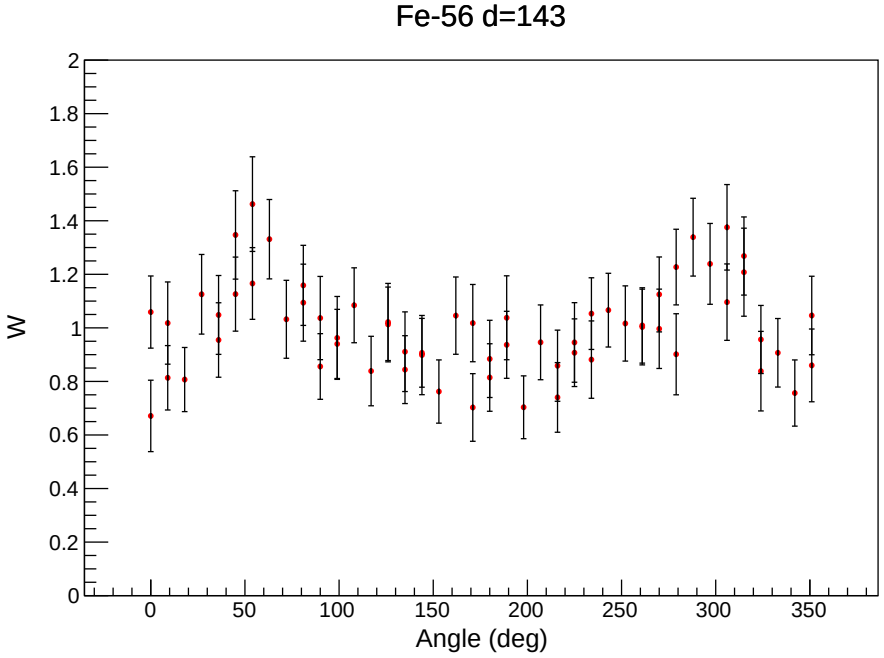

FIGURE B.11: ^{56}Fe TDRIV ϕ-dependent AC. γ-ray detectors $\theta = 46.5°$, time = 12.4 ps. See §6.1 for experimental details.

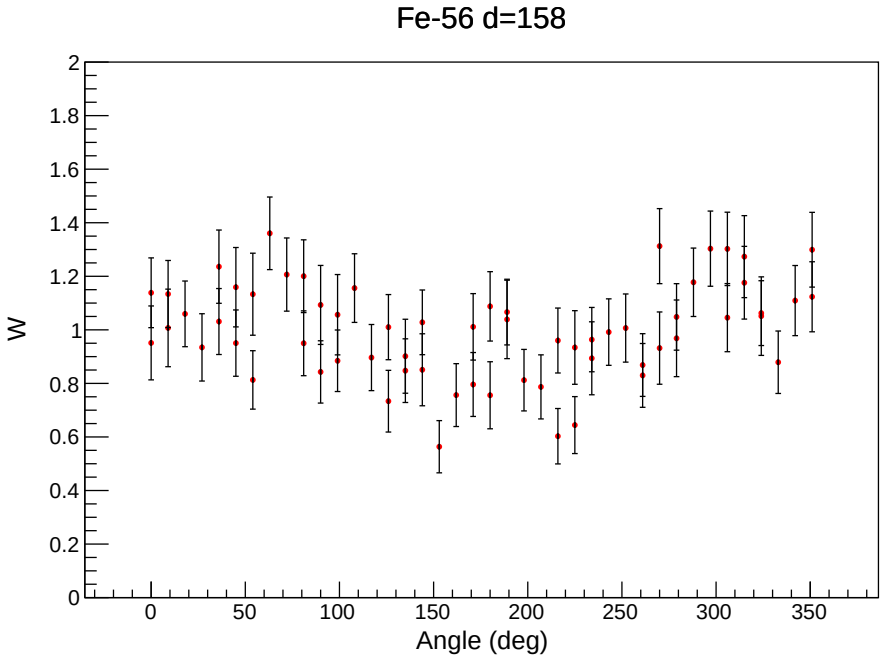

FIGURE B.12: ^{56}Fe TDRIV ϕ-dependent AC. γ-ray detectors $\theta = 46.5°$, time = 13.5 ps. See §6.1 for experimental details.

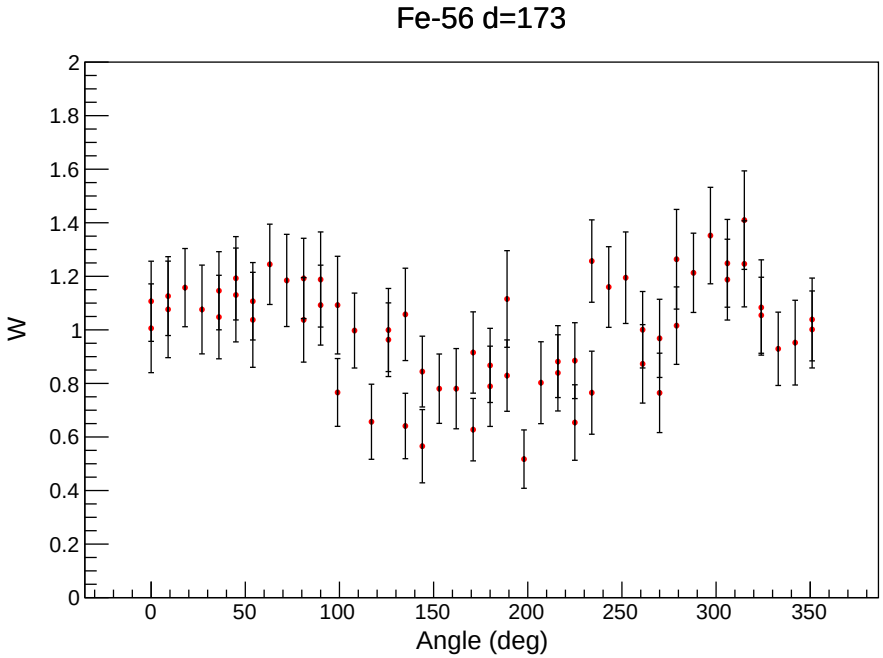

FIGURE B.13: ^{56}Fe TDRIV ϕ-dependent AC. γ-ray detectors $\theta = 46.5°$, time = 14.6 ps. See §6.1 for experimental details.

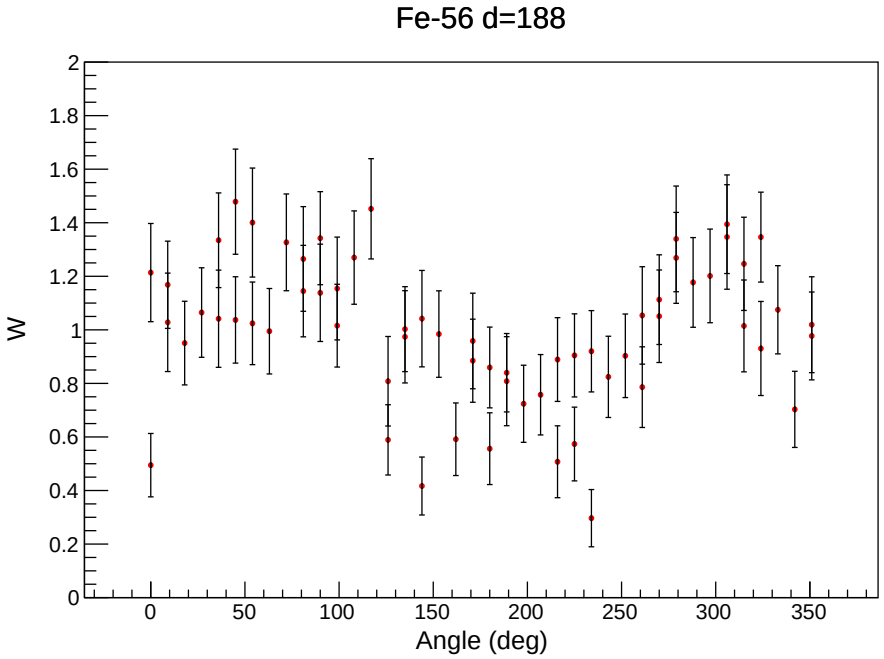

FIGURE B.14: ^{56}Fe TDRIV ϕ-dependent AC. γ-ray detectors $\theta = 46.5°$, time = 15.8 ps. See §6.1 for experimental details.

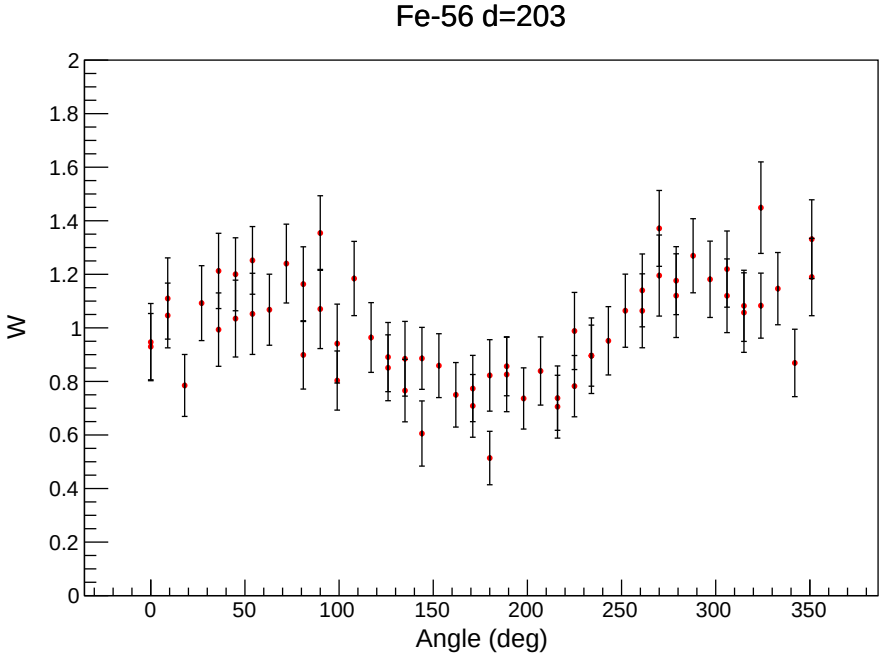

FIGURE B.15: ^{56}Fe TDRIV ϕ-dependent AC. γ-ray detectors $\theta = 46.5°$, time = 16.9 ps. See §6.1 for experimental details.

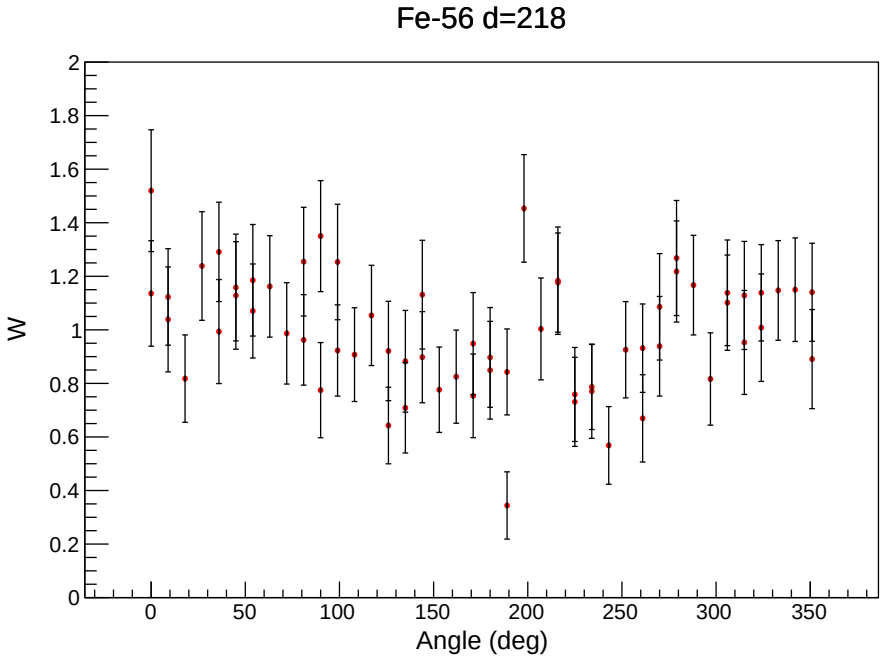

FIGURE B.16: ^{56}Fe TDRIV ϕ-dependent AC. γ-ray detectors $\theta = 46.5°$, time = 18.0 ps. See §6.1 for experimental details.

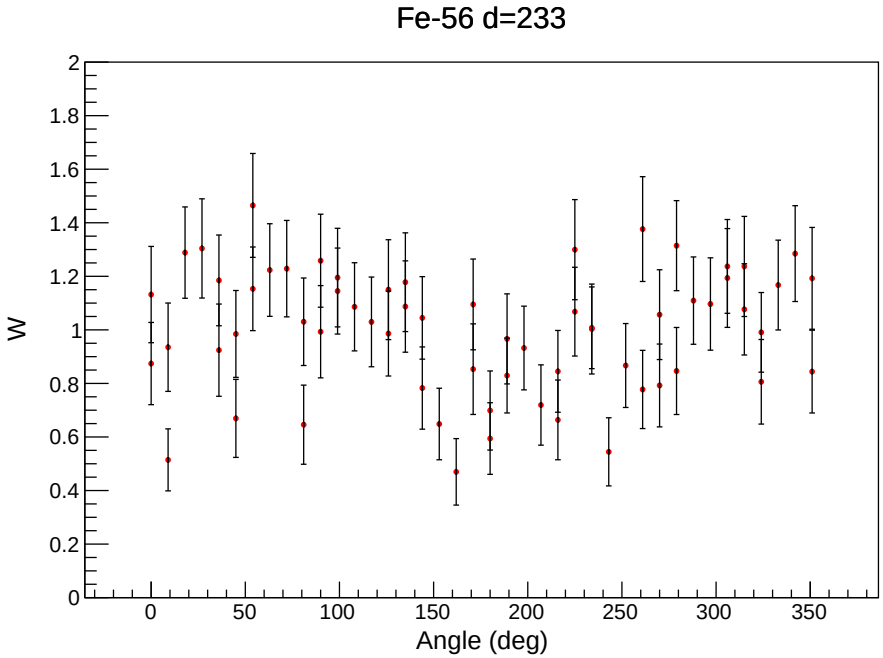

FIGURE B.17: ^{56}Fe TDRIV ϕ-dependent AC. γ-ray detectors $\theta = 46.5°$, time = 19.1 ps. See §6.1 for experimental details.

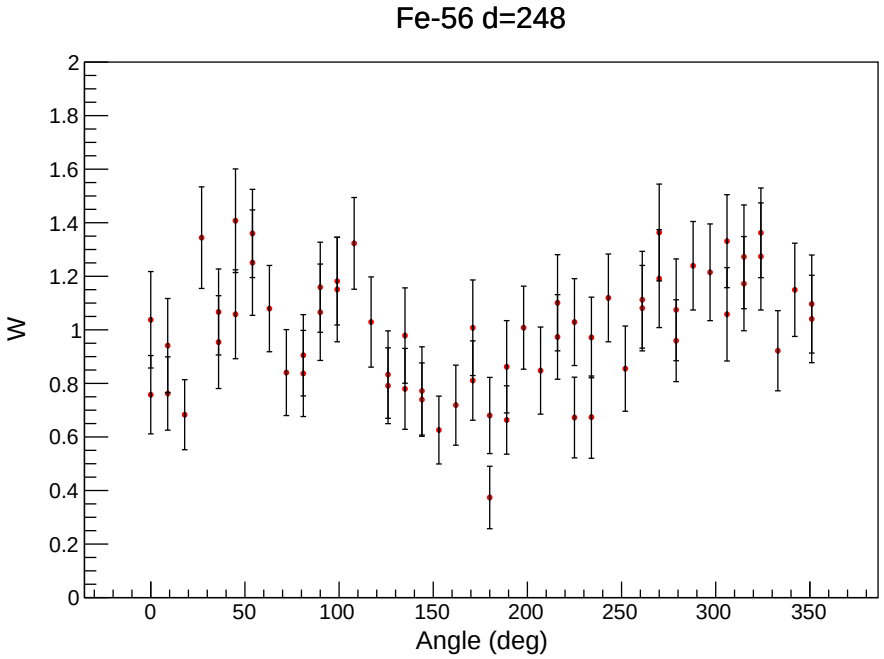

FIGURE B.18: ^{56}Fe TDRIV ϕ-dependent AC. γ-ray detectors $\theta = 46.5°$, time = 20.3 ps. See §6.1 for experimental details.

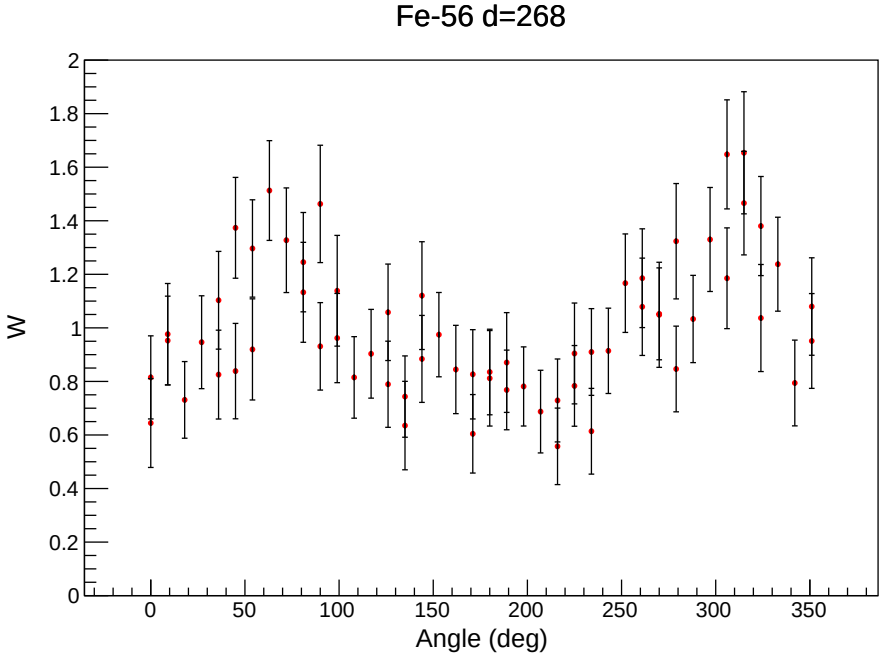

FIGURE B.19: ^{56}Fe TDRIV ϕ-dependent AC. γ-ray detectors $\theta = 46.5°$, time = 21.7 ps. See §6.1 for experimental details.

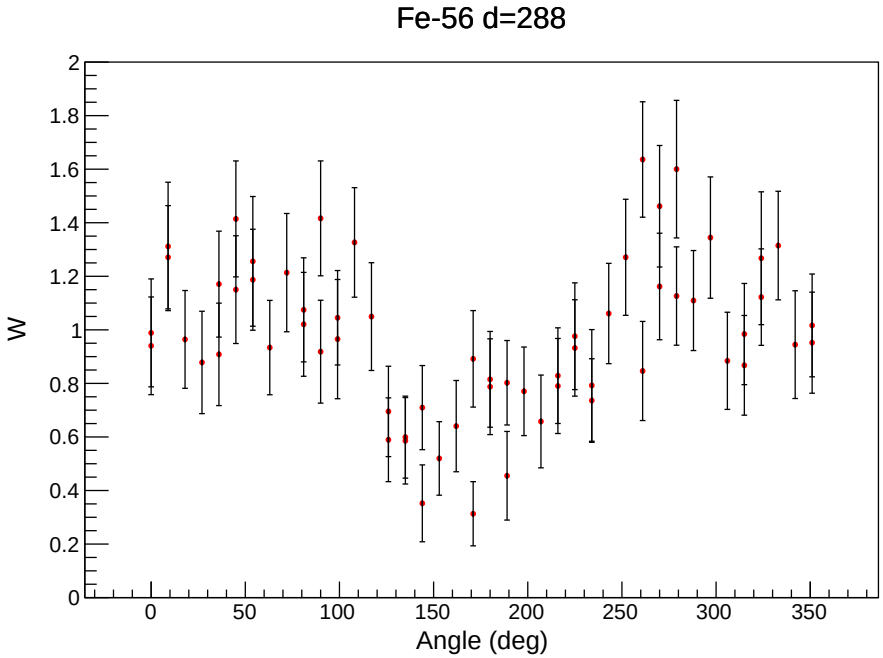

FIGURE B.20: ^{56}Fe TDRIV ϕ-dependent AC. γ-ray detectors $\theta = 46.5°$, time = 23.2 ps. See §6.1 for experimental details.

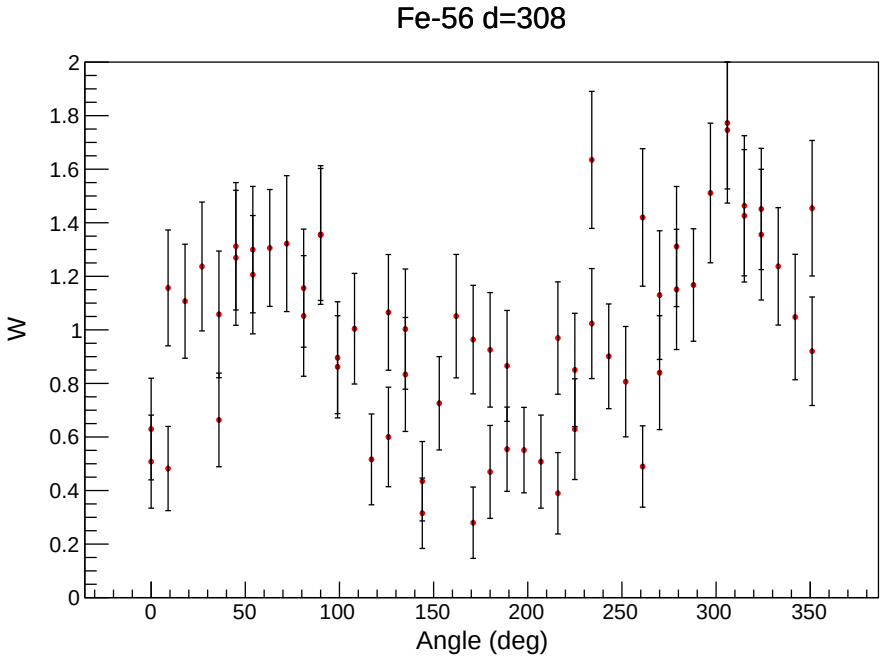

FIGURE B.21: ^{56}Fe TDRIV ϕ-dependent AC. γ-ray detectors $\theta = 46.5°$, time = 24.7 ps. See §6.1 for experimental details.

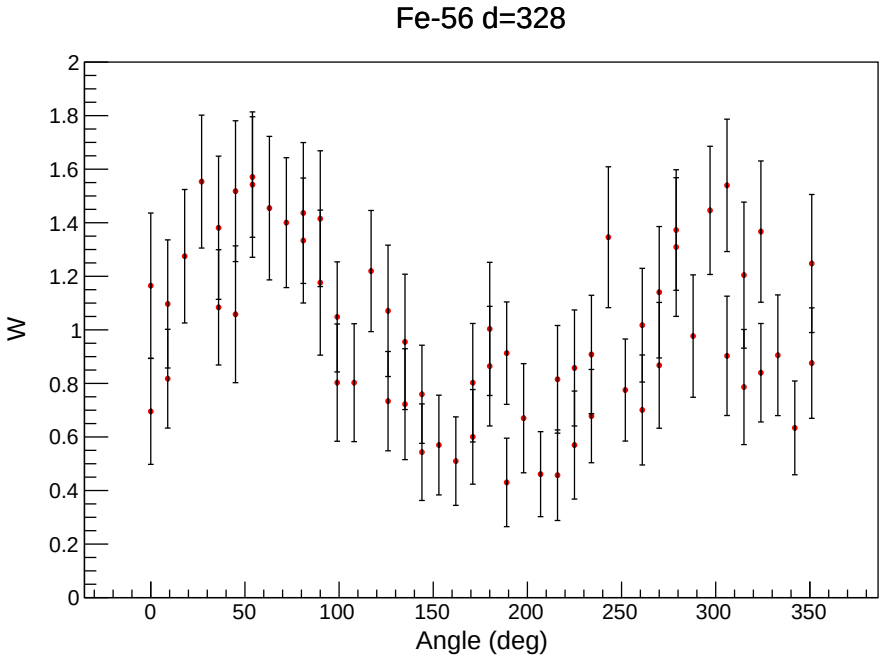

FIGURE B.22: ^{56}Fe TDRIV ϕ-dependent AC. γ-ray detectors $\theta = 46.5°$, time = 26.2 ps. See §6.1 for experimental details.

B.2 ^{54,56}Fe TIRIV ACs

This appendix section contains tabulated photopeak counts and angular-correlation (AC) plots from the time-integral recoil-in-vacuum (TIRIV) measurements on the 2_1^+ states in ^{54,56}Fe, described in §6.3. The data are separated by run and γ-ray detector.

TABLE B.1: Unscaled photopeak counts in Fig. B.23

ϕ	N	σ_N
0	4991	115
45	3357	70
90	1388	56
135	4513	78
180	5625	121

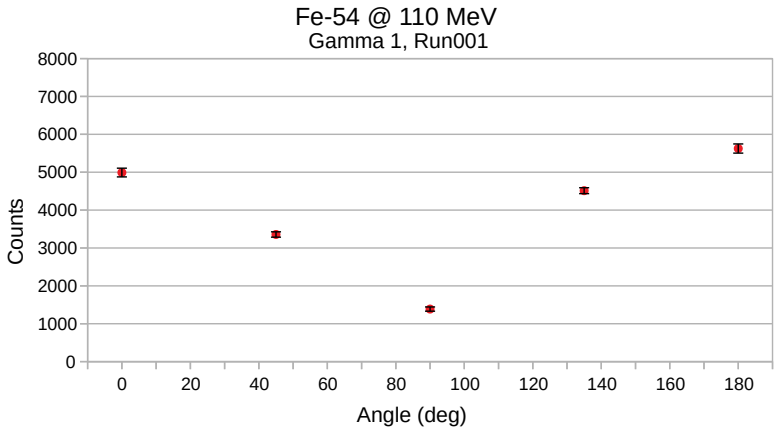

FIGURE B.23: ^{54}Fe TIRIV ϕ-dependent AC. γ-ray detector $\theta = 90°$. See §6.3 for experimental details.

TABLE B.2: Unscaled photopeak counts in Fig. B.24

ϕ	N	σ_N
0	1881	63
45	2211	48
90	3015	55
135	2779	53
180	1967	63

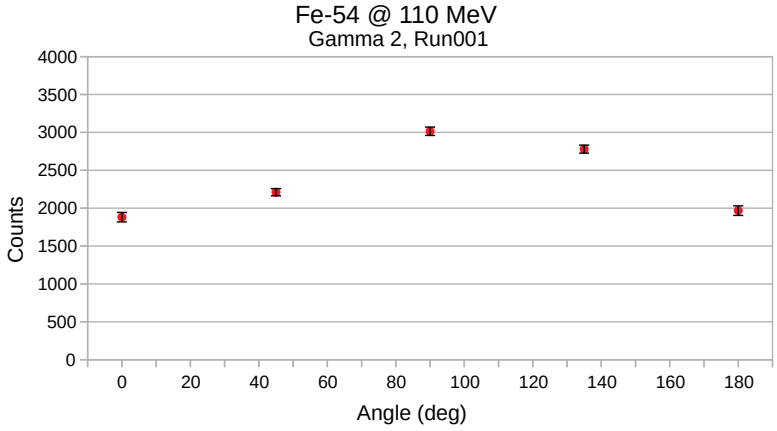

FIGURE B.24: ^{54}Fe TIRIV ϕ-dependent AC. γ-ray detector $\theta = 135°$. See §6.3 for experimental details.

TABLE B.3: Unscaled photopeak counts in Fig. B.25

ϕ	N	σ_N
0	2129	66
45	2852	54
90	2855	54
135	1872	44
180	1752	59

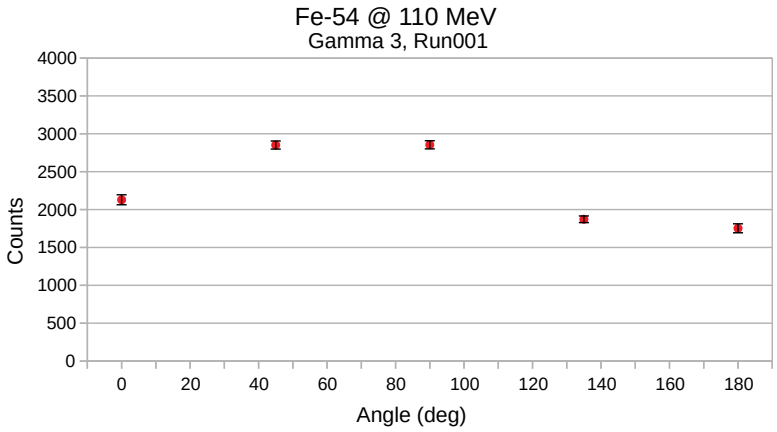

FIGURE B.25: ^{54}Fe TIRIV ϕ-dependent AC. γ-ray detector $\theta = 225°$. See §6.3 for experimental details.

TABLE B.4: Unscaled photopeak counts in Fig. B.26

ϕ	N	σ_N
0	5914	124
45	4423	77
90	1269	54
135	3792	72
180	5177	116

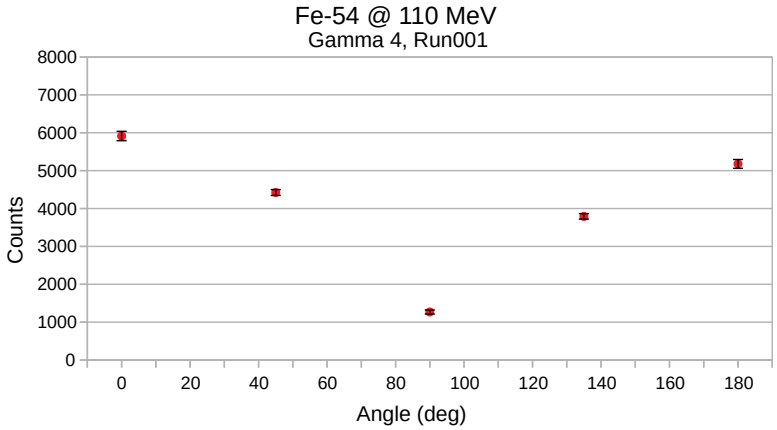

FIGURE B.26: ^{54}Fe TIRIV ϕ-dependent AC. γ-ray detector $\theta = 270°$. See §6.3 for experimental details.

TABLE B.5: Unscaled photopeak counts in Fig. B.27

ϕ	N	σ_N
0	4951	100
45	6559	77
90	6054	86
135	4323	66
180	3776	89

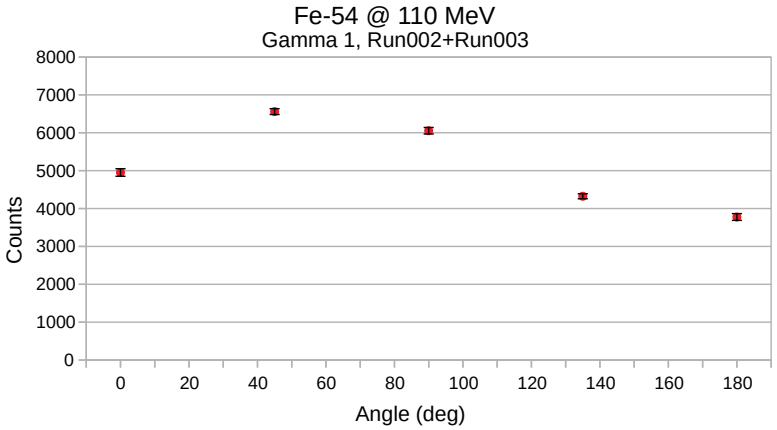

FIGURE B.27: ^{54}Fe TIRIV ϕ-dependent AC. γ-ray detector $\theta = 45°$. See §6.3 for experimental details.

TABLE B.6: Unscaled photopeak counts in Fig. B.28

ϕ	N	σ_N
0	1520	50
45	1680	36
90	2425	50
135	2328	43
180	1744	52

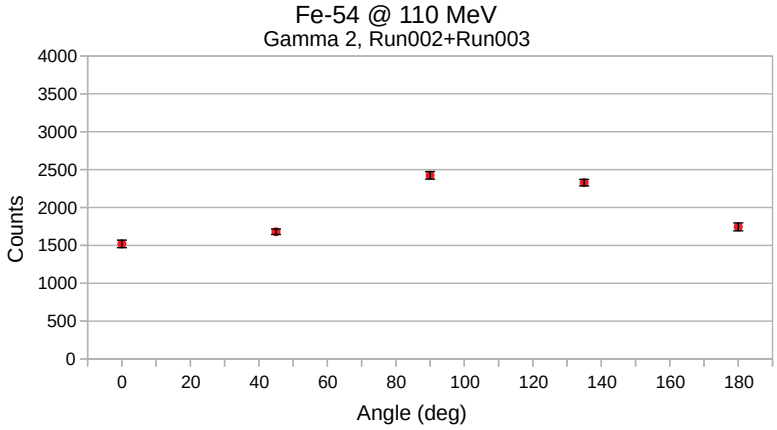

FIGURE B.28: ^{54}Fe TIRIV ϕ-dependent AC. γ-ray detector $\theta = 135°$. See §6.3 for experimental details.

TABLE B.7: Unscaled photopeak counts in Fig. B.29

ϕ	N	σ_N
0	1899	55
45	2464	44
90	2317	48
135	1646	36
180	1523	49

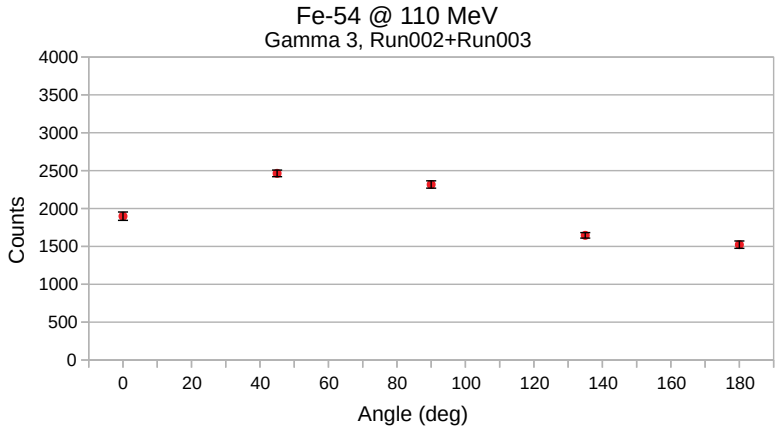

FIGURE B.29: ^{54}Fe TIRIV ϕ-dependent AC. γ-ray detector $\theta = 225°$. See §6.3 for experimental details.

TABLE B.8: Unscaled photopeak counts in Fig. B.30

ϕ	N	σ_N
0	3926	91
45	4247	65
90	6154	86
135	6285	76
180	4821	97

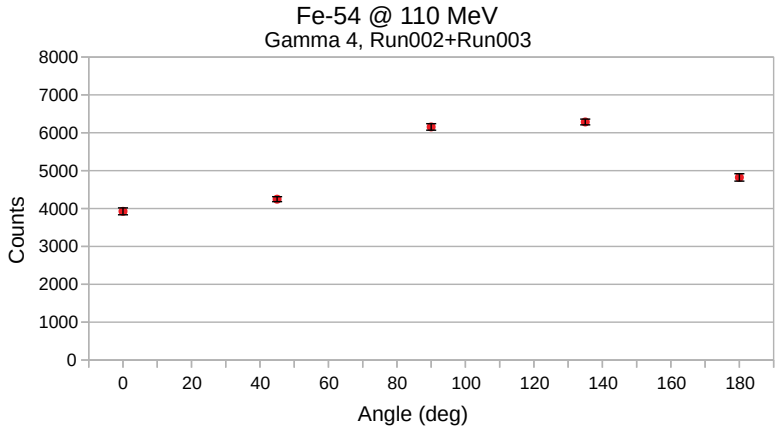

FIGURE B.30: ^{54}Fe TIRIV ϕ-dependent AC. γ-ray detector $\theta = 315°$. See §6.3 for experimental details.

TABLE B.9: Unscaled photopeak counts in Fig. B.31

ϕ	N	σ_N
0	13279	167
45	16444	128
90	16308	129
135	11960	111
180	10550	147

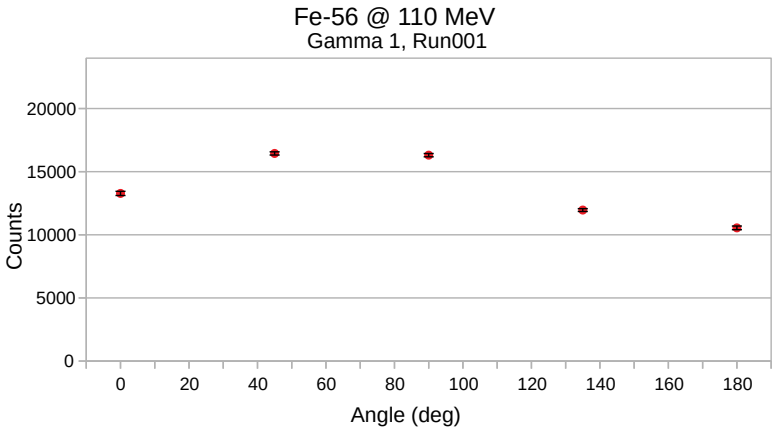

FIGURE B.31: ^{56}Fe TIRIV ϕ-dependent AC. γ-ray detector $\theta = 45°$. See §6.3 for experimental details.

TABLE B.10: Unscaled photopeak counts in Fig. B.32

ϕ	N	σ_N
0	4332	96
45	4678	69
90	6632	82
135	6423	81
180	5085	101

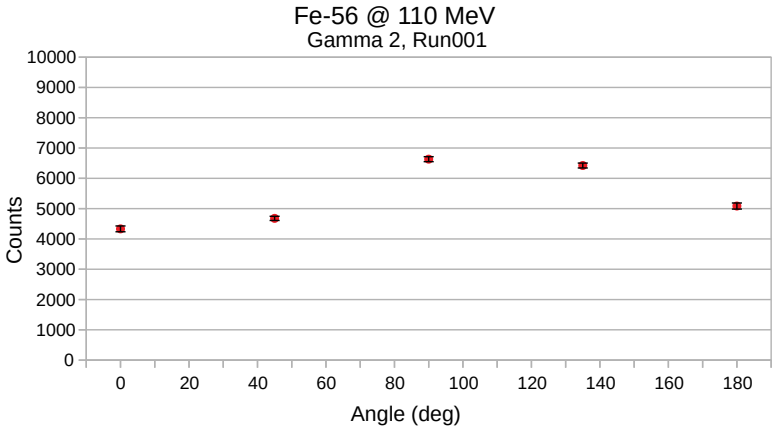

FIGURE B.32: ^{56}Fe TIRIV ϕ-dependent AC. γ-ray detector $\theta = 135°$. See §6.3 for experimental details.

TABLE B.11: Unscaled photopeak counts in Fig. B.33

ϕ	N	σ_N
0	5424	106
45	6171	78
90	6361	80
135	4779	70
180	4271	93

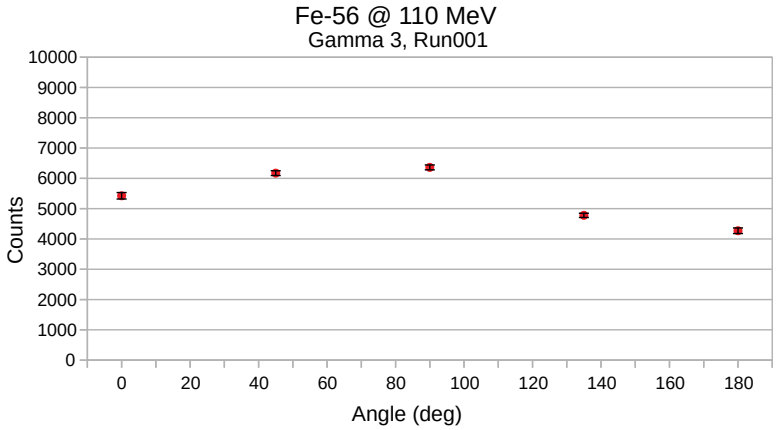

FIGURE B.33: ^{56}Fe TIRIV ϕ-dependent AC. γ-ray detector $\theta = 225°$. See §6.3 for experimental details.

TABLE B.12: Unscaled photopeak counts in Fig. B.34

ϕ	N	σ_N
0	10961	153
45	11780	109
90	15981	128
135	16271	129
180	13529	166

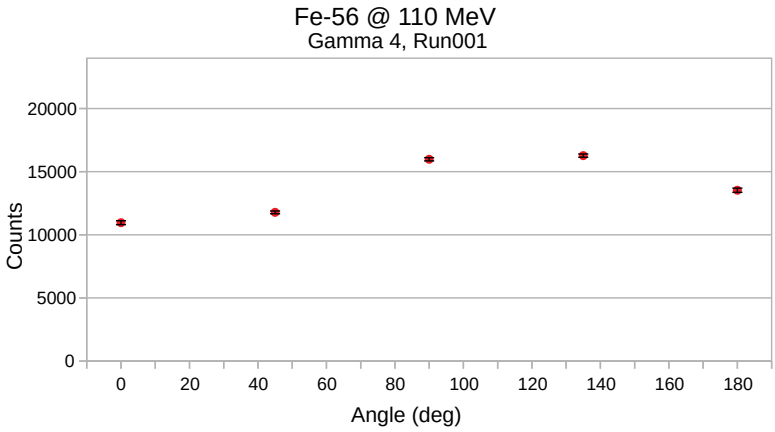

FIGURE B.34: TIRIV ϕ AC. γ-ray detector $\theta = 315°$. See §6.3 for experimental details.

TABLE B.13: Unscaled photopeak counts in Fig. B.35

ϕ	N	σ_N
0	16508	187
45	13047	116
90	9330	99
135	15544	126
180	18622	193

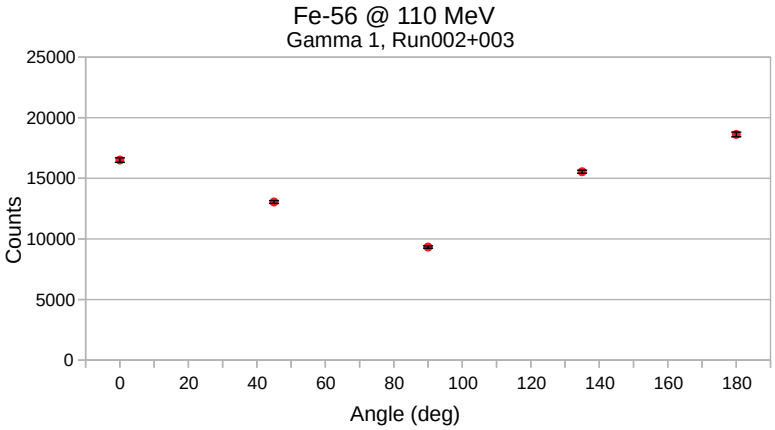

FIGURE B.35: ^{56}Fe TIRIV ϕ-dependent AC. γ-ray detector $\theta = 90°$. See §6.3 for experimental details.

TABLE B.14: Unscaled photopeak counts in Fig. B.36

ϕ	N	σ_N
0	6795	120
45	7344	87
90	9438	98
135	9553	98
180	7691	123

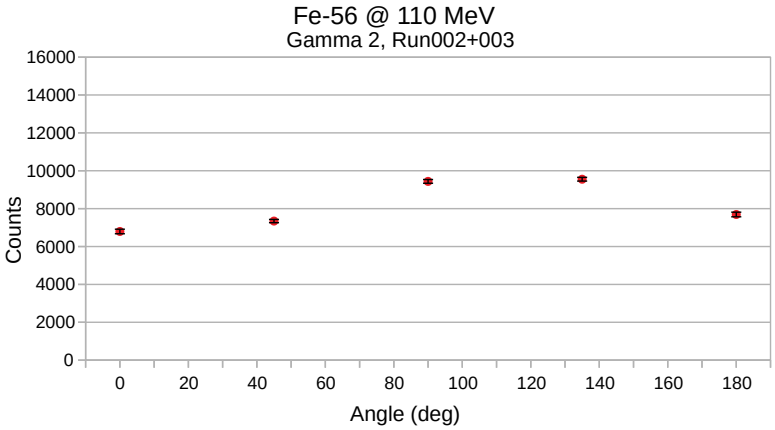

FIGURE B.36: ^{56}Fe TIRIV ϕ-dependent AC. γ-ray detector $\theta = 135°$. See §6.3 for experimental details.

TABLE B.15: Unscaled photopeak counts in Fig. B.37

ϕ	N	σ_N
0	8028	128
45	9661	98
90	9524	98
135	6719	82
180	6143	111

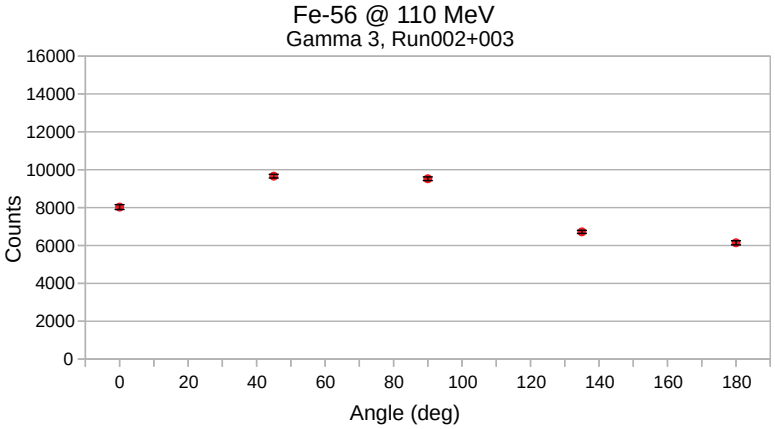

FIGURE B.37: ^{56}Fe TIRIV ϕ-dependent AC. γ-ray detector $\theta = 225°$. See §6.3 for experimental details.

TABLE B.16: Unscaled photopeak counts in Fig. B.38

ϕ	N	σ_N
0	18167	194
45	15164	124
90	9270	99
135	13523	117
180	16841	184

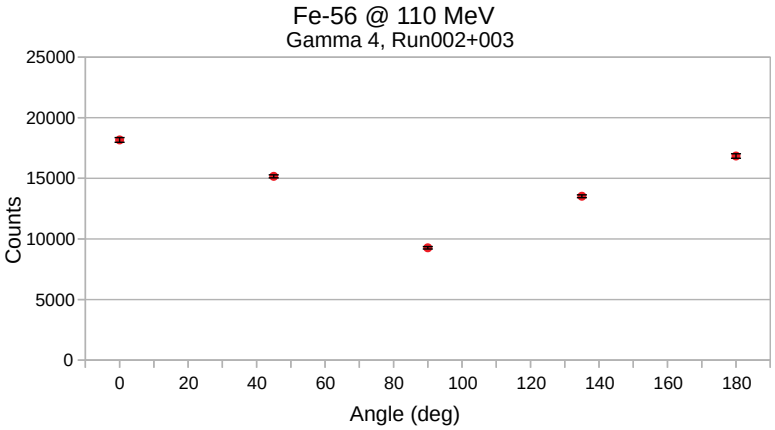

FIGURE B.38: ^{56}Fe TIRIV ϕ-dependent AC. γ-ray detector $\theta = 270°$. See §6.3 for experimental details.

B.3 ^{76}Ge TDRIV ACs

This appendix section contains tabulated photopeak counts and angular-correlation plots from the time-dependent recoil-in-vacuum measurement on the 2_1^+ state in ^{76}Ge, described in §6.4. The data are separated by γ-ray detector and plunger distance.

TABLE B.17: Unscaled 'stop' photopeak counts for Fig. B.39

ϕ	N	σ_N
0	9477	151
45	11576	121
90	11743	168
135	8800	108
180	7038	134

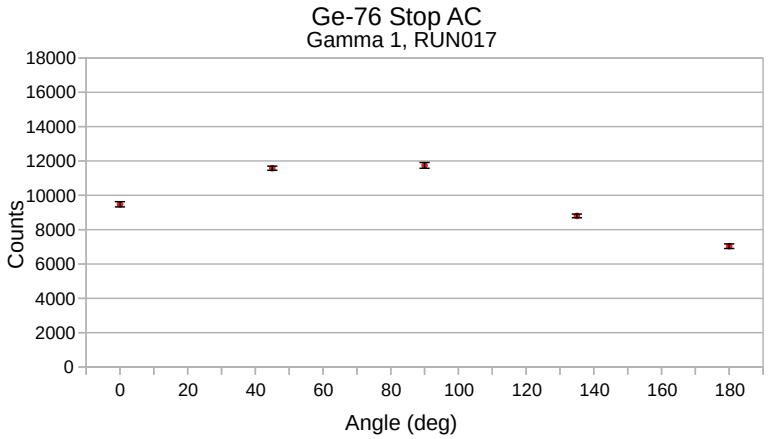

FIGURE B.39: ^{76}Ge TDRIV ϕ-dependent AC. γ-ray detector $\theta = 45°$, time = 6.77 ps. See §6.4 for experimental details.

TABLE B.18: Unscaled 'stop' photopeak counts in Fig. B.40

ϕ	N	σ_N
0	9321	159
45	11125	124
90	14683	197
135	13602	141
180	11365	179

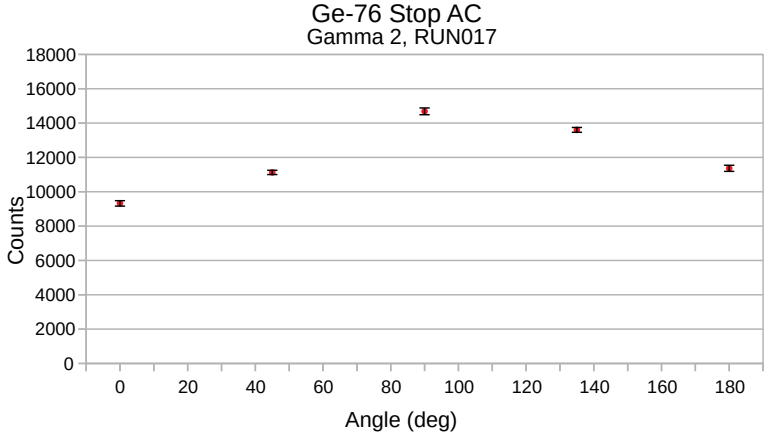

FIGURE B.40: ^{76}Ge TDRIV ϕ-dependent AC. γ-ray detector $\theta = 135°$, time = 6.77 ps. See §6.4 for experimental details.

TABLE B.19: Unscaled 'stop' photo-peak counts in Fig. B.41

ϕ	N	σ_N
0	11398	168
45	13393	133
90	12947	178
135	8927	110
180	7057	137

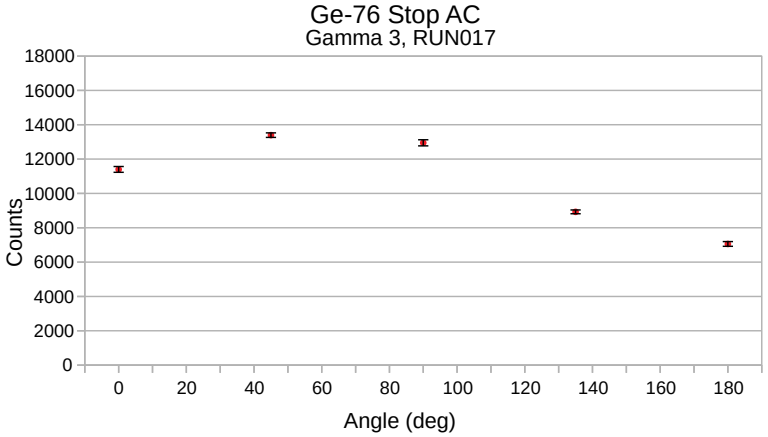

FIGURE B.41: ^{76}Ge TDRIV ϕ-dependent AC. γ-ray detector $\theta = 225°$, time = 6.77 ps. See §6.4 for experimental details.

TABLE B.20: Unscaled 'stop' photo-peak counts in Fig. B.42

ϕ	N	σ_N
0	7499	135
45	8659	104
90	11875	169
135	10879	120
180	8480	146

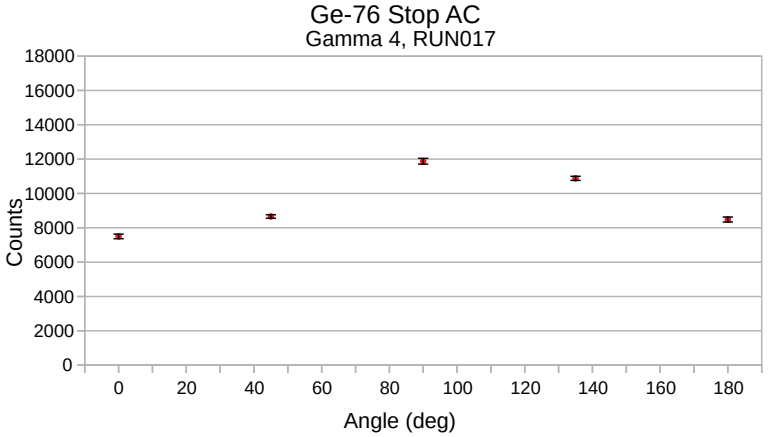

FIGURE B.42: ^{76}Ge TDRIV ϕ-dependent AC. γ-ray detector $\theta = 315°$, time = 6.77 ps. See §6.4 for experimental details.

TABLE B.21: Unscaled 'stop' photo-peak counts in Fig. B.43

ϕ	N	σ_N
0	5392	112
45	6168	87
90	6198	120
135	4332	76
180	3897	97

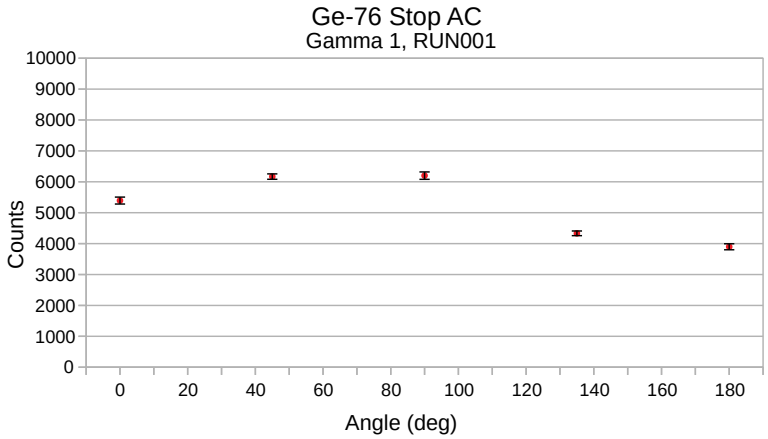

FIGURE B.43: ^{76}Ge TDRIV ϕ-dependent AC. γ-ray detector $\theta = 45°$, time = 8.75 ps. See §6.4 for experimental details.

TABLE B.22: Unscaled 'stop' photo-peak counts in Fig. B.44

ϕ	N	σ_N
0	4870	112
45	5864	88
90	7428	136
135	7118	101
180	5859	124

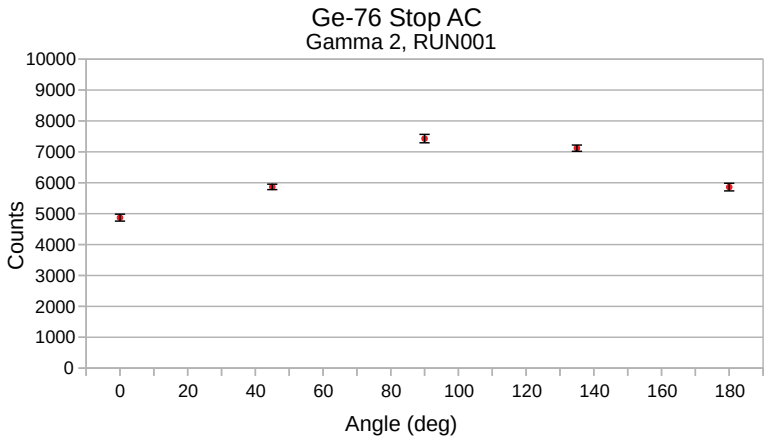

FIGURE B.44: ^{76}Ge TDRIV ϕ-dependent AC. γ-ray detector $\theta = 135°$, time = 8.75 ps. See §6.4 for experimental details.

TABLE B.23: Unscaled 'stop' photo-peak counts in Fig. B.45

ϕ	N	σ_N
0	5776	118
45	6832	93
90	6882	127
135	4528	78
180	4141	101

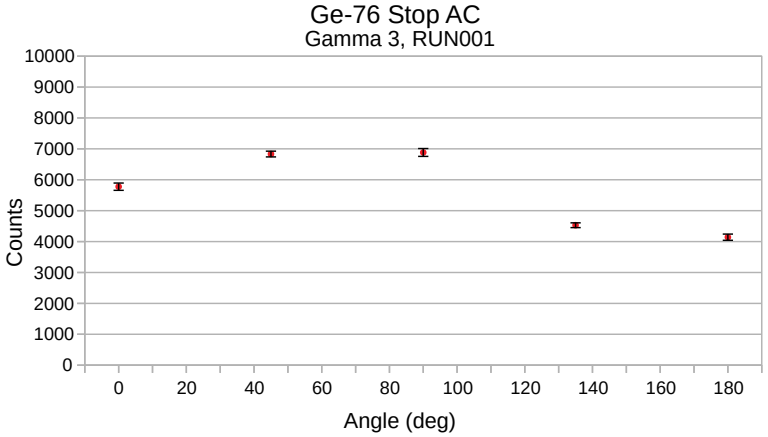

FIGURE B.45: ^{76}Ge TDRIV ϕ-dependent AC. γ-ray detector $\theta = 225°$, time = 8.75 ps. See §6.4 for experimental details.

TABLE B.24: Unscaled 'stop' photo-peak counts in Fig. B.46

ϕ	N	σ_N
0	3937	96
45	4712	75
90	6151	119
135	5712	88
180	4670	106

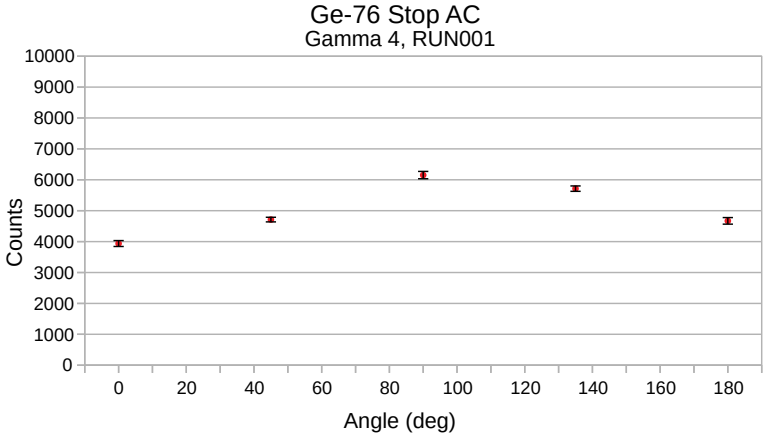

FIGURE B.46: ^{76}Ge TDRIV ϕ-dependent AC. γ-ray detector $\theta = 315°$, time = 8.75 ps. See §6.4 for experimental details.

TABLE B.25: Unscaled 'stop' photo-peak counts in Fig. B.47

ϕ	N	σ_N
0	9907	154
45	11248	118
90	11296	161
135	8346	104
180	7178	131

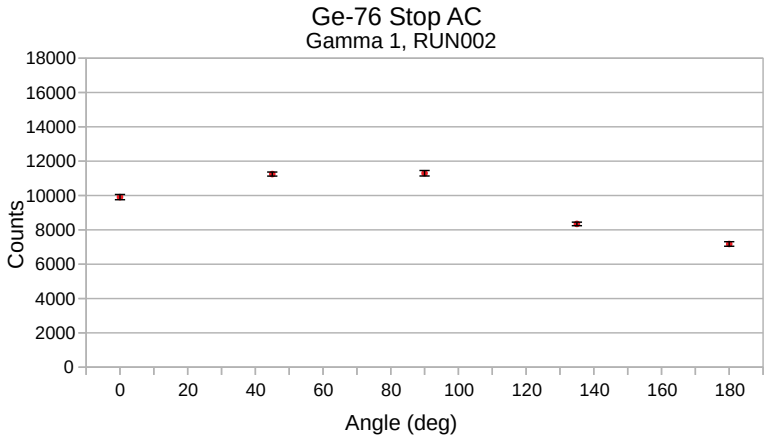

FIGURE B.47: ^{76}Ge TDRIV ϕ-dependent AC. γ-ray detector $\theta = 45°$, time = 10.3 ps. See §6.4 for experimental details.

TABLE B.26: Unscaled 'stop' photo-peak counts in Fig. B.48

ϕ	N	σ_N
0	9329	157
45	10562	119
90	13933	188
135	12290	132
180	10685	169

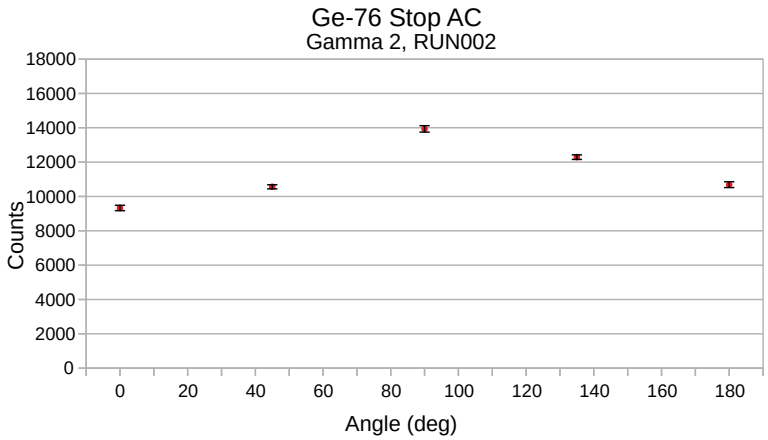

FIGURE B.48: ^{76}Ge TDRIV ϕ-dependent AC. γ-ray detector $\theta = 135°$, time = 10.3 ps. See §6.4 for experimental details.

TABLE B.27: Unscaled 'stop' photo-peak counts in Fig. B.49

ϕ	N	σ_N
0	11143	164
45	12522	126
90	11942	167
135	8564	106
180	8037	140

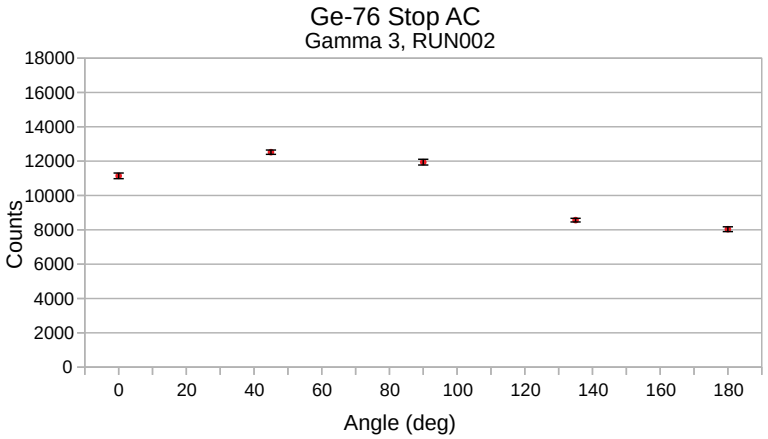

FIGURE B.49: ^{76}Ge TDRIV ϕ-dependent AC. γ-ray detector $\theta = 225°$, time = 10.3 ps. See §6.4 for experimental details.

TABLE B.28: Unscaled 'stop' photo-peak counts in Fig. B.50

ϕ	N	σ_N
0	7411	134
45	8627	103
90	10881	158
135	10161	115
180	8578	144

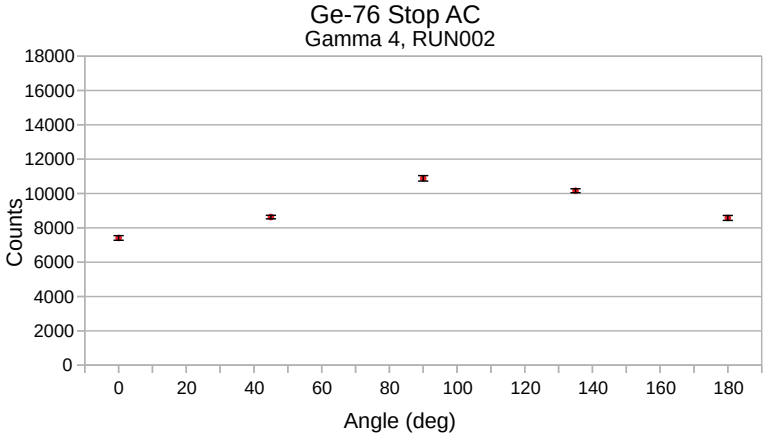

FIGURE B.50: ^{76}Ge TDRIV ϕ-dependent AC. γ-ray detector $\theta = 315°$, time = 10.3 ps. See §6.4 for experimental details.

TABLE B.29: Unscaled 'stop' photo-peak counts in Fig. B.51

ϕ	N	σ_N
0	10306	158
45	10914	116
90	11009	159
135	8237	103
180	7794	139

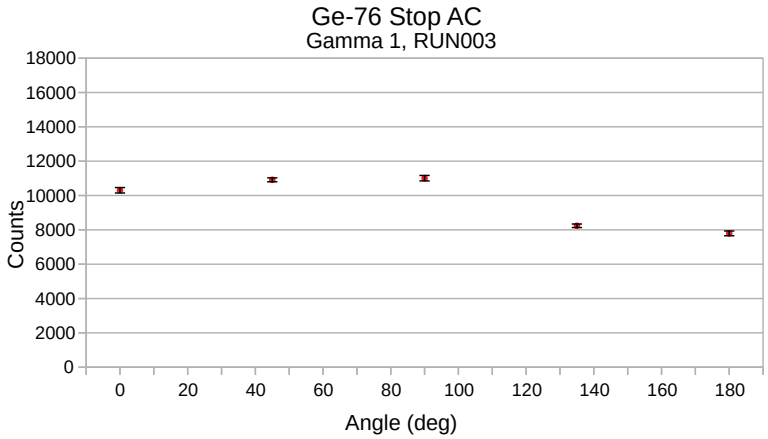

FIGURE B.51: ^{76}Ge TDRIV ϕ-dependent AC. γ-ray detector $\theta = 45°$, time = 12.6 ps. See §6.4 for experimental details.

TABLE B.30: Unscaled 'stop' photo-peak counts in Fig. B.52

ϕ	N	σ_N
0	9139	157
45	10225	117
90	13095	180
135	12237	132
180	11183	174

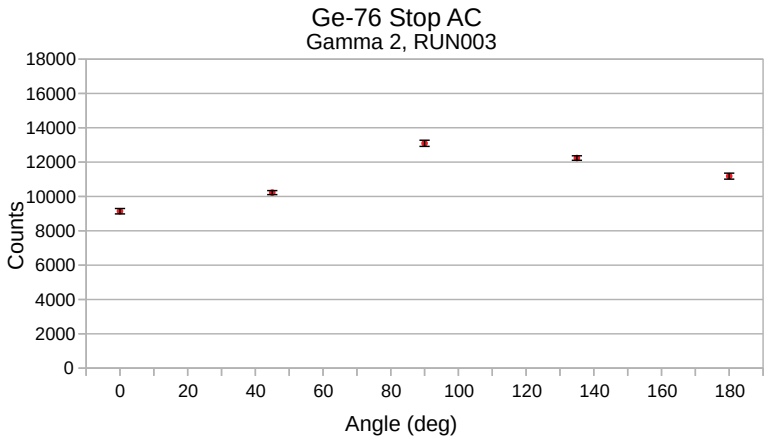

FIGURE B.52: ^{76}Ge TDRIV ϕ-dependent AC. γ-ray detector $\theta = 135°$, time = 12.6 ps. See §6.4 for experimental details.

TABLE B.31: Unscaled 'stop' photo-peak counts in Fig. B.53

ϕ	N	σ_N
0	11220	166
45	12280	124
90	11543	163
135	8311	104
180	8106	143

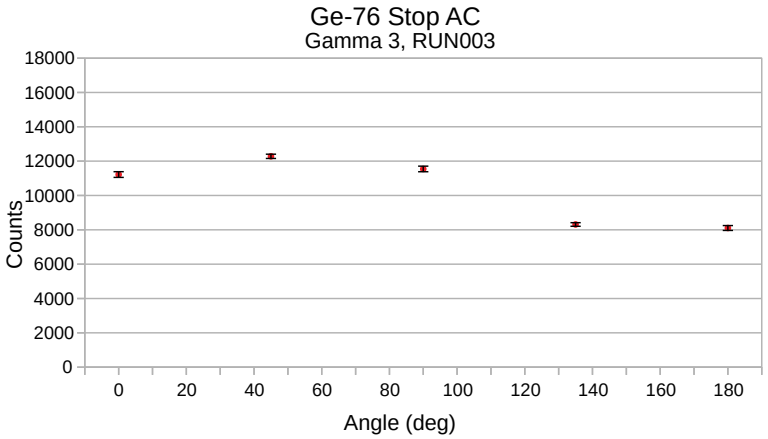

FIGURE B.53: ^{76}Ge TDRIV ϕ-dependent AC. γ-ray detector $\theta = 225°$, time = 12.6 ps. See §6.4 for experimental details.

TABLE B.32: Unscaled 'stop' photo-peak counts in Fig. B.54

ϕ	N	σ_N
0	7090	132
45	8397	101
90	9947	151
135	9912	113
180	8852	148

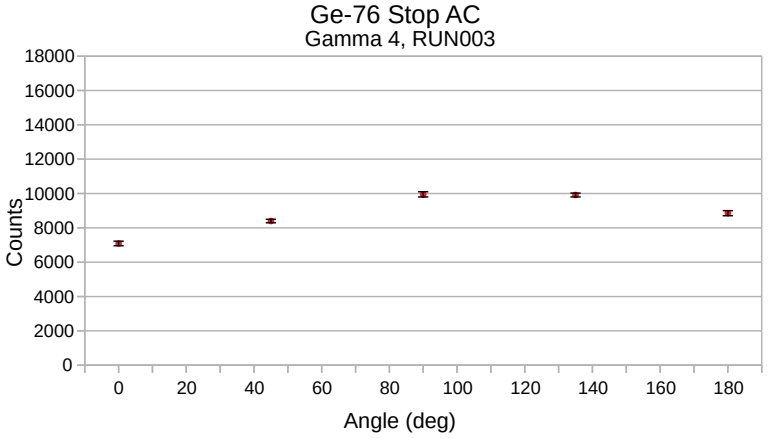

FIGURE B.54: ^{76}Ge TDRIV ϕ-dependent AC. γ-ray detector $\theta = 315°$, time = 12.6 ps. See §6.4 for experimental details.

TABLE B.33: Unscaled 'stop' photo-peak counts in Fig. B.55

ϕ	N	σ_N
0	7766	136
45	8568	102
90	8370	137
135	6720	92
180	5814	117

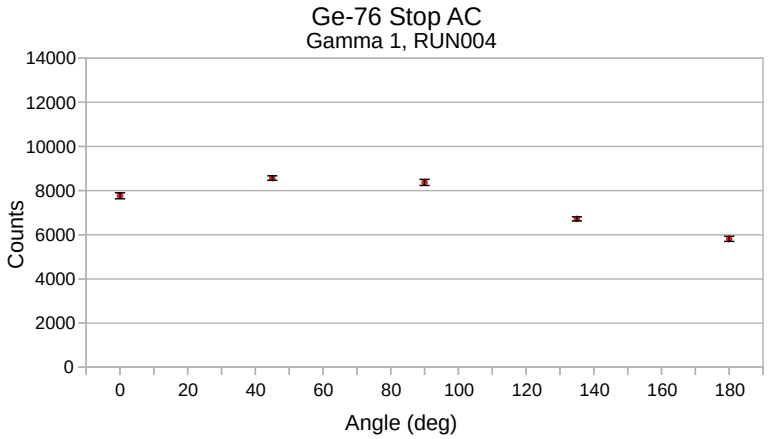

FIGURE B.55: ^{76}Ge TDRIV ϕ-dependent AC. γ-ray detector $\theta = 45°$, time = 14.5 ps. See §6.4 for experimental details.

TABLE B.34: Unscaled 'stop' photo-peak counts in Fig. B.56

ϕ	N	σ_N
0	7075	136
45	7946	102
90	10235	158
135	9571	115
180	8361	146

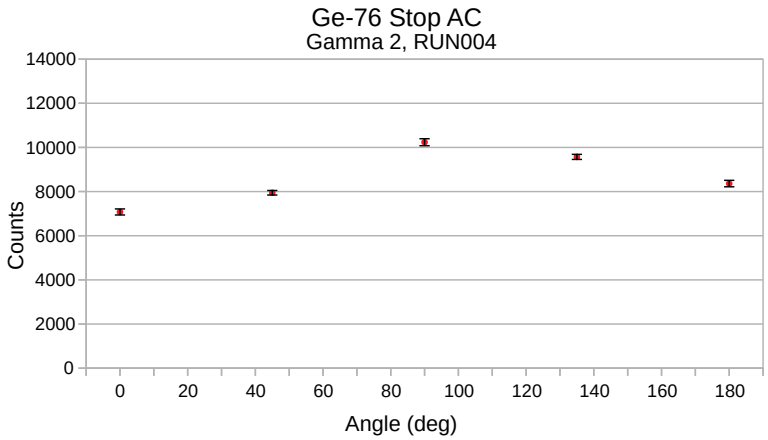

FIGURE B.56: ^{76}Ge TDRIV ϕ-dependent AC. γ-ray detector $\theta = 135°$, time = 14.5 ps. See §6.4 for experimental details.

TABLE B.35: Unscaled 'stop' photo-peak counts in Fig. B.57

ϕ	N	σ_N
0	8888	146
45	9268	107
90	9123	145
135	6456	91
180	6088	121

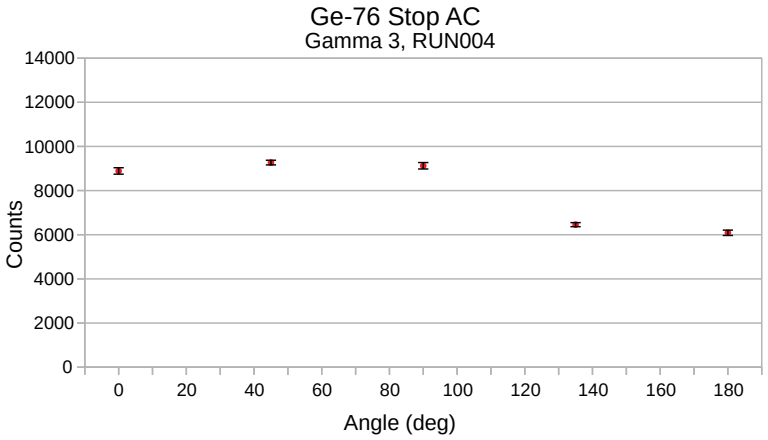

FIGURE B.57: ^{76}Ge TDRIV ϕ-dependent AC. γ-ray detector $\theta = 225°$, time = 14.5 ps. See §6.4 for experimental details.

TABLE B.36: Unscaled 'stop' photo-peak counts in Fig. B.58

ϕ	N	σ_N
0	5817	118
45	6421	88
90	7770	132
135	7878	100
180	6881	126

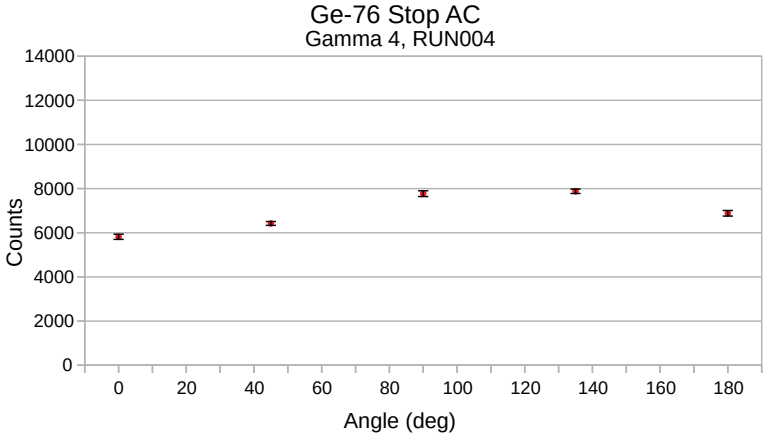

FIGURE B.58: ^{76}Ge TDRIV ϕ-dependent AC. γ-ray detector $\theta = 315°$, time = 14.5 ps. See §6.4 for experimental details.

TABLE B.37: Unscaled 'stop' photo-peak counts in Fig. B.59

ϕ	N	σ_N
0	6896	127
45	7504	95
90	7273	129
135	5535	84
180	5275	114

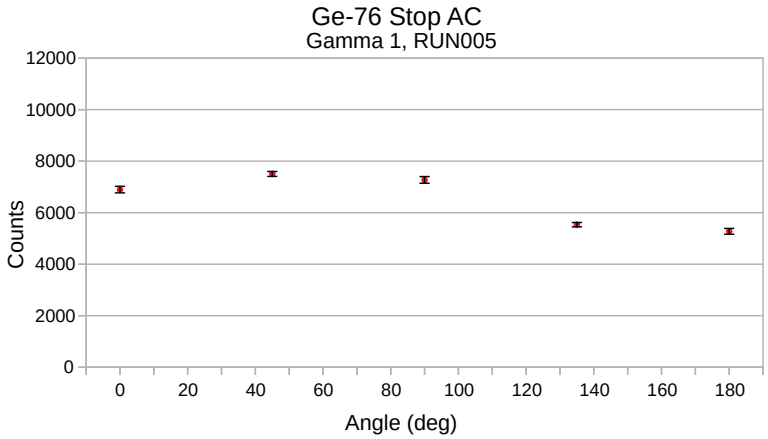

FIGURE B.59: ^{76}Ge TDRIV ϕ-dependent AC. γ-ray detector $\theta = 45°$, time = 16.5 ps. See §6.4 for experimental details.

TABLE B.38: Unscaled 'stop' photo-peak counts in Fig. B.60

ϕ	N	σ_N
0	6860	134
45	7495	99
90	9197	152
135	8317	107
180	7284	140

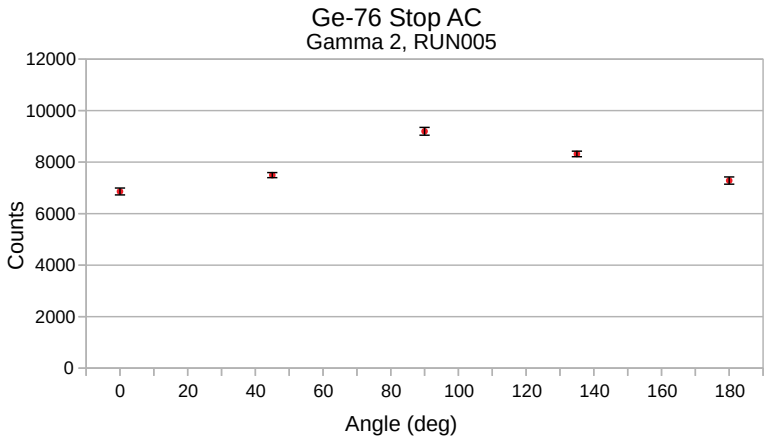

FIGURE B.60: ^{76}Ge TDRIV ϕ-dependent AC. γ-ray detector $\theta = 135°$, time = 16.5 ps. See §6.4 for experimental details.

TABLE B.39: Unscaled 'stop' photo-peak counts in Fig. B.61

ϕ	N	σ_N
0	7847	138
45	8243	101
90	7874	136
135	6040	89
180	5946	122

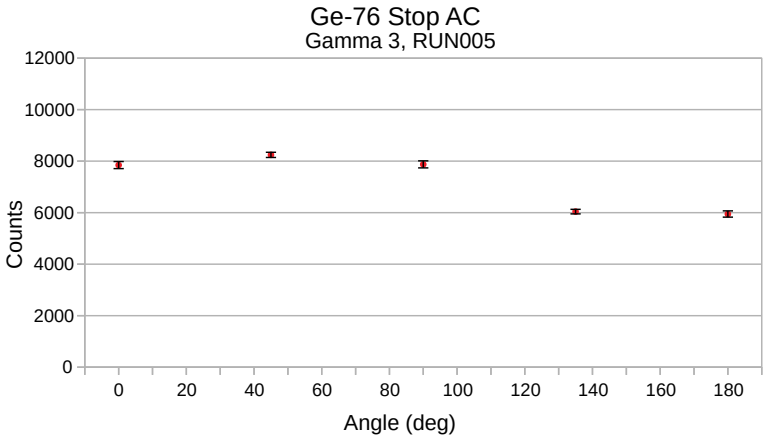

FIGURE B.61: ^{76}Ge TDRIV ϕ-dependent AC. γ-ray detector $\theta = 225°$, time = 16.5 ps. See §6.4 for experimental details.

TABLE B.40: Unscaled 'stop' photo-peak counts in Fig. B.62

ϕ	N	σ_N
0	5153	111
45	5771	83
90	7634	133
135	6951	94
180	6269	124

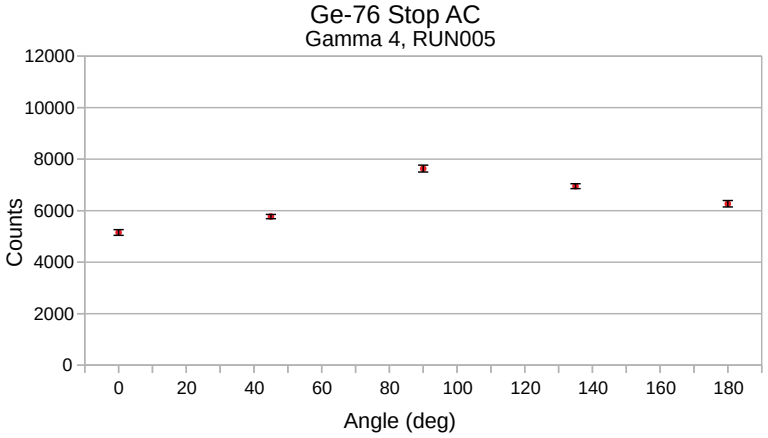

FIGURE B.62: ^{76}Ge TDRIV ϕ-dependent AC. γ-ray detector $\theta = 315°$, time = 16.5 ps. See §6.4 for experimental details.

TABLE B.41: Unscaled 'stop' photo-peak counts in Fig. B.63

ϕ	N	σ_N
0	7868	137
45	8551	102
90	8168	138
135	6712	93
180	6290	125

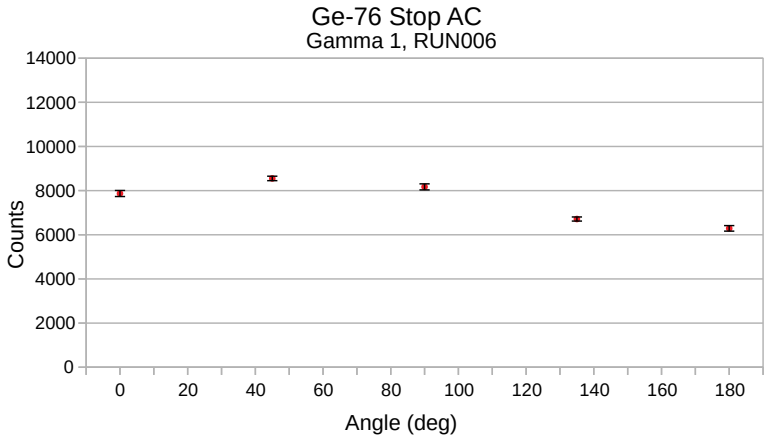

FIGURE B.63: ^{76}Ge TDRIV ϕ-dependent AC. γ-ray detector $\theta = 45°$, time = 19.1 ps. See §6.4 for experimental details.

TABLE B.42: Unscaled 'stop' photo-peak counts in Fig. B.64

ϕ	N	σ_N
0	7895	145
45	8129	104
90	10193	160
135	9810	118
180	8664	153

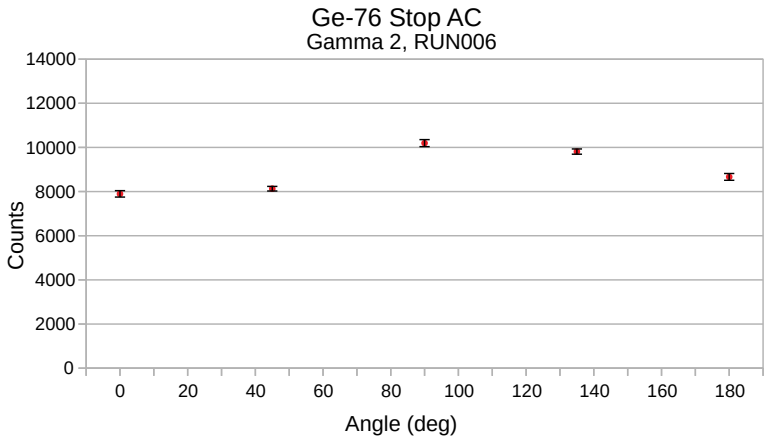

FIGURE B.64: ^{76}Ge TDRIV ϕ-dependent AC. γ-ray detector $\theta = 135°$, time = 19.1 ps. See §6.4 for experimental details.

TABLE B.43: Unscaled 'stop' photo-peak counts in Fig. B.65

ϕ	N	σ_N
0	9303	149
45	9671	109
90	8873	144
135	6805	95
180	6648	129

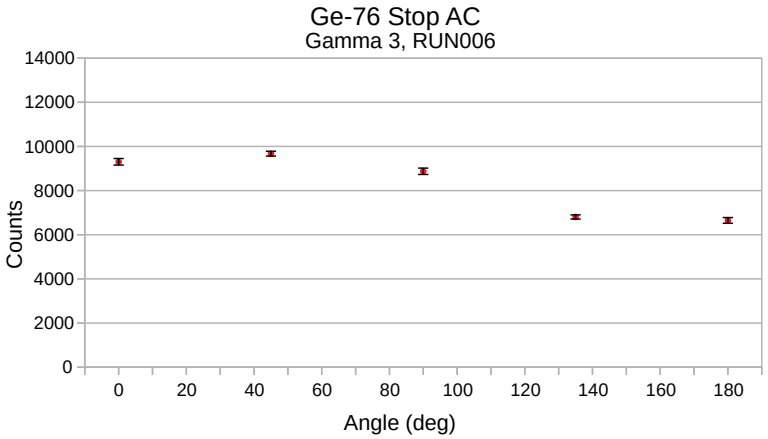

FIGURE B.65: ^{76}Ge TDRIV ϕ-dependent AC. γ-ray detector $\theta = 225°$, time = 19.1 ps. See §6.4 for experimental details.

TABLE B.44: Unscaled 'stop' photo-peak counts in Fig. B.66

ϕ	N	σ_N
0	6803	128
45	6492	89
90	8492	140
135	7876	101
180	7422	135

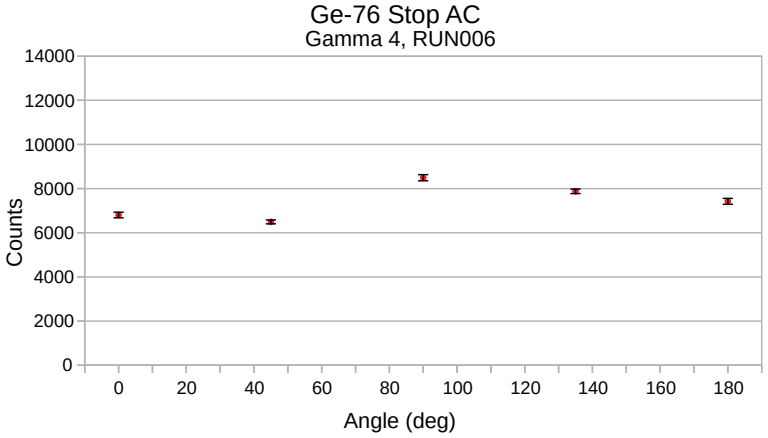

FIGURE B.66: ^{76}Ge TDRIV ϕ-dependent AC. γ-ray detector $\theta = 315°$, time = 19.1 ps. See §6.4 for experimental details.

TABLE B.45: Unscaled 'stop' photo-peak counts in Fig. B.67

ϕ	N	σ_N
0	8065	138
45	8205	99
90	8129	135
135	6073	88
180	5808	119

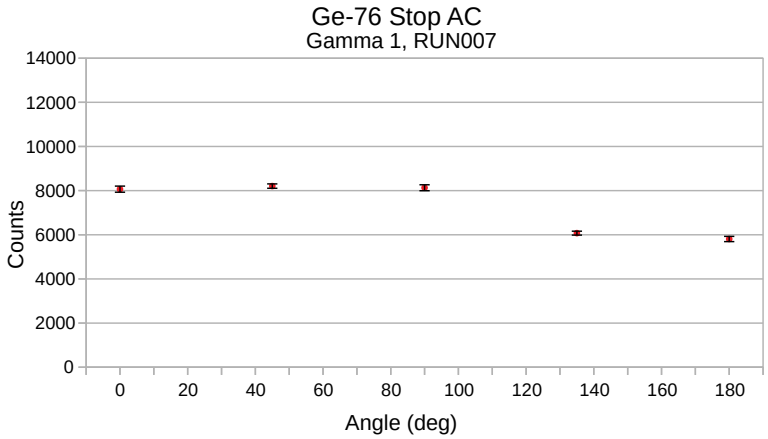

FIGURE B.67: ^{76}Ge TDRIV ϕ-dependent AC. γ-ray detector $\theta = 45°$, time = 20.8 ps. See §6.4 for experimental details.

TABLE B.46: Unscaled 'stop' photo-peak counts in Fig. B.68

ϕ	N	σ_N
0	7590	143
45	8169	104
90	9720	155
135	9201	114
180	8498	150

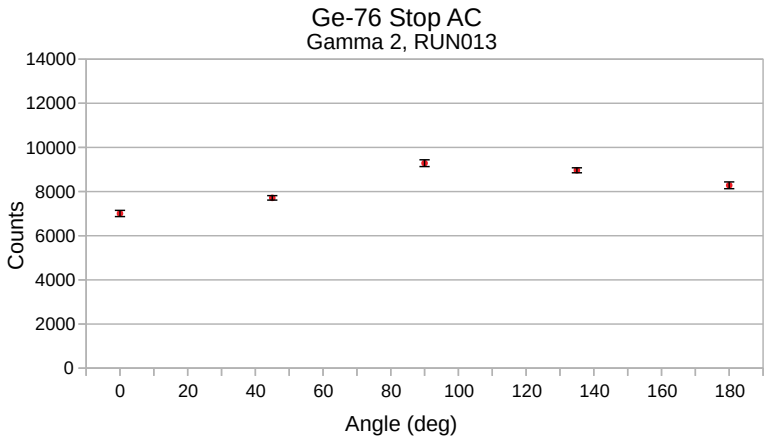

FIGURE B.68: ^{76}Ge TDRIV ϕ-dependent AC. γ-ray detector $\theta = 135°$, time = 20.8 ps. See §6.4 for experimental details.

TABLE B.47: Unscaled 'stop' photo-peak counts in Fig. B.69

ϕ	N	σ_N
0	8597	144
45	9140	106
90	9014	144
135	6799	95
180	6366	127

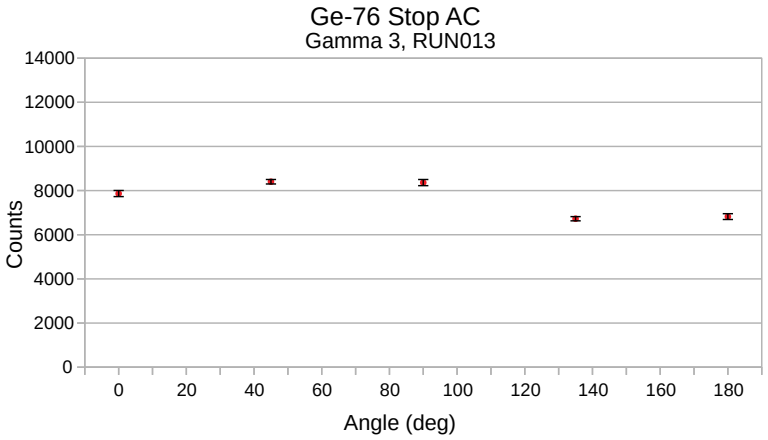

FIGURE B.69: ^{76}Ge TDRIV ϕ-dependent AC. γ-ray detector $\theta = 225°$, time = 20.8 ps. See §6.4 for experimental details.

TABLE B.48: Unscaled 'stop' photo-peak counts in Fig. B.70

ϕ	N	σ_N
0	6263	122
45	6775	90
90	8008	135
135	7526	98
180	6877	129

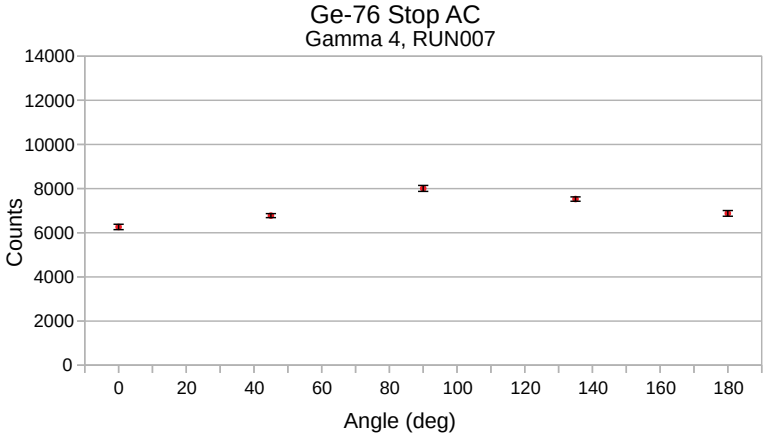

FIGURE B.70: ^{76}Ge TDRIV ϕ-dependent AC. γ-ray detector $\theta = 315°$, time = 20.8 ps. See §6.4 for experimental details.

TABLE B.49: Unscaled 'stop' photo-peak counts in Fig. B.71

ϕ	N	σ_N
0	7135	128
45	7667	96
90	7417	129
135	6160	89
180	5380	114

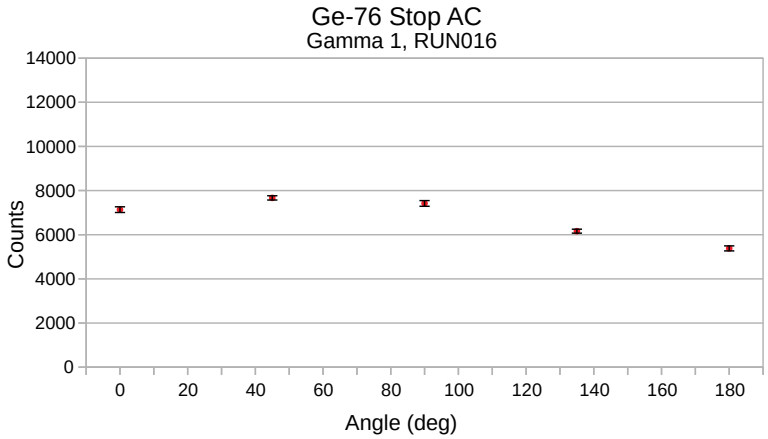

FIGURE B.71: ^{76}Ge TDRIV ϕ-dependent AC. γ-ray detector $\theta = 45°$, time = 24.8 ps. See §6.4 for experimental details.

TABLE B.50: Unscaled 'stop' photo-peak counts in Fig. B.72

ϕ	N	σ_N
0	7042	137
45	7732	101
90	8649	146
135	8689	111
180	7853	145

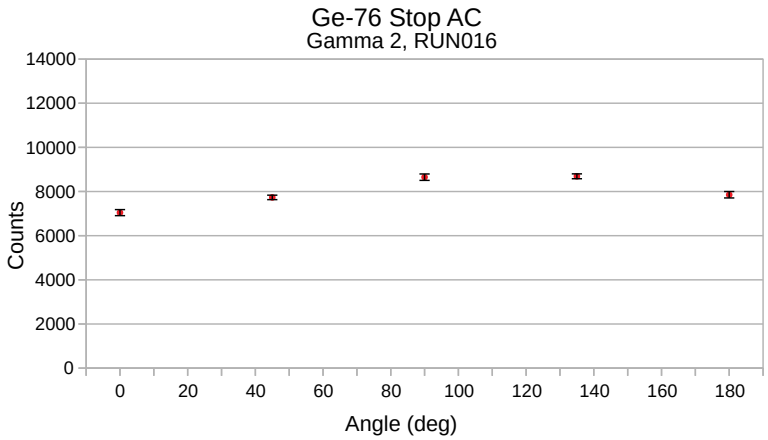

FIGURE B.72: ^{76}Ge TDRIV ϕ-dependent AC. γ-ray detector $\theta = 135°$, time = 24.8 ps. See §6.4 for experimental details.

TABLE B.51: Unscaled 'stop' photo-peak counts in Fig. B.73

ϕ	N	σ_N
0	8100	139
45	8413	102
90	8050	136
135	6541	93
180	6067	123

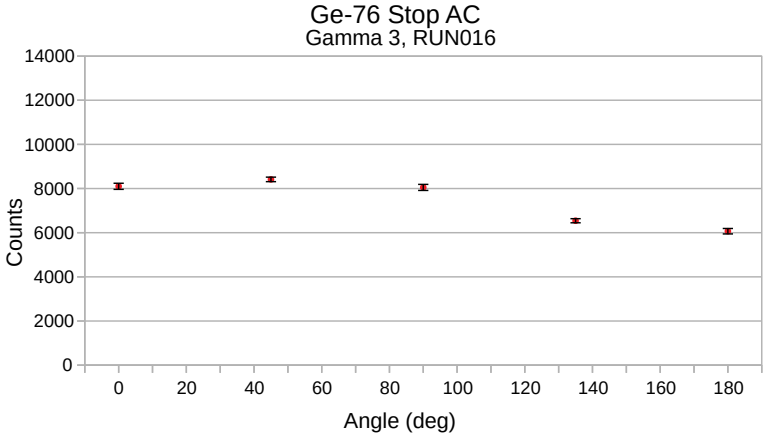

FIGURE B.73: ^{76}Ge TDRIV ϕ-dependent AC. γ-ray detector $\theta = 225°$, time = 24.8 ps. See §6.4 for experimental details.

TABLE B.52: Unscaled 'stop' photo-peak counts in Fig. B.74

ϕ	N	σ_N
0	5643	116
45	6187	87
90	7454	129
135	7205	96
180	6322	124

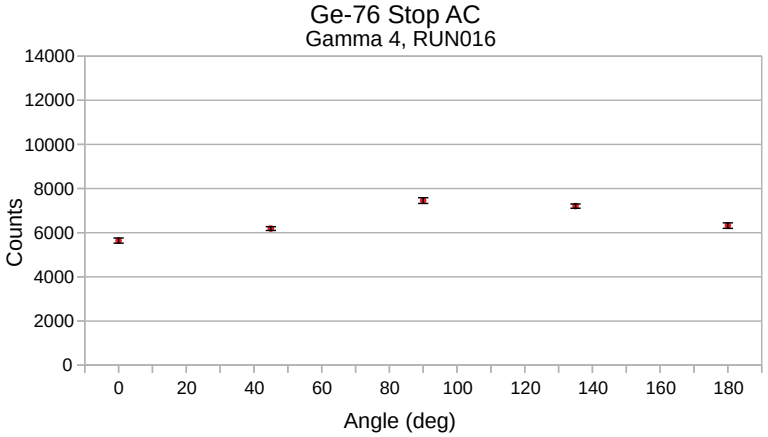

FIGURE B.74: ^{76}Ge TDRIV ϕ-dependent AC. γ-ray detector $\theta = 315°$, time = 24.8 ps. See §6.4 for experimental details.

TABLE B.53: Unscaled 'stop' photo-peak counts in Fig. B.75

ϕ	N	σ_N
0	7590	133
45	7480	95
90	7644	133
135	6400	91
180	6048	124

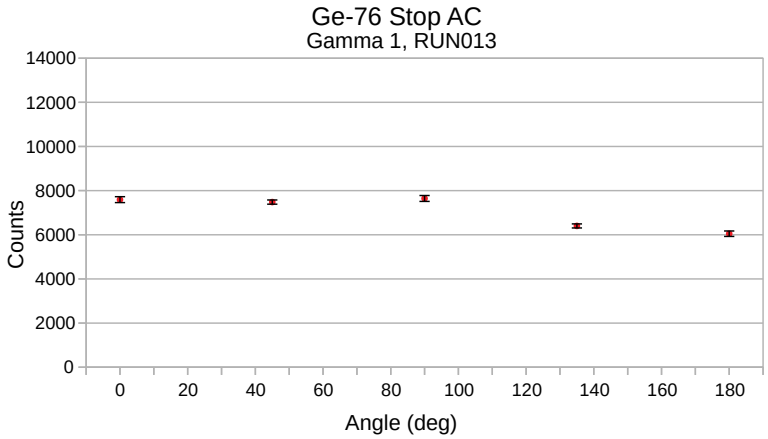

FIGURE B.75: ^{76}Ge TDRIV ϕ-dependent AC. γ-ray detector $\theta = 45°$, time = 30.9 ps. See §6.4 for experimental details.

TABLE B.54: Unscaled 'stop' photo-peak counts in Fig. B.76

ϕ	N	σ_N
0	7007	140
45	7714	102
90	9285	154
135	8963	114
180	8282	154

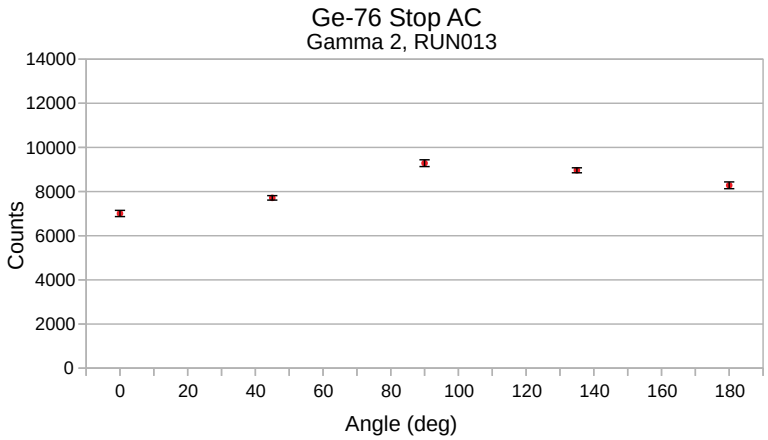

FIGURE B.76: ^{76}Ge TDRIV ϕ-dependent AC. γ-ray detector $\theta = 135°$, time = 30.9 ps. See §6.4 for experimental details.

TABLE B.55: Unscaled 'stop' photo-peak counts in Fig. B.77

ϕ	N	σ_N
0	7865	138
45	8401	101
90	8362	140
135	6725	95
180	6821	132

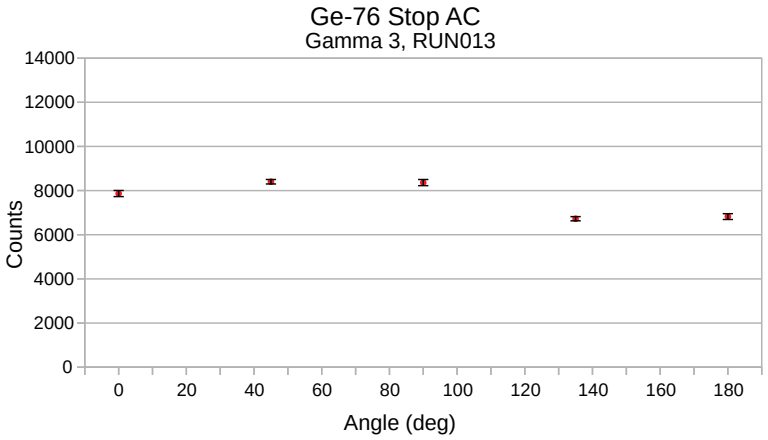

FIGURE B.77: ^{76}Ge TDRIV ϕ-dependent AC. γ-ray detector $\theta = 225°$, time = 30.9 ps. See §6.4 for experimental details.

TABLE B.56: Unscaled 'stop' photo-peak counts in Fig. B.78

ϕ	N	σ_N
0	5899	119
45	6545	89
90	7426	131
135	7209	97
180	6536	129

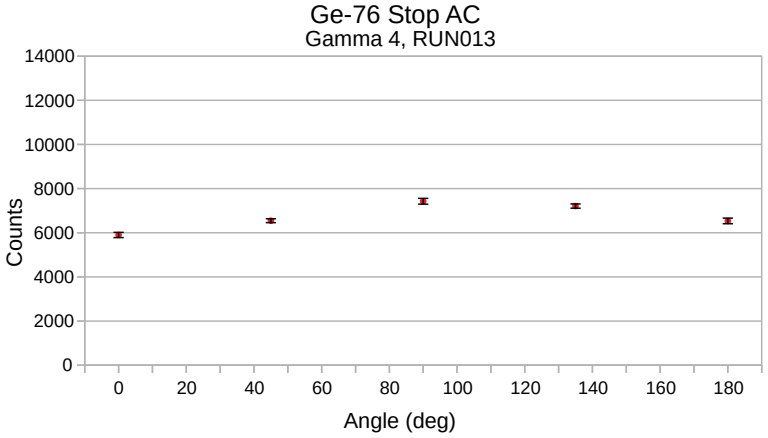

FIGURE B.78: ^{76}Ge TDRIV ϕ-dependent AC. γ-ray detector $\theta = 315°$, time = 30.9 ps. See §6.4 for experimental details.

TABLE B.57: Unscaled 'stop' photo-peak counts in Fig. B.79

ϕ	N	σ_N
0	8473	142
45	9033	104
90	8669	141
135	7260	97
180	6874	131

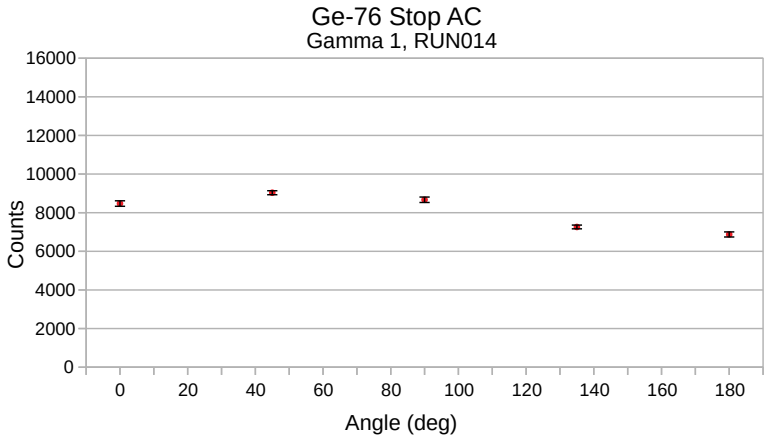

FIGURE B.79: ^{76}Ge TDRIV ϕ-dependent AC. γ-ray detector $\theta = 45°$, time = 34.5 ps. See §6.4 for experimental details.

TABLE B.58: Unscaled 'stop' photo-peak counts in Fig. B.80

ϕ	N	σ_N
0	9529	163
45	9660	116
90	10930	168
135	10174	122
180	9559	164

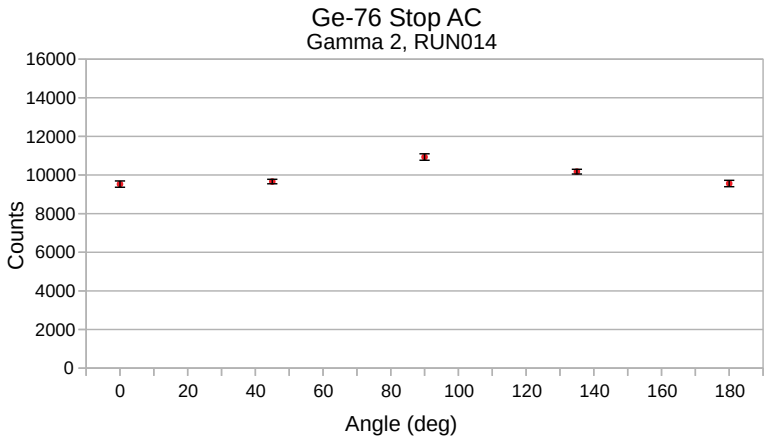

FIGURE B.80: ^{76}Ge TDRIV ϕ-dependent AC. γ-ray detector $\theta = 135°$, time = 34.5 ps. See §6.4 for experimental details.

TABLE B.59: Unscaled 'stop' photo-peak counts in Fig. B.81

ϕ	N	σ_N
0	9748	155
45	10357	113
90	10189	155
135	8153	105
180	7647	141

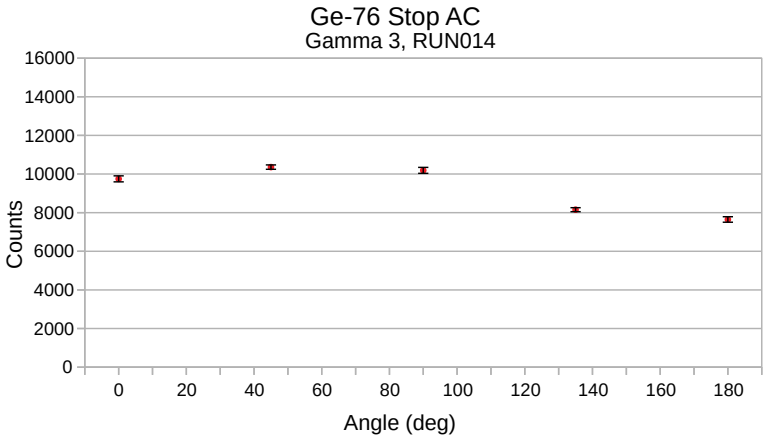

FIGURE B.81: ^{76}Ge TDRIV ϕ-dependent AC. γ-ray detector $\theta = 225°$, time = 34.5 ps. See §6.4 for experimental details.

TABLE B.60: Unscaled 'stop' photo-peak counts in Fig. B.82

ϕ	N	σ_N
0	7100	133
45	7993	98
90	9999	145
135	8225	103
180	7734	139

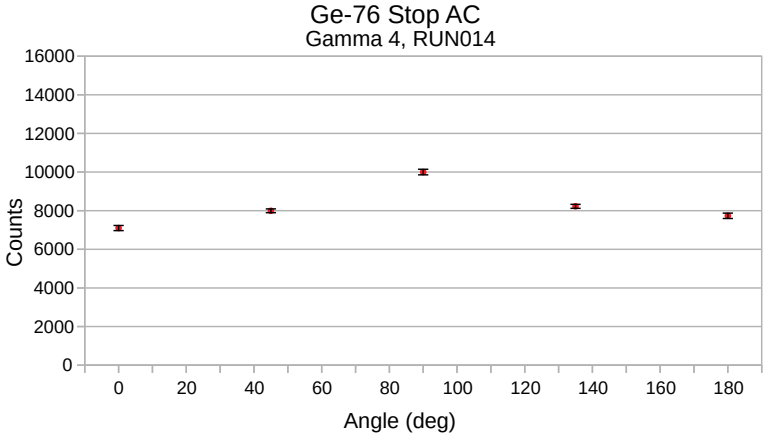

FIGURE B.82: ^{76}Ge TDRIV ϕ-dependent AC. γ-ray detector $\theta = 315°$, time = 34.5 ps. See §6.4 for experimental details.

TABLE B.61: Unscaled 'stop' photo-peak counts in Fig. B.83

ϕ	N	σ_N
0	6820	128
45	6988	92
90	7112	128
135	6041	89
180	5561	118

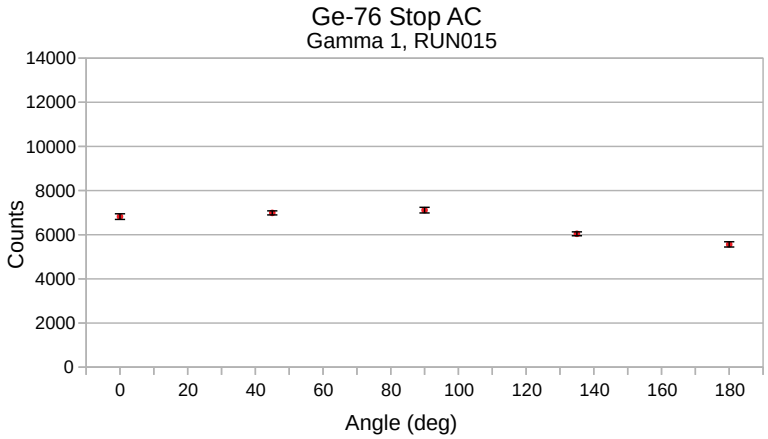

FIGURE B.83: ^{76}Ge TDRIV ϕ-dependent AC. γ-ray detector $\theta = 45°$, time = 38.4 ps. See §6.4 for experimental details.

TABLE B.62: Unscaled 'stop' photo-peak counts in Fig. B.84

ϕ	N	σ_N
0	7071	141
45	7500	101
90	8634	150
135	7739	108
180	7723	148

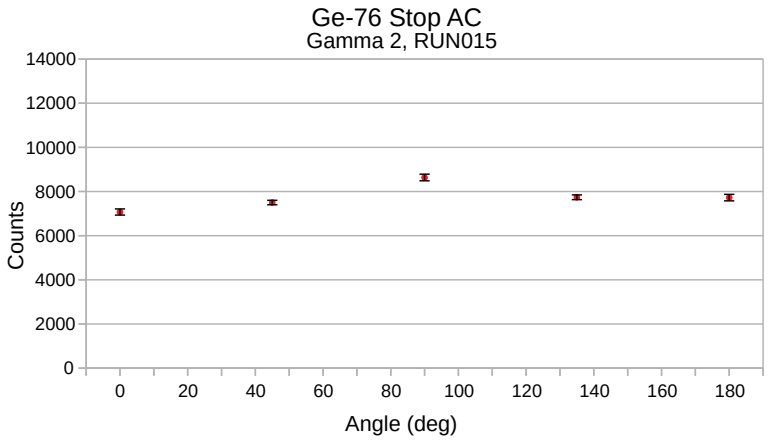

FIGURE B.84: ^{76}Ge TDRIV ϕ-dependent AC. γ-ray detector $\theta = 135°$, time = 38.4 ps. See §6.4 for experimental details.

TABLE B.63: Unscaled 'stop' photo-peak counts in Fig. B.85

ϕ	N	σ_N
0	7593	137
45	7930	99
90	7815	137
135	6434	94
180	6122	128

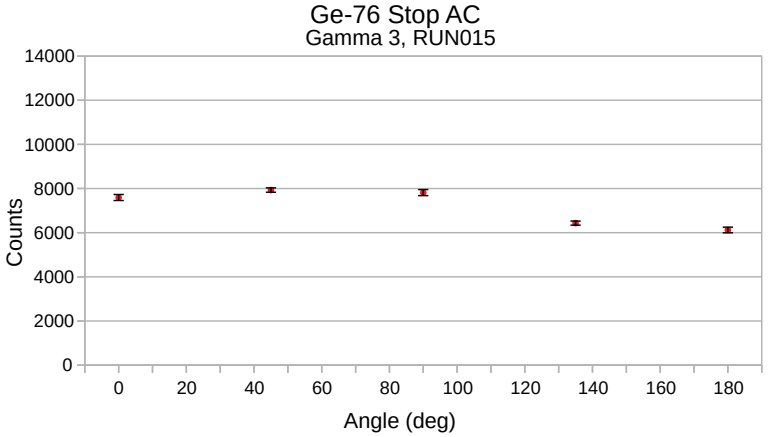

FIGURE B.85: ^{76}Ge TDRIV ϕ-dependent AC. γ-ray detector $\theta = 225°$, time = 38.4 ps. See §6.4 for experimental details.

TABLE B.64: Unscaled 'stop' photo-peak counts in Fig. B.86

ϕ	N	σ_N
0	5759	119
45	6356	88
90	6872	127
135	6915	95
180	6507	128

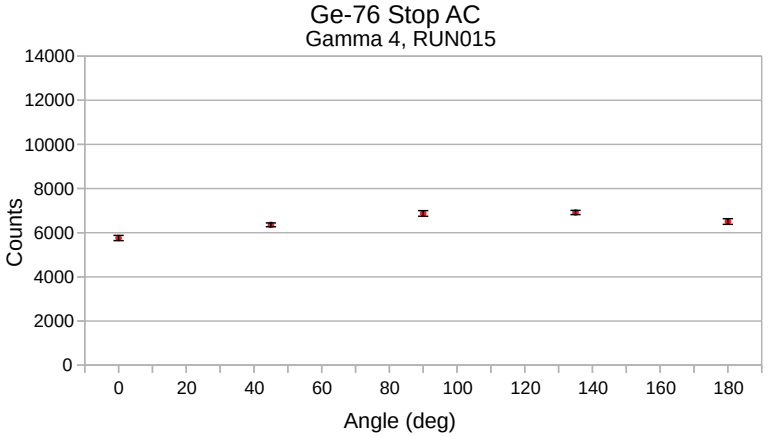

FIGURE B.86: ^{76}Ge TDRIV ϕ-dependent AC. γ-ray detector $\theta = 315°$, time = 38.4 ps. See §6.4 for experimental details.

Appendix C

RIV Simulate Example Data Input

This appendix contains two example **RIV Simulate** data input files, the first using the γ-particle index corresponding to the experimental setup, and the second using specified θ_γ and $\Delta\phi$ angles.

TABLE C.1: Example data file using the γ-particle index format, for use with **RIV Simulate**. Values may be space or tab separated, but the index $i_{\gamma p}$ and time t must be sequential. Counts N and uncertainty in counts σ_N are required, but uncertainty in time σ_t is optional. Note that the table heading is **not** to be included in the data file.

$i_{\gamma p}$	t	N	σ_N	σ_t
0	9.6	9907	154	
1	9.6	11248	118	
2	9.6	11296	161	
3	9.6	8346	104	
4	9.6	7178	131	
5	9.6	9329	157	
6	9.6	10562	119	
7	9.6	13933	188	
8	9.6	12290	132	
9	9.6	10685	169	
10	9.6	11143	164	
11	9.6	12522	126	
12	9.6	11942	167	
13	9.6	8564	106	
14	9.6	8037	140	
15	9.6	7411	134	
16	9.6	8627	103	
17	9.6	10881	158	
18	9.6	10161	115	
19	9.6	8578	144	

0	11.7	10306	158
1	11.7	10914	116
2	11.7	11009	159
3	11.7	8237	103
4	11.7	7794	139
5	11.7	9139	157
6	11.7	10225	117
7	11.7	13095	180
8	11.7	12237	132
9	11.7	11183	174
10	11.7	11220	166
11	11.7	12280	124
12	11.7	11543	163
13	11.7	8311	104
14	11.7	8106	143
15	11.7	7090	132
16	11.7	8397	101
17	11.7	9947	151
18	11.7	9912	113
19	11.7	8852	148
0	13.7	7766	136
1	13.7	8568	102
2	13.7	8370	137
3	13.7	6720	92
4	13.7	5814	117
5	13.7	7075	136
6	13.7	7946	102
7	13.7	10235	158
8	13.7	9571	115
9	13.7	8361	146
10	13.7	8888	146
11	13.7	9268	107
12	13.7	9123	145
13	13.7	6456	91
14	13.7	6088	121
15	13.7	5817	118
16	13.7	6421	88
17	13.7	7770	132
18	13.7	7878	100

19 13.7 6881 126

TABLE C.3: Example data file with $\Delta\phi$ and θ_γ values specified for each photopeak count, for use with **RIV Simulate**. Values may be space or tab separated, but the gamma-ray detector angle θ_γ and time t must be sequential. Counts N and uncertainty in counts σ_N are required, but uncertainty in time σ_t is optional. Note that the table heading is **not** to be included in the data file.

$\Delta\phi$	θ_γ	t	N	σ_N	σ_t
0	45	9.6	0.973	0.015	
45	45	9.6	1.105	0.012	
90	45	9.6	1.110	0.016	
135	45	9.6	0.820	0.010	
180	45	9.6	0.705	0.013	
0	135	9.6	0.774	0.013	
45	135	9.6	0.876	0.010	
90	135	9.6	1.156	0.016	
135	135	9.6	1.020	0.011	
180	135	9.6	0.887	0.014	
180	135	9.6	1.006	0.015	
135	135	9.6	1.130	0.011	
90	135	9.6	1.078	0.015	
45	135	9.6	0.773	0.010	
0	135	9.6	0.725	0.013	
180	45	9.6	0.765	0.014	
135	45	9.6	0.890	0.011	
90	45	9.6	1.123	0.016	
45	45	9.6	1.049	0.012	
0	45	9.6	0.885	0.015	
0	45	11.7	1.006	0.015	
45	45	11.7	1.066	0.011	
90	45	11.7	1.075	0.015	
135	45	11.7	0.804	0.010	
180	45	11.7	0.761	0.014	
0	135	11.7	0.771	0.013	
45	135	11.7	0.862	0.010	
90	135	11.7	1.104	0.015	
135	135	11.7	1.032	0.011	
180	135	11.7	0.943	0.015	
180	135	11.7	1.027	0.015	

135	135	11.7	1.125	0.011
90	135	11.7	1.057	0.015
45	135	11.7	0.761	0.010
0	135	11.7	0.742	0.013
180	45	11.7	0.756	0.014
135	45	11.7	0.895	0.011
90	45	11.7	1.061	0.016
45	45	11.7	1.057	0.012
0	45	11.7	0.944	0.016
0	45	13.7	0.983	0.017
45	45	13.7	1.084	0.013
90	45	13.7	1.059	0.017
135	45	13.7	0.850	0.012
180	45	13.7	0.736	0.015
0	135	13.7	0.772	0.015
45	135	13.7	0.867	0.011
90	135	13.7	1.117	0.017
135	135	13.7	1.044	0.013
180	135	13.7	0.912	0.016
180	135	13.7	1.052	0.017
135	135	13.7	1.097	0.013
90	135	13.7	1.080	0.017
45	135	13.7	0.764	0.011
0	135	13.7	0.720	0.014
180	45	13.7	0.788	0.016
135	45	13.7	0.870	0.012
90	45	13.7	1.053	0.018
45	45	13.7	1.068	0.014
0	45	13.7	0.933	0.017

Appendix D

GRASP2018 Calculation Results

This appendix contains atomic-structure properties calculated using GRASP2018 [79] and compared with the values in the NIST atomic spectra database [178]. Along with the atomic-structure information, the variance between the NIST and calculated values is shown. The variance between the two transition-rate calculation methods is also shown (See §2.4), which is an indicator of the calculated atomic wavefunction's self-consistency.

TABLE D.1: GRASP2018 calculation results for ^{56}Fe F-like valence-state ion energy levels, hyperfine-coupling frequency (A_J) and transition rates. GRASP energy levels are compared with NIST [178] values and the variance (var) is shown, as well as the variance (var) between the two different transition-rate calculations.

Energy (eV)					**Lower State**		**Transition rate (Hz)**		
NIST	**GRASP**	**Var**	$2J^\pi$	A_J (Hz)	**Energy**	$2J^\pi$	**Length**	**Velocity**	**Var**
0.00	0		3^-	2.52E+10					
12.72	12.73	0.0%	1^-	1.36E+11					
132.0	132.0	0.0%	1^+	4.59E+11	0.00	3^-	7.27E+10	7.78E+10	3.4%
					12.73	1^-	2.65E+10	2.82E+10	3.1%
771.4	774.7	0.2%	5^+	4.27E+10	0.00	3^-	8.19E+10	8.27E+10	0.5%
774.7	778.0	0.2%	3^+	7.06E+09	0.00	3^-	1.63E+12	1.64E+12	0.4%
					12.73	1^-	4.33E+10	4.36E+10	0.4%
782.4	784.6	0.1%	1^+	6.38E+10	0.00	3^-	1.55E+11	1.57E+11	0.5%
					12.73	1^-	5.01E+09	5.12E+09	1.0%
783.3	786.6	0.2%	3^+	3.54E+10	0.00	3^-	8.05E+11	8.10E+11	0.3%
					12.73	1^-	6.84E+10	6.90E+10	0.4%
786.4	789.8	0.2%	1^+	6.64E+09	0.00	3^-	1.20E+12	1.20E+12	0.3%
					12.73	1^-	1.37E+12	1.38E+12	0.4%
793.5	797.0	0.2%	5^+	6.61E+10	0.00	3^-	9.85E+11	9.91E+11	0.3%
794.0	797.5	0.2%	3^+	4.61E+10	0.00	3^-	1.74E+10	1.74E+10	0.1%
					12.73	1^-	1.20E+12	1.21E+12	0.4%
	804.9		3^-	2.23E+10	774.7	5^+	2.75E+09	2.69E+09	1.2%

			778.0	3^+	3.56E+08	3.46E+08	1.5%
			784.6	1^+	8.72E+08	9.17E+08	2.5%
			784.6	1^+	3.76E+07	3.62E+07	1.9%
			786.6	3^+	1.94E+06	1.76E+06	4.9%
			789.8	1^+	3.10E+05	2.87E+05	3.8%
			797.0	5^+	3.51E+05	3.07E+05	6.6%
			797.5	3^+	1.81E+05	1.61E+05	5.8%
805.4	5^-	2.27E+10	774.7	5^+	3.46E+09	3.38E+09	1.1%
			778.0	3^+	4.76E+07	4.57E+07	2.1%
			786.6	3^+	9.99E+06	9.72E+06	1.4%
			797.0	5^+	1.22E+05	1.06E+05	6.9%
			797.5	3^+	7.06E+03	5.82E+03	9.6%
808.8	1^-	3.01E+10	778.0	3^+	3.13E+09	3.06E+09	1.1%
			784.6	1^+	1.24E+09	1.33E+09	3.5%
			784.6	1^+	1.03E+08	9.95E+07	1.5%
			786.6	3^+	1.87E+07	1.77E+07	2.6%
			789.8	1^+	1.82E+07	1.79E+07	0.9%
			797.5	3^+	4.25E+06	3.90E+06	4.4%
809.4	7^-	1.69E+10	774.7	5^+	5.44E+09	5.35E+09	0.8%
			797.0	5^+	1.76E+05	1.59E+05	5.0%
809.5	5^-	2.09E+10	774.7	5^+	7.12E+07	7.07E+07	0.4%
	5^-	2.09E+10	778.0	3^+	3.94E+09	3.86E+09	1.0%
			786.6	3^+	5.40E+06	5.15E+06	2.4%
			797.0	5^+	1.15E+04	2.23E+04	31.8%
			797.5	3^+	8.43E+01	1.37E+02	23.7%
815.9	1^-	1.22E+10	778.0	3^+	2.14E+07	2.07E+07	1.7%
			784.6	1^+	6.22E+06	1.38E+07	37.9%
			784.6	1^+	7.02E+08	6.86E+08	1.1%
			786.6	3^+	2.37E+09	2.30E+09	1.3%
			789.8	1^+	4.51E+07	4.49E+07	0.2%
			797.5	3^+	2.92E+07	2.78E+07	2.5%
816.0	3^-	1.92E+10	774.7	5^+	6.53E+08	6.54E+08	0.0%
			778.0	3^+	4.26E+09	4.24E+09	0.3%
			784.6	1^+	1.04E+08	1.03E+08	0.5%
			784.6	1^+	5.29E+08	5.17E+08	1.1%
			786.6	3^+	1.68E+08	1.61E+08	2.0%
			789.8	1^+	2.99E+08	2.88E+08	1.9%
			797.0	5^+	2.63E+07	2.43E+07	3.9%
			797.5	3^+	1.37E+06	1.24E+06	5.0%

	816.3		1^-	2.73E+10	778.0	3^+	6.77E+08	6.68E+08	0.7%
					784.6	1^+	3.58E+09	3.50E+09	1.2%
					784.6	1^+	2.87E+09	2.81E+09	1.1%
					786.6	3^+	5.95E+08	5.80E+08	1.3%
					789.8	1^+	5.00E+07	4.80E+07	2.0%
					797.5	3^+	2.18E+05	1.69E+05	12.7%
815.2	817.2	0.1%	1^+	1.11E+11	0.00	3^-	2.37E+11	2.39E+11	0.5%
					12.73	1^-	8.51E+11	8.56E+11	0.3%
					804.9	3^-	1.91E+05	1.75E+05	4.5%
					808.8	1^-	1.29E+05	1.32E+05	1.2%
					815.9	1^-	7.77E+02	6.50E+02	8.9%
					816.0	3^-	1.78E-01	3.11E+02	99.9%
					816.3	1^-	1.56E+02	4.05E+01	58.7%
	818.2		3^-	2.76E+10	774.7	5^+	8.62E+08	8.60E+08	0.1%
					778.0	3^+	6.56E+08	6.60E+08	0.3%
					784.6	1^+	1.16E+08	8.70E+07	14.4%
					784.6	1^+	1.85E+09	1.82E+09	0.8%
					786.6	3^+	1.22E+09	1.20E+09	1.0%
					789.8	1^+	8.32E+05	8.28E+05	0.2%
					797.0	5^+	1.70E+08	1.62E+08	2.4%
					797.5	3^+	1.35E+07	1.31E+07	1.4%
					817.2	1^+	3.07E+02	4.23E+02	15.8%
	820.1		5^-	4.05E+09	774.7	5^+	2.09E+08	2.07E+08	0.5%
					778.0	3^+	3.23E+07	3.19E+07	0.5%
					786.6	3^+	4.71E+09	4.63E+09	0.8%
					797.0	5^+	3.32E+06	3.16E+06	2.5%
					797.5	3^+	1.75E+05	1.76E+05	0.2%
	820.6		3^-	1.48E+10	774.7	5^+	4.66E+08	4.66E+08	0.0%
					778.0	3^+	9.59E+07	9.49E+07	0.5%
					784.6	1^+	6.51E+09	6.52E+09	0.1%
					784.6	1^+	2.58E+09	2.55E+09	0.5%
					786.6	3^+	1.46E+09	1.44E+09	0.7%
					789.8	1^+	2.12E+08	2.08E+08	1.0%
					797.0	5^+	2.59E+08	2.47E+08	2.4%
					797.5	3^+	5.93E+06	5.77E+06	1.4%
					817.2	1^+	2.50E+04	1.95E+04	12.4%
	822.5		1^-	-2.57E+10	778.0	3^+	3.32E+08	3.29E+08	0.5%
					784.6	1^+	2.83E+08	3.19E+08	6.1%
					784.6	1^+	4.73E+08	4.66E+08	0.7%

			786.6	3^+	1.24E+08	1.20E+08	1.5%
			789.8	1^+	3.15E+09	3.10E+09	0.8%
			797.5	3^+	3.24E+08	3.13E+08	1.8%
			817.2	1^+	1.02E+05	9.24E+04	4.9%
823.2	3^-	1.01E+10	774.7	5^+	4.86E+08	4.90E+08	0.4%
			778.0	3^+	3.91E+08	3.93E+08	0.2%
			784.6	1^+	1.11E+09	1.12E+09	0.1%
			784.6	1^+	1.31E+07	1.31E+07	0.2%
			786.6	3^+	1.11E+09	1.09E+09	0.6%
			789.8	1^+	3.41E+09	3.36E+09	0.8%
			797.0	5^+	1.29E+08	1.23E+08	2.1%
			797.5	3^+	1.34E+07	1.24E+07	3.6%
			817.2	1^+	9.32E+04	7.02E+04	14.1%
827.5	5^-	5.09E+10	774.7	5^+	3.65E+06	3.66E+06	0.2%
			778.0	3^+	2.21E+05	2.27E+05	1.2%
			786.6	3^+	1.36E+07	1.34E+07	0.8%
			797.0	5^+	1.02E+09	9.95E+08	1.3%
			797.5	3^+	2.52E+09	2.45E+09	1.3%
830.1	7^-	3.41E+10	774.7	5^+	1.42E+07	1.42E+07	0.3%
			797.0	5^+	4.73E+09	4.64E+09	1.0%
832.0	3^-	4.52E+10	774.7	5^+	3.11E+07	3.11E+07	0.0%
			778.0	3^+	5.44E+08	5.50E+08	0.6%
			784.6	1^+	3.76E+09	3.85E+09	1.2%
			784.6	1^+	5.90E+05	5.06E+05	7.7%
			786.6	3^+	5.33E+08	5.34E+08	0.1%
			789.8	1^+	8.73E+03	1.79E+04	34.5%
			797.0	5^+	1.38E+07	1.44E+07	1.9%
			797.5	3^+	4.96E+09	4.89E+09	0.7%
			817.2	1^+	9.94E+05	1.05E+06	2.5%
833.5	5^-	3.83E+10	774.7	5^+	8.33E+07	8.43E+07	0.6%
			778.0	3^+	3.01E+05	3.90E+05	12.9%
			786.6	3^+	4.40E+07	4.41E+07	0.2%
			797.0	5^+	4.60E+09	4.54E+09	0.6%
			797.5	3^+	1.75E+09	1.73E+09	0.6%
839.2	3^-	3.27E+10	774.7	5^+	1.91E+08	1.98E+08	1.7%
			778.0	3^+	5.15E+09	5.27E+09	1.1%
			784.6	1^+	2.91E+10	2.95E+10	0.7%
			784.6	1^+	2.17E+08	2.23E+08	1.4%
			786.6	3^+	3.22E+09	3.27E+09	0.7%

			789.8	1^+	2.09E+09	2.12E+09	0.7%
			797.0	5^+	5.74E+09	5.77E+09	0.3%
			797.5	3^+	3.69E+08	3.66E+08	0.4%
			817.2	1^+	3.30E+05	5.02E+05	20.7%
842.2	1^-	1.17E+11	778.0	3^+	3.26E+08	3.34E+08	1.2%
			784.6	1^+	5.93E+10	5.92E+10	0.1%
			784.6	1^+	5.40E+06	5.53E+06	1.2%
			786.6	3^+	2.77E+08	2.83E+08	1.1%
			789.8	1^+	3.62E+09	3.68E+09	0.7%
			797.5	3^+	7.80E+09	7.85E+09	0.3%
			817.2	1^+	3.50E+08	3.33E+08	2.5%
847.0	5^+	1.49E+10	0.00	3^-	2.02E+08	2.52E+08	11.2%
			804.9	3^-	2.85E+09	2.88E+09	0.6%
			805.4	5^-	4.37E+09	4.41E+09	0.5%
			809.4	7^-	4.45E+08	4.51E+08	0.7%
			809.5	5^-	2.81E+05	3.31E+05	8.2%
			816.0	3^-	4.58E+07	4.63E+07	0.6%
			818.2	3^-	6.15E+05	5.58E+05	4.9%
			820.1	5^-	1.68E+07	1.69E+07	0.3%
			820.6	3^-	8.32E+06	8.36E+06	0.2%
			823.2	3^-	3.70E+05	3.87E+05	2.2%
			827.5	5^-	1.65E+03	2.69E+01	96.8%
			830.1	7^-	4.21E+05	4.78E+05	6.3%
			832.0	3^-	3.33E+04	3.53E+04	3.0%
			833.5	5^-	4.36E+05	4.60E+05	2.7%
			839.2	3^-	1.85E+04	2.33E+04	11.6%
847.1	7^+	1.01E+10	805.4	5^-	4.51E+09	4.57E+09	0.7%
			809.4	7^-	1.87E+09	1.90E+09	0.6%
			809.5	5^-	6.72E+08	6.85E+08	0.9%
			820.1	5^-	3.01E+06	3.02E+06	0.1%
			827.5	5^-	1.40E+05	1.44E+05	1.5%
			830.1	7^-	4.44E+05	4.37E+05	0.8%
			833.5	5^-	1.74E+03	2.29E+03	13.8%
847.7	3^+	2.22E+10	0.00	3^-	3.64E+09	3.67E+09	0.3%
			12.73	1^-	4.31E+10	4.32E+10	0.1%
			804.9	3^-	5.45E+09	5.51E+09	0.5%
			805.4	5^-	1.94E+09	1.96E+09	0.6%
			808.8	1^-	6.61E+08	6.66E+08	0.4%
			809.5	5^-	9.56E+06	9.85E+06	1.5%

			815.9	1^-	1.86E+06	2.00E+06	3.5%
			816.0	3^-	2.61E+06	2.44E+06	3.3%
			816.3	1^-	3.03E+07	2.99E+07	0.7%
			818.2	3^-	2.04E+07	2.00E+07	0.9%
			820.1	5^-	2.15E+07	2.21E+07	1.5%
			820.6	3^-	5.06E+05	5.55E+05	4.6%
			822.5	1^-	1.07E+07	1.09E+07	1.2%
			823.2	3^-	5.78E+05	5.84E+05	0.5%
			827.5	5^-	3.66E+04	7.25E+04	32.9%
			832.0	3^-	1.02E+06	1.10E+06	3.7%
			833.5	5^-	6.01E+05	6.10E+05	0.8%
			839.2	3^-	2.27E+02	1.33E+02	26.2%
			842.2	1^-	2.21E+04	2.05E+04	3.9%
848.9	1^+	3.83E+10	0.00	3^-	8.67E+08	8.16E+08	3.0%
			12.73	1^-	4.72E+10	4.75E+10	0.3%
			804.9	3^-	5.05E+09	5.11E+09	0.6%
			808.8	1^-	2.85E+09	2.89E+09	0.7%
			815.9	1^-	6.64E+07	6.47E+07	1.3%
			816.0	3^-	2.34E+07	2.44E+07	2.1%
			816.3	1^-	5.19E+07	5.17E+07	0.2%
			818.2	3^-	4.62E+07	4.71E+07	1.0%
			820.6	3^-	1.83E+07	1.86E+07	0.7%
			822.5	1^-	1.29E+07	1.34E+07	1.7%
			823.2	3^-	3.43E+06	3.61E+06	2.5%
			832.0	3^-	1.83E+06	1.73E+06	2.7%
			839.2	3^-	6.89E+04	6.16E+04	5.6%
			842.2	1^-	6.31E+03	4.02E+03	22.1%
850.0	9^+	1.17E+10	809.4	7^-	7.80E+09	7.92E+09	0.7%
			830.1	7^-	1.47E+05	1.52E+05	1.7%
851.3	7^+	1.44E+10	805.4	5^-	1.16E+09	1.18E+09	0.6%
			809.4	7^-	1.88E+08	1.89E+08	0.3%
			809.5	5^-	7.49E+09	7.60E+09	0.7%
			820.1	5^-	6.00E+04	5.07E+04	8.4%
			827.5	5^-	3.63E+05	3.49E+05	2.0%
			830.1	7^-	2.65E+05	2.48E+05	3.2%
			833.5	5^-	6.63E+04	6.28E+04	2.7%
851.7	3^-	7.05E+09	786.6	3^+	4.49E+07	4.50E+07	0.2%
			789.8	1^+	7.24E+07	7.41E+07	1.1%
			797.0	5^+	2.44E+08	2.39E+08	1.0%

					797.5	3^+	7.43E+07	7.29E+07	0.9%
					817.2	1^+	5.19E+09	5.15E+09	0.4%
					847.0	5^+	2.69E+07	2.83E+07	2.6%
					847.0	5^+	7.26E+01	7.08E+02	81.4%
					847.7	3^+	9.96E+07	1.02E+08	1.4%
					847.7	3^+	1.94E+02	6.30E+01	50.9%
					848.9	1^+	1.76E+10	1.69E+10	2.0%
					848.9	1^+	1.32E+07	1.43E+07	4.0%
					848.9	1^+	2.14E+01	1.15E+02	68.5%
	853.4		1^-	5.22E+10	786.6	3^+	4.95E+08	5.04E+08	1.0%
					789.8	1^+	3.19E+09	3.26E+09	1.0%
					797.5	3^+	2.75E+09	2.84E+09	1.5%
					817.2	1^+	5.10E+09	5.07E+09	0.2%
					847.7	3^+	4.00E+08	4.08E+08	0.9%
					847.7	3^+	4.23E+03	1.08E+03	59.3%
					848.9	1^+	6.09E+07	1.09E+08	28.4%
					848.9	1^+	1.65E+06	2.17E+06	13.7%
					848.9	1^+	1.53E+02	3.06E+02	33.2%
850.3	853.4	0.2%	1^+	-1.12E+10	0.00	3^-	2.64E+12	2.66E+12	0.4%
					12.73	1^-	1.24E+09	1.25E+09	0.5%
					804.9	3^-	3.72E+09	3.78E+09	0.8%
					808.8	1^-	3.50E+09	3.56E+09	0.9%
					815.9	1^-	1.98E+07	2.05E+07	1.8%
					816.0	3^-	1.01E+09	1.02E+09	0.3%
					816.3	1^-	2.42E+08	2.51E+08	1.8%
					818.2	3^-	5.64E+08	5.75E+08	1.0%
					820.6	3^-	9.28E+07	9.65E+07	1.9%
					822.5	1^-	1.19E+07	1.19E+07	0.2%
					823.2	3^-	8.60E+07	8.52E+07	0.5%
					832.0	3^-	3.12E+06	3.06E+06	0.9%
					839.2	3^-	1.29E+06	1.18E+06	4.3%
					842.2	1^-	3.54E+05	3.65E+05	1.6%
					851.7	3^-	9.42E+02	4.33E+00	99.1%
					853.4	1^-	1.80E-05	6.00E-05	53.8%
852.1	855.3	0.2%	3^+	4.10E+08	0.00	3^-	3.48E+12	3.51E+12	0.4%
					12.73	1^-	4.58E+11	4.61E+11	0.3%
					804.9	3^-	1.54E+08	1.57E+08	0.8%
					805.4	5^-	8.75E+08	8.93E+08	1.0%
					808.8	1^-	3.91E+09	3.98E+09	0.8%

					809.5	5^-	4.78E+08	4.83E+08	0.5%
					815.9	1^-	4.50E+07	4.61E+07	1.3%
					816.0	3^-	2.31E+09	2.35E+09	0.8%
					816.3	1^-	3.36E+07	3.33E+07	0.4%
					818.2	3^-	5.82E+08	5.86E+08	0.3%
					820.1	5^-	6.40E+06	7.03E+06	4.7%
					820.6	3^-	1.84E+08	1.87E+08	0.7%
					822.5	1^-	1.23E+07	1.18E+07	1.7%
					823.2	3^-	1.27E+08	1.29E+08	0.6%
					827.5	5^-	5.86E+06	5.38E+06	4.2%
					832.0	3^-	2.73E+07	2.74E+07	0.1%
					833.5	5^-	4.75E+06	4.76E+06	0.1%
					839.2	3^-	2.14E+06	1.94E+06	5.0%
					842.2	1^-	1.54E+06	1.50E+06	1.4%
					851.7	3^-	7.46E+00	5.51E+00	15.0%
					853.4	1^-	1.06E+01	1.64E+02	87.9%
853.1	856.3	0.2%	5^+	1.01E+10	0.00	3^-	4.54E+12	4.57E+12	0.4%
					804.9	3^-	7.93E+08	8.07E+08	0.8%
					805.4	5^-	6.07E+07	6.19E+07	0.9%
					809.4	7^-	4.27E+07	4.45E+07	2.0%
					809.5	5^-	3.15E+09	3.21E+09	0.9%
					816.0	3^-	4.39E+09	4.45E+09	0.7%
					818.2	3^-	2.80E+08	2.86E+08	1.1%
					820.1	5^-	5.92E+07	5.92E+07	0.0%
					820.6	3^-	1.25E+08	1.27E+08	0.7%
					823.2	3^-	3.36E+05	3.32E+05	0.5%
					827.5	5^-	9.04E+04	9.09E+04	0.2%
					830.1	7^-	7.10E+06	7.10E+06	0.0%
					832.0	3^-	4.26E+05	3.97E+05	3.5%
					833.5	5^-	1.06E+07	1.04E+07	0.7%
					839.2	3^-	7.92E+06	7.34E+06	3.8%
					851.7	3^-	2.40E+02	8.54E+02	56.1%
855.9	858.6	0.2%	1^+	2.62E+10	0.00	3^-	1.77E+11	1.79E+11	0.4%
					12.73	1^-	1.20E+11	1.20E+11	0.0%
					804.9	3^-	1.66E+08	1.70E+08	1.2%
					808.8	1^-	2.45E+04	8.38E+04	54.7%
					815.9	1^-	5.41E+09	5.48E+09	0.6%
					816.0	3^-	7.10E+06	6.69E+06	3.0%
					816.3	1^-	1.42E+09	1.44E+09	0.5%

			818.2	3^-	4.95E+08	4.97E+08	0.3%
			820.6	3^-	5.28E+08	5.31E+08	0.2%
			822.5	1^-	2.73E+07	2.81E+07	1.4%
			823.2	3^-	1.09E+08	1.12E+08	1.4%
			832.0	3^-	3.74E+07	3.69E+07	0.7%
			839.2	3^-	1.11E+05	1.07E+05	2.0%
			842.2	1^-	7.91E+05	7.66E+05	1.6%
			851.7	3^-	2.12E+04	1.60E+04	13.9%
			853.4	1^-	1.55E+04	8.50E+03	29.1%
859.3	3^+	1.22E+10	0.00	3^-	6.14E+11	6.18E+11	0.4%
			12.73	1^-	7.32E+10	7.43E+10	0.8%
			804.9	3^-	5.87E+07	5.99E+07	1.1%
			805.4	5^-	1.70E+07	1.75E+07	1.4%
			808.8	1^-	6.77E+06	6.52E+06	1.9%
			809.5	5^-	1.02E+08	1.06E+08	1.8%
			815.9	1^-	1.92E+09	1.94E+09	0.5%
			816.0	3^-	1.02E+09	1.04E+09	0.6%
			816.3	1^-	5.13E+09	5.19E+09	0.6%
			818.2	3^-	3.34E+08	3.36E+08	0.4%
			820.1	5^-	7.07E+06	6.96E+06	0.8%
			820.6	3^-	3.33E+08	3.37E+08	0.5%
			822.5	1^-	9.32E+07	9.41E+07	0.5%
			823.2	3^-	5.27E+07	5.28E+07	0.1%
			827.5	5^-	9.07E+05	1.00E+06	5.0%
			832.0	3^-	5.17E+06	5.31E+06	1.3%
			833.5	5^-	4.39E+06	4.27E+06	1.5%
			839.2	3^-	1.61E+06	1.48E+06	4.4%
			842.2	1^-	1.76E+05	1.62E+05	4.1%
			851.7	3^-	1.41E+04	8.84E+03	22.8%
			853.4	1^-	3.79E+03	8.12E+02	64.7%
859.5	5^+	1.47E+09	0.00	3^-	7.78E+08	7.24E+08	3.6%
			804.9	3^-	8.45E+07	8.55E+07	0.6%
			805.4	5^-	4.21E+08	4.28E+08	0.7%
			809.4	7^-	1.19E+08	1.22E+08	1.5%
			809.5	5^-	1.76E+07	1.83E+07	2.0%
			816.0	3^-	1.18E+09	1.19E+09	0.6%
			818.2	3^-	4.70E+09	4.76E+09	0.7%
			820.1	5^-	2.15E+08	2.16E+08	0.3%
			820.6	3^-	1.54E+09	1.56E+09	0.8%

					823.2	3^-	1.89E+06	1.95E+06	1.6%
					827.5	5^-	1.48E+03	1.14E+03	13.2%
					830.1	7^-	5.37E+05	4.88E+05	4.9%
					832.0	3^-	2.52E+05	2.53E+05	0.3%
					833.5	5^-	7.67E+06	7.76E+06	0.5%
					839.2	3^-	6.54E+04	8.50E+04	13.1%
					851.7	3^-	9.23E+03	4.25E+03	36.9%
	860.5		7^+	1.21E+09	805.4	5^-	2.10E+05	2.17E+05	1.7%
					809.4	7^-	1.63E+08	1.65E+08	0.8%
					809.5	5^-	1.28E+07	1.34E+07	2.0%
					820.1	5^-	7.45E+09	7.57E+09	0.8%
					827.5	5^-	4.13E+05	4.05E+05	1.0%
					830.1	7^-	3.70E+06	3.79E+06	1.2%
					833.5	5^-	1.95E+04	1.93E+04	0.7%
857.8	861.1	0.2%	3^+	1.71E+10	0.00	3^-	8.86E+11	8.92E+11	0.3%
					12.73	1^-	7.13E+11	7.20E+11	0.5%
					804.9	3^-	9.75E+07	9.96E+07	1.1%
					805.4	5^-	1.59E+08	1.63E+08	1.2%
					808.8	1^-	6.09E+06	6.01E+06	0.7%
					809.5	5^-	2.31E+07	2.45E+07	2.8%
					815.9	1^-	2.75E+09	2.78E+09	0.6%
					816.0	3^-	6.09E+07	6.27E+07	1.5%
					816.3	1^-	1.06E+09	1.08E+09	0.9%
					818.2	3^-	1.68E+09	1.70E+09	0.7%
					820.1	5^-	2.41E+08	2.42E+08	0.3%
					820.6	3^-	1.85E+09	1.87E+09	0.6%
					822.5	1^-	1.44E+07	1.46E+07	0.5%
					823.2	3^-	3.95E+08	4.01E+08	0.7%
					827.5	5^-	3.47E+07	3.31E+07	2.4%
					832.0	3^-	8.89E+07	9.02E+07	0.7%
					833.5	5^-	5.59E+07	5.60E+07	0.1%
					839.2	3^-	1.96E+06	1.89E+06	1.7%
					842.2	1^-	8.47E+06	8.35E+06	0.7%
					851.7	3^-	7.24E+02	1.41E+02	67.4%
					853.4	1^-	1.04E+04	1.35E+04	12.9%
855.9	863.0	0.4%	5^+	5.81E+09	0.00	3^-	3.90E+11	3.92E+11	0.3%
					804.9	3^-	5.56E+07	5.61E+07	0.4%
					805.4	5^-	2.76E+08	2.80E+08	0.7%
					809.4	7^-	6.15E+07	6.39E+07	1.9%

					809.5	5^-	2.75E+06	2.84E+06	1.5%
					816.0	3^-	8.31E+07	8.49E+07	1.1%
					818.2	3^-	5.57E+08	5.65E+08	0.7%
					820.1	5^-	1.73E+09	1.76E+09	0.8%
					820.6	3^-	1.85E+09	1.88E+09	0.8%
					823.2	3^-	3.65E+09	3.71E+09	0.9%
					827.5	5^-	2.31E+05	2.69E+05	7.6%
					830.1	7^-	1.08E+06	9.66E+05	5.5%
					832.0	3^-	1.64E+06	1.64E+06	0.3%
					833.5	5^-	5.45E+07	5.50E+07	0.5%
					839.2	3^-	9.15E+06	9.12E+06	0.2%
					851.7	3^-	1.62E+04	1.62E+04	0.2%
861.4	864.6	0.2%	3^+	-1.67E+10	0.00	3^-	2.44E+11	2.45E+11	0.2%
					12.73	1^-	1.14E+12	1.15E+12	0.3%
					804.9	3^-	9.31E+06	9.68E+06	2.0%
					805.4	5^-	9.16E+07	9.29E+07	0.7%
					808.8	1^-	4.82E+07	4.83E+07	0.1%
					809.5	5^-	9.68E+07	1.01E+08	2.3%
					815.9	1^-	7.88E+07	8.03E+07	0.9%
					816.0	3^-	2.70E+05	3.02E+05	5.6%
					816.3	1^-	7.92E+06	8.18E+06	1.6%
					818.2	3^-	7.26E+08	7.38E+08	0.8%
					820.1	5^-	1.89E+07	1.98E+07	2.1%
					820.6	3^-	2.47E+08	2.49E+08	0.4%
					822.5	1^-	5.37E+09	5.46E+09	0.9%
					823.2	3^-	8.84E+08	8.98E+08	0.8%
					827.5	5^-	1.44E+03	1.81E+03	11.5%
					832.0	3^-	4.13E+08	4.18E+08	0.7%
					833.5	5^-	1.39E+08	1.40E+08	0.1%
					839.2	3^-	2.75E+04	1.37E+04	33.6%
					842.2	1^-	3.56E+06	3.43E+06	1.8%
					851.7	3^-	1.43E+06	1.24E+06	6.9%
					853.4	1^-	2.63E+05	2.45E+05	3.5%
862.6	865.9	0.2%	5^+	1.09E+10	0.00	3^-	6.98E+12	7.03E+12	0.4%
					804.9	3^-	6.98E+07	7.15E+07	1.2%
					805.4	5^-	9.23E+04	9.00E+04	1.3%
					809.4	7^-	5.94E+04	6.46E+04	4.1%
					809.5	5^-	2.24E+08	2.29E+08	1.1%
					816.0	3^-	1.70E+08	1.74E+08	1.0%

					818.2	3^-	6.29E+08	6.37E+08	0.6%
					820.1	5^-	2.70E+08	2.74E+08	0.7%
					820.6	3^-	3.28E+09	3.33E+09	0.8%
					823.2	3^-	3.41E+09	3.47E+09	0.8%
					827.5	5^-	2.27E+08	2.30E+08	0.6%
					830.1	7^-	9.05E+07	9.01E+07	0.3%
					832.0	3^-	6.79E+06	6.45E+06	2.6%
					833.5	5^-	3.59E+08	3.62E+08	0.4%
					839.2	3^-	1.37E+08	1.35E+08	0.7%
					851.7	3^-	3.04E+05	3.53E+05	7.5%
	869.7		7^+	3.29E+10	805.4	5^-	4.31E+06	4.38E+06	0.9%
					809.4	7^-	3.12E+05	3.33E+05	3.2%
					809.5	5^-	8.06E+06	8.38E+06	1.9%
					820.1	5^-	3.10E+04	3.90E+04	11.5%
					827.5	5^-	7.77E+09	7.86E+09	0.6%
					830.1	7^-	5.16E+08	5.21E+08	0.5%
					833.5	5^-	1.54E+08	1.56E+08	0.7%
	870.0		9^+	2.52E+10	809.4	7^-	8.47E+06	8.60E+06	0.7%
					830.1	7^-	7.26E+09	7.37E+09	0.7%
	873.1		5^+	2.11E+10	0.00	3^-	1.34E+12	1.35E+12	0.4%
					804.9	3^-	3.63E+06	3.48E+06	2.1%
					805.4	5^-	3.08E+07	3.13E+07	0.9%
					809.4	7^-	5.87E+06	6.15E+06	2.4%
					809.5	5^-	2.85E+08	2.92E+08	1.4%
					816.0	3^-	1.14E+06	1.20E+06	2.4%
					818.2	3^-	4.36E+06	4.55E+06	2.2%
					820.1	5^-	2.31E+08	2.36E+08	1.1%
					820.6	3^-	8.73E+06	8.95E+06	1.2%
					823.2	3^-	2.04E+06	1.97E+06	1.8%
					827.5	5^-	1.49E+09	1.51E+09	0.7%
					830.1	7^-	1.63E+06	1.59E+06	1.3%
					832.0	3^-	5.56E+09	5.65E+09	0.8%
					833.5	5^-	1.17E+09	1.19E+09	1.0%
					839.2	3^-	9.92E+06	9.05E+06	4.6%
					851.7	3^-	1.54E+06	1.33E+06	7.2%
869.7	873.3	0.2%	1^+	4.14E+10	0.00	3^-	1.44E+13	1.45E+13	0.4%
					12.73	1^-	2.57E+12	2.60E+12	0.5%
					804.9	3^-	6.04E+07	6.13E+07	0.7%
					808.8	1^-	2.19E+08	2.23E+08	1.0%

					815.9	1^-	3.96E+08	4.03E+08	0.9%
					816.0	3^-	5.03E+08	5.14E+08	1.0%
					816.3	1^-	1.36E+08	1.42E+08	2.4%
					818.2	3^-	1.95E+09	1.98E+09	0.9%
					820.6	3^-	2.23E+09	2.29E+09	1.2%
					822.5	1^-	1.30E+08	1.31E+08	0.5%
					823.2	3^-	8.22E+08	8.42E+08	1.2%
					832.0	3^-	3.55E+08	3.62E+08	0.9%
					839.2	3^-	1.93E+09	1.93E+09	0.0%
					842.2	1^-	2.97E+08	3.07E+08	1.7%
					851.7	3^-	4.17E+07	4.65E+07	5.5%
					853.4	1^-	1.52E+06	8.38E+05	28.9%
	874.4		7^+	2.49E+10	805.4	5^-	2.25E+06	2.38E+06	2.7%
					809.4	7^-	8.28E+07	8.49E+07	1.3%
					809.5	5^-	2.88E+06	2.96E+06	1.4%
					820.1	5^-	1.91E+07	1.93E+07	0.7%
					827.5	5^-	9.08E+03	1.66E+03	69.1%
					830.1	7^-	2.98E+09	3.04E+09	0.9%
					833.5	5^-	5.78E+09	5.88E+09	0.8%
872.7	876.3	0.2%	3^+	1.23E+10	0.00	3^-	1.85E+13	1.86E+13	0.4%
					12.73	1^-	2.63E+12	2.65E+12	0.4%
					804.9	3^-	7.18E+07	7.35E+07	1.2%
					805.4	5^-	5.90E+07	6.11E+07	1.7%
					808.8	1^-	4.49E+08	4.65E+08	1.8%
					809.5	5^-	4.34E+08	4.55E+08	2.3%
					815.9	1^-	4.46E+08	4.60E+08	1.5%
					816.0	3^-	3.01E+08	3.13E+08	1.9%
					816.3	1^-	1.27E+09	1.30E+09	1.1%
					818.2	3^-	3.42E+08	3.52E+08	1.4%
					820.1	5^-	2.61E+08	2.67E+08	1.3%
					820.6	3^-	3.79E+08	3.85E+08	0.9%
					822.5	1^-	1.80E+09	1.83E+09	1.0%
					823.2	3^-	3.27E+07	3.33E+07	1.0%
					827.5	5^-	3.79E+08	3.83E+08	0.6%
					832.0	3^-	8.92E+08	9.02E+08	0.6%
					833.5	5^-	1.13E+09	1.15E+09	0.8%
					839.2	3^-	2.41E+09	2.41E+09	0.1%
					842.2	1^-	4.06E+08	4.06E+08	0.0%
					851.7	3^-	7.09E+04	6.76E+04	2.4%

					853.4	1^-	1.39E+06	1.52E+06	4.8%
872.9	876.6	0.2%	5^+	2.04E+10	0.00	3^-	1.82E+13	1.83E+13	0.4%
					804.9	3^-	2.46E+06	2.81E+06	6.6%
					805.4	5^-	1.15E+06	1.33E+06	7.6%
					809.4	7^-	5.65E+05	4.69E+05	9.3%
					809.5	5^-	4.73E+08	4.87E+08	1.4%
					816.0	3^-	9.05E+07	9.42E+07	2.0%
					818.2	3^-	4.21E+06	3.90E+06	3.8%
					820.1	5^-	6.38E+08	6.54E+08	1.2%
					820.6	3^-	2.97E+07	3.07E+07	1.6%
					823.2	3^-	1.05E+08	1.07E+08	1.0%
					827.5	5^-	3.30E+09	3.38E+09	1.1%
					830.1	7^-	3.95E+08	3.98E+08	0.4%
					832.0	3^-	1.39E+08	1.42E+08	1.1%
					833.5	5^-	2.40E+09	2.45E+09	1.0%
					839.2	3^-	2.47E+09	2.46E+09	0.2%
					851.7	3^-	4.51E+06	3.70E+06	9.9%
876.1	879.6	0.2%	3^+	3.72E+10	0.00	3^-	3.33E+12	3.35E+12	0.3%
					12.73	1^-	1.37E+13	1.38E+13	0.4%
					804.9	3^-	1.59E+04	1.49E+04	3.3%
					805.4	5^-	4.10E+05	4.34E+05	2.7%
					808.8	1^-	2.10E+07	2.26E+07	3.7%
					809.5	5^-	8.39E+07	8.70E+07	1.8%
					815.9	1^-	2.96E+07	3.15E+07	3.1%
					816.0	3^-	3.89E+07	3.93E+07	0.5%
					816.3	1^-	1.04E+06	1.18E+06	6.6%
					818.2	3^-	1.20E+07	1.27E+07	3.0%
					820.1	5^-	6.14E+07	6.25E+07	0.9%
					820.6	3^-	2.04E+08	2.08E+08	1.0%
					822.5	1^-	2.24E+07	2.32E+07	1.9%
					823.2	3^-	1.53E+09	1.57E+09	1.3%
					827.5	5^-	8.94E+08	9.06E+08	0.7%
					832.0	3^-	4.03E+09	4.13E+09	1.2%
					833.5	5^-	1.62E+08	1.66E+08	1.1%
					839.2	3^-	1.14E+09	1.15E+09	0.3%
					842.2	1^-	2.22E+09	2.24E+09	0.3%
					851.7	3^-	7.58E+06	7.76E+06	1.1%
					853.4	1^-	6.08E+07	5.70E+07	3.3%
877.1	880.7	0.2%	1^+	-3.53E+10	0.00	3^-	4.19E+12	4.22E+12	0.3%

					12.73	1^-	2.05E+13	2.07E+13	0.4%
					804.9	3^-	5.61E+04	8.24E+04	19.0%
					808.8	1^-	1.06E+06	1.10E+06	1.9%
					815.9	1^-	7.28E+05	7.09E+05	1.3%
					816.0	3^-	4.10E+07	4.34E+07	2.8%
					816.3	1^-	6.29E+08	6.45E+08	1.2%
					818.2	3^-	1.11E+06	1.15E+06	1.9%
					820.6	3^-	1.90E+08	1.93E+08	0.8%
					822.5	1^-	4.38E+09	4.49E+09	1.3%
					823.2	3^-	7.86E+08	8.11E+08	1.6%
					832.0	3^-	1.05E+09	1.07E+09	1.1%
					839.2	3^-	1.09E+09	1.09E+09	0.2%
					842.2	1^-	3.08E+09	3.10E+09	0.4%
					851.7	3^-	6.48E+06	7.01E+06	3.9%
					853.4	1^-	1.76E+08	1.71E+08	1.2%
890.9	892.1	0.1%	5^-	1.29E+11	847.0	5^+	4.10E+10	4.15E+10	0.6%
					847.0	5^+	3.55E+05	2.83E+05	11.2%
					847.1	7^+	2.56E+06	2.29E+06	5.6%
					847.7	3^+	5.71E+09	5.76E+09	0.4%
					847.7	3^+	1.77E+04	1.07E+04	24.9%
					851.3	7^+	1.06E+05	9.89E+04	3.4%
					855.3	3^+	8.39E+03	6.41E+03	13.4%
					856.3	5^+	9.50E+04	8.73E+04	4.2%
					859.3	3^+	9.80E+09	9.79E+09	0.1%
					859.3	3^+	6.24E+02	6.25E+02	0.1%
					859.5	5^+	3.00E+03	3.19E+03	3.1%
					860.5	7^+	3.06E+05	2.51E+05	9.8%
					861.1	3^+	3.51E+02	7.94E+02	38.7%
					863.0	5^+	1.35E+04	8.46E+03	23.0%
					864.6	3^+	1.74E+03	1.53E+03	6.4%
					865.9	5^+	5.43E+03	6.85E+03	11.6%
					869.7	7^+	1.03E+02	2.47E+02	41.3%
					873.1	5^+	2.14E+09	2.11E+09	0.6%
					873.1	5^+	6.70E+03	4.52E+03	19.4%
					874.4	7^+	9.98E+03	6.18E+03	23.5%
					876.3	3^+	9.64E+07	9.52E+07	0.6%
					876.3	3^+	9.13E+02	9.89E+01	80.4%
					876.6	5^+	3.53E+03	4.11E+02	79.1%
					879.6	3^+	9.50E+00	4.69E+01	66.4%

888.5	892.4	0.2%	5^+	1.68E+09	0.00	3^-	1.18E+12	1.19E+12	0.5%
					804.9	3^-	3.54E+06	3.78E+06	3.2%
					805.4	5^-	1.71E+06	1.73E+06	0.5%
					809.4	7^-	1.86E+06	1.79E+06	1.9%
					809.5	5^-	2.31E+07	2.37E+07	1.4%
					816.0	3^-	2.06E+06	2.23E+06	4.0%
					818.2	3^-	6.83E+06	6.58E+06	1.9%
					820.1	5^-	5.19E+06	5.21E+06	0.2%
					820.6	3^-	5.22E+06	5.12E+06	1.0%
					823.2	3^-	2.02E+04	1.14E+04	27.7%
					827.5	5^-	4.40E+06	4.22E+06	2.1%
					830.1	7^-	1.43E+08	1.49E+08	2.3%
					832.0	3^-	7.90E+06	8.48E+06	3.5%
					833.5	5^-	3.00E+08	3.06E+08	1.0%
					839.2	3^-	7.30E+05	3.28E+05	38.0%
					851.7	3^-	7.84E+09	7.94E+09	0.6%
					892.1	5^-	8.31E-02	2.86E-03	93.3%
890.7	894.7	0.2%	3^+	4.40E+09	0.00	3^-	7.35E+10	7.42E+10	0.5%
					12.73	1^-	1.27E+13	1.28E+13	0.4%
					804.9	3^-	6.14E+06	6.46E+06	2.6%
					805.4	5^-	2.22E+06	2.19E+06	0.6%
					808.8	1^-	1.44E+06	1.23E+06	8.1%
					809.5	5^-	9.82E+03	1.89E+04	31.5%
					815.9	1^-	5.45E+06	5.03E+06	4.0%
					816.0	3^-	6.74E+07	6.97E+07	1.7%
					816.3	1^-	1.17E+07	1.29E+07	4.9%
					818.2	3^-	6.40E+07	6.65E+07	1.9%
					820.1	5^-	1.59E+06	1.62E+06	1.0%
					820.6	3^-	7.19E+06	7.22E+06	0.2%
					822.5	1^-	6.51E+07	6.88E+07	2.7%
					823.2	3^-	2.31E+08	2.39E+08	1.7%
					827.5	5^-	8.71E+07	9.44E+07	4.0%
					832.0	3^-	9.42E+07	9.90E+07	2.5%
					833.5	5^-	1.24E+07	1.20E+07	1.8%
					839.2	3^-	6.73E+06	7.49E+06	5.3%
					842.2	1^-	1.44E+09	1.47E+09	1.3%
					851.7	3^-	1.53E+09	1.54E+09	0.4%
					853.4	1^-	6.10E+09	6.12E+09	0.1%
					892.1	5^-	4.09E-01	2.32E-01	27.7%

892.4	896.6	0.2%	3^-	1.64E+11	817.2	1^+	6.38E+07	6.36E+07	0.2%
					847.0	5^+	2.41E+10	2.44E+10	0.8%
					847.0	5^+	7.31E+05	5.86E+05	11.0%
					847.7	3^+	1.37E+10	1.39E+10	0.5%
					847.7	3^+	3.96E+05	3.01E+05	13.7%
					848.9	1^+	4.91E+11	4.99E+11	0.8%
					848.9	1^+	1.45E+10	1.45E+10	0.3%
					848.9	1^+	1.52E+05	1.25E+05	9.8%
					853.4	1^+	1.63E+06	1.68E+06	1.5%
					855.3	3^+	2.95E+06	2.75E+06	3.4%
					856.3	5^+	4.72E+06	4.64E+06	0.9%
					858.6	1^+	3.26E+09	3.25E+09	0.1%
					858.6	1^+	7.86E+04	8.03E+04	1.1%
					859.3	3^+	7.33E+07	7.68E+07	2.3%
					859.3	3^+	5.29E+05	4.84E+05	4.4%
					859.5	5^+	3.55E+05	2.88E+05	10.4%
					861.1	3^+	7.85E+05	7.58E+05	1.7%
					863.0	5^+	1.06E+06	1.00E+06	2.9%
					864.6	3^+	1.92E+03	3.16E+03	24.3%
					865.9	5^+	5.03E+06	5.00E+06	0.2%
					873.1	5^+	4.79E+07	4.59E+07	2.1%
					873.1	5^+	6.24E+05	5.35E+05	7.7%
					873.3	1^+	2.07E+06	2.31E+06	5.5%
					876.3	3^+	2.05E+09	2.01E+09	0.7%
					876.3	3^+	3.30E+06	2.78E+06	8.6%
					876.6	5^+	4.62E+06	4.36E+06	2.9%
					879.6	3^+	3.29E+05	3.13E+05	2.5%
					880.7	1^+	1.79E+05	1.17E+05	20.8%
					892.4	5^+	4.04E+03	4.17E+03	1.5%
					894.7	3^+	5.64E-01	4.61E+01	97.6%
895.7	902.3	0.4%	1^-	2.00E+11	817.2	1^+	2.75E+08	2.75E+08	0.1%
					847.7	3^+	3.56E+10	3.62E+10	0.8%
					847.7	3^+	1.75E+05	1.26E+05	16.4%
					848.9	1^+	3.20E+11	3.26E+11	0.8%
					848.9	1^+	1.04E+10	1.05E+10	0.4%
					848.9	1^+	6.82E+05	5.71E+05	8.8%
					853.4	1^+	5.40E+05	6.01E+05	5.3%
					855.3	3^+	2.56E+03	3.20E+02	77.8%
					858.6	1^+	2.06E+09	2.05E+09	0.2%

					858.6	1^+	2.61E+05	1.99E+05	13.5%
					859.3	3^+	1.84E+10	1.86E+10	0.6%
					859.3	3^+	2.99E+05	2.65E+05	6.0%
					861.1	3^+	1.56E+06	1.43E+06	4.0%
					864.6	3^+	6.51E+05	6.77E+05	1.9%
					873.3	1^+	5.45E+05	7.54E+05	16.1%
					876.3	3^+	6.02E+08	5.81E+08	1.8%
					876.3	3^+	5.62E+05	5.06E+05	5.2%
					879.6	3^+	2.53E+06	2.30E+06	4.9%
					880.7	1^+	1.76E+06	1.50E+06	8.0%
					894.7	3^+	1.39E+05	1.33E+05	2.1%
899.0	903.1	0.2%	3^-	8.42E+10	817.2	1^+	1.22E+09	1.22E+09	0.0%
					847.0	5^+	1.05E+10	1.07E+10	0.9%
					847.0	5^+	7.44E+05	7.48E+05	0.3%
					847.7	3^+	9.60E+09	9.72E+09	0.6%
					847.7	3^+	2.04E+05	2.05E+05	0.3%
					848.9	1^+	7.39E+11	7.50E+11	0.8%
					848.9	1^+	7.97E+09	8.04E+09	0.4%
					848.9	1^+	2.61E+03	3.29E+03	11.5%
					853.4	1^+	4.45E+06	4.67E+06	2.3%
					855.3	3^+	1.16E+07	1.10E+07	2.6%
					856.3	5^+	2.30E+07	2.24E+07	1.3%
					858.6	1^+	1.99E+09	1.97E+09	0.3%
					858.6	1^+	1.45E+05	1.64E+05	6.3%
					859.3	3^+	1.53E+10	1.54E+10	0.4%
					859.3	3^+	1.52E+06	1.48E+06	1.4%
					859.5	5^+	1.78E+05	1.84E+05	1.5%
					861.1	3^+	1.72E+06	1.78E+06	1.8%
					863.0	5^+	7.18E+05	7.62E+05	3.0%
					864.6	3^+	2.94E+05	3.26E+05	5.3%
					865.9	5^+	2.09E+07	2.06E+07	0.6%
					873.1	5^+	2.96E+08	3.24E+08	4.5%
					873.1	5^+	2.93E+06	2.63E+06	5.3%
					873.3	1^+	9.36E+06	9.98E+06	3.2%
					876.3	3^+	1.43E+09	1.43E+09	0.2%
					876.3	3^+	1.91E+07	1.71E+07	5.5%
					876.6	5^+	2.79E+07	2.64E+07	2.8%
					879.6	3^+	2.42E+06	2.26E+06	3.3%
					880.7	1^+	1.41E+06	1.12E+06	11.5%

892.4	5^+	3.01E+05	2.36E+05	12.1%	
894.7	3^+	9.50E+03	7.56E+03	11.3%	

TABLE D.3: GRASP2018 calculation results for ^{56}Fe Ne-like valence-state ion energy levels, hyperfine-coupling frequency (A_J) and transition rates. GRASP energy levels are compared with NIST [178] values and the variance (var) is shown, as well as the variance (var) between the two different transition-rate calculations.

Energy (eV)					**Lower State**		**Transition rate (Hz)**		
NIST	**GRASP**	**Var**	$2J^\pi$	A_J (Hz)	**Energy**	$2J^\pi$	**Length**	**Velocity**	**Var**
0.00	0.00		0^+	0.00E+00					
725.24	728.99	0.3%	4^-	1.01E+10					
727.14	730.89	0.3%	2^-	4.48E+10	0.00	0^+	9.41E+11	9.68E+11	1.4%
737.86	741.61	0.3%	0^-	0.00E+00					
739.05	742.81	0.3%	2^-	1.86E+09	0.00	0^+	8.10E+11	8.32E+11	1.3%
755.49	759.04	0.2%	2^+	2.71E+10	728.99	4^-	3.37E+09	3.26E+09	1.7%
					741.61	0^-	1.03E+07	9.61E+06	3.5%
					742.81	2^-	1.22E+08	1.18E+08	1.7%
					742.81	2^-	1.15E+07	1.06E+07	4.3%
758.99	762.51	0.2%	4^+	9.74E+09	728.99	4^-	2.48E+09	2.42E+09	1.3%
					742.81	2^-	2.45E+09	2.38E+09	1.5%
					742.81	2^-	1.58E+05	1.18E+05	14.6%
760.61	764.12	0.2%	6^+	0.00E+00	728.99	4^-	6.17E+09	6.04E+09	1.0%
761.74	765.24	0.2%	2^+	1.56E+10	728.99	4^-	3.27E+08	3.19E+08	1.2%
					741.61	0^-	5.17E+06	4.94E+06	2.2%
					742.81	2^-	5.46E+09	5.33E+09	1.2%
					742.81	2^-	2.02E+05	2.37E+05	8.0%
763.55	767.05	0.2%	4^+	5.48E+09	728.99	4^-	4.30E+09	4.22E+09	0.9%
					742.81	2^-	3.12E+09	3.05E+09	1.1%
					742.81	2^-	2.32E+07	2.20E+07	2.8%
768.98	772.58	0.2%	0^+	0.00E+00	742.81	2^-	7.43E+09	7.46E+09	0.2%
					742.81	2^-	1.15E+09	1.07E+09	3.4%
771.06	774.58	0.2%	2^+	3.72E+10	728.99	4^-	1.27E+07	1.27E+07	0.1%
					741.61	0^-	1.98E+09	1.93E+09	1.3%
					742.81	2^-	3.14E+07	3.04E+07	1.6%
					742.81	2^-	2.76E+09	2.67E+09	1.6%
774.31	777.82	0.2%	2^+	4.73E+10	728.99	4^-	7.98E+08	7.94E+08	0.3%
					741.61	0^-	3.99E+09	3.91E+09	1.0%

					742.81	2^-	2.53E+06	2.43E+06	2.2%
					742.81	2^-	2.20E+09	2.15E+09	1.1%
774.69	778.20	0.2%	4^+	1.68E+10	728.99	4^-	1.06E+08	1.05E+08	0.4%
					742.81	2^-	7.91E+07	7.95E+07	0.2%
					742.81	2^-	6.31E+09	6.17E+09	1.1%
787.72	792.17	0.3%	0^+	0.00E+00	742.81	2^-	1.11E+10	1.19E+10	3.4%
					742.81	2^-	1.28E+10	1.34E+10	2.2%
801.43	805.26	0.2%	0^-	0.00E+00	759.04	2^+	1.12E+10	1.13E+10	0.2%
					765.24	2^+	3.32E+08	2.92E+08	6.4%
					774.58	2^+	2.93E+05	1.23E+06	61.5%
					777.82	2^+	1.25E+08	1.34E+08	3.7%
802.40	806.21	0.2%	2^-	1.36E+10	0.00	0^+	8.80E+10	8.95E+10	0.9%
					759.04	2^+	9.39E+09	9.51E+09	0.6%
					762.51	4^+	8.89E+08	8.15E+08	4.3%
					765.24	2^+	2.84E+07	3.56E+07	11.2%
					767.05	4^+	1.09E+09	1.09E+09	0.2%
					772.58	0^+	1.68E+08	1.67E+08	0.4%
					774.58	2^+	2.87E+06	4.37E+05	73.5%
					777.82	2^+	4.42E+07	4.13E+07	3.4%
					778.20	4^+	1.71E+07	2.61E+07	20.7%
					792.17	0^+	9.36E+03	3.50E+03	45.6%
804.21	808.03	0.2%	4^-	9.89E+09	759.04	2^+	5.30E+09	5.37E+09	0.7%
					762.51	4^+	7.88E+08	8.44E+08	3.4%
					764.12	6^+	4.14E+08	3.52E+08	8.1%
					765.24	2^+	1.05E+09	1.07E+09	1.2%
					767.05	4^+	3.66E+09	3.71E+09	0.7%
					774.58	2^+	1.42E+07	1.26E+07	5.8%
					777.82	2^+	1.53E+07	1.35E+07	6.2%
					778.20	4^+	4.92E+07	4.00E+07	10.3%
804.26	808.20	0.2%	8^-	0.00E+00	764.12	6^+	1.11E+10	1.13E+10	0.6%
806.73	808.94	0.1%	6^-	6.48E+09	762.51	4^+	1.10E+10	1.11E+10	0.5%
					764.12	6^+	1.71E+09	1.75E+09	1.0%
					767.05	4^+	1.10E+08	1.11E+08	0.6%
					778.20	4^+	3.44E+06	2.86E+06	9.2%
806.73	810.62	0.2%	4^-	9.79E+09	759.04	2^+	3.73E+08	3.78E+08	0.6%
					762.51	4^+	4.88E+09	5.01E+09	1.3%
					764.12	6^+	2.27E+08	2.39E+08	2.4%
					765.24	2^+	7.74E+09	7.85E+09	0.7%
					767.05	4^+	7.45E+05	1.04E+06	16.3%

					774.58	2^+	5.05E+06	3.94E+06	12.4%
					777.82	2^+	4.49E+06	4.26E+06	2.6%
					778.20	4^+	6.35E+04	6.11E+04	1.9%
807.80	811.69	0.2%	6^-	0.00E+00	762.51	4^+	8.09E+07	8.65E+07	3.4%
					764.12	6^+	2.60E+09	2.72E+09	2.3%
					767.05	4^+	9.51E+09	9.69E+09	1.0%
					778.20	4^+	9.25E+06	8.36E+06	5.0%
812.37	816.41	0.2%	2^-	3.39E+10	0.00	0^+	5.82E+12	5.87E+12	0.4%
					759.04	2^+	5.65E+07	5.80E+07	1.4%
					762.51	4^+	6.80E+08	7.08E+08	2.0%
					765.24	2^+	7.03E+09	7.30E+09	1.8%
					767.05	4^+	1.95E+06	3.75E+06	31.5%
					772.58	0^+	5.49E+09	5.58E+09	0.8%
					774.58	2^+	1.60E+08	1.61E+08	0.3%
					777.82	2^+	1.92E+08	1.85E+08	1.9%
					778.20	4^+	4.94E+07	6.42E+07	13.1%
					792.17	0^+	4.79E+07	4.78E+07	0.1%
817.60	821.51	0.2%	4^-	-7.08E+07	759.04	2^+	2.67E+07	2.71E+07	0.8%
					762.51	4^+	6.32E+07	7.21E+07	6.6%
					764.12	6^+	2.31E+06	2.10E+06	4.8%
					765.24	2^+	1.80E+06	2.21E+06	10.3%
					767.05	4^+	2.03E+07	2.19E+07	3.7%
					774.58	2^+	1.14E+10	1.15E+10	0.7%
					777.82	2^+	1.58E+08	1.60E+08	0.6%
					778.20	4^+	1.49E+09	1.50E+09	0.4%
818.41	822.27	0.2%	4^-	4.67E+09	759.04	2^+	7.38E+07	7.32E+07	0.4%
					762.51	4^+	2.29E+08	2.34E+08	1.1%
					764.12	6^+	1.34E+08	1.77E+08	13.9%
					765.24	2^+	2.33E+07	2.52E+07	3.9%
					767.05	4^+	5.91E+08	6.15E+08	2.1%
					774.58	2^+	3.95E+05	5.01E+05	11.8%
					777.82	2^+	9.87E+09	1.00E+10	0.9%
					778.20	4^+	1.07E+09	1.09E+09	1.1%
818.93	822.85	0.2%	6^-	0.00E+00	762.51	4^+	3.38E+06	3.54E+06	2.2%
					764.12	6^+	1.28E+08	1.45E+08	6.2%
					767.05	4^+	1.33E+07	1.38E+07	1.8%
					778.20	4^+	1.16E+10	1.18E+10	0.9%
825.70	830.12	0.3%	2^-	-1.80E+10	0.00	0^+	2.30E+13	2.32E+13	0.4%
					759.04	2^+	7.92E+06	9.68E+06	10.0%

762.51	4^+	1.44E+07	2.89E+07	33.5%
765.24	2^+	1.79E+09	1.93E+09	3.6%
767.05	4^+	5.97E+07	4.73E+07	11.6%
772.58	0^+	7.00E+08	7.11E+08	0.8%
774.58	2^+	5.52E+09	5.77E+09	2.2%
777.82	2^+	2.86E+09	2.98E+09	1.9%
778.20	4^+	2.19E+08	2.04E+08	3.5%
792.17	0^+	3.58E+09	3.61E+09	0.4%

TABLE D.5: GRASP2018 calculation results for ^{56}Fe Na-like valence-state ion energy levels, hyperfine-coupling frequency (A_J) and transition rates. GRASP energy levels are compared with NIST [178] values and the variance (var) is shown, as well as the variance (var) between the two different transition-rate calculations.

Energy (eV)					**Lower State**		**Transition rate (Hz)**		
NIST	**GRASP**	**Var**	$2J^\pi$	A_J (Hz)	**Energy**	$2J^\pi$	**Length**	**Velocity**	**Var**
0.00	0.00		1^+	9.56E+10					
34.37	34.36	0.0%	1^-	2.82E+10	0.00	1^+	6.17E+09	6.12E+09	0.4%
36.97	36.96	0.0%	3^-	4.84E+09	0.00	1^+	7.70E+09	7.67E+09	0.2%
83.75	83.82	0.0%	3^+	2.14E+09	34.36	1^-	1.49E+10	1.50E+10	0.4%
					36.96	3^-	2.54E+09	2.55E+09	0.3%
84.11	84.18	0.0%	5^+	6.02E+08	36.96	3^-	1.56E+10	1.57E+10	0.5%
231.57	231.72	0.0%	1^+	3.64E+10	34.36	1^-	1.10E+11	1.10E+11	0.1%
				3.64E+10	36.96	3^-	2.26E+11	2.27E+11	0.1%
245.20	245.35	0.0%	1^-	1.09E+10	0.00	1^+	2.07E+11	2.07E+11	0.0%
					83.82	3^+	7.96E+10	8.02E+10	0.4%
					231.72	1^+	1.45E+09	1.44E+09	0.3%
246.19	246.36	0.0%	3^-	1.88E+09	0.00	1^+	1.96E+11	1.96E+11	0.0%
					83.82	3^+	7.66E+09	7.71E+09	0.3%
					84.18	5^+	6.92E+10	6.98E+10	0.4%
					231.72	1^+	1.80E+09	1.80E+09	0.2%
263.43	263.59	0.0%	3^+	8.84E+08	34.36	1^-	3.48E+11	3.47E+11	0.1%
					245.35	1^-	3.33E+09	3.34E+09	0.2%
					246.36	3^-	7.11E+10	7.09E+10	0.1%
					246.36	3^-	5.63E+08	5.64E+08	0.1%
263.59	263.75	0.0%	5^+	3.03E+08	246.36	3^-	4.24E+11	4.23E+11	0.1%
					246.36	3^-	3.47E+09	3.49E+09	0.2%
270.90	271.12	0.0%	5^-	2.10E+08	83.82	3^+	9.16E+11	9.14E+11	0.1%

					84.18	5^+	6.53E+10	6.52E+10	0.1%
					263.59	3^+	1.86E+08	1.86E+08	0.1%
					263.75	5^+	1.24E+07	1.24E+07	0.2%
270.96	271.18	0.0%	7^-	1.02E+08	84.18	5^+	9.79E+11	9.78E+11	0.1%
					263.75	5^+	1.91E+08	1.91E+08	0.1%
330.00	330.40	0.1%	1^+	1.76E+10	34.36	1^-	5.04E+10	5.05E+10	0.1%
					245.35	1^-	3.38E+10	3.38E+10	0.0%
					246.36	3^-	1.03E+11	1.04E+11	0.1%
					246.36	3^-	6.95E+10	6.95E+10	0.0%
336.89	337.12	0.0%	1^-	5.37E+09	0.00	1^+	1.20E+11	1.20E+11	0.0%
					83.82	3^+	3.23E+10	3.27E+10	0.5%
					231.72	1^+	3.95E+10	3.94E+10	0.1%
					263.59	3^+	3.63E+10	3.63E+10	0.1%
					330.40	1^+	4.60E+08	4.58E+08	0.3%
337.38	337.62	0.0%	3^-	9.26E+08	0.00	1^+	1.15E+11	1.15E+11	0.0%
					83.82	3^+	3.12E+09	3.15E+09	0.5%
					84.18	5^+	2.81E+10	2.84E+10	0.6%
					231.72	1^+	3.71E+10	3.70E+10	0.1%
					263.59	3^+	3.50E+09	3.50E+09	0.0%
					263.75	5^+	3.17E+10	3.17E+10	0.1%
					330.40	1^+	5.71E+08	5.69E+08	0.2%
345.67	345.94	0.0%	3^+	4.47E+08	34.36	1^-	2.04E+11	2.03E+11	0.2%
					245.35	1^-	5.69E+10	5.68E+10	0.1%
					246.36	3^-	4.12E+10	4.10E+10	0.2%
					246.36	3^-	1.18E+10	1.18E+10	0.1%
					271.12	5^-	6.61E+09	6.58E+09	0.3%
					337.12	1^-	1.04E+09	1.04E+09	0.1%
					337.62	3^-	1.75E+08	1.75E+08	0.0%
345.74	346.02	0.0%	5^+	1.62E+08	246.36	3^-	2.46E+11	2.45E+11	0.2%
					246.36	3^-	7.02E+10	7.00E+10	0.1%
					271.12	5^-	3.11E+08	3.09E+08	0.3%
					271.18	7^-	6.25E+09	6.21E+09	0.3%
					337.62	3^-	1.08E+09	1.09E+09	0.1%
349.46	349.72	0.0%	5^-	1.09E+08	84.18	5^+	2.38E+10	2.37E+10	0.2%
					263.59	3^+	1.54E+11	1.54E+11	0.0%
					263.75	5^+	1.10E+10	1.10E+10	0.0%
					345.94	3^+	3.34E+11	3.33E+11	0.1%
					345.94	3^+	8.40E+07	8.34E+07	0.4%
					346.02	5^+	5.60E+06	5.55E+06	0.4%

349.50	349.76	0.0%	7^-	5.13E+07	84.18	5^+	3.56E+11	3.55E+11	0.1%
					263.75	5^+	1.65E+11	1.65E+11	0.0%
					346.02	5^+	8.61E+07	8.55E+07	0.3%
349.97	350.14	0.0%	7^+	4.44E+07	271.12	5^-	2.70E+11	2.70E+11	0.0%
					271.18	7^-	9.99E+09	9.97E+09	0.1%
					349.72	5^-	6.58E+04	6.56E+04	0.1%
					349.76	7^-	1.93E+03	1.93E+03	0.2%
349.98	350.16	0.0%	9^+	2.79E+07	271.18	7^-	2.80E+11	2.79E+11	0.0%
					349.76	7^-	6.33E+04	6.23E+04	0.8%
381.38	381.57	0.0%	1^+	9.81E+09	34.36	1^-	2.74E+10	2.74E+10	0.0%
					245.35	1^-	1.73E+10	1.72E+10	0.2%
					246.36	3^-	5.61E+10	5.61E+10	0.0%
					246.36	3^-	3.54E+10	3.53E+10	0.2%
					337.12	1^-	1.30E+10	1.30E+10	0.1%
					337.62	3^-	2.67E+10	2.67E+10	0.1%
385.14	385.36	0.0%	1^-	3.02E+09	0.00	1^+	7.14E+10	7.12E+10	0.1%
					231.72	1^+	2.64E+10	2.63E+10	0.3%
					263.59	3^+	1.70E+10	1.69E+10	0.1%
					330.40	1^+	1.14E+10	1.14E+10	0.3%
					345.94	3^+	1.67E+10	1.68E+10	0.4%
					345.94	3^+	1.67E+10	1.66E+10	0.1%
					381.57	1^+	1.79E+08	1.79E+08	0.1%
385.45	385.64	0.0%	3^-	5.21E+08	0.00	1^+	6.87E+10	6.85E+10	0.1%
					84.18	5^+	1.45E+10	1.46E+10	0.4%
					231.72	1^+	2.51E+10	2.50E+10	0.3%
					263.59	3^+	1.64E+09	1.63E+09	0.2%
					263.75	5^+	1.48E+10	1.48E+10	0.1%
					330.40	1^+	1.07E+10	1.06E+10	0.3%
					345.94	3^+	1.61E+09	1.62E+09	0.3%
					345.94	3^+	1.61E+09	1.61E+09	0.1%
					346.02	5^+	1.46E+10	1.45E+10	0.1%
					381.57	1^+	2.22E+08	2.22E+08	0.0%
390.06	390.30	0.0%	3^+	2.55E+08	34.36	1^-	1.21E+11	1.20E+11	0.3%
					245.35	1^-	4.05E+10	4.02E+10	0.3%
					246.36	3^-	2.43E+10	2.41E+10	0.3%
					246.36	3^-	8.28E+09	8.23E+09	0.3%
					271.12	5^-	2.82E+09	2.75E+09	1.3%
					337.12	1^-	1.47E+10	1.46E+10	0.3%
					337.62	3^-	3.08E+09	3.07E+09	0.3%

					349.72	5^-	4.74E+09	4.68E+09	0.6%
					385.36	1^-	4.04E+08	4.06E+08	0.2%
					385.64	3^-	6.80E+07	6.82E+07	0.2%
390.14	390.35	0.0%	5^+	9.54E+07	246.36	3^-	1.45E+11	1.44E+11	0.3%
					246.36	3^-	4.94E+10	4.91E+10	0.3%
					271.12	5^-	1.33E+08	1.29E+08	1.3%
					271.18	7^-	2.66E+09	2.59E+09	1.3%
					337.62	3^-	1.83E+10	1.82E+10	0.3%
					349.72	5^-	2.23E+08	2.20E+08	0.6%
					349.76	7^-	4.48E+09	4.42E+09	0.6%
					385.64	3^-	4.22E+08	4.23E+08	0.2%
392.178	392.46	0.0%	5^-	6.33E+07	263.59	3^+	8.50E+10	8.48E+10	0.1%
					263.75	5^+	6.07E+09	6.05E+09	0.1%
					345.94	3^+	1.63E+11	1.62E+11	0.2%
					345.94	3^+	4.00E+10	3.99E+10	0.0%
					346.02	5^+	2.86E+09	2.86E+09	0.1%
					350.14	7^+	8.30E+08	8.22E+08	0.4%
					390.30	3^+	3.82E+07	3.78E+07	0.6%
					390.35	5^+	1.16E+10	1.15E+10	0.3%
					390.35	5^+	2.54E+06	2.51E+06	0.6%
392.186	392.48	0.0%	7^-	2.94E+07	263.75	5^+	9.09E+10	9.07E+10	0.1%
					346.02	5^+	4.29E+10	4.28E+10	0.0%
					350.14	7^+	2.29E+07	2.27E+07	0.4%
					350.16	9^+	8.05E+08	7.97E+08	0.5%
					390.35	5^+	1.74E+11	1.73E+11	0.2%
					390.35	5^+	3.91E+07	3.86E+07	0.6%

Bibliography

[1] A. Abragam and R. V. Pound. "Influence of Electric and Magnetic Fields on Angular Correlations". In: *Phys. Rev.* 92 (1953), pp. 943–962. DOI: 10.1103/PhysRev.92.943.

[2] B. M. Adams, D. Eccleshall, and M. J. L. Yates. "Coulomb Excitation Produced by Oxygen Ions". In: *Proc. Conf. React. Compl. Nucl.* Vol. 2. John Wiley and Sons, Inc., New York, 1990, p. 95.

[3] K. Alder. "Beiträge zur Theorie der Richtungskorrelation". In: *Helv. Phys. Acta* 25 (1952), pp. 235–258. DOI: 10.5169/seals-112308.

[4] K. Alder and A. Winther. *Coulomb Excitation; a collection of reprints*. New York: Academic Press, 1966.

[5] K. Alder and A. Winther. *Electromagnetic excitation; theory of Coulomb excitation with heavy ions*. Amsterdam / Oxford: North-Holland Publishing Company, 1975.

[6] K. Alder et al. "Study of Nuclear Structure by Electromagnetic Excitation with Accelerated Ions". In: *Rev. Mod. Phys.* 28 (1956), pp. 432–542. DOI: 10.1103/RevModPhys.28.432.

[7] D. G. Alkhazov et al. "Coulomb Excitation of Nuclear Levels in Spherical Even-Even Nuclei". In: *Izvest. Akad. Nauk SSSR: Ser. Fiz.* 23 (1959), p. 223.

[8] J. M. Allmond et al. "Magnetic moments of 2_1^+ states in ^{124,126,128}Sn". In: *Phys. Rev. C* 87 (2013), p. 054325. DOI: 10.1103/PhysRevC.87.054325.

[9] S. S. Anderssen and A. E. Stuchbery. "Measured static hyperfine magnetic fields following implantation of Pt into Fe interpreted as evidence for pre-equilibrium effects". In: *Hyp. Int.* 96 (1995), pp. 1–22.

[10] F. Andreozzi et al. "Realistic shell-model calculations for neutron deficient Sn isotopes". In: *Phys. Rev. C* 54 (1996), pp. 1636–1640. DOI: 10.1103/PhysRevC.54.1636.

[11] H. R. Andrews et al. "Calibration of the transient magnetic field for rare-earth nuclei in iron: applicaiton to g-factors of high spin states in ^{152,154}Sm". In: *Nuc. Phys. A* 383 (1982), pp. 509–529. DOI: 10.1016/0375-9474(82)90088-4.

[12] D. S. Andreyev et al. "Coulomb Excitation of the First Levels of Spherical Even Nuclei by Multiply Charged Ions". In: *Nucl. Phys.* 19 (1960), p. 400. DOI: 10.1016/0029-5582(60)90251-0.

[13] H. Appel and W. Mayer. "q-factor measurement on the first excited state of Fe^{56} using internal magnetic fields". In: *Nucl. Phys.* 43 (1963), pp. 393–404. DOI: 10.1016/0029-5582(63)90360-2.

[14] A. D. Ayangeakaa et al. "Shape coexistence and the role of axial asymmetry in ^{72}Ge". In: *Phys. Lett. B* 754 (2016), pp. 254–259. DOI: 10.1016/j.physletb.2016.01.036.

[15] CC BY-SA 3.0 Bakken English Wikipedia. URL: https://commons.wikimedia.org/w/index.php?curid=15039395.

[16] B. R. Barrett, P. Navrátil, and J. P. Vary. "Ab initio no core shell model". In: *Progress in Particle and Nuclear Physics* 69 (2013), pp. 131–181. DOI: 10.1016/j.ppnp.2012.10.003.

[17] M. S. Basunia and A. M. Hurst. "Nuclear Data Sheets for $A = 26$". In: *Nuclear Data Sheets* 134 (2016), pp. 1–148. DOI: 10.1016/j.nds.2016.04.001.

[18] R. B. Begzhanov et al. "Lifetime of the 0.845 MeV Level of the Fe^{56} Nucleus". In: *Zh. Eksperim. i Teor. Fiz.* 44 (1963), p. 137.

[19] L. C. Beidenharn and M. E. Rose. "Theory of Angular Correlations of Nuclear Radiations". In: *Rev. Mod. Phys.* 25 (1953), pp. 729–777. DOI: 10.1103/RevModPhys.25.729.

[20] J. Bellicard and P. Barreau. "Etude des Niveaux de Vibration des Isotopes du Fer par Diffusion Inelastique d'Electrons de 150 MeV". In: *Nucl. Phys.* 36 (1962), p. 476. DOI: 10.1016/0029-5582(62)90471-6.

[21] I. Ben-Zvi et al. "Precession measurements following Coulomb excitation with oxygen ions (VI). Hyp. Int. of nuclei in highly ionized atoms". In: *Nuc. Phys. A* 121 (1968), pp. 592–611. DOI: 10.1016/0375-9474(68)90110-3.

[22] N. Benczer-Koller and G. J. Kumbartzki. "Magnetic moments of short-lived excited nuclear states: measurements and challenges". In: *J. Phys. G* 34 (2007), R321. DOI: 10.1088/0954-3899/34/9/R01.

[23] M. Blume. "Perturbed angular correlations: Perturbation factor for arbitrary correlation time". In: *Nucl. Phys. A* 167 (1971), pp. 81–86. DOI: 10.1016/0375-9474(71)90583-5.

[24] R. Bock, ed. *Heavy Ion Collisions*. Vol. 3. North-Holland Pub. Co., 1982.

[25] A. Bohr and B. R. Mottelson. *Nuclear Structure*. Vol. 1. New York, New York 10016: W. A. Benjamin, INC., 1969.

[26] Niels Bohr and John Archibald Wheeler. "The Mechanism of Nuclear Fission". In: *Phys. Rev.* 56 (1939), pp. 426–450. DOI: 10.1103/PhysRev.56.426.

[27] E. C. Booth, B. Chasan, and K. A. Wright. "Nuclear Resonance Fluorescence from Light and Medium Weight Nuclei". In: *Nucl. Phys.* 57 (1964), p. 403. DOI: 10.1016/0029-5582(64)90338-4.

[28] R. R. Borchers et al. "Evidence for Transient Hyperfine Fields on Fast Ions in Ferromagnetic Media". In: *Phys. Rev. Lett.* 20 (1968), pp. 424–427. DOI: 10.1103/PhysRevLett.20.424.

[29] R. R. Borchers et al. "Magnetic Moments of 2^+ States in Even Te Nuclei". In: *Phys. Rev. Lett.* 17 (1966), pp. 1099–1102. DOI: 10.1103/PhysRevLett.17.1099.

[30] F. Bosch and H. Spehl. "Asymptotic attenuation coefficients in random perturbations of Angular Correlations". In: *Z. Phys. A* 280 (1977), pp. 329–339. DOI: 10.1007/BF01435441.

[31] F. Bosch and H. Spehl. "Gamma-ray angular correlations perturbed by a stochastic Gaussian-Markov process". In: *Z. Phys.* 253 (1972), pp. 257–268. DOI: 10.1007/BF02033324.

[32] F. Bosch and H. Spehl. "Influence of electronic deexcitation cascades on gamma-ray angular correlations in highly stripped free ions". In: *Hyp. Int.* 1 (1975), pp. 255–263. DOI: 10.1007/BF01022458.

[33] J. M. Brennan et al. "Magnetic moments of the 2^+ first excited states of even iron isotopes". In: *Phys. Rev. C* 16 (1977), pp. 899–901. DOI: 10.1103/PhysRevC.16.899.

[34] J. M. Brennan et al. "On the nature of the dynamic magnetic fields acting on fast moving ions in magnetic materials". In: *Hyp. Int.* 4 (1978), pp. 267–277. DOI: 10.1007/BF01021837.

[35] P.G. Bricault. "Review of radioactive ion beam accelerators". In: *Proceedings of the 1997 Particle Accelerator Conference (Cat. No.97CH36167)*. Vol. 1. 1997, 925–929 vol.1. DOI: 10.1109/PAC.1997.749884.

[36] R. Broda et al. "$N = 40$ Neutron Subshell Closure in the ^{68}Ni Nucleus". In: *Phys. Rev. Lett.* 74 (1995), pp. 868–871. DOI: 10.1103/PhysRevLett.74.868.

[37] R. Broda et al. "$N = 40$ Neutron Subshell Closure in the ^{68}Ni Nucleus". In: *Phys. Rev. Lett.* 74 (1995), pp. 868–871. DOI: 10.1103/PhysRevLett.74.868.

[38] B. A. Brown and A. F. Lisetskiy. "JJ44B effective interaction". In: *Unpublished* (2012).

[39] B. A. Brown and W. D. M. Rae. "The Shell-Model Code NuShellX@MSU". In: *Nuclear Data Sheets* 120 (2014), pp. 115–118. DOI: 10.1016/j.nds.2014.07.022.

[40] B. A. Brown and B. H. Wildenthal. "Status of the Nuclear Shell Model". In: *Ann. Rev. Nucl. Part. Sci.* 38 (1988), pp. 29–66. DOI: 10.1146/annurev.ns.38.120188.000333.

[41] R. Brun and F. Rademakers. "ROOT — An object oriented data analysis framework". In: *Nucl. Inst. Meth. Phys. Res. A* 389 (1997), pp. 81–86. DOI: 10.1016/S0168-9002(97)00048-X.

[42] J. C. Bryan. *Introduction to Nuclear Science*. CRC Press, 2013. ISBN: 978-1-4398-9893-2.

[43] T. Brage C. Froese Fischer and P. Jönsson. *Computational Atomic Structure: An MCHF Approach*. Inst. Phys. Pub. Bristol and Philadelphia, 1997.

[44] P. T. Callaghan, N. J. Stone, and B. G. Turrell. "Combined lattice-location–hyperfine-interaction experiment on Se implanted in Fe and Co". In: *Phys. Rev. B* 10(3) (1974), pp. 1075–1083. DOI: 10.1103/PhysRevB.10.1075.

[45] J. A. Camberson et al. "Reorientation Measurement in ^{56}Fe". In: *Can. J. Phys.* 50 (1972), p. 475. DOI: 10.1139/p72-066.

[46] A. Capitanio. *The Skew-Normal and Related Families*. Cambridge University Press, 2013. ISBN: 9781107729315.

[47] R. F. Casten. *Nuclear Structure From A Simple Perspective*. New York, United States: Oxford University Press Inc, 1990. ISBN: 9780195045994.

[48] S. K. Chamoli et al. "Measured g factors and the tidal-wave description of transitional nuclei near $A = 100$". In: *Phys. Rev. C* 83 (2011), p. 054318. DOI: 10.1103/PhysRevC.83.054318.

[49] X. Chen et al. "Time-dependent Monte Carlo calculations of recoil-in-vacuum g-factor data for ^{122,126,130,132}Te". In: *Phys. Rev. C* 87 (2013), p. 044305. DOI: 10.1103/PhysRevC.87.044305.

[50] P. Choudhary, P. C. Srivastava, and P. Navrátil. "Ab initio no-core shell model study of $^{10--14}$B isotopes with realistic NN interactions". In: *Phys. Rev. C* 102 (2020), p. 044309. DOI: 10.1103/PhysRevC.102.044309.

[51] S. Cohen and D. Kurath. "Effective interactions for the 1p shell". In: *Nucl. Phys.* 73 (1965), pp. 1–24. DOI: 10.1016/0029-5582(65)90148-3.

[52] L. Coraggio et al. "Shell-model calculations and realistic effective interactions". In: *Prog. Part. Nucl. Phys.* 62 (2009), pp. 135–182. DOI: 10.1016/j.ppnp.2008.06.001.

[53] "Coulomb Excitation of N = 28 Nuclei". In: *AECL* 3996 (1971), p. 16.

[54] K. Dybdal, J. L. Eberhardt, and N. Rud. "Importance of Polarization of Bound Projectile s Electrons for Transient Magnetic Fields". In: *Phys. Rev. Lett.* 42 (1979), pp. 592–595. DOI: 10.1103/PhysRevLett.42.592.

[55] K. Dybdal, J. S. Forster, and N. Rud. "Discontinuity in the Transient Magnetic Field around $Z_1 = 9$ and $Z_2 = 26$". In: *Phys. Rev. Lett.* 43 (1979), pp. 1711–1715. DOI: 10.1103/PhysRevLett.43.1711.

[56] M. C. East et al. "g factor of the first excited state in ^{56}Fe and implications for transient-field calibration in the Fe region". In: *Phys. Rev. C* 79 (2009), p. 024303. DOI: 10.1103/PhysRevC.79.024303.

[57] M. C. East et al. "Relative g-factor measurements in ^{54}Fe, ^{56}Fe, and ^{58}Fe". In: *Phys. Rev. C* 79 (2009), p. 024304. DOI: 10.1103/PhysRevC.79.024304.

[58] J. L. Eberhardt and K. Dybdal. "The velocity and Z dependence of the transient magnetic field in iron". In: *Hyp. Int.* 7 (1979), pp. 387–399. DOI: 10.1007/BF01021522.

[59] J. L. Eberhardt et al. "Anomalously large transient field through polarized electron capture". In: *Phys. Lett. B* 56 (1975), pp. 329–331. DOI: 10.1016/0370-2693(75)90311-1.

[60] J. L. Eberhardt et al. "Large transient magnetic fields at high ion velocities in polarized iron". In: *Hyp. Int.* 3 (1977), pp. 195–212. DOI: 10.1007/BF01021550.

[61] J. L. Eberhardt et al. "Transient field measurements of $g-$factors for ^{24}Mg AND ^{26}Mg". In: *Nucl. Phys. A* 229.1 (1974), pp. 162–178. ISSN: 0375-9474. DOI: 10.1016/0375-9474(74)90683-6.

[62] B. Elbek, H. E. Grove, and B. Herskind. "Coulomb Excitation of Levels in Cu^{63} and Cu^{65}". In: *Kgl. Danske Videnskab. Selskab.: Mat.-Fys. Medd* 34.8 (1964).

[63] J. P. Elliott and A. M. Lane. "Evidence for Two-Body Spin-Orbit Forces in Nuclei". In: *Phys. Rev.* 96 (1954), pp. 1160–1162. DOI: 10.1103/PhysRev.96.1160.

[64] W. M. Elsasser. In: *J. Phys. Rad.* 5 (1934), p. 625.

[65] T. Engeland et al. "Large shell model calculations with realistic effective interaction". In: *Phys. Scr.* T56 (1995), pp. 58–66. DOI: 10.1088/0031-8949/1995/t56/009.

[66] R. Ernst et al. "Shell structure of Ti and Cr nuclei from measurements of g factors and lifetimes". In: *Phys. Rev. C* 62 (2000), p. 024305. DOI: 10.1103/PhysRevC.62.024305.

[67] M. A. Eswaran et al. "Lifetimes of Excited States in Cu^{63}, Cu^{65}, Ni^{62} and Fe^{56} by Doppler Shift Attenuation Measurements". In: *Nucl. Phys.* 66 (1965), p. 401. DOI: 10.1016/0029-5582(65)90188-4.

[68] C. Fahlander, K. Johansson, and G. Possnert. "The Magnetic Moment of the Excited $5/2^-$ State in the ^{57}Fe". In: *Phys. Scr.* 20 (1979), pp. 163–164. DOI: 10.1088/0031-8949/20/2/007.

[69] C. Fahlander et al. "The g-factors of the first 2+ states in ^{50,54}Cr, ^{54}Fe and ^{70}Ge". In: *Nucl. Phys. A* 291 (1977), pp. 241–248. DOI: 10.1016/0375-9474(77)90209-3.

[70] U. Fano. "Geometrical Characterization of Nuclear States and the Theory of Angular Correlations". In: *Phys. Rev.* 90 (1953), pp. 577–579. DOI: 10.1103/PhysRev.90.577.

[71] R. B. Firestone. "Nuclear Data Sheets for $A = 24$". In: *Nuclear Data Sheets* 108 (2007), pp. 2319–2392. DOI: 10.1016/j.nds.2007.10.001.

[72] C. Froese Fischer. "A general multi-configuration Hartree-Fock program". In: *Comp. Phys. Comm.* 14 (1978), pp. 145–153. DOI: 10.1016/S0010-4655(84)82661-2.

[73] C. Froese Fischer. "A general multi-configuration Hartree-Fock program". In: *Comp. Phys. Comm.* 64 (1991), pp. 431–454. DOI: 10.1016/0010-4655(91)90137-A.

[74] C. Froese Fischer. "A multi-configuration Hartree-Fock program". In: *Comp. Phys. Comm.* 1 (1969), pp. 151–166. DOI: 10.1016/0010-4655(70)90002-0.

[75] C. Froese Fischer. "A multi-configuration Hartree-Fock program with improved stability". In: *Comp. Phys. Comm.* 4 (1972), pp. 107–116. DOI: 10.1016/S0010-4655(84)82400-5.

[76] C. Froese Fischer. "General Hartree-Fock program". In: *Comp. Phys. Comm.* 43 (1987), pp. 355–365. DOI: 10.1016/0010-4655(87)90053-1.

[77] C. Froese Fischer. "The MCHF atomic-structure package". In: *Comp. Phys. Comm.* 64 (1991), pp. 369–398. DOI: 10.1016/0010-4655(91)90133-6.

[78] C. Froese Fischer et al. "Advanced multiconfiguration methods for complex atoms: I. Energies and wave functions". In: *J. Phys. B* 49 (2016), p. 182004. DOI: 10.1088/0953-4075/49/18/182004.

[79] C. Froese Fischer et al. "GRASP2018—A Fortran 95 version of the General Relativistic Atomic Structure Package". In: *Comp. Phys. Comm.* 237 (2019), pp. 184–187. DOI: 10.1016/j.cpc.2018.10.032.

[80] K. T. Flanagan et al. "Nuclear Spins and Magnetic Moments of ^{71,73,75}Cu: Inversion of $\pi 2p_{3/2}$ and $\pi 1f_{5/2}$ Levels in ^{75}Cu". In: *Phys. Rev. Lett.* 103 (2009), p. 142501. DOI: 10.1103/PhysRevLett.103.142501.

[81] M. Forterre et al. "The sign of the magnetic moment of the first 2+ state in ^{18}O". In: *Phys. Lett. B* 55 (1975), pp. 56–58. DOI: 10.1016/0370-2693(75)90186-0.

[82] M. Forterre et al. "Transient field at nitrogen nuclei recoiling in iron and the magnetic moment of the ^{15}N first excited state". In: *Phys. Rev. C* 11 (1975), pp. 1976–1982. DOI: 10.1103/PhysRevC.11.1976.

[83] H. Frauenfelder. "Angular correlation of nuclear radiation". In: *Ann. Rev. Nucl. Sci.* 2 (1953), pp. 129–162. DOI: 10.1146/annurev.ns.02.120153.001021.

[84] C. Froese Fischer et al. "GRASP2018–A Fortran 95 version of the General Relativistic Atomic Structure Package". In: *Mendeley Data v1* (2019). DOI: 10.17632/x574wpp2vg.1.

[85] C. Le Galliard. *IPN Orsay - ORGAM*. Tech. rep. IPN Orsay, University of South Paris, France: IPN Orsay, 2019. URL: http://ipnwww.in2p3.fr/Orgam?lang=en.

[86] G. Gamow. "Mass defect curve and nuclear constitution". In: *Proc. Roy. Soc. A* 126 (1930). DOI: 10.1098/rspa.1930.0032.

[87] P. E. Garrett, J. L. Wood, and S. W. Yates. "Critical insights into nuclear collectivity from complementary nuclear spectroscopic methods". In: *Phys. Scr.* 93 (2018), p. 063001. DOI: 10.1088/1402-4896/aaba1c.

[88] M. Goeppert-Mayer. "On Closed Shells in Nuclei. II". In: *Phys. Rev.* 75 (1949), pp. 1969–1970. DOI: 10.1103/PhysRev.75.1969.

[89] G. Goertzel. "Angular Correlation of Gamma-Rays". In: *Phys. Rev.* 70 (1946), pp. 897–909. DOI: 10.1103/PhysRev.70.897.

[90] M. B. Goldberg et al. "Spin precession of the $^{12}C(2_1^+)$ state on recoil in polarized iron". In: *Hyp. Int.* 1 (1975), pp. 429–434. DOI: 10.1007/BF01022473.

[91] G. Goldring. "Hyp. Int. in Isolated Ions". In: *Heavy Ion Collisions*. Ed. by R. Bock. Vol. 3. North-Holland Pub. Co., 1982, p. 483.

[92] G. Goldring et al. "Hyperfine field and correlation time measurements of Sm ions recoiling into gas and vacuum by the longitudinal decoupling method". In: *Hyp. Int.* (1977), pp. 283–290. DOI: 10.1007/BF01021700.

[93] L. Grodzins. "Magnetic Dipole Moments of Excited Nuclear States". In: *Ann. Rev. Nucl. Sci.* 18 (1968), pp. 291–342. DOI: 10.1146/annurev.ns.18.120168.001451.

[94] L. Grodzins, R. Borchers, and G. B. Hagemann. "Effective magnetic fields at Sm, Gd and Dy nuclei in metallic Fe following coulomb excitation implantation". In: *Phys. Lett.* 21 (1966), pp. 214–217. DOI: 10.1016/0031-9163(66)90320-9.

[95] C. Guénaut et al. "High-precision mass measurements of nickel, copper, and gallium isotopes and the purported shell closure at $N = 40$". In: *Phys. Rev. C* 75 (2007), p. 044303. DOI: 10.1103/PhysRevC.75.044303.

[96] M. R. Gunye. "Static quadrupole moments and $B(E2)$ values in *sd*-shell nuclei". In: *Phys. Lett. B* 37 (1971), pp. 125–127. DOI: 10.1016/0370-2693(71)90031-1.

[97] J. B. Gupta and J. H. Hamilton. "Empirical study of the shape evolution and shape coexistence in Zn, Ge and Se isotopes". In: *Nucl. Phys. A* 983 (2019), pp. 20–37. DOI: 10.1016/j.nuclphysa.2018.12.009.

[98] G. Gürdal et al. "Measurements of $g(4_1^+, 2_2^+)$ in ^{70,72,74,76}Ge: Systematics of low-lying structures in $30 \leq Z \leq 40$ and $30 \leq N \leq 50$ nuclei". In: *Phys. Rev. C* 88 (2013), p. 014301. DOI: 10.1103/PhysRevC.88.014301.

[99] C. Broude H. E. Gove. "Coulomb Excitation in Nuclei from $A = 23$ to $A = 60$ Using O^{16} Ions". In: *Proc. Conf. React. Compl. Nucl.* Vol. 2. John Wiley and Sons, Inc., New York, 1990, p. 57.

[100] D. R. Hamilton. "On Directional Correlation of Successive Quanta". In: *Phys. Rev.* 58 (1940), pp. 122–131. DOI: 10.1103/PhysRev.58.122.

[101] M. Hass et al. "Direct evidence for enhanced transient fields on fast ^{56}Fe ions recoiling through thin iron". In: *Phys. Rev. C* 14 (1976), pp. 2119–2125. DOI: 10.1103/PhysRevC.14.2119.

[102] M. Hass et al. "Magnetic moments of the 2_1^+ states of even Ni isotopes". In: *Phys. Rev. C* 17 (1978), pp. 997–1000. DOI: 10.1103/PhysRevC.17.997.

[103] O. Häusser et al. "Large transient magnetic fields for rare-earth ions recoiling in gadolinium and g-factors of high-spin states in 156, 158, 160Gd". In: *Nucl. Phys. A* 406 (1983), pp. 339–368. DOI: 10.1016/0375-9474(83)90466-9.

[104] O. Häusser et al. "Transient magnetic fields for large-Z atoms recoiling through gadolinium". In: *Nucl. Phys. A* 412 (1984), pp. 141–158. DOI: 10.1016/0375-9474(84)90389-0.

[105] O. Haxel, J. H. D. Jensen, and H. E. Suess. "On the "Magic Numbers" in Nuclear Structure". In: *Phys. Rev.* 75 (1949), pp. 1766–1766. DOI: 10.1103/PhysRev.75.1766.2.

[106] G. M. Heestand et al. "g-Factors for 2^+ states of doubly even nuclei (Ge, Se, Mo, Ru, Pd, Cd and Te)". In: *Nuc. Phys. A* 133 (1969), pp. 310–320. DOI: 10.1016/0375-9474(69)90633-2.

[107] J. Heisenberg, J. S. McCarthy, and I. Sick. "Inelastic Electron Scattering from Several Ca, Ti and Fe Isotopes". In: *Nucl. Phys. A* 164 (1971), p. 353. DOI: 10.1016/0375-9474(71)90219-3.

[108] W. Heisenberg. "On the structure of atomic nuclei". In: *Z. Phys.* 77 (1932), pp. 1–11. DOI: 10.1007/BF01342433.

[109] J. G. Hirsch and P. C. Srivastava. "Shell model description of Ge isotopes". In: *J. Phys. Conf.* 387 (2012), p. 012020. DOI: 10.1088/1742-6596/387/1/012020.

[110] M. Honma et al. "Effective interaction for pf-shell nuclei". In: *Phys. Rev. C* 65 (2002), p. 061301. DOI: 10.1103/PhysRevC.65.061301.

[111] M. Honma et al. "New effective interaction for f_5pg_9-shell nuclei". In: *Phys. Rev. C* 80 (2009), p. 064323. DOI: 10.1103/PhysRevC.80.064323.

[112] M. Honma et al. "New effective interaction for pf-shell nuclei and its implications for the stability of the $N = Z = 28$ closed core". In: *Phys. Rev. C* 69 (2004), p. 034335. DOI: 10.1103/PhysRevC.69.034335.

[113] R. E. Horstman et al. "Recoil-distance measurements of g-factors for ^{24}Mg(2_1^+) and ^{20}Ne(2_1^+)". In: *Nucl. Phys. A* 248 (1975), pp. 291–316. DOI: 10.1016/0375-9474(75)90167-0.

[114] G. K. Hubler, H. W. Kugel, and D. E. Murnick. "Nuclear magnetic moments of very short-lived states via the transient-field implantation perturbed-angular-correlation technique". In: *Phys. Rev. C* 9 (1974), pp. 1954–1964. DOI: 10.1103/PhysRevC.9.1954.

[115] U. Littmark J. F. Ziegler J. P. Biersack. *The Stopping and Range of Ions in Solids*. Vol. 1. Pergamon, New York, 1985. ISBN: 008021603X.

[116] J. Jakob G.and Cub et al. "On the ion beam stopping power dependence of transient magnetic fields in Fe- and Gd-hosts". In: *Z. Phys. D* 32 (1994), pp. 7–11. DOI: 10.1007/BF01425916.

[117] F. James. *MINUIT – Function Minimization and Error Analysis*. 1998. URL: https://cds.cern.ch/record/2296388/files/minuit.pdf.

[118] P. Jönsson et al. "New version: Grasp2K relativistic atomic structure package". In: *Comp. Phys. Comm.* 184 (2013), pp. 2197–2203. DOI: 10.1016/j.cpc.2013.02.016.

[119] P. Jönsson et al. "The grasp2K relativistic atomic structure package". In: *Comp. Phys. Comm.* 177 (2007), pp. 597–622. DOI: 10.1016/j.cpc.2007.06.002.

[120] P. Jönsson et al. "The grasp2K relativistic atomic structure package". In: *Comp. Phys. Comm.* 177 (2007), pp. 597–622. DOI: 10.1016/j.cpc.2007.06.002.

[121] K. Kaneko, M. Hasegawa, and T. Mizusaki. "Shape transition and oblate-prolate coexistence in $N = Z$ fpg-shell nuclei". In: *Phys. Rev. C* 70 (2004), p. 051301. DOI: 10.1103/PhysRevC.70.051301.

[122] W. H. Kelly and G. B. Beard. "Nuclear Resonance Fluorescence Measurements in the 845 keV Level in Fe^{56}". In: *Nucl. Phys.* 27 (1961), p. 188. DOI: 10.1016/0029-5582(61)90344-3.

[123] T. Kibédi. *AveTools v3.0*. 2014. URL: https://www-nds.iaea.org/public/ensdf_pgm/utility/avetools/AveTools.pdf.

[124] K. Kitao, Y. Tendow, and A. Hashizume. "Nuclear Data Sheets for $A = 120$". In: *Nuclear Data Sheets* 96 (2002), p. 241.

[125] G. F. Knoll. *Radiation Detection and Measurement, Third Edition*. John Wiley & Sons, Inc., 2000. ISBN: 0-471-07338-5.

[126] Yu. G. Kosyak, D. K. Kaipov, and L. V. Chekushina. "Study of the Excited States of ^{56,58}Fe by the $(n, n'\gamma)$ Reaction". In: *Izv. Akad. Nauk SSSR: Ser. Fiz.* 47 (1983), p. 2118.

[127] K. S. Krane. *Introductory Nuclear Physics*. 111 River St, Hoboken, NJ 07030: John Wiley and Sons, Inc., 1988. ISBN: 978-0-471-80553-3.

[128] K. S. Krane. "Solid-angle correction factors for coaxial Ge(Li) detectors". In: *Nucl. Instr. Meth.* 98 (1972), pp. 205–210. DOI: 10.1016/0029-554X(72)90099-7.

[129] A. Kusoglu et al. "Magnetism of an Excited Self-Conjugate Nucleus: Precise Measurement of the g Factor of the 2_1^+ State in ^{24}Mg". In: *Phys. Rev. Lett.* 114 (6 2015), p. 062501. DOI: 10.1103/PhysRevLett.114.062501.

[130] G. J. Lampard et al. "Systematics of gyromagnetic ratios of the 2_1^+ states in even Ge isotopes". In: *Aus. J. Phys.* 40 (1987), pp. 117–123. DOI: 10.1071/PH870117.

[131] K. Langanke et al. "How magic is the magic ^{68}Ni nucleus?" In: *Phys. Rev. C* 67 (2003), p. 044314. DOI: 10.1103/PhysRevC.67.044314.

[132] M. J. Le Vine, E. K. Warburton, and D. Schwalm. "Static quadrupole moments for the 2^+ states of ^{54,56,58}Fe". In: *Phys. Rev. C* 23 (1981), pp. 244–252. DOI: 10.1103/PhysRevC.23.244.

[133] R. Lecomte et al. "Evidence of a spherical to prolate shape transition in the germanium nuclei". In: *Phys. Rev. C* 22 (1980), pp. 1530–1533. DOI: 10.1103/PhysRevC.22.1530.

[134] R. F. Leslie. "Developing the recoil-in-vacuum technique for magnetic moment measurements on fission fragments and radioactive beams". PhD thesis. The Australian National University, 2015. URL: http://hdl.handle.net/1885/156194.

[135] P. M. S. Lesser et al. "Static Electric Quadrupole Moments of the First Excited States of ^{56}Fe And the Even Titanium Nuclei". In: *Nucl. Phys. A* 190 (1972), p. 597. DOI: 10.1016/0375-9474(72)90859-7.

[136] J. Lindhard and A. Winther. "Transient fields acting on heavy ions during slowing-down in magnetized materials". In: *Nucl. Phys. A* 166 (1971), pp. 413–435. DOI: 10.1016/0375-9474(71)90898-0.

[137] C. J. Lister et al. "Gamma radiation from the N=Z nucleus $^{80}_{40}$Zr$_{40}$". In: *Phys. Rev. Lett.* 59 (1987), pp. 1270–1273. DOI: 10.1103/PhysRevLett.59.1270.

[138] A. S. Litvinenko et al. "Electric Excitation of $E2$ and $E3$ Transitions in ^{54,56,58}Fe and ^{62}Ni". In: *Ukr. Fiz. Zh.* 17 (1972), p. 1210.

[139] J. Ljungvall et al. "Onset of collectivity in neutron-rich Fe isotopes: Toward a new island of inversion?" In: *Phys. Rev. C* 81 (2010), p. 061301. DOI: 10.1103/PhysRevC.81.061301.

[140] J. Ljungvall et al. "Shape Coexistence in Light Se Isotopes: Evidence for Oblate Shapes". In: *Phys. Rev. Lett.* 100 (2008), p. 102502. DOI: 10.1103/PhysRevLett.100.102502.

[141] J. Ljungvall et al. "The Orsay Universal Plunger System". In: *Nucl. Inst. Meth. A* 679 (2012), pp. 61–66. DOI: 10.1016/j.nima.2012.03.041.

[142] S. P. Lloyd. "The Angular Correlation of Two Successive Nuclear Radiations". In: *Phys. Rev.* 85 (1952), pp. 904–911. DOI: 10.1103/PhysRev.85.904.

[143] M. Galassi *et al. GNU Scientific Library Reference Manual (3rd Ed.)* Network Theory Ltd., 2009. ISBN: 0954612078. URL: http://www.gnu.org/software/gsl/.

[144] J. B. Marion and F. C. Young. *Nuclear Reaction Analysis*. North-Holland Publishing Company–Amsterdam, 1968.

[145] B. P. McCormick et al. "First-excited state g factors in the stable, even Ge and Se isotopes". In: *Phys. Rev. C* 100 (2019), p. 044317. DOI: 10.1103/PhysRevC.100.044317.

[146] B. P. McCormick et al. "Modelling hyperfine interactions for nuclear g-factor measurements". In: *EPJ Web Conf.* 232 (2020), p. 04009. DOI: 10.1051/epjconf/202023204009.

[147] B. P. M^{c}Cormick et al. "Probing the $N = 14$ subshell closure: g factor of the ^{26}Mg(2_1^+) state". In: *Phys. Lett. B* 779 (2018), pp. 445–451. DOI: 10.1016/j.physletb.2018.02.032.

[148] J. B. McGrory and B. H. Wildenthal. "Large-Scale Shell-Model Calculations". In: *Ann. Rev. Nucl. Part. Sci.* 30 (1980), pp. 383–436. DOI: 10.1146/annurev.ns.30.120180.002123.

[149] T. J. Mertzimekis et al. "Systematics of first 2^+ state g factors around mass 80". In: *Phys. Rev. C* 68 (2003), p. 054304. DOI: 10.1103/PhysRevC.68.054304.

[150] F. R. Metzger. "Lifetime and g-factor of the first excited state in Fe^{56}". In: *Nucl. Phys.* 27 (1961), pp. 612–619. DOI: 10.1016/0029-5582(61)90306-6.

[151] G. van Middelkoop et al. "Larger Transient Field for ^{19}F in Co than in Fe: Evidence for the Atomic Nature of the Transient Field". In: *Phys. Rev. Lett.* 40 (1978), pp. 24–27. DOI: 10.1103/PhysRevLett.40.24.

[152] J. Murray, T. A. McMath, and J. A. Cameron. "Nuclear g factors of the first excited states of ^{76}Se and ^{122}Te". In: *Can. J. P.* 45 (1967), pp. 1821–1831. DOI: 10.1139/p67-141.

[153] F. Naqvi et al. "Test of the $\pi g_{7/2}$ subshell closure at $Z = 58$". In: *Phys. Lett. B* 728 (2014), pp. 303–307. DOI: 10.1016/j.physletb.2013.11.057.

[154] P. Navrátil, J. P. Vary, and B. R. Barrett. "Large-basis ab initio no-core shell model and its application to ^{12}**C**". In: *Phys. Rev. C* 62 (2000), p. 054311. DOI: 10.1103/PhysRevC.62.054311.

[155] V. S. Nikolaev and I. S. Dmitriev. "On the equilibrium charge distribution in heavy element ion beams". In: *Phys. Lett. A* 28 (1968), pp. 277–278. DOI: 10.1016/0375-9601(68)90282-X.

[156] R. Nordhagen, B. Elbek, and B. Herskind. "Collective States in ^{59}Co". In: *Nucl. Phys. A* 104 (1967), p. 353. DOI: 10.1016/0375-9474(67)90562-3.

[157] A. Obertelli et al. "Shape evolution in self-conjugate nuclei, and the transitional nucleus ^{68}Se". In: *Phys. Rev. C* 80 (2009), p. 031304. DOI: 10.1103/PhysRevC.80.031304.

[158] T. Otsuka et al. "Evolution of Nuclear Shells due to the Tensor Force". In: *Phys. Rev. Lett.* 95 (2005), p. 232502. DOI: 10.1103/PhysRevLett.95.232502.

[159] T. Otsuka et al. "Evolution of shell structure in exotic nuclei". In: *Rev. Mod. Phys.* 92 (2020), p. 015002. DOI: 10.1103/RevModPhys.92.015002.

[160] T. Otsuka et al. "Magic Numbers in Exotic Nuclei and Spin-Isospin Properties of the *NN* Interaction". In: *Phys. Rev. Lett.* 87 (2001), p. 082502. DOI: 10.1103/PhysRevLett.87.082502.

[161] T. Otsuka et al. "Monte Carlo shell model for atomic nuclei". In: *Prog. Part. Nucl. Phys.* 47 (2001), pp. 319–400. DOI: 10.1016/S0146-6410(01)00157-0.

[162] T. Otsuka et al. "Monte Carlo shell model for atomic nuclei". In: *Prog. Part. Nucl. Phys.* 47 (2001), pp. 319–400. DOI: 10.1016/S0146-6410(01)00157-0.

[163] T. Otsuka et al. "Novel Features of Nuclear Forces and Shell Evolution in Exotic Nuclei". In: *Phys. Rev. Lett.* 104 (2010), p. 012501. DOI: 10.1103/PhysRevLett.104.012501.

[164] C. Ouellet and B. Singh. "Nuclear Data Sheets for $A = 32$". In: *Nuclear Data Sheets* 112 (2011), pp. 2199–2355. DOI: 10.1016/j.nds.2011.08.004.

[165] E. Padilla-Rodal et al. "B(E2)↑ Measurements for Radioactive Neutron-Rich Ge Isotopes: Reaching the N=50 Closed Shell". In: *Phys. Rev. Lett.* 94 (2005), p. 122501. DOI: 10.1103/PhysRevLett.94.122501.

[166] A. Pakou et al. "Transient magnetic field measurements for even Ge isotopes". In: *J. Phys. G* 10 (1984), pp. 1759–1764. DOI: 10.1088/0305-4616/10/12/014.

[167] F. A. Parpia, C. Froese Fischer, and I. P. Grant. "GRASP92: A package for large-scale relativistic atomic structure calculations". In: *Comp. Phys. Comm.* 94 (1996), pp. 249–271. DOI: 10.1016/0010-4655(95)00136-0.

[168] S. K. Patra and C. R. Praharaj. "Shapes of exotic nuclei in the mass $A = 70$ region". In: *Phys. Rev. C* 47 (1993), pp. 2978–2981. DOI: 10.1103/PhysRevC.47.2978.

[169] D. Pelte and D. Schwalm. "In-beam Gamma-ray Spectroscopy with Heavy Ions". In: *Heavy Ion Collisions*. Ed. by R. Bock. Vol. 3. North-Holland Pub. Co., 1982, p. 161.

[170] R. J. Peterson, H. Theissen, and W. J Alston. "Inelastic Electron Scattering from ^{56}Fe". In: *Nucl. Phys. A* 153 (1970), p. 610. DOI: 10.1016/0375-9474(70)90795-5.

[171] A. Petrovici et al. "Some new aspects of the shape coexistence in the $A = 70$ mass region". In: *Nucl. Phys. A* 517 (1990), pp. 108–124. DOI: 10.1016/0375-9474(90)90263-L.

[172] ANU Nuclear Physics. *Legacy DAQ - Nuclear wiki*. 2015. URL: http://rspewiki.anu.edu.au/nuc/index.php/Legacy_DAQ.

[173] A. R. Poletti et al. "Nuclear spectroscopy with lithium beams. II. High-spin states in ^{52}Cr, ^{54}Mn, ^{54}Fe, and ^{56}Fe". In: *Phys. Rev. C* 10 (1974), pp. 2329–2339. DOI: 10.1103/PhysRevC.10.2329.

[174] *Private communication with Praveen Srivastava (unpublished)*. 2020.

[175] G. Racah. "Directional Correlation of Successive Nuclear Radiations". In: *Phys. Rev.* 84 (1951), pp. 910–912. DOI: 10.1103/PhysRev.84.910.

[176] P. Raghavan, M. Senba, and R. S. Raghavan. "Hyperfine magnetic fields at ^{67}Ge in Fe, Co and Ni". In: *Hyp. Int.* 4 (1978), pp. 330–337. DOI: 10.1007/BF01021846.

[177] M. U. Rajput and T. D. Mac Mahon. "Techniques for evaluating discrepant data". In: *Nucl. Instr. Meth. A* 312 (1992), pp. 289–295. DOI: 10.1016/0168-9002(92)90171-Y.

[178] Y. Ralchenko. In: *NIST* Atomic Spectral Database (2019). URL: https://www.nist.gov/pml/atomic-spectra-database.

[179] S. Raman, C. W. Nestor, and P. Tikkanen. "TRANSITION PROBABILITY FROM THE GROUND TO THE FIRST-EXCITED 2+ STATE OF EVEN-EVEN NUCLIDES". In: *At. Data Nucl. Data Tables* 78 (2001), pp. 1–128. DOI: 10.1006/adnd.2001.0858.

[180] G. N. Rao. "Dilute-impurity hyperfine fields in Fe, Co, Ni and Gd". In: *Atom. Data Nucl. Data Tables* 15 (1975), pp. 553–576. DOI: 10.1016/0092-640X(75)90016-9.

[181] F. Recchia et al. "Toward the $N = 40$ sub-shell closure in Co isotopes and the new island of inversion". In: *Phys. Scr.* T150 (2012), p. 014034. DOI: 10.1088/0031-8949/2012/t150/014034.

[182] W. A. Richter, S. Mkhize, and B. A. Brown. "*sd*-shell observables for the USDA and USDB Hamiltonians". In: *Phys. Rev. C* 78 (2008), p. 064302. DOI: 10.1103/PhysRevC.78.064302.

[183] H. J. Rose and D. M. Brink. "Angular Distributions of Gamma Rays in Terms of Phase-Defined Reduced Matrix Elements". In: *Rev. Mod. Phys.* 39 (1967), pp. 306–347. DOI: 10.1103/RevModPhys.39.306.

[184] M. E. Rose. "The Analysis of Angular Correlation and Angular Distribution Data". In: *Phys. Rev.* 91 (1953), pp. 610–615. DOI: 10.1103/PhysRev.91.610.

[185] D. J. Rowe and J. L. Wood. *Fundamentals of Nuclear Models*. WORLD SCIENTIFIC, 2010. DOI: 10.1142/6209.

[186] C. Scherer. "Gamma-gamma angular correlations: A model for statistical perturbation with any correlation time". In: *Nucl. Phys. A* 157 (1970), pp. 81–92. DOI: 10.1016/0375-9474(70)90099-0.

[187] G. Schiwietz and P.L. Grande. "Improved charge-state formulas". In: *Nucl. Instrum. Meth. Phys. Res. B* 175–177 (2001), pp. 125–131.

[188] M. Shamsuzzoha Basunia. "Nuclear Data Sheets for $A = 22$". In: *Nuclear Data Sheets* 127 (2015), pp. 69–190. DOI: 10.1016/j.nds.2015.07.002.

[189] M. Shamsuzzoha Basunia. "Nuclear Data Sheets for $A = 28$". In: *Nuclear Data Sheets* 114 (2013), pp. 1189–1291. DOI: 10.1016/j.nds.2013.10.001.

[190] M. Shamsuzzoha Basunia. "Nuclear Data Sheets for $A = 30$". In: *Nuclear Data Sheets* 111 (2010), pp. 2331–2424. DOI: 10.1016/j.nds.2010.09.001.

[191] N. K. B. Shu et al. "Velocity dependence of the dynamic magnetic field acting on swift O and Sm ions". In: *Phys. Rev. C* 21 (1980), pp. 1828–1837. DOI: 10.1103/PhysRevC.21.1828.

[192] K. Siegbahn. *Alpha-, Beta- and Gamma-Ray Spectroscopy*. North Holland, 1979. ISBN: 978-0-4445-9699-4.

[193] O. Sorlin. "Shell Evolutions and Nuclear Forces". In: *Eur. Phys. J. Web Conf.* 66 (2014), p. 01016. DOI: 10.1051/epjconf/20146601016.

[194] K.-H. Speidel et al. "Evidence for electron orbital dependence of ion-beam induced attenuations of transient magnetic fields". In: *Z. Phys. D* 22 (1991), pp. 371–374. DOI: 10.1007/BF01438558.

[195] K.-H. Speidel et al. "Shell closure effects in the stable $^{74-82}$Se isotopes from magnetic moment measurements using projectile excitation and the transient field technique". In: *Phys. Rev. C* 57 (1998), pp. 2181–2188. DOI: 10.1103/PhysRevC.57.2181.

[196] K. H. Speidel et al. "The $g-$factor of the first excited 2^+ state in ^{26}Mg from transient field precession measurements". In: *Phys. Lett. B* 102 (1981), pp. 6–8. DOI: 10.1016/0370-2693(81)90200-8.

[197] G. D. Sprouse and S. S. Hanna. "Lifetimes and Magnetic Moments of Levels in ^{57}Fe". In: *Nucl. Phys. A* 137 (1969), p. 658. DOI: 10.1016/0375-9474(69)90100-6.

[198] P. C. Srivastava and M. J. Ermamatov. "Comparison of shell model results for even–even Se isotopes". In: *Phys. Scr.* 88 (2013), p. 045201. DOI: 10.1088/0031-8949/88/04/045201.

[199] P. C. Srivastava and I. Mehrotra. "Large-scale shell-model calculations for even-odd $^{61-65}$Fe isotopes". In: *Phys. Atom. Nuclei* 73 (2010), pp. 1656–1659. DOI: 10.1134/S1063778810100030.

[200] M. Stanoiu et al. "$N = 14$ and 16 shell gaps in neutron-rich oxygen isotopes". In: *Phys. Rev. C* 69 (2004), p. 034312. DOI: 10.1103/PhysRevC.69.034312.

[201] D. Steppenbeck et al. "Evidence for a new nuclear 'magic number' from the level structure of ^{54}Ca". In: *Nature* 502 (2013), pp. 207–10. DOI: 10.1038/nature12522.

[202] N. J. Stone, J. R. Stone, and P. Jönsson. "A priori calculations of Hyp. Int. in highly ionized atoms: g-factor measurements on aligned pico-second states populated in nuclear reactions". In: *Hyp. Int.* 197 (2010), pp. 29–35. DOI: 10.1007/s10751-010-0235-y.

[203] N. J. Stone et al. "Calibration of Recoil-In-Vacuum attenuations from first principles: comparison with recent experimental data on Fe isotopes". In: *Hyp. Int.* 230 (2015), pp. 169–174. DOI: 10.1007/s10751-014-1110-z.

[204] N. J. Stone et al. "First Nuclear Moment Measurement with Radioactive Beams by the Recoil-in-Vacuum Technique: The g Factor of the 2_1^+ State in ^{132}Te". In: *Phys. Rev. Lett.* 94 (2005), p. 192501. DOI: 10.1103/PhysRevLett.94.192501.

[205] N. J. Stone et al. "The Hyperfine Field of Selenium in Iron and the Magnetic Dipole Moment of ^{75}Se". In: *Hyp. Int.* 133 (2001), pp. 117–120. DOI: 10.1023/A:1012269720057.

[206] A. E. Stuchbery. "Free-ion hyperfine fields and magnetic-moment measurements on radioactive beams: progress and outlook". In: *Hyp. Int.* 220 (2013), pp. 29–45. DOI: 10.1007/s10751-012-0683-7.

[207] A. E. Stuchbery. "γ-ray angular distributions and correlations after projectile-fragmentation reactions". In: *Nucl. Phys. A* 723 (2003), pp. 69–92. DOI: 10.1016/S0375-9474(03)01157-6.

[208] A. E. Stuchbery. "Transient-field strengths for high-velocity light ions and applications to g-factor measurements on fast exotic beams". In: *Phys. Rev. C* 69 (2004), p. 064311. DOI: 10.1103/PhysRevC.69.064311.

[209] A. E. Stuchbery, G. J. Lampard, and H. H. Bolotin. "Transient field measurements of g-factors in ^{194,196,198}Pt; $g(2_1^+)$ systematics in transitional W, Os, Pt nuclei". In: *Nucl. Phys. A* 528 (1991), pp. 447–464. DOI: 10.1016/0375-9474(91)90098-Q.

[210] A. E. Stuchbery and M. P. Robinson. "Perturbed γ–γ correlations from oriented nuclei and static moment measurements I: formalism and principles". In: *Nucl. Instrum. Meth. Phys. Res. A* 485 (2002), pp. 753–767. DOI: 10.1016/S0168-9002(01)02114-3.

[211] A. E. Stuchbery, C. G. Ryan, and H. H. Boloton. "Disparity between the transient hyperfine fields for Pt and Os in Fe; an electron vacancy sharing interpretation". In: *Hyp. Int.* 13 (1983), pp. 275–295. DOI: 10.1007/BF01027258.

[212] A. E. Stuchbery and N. J. Stone. "Recoil in vacuum for Te ions: Calibration, models, and applications to radioactive-beam g-factor measurements". In: *Phys. Rev. C* 76 (2007), p. 034307. DOI: 10.1103/PhysRevC.76.034307.

[213] A. E. Stuchbery et al. "Apparatus for in-beam Hyp. Int. and g-factor measurements: Design and operation". In: *Nucl. Inst. Meth. A* 951 (2020), p. 162985. DOI: 10.1016/j.nima.2019.162985.

[214] A. E. Stuchbery et al. "Electromagnetic properties of the 2_1^+ state in ^{134}Te: Influence of core excitation on single-particle orbits beyond ^{132}Sn". In: *Phys. Rev. C* 88 (2013), p. 051304. DOI: 10.1103/PhysRevC.88.051304.

[215] A. E. Stuchbery et al. "First-excited state g factor of ^{136}Te by the recoil in vacuum method". In: *Phys. Rev. C* 96 (2017), p. 014321. DOI: 10.1103/PhysRevC.96.014321.

[216] A. E. Stuchbery et al. "Perturbed angular correlations for Gd in gadolinium: In-beam comparisons of relative magnetizations". In: *Nucl. Inst. Meth. B* 252 (2006), pp. 230–244. DOI: 10.1016/j.nimb.2006.09.004.

[217] A. E. Stuchbery et al. "Systematic measurements of transient fields for W, Os and Pt ions traversing Fe". In: *Hyp. Int.* 88 (1994), pp. 97–119. DOI: 10.1007/BF02068707.

[218] A. E. Stuchbery et al. "Transient-field strength measurements for ^{52}Cr traversing Fe hosts at high velocity and polarization transfer mechanisms". In: *Hyp. Int.* 36 (1987), pp. 75–96. DOI: 10.1007/BF02396850.

[219] A. E. Stuchbery et al. "Transient fields for Ag and Pd ions in Fe and Co; g-Factor measurements of the lowest 3/2– and 5/2– states in ^{107,109}Ag". In: *Hyp. Int.* 20 (1984), pp. 119–134. DOI: 10.1007/BF02059484.

[220] Andrew E. Stuchbery and Eva Bezakova. "Thermal-Spike Lifetime from Picosecond-Duration Preequilibrium Effects in Hyperfine Magnetic Fields Following Ion Implantation". In: *Phys. Rev. Lett.* 82 (1999), pp. 3637–3640. DOI: 10.1103/PhysRevLett.82.3637.

[221] J. J. Sun et al. "Spectroscopy of ^{74}Ge: From soft to rigid triaxiality". In: *Phys. Lett. B* 734 (2014), pp. 308–313. DOI: https://doi.org/10.1016/j.physletb.2014.05.069.

[222] T. Williams, C. Kelley *et al. Gnuplot 5.2: an interactive plotting program*. http://gnuplot.sourceforge.net/. 2017.

[223] N. Takigawa and K. Washiyama. *Fundamentals of Nuclear Physics*. Springer Japan, 2017. ISBN: 978-4-431-55377-9.

[224] I. Talmi and I. Unna. "Order of Levels in the Shell Model and Spin of Be^{11}". In: *Phys. Rev. Lett.* 4 (1960), pp. 469–470. DOI: 10.1103/PhysRevLett.4.469.

[225] G. M. Temmer and N. P. Heydenburg. "Coulomb Excitation of Medium-Weight Nuclei". In: *Phys. Rev.* 104 (1956), pp. 967–980. DOI: 10.1103/PhysRev.104.967.

[226] J. R. Terry et al. "Single-neutron knockout from intermediate energy beams of ^{30,32}Mg: Mapping the transition into the "island of inversion"". In: *Phys. Rev. C* 77 (2008), p. 014316. DOI: 10.1103/PhysRevC.77.014316.

[227] E. K. Warburton, J. A. Becker, and B. A. Brown. "Mass systematics for $A = 29 - 44$ nuclei: The deformed $A \sim 32$ region". In: *Phys. Rev. C* 41 (1990), pp. 1147–1166. DOI: 10.1103/PhysRevC.41.1147.

[228] D. Ward et al. "Measurement of g-factors in ^{170}Yb, ^{172}Yb and ^{174}Yb by transient field interaction at high recoil velocities". In: *Nucl. Phys. A* 330 (1979), pp. 225–242. DOI: 10.1016/0375-9474(79)90547-5.

[229] N. Warr et al. "MINIBALL: A Gamma-ray spectrometer for exotic beams". In: *Capture Gamma-Ray Spectroscopy and Related Topics*. 2003, pp. 490–496. DOI: 10.1142/9789812795151_0063.

[230] XIA. *Pixie-16 Data Sheet*. XIA LLC, 31057 Genstar Rd. Hayward CA 94544 USA. URL: https://www.xia.com/wp-content/uploads/2018/05/Pixie-16_flyer_190327.pdf.

[231] P. C. Zalm et al. "Velocity and atomic number dependence of the transient magnetic field in iron". In: *Hyp. Int.* 5 (1977), pp. 347–360. DOI: 10.1007/BF01021706.

[232] J. F. Ziegler. *James Ziegler – SRIM & TRIM*. 2013. URL: http://www.srim.org/.

[233] A. Zucker, E. C. Halbert, and F. T. Howard. *Proc. Conf. Reactions between Complex Nuclei*. Vol. 2. John Wiley and Sons, Inc., New York, 1990.